MAYNOOTH UNIVERSITY

DOCTORAL THESIS

---

# Outflows from young stars: Investigating angular momentum removal with Integral Field Spectroscopy

---

*Author:*
Matthew Birney

*Supervisor:*
Dr. Emma Whelan

*Head of Department:*
Dr. Neil Trappe

*A thesis submitted in fulfilment of the requirements for the degree of Doctor of Philosophy in the*

Star and Planet Formation group
Department of Physics
Faculty of Science and Engineering

*This thesis has been prepared in accordance with the PhD regulations of Maynooth University and is subject to copyright. For more information see PhD Regulations (December 2022).*

February 2025

# Declaration of Authorship

I, Matthew Birney, declare that this thesis titled, "Outflows from young stars: Investigating angular momentum removal with Integral Field Spectroscopy" and the work presented in it are my own. I confirm that:

- This work was done wholly or mainly while in candidature for a research degree at this University.
- Where any part of this thesis has previously been submitted for a degree or any other qualification at this University or any other institution, this has been clearly stated.
- Where I have consulted the published work of others, this is always clearly attributed.
- Where I have quoted from the work of others, the source is always given. With the exception of such quotations, this thesis is entirely my own work.
- I have acknowledged all main sources of help.
- Where the thesis is based on work done by myself jointly with others, I have made clear exactly what was done by others and what I have contributed myself.

Signed: 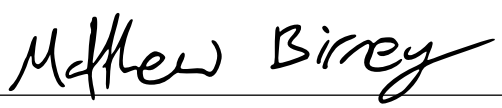

Date: 01/09/2025

*"What is the point of worrying oneself too much about what one could or could not have done to control the course one's life took? Surely it is enough that the likes of you and I at least try to make our small contribution count for something true and worthy. And if some of us are prepared to sacrifice much in life in order to pursue such aspirations, surely that in itself, whatever the outcome, cause for pride and contentment."*

*"The Remains of the Day"* – Kazuo Ishiguro

# *Abstract*

**Outflows from young stars:**
**Investigating angular momentum removal**
**with Integral Field Spectroscopy**

by Matthew Birney

Outflows from young stars play a fundamental role in the process of star formation, acting as a dominant mechanism for angular momentum extraction from the star-disc system, regulating accretion onto the star. These powerful ejections, composed of high-velocity, collimated jets and slower-moving, wide-angled winds, are intrinsically linked to accretion and are launched perpendicularly to the disc surrounding the star. However, the exact mechanism for how these outflows are driven, the impact that they have on mass and angular momentum extraction, and subsequently, the impact they have on disc evolution and planet formation, is not well-constrained. This thesis presents an observational study of protostellar outflows from low-mass stars, primarily with the use of Integral Field Spectroscopy (IFS) with VLT (the Very Large Telescope) instruments, such as SINFONI, MUSE, and ERIS, allowing the spatial and kinematical analysis of these outflows in various emission tracers.

A morphological and kinematical study of the HH 46/47 outflow in the near-infrared (NIR) using SINFONI reveals a stratified outflow structure in kinematics, chemistry, and temperature, and the presence of a velocity gradient transverse to the flow direction, providing insights into the launching mechanism. The investigation of the RU Lupi outflow in optical forbidden emission lines with MUSE presents the first images of the jet and low-velocity component of the outflow, allowing their kinematics, extents, and widths to be determined, and additionally the outflow efficiency to be explored, providing constraints on the launching mechanism. A multi-epoch proper motion analysis of the HH 46/47 outflow, using observations spanning nearly three decades, is presented, enabling a detailed characterisation of the temporal evolution of the outflow. The results presented in this thesis showcase the powerful use of IFS in the study of outflows, and offer new constraints on the outflow driving mechanisms and their role in angular momentum removal, contributing to our understanding of star formation.

# Publications

Birney, M., C. Dougados, E. T. Whelan, B. Nisini, S. Cabrit, and Y. Zhang (2024a). "A kinematical study of the launching region of the blueshifted HH 46/47 outflow with SINFONI K-band observations". In: *Astronomy and Astrophysics* Vol. 692, A143. DOI: 10.1051/0004-6361/202451433. arXiv: 2407.07233 [astro-ph.SR]

Birney, M., E. T. Whelan, C. Dougados, I. Pascucci, A. Murphy, L. Flores-Rivera, M. Flock, and A. Kirwan (2024b). "Forbidden emission line spectro-imaging of the RU Lupi jet and low-velocity component". In: *Astronomy and Astrophysics* Vol. 692, L5. DOI: 10.1051/0004-6361/202452402. arXiv: 2409.19112 [astro-ph.SR]

# *Acknowledgements*

Firstly, I would like to extend my sincerest gratitude to my supervisor, Dr. Emma Whelan, for her support at every stage and in every aspect of my PhD journey. Thank you for giving me this amazing opportunity, and your help with everything. I am grateful for you sharing your expansive expertise and knowledge with me, helping write project proposals and papers, and for gently steering me to explore new avenues of research. Thank you for encouraging me to present my work at conferences and meetings at every opportunity, allowing my confidence and determination to grow. I greatly appreciate you introducing me to friends and collaborators all over the world. Without your help, this project would have been a much more difficult undertaking.

I would like to acknowledge the huge support and contributions from my collaborators. I would like to express my gratitude to Dr. Catherine Dougados, who shared her extensive knowledge of the field and technical expertise with me, and for inviting me to work with her at IPAG, Grenoble numerous times. Thank you to Dr. Fernando Comerón for inviting me to work with him at ESO's headquarters in Garching, and for sharing with me his legacy expertise in the field. Thank you to the collaborators on my papers for their invaluable discussions and insightful comments throughout the process; Emma Whelan, Catherine Dougados, Sylvie Cabrit, Brunella Nisini, Ilaria Pascucci, Lizxandra Flores-Rivera, Mario Flock, Yichen Zhang, and of course my former office mates, Aisling Murphy and Andrew Kirwan. Thank you also to Carlo Manara, Jochen Eislöffel, Andrea Banzatti, Patrick Kavanagh, Tom Ray, Antonella Natta, and Donna Rodgers-Lee for their helpful discussions.

Thank you to everyone in the Physics department, where I have spent the past eight years. I would not be in this position without their expert teaching and guidance throughout the years. Thank you for the coffee room chats and great Christmas parties. Thank you to my fellow postgrads and postdocs in the department, both past and present; Donnacha, Aisling, Andrew, Julianne, David, Joe B., Daithí, James, Phillip, John, Stephen, Aonghus, Noah, Darren, Jack, Aoibhinn, Hannah, Dale, Cathal, Seán, Aoife, Sabrina, Aparna, Saoirse W., Joe McC., Kay, Lewis, Mohsen, Jeroen, Pawel, Gary, Saoirse D., Daxal, Pelle, Eddie, Samuel, Pan, Emilija, Milosz. Thank you for making it more than worthwhile to come into the office every day, and for unscheduled pints.

Thank you to everyone at the DIAS Fitzwilliam office for welcoming me in, and for the helpful discussions provided at the star formation meetings. Thank you to the DUSTBIN collective for the insightful meetings, presentations, and drinks every month, I made some great friends. Thank you to the friends I made at IPAG, at ESO (Beer Fridays!), at summer schools, and at conferences. Thank you to the friends outside of physics, who continue to positively impact my life in many ways. Thank you to the two doors down crew, both past and present. I couldn't have asked for a better gang to spend the last four years with.

Thank you to my parents, Colin and Brigid, who allowed me to follow my own path in life and supported me wholly every step of the way. I wouldn't be where I am today without you. Thank you to my brothers, John and David, and my sisters, Emma and Michelle, who regularly have to put up with me telling them about how cool physics is, most of the time against their will. Thank you for the endless fun. I hope that you also follow your own paths. Thank you to my extended family - grandparents, aunts, uncles, cousins, in-laws, and those who may become family in the future - for their support of my endeavours.

Finally, I wish to express my deepest gratitude to Eibhlin for your unwavering support, patience, and encouragement in every way and at every moment throughout this journey. This would not have been possible without you.

*This work was sponsored by the John & Pat Hume Doctoral Scholarship and the National University of Ireland (NUI) Travelling Doctoral Studentship.*

# Contents

**Declaration of Authorship** i

**Abstract** iii

**Publications** iv

**Acknowledgements** v

**1 Introduction** 1

1.1 Low-mass star formation . . . 3

1.1.1 The collapse of molecular clouds . . . 3

1.1.2 Protostellar evolution . . . 8

Class 0 objects . . . 9

Class I objects . . . 10

Class II objects . . . 12

Class III objects . . . 12

1.2 Accretion processes . . . 14

1.2.1 The transport of angular momentum . . . 16

1.2.2 The accretion mechanism . . . 17

1.3 Ejection processes . . . 20

1.3.1 Outflow launching . . . 22

The X-wind model . . . 24

The disc wind model . . . 25

Stellar winds . . . 27

1.3.2 Outflow shocks and observational tracers . . . 28

Shocks in outflows . . . 28

Outflow emission . . . 30

1.3.3 Outflow evolution . . . 35

Embedded class 0 outflows . . . 36

Class I outflows . . . 37

Evolved class II outflows . . . 38
1.3.4 Discerning the launching mechanism . . . 39
1.3.5 Disc dispersal and implications for planet formation . . . 45
1.4 Summary of contributions to field . . . 46
Methods and analysis techniques . . . 46
HH 46/47 . . . 47
RU Lupi . . . 48

**2 Telescopes and instrumentation** **49**
2.1 ESO's VLT . . . 49
2.2 Integral Field Spectroscopy (IFS) . . . 51
2.3 Instrumentation . . . 54
2.3.1 SINFONI . . . 54
2.3.2 MUSE . . . 56
2.3.3 ERIS . . . 59
2.3.4 Other instruments . . . 60
EMMI . . . 60
EFOSC2 . . . 60
FORS2 . . . 61
ISAAC . . . 61
HAWK-I . . . 61

**3 Reduction and analysis of integral field observations** **62**
3.1 Tools for data cube analysis . . . 62
3.1.1 Gaussian fitting . . . 63
3.2 SINFONI observations . . . 64
3.3 SINFONI data reduction and analysis . . . 65
3.3.1 Data reduction pipeline . . . 65
3.3.2 Wavelength recalibration . . . 66
3.3.3 Uneven slit effect correction . . . 74
3.3.4 Flux calibration . . . 76
3.3.5 Telluric correction . . . 83
3.3.6 Spatial resampling . . . 88
3.3.7 Continuum subtraction and scattered emission removal 88
3.4 MUSE observations . . . 97
3.4.1 0104.C-0919(B) observations . . . 97
3.4.2 106.21EN.001 observations . . . 99

3.5 MUSE data reduction and analysis . . . 99
3.5.1 Data cube coadding . . . 100
3.5.2 Continuum subtraction . . . 100
3.6 ERIS observations . . . 102
3.7 ERIS data reduction and analysis . . . 104
3.7.1 Continuum subtraction . . . 104
3.7.2 Principal component analysis . . . 105

**4 A kinematical study of the HH 46/47 outflow with SINFONI 108**
4.1 Introduction . . . 108
4.1.1 HH 46/47 . . . 111
4.2 Results . . . 114
4.2.1 Morphology . . . 119
4.2.2 Kinematics . . . 127
4.2.3 $H_2$ velocity centroid maps . . . 136
Preliminary ERIS results . . . 142
4.3 Discussion . . . 143
4.3.1 Layering of emission and axial asymmetries . . . 144
4.3.2 Origin of the $H_2$ transverse velocity gradient . . . 151
4.4 Summary and conclusions . . . 156

**5 Spectro-imaging of the RU Lupi jet and low-velocity component 160**
5.1 Introduction . . . 160
5.1.1 RU Lupi . . . 163
5.2 Results . . . 163
5.2.1 Morphology of the outflow components . . . 164
5.2.2 Structure of the outflow components . . . 187
5.2.3 Outflow efficiency . . . 200
5.3 Discussion . . . 210
5.3.1 Interpretation of the outflow structure . . . 210
5.3.2 Implications of the outflow efficiency . . . 215
5.4 Summary and conclusions . . . 219

**6 The proper motions of the HH 46/47 outflow 222**
6.1 Introduction . . . 222
6.2 Observations and data reduction . . . 227
6.2.1 EMMI 1991 observations . . . 227
6.2.2 EMMI 1995 observations . . . 228

6.2.3 EFOSC2 2002 observations . . . 228
6.2.4 EMMI 2006 observations . . . 229
6.2.5 FORS2 2018 observations . . . 229
6.2.6 ISAAC 2001 observations . . . 230
6.2.7 HAWK-I 2019 observations . . . 230
6.3 Astrometric alignment . . . 231
6.4 Results . . . 233
6.4.1 The proper motions in [S II] emission . . . 234
1991 – 1995 epoch . . . 235
1995 – 2002 epoch . . . 240
2002 – 2006 epoch . . . 245
2006 – 2018 epoch . . . 249
6.4.2 The proper motions in $H_2$ emission . . . 254
6.5 Discussion . . . 261
6.6 Summary and conclusions . . . 271

**7 Conclusions and future work** **274**
7.1 Summary of findings . . . 277
7.1.1 The kinematical study of the HH 46/47 outflow with SINFONI . . . 277
7.1.2 The spectro-imaging study of the RU Lupi outflow . . . 278
7.1.3 The proper motions study of the HH 46/47 outflow . . . 280
7.2 Future work . . . 281

**Bibliography** **285**

# List of Figures


1.1 Taurus molecular cloud B211/B213 filament . . . . . 4
1.2 Typical SED profiles of different YSO classes . . . . . 10
1.3 Evolutionary stages of YSO formation . . . . . 11
1.4 HL Tau disc as observed with ALMA . . . . . 15
1.5 Magnetospheric accretion mechanism illustration . . . . . 18
1.6 HH 211 outflow as observed with JWST NIRCam . . . . . 20
1.7 The X-wind model . . . . . 25
1.8 The disc wind model . . . . . 26
1.9 Kinematical decomposition of emission lines . . . . . 34

2.1 The VLT observatory . . . . . 50
2.2 The instruments installed on the VLT . . . . . 50
2.3 Illustration of a 3D data cube . . . . . 52
2.4 The SINFONI instrument . . . . . 54
2.5 Illustration of the image slicing technique used in IFS . . . . . 56
2.6 The MUSE instrument . . . . . 57
2.7 Illustration of the MUSE image slicing technique . . . . . 58
2.8 The ERIS instrument . . . . . 59

3.1 Wavelength offset maps produced using Gaussian fitting . . . . 68
3.2 Wavelength offset histograms . . . . . 69
3.3 Theoretical emission spectrum from Earth's upper atmosphere . 69
3.4 Example spectrum containing OH emission lines . . . . . 70
3.5 2D wavelength offset map using cross correlation . . . . . 71
3.6 Linear fits to horizontal rows of 2D wavelength offset map . . . 72
3.7 Wavelength calibration map . . . . . 73
3.8 Uneven slit effect correction map . . . . . 76
3.9 Effect of applying uneven slit effect correction to $H_2$ emission . 77
3.10 log(flux) vs. log(wavelength) for HD 67954 . . . . . 80
3.11 log(flux) vs. log(wavelength) for HD 73105 . . . . . 81

3.12 Integrated HD 67954 stellar spectrum with polynomial fit applied 82
3.13 Flux calibrated integrated HD 67954 stellar spectrum . . . . . 82
3.14 Flux calibrated integrated HD 73105 stellar spectrum . . . . . 83
3.15 Flux correction function . . . . . 84
3.16 Telluric standard star spectrum with smooth spline fit . . . . . 85
3.17 Normalised telluric standard star spectrum . . . . . 85
3.18 Science spectrum with telluric spectrum overplotted . . . . . 86
3.19 Spectrum before and after telluric correction . . . . . 87
3.20 HH 46/47 continuum emission . . . . . 89
3.21 Scattered emission removal routine applied to the $H_2$ emission . 91
3.22 Line to continuum ratio plots ($H_2$ and [Fe II]) . . . . . 93
3.23 Effect of scattered emission removal on $H_2$ emission . . . . . 94
3.24 Line to continuum ratio plots (Br-$\gamma$) . . . . . 96
3.25 Baseline continuum subtraction for jet-tracing emission lines . . 98
3.26 Continuum subtraction oversubtraction example . . . . . 102
3.27 Baseline continuum subtraction for outflow tracing lines . . . . 103
3.28 Visual artefacts in ERIS images . . . . . 106

4.1 NIRCam image of HH 46/47 outflow . . . . . 112
4.2 HH 46/47 spectral extraction locations . . . . . 115
4.3 HH 46/47 spectrum extracted from source position . . . . . 116
4.4 HH 46/47 spectrum extracted from jet knot . . . . . 117
4.5 HH 46/47 spectra extracted from bright $H_2$ features . . . . . 118
4.6 Morphology of continuum emission . . . . . 120
4.7 Morphology of HH 46/47 in $H_2$ 1-0 S(1) emission . . . . . 122
4.8 Morphologies of HH 46/47 outflow in $H_2$ emission . . . . . 124
4.9 Morphology of outflow in [Fe II] and Br-$\gamma$ emission . . . . . 125
4.10 Morphologies of HH 46/47 outflow in [Fe II] emission . . . . . 126
4.11 Morphologies of HH 46/47 in CO emission . . . . . 128
4.12 HH 46/47 $H_2$ 1-0 S(1) emission channel map . . . . . 130
4.13 HH 46/47 [Fe II] emission channel map . . . . . 131
4.14 HH 46/47 Br-$\gamma$ emission channel map . . . . . 133
4.15 PV diagram in [Fe II] emission . . . . . 134
4.16 PV diagram in Br-$\gamma$ emission . . . . . 135
4.17 Transverse PV diagram in $H_2$ emission . . . . . 137
4.18 Radial velocity centroid maps in $H_2$ emission . . . . . 138
4.19 radial velocity centroid map in [Fe II] emission . . . . . 141

4.20 ERIS radial velocity centroid map in $H_2$ emission . . . . . 142
4.21 SINFONI three-colour image displaying the outflow cavity and jet compared to HST observations of the jet . . . . . 145
4.22 SINFONI $H_2$ cavity compared to the $^{12}CO$ molecular outflow as observed by ALMA . . . . . 146

5.1 RU Lupi spectrum extracted from source . . . . . 165
5.2 RU Lupi jet integrated intensity map in [O I] emission . . . . . 167
5.3 RU Lupi jet integrated intensity map in [S II] emission . . . . . 168
5.4 RU Lupi jet integrated intensity map in [N II] and [Fe II] emission 169
5.5 Jet in [S II] emission displaying measured position angle . . . . . 171
5.6 Line profiles of [O I] 6300 Å and [S II] 6731 Å emission . . . . . 172
5.7 Channel maps of [O I] 6300 Å and [S II] 6731 Å emission . . . . . 174
5.8 Channel maps of [N II] 6583 Å and [S II] 6731 Å emission . . . . 175
5.9 Line to continuum ratio maps in [O I] and [S II] emission . . . . . 176
5.10 Line to continuum ratio maps in [N II] and [S II] emission . . . . 178
5.11 PSFs used in deconvolution . . . . . 179
5.12 Channel maps of [O I] emission after deconvolution . . . . . 180
5.13 Channel maps of [S II] emission after deconvolution . . . . . 181
5.14 Channel maps of [N II] and [S II] emission after deconvolution . 182
5.15 Channel maps of [O I] emission after deconvolution (alternate observation) . . . . . 184
5.16 Channel maps of [S II] emission after deconvolution (alternate observation) . . . . . 185
5.17 Channel maps of [O I] emission after deconvolution (alternate observation) . . . . . 186
5.18 PV diagrams of [O I] and [S II] emission . . . . . 189
5.19 PV diagrams of [N II] and [Fe II] emission . . . . . 190
5.20 Transverse PV diagrams of [O I] and [S II] emission . . . . . 192
5.21 Line profiles extracted from transverse PV diagrams in [O I] and [S II] emission . . . . . 193
5.22 Transverse PV diagrams of [N II] and [Fe II] emission . . . . . 195
5.23 Line profiles extracted from transverse PV diagrams in [N II] and [Fe II] emission . . . . . 196
5.24 FWHM measurements along the outflow axis . . . . . 199
5.25 Normalised flux measurements along the outflow axis . . . . . 201
5.26 Outflow centroid measurements along the outflow axis . . . . . 202

5.27 Measured line flux and mass accretion rates as a function of spectral extraction aperture size . . . . . 205

6.1 Labelled FORS2 H$\alpha$ image of the HH 46/47 outflow . . . . . 224
6.2 Proper motions data observation timeline . . . . . 228
6.3 Example affine transformation solution using ASTROALIGN . 232
6.4 Example of shock feature centroid retrieval . . . . . 234
6.5 EMMI 1995 and EMMI 1991 observations difference image . . . 237
6.6 EMMI 1991 – EMMI 1995 shock features identification . . . . . 238
6.7 EFOSC2 2002 and EMMI 1995 observations difference image . . 242
6.8 EMMI 1995 – EFOSC2 2002 shock features identification . . . . 243
6.9 EMMI 2006 and EFOSC2 2002 observations difference image . . 246
6.10 EFOSC2 2002 – EMMI 2006 shock features identification . . . . 247
6.11 FORS2 2018 and EMMI 2006 observations difference image . . . 251
6.12 EMMI 2006 – FORS2 2018 shock features identification . . . . . 252
6.13 HAWK-I 2019 and ISAAC 2001 observations difference image . 257
6.14 ISAAC 2001 - HAWK-I 2019 shock features identification . . . . 258
6.15 Position velocity diagrams of proper motions measurements . . 262

# List of Tables


3.1 Zero-magnitude fluxes of stars in the J, H, & K passbands . . . . 78
3.2 Standard star's magnitudes and flux densities in the J, H, & K bands . . . . . 79

4.1 Typical gas properties for emission tracers in SINFONI data . . 110
4.2 Identified emission lines in the SINFONI observations of HH 46/47 . . . . . 119
4.3 Velocity difference between the left and right side of the $H_2$ cavity at various heights along the outflow . . . . . 139
4.4 Specific angular momenta calculations of the $H_2$ cavity rotation at various heights ($z$) along the outflow. . . . . 153

5.1 Identified emission lines in the MUSE observations of RU Lupi 166
5.2 Typical gas properties for emission tracers in MUSE data . . . . 166
5.3 Launch radii and full opening angles of the jet, HVC1, and LVC 198
5.4 $F_{\rm line}$ and $L_{\rm line}$ for selected accretion-tracing emission lines . . . . 205
5.5 $L_{\rm acc}$ – $L_{\rm line}$ linear relationship results . . . . . 206
5.6 Measured accretion luminosities and mass accretion rates . . . . 207

6.1 Summary of previous proper motions in the HH 46/47 outflow 226
6.2 Proper motions study imaging data . . . . . 227
6.3 Proper motions in [S II] emission 1991 – 1995 . . . . . 239
6.4 Proper motions in [S II] emission 1995 – 2002 . . . . . 244
6.5 Proper motions in [S II] emission 2002 – 2006 . . . . . 248
6.6 Proper motions in [S II] emission 2006 – 2018 . . . . . 253
6.7 Proper motions in $H_2$ emission 2001 – 2019 . . . . . 259
6.8 Multi-epoch proper motions in [S II] emission 1991 – 2018 . . . . 265
6.9 Summary of proper motions in the HH 46/47 outflow . . . . . 267

# List of Abbreviations

| | |
|---|---|
| **2MASS** | Two Micron All-Sky Survey |
| **ALMA** | Atacama Large Millimeter/submillimeter Array |
| **AO** | Adaptive Optics |
| **BC** | Broad Component |
| **BERV** | Barycentric Earth Radial Velocity |
| **CCD** | Charge-Coupled Device |
| **CSA** | Canadian Space Agency |
| **CTTS** | Classical T Tauri Star |
| **DSHARP** | Disc Substructures at High Angular Resolution Project |
| **EFOSC2** | ESO Faint Object Spectrograph and Camera v.2 |
| **EMMI** | ESO Multi-Mode Instrument |
| **ERIS** | Enhanced Resolution Imager and Spectrograph |
| **ESA** | European Space Agency |
| **ESO** | European Southern Observatory |
| **FEL** | Forbidden Emission Line |
| **FIR** | Far-infrared |
| **FORS2** | FOcal Reducer/low dispersion Spectrograph 2 |
| **FOV** | Field Of View |
| **FUV** | Far-Ultraviolet |
| **FWHM** | Full-Width at Half-Maximum |
| **GMC** | Giant Molecular Cloud |
| **HAWK-I** | High Acuity Wide field K-band Imager |
| **HH** | Herbig-Haro |
| **HST** | Hubble Space Telescope |
| **HVC** | High-Velocity Component |
| **IFS** | Integral-Field Spectroscopy |
| **IFU** | Integral-Field Unit |
| **IR** | Infrared |
| **IRAF** | Image Reduction and Analysis Facility |

| | |
|---|---|
| **IRS** | Infrared Source |
| **ISAAC** | Infrared Spectrometer And Array Camera |
| **ISM** | Interstellar Medium |
| **JWST** | James Webb Space Telescope |
| **LSR** | Local Standard of Rest |
| **LVC** | Low-Velocity Component |
| **MHD** | Magnetohydrodynamic |
| **MIR** | Mid-infrared |
| **MIRI** | Mid-Infrared Instrument |
| **MRI** | Magnetorotational Instability |
| **MUSE** | Multi Unit Spectroscopic Explorer |
| **NAOJ** | National Astronomical Observatory of Japan |
| **NASA** | National Aeronautics and Space Administration |
| **NC** | Narrow Component |
| **NFM** | Narrow Field Mode |
| **NIR** | Near-infrared |
| **NIRCam** | Near-Infrared Camera |
| **NIRSpec** | Near-Infrared Spectrograph |
| **NOAO** | National Optical Astronomy Observatory |
| **NRAO** | National Radio Astronomy Observatory |
| **PA** | Position Angle |
| **PE** | Photoevaporation |
| **PMS** | Pre-Main Sequence |
| **PSF** | Point Spread Function |
| **PV** | Position-Velocity |
| **SED** | Spectral Energy Distribution |
| **SINFONI** | Spectrograph for INtegral Field Observations in the NIR |
| **SMC** | Small Molecular Cloud |
| **S/N** | Signal-to-Noise ratio |
| **TD** | Transition Disc |
| **UT** | Unit Telescope |
| **UV** | Ultraviolet |
| **VLT** | Very Large Telescope |
| **WFM** | Wide Field Mode |
| **WTTS** | Weak-line T Tauri Star |
| **YSO** | Young Stellar Object |

*For those who encouraged me to reach for the stars*

# Chapter 1

# Introduction

*"What transforms this world is - knowledge. Do you see what I mean? Nothing else can change anything in this world. Knowledge alone is capable of transforming the world, while at the same time leaving it exactly as it is. When you look at the world with knowledge, you realize that things are unchangeable and at the same time are constantly being transformed."*

*"The Temple of the Golden Pavilion"* – Yukio Mishima

We have always looked to the stars. From ancient civilisations who crafted myths, based religious beliefs, charted navigation, and marked the passing of the seasons around the stars, to modern astronomers who gaze at the stars, studying their formation, lives, and deaths. Stars remain central to our quest of understanding the universe. The study of the stars is, at its core, an exploration of our own origins. When we study star formation, we are not merely ascertaining how giant spheres of gas form, ignite, and burn brightly, we are peering into the processes that made life itself possible. How is it that life sparks in the cold and dark regions of space? After the Big Bang, the hydrogen, helium, and small amounts of lithium present in the universe went on to form the first stars, whereby heavier elements, such as the oxygen, carbon, nitrogen, and other elements essential to life, were formed through stellar nucleosynthesis. For thousands of years we thought of stars as timeless and constant, but we now know that they are far from static, they are dynamic bodies that are born in clouds of gas, evolving over millions of years, shaping their surroundings, and ultimately dying in spectacular fashion.

Among the many aspects of star formation, one intriguing and exciting process, which this thesis focusses on, is the generation of bipolar outflows of material from young forming stars. Outflows from young accreting stars are ubiquitous, and are thought to be not only a by-product, but fundamental to star formation. These powerful ejections of gas and dust permit the accretion of matter onto a star, influence the planet formation process, and impact the structure and dynamics of their surrounding molecular cloud. The study of outflows requires detailed observations across multiple wavelengths, to discern their structures and compositions, their kinematics, how they are launched, and how these dynamic objects interact with their environments. Modern advances in observational astronomy has allowed us to learn much about these outflows, using instrumentation such as high-resolution spectroscopy and Integral Field Spectroscopy (IFS), providing vital information for verifying theoretical models of these flows.

This thesis presents analysis of outflows from low-mass stars in the optical and near-infrared (NIR) wavelength regimes, primarily using observations collected with the European Southern Observatory's Very Large Telescope (ESO VLT). The outflows studied in this work are the HH 46/47 outflow, where HH stands for Herbig-Haro object (Herbig, 1951; Haro, 1952), and the outflow emanating from RU Lupi. This thesis aims to characterise the morphology, kinematics and structure of these outflows, thereby shedding light on their driving mechanism and their influence on the star formation process.

The structure of the thesis is as follows:

- *Chapter 1* provides an introduction to star formation and evolution, with particular focus on low-mass stars, comparable to our sun. I will discuss how these stars gather mass through accretion, and how the launching of outflows is intrinsically linked with this process. I will explore the models for outflow launching, how one can observationally study outflows, how these outflows evolve along with the star, and how one can use observational findings to constrain the launching mechanism.
- *Chapter 2* discusses the observational technique of IFS, and the telescopes and instrumentation used in this project.
- *Chapter 3* discusses the data reduction and analysis techniques performed on the integral field data before the presentation of the results.

- *Chapter 4* presents the kinematical and morphological study of the launching region of the blueshifted HH 46/47 outflow with SINFONI K-band observations.
- *Chapter 5* presents the study of the outflow emanating from RU Lupi in optical forbidden emission lines with MUSE observations, with particular focus on the jet and low-velocity component.
- *Chapter 6* presents the proper motions study of the HH 46/47 outflow, with imaging observations from 1991 to 2018 in [S II] emission, and from 2001 to 2019 in $H_2$ emission.
- *Chapter 7* discusses the overall conclusions of this thesis, with summaries of the findings from the individual studies, and highlights future work to be undertaken to further probe the conclusions drawn from the project.

## 1.1 Low-mass star formation

### 1.1.1 The collapse of molecular clouds

Stars form within relatively dense, cold clouds of molecular gas, referred to as molecular clouds (e.g. Lada, 1976). These can be divided into two types, small molecular clouds (SMCs) and giant molecular clouds (GMCs). Molecular clouds are observationally defined as gravitationally bound over-densities in the interstellar medium (ISM), and much of our understanding of star formation arises from observations of nearby star-forming regions in the ISM. However, one can now perform less biased star formation studies by observing star forming regions outside of our own galaxy, such as extragalactic H II regions, the Magellanic Clouds, and the full discs of nearby galaxies (e.g. Wilson and Scoville, 1990; Fukui et al., 2001; Fukui and Kawamura, 2010). Molecular hydrogen ($H_2$) comprises most of the gas in these molecular clouds, as atomic hydrogen tends to form the more stable $H_2$ molecule in low-temperature, relatively dense regions (Tacconi, Genzel, and Sternberg, 2020), but emission from $H_2$ in molecular clouds is difficult to observe. Instead, SMCs and GMCs are generally observed in low-density tracers such as carbon monoxide (CO) emission, due to its high abundance (the second-most abundant molecule) and capability of emitting at low temperatures. Typical sizes of molecular clouds range from 10 pc to 100 pc, and have total masses of $\sim 10^2\ M_\odot$, in the case of

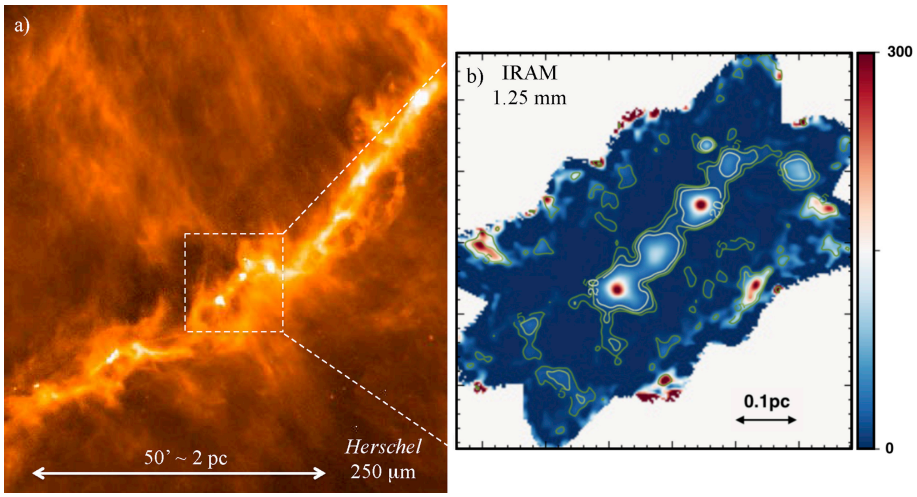


FIGURE 1.1: Panel a: Taurus B211/B213 filament in the Taurus molecular cloud (Palmeirim et al., 2013; Marsh et al., 2016) from Herschel/SPIRE in 250 μm dust continuum emission. There are several dense regions seen along the filamentary structure. Panel b: IRAM/NIKA 1.25 mm dust continuum emission image (Bracco et al., 2017) of the central part of the Herschel image in panel 'a'. There are at least three prominent dense cores seen in this emission along the filament.

SMCs, and $10^4 - 10^6$ $M_\odot$, in the case of GMCs (Ray, 2007; Hartmann, 2009). The molecular gas in these regions generally has temperatures of 10 – 100 K, and mean densities of $n_{H_2} = 100$ cm$^{-3}$ (e.g. Scoville et al., 1987; Dame, Hartmann, and Thaddeus, 2001).

GMCs form rapidly ($t \sim 10^6$ yrs), evolve, and disperse quickly ($t \sim 10^7$ yrs) in comparison to their host galaxies. They are thought to arise from a combination of processes that lead to compression, cooling, and fragmentation of the larger-scale and more diffuse ISM. Dobbs et al. (2014) propose many formation mechanisms for GMCs, such as gravitational-induced compression of unstable regions, converging filamentary gas flows in the ISM, spiral-arm induced collisions, and supernovae shock wave-induced compression. As the gas in GMCs is mostly hydrogen in its molecular form, there is a conversion of the mainly atomic hydrogen in the ISM material into $H_2$. This conversion requires shielding from the ambient background stellar far-ultraviolet (FUV) radiation which photodissociates $H_2$. This shielding can take the form of dust attenuation of the FUV light, and molecular self-shielding, where $H_2$ located at the cloud surface absorbs FUV photons, reducing the intensity of the available radiation to dissociate $H_2$ deeper in the cloud (Sternberg et al., 2014).

GMCs are highly structured, displaying networks of filamentary structures comprising of gas and dust (Bally et al., 1987; André et al., 2014; Pineda et al., 2023). This internal structure is produced by many factors including gravity, turbulence and propagating shocks, magnetic fields, heating and cooling, and chemistry. Many of these effects derive from stellar feedback (Chevance et al., 2023). Within these filaments there are relatively dense clumps ($n_{\mathrm{H_2}} > 10^4$ cm$^{-3}$), or molecular cores, that determine where stars form within the cloud (Inutsuka, 2012; André et al., 2010; Hacar et al., 2023). Figure 1.1 displays a the B211/B213 filament in the well-studied Taurus molecular cloud (André, 2017). There are several dense cores, typically referred to as prestellar cores, seen along the filament. The kinetic energy associated with GMCs is often assumed as being comparable to gravitational potential energy, and that they are in virial equilibrium (Larson, 1981), meaning the internal forces within the gravitationally bound system are balanced such that the system neither collapses under its own gravity nor expands indefinitely. The kinetic energy in these clouds of molecular material comes from the random motions of the gas particles such as an internal gas pressure from thermal energy. These clouds often exhibit turbulent motions, and in addition, large-scale shear and rotational motion.

In order for stars to form in these GMCs, it is necessary that the self-gravity of the cloud overcomes the resisting forces of thermal gas pressure and kinetic turbulent motions. It is known that the star formation efficiency of GMCs, in terms of the total fraction of the parent clouds mass converted into stars over the clouds lifetime, is low (Chevance et al., 2023), with efficiency estimations of $\sim 1\%$. There are many hypothesis as to what triggers gravitational collapse, such as galactic interactions, and stellar winds compressing the cloud, however, the fragmentation of GMCs into self-gravitating cloudlets is still not well understood (Hartmann, 2009). There are two proposed scenarios for the collapse of GMCs. Firstly, due to turbulent motion in the cloud, and in the filaments within the cloud, only a small fraction of the cloud fragments into localised densities, which further collapse to form stars (e.g. Dobbs, Burkert, and Pringle, 2011). Secondly, there is a global, hierarchical collapse of the cloud (e.g. Vázquez-Semadeni et al., 2019), where self gravity causes the entire GMC to undergo gravitational contraction, driving motions within the cloud, forming filamentary structures, which further collapse. As the internal structure of GMCs is filamentary and clumpy, the small scale structures can collapse

and form stars even though the large scale structure is not necessarily gravitationally bound (e.g. Henshaw et al., 2014). The isolated local collapse scenario explains the low star formation efficiency of GMCs by the fact that only a small fraction of the gas actually goes on to form stars (e.g. Dobbs, Burkert, and Pringle, 2011). In the global hierarchical scenario, only stellar feedback mechanisms restrict the star formation efficiency from rising. At present, there is observational support for both scenarios.

Once a prestellar core is formed, which are pre-cursors to protostars and generally found in chains along the filaments of the GMCs, it evolves rapidly, on typical timescales of $< 10^6$ years, towards a centrally condensed configuration. This occurs once the core exceeds the Jeans length, or Jeans mass, where the internal gas pressure of the pre-stellar core can no longer support it against the gravitational pressure (Jeans, 1902). Once this criterion is met, and assuming the prestellar core is mostly spherical, non-rotating, and pressure-less, the core collapses rapidly in a runaway fashion. This happens on the order of a free-fall collapse, where there are no forces opposing the gravitational collapse, the timescale of which is shown in Equation 1.1 (Hartmann, 2009). Here, $t_{\rm ff}$ is the time for the cloud core to collapse completely, $G$ is the gravitational constant, and $\rho_0$ is the initial density of the core. As this self-gravitational collapse begins in the cores, the inner region collapses faster than the surrounding envelope of the core, therefore the resultant newborn protostar is heavily embedded in their dense molecular envelopes.

$$t_{\rm ff} = \sqrt{\frac{3\pi}{32 G \rho_0}} \tag{1.1}$$

There is a so-called first core (Larson, 1969) during the collapse, which is in temporary hydrostatic equilibrium, where the outward thermal pressure halts the gravitational collapse of the inner region. Hydrostatic equilibrium is defined in Equation 1.2, where $P(r)$, $M(r)$, and $\rho(r)$ are the pressure, mass, and density contained within radius $r$. The radius of the first core is of au scales (Inutsuka, 2012). The central density of this first core increases, as mass is accreted from the surrounding envelope, and because the gas is now optically thick, making radiative cooling inefficient, the core increases in temperature, until the $H_2$ begins to dissociate into atomic hydrogen at temperatures of approximately 1800 K. A second collapse then begins, as thermal energy is

extracted from the system in this reaction, and gravitational forces dominate again, leading to the birth of a stellar core once a new hydrostatic equilibrium is established (Saigo, Tomisaka, and Matsumoto, 2008). Once interior temperatures of the stellar core reach approximately $10^5$ – $10^6$ K, deuterium fusion begins and a protostar is born.

$$\frac{\mathrm{d}P(r)}{\mathrm{d}r} = \frac{GM(r)\rho(r)}{r^2} \tag{1.2}$$

In going from the large size of the parent molecular cloud to a typical size of a stellar system, there is a dramatic and fast reduction in size. Any small rotational movement in the parent molecular cloud is amplified by an enormous amount by the conservation of angular momentum during the gravitational collapse (Tscharnuter, 1987; Hartmann, 2009). Molecular clouds in the disc of our Galaxy have intrinsic angular momentum that is partly due to galactic rotation (Inutsuka, 2012). This conservation of angular momentum leads to the production of a rapidly rotating disc surrounding the smaller stellar core. Most of the mass of the final star is thought to be accreted from this rotationally supported disc, where infalling material from the core falls onto the disc rather than the central, pressure-supported protostar (Shu, Adams, and Lizano, 1987).

Molecular clouds are observed to be threaded by magnetic field lines (Zhang et al., 2014; Arzoumanian et al., 2021; Pattle et al., 2023), where the orientation of the field can be inferred with linear polarisation measurements due to aligned dust grains in the clouds, and the field strengths can be derived from Zeeman splitting (Ray, 2007). Charged particles preferentially travel along magnetic fields due to their motion and the Lorentz force, shown in Equation 1.3, where $\rho\vec{E}$ is the electric force density, $\vec{J}$ is the current density, and $\vec{B}$ is the magnetic field. As there exists ionisation in the molecular cloud, there is a coupling between the gas motion and the magnetic field. Furthermore, there exists a coupling between ions and neutrals, through collisions, ensuring that even the neutral gas is subject to the same Lorentz force as the ions. As the gas collapses, the magnetic field lines are dragged towards the centre of mass, which produces a characteristic hour-glass shape (Mestel, 1966; Redaelli et al., 2019). This magnetic pinching also leads to the formation of a flattened structure surrounding the protostar (Galli and Shu, 1993). These magnetic field

lines exert a torque opposing the rotation of the disc, providing a form of angular momentum transport to slow down the rotation of the disc, referred to as magnetic braking. In tandem to the formation of this rotating disc, the pinched magnetic field lines at the centre of the collapse become wound-up just after the formation of a protostar. This is followed by the driving of a bipolar outflow, perpendicular to the disc, whose production is closely related to accretion. Many mechanisms for the magnetic launching of outflows have been proposed, such as the disc wind model (Blandford and Payne, 1982; Pudritz and Norman, 1983; Konigl and Pudritz, 2000) and the 'X-wind' model (Shu et al., 1994; Shu et al., 2000), and these are discussed in Section 1.3. Collimation of the outflow is achieved due to the hoop stress of piled-up toroidal field lines (Pudritz and Ray, 2019). In addition to magnetic braking, the outflowing gas also removes angular momentum from the system (Kuffmeier, 2024).

$$\vec{F}_{\text{Lorentz}} = \rho\vec{E} + \vec{J} \times \vec{B} \tag{1.3}$$

### 1.1.2 Protostellar evolution

In the low mass regime (M $< 2\ M_{\odot}$), the protostar stage and following pre-main sequence stage of a young stellar object's (YSOs: Strom, 1972) life is historically divided into four evolutionary stages. These stages are based on the infrared (IR) excess of the star's spectral energy distribution (SED) in the wavelength interval of 2.2 – 20 μm (Lada, 1987). As the star evolves, the surrounding envelope dissipates, followed by the disc. As these are cooler than the central YSO, they emit reprocessed photons[1] at longer wavelengths, producing this IR excess. The four stages of YSO evolution can be observationally classified as intervals of the spectral index, $\alpha$, shown in equation 1.4. Here, $F_{\lambda}$ is the flux density at some wavelength. Class I objects have $\alpha > 0.3$, class II objects have $-0.3 > \alpha > -1.6$, and class III sources have $\alpha < -1.6$ (Dunham et al., 2014). Greene et al. (1994) added a fourth class, the so-called Flat-SED sources, with $0.3 > \alpha > -0.3$. Class 0 objects were later added to account for protostars too deeply embedded to be detected at wavelengths $< 20$ μm. These objects are inferred through other means such as outflow presence (André, Ward-Thompson, and Barsony, 1993). Class 0/I objects are referred to as

[1]Reprocessed light refers to radiation emitted by the YSO, generally optical or UV photons, that is absorbed by the disc material, heating it to some degree, and subsequently re-emitting the radiation at longer wavelengths.

protostars, and class II/III objects are referred to as pre-main sequence stars or T Tauri stars. Figure 1.2 presents the characteristic SED profiles for class 0, I, II, and III objects. Figure 1.3 presents an illustration of the evolutionary stages of low-mass star formation. YSOs are more luminous than their subsequent main sequence phase due to their larger radii and accretion activity.

$$\alpha = \frac{\mathrm{dlog}(\lambda F_\lambda)}{\mathrm{dlog}\lambda} \tag{1.4}$$

Intermediate mass stars ($M = 2\ M_\odot - 8\ M_\odot$) follow a similar evolutionary track, and observational classifications of the evolutionary stages have also been defined (Hillenbrand et al., 1992; Waters and Waelkens, 1998). There exists class 0/I analogues in the intermediate mass regime, and class II/III analogues, referred to as Herbig Ae/Be stars (Herbig, 1960), which are hotter and more luminous than their low-mass counterparts, and host weaker magnetic fields. More massive stars ($\gtrsim 8\ M_\odot$) evolve very quickly, sometimes reaching the main sequence whilst still embedded in their parent envelopes, producing ultra-compact H II regions, where the hydrogen-fusing central star ionises the surrounding gas (Wood and Churchwell, 1989; Hoare et al., 2007).

#### Class 0 objects

Class 0 YSOs are low-mass protostars in the earliest stages of formation. They are objects heavily embedded within their roughly spherical, opaque parent envelope of gas and dust, and so are not detected at NIR or mid-infrared (MIR) wavelengths (Hartmann, 2009). Their presence can however be inferred through other means, such as bipolar outflows, and they can be detected in cool, sub-mm wavelengths as a peak in continuum emission within the cloud indicating the presence of a compact object. Their observed SEDs, shown in Figure 1.2, are dominated by thermal, approximately blackbody, emission from the surrounding dust, at bolometric temperatures of at most, a few 10's of Kelvin. This stage is short-lived and typically persists for $<$ 100,000 years (Tsukamoto et al., 2023), and these early stages of formation are accompanied by high mass accretion rates ($\dot{M}_{\mathrm{acc}}$), where the embedded core and surrounding disc is accreting from the much larger and more massive infalling envelope. As a consequence of this high accretion activity, class 0 objects are accompanied by powerful outflows, which are mostly molecular (e.g. Podio et al., 2016;

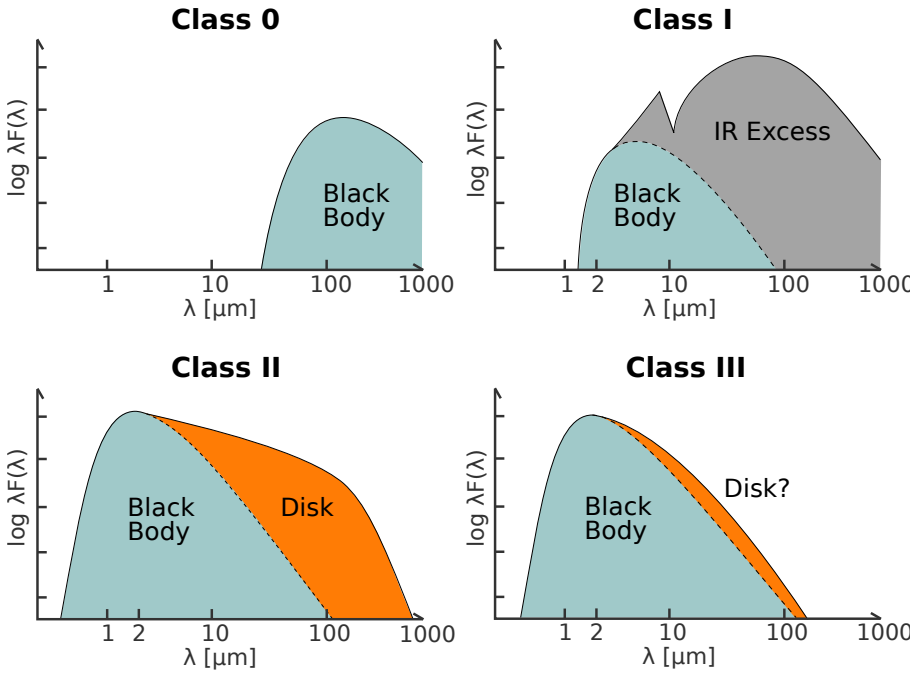


FIGURE 1.2: An illustration of typical SED profiles of different YSO classes. Figure from Persson (2014b).

Jhan and Lee, 2021; Ray et al., 2023) (see Figure 1.3), as accretion activity and outflow activity are intrinsically linked (Hartigan, Edwards, and Ghandour, 1995; Hartmann, 2009).

### Class I objects

In class I objects, the mass of the central source continues to grow slowly, with the gas and dust continuing to fall onto the now massive disc, and from the disc onto the evolved accreting protostar. This depletes the surrounding envelope enough so that the protostar becomes detectable at IR wavelengths (Hartmann, 2009). Their SEDs, shown in Figure 1.2, therefore display a shifted blackbody spectrum, at shorter wavelengths than that seen at the class 0 stage, with a strong IR excess, indicating the presence of a heated accretion disc (Kogure and Leung, 2010), along with contribution from the less dense envelope (Ray and Ferreira, 2021). The slope or the peak of the SED is used to determine how much the surrounding envelope has depleted, and the protostar now has a mass comparable to or greater than the envelope. This stage typically begins at 100,000 – 200,000 years and persists for $\sim$ 500,000 years, and the accretion rate is somewhat diminished from the class 0 stage, but still strong. Consequently, there are also jet-like molecular outflows present in this

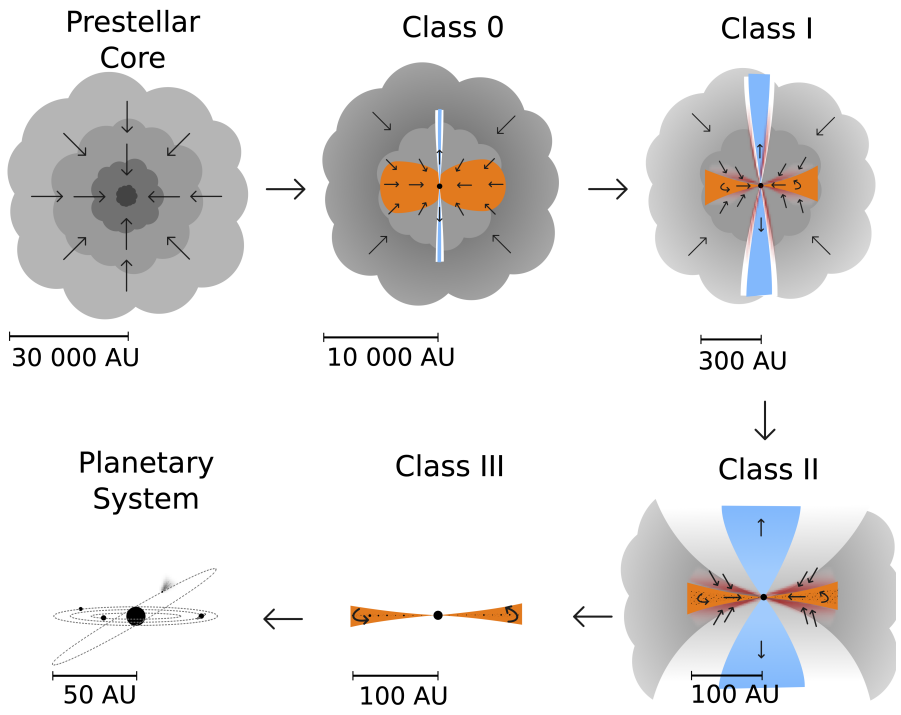


FIGURE 1.3: An illustration of the evolutionary stages of YSO formation. Grey represents the surrounding envelope, blue represents the bipolar outflow, and orange represents the flattened, rotating disc. Class 0 and I objects are considered protostars, and class II and III objects are classified as PMS stars. Figure from Persson (2014a).

stage (see Figure 1.3), but less powerful, suggesting a decrease in the mass accretion rate over time. The bipolar outflows carve out cavities in the surrounding material, further clearing the envelope.

### Class II objects

Class II objects correspond to the observationally classified classical T Tauri star (CTTS) phase of star formation, for low-mass stars (Joy, 1945; Herbig, 1962; Bertout, 1989). The corresponding phase for intermediate mass stars ($M = 2$ $M_\odot$ – 8 $M_\odot$) is the Herbig Ae/Be stage (Herbig, 1960). The class II stage corresponds to the transition of a protostar to a pre-main sequence (PMS) star. They are defined by the lack of a substantial envelope surrounding the star, but still have a heated accretion disc (see Figure 1.3), producing the observed falling excess IR emission in their SED profiles (Figure 1.2). The emission from the disc progressively becomes more negligible and the SED comes to resemble a pure stellar photosphere. The peak of the SED shifts to shorter wavelengths and hence, class II objects are detectable at optical wavelengths (Hartmann, 2009), with bolometric temperatures of $T_{\rm bol} \approx 650$ – 2,880 K. This stage of low-mass star formation begins at approximately 1 Myr, and persists for millions of years. The mass accretion rate drops significantly in this stage, as the envelope has dissipated and the accretion disc is solely feeding the central star, and consequently, the outflows are significantly less powerful than in the earlier stages. CTTSs are defined as having strong emission lines in their spectra at optical wavelengths (Hartmann, 2009; Krumholz, 2017), such as the H Balmer lines (H$\alpha$, H$\beta$,...). There exists velocity broadening of these emission lines, indicating accretion activity, as the high-velocities of these lines traces material accelerated toward the central star (Greene et al., 1994). The strength of these accretion-tracing emission lines, in the ultraviolet (UV) and optical wavelength regimes, vary significantly on very short timescales, hours to months, indicating that accretion is a variable process. The flat-SED class exhibits relatively flat SED profiles in the MIR, distinct from both class I and class II, and as such is thought to be a transition between the two classes (André et al., 2004).

### Class III objects

Class III YSOs represent the final stage of star formation before the main-sequence. Both the surrounding envelope and surrounding accretion disc are by now almost completely depleted or dispersed. The observed SED resembles

a stellar blackbody curve, with a greatly diminished IR excess (André, 2002), see Figure 1.2. The IR excess exists primarily in the MIR to far-infrared (FIR) indicating that the remaining material in the disc is cool and located far from the central star (Greene et al., 1994). The accretion tracing emission lines, which are strong in the CTTS phase, have also weakened or disappeared, indicating low accretion activity (Cieza et al., 2007). These classes of stars, with little IR excess and weak accretion-tracing emission lines are referred to as weak-line T Tauri stars (WTTS). This stage begins at approximately 10 Myrs and persists for a few million years, leading directly into the main-sequence. The central PMS stars have bolometric temperatures of $T_{\rm bol} > \sim$ 2,880 K. As a consequence of this low accretion activity, the outflows are no longer present (see Figure 1.3).

There also exists a phase of a circumstellar, or protoplanetary, disc's evolution between the class II and class III stages, classified as a transitional disc (TD) (Strom et al., 1989). They represent an intermediate stage in the disc evolution, where the disc transitions from a massive, gas-rich , optically thick disc, to a sparse debris disc (Ercolano and Pascucci, 2017). These discs exist around T Tauri stars, both CTTSs and WTTSs, defined as a disc structure that hosts a large gap between the inner disc radius and the star. They are identified by observing the SED, if much of the optically thick material, such as dust, in the inner disc region has depleted, the NIR excess will be low, with MIR and FIR excess dominating the SED (Espaillat et al., 2014). This points to a TD with no dust in the inner disc region (Krumholz, 2017). TDs can also now be directly imaged due to recent advances in observatories and observational techniques. The process for this inside-out clearing of dust is currently debated, with photoevaporation (PE) of dust in the inner disc region due to the central source (Ercolano and Pascucci, 2017; Picogna et al., 2019), the presence of forming planets clearing the local dust (Ginski et al., 2016; Maucó et al., 2018; Andrews, 2020), and radial magnetised winds clearing the inner disc region (Wang and Goodman, 2017; Martel and Lesur, 2022), being proposed as possible mechanisms. A caveat to point out is that this evolutionary model based solely on the IR excess of SEDs is currently debated. For example, there is some work that suggests that CTTSs do not evolve into WTTSs, and that they are instead distinct populations (e.g. Littlefair et al., 2004), although WTTSs are generally accepted as being older than CTTSs (e.g. Armitage, Clarke, and Palla, 2003).

Throughout these evolutionary stages of low-mass star formation, planet

formation is simultaneously occurring alongside disc evolution, as these processes influence one another. The first stages of planet formation likely take place as early as the class 0/I stages, with observations of disc substructures indicative of planet-disc interactions (e.g. Zhang et al., 2018; Xu and Armitage, 2023; van't Hoff et al., 2023). In class II sources, large gaps in discs, potentially due to planet-disc interactions, and embedded protoplanets are commonly seen (Armitage, 2015).

Further gravitational contraction of the central object eventually causes the PMS star to join the main-sequence, defined by the onset of hydrogen fusion. This begins when the core temperature is sufficient to ignite the proton-proton (p-p) chain reaction at temperatures of $> 10^7$ K. This leads to the production of helium (He), where this process of nuclear fusion halts the gravitational contraction of the star, allowing it to achieve hydrostatic equilibrium, where the gravitational force is balanced by the pressure generated via fusion of H into He. Other H $\rightarrow$ He fusion reactions can take place with increasing core temperatures, such as the Carbon-Nitrogen-Oxygen (CNO) cycle. The p-p chain dominates hydrogen fusion in stars with masses $< 1.3\ M_{\odot}$, and the CNO cycle dominates in stars with masses $> 1.3\ M_{\odot}$ due to their higher core temperatures.

## 1.2 Accretion processes

The mass of a newly-formed protostar increases by accreting material from the collapsing cloud. As described in Section 1.1.1, the collapse of a protostellar cloud results in the formation of a rotating, flattened disc, due to the conservation of angular momentum (see Figure 1.4). Approximately 99% of the mass in these circumstellar discs, assuming they inherit their composition from their parent molecular clouds, is made up of gas, and the remaining 1% is made up of refractory material, or dust (Bohlin and Drake, 1978). These discs have typical radii of a few hundred au, as measured in mm-dust emission, however, gas disc sizes are generally found to be several times larger than the dust disc, suggesting the inward drift of mm-sized particles (e.g. Ansdell et al., 2018; Sanchis et al., 2021). Disc formation is closely followed by a much longer phase of disc accretion, whereby angular momentum in the disc is either redistributed to larger radial distances, or removed from the disc, to allow the inspiral of disc material onto the central star. Most of the mass contained in the disc after

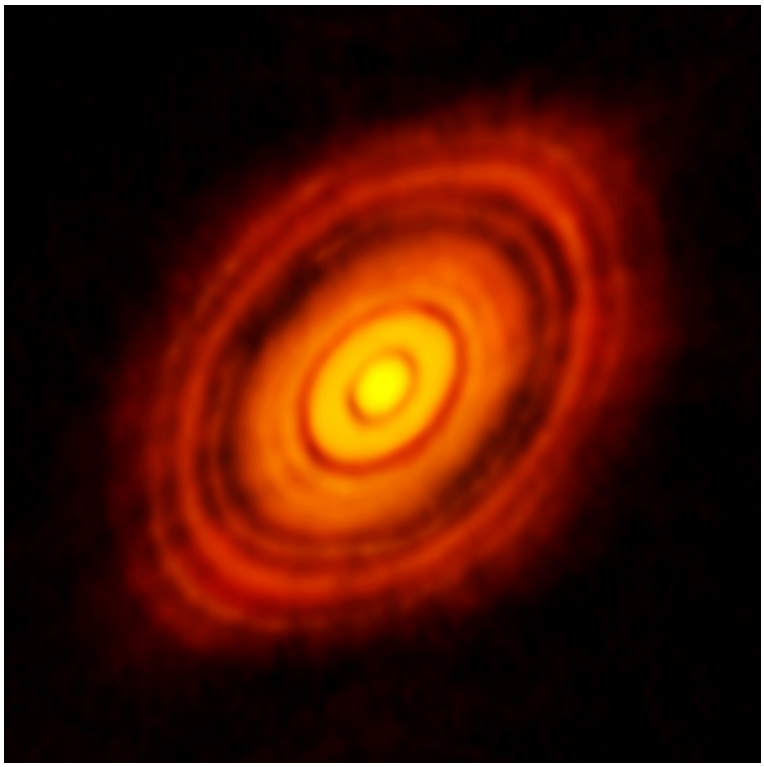

FIGURE 1.4: An ALMA image of the disc surrounding the class I/II object HL Tau in 1.3 mm dust continuum emission, displaying rings and gaps. Credit: ALMA(ESO/NAOJ/NRAO); C. Brogan, B.Saxton (NRAO/AUI/NSF).

formation will end up in the central star, with some fraction reserved for the possible formation of planets (Hartmann, 2009), and most of the stellar mass is assembled during the early stages of evolution (class 0/I). Accretion discs deliver material onto their central stars at typical rates of $10^{-10}$ – $10^{-7}$ $M_{\odot}$ yr$^{-1}$ (Venuti et al., 2014; Hartmann, Herczeg, and Calvet, 2016; Manara et al., 2016). Their formation, evolution, and subsequent dispersal is closely related to the amount of angular momentum the disc harbours. Discs often display complex substructures, including rings, gaps, spirals, and crescents, the origin of which is an active field (Andrews et al., 2018; Ginski et al., 2021; Bae et al., 2023). Angular momentum transport within the disc, and removal from the system, is therefore critical to understanding the evolution of discs around YSOs (Lesur et al., 2023).

### 1.2.1 The transport of angular momentum

How the angular momentum in the disc is transported radially outward, or removed from the inner disc region, both of which permits accretion of material onto the central star, is an ongoing challenge in star formation (Pudritz and Ray, 2019; Manara et al., 2023). However, there are two likely mechanisms for angular momentum transport; via viscous turbulence or by magnetically launched outflows. The standard model for disc evolution is based on classical disc accretion theory, whereby some form of viscosity in the disc, generally attributed to turbulence in the disc generated by magnetohydrodynamic (MHD) processes such as magnetorotational instabilities (MRIs) (Balbus and Hawley, 1991; Armitage, 2011), hydrodynamical instabilities such as the vertical-shear instability (VSI) (Nelson, Gressel, and Umurhan, 2013), or gravitational instabilities (Rice, Lodato, and Armitage, 2005), leads to the outward transfer of angular momentum. Viscosity arising from turbulence in the disc refers to the effective internal friction of differential motion within the disc, whereby neighbouring layers of the disc rotate at different angular velocities due to the differential rotation. The angular velocity of a circumstellar disc is roughly Keplerian (Hartmann, 2009), meaning the angular velocity decreases with distance from the central star.

Whilst radial angular momentum transport is likely driven by turbulent or viscous mechanisms in discs, where class I discs were found to be more radially compact compared to their class II counterparts, supporting the idea of viscous angular momentum transport (Najita and Bergin, 2018), it is likely not the dominant angular momentum redistribution mechanism (Manara et al., 2023). For example, it is now accepted that MRI is largely suppressed in the planet-forming regions of the disc, $r \approx 1 - 30$ au, due to insufficient disc ionisation and non-ideal MHD effects, such as Ohmic resistivity, ambipolar diffusion, and the Hall drift (Bai and Stone, 2013; Turner et al., 2014; Lesur et al., 2023; Pascucci et al., 2023). Other processes must be contributing to angular momentum transport, thus enabling accretion onto the central star. Magnetically launched outflows from the disc surface, MHD disc winds, are a strong candidate for removing angular momentum from the disc, rather than transporting it outward, with numerical simulations and theoretical models showing that MHD disc winds should dominate the accretion process (Bai and Stone, 2013; Gressel and Pessah, 2015; Béthune, Lesur, and Ferreira, 2017; Bai et al., 2016; Bai, 2017). The MHD wind is launched by the magnetic field threading the

disc, where the exchange of angular momentum of material in the disc, which decreases in rotational velocity, and material in the outflow, which increases in angular velocity, is mediated by the magnetic field (Blandford and Payne, 1982; Manara et al., 2023). Torque ($\tau$), shown in Equation 1.5, is a measure of the rotational force acting on an object about a pivot point, and is proportional to the position vector ($\vec{r}$) from the pivot point to the point where the force is applied, the lever arm, and the force ($\vec{F}$). Magnetic Torque in accretion discs arises from the interaction of magnetic field with the rotating material in the disc transferring angular momentum outward, and therefore the amount of angular momentum removed by the magnetically launched wind increases with increasing disc radius, as the magnetic lever arm increases.

$$\tau = \vec{r} \times \vec{F} \tag{1.5}$$

### 1.2.2 The accretion mechanism

Whatever the mechanism for angular momentum removal from the inner disc region, accretion of material onto the central star will follow. Mass accretion onto low-mass stars ($< 2\ M_{\odot}$) is currently understood to occur through the observationally supported process of magnetospheric accretion (Uchida and Shibata, 1985; Koenigl, 1991; Hartmann, Hewett, and Calvet, 1994; Bouvier et al., 2007), where gas and dust from the ionised inner disc is channelled in funnels along magnetic field lines, crashing onto the stellar surface (Camenzind, 1990; Ostriker and Shu, 1995). Accretion of material occurs from the magnetic truncation radius ($R_{\mathrm{t}}$) of the disc, where the approximately dipole stellar magnetic field has truncated the inner disc. This truncation occurs where the magnetic pressure of the stellar magnetosphere ($P_{\mathrm{B}}$) balances the ram pressure of the accreting material ($P_{\mathrm{ram}}$), caused by the bulk motion of the fluid, shown in equation 1.6, where $B$ is the magnetic field strength, $\mu_0$ is the vacuum permeability, $\rho$ is the gas density, and $v$ is the Keplerian velocity of the gas at the radius in question. The magnetic truncation radius is typically close to, but within, the co-rotation radius ($R_{\mathrm{c}}$) of the disc, defined as the radius at which the angular velocity of disc material is equal to the stellar rotation period (Bouvier et al., 2007). This inner disc disruption is observationally supported with sufficient field strengths detected at the truncation radius, typically a few stellar radii (Johns-Krull, 2007), in CTTSs (e.g. Johns-Krull, Valenti, and Koresko,

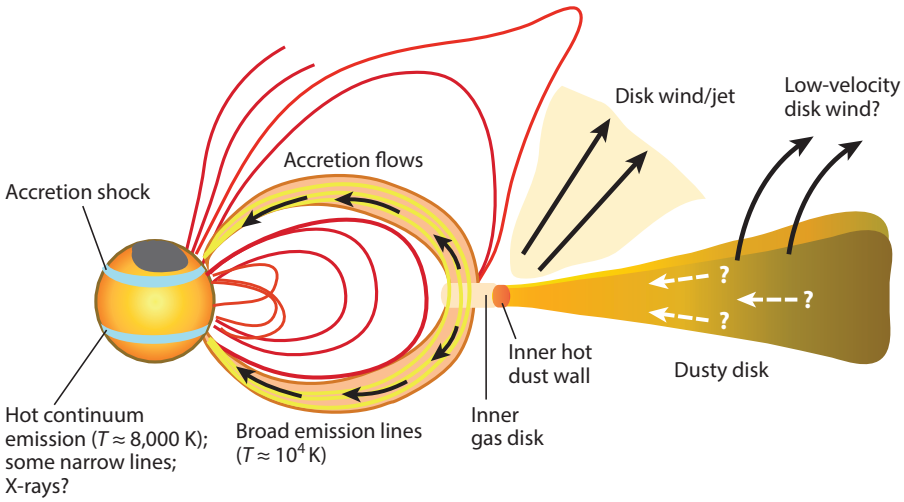


FIGURE 1.5: An illustration of the magnetospheric accretion mechanism. The stellar magnetosphere truncates the inner disc near the co-rotation radius. Magnetic field lines, connected to the disc, channel material at near free-fall velocities that shock the stellar surface at high latitudes. Figure from Hartmann, Herczeg, and Calvet (2016).

1999; Symington et al., 2005). As the truncation radius is located within the co-rotation radius, the disc material here rotates faster than the star and therefore transfers angular momentum to the star, spinning it up. Here, magnetically launched outflows are again invoked to regulate the star's rotation rate, by carrying away excess angular momentum. The temperature of disc material at the truncation radius is approximately $> 10^3$ K, due to radiation heating from the central star, and the dust begins to sublimate. These inner disc temperatures are high, ensuring sufficient ionisation for strong coupling between the gas and the magnetic field (Koenigl, 1991).

$$\frac{B^2}{2\mu_0} \approx \rho v^2 \tag{1.6}$$

The captured disc material is channelled along the magnetic field lines in funnel flows, as illustrated in Figure 1.5. The material in the infalling accretion flows accelerates to near local free-fall velocities ($\sim 10^2$ km s$^{-2}$) (Bonnell et al., 1998), producing broad emission lines arising from gas temperatures of $T \approx 8{,}000$ K (Calvet and Hartmann, 1992; Hartmann, Hewett, and Calvet, 1994), and impacts the stellar surface at high latitudes, producing accretion shocks on the stellar surface. The gas at the stellar surface is briefly shock-heated to temperatures of the order of $10^6$ K, resulting in X-ray emission, which is absorbed

and re-radiated at lower temperatures, producing strong UV-optical continuum excess, along with some relatively narrow emission lines. The clearest observational signatures of accretion come from this UV continuum, narrow line emission, and the broad emission lines from the accretion flows (Calvet and Hartmann, 1992; Hartmann, Hewett, and Calvet, 1994). Accretion is known to be a variable process, with temporal changes in the star-disc connection and the flow of gas through the disc (Bally, 2016; Fischer et al., 2023). Periods of high-accretion, or bursts, can have durations as short as hours or, more rarely, as long as months or decades. The spectra from accreting low-mass stars often show optical and NIR emission lines with characteristic inverse P Cygni profiles, where there is strong emission centred around the rest wavelength of the line, arising from the shock-heated gas, and a superimposed redshifted absorption feature, indicating the presence of infalling material in the accretion funnel that absorbs stellar radiation (Edwards et al., 1994). The width of the absorption features indicates the bulk motion of the infalling material at velocities of $\sim 10^2$ km s$^{-2}$. Magnetospheric accretion may not be the dominant accretion model for intermediate and higher mass stars ($\gtrsim 4\ M_\odot$) where stellar magnetospheres are weaker (Wichittanakom et al., 2020), and possibly for high accretion periods of low mass stars, such as FU Ori objects, where the broad emission lines from the accretion columns disappear. A proposed mechanism for disc accretion in these objects is boundary layer accretion. This occurs when the ram pressure of the accreting material pushes the magnetic field back to the stellar surface, allowing material in the disc to accrete directly onto the equatorial region of the stellar surface (Hartmann, 2009).

The luminosity of the UV excess and broad emission lines in the accretion flows can be directly measured as the accretion luminosity ($L_{\rm acc}$), which is essentially a measure of the gravitational potential energy that is converted into radiation. The combination of the $L_{\rm acc}$ with the stellar mass and radius ($M_\star$, $R_\star$) can be used to estimate the mass accretion rate ($\dot{M}_{\rm acc}$) (Hartmann, Herczeg, and Calvet, 2016), generally measured in solar masses per year ($M_\odot$ yr$^{-1}$). Uncertainties arise in this conversion from $L_{\rm acc}$ to $\dot{M}_{\rm acc}$, particularly, due to the estimations of the stellar parameters $M_\star$ and $R_\star$, and due to potential variability in the accretion rate (Manara et al., 2023). Typical accretion variability in PMS stars peaks at a factor of $\sim 3$ on timescales of days to weeks (e.g. Biazzo et al., 2012; Costigan et al., 2014; Venuti et al., 2014; Hartmann, Herczeg, and Calvet, 2016; Robinson and Espaillat, 2019).

FIGURE 1.6: A three-colour image of the bipolar HH 211 outflow as observed with JWST NIRCam. Credit: ESA/Webb, NASA, CSA, T. Ray (Ray et al., 2023).

## 1.3 Ejection processes

Outflows are ubiquitous to accreting YSOs (class 0/I/II), and are observed across the wavelength range, from X-rays to radio (See Figure 1.6). As accretion begins early in the star formation process, so does the driving of bipolar outflows, launched perpendicularly to the accretion disc surrounding the YSO, as ejection is intrinsically linked with accretion (Hartigan, Edwards, and Ghandour, 1995; Edwards, 2009; Ray and Ferreira, 2021). As discussed in Section 1.2, outflows may be fundamental to the star formation process, removing angular momentum from the star-disc system, thus permitting accretion onto the central star. The initial angular momentum present in prestellar cores needs to be reduced by several orders of magnitude in order to permit a star or a multiple star system to form (Belloche, 2013). The strength of outflows is also dependent on the evolutionary status of the star, with younger stars possessing more powerful outflows, in line with their higher accretion rates (Ray and Ferreira,

2021). Outflows may also significantly influence disc evolution and potentially planet formation and planetary migration, as they may interact with the planet forming regions of the disc (Pascucci et al., 2023).

Outflows are composed of high-velocity ($\gtrsim 100$ km s$^{-1}$), collimated gas, referred to as jets, and low-velocity ($\lesssim 30$ km s$^{-1}$), wide-angled winds (Reipurth and Bally, 2001; Frank et al., 2014; Pascucci et al., 2023). Outflow emission is mostly characterised by line emission, which arises primarily from the cooling regions of shocks generated by the outflow. Herbig-Haro (HH) objects, which are small, bright regions of nebulosity, were discovered in the early 1950's (Herbig, 1951; Haro, 1952), and were later ascertained to arise from outflows from forming stars. HH objects are created when the high-velocity, collimated jet component of the outflow impacts and interacts with the surrounding medium, creating shocked regions of gas. The fast, axial jets often exhibit bright, knotty substructures within the jet axis (internal shocks), arising from high-velocity material catching up with and impacting material ahead of it (Tsukamoto et al., 2023). The presence of these internal shocks indicates episodic variations in the velocity or the mass outflow rate of the flow (Caratti o Garatti et al., 2006), which may be the result of variable accretion. The outflowing gas can also interact with the surrounding envelope of quiescent material, creating shocked regions, such as terminal bow shock structures (Hartigan, 2003; Arce et al., 2007). Lower-velocity, wider-outflow components surrounding the bases of jets were first discovered by Davis (2002) using NIR narrow-band molecular hydrogen ($H_2$) imaging. Outflows can also entrain material, where ambient material in the surrounding envelope or ISM is swept up, accelerated, and subsequently entrained by the flow (Arce et al., 2013). Cavities, surrounding the outflow, which are defined as hollow, low-density regions created by the outflow, are also well documented phenomena (Habel et al., 2021). The origin of these hollow outflow cavities is currently debated. They may be directly or partly tracing intrinsic wide-angled disc winds originating from the disc surface (de Valon et al., 2022; López-Vázquez et al., 2024), either by magnetic or thermal processes. The cavities may be tracing an interaction region between some kind of wide-angled disc wind and the surrounding medium, be it a static or infalling envelope. They may also be produced by the stacking of successive jet bow shocks from a collimated, variable jet propagating into a density-stratified surrounding medium (Rabenanahary et al., 2022).

### 1.3.1 Outflow launching

The mechanism for launching outflows remains a major open question in star formation (e.g. Frank et al., 2014; Ray and Ferreira, 2021; Pascucci et al., 2023). However, magnetically launched outflows are a promising candidate for producing these fast, collimated jets and lower-velocity, wide-angled winds (e.g. Donati et al., 2010; Bjerkeli et al., 2016; Lee et al., 2017; Lee et al., 2021). Furthermore, it has been shown that magnetised outflows are consequently obtained if a large scale magnetic field is present in the disc (Suzuki and Inutsuka, 2009; Fromang et al., 2013; Bai and Stone, 2013). Thermally-launched photoevaporative winds, where high-energy radiation (UV and X-rays) originating from the central source generate a thermal pressure in the disc surface, are also thought to be present, especially at later stages of pre-main sequence star evolution (e.g. Alexander et al., 2014; Ercolano and Pascucci, 2017).

Outflows are likely launched magneto-centrifugally (Blandford and Payne, 1982), via MHD processes. As stated earlier, open magnetic field lines thread the accretion disc, and as there exists a fraction of ionisation in the disc, there is a coupling between the ionised disc material and the magnetic field lines due to the Lorentz force, referred to as the frozen-in flux condition in magnetohydrodynamics (Priest and Forbes, 2000). In a conductive plasma, and assuming an ideal MHD situation (where resistivity is taken to be negligible), the magnetic field lines move with the plasma, as if they are anchored in the disc (Ferreira, 2013; Bally, 2016; Konigl and Pudritz, 2000)[2]. The Lorentz force ties the magnetic field lines to the rotating, partially ionised plasma, preventing the field lines from slipping relative to the Keplerian rotating disc. Due to the differential rotation of the disc, the magnetic field lines co-rotating with the disc become wound-up, creating a helical hour-glass-like structure. The magnetic field has both poloidal and toroidal components, where the poloidal component refers to the component of the magnetic field threading the disc, extending away from the plane of the disc, and the toroidal component refers the component of the magnetic field that wraps around the axis of rotation, encircling it in a toroidal fashion. The poloidal magnetic field lines therefore act like tracks along which ionised material is guided. As the magnetic field

[2]Outflows are also launched from magnetised discs for which non-ideal MHD effects (Ohmic resistivity, ambipolar diffusion, the Hall drift,...) dominate the physics of how magnetic fields are coupled to the gas and dust, due to an ionised layer at the disc surface (Pudritz and Ray, 2019; Lesur et al., 2023).

lines are inclined with respect to the disc surface, there is a component of centrifugal force, felt by the rotating disc material, along the magnetic field lines. This generates a magnetic torque. The centrifugal force acts radially outward from the centre of the rotating disc in the rotational plane, therefore pushing disc material away from the axis of rotation. As the ionised material follows the magnetic field lines outwards, the centrifugal force accelerates the material outward along the field line (Blandford and Payne, 1982). The rotational energy of the disc is transferred, and converted, to the kinetic energy of to the accelerated material via the magnetic field (Manara et al., 2023).

The collimation of the outflow is then achieved due to the hoop stress of piled-up toroidal field lines (Pudritz and Ray, 2019). The winding-up of field lines occurs at the Alfvén point, or radius, when the poloidal flow velocity ($v_{\rm flow}$) approximately equals the Alfvén velocity ($v_{\rm A}$) in the poloidal plane. The Alfvén velocity, given in Equation 1.7 [3], is the characteristic velocity of MHD Alfvén waves, transverse waves that propagate through a plasma in the direction of the magnetic field lines. Beyond the Alfvén point, the plasma transitions from being magnetically dominated, where field lines control the motion of the flow, to inertially dominated, where the inertia of the flow stretches and twists the magnetic field, preventing it from relaxing back to it's original configuration, the frozen-in condition of MHD. This results in the generation of a strong toroidal field component, which increasingly becomes dominant with distance from the central star. The strong toroidal component of the field beyond the Alfvén point creates a magnetic tension that acts inward towards the axis of the flow, effectively collimating the outflow.

$$v_{\rm A} = \frac{B}{\sqrt{\mu_0 \rho}} \tag{1.7}$$

The magnetic lever arm parameter ($\lambda$), shown in Equation 1.8, is a dimensionless parameter that quantifies the efficiency at which the magneto-centrifugally launched outflow extracts angular momentum from the star-disc system. It is defined as the ratio of the square of the cylindrical Alfvén radius ($r_{\rm A}$), to the square of the footpoint of the outflow, or the launch radius ($r_0$). If the magnetic lever arm parameter is significant ($\lambda \gtrsim 2$), then magnetic

[3] Here, $B$ is the magnetic field strength, $\mu_0$ is the vacuum permeability, and $\rho$ is the mass density of the plasma.

tension accelerates the outflow, causing the outflow to super-rotate with respect to the local Keplerian rotation velocity at $r_0$ at the disc surface (Pascucci et al., 2023). The magnetic lever arm acts similar to a mechanical lever arm, whereby it exerts a magnetic torque (see Equation 1.5) on rotating material at $r_0$. This torque is responsible for removing angular momentum from the outflow launching region. If a longer lever arm is present, where $r_{\rm A}$ is larger, then angular momentum is more efficiently extracted from the system. Beyond the Alfvén radius, where magnetic forces gradually become negligible, then the final outflow velocity, or asymptotic velocity of the flow, is related to the magnetic lever arm parameter and given by the Bernoulli invariant, shown in Equation 1.9 (Blandford and Payne, 1982; Cabrit, 2007), where $v_{\rm Kep}(r_0)$ is the Keplerian velocity ($v_{\rm Kep}(r_0) = \sqrt{GM_\star/r_0}$) of the disc material at the outflow launch radius ($r_0$).

$$\lambda = \left(\frac{r_{\rm A}}{r_0}\right)^2 \tag{1.8}$$

$$v_{\rm flow} \simeq \sqrt{2\lambda - 3}\, v_{\rm Kep}(r_0) \tag{1.9}$$

Within the mechanism of magneto-centrifugally launched outflows, there are broadly two competing models to explain this phenomenon; the 'X-wind' model (Shu et al., 1994; Shu et al., 2000), and the disc wind model (Pudritz and Norman, 1983; Konigl and Pudritz, 2000; Pudritz et al., 2007).

**The X-wind model**

The 'X-wind' model proposes that the outflow is launched from a narrow annulus on the disc, at the interface where the stellar magnetosphere interacts directly with the inner disc edge, the co-rotation radius. At this radius the magnetic field switches from its closed configuration, where field lines associated with the stellar magnetosphere are connected to those threading the inner disc edge, to an open one, where field lines open up and diffuse beyond the co-rotation radius. This narrow radial ring is known as the 'X-point'. Due to the proximity to the central star, the inner disc is fully ionised, resulting in a strong coupling between the magnetic field and the disc gas. Disc material at this radius is therefore magneto-centrifugally accelerated along the open field

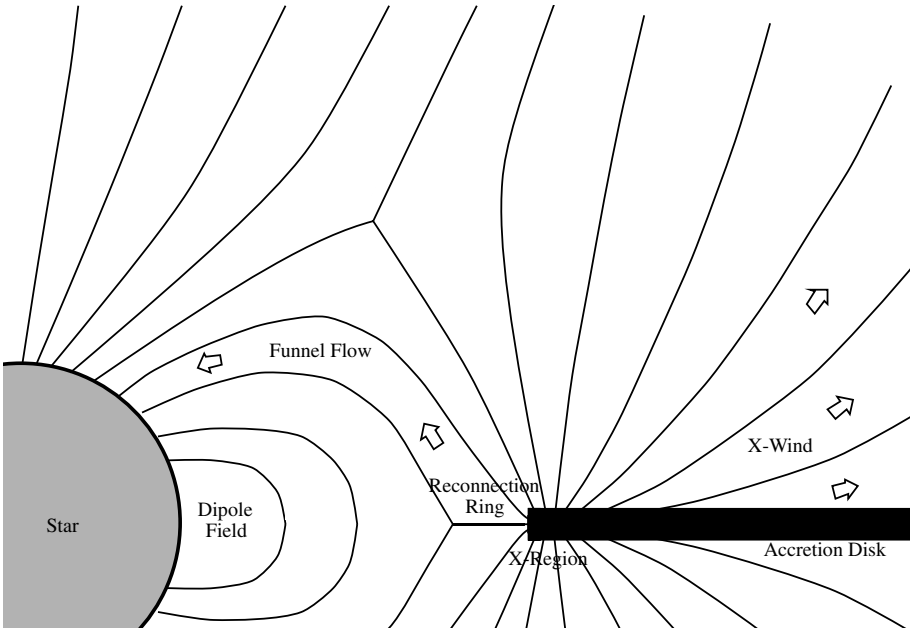


FIGURE 1.7: A schematic of the X-wind model. At the 'X-point'(labelled X-region in this diagram), magnetic field lines diffuse outward beyond the co-rotation radius. Strongly ionised material is magneto-centrifugally launched along the open field lines at this narrow annulus. Magnetic field lines are represented by black lines and the arrows show the channelling of inner disc material. Figure adapted from Shu et al. (2000).

lines, removing angular momentum from the disc material in this localised region, and removing a significant fraction of the incoming mass. In this case, the angular momentum removal from the disc is only partially resolved as material still has to be transported inward within the disc to this inner radius (Camenzind, 1990; Shu et al., 1994; Fendt, 2009; Čemeljić, Shang, and Chiang, 2013). High-velocity, collimated jets and slower-moving wide-angled winds are predicted with this model (Shang et al., 2020), with the wide-angled winds originating from the more inclined field lines at the 'X-point'. In this model, the expected outflow ejection radius is of the order of $\sim 0.1 - 0.5$ au (Bjerkeli et al., 2016; Pascucci et al., 2023).

### The disc wind model

The disc wind model proposes that the outflow is instead launched from a range of disc radii, from the co-rotation radius outward, where the high-velocity, collimated jet component is launched from the innermost regions of the disc, whilst the launching region of the lower-velocity wide-angled outflow component is launched further radially extended along the disc (Konigl and

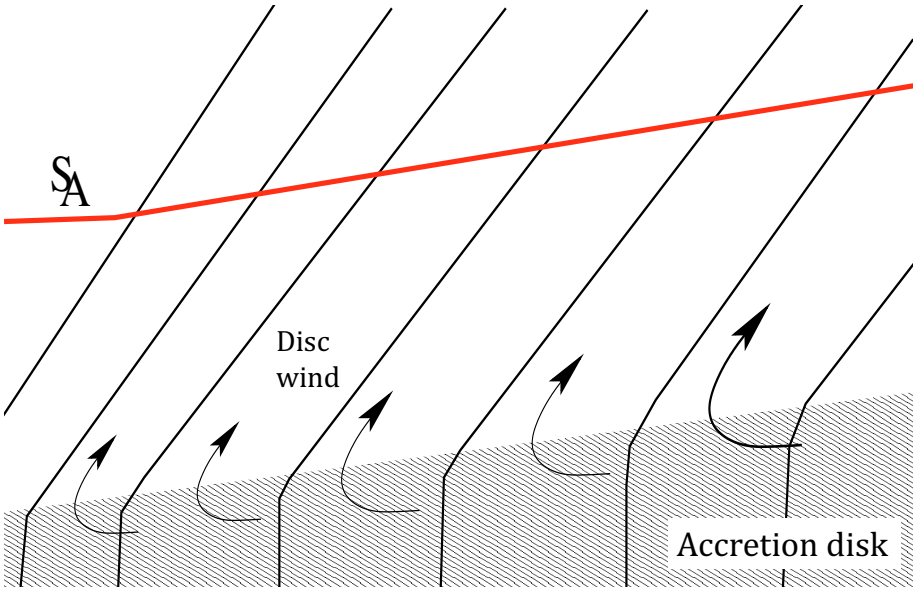


FIGURE 1.8: A schematic of the disc wind model. The outflow is launched from an extended radial region from open magnetic field lines anchored in the disc. The outflow velocities launched from the disc decrease with increasing disc radius, generating a nested, onion-like kinematic structure to the flow. Magnetic field lines are represented by black lines and the arrows show the channelling of disc material. The red line, labelled $S_A$, refers to the Alfvén surface, where the poloidal flow velocity ($v_{\rm flow}$) approximately equals the Alfvén velocity ($v_A$) in the poloidal plane. Figure adapted from Ferreira, Dougados, and Cabrit (2006).

Pudritz, 2000; Pudritz et al., 2007). This model necessitates that the poloidal magnetic field lines threading the disc are radially spread along the disc, providing a range of outflow launching radii. In the disc wind model a continuum of outflow velocities is expected, with outflow velocities decreasing with increasing disc radius, generating a nested, onion-like kinematic structure (de Valon et al., 2020; Pascucci et al., 2023). Disc wind models predict a greater fraction of angular momentum removal from the star-disc system, as the outflow driving region extends further radially along the disc from the driving source, and angular momentum increases with disc radii (Anderson et al., 2003; Ferreira, Dougados, and Cabrit, 2006; Pudritz and Ray, 2019; Lee et al., 2021). Disc winds are naturally more influential in disc evolution, and later planet formation, as they interact with a greater disc area in comparison to the 'X-wind' model.

### Stellar winds

Further to these two competing outflow launching mechanisms, there also likely exists self-collimated, MHD stellar winds, launched directly from open polar magnetic field lines from the star itself (Matt and Pudritz, 2005; Ferreira, Dougados, and Cabrit, 2006; Cranmer, 2008). Stars rotating near their break-up velocity, where the centrifugal force equals the gravitational force, can provide enough rotational energy to magneto-centrifugally accelerate stellar winds. However, protostars and T Tauri stars are relatively slow rotators (Bouvier et al., 1997; Scholz, Eislöffel, and Mundt, 2009; Ray and Ferreira, 2021), and therefore the stellar wind must be driven by a pressure gradient, either thermal in nature (Sauty and Tsinganos, 1994; Sauty, Trussoni, and Tsinganos, 2002) or from turbulent Alfvén waves (Hartmann, Avrett, and Edwards, 1982). In magnetospheric accretion, inner disc material is channelled along stellar field lines producing shocks at the stellar surface. Some post-shocked material may preserve high-temperatures thus allowing for a thermally driven outflow. Additionally, the magnetospheric accretion shocks efficiently generate turbulent Alfvén waves, providing a sufficient magnetic pressure gradient to launch and MHD outflow from the stellar surface. As this outflow launching is connected to the accretion mechanism, it is referred to as the accretion-powered stellar winds model (Matt and Pudritz, 2005). This produces an enhanced stellar wind which removes angular momentum along the open magnetic field lines connected to the stellar surface, contributing to the rotational braking of the star (Matt et al., 2012). However, it has been shown that such stellar winds are unlikely to carry a significant portion of mass-flux, requiring an extremely efficient conversion of thermal/wave energy into the kinetic energy of the outflow (Ferreira, Dougados, and Cabrit, 2006; Cabrit, 2007). Additionally, large amounts of energy are required to both launch this stellar wind and provide the observed accretion luminosities originating from the accretion shocks. This large amount of energy required implies a correspondingly high mass accretion rate, resulting in a greater spin-up torque acting on the star, which is difficult to balance with the amount of angular momentum these winds can extract from the rotating star (Ray and Ferreira, 2021). Therefore, stellar winds are generally not considered dominant in outflow launching.

The modern consensus is that there is likely a combination of models contributing to outflow launching, resulting in a layered, multi-component MHD

outflow structure (Frank et al., 2014; Bally, 2016; Ray and Ferreira, 2021). High-velocity, collimated jets originate in the inner disc region, and from the protostar itself, where magnetisation is expected to be the strongest, with stellar winds, the 'X-wind' model, and the disc wind model working together to achieve this hot, fast, axial flow. Meanwhile, wider, slower, and cooler winds surround the jet in a kinematically stratified structure. Observational discrimination between outflow launching models is discussed in Section 1.3.4.

### 1.3.2 Outflow shocks and observational tracers

Outflows emit radiation across the electromagnetic spectrum. This emission is generally characterised by line emission, which arises primarily from the cooling regions behind shocks generated by the outflow (Tsukamoto et al., 2023). Shocks are generated by the outflow when supersonic flows impact and interact with slower-moving, previously ejected material, or stationary material, in the surrounding envelope, dissipating the kinetic energy of the flow into thermal energy and radiation (Hartigan, 2003).

#### Shocks in outflows

Shocks, which are abrupt discontinuities in the gas properties, such as temperature, density, and pressure, are produced when a fluid disturbance moves through a medium faster than the local sound speed of the medium, so a pressure wave cannot precede the disturbance. Such a disturbance, which exceeds the local sound ($c_s$) speed is referred to as supersonic. The Mach number ($M$) is used to indicate the extent to which the velocity of the disturbance exceeds the sound speed of the gas, and it is defined as ratio of the flow velocity to the local sound speed ($M = v_{jet}/c_s$). Typical jet temperatures are $\sim 10^4$ K, implying local sound speeds of $\sim 10$ km s$^{-1}$. The velocities of jets ($v_{jet}$) therefore clearly exceed the local sound speed, making them highly supersonic (Ray and Ferreira, 2021), with high Mach numbers. Higher Mach numbers correspond to stronger shocks. Gas conditions in the medium ahead of a shock, the pre-shock region (upstream), change almost instantaneously with the passage of a shock. The shock wave transforms a large portion of the kinetic energy associated with the shock into thermal energy, referred to as shock heating, dramatically raising the temperature and the pressure, due to compression, of the gas behind the shock, the post-shock region (downstream) (Draine and McKee, 1993). The

post-shock region contains material that has undergone compression, heating, and ionisation. Across the shock, mass, energy and momentum must be conserved. These conservation rules can be expressed as the Rankine-Hugoniot conditions (Rankine, 1870; Hugoniot, 1887).

The most familiar type of shock is a jump shock (J-shock), which are shocks characterised by the abrupt discontinuities in the medium. These shocks tend to dominate in high velocity regimes where magnetic field strengths are relatively insignificant (Hartigan, 2003). In contrast, continuous shocks (C-shocks), the transition between the pre-shock and post-shock conditions is spread over a larger spatial region. This is due to the crucial role magnetic fields play in these shocks. If significant magnetic fields are present, the ions and neutrals are necessarily treated as separate fluids (Draine and McKee, 1993). When the shock is supersonic, but submagnetosonic (below the Alfvén velocity), magnetic waves can form a magnetic precursor that influences the ions in the pre-shock region before the shock arrives, leading to a smoother rise in temperature and density. C-shocks necessitate that the pre-shock region is partially ionised for the magnetic precursor to have a significant effect, but not ionised to a high enough degree to allow for effective coupling between ions and neutrals through collisions. Further to magnetic precursors, there are also radiative precursors, where radiation generated in the post-shock region and shock front can heat and ionise gas in the pre-shock region, again leading to an extended zone of altered gas conditions across the shock (Shull and McKee, 1979).

Shocks in outflows can generally be characterised as internal shocks, referred to as working surfaces, and terminal shocks. Terminal shocks occur when the leading edge of the supersonic outflow collides with the relatively static, or infalling, surrounding envelope of quiescent material, or with ambient ISM material. These shocks convert the bulk of the kinetic energy of the outflow into heat, light, and momentum transfer to the ambient material. Terminal shocks often produce large arc-shaped features in the pre-shock region where ambient material is accelerated and deflected outward, called bow shocks, which appear as curved shock fronts, where the apex of the bow feature corresponds to the highest velocity relative to the ambient medium, with slower regions extending along its wings (Hartigan, 2003; Arce et al., 2007). Mach discs, a type of shock that arises behind the bow shock in the outflowing material itself, mark where the outflow abruptly decelerates and compresses

as it encounters the bow shock (Bally, 2016). Mach discs do not occur if the generated bow feature moves faster than the outflow, as might happen if the outflow velocity decreases with time (Hartigan, 2003).

Internal shocks, or working surfaces, occur primarily in the outflow axis as a result of velocity variations in the outflow, as more rapidly advancing material catches up with, and impacts slower material ahead of it. Therefore the strength of the shock produced depends not on the outflow velocity with respect to the source, but instead the relative difference between the outflow velocity and the material it is impacting (Ray and Ferreira, 2021). These internal surfaces comprise both forward and reverse shocks, with the forward shock compressing the medium ahead of it, and the reverse shock heating the trailing jet material. As accretion in known to be a variable process (Bally, 2016; Fischer et al., 2023), the outflow consequently has variable launching of material (Caratti o Garatti et al., 2006), resulting in the production of knot-like substructures along the outflow axis, each representing active internal working surfaces. The presence of working surfaces is supported by the observed shock velocities of these knots in jets, which are typically only a few 10's of km $s^{-1}$ (Hartigan, Morse, and Raymond, 1994), whereas bulk jet velocities are measured to be much higher (100's of km $s^{-1}$) from proper motion measurements, which provides tangential velocities, and spectroscopy of outflow-tracing emission lines, which provides radial velocities.

**Outflow emission**

The visibility of outflows is made possible by the radiative cooling of the shock-heated gas in the flow. The shocks are collisional, meaning the heating of particles in the gas is due to particle-particle collisions. These collisions result in the raising of atoms to excited states, where the electrons in the atom are raised to higher energy levels due to the transfer of kinetic energy to the bound electron (Hartigan, 2003). The ionisation of atoms can also occur, whereby the atom absorbs enough energy to overcome the binding energy of the electrons, resulting in the atom losing one or more electrons. This produces positively charged ions. The cooling of the gas in the post-shock regions occurs efficiently with the emission of photons, in the form of line emission (Ray and Ferreira, 2021), referred to as radiative decay. Emission lines arise when the atom (neutral or ionised) transitions from the excited bound state to a lower energy bound state. This occurs when an electron in that atom drops from a discrete energy

level, with energy $E_2$, to a lower energy level, with energy $E_1$, thus using the energy difference to emit a photon (Planck, 1901; Einstein, 1965; Bohr, 1913). The analysis of these spectral emission lines is paramount to all fields of astrophysics. The emission lines represent specific atomic or molecular transitions, resulting in the emission of specific photons. The energy of an emitted photon is equal to the energy difference between the two states in the transition, and is given by Equation 1.10, where $h$ is Planck's constant, and $\nu$ is the frequency of the emitted photon. The probability of a given spontaneous radiative decay occurring is given by the Einstein $A_{21}$ ($s^{-1}$) coefficient, where '2' represents the higher energy level, and '1' represents the lower. The radiative lifetime ($\tau_2$) of the excited state is inversely proportional to the Einstein $A_{21}$ coefficient, meaning higher values of $A_{21}$ correspond to shorter lifetimes of the excited state. The intensity of emission lines is proportional to the product of the $A_{21}$ coefficient and the population of the excited state. Collisional de-excitation of atoms and molecules can also occur, where a particle-particle collision de-excites the excited atom or molecule to a lower excited state. In high-density regions, collisional de-excitation can dominate over radiative decay.

$$E_2 - E_1 = h\nu \tag{1.10}$$

In outflows, one sees emission in both permitted emission lines and forbidden emission lines (FELs). Permitted emission lines, arising from electric dipole transitions, have high $A_{21}$ coefficients, meaning their excited states are short-lived. However, FELs, arising from magnetic dipole or electric quadrupole transitions, have much lower $A_{21}$ coefficients, meaning they have long-lived excited states, described as metastable. Atomic FELs are denoted with square brackets, and are not strictly forbidden transitions, rather, they have very low probabilities of occurring in typical laboratory conditions. However, the relatively low-densities associated with the post-shock regions in outflows allow such long-lived excited states to decay radiatively, rather than from collisional de-excitation. In contrast, permitted lines generally arise from higher density and higher temperature regions, for example near the base of the outflow, where accretion and outflow-launching processes dominate, or at energetic shocks in the flow. Often, FELs dominate the emission originating in post-shock gas in outflows, as they are generally too cool to produce strong permitted emission lines, due to the inability to significantly populate their

upper energy levels (Hartigan, 2008). An emission line is said to have reached its critical density at a gas density when the rate of radiative decay equals the rate of collisional de-excitation (Hartigan, Edwards, and Ghandour, 1995). This can occur in high-density regions where there are more particles available for collisions. If this critical density is exceeded for a particular emission line, then it is more likely that the excited particles will de-excite collisionally rather than decay radiatively. This results in the quenching of a particular emission line, if the density is high enough, where collisional de-excitation prevents photons being emitted, as the excited particles loose energy through collisions before they can spontaneously emit a photon (Hartigan, 2008). As different emission lines have different critical densities, one can probe regions of differing densities with differing emission lines. The critical densities of emission lines in the context of shocks generated in outflows is generally only applicable to FELs. In permitted emission lines, as the $A_{21}$ coefficients are much higher, the critical densities of these lines are correspondingly much higher due to the fact that collisional de-excitation is unlikely to compete with their rapid radiative decay.

One sees outflow emission in a plethora of emission lines, from molecular, atomic, and ionic transitions, spanning the electromagnetic spectrum. In the optical and IR wavelength regimes, one sees outflow emission in permitted emission lines such as the strong hydrogen recombination lines in the Balmer (H$\alpha$, H$\beta$), Paschen (Pa-$\beta$), and Brackett (Br-$\gamma$) series of hydrogen (Bally, 2016). One also sees a variety of atomic FELs (from oxygen, nitrogen, sulphur, iron, silicon, calcium, neon, etc.) in various states of ionisation, such as [O I], [O II], [O III], [N II], [S I], [S II], [Fe II], [Si II], [Ca II], [N II] and so on. One also sees molecular emission from species such as molecular hydrogen and carbon monoxide ($H_2$, CO), tracing regions of the outflow with weaker shocks and material entrained by the outflow. At radio wavelengths, one sees predominantly molecular emission lines such as CO, SO, and SiO. The low-velocity component of an outflow is well-traced by purely rotational transitions of CO, due to the molecules abundance and ease of excitation. As the gas in the post-shock region cools by radiative decay, one observes progressively lower ionisation emission lines. For example, an energetic high-velocity shock may emit [O III] emission lines close to the shock front, followed by lines of [O II], and lastly [O I] (Dopita, 1976).

Spectroscopy of emission lines allow measurements of the radial velocity

($v_{\rm rad}$) of the emitting gas, through the Doppler shifting of the emission line. Doppler shifting refers to the offset in an emission line's rest wavelength, the wavelength the emission line emits at if the emitting source is stationary, and the observed wavelength, due to the relative motion of the emitting region towards or away from the observer. Redshifted emission lines refer to the shifting of the emission line to longer wavelengths due to the emitting region moving away from the observer. Blueshifted emission lines refer to the shifting of the emission line to shorter wavelengths due to the emitting region moving towards the observer. The measurement of spectral emission lines also allow the determination of an outflow's fundamental parameters, such as temperature, electron density, and ionisation fraction (Frank et al., 2014; Ray and Ferreira, 2021). These properties are measured from the ratios of the intensities associated with different emission lines. For example, the electron density ($n_{\rm e}$) can be derived from the ratio of the [S II] doublet at 6716 Å and 6731 Å (Bacciotti and Eislöffel, 1999; Osterbrock and Ferland, 2006), which have closely spaced energy levels. As $n_{\rm e}$ increases in dense regions, collisional de-excitation increasingly competes with radiative decay. The [S II] line at 6716 Å has a comparatively lower critical density than the [S II] $\lambda$ 6731 Å emission line, meaning that as the density increases, the [S II] $\lambda$ 6716 Å emission line increasingly becomes quenched, therefore reducing the ratio of the two emission lines (Hartigan and Morse, 2007). The gas temperature can be derived from atomic transitions with energy levels that have significantly different excitation energies. The population of higher-energy states increases with temperature, as at high temperatures, collisional excitations are more energetic, sufficiently populating higher energy levels. If a higher energy level is sufficiently populated, then radiative emission from this energy level becomes stronger, therefore increasing the line strength relative to emission lines originating from lower energy levels (Bacciotti and Eislöffel, 1999; Hartigan and Morse, 2007). The ionisation fraction can be derived using emission lines from the same element, but from different ions of that element. For example, a ratio of [O II] (singly ionised oxygen) to [O III] (doubly ionised oxygen), will provide information of the degree on ionisation. A low ratio suggests that there is a high degree of ionisation, as there is more emission from the more ionised [O III], and vice versa.

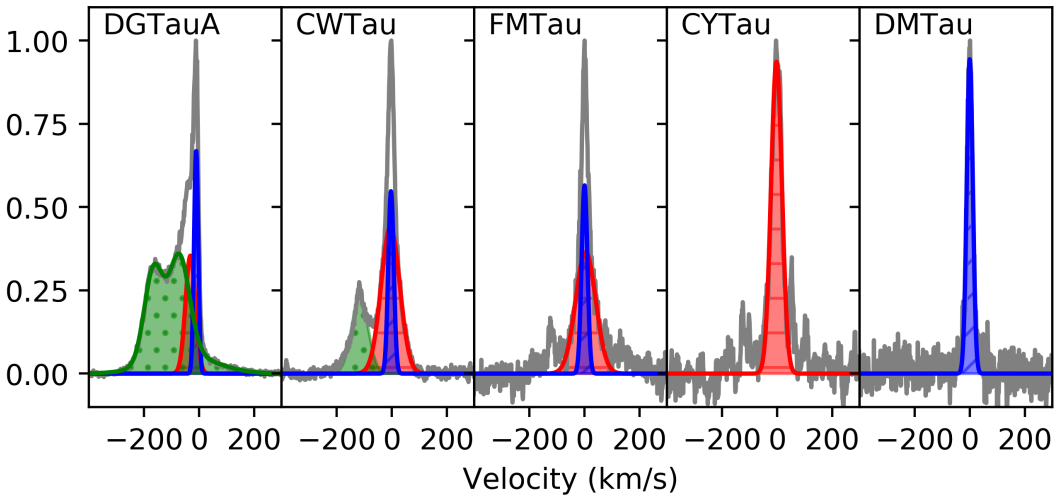


FIGURE 1.9: A sample of [O I] $\lambda$ 6300 Å emission line profiles from various objects. The y-axis represents the normalised flux of the emission lines. The line profiles are kinematically decomposed into HVCs (green regions), and LVCs (blue and red regions). The LVC is further decomposed into BCs (red regions) and NCs (blue regions). The spectra are taken from Banzatti et al. (2019), with the kinematic decompositions following Simon et al. (2016). Figure from Pascucci et al. (2023).

High-resolution spectroscopy has revealed that the spectral profiles of emission lines tracing outflows (generally from class II objects) often display various velocity components, with high-velocity components (HVC) and low-velocity components (LVC) (Kwan and Tademaru, 1988; Hartigan, Edwards, and Ghandour, 1995) (See Figure 1.9). The neutral oxygen forbidden emission line ([O I]) at 6300 Å is an excellent example of a bright FEL displaying this multi-component line profile, due to the large abundance of oxygen and favourable excitation conditions, almost always displaying a LVC and frequently displaying a HVC (McGinnis et al., 2018; Nisini et al., 2018). The HVC ($v_{\rm peak} > 30$ km s$^{-1}$), whose emission region extends far from the central source, is widely accepted to be tracing the collimated jet component of the outflow (Hirth, Mundt, and Solf, 1997; Hartigan and Morse, 2007). In contrast, the exact physical process that the LVC ($v_{\rm peak} < 30$ km s$^{-1}$), whose emission region is spatially compact (Fang et al., 2023a), is tracing is less clear, however, it is a strong candidate for an MHD disc wind tracer (Kwan and Tademaru, 1988; Kwan and Tademaru, 1995; Simon et al., 2016; Whelan et al., 2021). These velocity components in the line profiles are likely tracing a stratified velocity structure in the outflow, with high-velocity, collimated gas at the central outflow axis, the jet, surrounded by a slower-moving, less collimated flow

(Bacciotti et al., 2000). Spectroastrometric analysis has shown that the HVC displays an initial increase in velocity as distance from the central source increases, consistent with an accelerating jet, whereas the LVC has been shown to display a decrease in velocity with increasing distances from the source, compatible with a disc wind origin, with the sampling of flow streamlines at increasing disc radii (Whelan et al., 2021). The LVC can be further decomposed into a broad component (BC) and a narrow component (NC), based on the full width at half maximum (FWHM) of the emission line profile (Simon et al., 2016; McGinnis et al., 2018). The BC has a FWHM between $\sim 40$ – 100 km s$^{-1}$ and a peak velocity of $\sim -10$ km s$^{-1}$, and the NC has a FWHM of $\sim 10$ – 30 km s$^{-1}$ and a peak velocity of $\sim -3$ km s$^{-1}$ (Rigliaco et al., 2013; Simon et al., 2016; Fang et al., 2018; Banzatti et al., 2019). The radial velocities and relatively large FWHMs associated with the BC point to an MHD disc wind origin (Simon et al., 2016), but the origin of the NC is less clear. The NC may be partly tracing a photoevaporative wind (Font et al., 2004; Ercolano and Owen, 2010; Gorti et al., 2011; Rab et al., 2023). However, mounting evidence, such as the correlation of the NC's velocities and FWHMs with the BC, and the origin of emission deep within the gravitational potential well of the central star, point to the NC to be predominantly tracing an MHD disc wind (Pascucci et al., 2023).

### 1.3.3 Outflow evolution

Young, less evolved sources are characterised by powerful outflows, and the outflow power is found to be strongly correlated to the accretion luminosity, indicating a strong relation between accretion and ejection activity (Ray and Ferreira, 2021). More evolved sources display decreased mass accretion rates and consequently, weaker outflows, due to disc dissipation. This points to an evolution of the outflow, and an evolution of the accretion activity in line with the evolution of the object itself. Characteristic ages of class 0 sources are of the order of $10^4$ years, class I $\sim 10^5$ years, and class II $\sim 10^{5.5}$ – $10^7$ years (Pascucci et al., 2023). Outflows from class 0/I/II sources share many common features, including highly-collimated jets, and wider winds, implying that the accretion mechanism and ejection mechanism is consistent over a range of ages and accretion rates. There exists a distinction in morphology between jets and winds, in that jets display a variable knotty structure advancing along the flow, whilst slow-moving winds appear smooth in structure, with little collimation. There

is growing evidence that the slow disc winds, not the jets, are dominating mass outflow (Pascucci et al., 2023).

**Embedded class 0 outflows**

Outflows from these young embedded sources are powerful, and extend far from the driving source, on scales of 0.1 – 5 pc (Pascucci et al., 2023). These powerful outflows interact strongly with their parent envelope, generating bow shock features and opening cavities at the launching region. These cavities are filled by wide-angle winds and shocked jet material, most likely being produced by the wide-angled wind itself or, in the absence of a wind, by the lateral splash of shocked jet fluid produced by ejection-velocity variations (Bally, 2016). Class 0 sources have high mass accretion rates, between $\dot{M}_{\rm acc} = 10^{-5} - 10^{-6}\ M_{\odot}\ {\rm yr}^{-1}$ (Lee, 2020), and consequently, high mass outflow rates. They are composed of high-velocity collimated jets and wider, colder, and slower-moving molecular outflows, resulting from jet-driven entrainment of surrounding material or directly tracing disc winds. The jet component is often probed in atomic emission lines such as [S II] or [Fe II] (Frank et al., 2014; Bally, 2016), but class 0 jets are predominantly traced in molecular emission from $H_2$, and high-J, pure rotational lines of CO, SiO, and SO (Lee, 2020; Ray et al., 2023). The semi-opening angles measured for these highly collimated jets are $\sim 1°–4°$ (Lee, 2020; Bjerkeli et al., 2019). Mass outflow rates ($\dot{M}_{\rm out}$) from the jet component are of the order of $\sim 20\%$ of the mass accretion rate onto the central source, derived from CO emission (Lee, 2020), and $\sim 10\%$ of the mass accretion rate from optical and IR atomic lines (Hartigan, Morse, and Raymond, 1994; Bally, 2016). The wide-angled outflow component from these sources is observed in lower excitation molecular transitions such as those from SO and $SO_2$. The semi-opening angles of these wider flows is expectedly larger than the jet component, with values ranging from $\sim 20°–45°$ (Lee et al., 2018; de Valon et al., 2020; Lee et al., 2021). Mass outflow rates in the wide-angled wind are measured to be of the order of the mass accretion rate ($\dot{M}_{\rm out} \approx \dot{M}_{\rm acc}$) (de Valon et al., 2020). If this is found to be typical, then one can conclude that the wide-angled wind component of the outflow ejects significantly more mass than the jet, limiting the amount of parent envelope mass ending up in the central star, and contributing strongly to disc evolution, dissipating the disc mass reservoir. These wide-angled molecular outflows display launch regions radially beyond 20 au from the central source, hinting at material ejected directly

from the disc surface (Launhardt et al., 2009; Bjerkeli et al., 2016; Tabone et al., 2017; de Valon et al., 2020; Lee et al., 2018; Zhang et al., 2018; Pascucci et al., 2023). Furthermore, they often show a nested velocity structure with progressively lower outflow speeds and larger specific angular momenta, as the disc radii increase.

**Class I outflows**

Transitioning to class I outflows, the cavity opened by the outflow is generally wider, with the winds inflating the cavity (Offner et al., 2011). The wide-angled winds progressively emerge more clearly, extending over a few hundred au along the jet (Garcia Lopez et al., 2010). The outflows are less powerful than their class 0 counterparts, but observably faster-moving, and generally extend further from the driving source, simply due to their dynamical age (Bally, 2016). As the outflows grow larger than the size of their parent core, or cloud, they blow out and interact with the surrounding ISM, depositing momentum. Class I sources have lower mass accretion rates, between $\dot{M}_{\rm acc} = 10^{-6} - 10^{-9}$ $M_\odot$ yr$^{-1}$ (Alcalá et al., 2014; Fiorellino et al., 2021), and consequently, lower mass outflow rates. Jet tracers switch to predominantly atomic emission lines such as H$\alpha$, [O I], [S II], and [Fe II], reflecting the decreasing interaction with the diminishing molecular envelope, and the increasing jet gas excitation and ionisation (Nisini et al., 2015). However, $H_2$ remains an important tracer of jet emission (Bally, 2016). The narrow semi-opening angles measured for these highly collimated jets remain relatively unchanged compared to those originating from class 0 sources (Erkal et al., 2021b). Mass outflow rates ($\dot{M}_{\rm out}$) from the jet component are of the order of $\sim 10\%$ of the mass accretion rate onto the central source, derived from optical and IR atomic emission lines (Ray and Ferreira, 2021). The wide-angled outflow component from these sources is observed in lower excitation molecular transitions such as those from $H_2$ and CO (Beck et al., 2008; Güdel et al., 2018). The semi-opening angles of these wider flows is, again, expectedly larger than the jet component, with values ranging from $\sim 20°$– $40°$ (Launhardt et al., 2009; Davis et al., 2011; Garcia Lopez et al., 2013; Zapata et al., 2015; Delabrosse et al., 2024). Mass outflow rates in the wide-angled wind are measured to be of the order of the mass accretion rate ($\dot{M}_{\rm out} \approx \dot{M}_{\rm acc}$) (Lesur, 2021; de Valon et al., 2022). These wide-angled molecular outflows display launch regions radially beyond 5 au from the central

source, again hinting at material ejected directly from the disc surface (Bjerkeli et al., 2016; de Valon et al., 2022; Pascucci et al., 2023).

**Evolved class II outflows**

In the class II stage, the accretion rate drops significantly due to a clearing of available material, as these objects are characterised by their relatively sparse envelopes and prominent discs. Class II sources span a wide range of accretion rates, encompassing sources with full dust discs and outflows, to sources with dissipating discs and no evidence of jet launching. The mass accretion rates for these sources typically ranges from $\dot{M}_{\rm acc} = 10^{-8} - 10^{-12}$ $M_\odot$ yr$^{-1}$ (Alcalá et al., 2014; Manara et al., 2017; Nisini et al., 2018; Manara et al., 2023), however, there exists a handful of high accretors in the class II phase with mass accretion rates $> 10^{-8}$ $M_\odot$ yr$^{-1}$. Due to the lower accretion rates, the outflow weakens, spatially extending less from their central sources, and displaying greatly reduced environmental interaction, due to the dissipation of the envelope. Jet tracers remain predominantly atomic, with the exception of $H_2$ emission, with emission in lines such as H$\alpha$, [O I], [S II], and [Fe II] (Ray et al., 2007; Bally, 2016). The narrow semi-opening angles measured for these collimated jets are reminiscent of class I jets, with semi-opening angles of $< 5°$ (Pascucci et al., 2023). Unlike their class 0/I counterparts, whose outflows are generally spatially resolved, much of what is inferred from class II outflows comes from spectroscopy of spatially unresolved forbidden emission lines, with [O I] $\lambda$ 6300 Å being one of the most dominant tracers due to it's abundance, being detected in 80 – 90% of accreting class II objects. The components of these spatially unresolved outflows are differentiated by HVCs and LVCs, as discussed in Section 1.3.2. Mass outflow rates ($\dot{M}_{\rm out}$) from the jet are again of the order of $\sim 10\%$ of the mass accretion rate onto the central source, derived from optical and IR atomic emission lines (Hartigan, Edwards, and Ghandour, 1995; Nisini et al., 2018; Ray and Ferreira, 2021). The wide-angled outflow component from these sources is again observed in lower excitation molecular transitions such as those from $H_2$ and CO (Beck et al., 2008; Güdel et al., 2018), however, optical forbidden lines such as those from [O I] and [S II] are also well-established tracers of wide-angled winds, often tracing very compact emission (Natta et al., 2014; McGinnis et al., 2018; Nisini et al., 2018; Whelan et al., 2021; Whelan, Murphy, and Pascucci, 2023; Fang et al., 2023b). The semi-opening angles estimated for these wide-angled flows range from $\sim 25°$– $35°$ (Agra-Amboage

et al., 2014; Güdel et al., 2018; Louvet et al., 2018; Garufi et al., 2020), and often show layering in emission, with higher-velocity $H_2$ emission being nested within the lower excitation and slower-moving CO emission (Pascucci et al., 2024). Mass outflow rates in the wide-angled wind are again measured to be of the order of the mass accretion rate ($\dot{M}_{\rm out} \approx \dot{M}_{\rm acc}$) (Louvet et al., 2018; Pascucci et al., 2023), but can be comparable to the jet mass loss rate in some cases ($\sim 10\%$ $\dot{M}_{\rm acc}$). However, these low mass outflow rates derived predominantly from spatially unresolved optical FELs have associated uncertainties, originating from assumed gas temperatures and wind geometries, especially the vertical extent of the wind (Natta et al., 2014; Fang et al., 2018). If these wide-angled winds are predominantly molecular (e.g. Pascucci et al., 2020), then these optically inferred mass outflow rates are lower limits. The LVCs or wind components from class II sources also display evidence of originating from extended disc radii (Pascucci et al., 2023).

### 1.3.4 Discerning the launching mechanism

Discerning the exact mechanism behind outflow launching, and in doing so, unravelling the significance that outflows play in star formation, disc evolution, and planet formation, is challenging, and requires observations of the launching region of the outflow. The need for such observations is due to loss of information once the outflow starts interacting with the surrounding ambient material, and once the outflow starts self-interacting, resulting in complex shock features that tell one little about the launching mechanism. It is observationally difficult to discern the launching mechanism with current instrumentation (Frank et al., 2014), since the acceleration and collimation regions of outflows are located close to the driving source. Furthermore, the launching regions are often deeply embedded, especially in early evolutionary stages when the outflows are at their most powerful. Moreover, it is not just spatial information, but velocity information that is required (which requires spatially and spectrally resolved line emission), since different models predict very different kinematic behaviour in the vicinity of the launch zone. However, advances in ground-based adaptive-optics (AO) for optical and NIR Integral Field Spectrometers (IFS; Section 2.2) are allowing the investigation of launch regions of outflows, providing both spatial and spectral information (Dougados, 2008; Ray and Ferreira, 2021). Further to this, the new generation of spectro-interferometric instruments, such as GRAVITY (Eisenhauer et

al., 2011; Labdon et al., 2019), are beginning to allow the measurement of the extent, position, and velocity of line emission very close to the driving source.

The mapping of line emission close to the driving source permits the discrimination between the various outflow launching models (X-winds, disc winds, and stellar winds), which predict outflow emission to have different initial spatial widths and kinematic properties. Measuring the terminal velocity of the outflow, which is reached at tens of au, can provide some clues to the launching mechanism (Ray and Ferreira, 2021). Disc winds, for example, are expected to have velocities proportional to the Keplerian velocity at the launching radius, while stellar winds are thought to exhibit a different velocity scaling. The disc wind model also predicts that line emission should originate from an extended region in the disc plane, straddling the central source, whereas the X-wind model predicts that line emission should originate from a much more compact and confined region, near the co-rotation radius of the disc. Furthermore, for spatially resolved emission, one can probe the velocity structure of the outflow. For example, the disc wind model predicts a layered kinematic stratification perpendicular to the outflow axis, as the wind is launched from the disc surface at different radii at local Keplerian velocities, and later accelerates towards the Alfvén radius (Ferreira, 2009). This kinematic stratification, sometimes analogised to onion-like layering, with velocity decreasing with increasing polar angle points to radially extended disc winds launched from the co-rotation radius outwards (Lavalley-Fouquet, Cabrit, and Dougados, 2000). In addition, outer streamlines in the radially extended disc wind are predicted to be cooler than inner streamlines, and hence they will be highlighted in lower-excitation emission lines, such as those from CO (Delabrosse et al., 2024), producing a layering in chemistry also. The detection of emission in molecular material, such as emission in CO and SiO, may be tracing material lifted directly from the disc, thus pointing towards a disc wind. In contrast, the X-wind model is not expected to display a spatially layered kinematic structure, as the launch region is concentrated near the inner edge of the disc. Both X-winds and stellar winds are launched close to the driving source, implying higher temperatures. In this case, molecular material is dissociated and ionised, meaning molecular winds are not expected in these models. However, it is possible that the molecular component seen in outflows is not tracing a disc wind, where material is lifted directly from the disc (Louvet et al., 2018; de Valon et al., 2022; López-Vázquez et al., 2024), but instead is

tracing jet-entrained molecular material from the surrounding envelope (Arce et al., 2013; Rabenanahary et al., 2022).

A key diagnostic for confirming magneto-centrifugally launched outflow models is outflow rotation (Pudritz and Ray, 2019; Ray and Ferreira, 2021). If outflows are launched from a rotating star-disc system as MHD outflows, then they themselves are expected to rotate in the same sense as the disc, carrying away angular momentum from the star and disc. Disc wind, X-wind, and stellar wind models therefore all predict outflow rotation, however, the key discrimination between these models is the amount of angular momentum transported in the outflow. The amount of angular momentum per unit mass contained in an outflow is a function of the outflow launching radius, with winds launched at larger disc radii carrying more angular momentum. This results in an important difference between outflows launched from extended disc regions and outflows launched near the co-rotation radius, as is the prediction for X-wind models, with the former extracting more angular momentum flux per unit mass. Therefore, measurements of outflow rotation that lead to estimates of specific angular momentum are critical for constraining MHD outflow launching models, providing information as to where the outflow was launched from.

Detecting jet rotation is observationally challenging due to the difficulty in spatially resolving the jet axis, transverse to the flow direction (Dougados et al., 2000), and measuring systematic shifts in the radial velocity across the jet axis. Furthermore, the toroidal velocity is expected to be only a small fraction of the poloidal velocity (Frank et al., 2014). Early searches for jet rotation were performed with the Space Telescope Imaging Spectrograph (STIS) on HST (Hubble Space Telescope) (Bacciotti et al., 2002; Woitas et al., 2005; Coffey et al., 2007). These studies were performed by orientating the spectrometer slit either parallel or transverse to the outflow axis, and as close as possible to the central star, to minimise false rotation signatures originating in outflow interaction with the environment. The radial velocity differences between each side of the jet, equidistant from the jet axis, were of the order of $5 - 25$ km s$^{-1}$. These outflow rotation measurements placed the wider components of the flows as originating from disc radii up to 2 au, therefore favouring the disc wind model (Coffey, 2017). However, as this method does not resolve the innermost layers of the outflow, at the jet axis, one cannot exclude stellar wind or X-wind components (Frank et al., 2014).

Wider-angled components of the outflow can offer more information about angular momentum transport. As the lateral component of these wide-angled winds can more readily be spatially resolved, obtaining outflow rotation measurements is more promptly achievable (Tabone et al., 2017; Zhang et al., 2018). Measuring outflow rotation signatures using only the high-velocity jet counterparts is more challenging and requires high-angular resolution observations (Coffey et al., 2004; Coffey et al., 2007; Lee et al., 2017). A means of achieving high-angular resolution, and probing outflows close to their launching regions where there exists high extinction, is to use millimetre-interferometry, such as that offered with ALMA (The Atacama Large Millimeter/submillimeter Array). Using this approach, molecular outflow rotation has been confirmed in many cases, Orion Source I (Hirota et al., 2017), TMC-1A (Bjerkeli et al., 2016), HH 212 (Lee et al., 2017), HH 211 (Lee et al., 2018), HH 30 (Louvet et al., 2018), OMC2/FIR6b (Matsushita et al., 2021), and several outflows in NGC1333 (Choi, Kang, and Tatematsu, 2011; Chen et al., 2016; Zhang et al., 2018). Rotating molecular cavities have also been confirmed in all evolutionary stages of low-mass star formation, in class 0 objects (e.g. HH 212, IRAS 4C in Tabone et al., 2017 and Zhang et al., 2018), in class I objects (e.g. TMC 1A and DG Tau B in Bjerkeli et al., 2016 and de Valon et al., 2020), and in class II objects (e.g. HH 30 in Louvet et al., 2018). In these confirmations of outflow rotation, the outflow launching regions were inferred to be up to, and beyond, disc radii of 10 au (Tsukamoto et al., 2023), subsequently favouring the disc wind model. However, cases of counter-rotation have also been observed, where the outflow rotation signature is opposite to the disc rotation direction (Cabrit et al., 2006; Louvet et al., 2016). This could be due to asymmetric shocks, outflow precession, and wiggling in the outflow (Cabrit et al., 2006; Cerqueira et al., 2006; Coffey et al., 2015; Louvet et al., 2016; Erkal et al., 2021a). Therefore, inferred outflow launching radii from outflow rotation measurements are likely upper limits (Pascucci et al., 2023).

Combining measured mass outflow rates ($\dot{M}_{\rm out}$) from outflows with rotation measurements allows the angular momentum contained within the outflow to be derived (Maurri et al., 2014). If the outflow is responsible for removing excess angular momentum from the disc, therefore permitting accretion, the mass outflow rate and the mass accretion rate have the relation presented in Equation 1.11. Here, $\Omega$ is the angular velocity at the launching radius of the outflow ($r$), which can be approximated by the Keplerian rotation frequency,

and $r_A$ is the Alfvén radius (Pelletier and Pudritz, 1992; Bai et al., 2016; Pascucci et al., 2023). The collimated jet component of outflows is typically observed to have a mass outflow to mass accretion rate ratio of 0.01 – 0.1, meaning the majority of the angular momentum must be removed by winds.

$$\dot{M}_{acc}(r)\frac{d}{dr}(r^2\Omega) \simeq \frac{d\dot{M}_{out}(r)}{dr}\Omega(r_A^2 - r^2) \tag{1.11}$$

The left term in Equation 1.11 is the angular momentum flux extracted to allow accretion from the disc at a radius $r$ ($\dot{J}_{acc}$), and the right term in the relation is the angular momentum flux contained in the outflow at that radius ($\dot{J}_{out}$). If the outflow is launched from a narrow radial region, at a launch point $r_0$, as in the X-wind model, then the derivative terms can be replaced with local values, resulting in $\dot{J}_{acc} \approx \dot{M}_{acc}\Omega {r_0}^2$, and $\dot{J}_{out} \approx \dot{M}_{out}\Omega\,({r_A}^2 - {r_0}^2)$. It follows that the ratio of the mass outflow rate to the mass accretion rate can be written as shown in Equation 1.12, where $\lambda$ is the magnetic lever arm parameter (Blandford and Payne, 1982), as defined in Section 1.3.1. As the launching radius is fixed in the X-wind model, the momentum removed by the jet will have an approximately uniform value (Frank et al., 2014). It is expected in the X-wind model that the outflow is launched within the Alfvén radius, and therefore the expected mass outflow rate is a fraction, potentially nearing unity, of the mass accretion rate.

$$\frac{\dot{M}_{out}(r_0)}{\dot{M}_{acc}(r_0)} \sim \frac{r_0^2}{r_A^2} \approx \lambda^{-1} \tag{1.12}$$

Conversely, if the outflow is launched from extended disc radii, as in the disc wind model, the derivative terms in Equation 1.11 cannot be ignored, and one expects a gradient of momenta across the base of the extended outflow. The predicted ratio of the mass outflow rate to mass accretion rate in this case is presented in Equation 1.13. Here, $r_{in}$ is the innermost radius that the outflow launches from, the co-rotation radius, $r_{out}$ is the outer limit of the outflow launching radius, and $f_J$ is the fraction of angular momentum extracted from a disc radius $r$, and it is assumed that this fraction is constant with disc radius[4]. This shows that the mass outflow rate, integrated for the entire flow, for a radially extended disc wind can exceed the mass accretion rate onto the central star,

[4]See Ferreira (1997) and Pascucci et al. (2023) for details of the derivation.

occurring at $r_{\rm in}$. For example, recent MHD simulations of disc winds predict $\lambda \sim 2$, and $r_{\rm out}/r_{\rm in} > 10$, and assuming that accretion is permitted purely by the outflow removing angular momentum ($f_J \approx 1$), one expects mass outflow rates of more than twice the mass accretion rate at the inner launching radius (Pascucci et al., 2023). Therefore mass outflow rate measurements, in combination with mass accretion rate measurements, can help discriminate between magneto-centrifugally launched outflow models, and inform if outflows are extracting enough angular momentum to drive accretion.

$$\frac{\dot{M}_{\rm out}}{\dot{M}_{\rm acc}(r_{\rm in})} = \left[ \left( \frac{r_{\rm out}}{r_{\rm in}} \right)^{f_J/[2(\lambda-1)]} - 1 \right] \tag{1.13}$$

Another method of differentiating between outflow launching mechanisms, is to map the magnetic field strength and orientation in the launching region, however, observationally measuring the magnetic field in this region is challenging (Pudritz and Ray, 2019). Radially extended disc winds necessitate organised, large-scale magnetic fields, whist X-winds instead rely on strong stellar magnetospheres. The orientation of the fields can be inferred from linear polarisation measurements due to aligned dust grains (Ray, 2007), however, in embedded sources, it is difficult to peer through outer dust grains. Magnetic field strengths can be derived from Zeeman splitting of emission lines (Hartigan, Morse, and Raymond, 1994), however, interpreting results is not straightforward. Therefore, deriving information about the strength, orientation, and extent of the magnetic field in this region relies on proxies, generally from observable outflow properties such as the degree of collimation further from the source, and the outflow velocity structure. The presence of magnetic fields can also be indirectly inferred from outflow rotation (Pudritz and Ray, 2019; Pascucci et al., 2023). The degree of rotation, as discussed above, depends on where the outflow is launched from. In the case of the X-wind model the expected rotation is small, whereas in the disc wind model, one expects any measured outflow rotation to be correspondingly higher, as the amount of angular momentum increases with increasing disc radii (Ferreira, Dougados, and Cabrit, 2006). There is very little observational data on magnetic fields threading the inner disc region, where the outflow is launched from. However, the stellar surface magnetic fields of class II/III sources is known to be of the order of several kG (Donati et al., 2020), as derived from Zeeman splitting measurements. Measurements of field strengths in the innermost regions of accretion

discs is sparse, but Donati et al. (2005) show that the inner disc of FU Ori has similar field strengths to the parent star surface. These values of magnetic field strength, coupled with typical outflow velocities, temperatures and densities, are well capable of launching magnetically driven outflows (Tsukamoto et al., 2023).

### 1.3.5 Disc dispersal and implications for planet formation

Outflows are also thought to be integral to the eventual clearing of the protoplanetary disc and influential in the process of planet formation. Disc evolution is driven by accretion onto the central source, but outflows likely contribute significantly to mass loss from the disc throughout the lifetime of the disc, over several million years (Alexander et al., 2014). This evolutionary phase of disc dispersal is broadly associated with class II/III sources, but a variety of different physical processes contribute to the observed properties of individual discs in the process of dispersal. It is thought that the process of photoevaporation, now directly detectable, is the most plausible mechanism for disc dispersal, where the disc gradually disperses and transitions into a planetary system. Although photoevaporation can explain the inside-out clearing of dust in the later stages of discs lives in many cases, other mechanisms are likely occurring concurrently, such as interactions with forming planets and magnetically launched disc winds, as discussed in Section 1.1.2. The inside-out clearing of discs is confirmed observationally by transitional discs, discs that have large (tens of au) inner cavities. These can be observed through SED observations, with dips in the NIR part of the SED (Espaillat et al., 2014), and through increasing spatially resolved observations of discs (Ginski et al., 2016; van der Marel, 2023).

The presence of outflows likely affects planet formation, especially in the case of radially extended disc winds which are launched directly from planet-forming regions in the disc. Planet formation likely begins early in the disc lifetime, with significant substructures observed in discs around young objects, such as the class I object HL Tau (Figure 1.4) (Drazkowska et al., 2023). At these early stages of star formation, outflows are powerful and can therefore have a strong influence on the planet formation process. Radially extended disc winds may regulate the surface density of the disk, potentially shaping

the radial distribution of solids and therefore affecting the locations of pressure traps where dust accumulates (Morbidelli and Raymond, 2016; Carrera et al., 2017). Outflows may also correlate to the presence of various disc substructures, such as rings, gaps, and cavities, influencing planetary migration and altering the mass distribution of forming planets (Ogihara, Morbidelli, and Guillot, 2015; Béthune, Lesur, and Ferreira, 2017). Mass-loss throughout the disc lifetime may also influence, or even trigger, planet formation, by preferentially depleting the disc of gas, enhancing the fractional abundances of both dust and heavy elements (Gorti, Hollenbach, and Dullemond, 2015; Pudritz and Ray, 2019). Furthermore, outflows may drive significant turbulence in the disc (Miotello et al., 2023), affecting the collisional dynamics of dust grains and facilitating or hindering planetesimal formation. In the case of outflows enhancing turbulence in the disc, planetesimals likely form more efficiently due to the prevention of excessive grain settling to the disc mid-plane, and due to enhanced local solid concentrations through streaming instabilities. Conversely, strong disc winds could deplete the disk too rapidly, therefore shortening the amount of time for planet formation to occur and subsequently influencing the final architecture of planetary systems.

## 1.4 Summary of contributions to field

This section briefly highlights the contributions that this work adds to the field of star formation, with a focus on the HH 46/47 outflow system and CTTS RU Lupi.

#### Methods and analysis techniques

This work develops and applies a collection of robust IFS data reduction and analysis techniques, as discussed in detail in Section 3. These techniques include Gaussian fitting, uneven slit correction, careful continuum subtraction, flux calibration, telluric correction, Lucy-Richardson deconvolution, and PCA approaches for the analyses of SINFONI/ERIS/MUSE data cubes. Some of these reduction techniques are standard in the field, however, others are specialised correction techniques often overlooked by similar studies. Novel, and important, data analysis techniques implemented in this work are the wavelength recalibration technique using OH lines present in the spectra as a reference point, and the production of line to continuum ratio maps, allowing the

disentanglement of true line emission from scattered nebulosity. Implementing these methods enabled high confidence in kinematic results and enabled the determination of the true spatial distribution of intrinsic emission, critical when investigating the kinematics and morphology of outflow emitting regions close to their driving sources.

**HH 46/47**

Prior studies established the bipolar HH 46/47 outflow system as an excellent example of isolated star formation, consisting of high-velocity jets and wide-angled winds. This work contributes to the wealth of information on this object by providing spatially resolved kinematics of the launching region of the blueshifted outflow, observations which are necessary to characterise the launching mechanism of the flow. Utilising NIR SINFONI K-band observations, the inner few arcseconds of the blueshifted flow were mapped in atomic and molecular emission tracers. These observations revealed a radially stratified structure in kinematics, chemistry, and temperature, with hot, high-velocity emission in the centre of the flow, indicative of a disc wind launching mechanism. A velocity gradient transverse to the outflow direction was detected for the first time in $H_2$ emission. Purely rotational motion was ruled out as the primary contributor to this signal and was instead attributed to inhomogeneous density of the ambient medium or the presence of a secondary outflow. This work demonstrated the effectiveness of IFS in obtaining launch diagnostics close to the driving source of the outflow, and the feasibility of performing rotation measurements, whilst also warning against the misinterpretation of transverse velocity gradients as purely due to rotational motion. These results provide direct observational constraints that favour a layered, disc wind dominated launching mechanism.

Furthermore, this work provides multi-epoch proper motions of shock features in this outflow over a long temporal baseline in [S II] and $H_2$ emission. As well as collating previous proper motions studies, which focused on few shock features and shorter baselines, presented here is acceleration and deceleration signatures, and morphological and brightness variability, both highlighting episodic ejection and ambient medium asymmetries. These results provide constraints on how outflows carve and evolve their surrounding mediums.

**RU Lupi**

Prior studies of the CTTS RU Lupi established the forming star as having high accretion activity and a variable luminosity. Spectroscopic and spectro-astrometric evidence of an outflow comprising of a high-velocity jet and slower wind existed. Presented here are the first spatially resolved observations of the outflow emanating from RU Lupi, proving an accurate PA for the flow and the first outflow width measurements. The outflow emission was kinematically decomposed into high and low-velocity, highlighting the morphological differences between these kinematic features. Radial stratification of the outflow in velocity was observed, again favouring a disc wind launching mechanism, and geometric constraints were placed on the launching radii of the different kinematic components of the outflow. The height of the wide-angled wind could be measured for the first time, providing much needed constraints on the mass outflow rate. Together with the measured mass accretion rate, the outflow efficiency of the jet and wind was estimated. The resulting efficiency of the jet was as expected, however the efficiency of the wind was very low, suggesting that the bulk of the mass flux in the winds from CTTSs is not contained in atomic tracers.

# Chapter 2

# Telescopes and instrumentation

In this chapter, the telescopes and instrumentation used in this project are outlined. The work presented in this thesis is largely performed using observations from Integral field spectrographs.

## 2.1 ESO's VLT

The majority of observational data presented and analysed in this thesis was gathered by instruments installed on the European Southern Observatory's (ESO's) Very Large Telescope (VLT), shown in Figure 2.1. The VLT facility, part of Paranal Observatory[1] atop Cerro Paranal in the Atacama Desert in Chile, is an optical and infrared telescope at an altitude of 2636 m. The facility consists of four Unit Telescopes (UTs), each in an altitude-azimuth mount and equipped with an 8.2 m diameter primary mirror (M1), and four movable 1.8 m Auxiliary Telescopes (ATs). Each of the UTs (UT1 'Antu', UT2 'Kueyen', UT3 'Melipal', UT4 'Yepun') are of Ritchey-Chrétien Cassegrain design and host various instruments specifically designed for different observational needs. These include wide-field imagers, adaptive optics corrected cameras and spectrographs, as well as high-resolution and multi-object spectrographs, covering a broad spectral region, from the ultraviolet (300 nm) to the mid-infrared (24 μm). The UTs can be used individually with a specific instrument, or they can be combined to form an optical interferometer called the Very Large Telescope Interferometer (VLTI). Figure 2.2 displays the four UTs and the corresponding instruments installed on them.

[1] Telescopes at ESO's Paranal observatory.

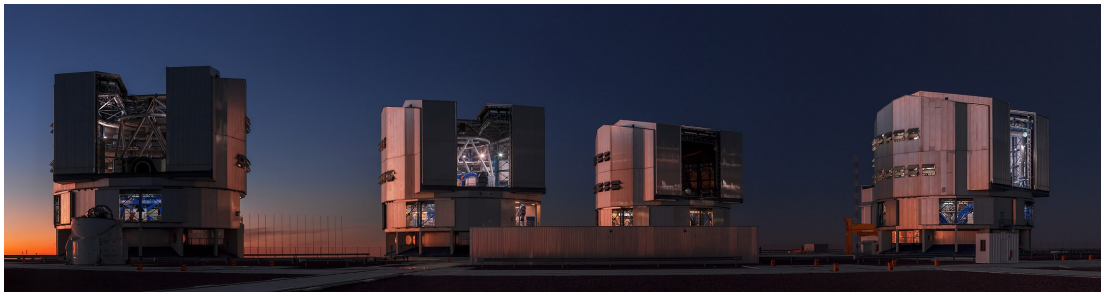

FIGURE 2.1: The four unit telescopes of the VLT at Paranal observatory. Credit: ESO/B. Tafreshi.

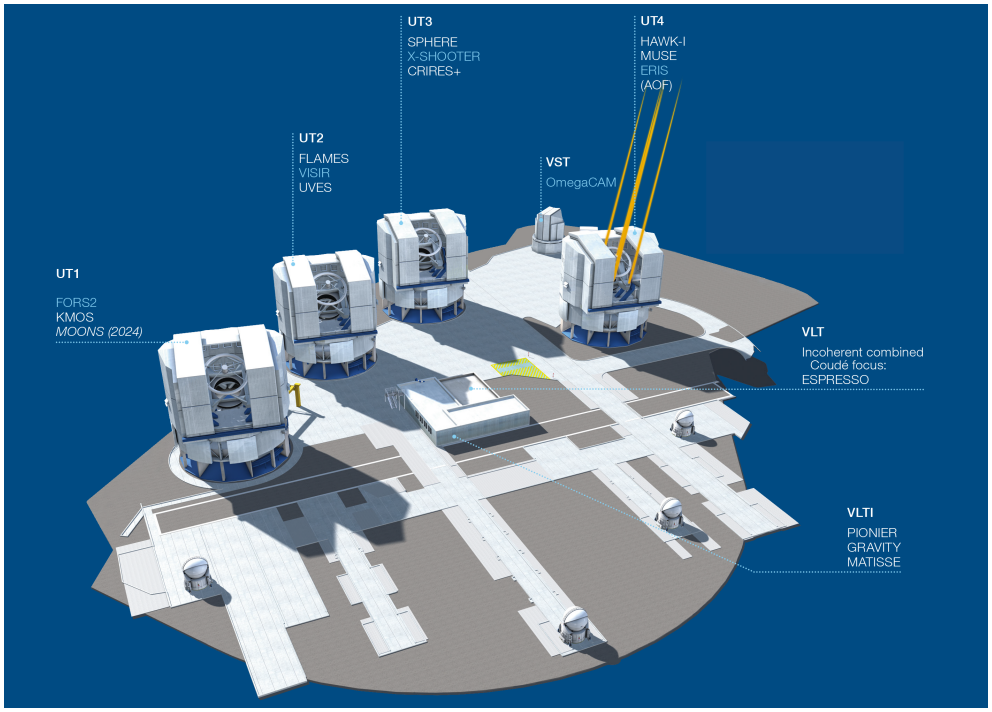


FIGURE 2.2: The telescopes and instruments of Paranal observatory. Instruments listed in blue are positioned at the Cassegrain foci of the telescopes. MOONS has not yet achieved first light. Credit: ESO.

Each of the UTs host a 1.1 m diameter hyperbolic secondary mirror (M2), and a flat tertiary mirror (M3) that reflects the incoming light to one of two instruments located at the Nasmyth foci on either side of the telescope. The tertiary mirror can also be tilted aside so that light from M2 can focus at the Cassegrain focus below the centre of M1, where another instrument is located. A Coudé focus can also be achieved using the M3 mirror to divert light to the Nasmyth focus and subsequent mirrors in an optical train. From the Coudé focus, light can be further relayed to be physically interfered in the VLTI with the other UTs. The VLT utilises advanced adaptive optics (AO) to counteract the blurring and distortion of light as it passes through Earths turbulent atmosphere. The AO systems employ wavefront sensors, which measure the distortions of the wavefronts incident on the telescopes. These distortions are processed by a real-time computer which controls a deformable mirror which deforms to counteract the wavefront distortions. In order for accurate tracking and correction of atmospheric distortions, the AO module requires a bright natural guide star (NGS) close to the object being observed. In the case of limited availability of sufficiently bright natural guide stars, sodium lasers can be used to produce artificial laser guide stars (LGS), by exciting sodium atoms in Earth's upper atmosphere.

## 2.2 Integral Field Spectroscopy (IFS)

The technique of Integral Field Spectroscopy (IFS) is a powerful tool for astronomical observations, as it combines two well established astronomical techniques, imaging and spectroscopy. Imaging provides one with a two - dimensional (2D) view of the astronomical object in question. One can learn much about the morphology of the object using imaging. Multi-epoch imaging can provide more information, where one can study the temporal variations of the object in terms of movement and brightness. A limitation associated with imaging is that there is no spectral information. Multiple observations of the object can of course be performed in different wavelength bands using filters, however the spectral information is still limited and this increases the observation time required. In contrast, spectroscopy will provide one with a spectrum from the light emitted, absorbed, or reflected by the object. Using spectroscopy, one can learn much information about the object being studied, such as the composition, temperature, movement, etc., based on emission or absorption

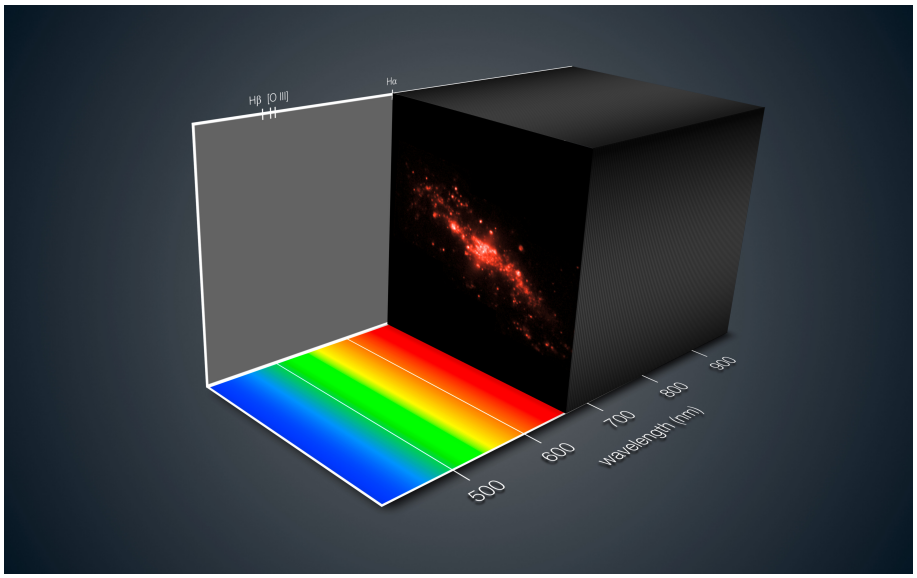


FIGURE 2.3: Illustration of a 3D data cube produced using IFS. Credit: ESO/MUSE consortium/R. Bacon/L. Calçada.

lines present in the spectrum. However, with spectroscopy, the spatial information is constrained, with observations often restricted to a narrow slit. IFS employs the use of an Integral Field Unit (IFU) to combine these two techniques into one, producing a 3D data cube, where every spatial pixel has a corresponding spectrum, providing spectroscopic information over an extended field of view. This allows extremely efficient data collection, where imaging and spectroscopy are performed simultaneously in one observation.

IFS data cubes have two axes which represent the spatial dimensions and a third axis which contains the spectral information. An illustration of an IFS data cube is displayed in Figure 2.3. Obtaining detailed spatial and spectral information simultaneously is invaluable, in that localised 1D spectra[2] can be extracted from features of interest from the science object, allowing the derivation of physical parameters as a function of position. Furthermore, narrow-band or wide-band imaging can be achieved by integrating 2D spatial slices within the cube along the spectral axis. Observations with IFUs can also be used to mimic long-slit spectroscopic observations[3]. This can be achieved by placing a pseudo-slit at some desired orientation across the observation, resulting in a 2D cut through the data cube where one axis contains wavelength

[2]A 1D spectrum represents light intensity as a function of wavelength.

[3]This produces 2D spectra, which displays how the intensity of light varies as a function of wavelength and position along a spatial dimension.

information, along the dispersion axis of the cube, and the other axis contains spatial information, along the length of the slit. When studying protostellar outflows from young stars one can, for example, place a pseudo-slit along the axis of the outflow allowing us to study the kinematics of features along the outflow, or one can place the pseudo-slit transverse to the outflow direction, providing us with a cross section along the outflow axis, which again can be used to probe the velocity structure surrounding the jet axis.

IFS data is advantageous in many ways. The technique allows the rapid collection of a large dataset and nullifies the requirement of separate continuum observations as the data cube will contain continuum emission along the spectral axis. The orientation of the detector is not as crucial as it is when performing long-slit spectroscopic observations as the choice of pseudo-slit orientation is unrestricted, and can be done after the observation. One trade-off associated with IFS data is that the spatial resolution is often not as high as with dedicated imaging instruments, and the FOV (Field Of View) is often not as wide. The spectral resolution also suffers when compared to dedicated high-resolution spectroscopic instruments.

Utilising the technique of IFS to investigate outflows provides one with powerful insights into many features of these phenomena. The spatial extent of the outflows can be mapped, allowing the investigation of their morphology in different emission lines, both atomic and molecular, therefore gathering information on substructures within the flow, such as internal shock fronts, and the interaction of the flow with the surrounding environment. The kinematical structure of the outflow can be investigated, again in different emission tracers, using the wavelength information to derive radial velocities. Spatially resolved maps of the fundamental outflow parameters, such as temperature, electron density, and ionisation fraction can be derived from emission line ratios, as discussed in Section 1.3.2. A limitation associated with using IFS instruments to study outflows is their restrictive FOV when compared with dedicated imaging instruments. Outflows are regularly extended objects, meaning a choice has to be made to study only one section of the outflow with an IFU. Of course, the entire extent of the outflow can be mapped by availing of multiple observations and mosaicing, but this is observationally time consuming and can introduce regions of lower quality data if observing conditions change over the observation period.

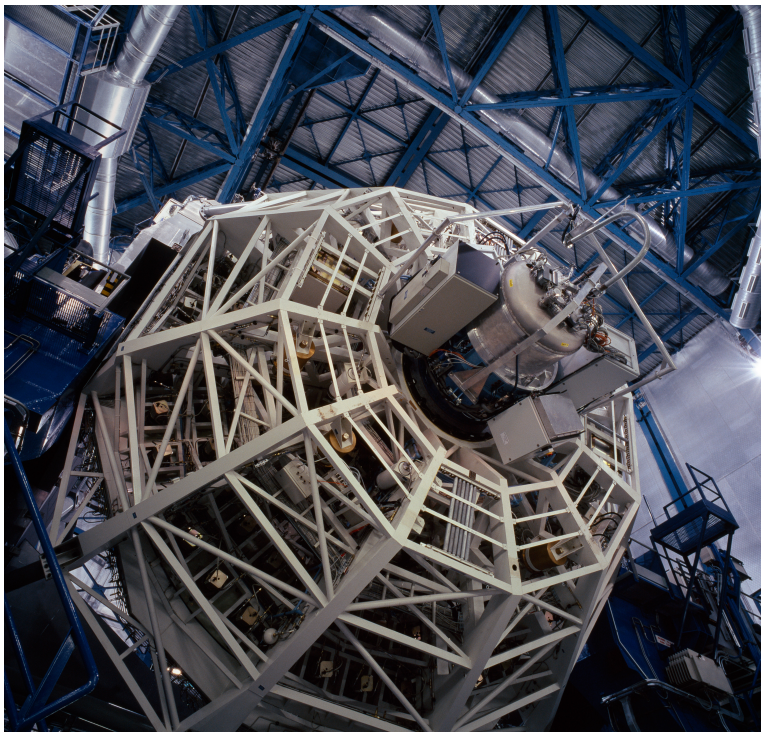

FIGURE 2.4: The SINFONI instrument mounted at the Cassegrain focus of the VLT's 4$^{th}$ unit telescope (UT4). Credit: ESO.

## 2.3 Instrumentation

### 2.3.1 SINFONI

SINFONI (the Spectrograph for INtegral Field Observations in the Near Infrared) was an AO assisted IFS, which was installed on the 4$^{th}$ unit telescope (UT4), and briefly UT3, at ESO's VLT at Paranal Observatory, Chile (See Figure 2.4). SINFONI was decommissioned in 2019 to make way for its successor, ERIS (See Section 2.3.3). SINFONI operated in the NIR part of the electromagnetic spectrum from 1.10 μm to 2.45 μm, with a spectral sampling of 0.25 nm pixel$^{-1}$. The instrument operated with four gratings, J (1.10 μm to 1.40 μm), H (1.45 μm to 1.85 μm), K (1.95 μm to 2.45 μm), H+K (1.45 μm to 2.45 μm) providing a spectral resolving power of $\sim$ 2000, 3000, 4000 in the J, H, K gratings respectively and $\sim$ 1500 in the H+K grating (Eisenhauer et al., 2003). The spectral resolving power ($R$), or spectral resolution, is defined as the smallest difference in wavelength space ($\Delta\lambda$) that can be resolved at a wavelength ($\lambda$), as shown in Equation 2.1.

$$R = \frac{\lambda}{\Delta\lambda} \tag{2.1}$$

SINFONI belongs to a category of IFUs that use an image slicing technique which relies on reflective optics, where the incoming light from the telescope is collected over a 2D FOV, which is then segmented into narrow slices. This is achieved when the incoming light is incident on narrow mirror slices, each of which have different tilt angles with respect to one another. The diverging beams from each mirror, which each represent a spatial section of the original FOV, are rearranged so that they lie next to one another in a continuous linear path. This is to ensure that the light can be processed by a long-slit spectrograph. The slices are individually sent to a long-slit spectrograph where the light from each slice is dispersed into its constituent wavelengths, resulting in a spectrum which is recorded by the instrument detector. Finally, the slices are re-assembled to restore their original spatial positions, where each spatial pixel now has an associated spectrum, essentially constructing a 3D data cube. An illustration of the image slicing IFS technique is displayed in Figure 2.5.

SINFONI operated in three modes; with FOVs of $8\farcs0 \times 8\farcs0$, $3\farcs0 \times 3\farcs0$, and $0\farcs8 \times 0\farcs8$, corresponding to spatial samplings of $0\farcs25$, $0\farcs1$, and $0\farcs025$ pixel$^{-1}$ respectively. The SINFONI FOV was sliced into 32 slitlets which is imaged onto 64 pixels of the detector, resulting in $32 \times 64 = 2048$ spectra of the imaged region. The detector was a Rockwell 2k $\times$ 2k Hawaii 2RD array that operated at 84 K. SINFONI was equipped with AO to counteract the blurring and distortion of light as it passes through Earths turbulent atmosphere. Observations could however be done without the use of AO, wherein the spatial resolution was dictated by the seeing of the observation[4].

SINFONI's FOV was suited to study the launching region outflows. One can study the morphology of the base of the outflow, close to the driving source, and investigate the interaction of the outflow with the surrounding medium that the outflow is expanding into. The NIR wavelength regime is an interesting region in which to study outflows. Instruments in this wavelength regime can also achieve high spatial resolution due to more effective AO in this

[4]The seeing refers to the blurring of astronomical images due to turbulence in Earth's atmosphere, and is quantified as the full width at half maximum (FWHM) of the star's PSF (Point Spread Function).

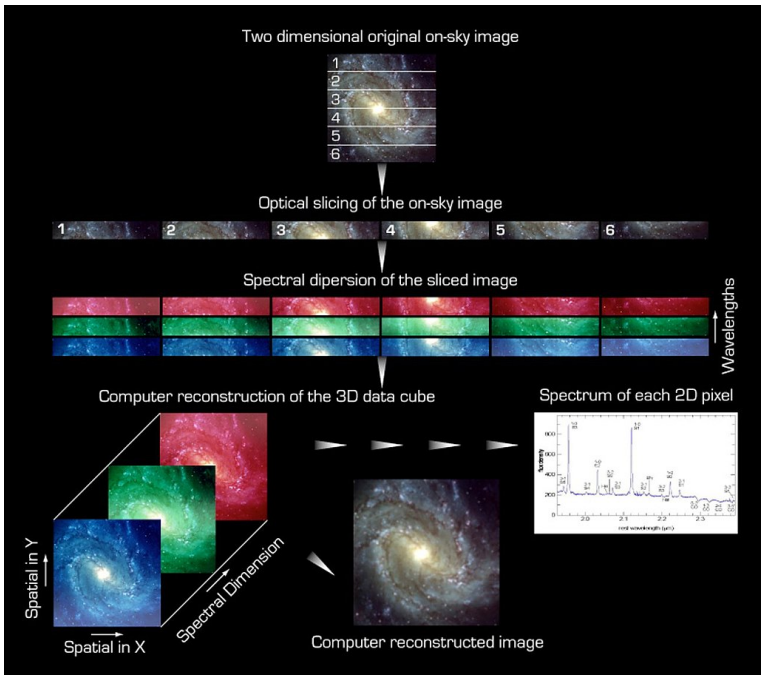


FIGURE 2.5: Illustration of the image slicing technique used in IFS instruments producing a 3D data cube. The FOV (*top*) is sliced into small slitlets which are recombined into a pseudo long-slit before being dispersed. The dispersed light is reconstructed into a data cube. Credit: ESO.

part of the spectrum, in comparison to the optical. Atmospheric turbulence affects shorter wavelengths more severely than longer wavelengths, where the Strehl ratio[5] at longer wavelengths is higher, making AO corrections easier to implement. This attainable high-angular resolution allows the study of outflow morphology, particularly of substructures within the flow. Observing the outflow in different emission tracers, such as atomic FELs and molecular emission lines, allow one to probe different components of the outflow. In this work, SINFONI is utilised in the study of the HH 46/47 outflow presented in Chapter 4.

### 2.3.2 MUSE

MUSE (the Multi Unit Spectroscopic Explorer) is an AO assisted IFS, a second-generation instrument installed on the 4$^{th}$ unit telescope (UT4) at ESO's VLT at Paranal Observatory, Chile (See Figure 2.6). MUSE operates in the optical

[5]The Strehl ratio, having a value between 0 and 1, is defined as the ratio of the peak intensity of the observations PSF, to the theoretical peak intensity for a perfect diffraction-limited system. Higher Strehl ratios correspond to sharper images with a greater fraction of light concentrated in the PSF core.

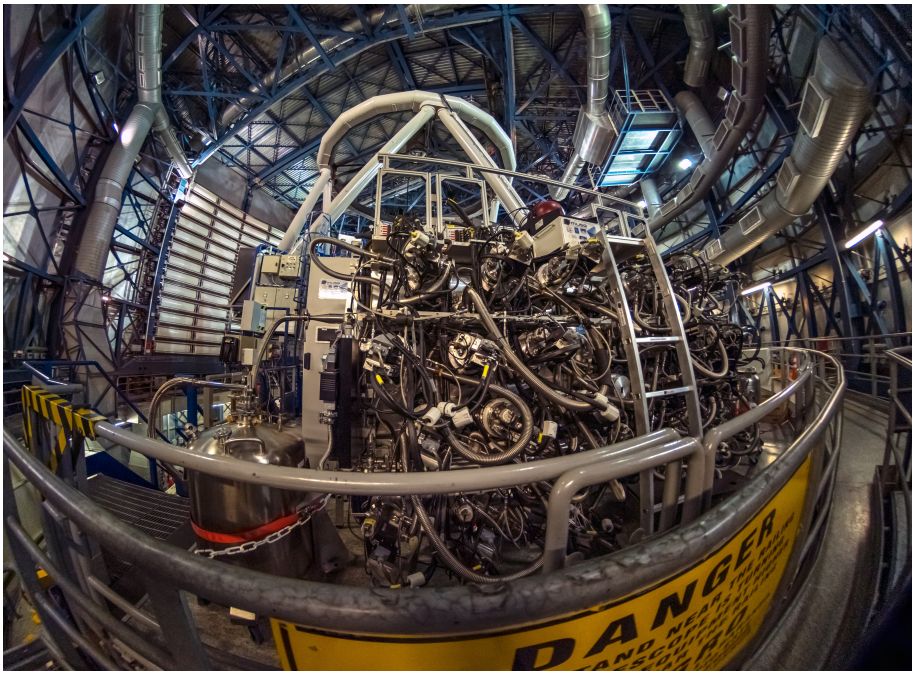


FIGURE 2.6: The MUSE instrument installed at one of the Nasmyth foci of the VLT's 4$^{\text{th}}$ unit telescope (UT4). Credit: ESO/Z. Bardon.

part of the electromagnetic spectrum, extending slightly into the NIR, from 465 nm to 930 nm. The instrument features a Wide Field Mode (WFM), with an FOV of $1'.0 \times 1'.0$ and a spatial sampling of $0''.20$ pixel$^{-1}$, and a Narrow Field Mode (NFM), with an FOV of $7''.5 \times 7''.5$ and a spatial sampling of $0''.025$ pixel$^{-1}$ (Bacon et al., 2010). The spectral resolving power varies from $R \approx 1700$ in the blue end of the wavelength range to $R \approx 3400$ in the red end, at a spectral sampling of 0.125 nm pixel$^{-1}$. MUSE makes use of the AO module GALACSI (Ground Atmospheric Layer Adaptive Corrector for Spectroscopic Imaging), which employs four sodium laser guide stars (LGS) that produce artificial guide stars in Earth's upper atmosphere. This optical AO system requires finer and faster corrections, in comparison to NIR AO systems, due to the correspondingly smaller spatial scale of atmospheric turbulence distortions at optical wavelengths.

Like SINFONI, MUSE is also an image slicer IFU. The 2D FOV is split into 24 sub-fields, where each of these optical beams are further segmented into 48 slices. These slices are rearranged into a single linear path and enter the spectrograph to disperse the light. As each of the 24 sub-fields are further segmented and passed into a spectrograph, MUSE requires 24 identical spectrographs. The light from each of the spectrographs is imaged onto a 4k $\times$ 4k,

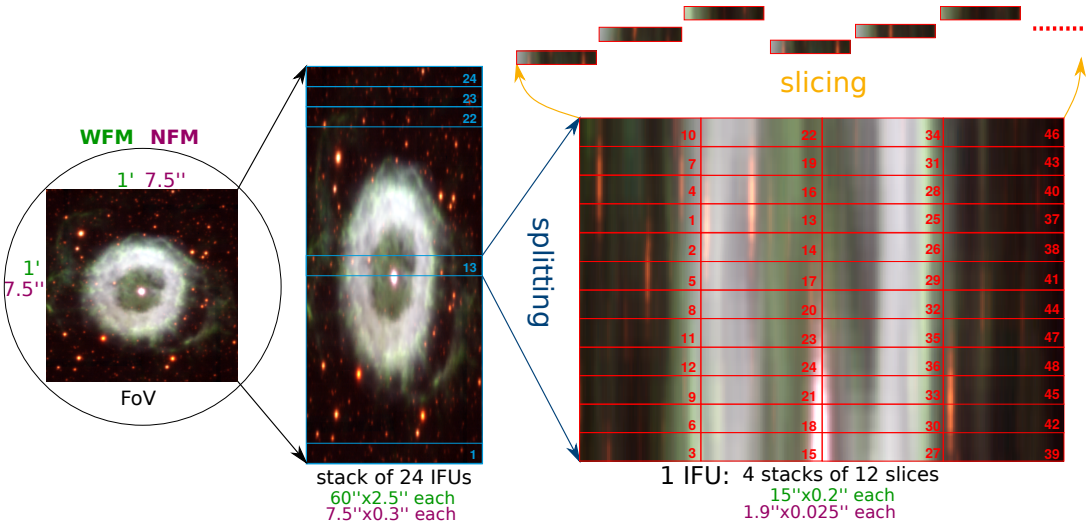


FIGURE 2.7: Illustration of the MUSE image slicing technique. The FOV (*left*) is segmented into 24 subfields. Each of these subfields are further sliced into 48 slitlets which are recombined into a pseudo long-slit before being dispersed. The dispersed light is reconstructed into a data cube (Weilbacher et al., 2020).

15 µm pixel CCD (Charge-Coupled Device) operated at 163 K. A schematic of the MUSE image slicing technique is displayed in Figure 2.7 (Weilbacher et al., 2020).

Both of MUSE's FOVs are suited to study different aspects of outflows. MUSE operated in WFM provides a relatively large FOV for an IFS instrument. This allows one to map a large extent of the outflow. MUSE operated in NFM provides a much greater spatial resolution, allowing the launching region of the outflow close to the driving source to be studied, at the cost of a much reduced FOV. The AO provided in NFM also provides a much sharper correction than that in WFM, using GALACSI's laser tomography adaptive optics (LTAO) system, which corrects turbulence at multiple altitudes. The optical-NIR wavelength regime is a valuable portion of the electromagnetic spectrum in which to study outflows. In this region there are a wide range of emission lines that trace shocked emission from outflows. MUSE in NFM is utilised in the study of the outflow from RU Lupi presented in Chapter 5.

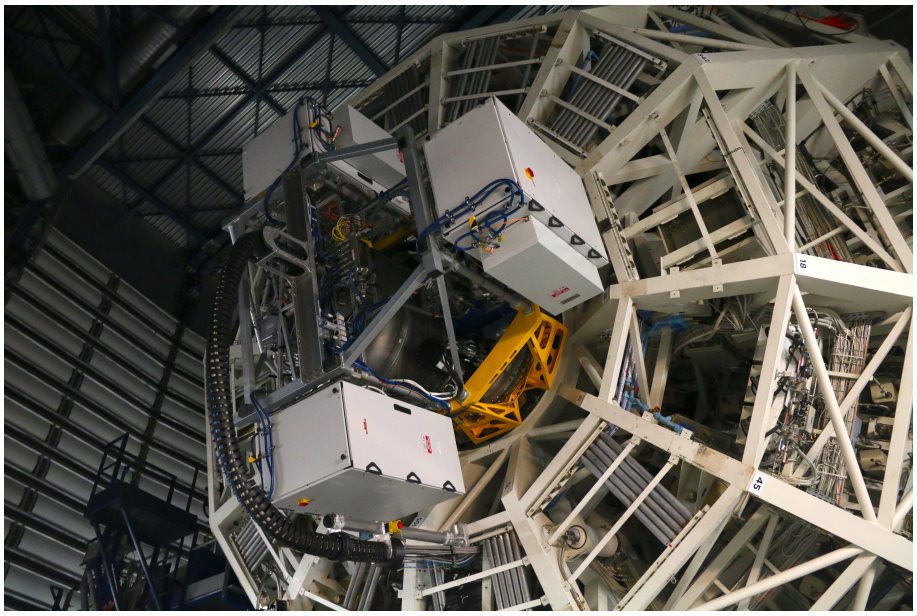

FIGURE 2.8: The ERIS instrument installed at the Cassegrain focus of the VLT's 4$^{\text{th}}$ unit telescope (UT4). Credit: UKATC/W. Taylor.

### 2.3.3 ERIS

ERIS (The Enhanced Resolution Imager and Spectrograph) is a near-infrared instrument installed on UT4, the 4$^{\text{th}}$ unit telescope of the VLT at Paranal Observatory, Chile (See Figure 2.8). ERIS was installed in February 2022, and achieved first light in November 2022. The instrument succeeds ESO's SINFONI and NACO instruments. It has two science arms; SPIFFIER and NIX. SPIFFIER is an IFS covering the J to K bands, NIX is an imager covering the J to M bands. SPIFFIER can operate in 12 grating configurations; 3 low-resolution ($R \approx 5000$) configurations, covering the J, H and K bands, and 9 high-resolution ($R \approx 10{,}000$) configurations, 3 for each broader band. SPIFFIER can operate in three modes; with an FOV of $8\farcs0 \times 8\farcs0$ with a spatial resolution of $0\farcs25$ pixel$^{-1}$, with an FOV of $3\farcs2 \times 3\farcs2$ with a spatial resolution of $0\farcs1$ pixel$^{-1}$, and with an FOV of $0\farcs8 \times 0\farcs8$ with a spatial resolution of $0\farcs025$ pixel$^{-1}$. Like SINFONI and MUSE, SPIFFIER is also an image slicer IFU. The 2D FOV is split into 32 slitlets, which is then rearranged into a pseudo-slit which is then focussed onto a spectrograph. The light from the spectrograph is imaged onto a 2k $\times$ 2k, 18 µm pixel HAWAII 2RG detector operated at 77 K.

NIX can do short-wavelength imaging (1.0 – 2.5 µm) with an FOV of $27\farcs0 \times 27\farcs0$, and a spatial resolution of $0\farcs013$ pixel$^{-1}$, or with an FOV of $55\farcs0 \times 55\farcs0$, and a spatial resolution of $0\farcs027$ pixel$^{-1}$, in broad or narrow-band filters.

NIX can also do long-wavelength imaging (2.5 – 5.0 μm) with an FOV of $27''.0 \times 27''.0$, and a spatial resolution of $0''.013$ pixel$^{-1}$ in broad or narrow-band filters. Preliminary results from ERIS on the HH 46/47 outflow are presented in Section 4.2.3 in Chapter 4.

### 2.3.4 Other instruments

The following instruments were utilised for optical and NIR narrow-band imaging of the HH 46/47 outflow, for the proper motions study of the outflow presented in Chapter 6.

#### EMMI

EMMI (ESO Multi-Mode Instrument) was a wide-field imager, long-slit spectrograph, multi-object spectrograph and an echelle spectrograph installed on the New Technology Telescope (NTT) at La Silla Observatory, Chile. The spectrograph could perform low-resolution ($R \approx 300$ – 2000) and medium-to-high-resolution ($R \approx 5000$ – 15000) spectroscopy. EMMI covered a broad wavelength range, with a 'blue arm' in the near-ultraviolet (NUV) to optical ($\lambda$: 300 – 500 nm) and a 'red arm' in the optical to near-infrared ($\lambda$: 400 – 1100 nm). The wide-field imager had a spatial resolution of $0''.37$ pixel$^{-1}$ in the blue imager and $0''.44$ pixel$^{-1}$ in the red imager, and a maximum FOV of $7'.6 \times 7'.6$. In 1993, the detector was upgraded to a Tektronix CCD (TEK), allowing an upgrade of the red arm of the instrument to a higher spatial resolution of $0''.26$ pixel$^{-1}$, and a wider FOV of $8'.9 \times 8'.9$. In 1997, EMMI was upgraded again with an MIT Lincoln Laboratory (MIT LL) 2048 × 4096 pixel mosaic detector, allowing a spatial resolution of $0''.1665$ pixel$^{-1}$, and an FOV of $4'.5 \times 9'.0$.

#### EFOSC2

EFOSC2 (the ESO Faint Object Spectrograph and Camera v.2) is a multi-mode instrument, capable of imaging, low-to-medium-resolution spectroscopy, polarimetry, and multi-object spectroscopy, that was installed on the ESO-3.6 metre telescope at La Silla Observatory. It operates primarily in the optical regime, with a wavelength range between 305 nm and 1110 nm. The FOV of the imager is $4'.1 \times 4'.1$ with a spatial sampling of $0''.12$ pixel$^{-1}$. The spectral resolution ranges from $R \approx 200$ – 2000 depending on the grating and slit width.

### FORS2

FORS2 (FOcal Reducer/low dispersion Spectrograph 2) is a multi-mode instrument installed on UT1, the 1st unit telescope of the VLT at Paranal Observatory. The instrument is capable of imaging, polarimetry, long-slit spectroscopy, and multi-object spectroscopy. The instrument operates primarily in the optical with a wavelength range of 330 nm to 1100 nm. FORS2 imaging can operate with two different magnifications, an FOV of $7'.1 \times 7'.1$ with a spatial sampling of $0''.25$ pixel$^{-1}$ (with the standard resolution collimator), and an FOV of $4'.25 \times 4'.25$ with a spatial sampling of $0''.125$ pixel$^{-1}$ (with the high resolution collimator). The instrument's spectral resolution varies from $R \approx 260 - 2600$.

### ISAAC

ISAAC (Infrared Spectrometer And Array Camera) was an imager and spectrograph installed on UT3, the 3rd unit telescope of the VLT at Paranal Observatory. The instrument operated in the near to mid-infrared with a wavelength range of 1 μm to 5 μm. The instrument could operate in either the short-wavelength (SW) imaging mode (1 μm to 2.5 μm) or long-wavelength (LW) imaging mode (2.9 μm to 5 μm). In SW mode, the instrument provided an FOV of $2'.5 \times 2'.5$ with a spatial sampling of $0''.148$ pixel$^{-1}$, and in LW mode the FOV was $1'.2 \times 1'.2$ with a spatial sampling of $0''.071$ pixel$^{-1}$. The spectral resolution of the instrument varied from $R \approx 500 - 3000$.

### HAWK-I

HAWK-I (the High Acuity Wide field K-band Imager) is a wide-field imager installed on UT4, the 4th unit telescope of the VLT at Paranal Observatory. The instrument operates in the near-infrared from 0.85 μm to 2.5 μm and offers 10 observing filters in two filter wheels, 4 broad-band filters and 6 narrow-band filters. The FOV is $7'.5 \times 7'.5$ with a spatial sampling of $0''.106$ pixel$^{-1}$. The instrument offers AO with the VLT's Ground Layer Adaptive Optics (GLAO) mode.

# Chapter 3

# Reduction and analysis of integral field observations

In this chapter, I will discuss the data reduction and analysis techniques performed on the integral field data before the presentation of the results. All datasets were first processed with data reduction pipelines provided by ESO. These pipelines performed general data reduction techniques, converting raw instrument data into IFS data cubes, as discussed in Sections 3.3.1, 3.5, 3.7. Additional data reduction and analysis was required before the extraction of results, resulting in the production of custom scripts. These methods are described in detail in Sections 3.3.2 – 3.3.7 for SINFONI, Sections 3.5.1 – 3.5.2 for MUSE, and Sections 3.7.1 – 3.7.2 for ERIS.

## 3.1 Tools for data cube analysis

Python was selected as the primary coding language for this work and was used extensively in the data analysis of the data cubes and the presented results. Several libraries in Python were employed for the analysis, including SciPy (Virtanen et al., 2020) and Astropy (Astropy Collaboration et al., 2013; Astropy Collaboration et al., 2018; Astropy Collaboration et al., 2022). Further to this, a significant portion of the analysis required the production of custom Python scripts designed specifically for these instruments and datasets. Python was also essential for the visualisation and presentation of results, where the library Matplotlib (Hunter, 2007) was almost exclusively used.

Python scripts were developed to interact with and examine data cubes. These included modules that allowed for analysis of the data, for example,

slicing of the data cubes, allowing 2D images to be extracted along the spectral axis of the cube. Additionally, modules were developed that allowed integrated images to be extracted, where multiple 2D image slices are collapsed into a single image. The extraction of sub-cubes was also essential where a select portion of the data cube was extracted between two wavelength values of choice. Modules were developed that allowed for the placement of pseudo-longslits across the FOV of the observations to extract spectra, mimicking longslit spectroscopy, and for spectra to be extracted from a feature of interest by use of an aperture. Cube rotation was also an essential tool for ease of analysis, where cubic interpolation was implemented post-rotation to ensure image quality and flux conservation. Tools such as those used for wavelength recalibration, uneven slit correction, flux calibration, telluric correction, continuum subtraction, scattered light removal, and Gaussian fitting were also developed and are discussed in detail in the following sections.

### 3.1.1 Gaussian fitting

The statistical method of modelling data points by fitting a Gaussian profile to them is used extensively in this work. A Gaussian profile, also known as the normal distribution, is a powerful analysis tool in the study of astronomical data, as a significant portion of astrophysical phenomena and instrumental effects naturally produce Gaussian shaped features, or can be well approximated by them. The general form of the Gaussian profile is shown in Equation 3.1. Here, $A$ is the amplitude of the Gaussian, $\mu$ is the mean of the distribution or the centre of the peak, and $\sigma$ is the standard deviation of the distribution. The FWHM of the Gaussian profile is related to the standard deviation, as shown in Equation 3.2, and is an intuitive measure of the width of the profile.

$$G(x) = A\, e^{-\frac{(x-\mu)^2}{2\sigma^2}} \tag{3.1}$$

$$\mathrm{FWHM} = 2\sqrt{2\ln(2)}\,\sigma \tag{3.2}$$

Fitting of Gaussian profiles is used in this work for spectral emission line

characterisation. This allows the derivation of the emission lines central wavelength, the width of the line and the intensity of the line. The fitting of Gaussian profiles is also used in determining precise positions of objects and object features. The uncertainty of the mean of the distribution, $\sigma_\mu$, or the centre of the peak, is related to the FWHM and the signal to noise ratio (S/N) of the observation as shown in Equation 3.3.

$$\sigma_\mu = \frac{\mathrm{FWHM}}{2\sqrt{2\ln 2} \times \mathrm{S/N}} \tag{3.3}$$

Relating the central wavelength measured for an emission line to the emission lines rest wavelength allows the radial velocity of the emitting region to be calculated. This is achieved using the Doppler shift of the emission line, shown in Equation 3.4, where $\Delta\lambda$ is the wavelength offset from the rest wavelength ($\lambda_{\mathrm{rest}}$), and $c$ is the speed of light in a vacuum. When utilising spectrographic observations with the intention of calculating radial velocities, the motion of the observatory location must be considered. One must correct for the Earth's movement in relation to the centre of mass, or the barycentre, of the solar system. This is known as the Barycentric Earth Radial Velocity (BERV) correction. Further to this, one must correct for the mean motion of material in the Milky Way in the neighbourhood of the sun, in other words the mean motion of material in a 100 pc radius from the sun as they orbit the centre of the galaxy. This adjustment allows the measured radial velocities to be expressed relative to a common reference frame called the Local Standard of Rest (LSR).

$$v_{\mathrm{rad}} = \frac{\Delta\lambda}{\lambda_{\mathrm{rest}}} \times c \tag{3.4}$$

## 3.2 SINFONI observations

Observations of the HH 46/47 outflow were obtained with ESO's SINFONI on the 27$^{\mathrm{th}}$ of November 2018 under ESO Program ID 0102.C-0615(A) (PI: C. Dougados). The target, HH 46/47, is discussed further in Section 4.1.1. The NIR observations were obtained using the K-band grating (1.95 – 2.45 μm) with a resolving power of R = 4000. The FOV chosen was $8\farcs0 \times 8\farcs0$ providing a spatial sampling of $0\farcs125 \times 0\farcs250$ (Eisenhauer et al., 2003). This FOV was chosen as it was well suited to encompass the base of the blueshifted outflow.

The detector was rotated 60° so that the vertical axis of the detector was parallel to the approximate CO outflow position angle (PA) (Zhang et al., 2019). This rotation was implemented to maximise the amount of outflow emission within the FOV.

The observations consisted of ten exposures of 150 s each providing an on target exposure time of 1500 s. The average seeing of the science observation was $0''.81$ and the airmass (Section 3.3.4) varied from 1.127 to 1.125. It was not possible to use the instruments AO correction due to a lack of a suitable bright point source nearby, resulting in the observation being limited by the atmospheric seeing of the night of observation. This potentially hampers the detection of fine structure present in the observation. Three exposures of 300 s were also taken for sky exposures. Two standard stars, HD 67954 (HIP 039774) and HD 73105 (HIP 042038), were also observed for flux calibration and telluric correction. The goal of the observations was to extract the 2D spatial and kinematic distribution of atomic and molecular emission lines at the base of the blueshifted outflow.

## 3.3 SINFONI data reduction and analysis

### 3.3.1 Data reduction pipeline

The data was reduced using ESO's SINFONI data reduction pipeline (Version 3.3.0) and run with ESOReflex (Freudling et al., 2013). Standard calibration files were used in the reduction. Input files include reference files (reference bad pixel map & arc line reference table), the raw frames (dark frames, flat fields, fibre frames, arc lamp frames, sky frames, telluric standard star frames, PSF frames, & science frames), and calibration products (bad pixel maps, distortion table, master flat field, master darks, slitlet distances, slitlet edge positions, & wavelength maps). More information on these input files can be found in the SINFONI user manual[1].

The data reduction pipeline was run using ESOReflex, a graphical user interface (GUI) provided with the pipeline. ESOReflex provides visual information about the data reduction steps and automates the procedure of data reduction. The data cube was corrected for bad pixels, flat-fielding, bias and

[1]SINFONI User Manual

dark signal, sky emission and a first order wavelength calibration was done using arc lamp wavelength solutions.

### 3.3.2 Wavelength recalibration

The spectral resolution of SINFONI in the K-band is approximately R = 4000 or 2.45 Å, which translates to a velocity resolution of 75 km $s^{-1}$. The spectral sampling size in terms of velocity is 38 km $s^{-1}$ at 1.95 μm and 30 km $s^{-1}$ at 2.45 μm. The first order wavelength calibration was performed using the standard procedure, applying a wavelength solution using arc lamps with well measured wavelengths as reference, with the SINFONI data reduction pipeline. However, wavelength calibration errors of approximately $\pm$ 30 km $s^{-1}$ were observed in the final data cube after data reduction using the SINFONI pipeline, which are not optimal for kinematical analysis. These calibration errors were measured by re-reducing the data with the data reduction pipeline again, but omitting the sky subtraction step from the process. This resulted in a science data cube that contained the OH telluric emission lines. These emission lines arise from the emission of hydroxyl radicals (OH) in Earth's upper atmosphere. OH molecules are produced through various chemical reactions, often involving atomic hydrogen (H) and ozone ($O_3$), and are typically found in the NIR part of the electromagnetic spectrum (0.67 – 2.62 μm) (Rousselot et al., 2000). As these lines have a radial velocity of 0 km $s^{-1}$ with respect to Earth's surface, they serve as a valuable tool for wavelength calibration. A selection of bright OH emission lines present in the observations spectrum, at various points across the FOV, were fit with Gaussian profiles. The centroid of the Gaussian fit was taken as the radial velocity of the emission line, and measurements of these lines yielded results of approximately $\pm$ 30 km $s^{-1}$ across the FOV. In order to increase the wavelength, or radial velocity calibration accuracy, a more rigorous wavelength calibration technique needed to be employed. A 2D wavelength correction map could be produced using these OH lines as a velocity reference point, accounting for possible wavelength drifts across the FOV of the observation.

As a first attempt to produce this 2D wavelength correction map, a selection of OH emission lines, located spectrally close to emission lines of interest, were fit with Gaussian profiles. These OH lines were fit at every spatial pixel in the cube and their wavelength offset from the known rest wavelength was

recorded. This effectively produced a 2D wavelength offset map for each OH line measured. Examples of these 2D wavelength offset maps are displayed in Figure 3.1. These maps were produced to correct the wavelength offset for the molecular hydrogen ($H_2$) emission line at 2.12 μm ($H_2$ 1-0 S(1)). The wavelength offsets derived from these maps are centred at approximately 2 Å, and vary from $\sim 1 - 3$ Å. In order to estimate the amount of uncertainty associated with the wavelength offsets calculated, the 2D maps were collapsed into histograms. The root mean square (RMS), or $\approx 1$ standard deviation, was taken as the uncertainty of the wavelength offset calculated across the FOV of the observation. These histograms produced for the four OH lines used are displayed in Figure 3.2. These uncertainty values are approximately $0.2 - 0.3$ Å. The spectral sampling of SINFONI is 0.25 nm, or 2.5 Å, meaning uncertainties achieved are of the order of $1/10^{\text{th}}$ of the spectral pixel size. The 2D wavelength offset maps could then be averaged, resulting in a more accurate wavelength calibration map than that provided by the data reduction pipeline.

Whilst the method of fitting individual OH lines, located near to emission lines of interest, with Gaussian profiles worked sufficiently, the process was deemed time consuming due to the number of OH lines present in the data cube (See Figure 3.3) and the fact that these OH lines needed to be fit at each individual spaxel (spatial pixel) across the FOV of the observation. Instead, another more efficient method was used to wavelength calibrate the data cube using the OH lines as velocity reference points. A cross-correlation method was chosen to produce a 2D wavelength correction map by comparing the OH emission lines present in the science cube spectra with a theoretical night-sky spectrum of emission from the upper atmosphere. The cross-correlation routine used was from the Toolkit for Exoplanet deTection and chaRacterization with IfS (TExTRIS) (Bonnefoy et al., 2014; Petrus et al., 2021; Palma-Bifani et al., 2023; Demars et al., 2023). The ESO SKYCALC tool[2] (Noll et al., 2012; Jones et al., 2013) was used to generate a synthetic night-sky spectrum that matched the night of observation and observatory location. This generated spectrum is displayed in Figure 3.3. The synthetic spectrum had a spectral resolution of R = 100,000 and was convolved with a Gaussian in order to downscale the spectral resolution to match that of the SINFONI K-band observations. An example spectrum extracted from the source position in the science cube containing OH sky lines is displayed in Figure 3.4.

[2]ESO SKYCALC tool

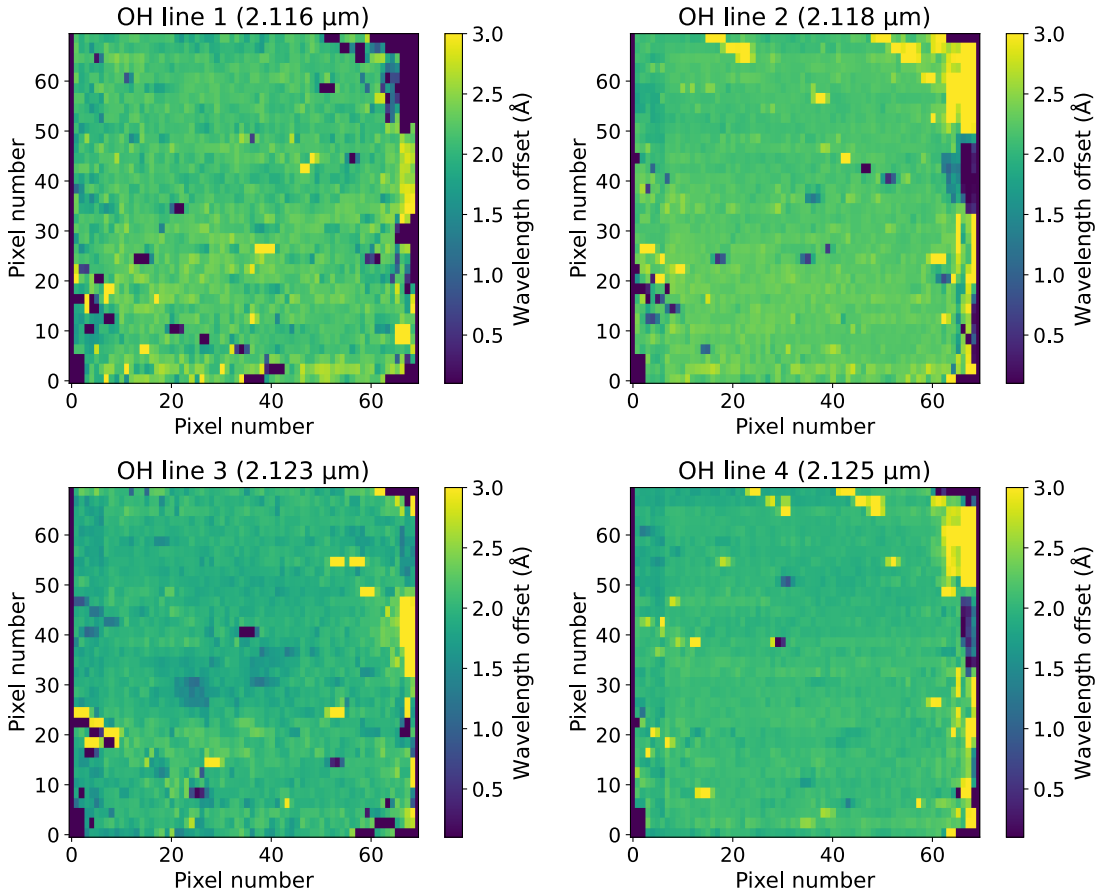


FIGURE 3.1: 2D wavelength offset maps produced using Gaussian fitting of OH lines located near to the $H_2$ 1-0 S(1) emission line at 2.12 μm. Wavelength offsets derived from the maps are centred at approximately 2 Å.

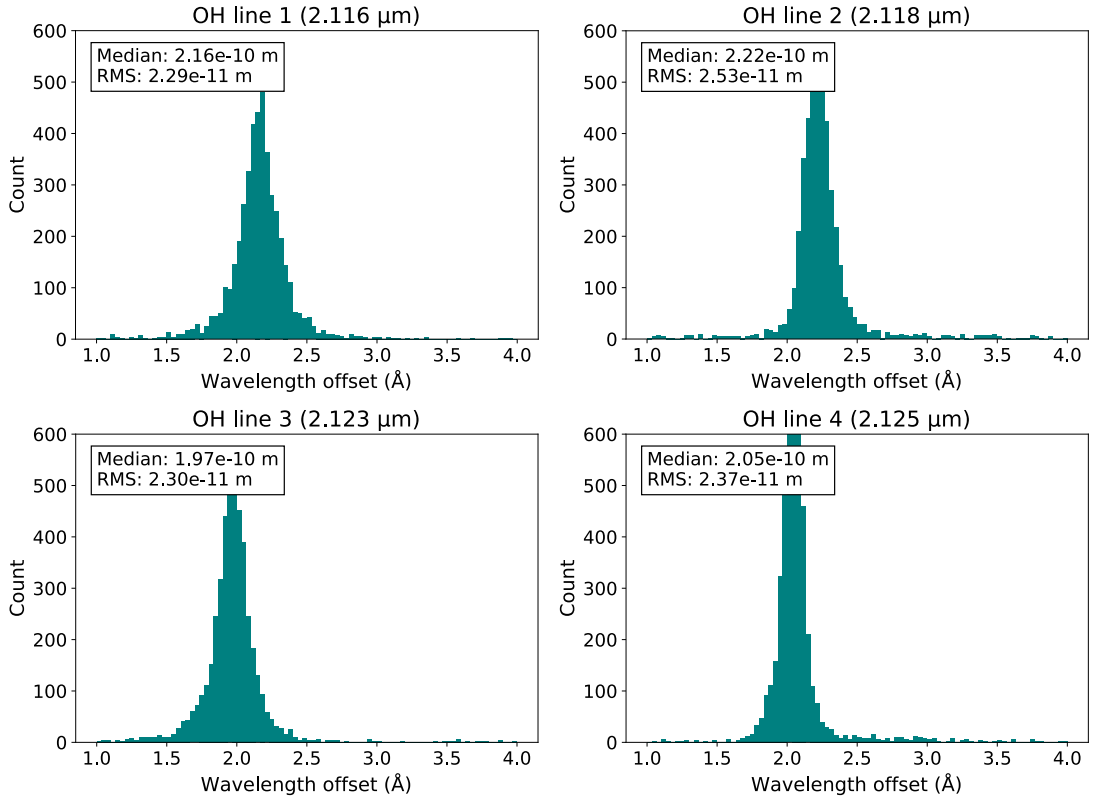


FIGURE 3.2: Wavelength offset histograms produced using Gaussian fitting of OH lines located near to the $H_2$ 1-0 S(1) emission line at 2.12 μm. The median value for the wavelength offset calculated using each of the four OH lines is approximately 2 Å. The uncertainty associated with these derived wavelength offsets is taken as the RMS of the distribution. The uncertainty varies from 0.2 – 0.3 Å.

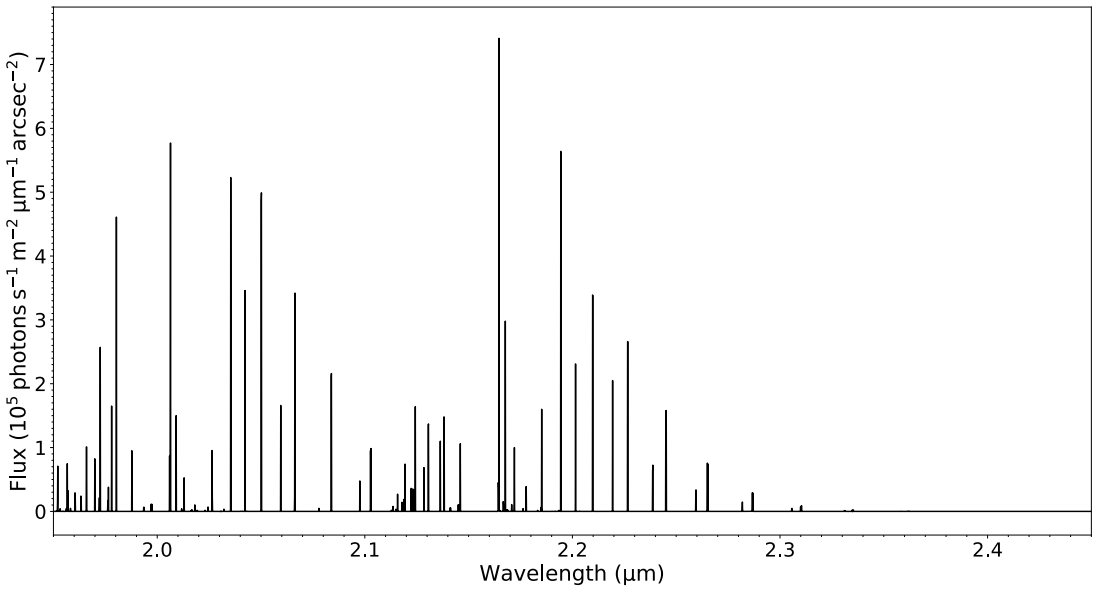


FIGURE 3.3: Theoretical night-sky spectrum of emission from Earth's upper atmosphere generated using ESO's SKYCALC tool.

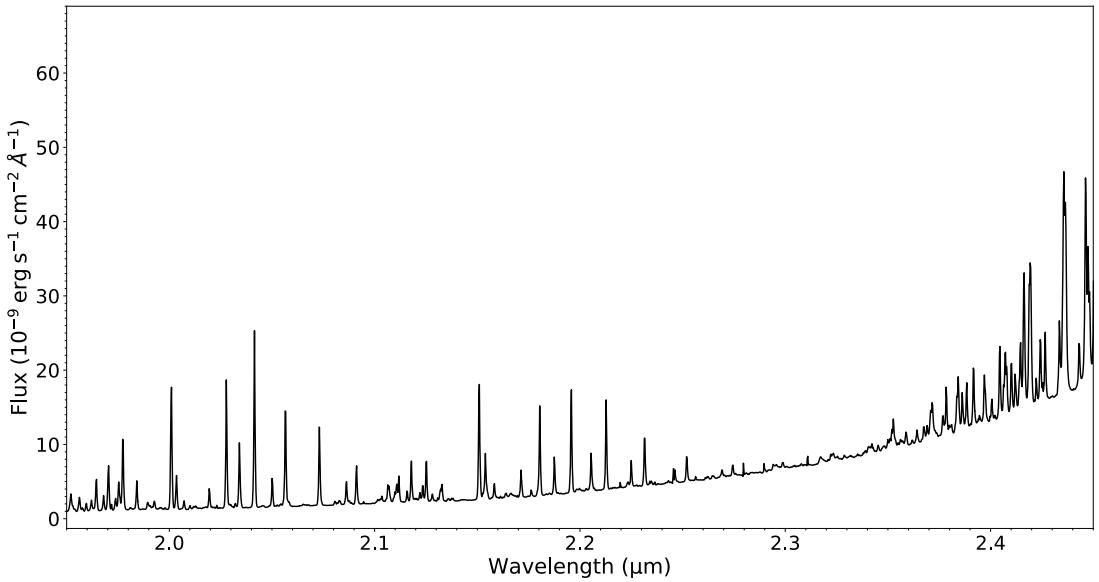


FIGURE 3.4: Example science spectrum containing OH sky lines extracted from the HH 46/47 source position.

The cross-correlation procedure compares the spectral positions of all of the OH lines in the science cube with the theoretical positions in the synthetic night sky spectrum, at each spectrum across the FOV of the cube, and calculates the wavelength offset between the two around a desired spectral region. The cross-correlation method was run in a spectral region centred on the $H_2$ 2.12 μm emission line with care taken to avoid large telluric absorption bands within the spectral window. A 2D wavelength correction map was produced, where each pixel in the map corresponded to a wavelength offset between the OH lines in the science spectra and theoretical spectrum. This 2D map is displayed in Figure 3.5. Each wavelength offset was then converted into a radial velocity using Doppler shift (Equation 3.4).

A linear trend was observed in each of the horizontal rows of pixels in the 2D map. This trend is in accordance with the orientation of the horizontal slicing mirrors of the beam splitter present in the SINFONI IFU. Each horizontal row of pixels in the 2D wavelength correction map was isolated and a linear fit was applied to the data points. A selection of these linear fits are displayed in Figure 3.6. The uncertainty of the fits is estimated as the standard deviations of the residuals of the horizontal linear fits. Each linear fit was compiled into a 2D wavelength correction map. This final wavelength correction map is shown in Figure 3.7. This method of precise wavelength calibration was also performed on SINFONI observations in Delabrosse et al. (2024).

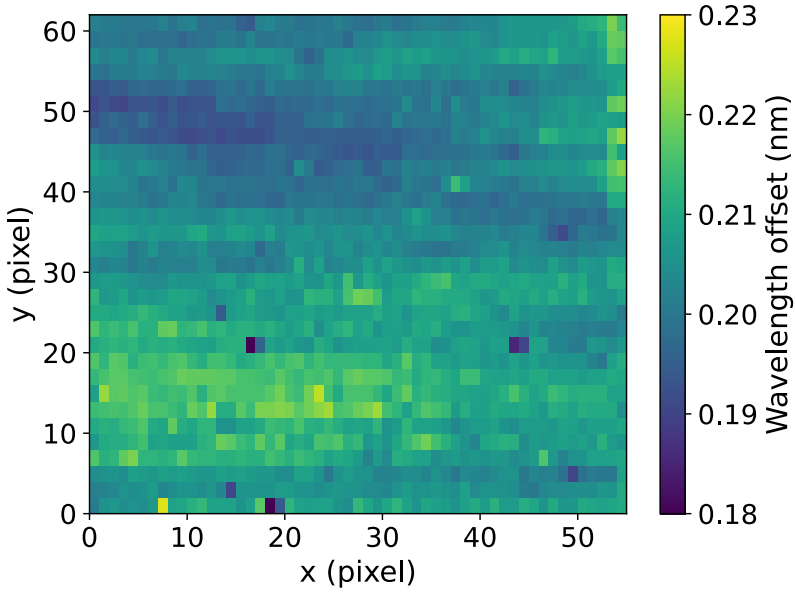


FIGURE 3.5: 2D wavelength correction map produced using cross correlation of the science cube and the theoretical night sky spectrum. Each pixel in the map corresponds to a wavelength offset between the OH lines in the science spectra and theoretical spectrum.

This final wavelength correction map was applied to the SINFONI data cube, effectively obtaining a more accurate wavelength calibration than that offered with the standard arc lamp wavelength calibration. The relative uncertainty associated with this wavelength correction map, calculated from the standard deviations of the residuals of the horizontal linear fits, is $\pm$ 0.55 km s$^{-1}$. The absolute error associated with the map is estimated to be $\pm$ 0.62 km s$^{-1}$. This was calculated by computing the wavelength correction map in several narrow wavelength intervals throughout the spectral axis, allowing the variation in wavelength/velocity correction values as a function of the central wavelength to be estimated. Summing the absolute and relative error in quadrature, the total uncertainty of the wavelength calibration procedure is retrieved to be $\pm$ 0.83 km s$^{-1}$. Note that this value is not the final uncertainty on individual line centroid velocities, but rather the velocity associated with the wavelength recalibration procedure.

There are also systematic errors that arise when using this wavelength calibration method that must be considered, as a single average wavelength correction value is derived for each spatial pixel over a range of wavelengths. Delabrosse et al. (2024) noticed when applying the 2D wavelength correction

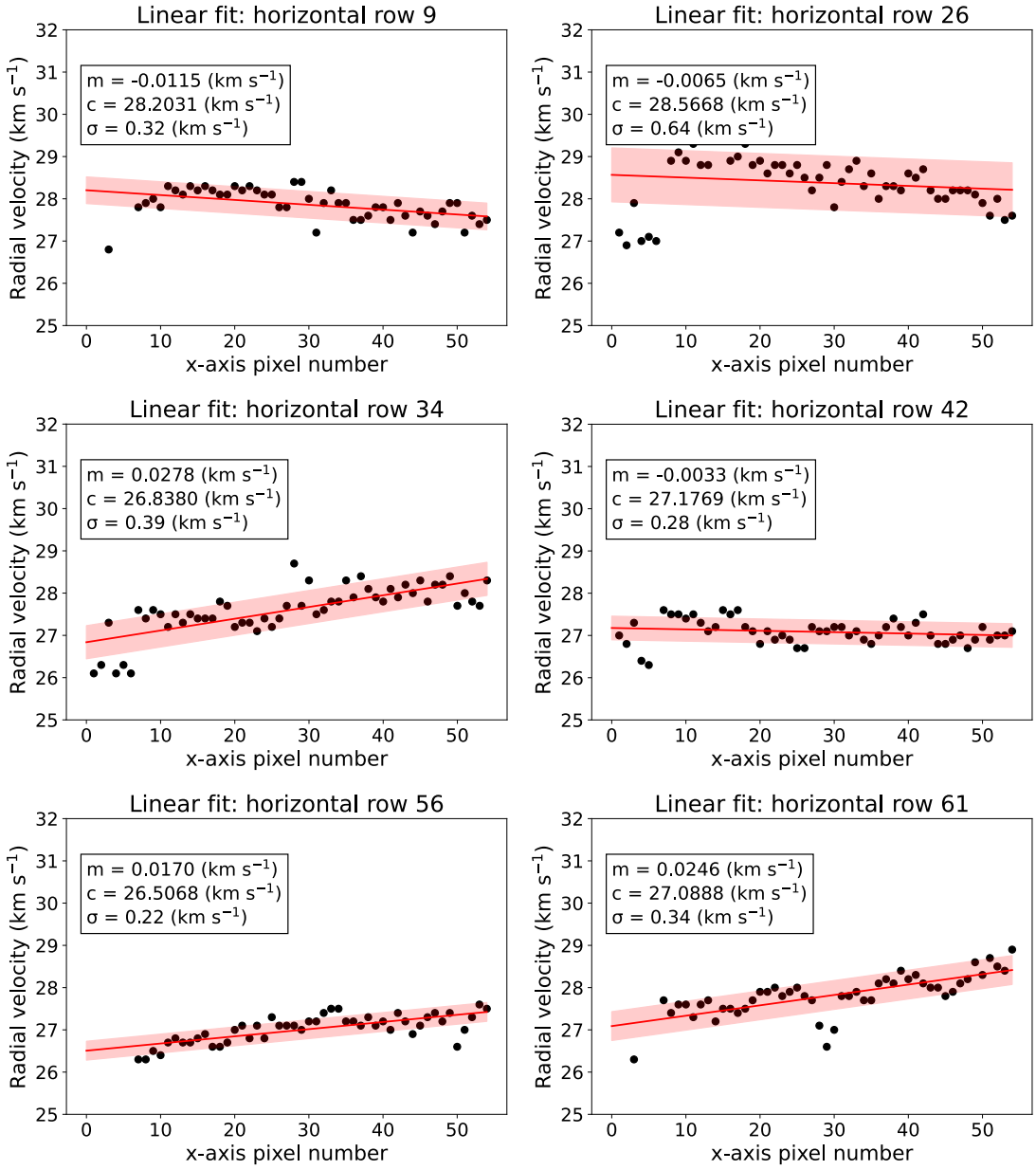


FIGURE 3.6: A selection of horizontal rows in the 2D wavelength offset map (Fig. 3.5) with linear fits applied to the data points. The inserted text boxes display the slope (m) of the linear fit, the intercept (c), the correlation coefficient ($R^2$), and the standard deviation ($\sigma$) of the data points with respect to the linear fit.

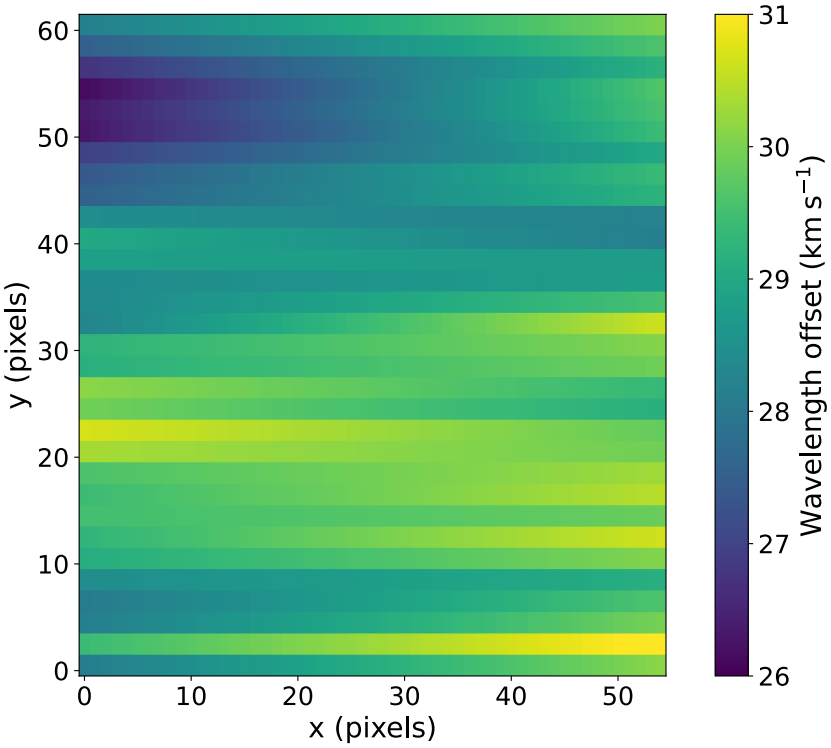


FIGURE 3.7: 2D wavelength calibration map produced by the compiling linear fits (e.g. Figure 3.6) to the horizontal rows of the wavelength offset map in Figure 3.5.

map to individual OH lines in the vicinity of the $H_2$ 2.12 μm emission line, there existed systematic offsets from the individual OH line's actual rest wavelength. These systematic uncertainties produce absolute errors of the order of 0.4 km $s^{-1}$, retrieved from Gaussian centroid offsets from the OH lines' known wavelengths, and relative uncertainties of the order of 0.9 km $s^{-1}$, retrieved from the standard deviation of wavelength correction values in the 2D wavelength correction map applied to the OH lines. The same values are adopted here as similar results were found, as expected using the same wavelength calibration method. Therefore, a $1\sigma$ uncertainty associated with the wavelength calibration of $\pm$ 1.0 km $s^{-1}$ is estimated.

In order to express radial velocity measurements correctly, the motion of the observatory location must be considered. ESO's data reduction pipeline corrects for the Earth's movement in relation to the barycentre of the solar system, the BERV correction. Further to this, the data was corrected for the mean motion of material in the Milky Way in the neighbourhood of the sun, allowing the measured radial velocities to be expressed relative to the common LSR reference frame. The LSR velocity of the object was calculated using the `rvcorrect` package in IRAF[3] (Image Reduction and Analysis Facility). The input parameters include the time and date of the observation, the direction of the observation, the location of the observatory, and the direction and magnitude of the solar motion relative to the LSR. The `rvcorrect` package then outputs the magnitude and direction of the radial velocity correction required to place the observation in the LSR reference frame. In the case of the SINFONI observations of HH 46/47, the LSR velocity correction is $v_{\mathrm{LSR}} = -4.42$ km $s^{-1}$. As the objective of the observations was to study the HH 46/47 outflow, the kinematical measurements are expressed with respect to the reference frame of the central driving source of the outflow. The LSR velocity of the dark cloud that the outflow emanates from is $v_{\mathrm{Cloud}} = +5.53$ km $s^{-1}$ (van Kempen et al., 2009) and this final radial velocity correction was applied.

### 3.3.3 Uneven slit effect correction

The uneven slit effect is an instrumental limitation associated with spectrometers due to the non-uniform illumination of the slit, or an illumination gradient

[3]IRAF is distributed by the National Optical Astronomy Observatory (NOAO), which is operated by the Association of the Universities for Research in Astronomy, inc. (AURA) under cooperative agreement with the National Science Foundation.

within the slit. In the case of IFUs, the slicing mirrors, which individually behave like long-slit spectrographs, are illuminated non-uniformly, introducing a spurious wavelength shift in the spectral axis between on-axis and off-axis light. Incoming light that enters the slicing mirror or slitlet at a point above the slitlet centre will have an opposite wavelength bias when compared with incoming light entering the slit at a point below the slitlet centre (Whelan and Garcia, 2008). In the case of these observations, the effect arises due to the slope of the PSF creating a non-uniform brightness gradient within the slit. The resulting spurious wavelength shift depends on how strong the local brightness gradient is across the slit.

The generation of a further 2D wavelength correction map was necessary in order to correct for these illusory wavelength shifts due to uneven slit illumination. In the case of these observations, the generation of a wavelength correction map for the $H_2$ 1-0 S(1) emission line at 2.12 μm was needed as optimal confidence in the radial velocity measurements of the molecular outflow was required. With regard to the SINFONI instrument, the horizontal slicing mirrors can introduce spurious wavelength shifts up to a few km $s^{-1}$ (Agra-Amboage et al., 2014). In order to correct for uneven slit illumination, the method outlined in Agra-Amboage et al. (2014) and Erkal et al. (2021a) is followed. First, the distribution of incoming light, by spectrally integrating the emission line of interest and the local continuum emission either side of the emission line, is modelled. The brightness centroid and its displacement with respect to the centre of the slitlet at each spaxel in the data cube is then estimated. The spurious wavelength shift, expressed in terms of a velocity shift, is calculated using the adapted formula, derived by Marconi et al. (2003), shown in Equation 3.5.

$$\Delta v(x_0, y_0) = \frac{\delta u}{\delta y} \times \frac{\iint I_{\mathrm{mod}}(u, v) \times (v - y_0)\, \mathrm{d}u\, \mathrm{d}v}{\iint I_{\mathrm{mod}}(u, v)\, \mathrm{d}u\, \mathrm{d}v} \tag{3.5}$$

Here, $\delta u$ is the spectral pixel sampling, $\delta y$ is the width of the slitlet, and $I_{\mathrm{mod}}$ is the modelled light intensity integrated over a single spaxel of detector coordinates $(x_0, y_0)$. Figure 3.8 displays the 2D wavelength correction map computed around the $H_2$ 1-0 S(1) emission line. Velocity corrections here vary from $-$ 5 km $s^{-1}$ to $+$ 10 km $s^{-1}$. As expected, the velocity corrections have a strong variation in the vertical, or dispersion direction, due to the nature of

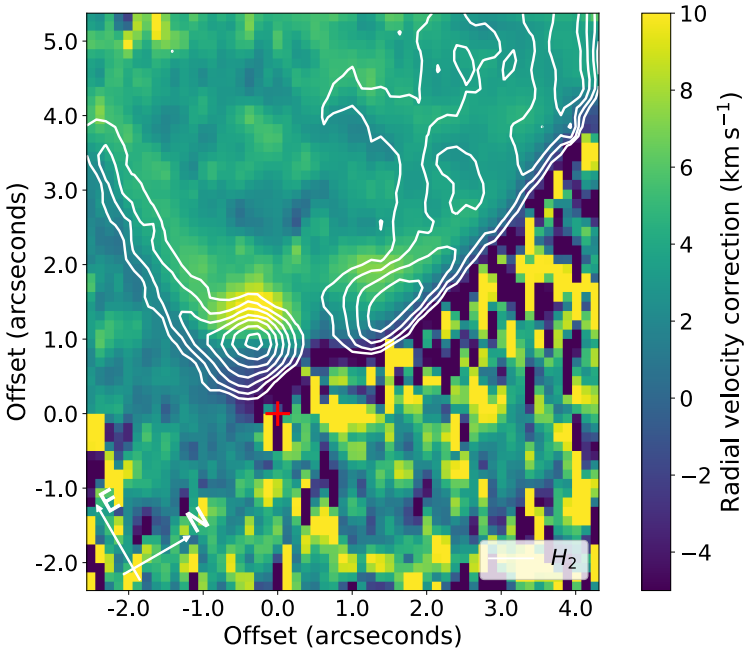


FIGURE 3.8: 2D wavelength correction map required to amend illusory wavelength/velocity shifts due to uneven slit illumination. $H_2$ emission is overplotted in white contour lines. The continuum peak position is marked with a red plus symbol. Contour levels begin at $3\sigma$ of the background emission and increase by factors of 1.5.

the horizontal slicing mirrors present in the SINFONI instrument. The effect due to uneven slit illumination is more prominent in brighter and more compact emission, as can be seen in Figure 3.8, where the velocity corrections are strongest near the $H_2$ emission knot located east of the source position marked by a red plus, and in the $H_2$ cavity walls. More information on the morphology of the $H_2$ emission is discussed in Section 4.2.1.

The effect of applying this wavelength or velocity correction map to the radial velocity map of $H_2$ 1-0 S(1) emission is displayed in Figure 3.9. The radial velocity of the $H_2$ emission varies from $v = 0$ to $-40$ km s$^{-1}$.

### 3.3.4 Flux calibration

Flux calibration is necessary to convert the light intensity units from arbitrary detector counts to physical units. Flux calibration was performed on the SINFONI data cube using the two standard star observations that were part of the same observation run. Standard stars are beneficial for calibration as they

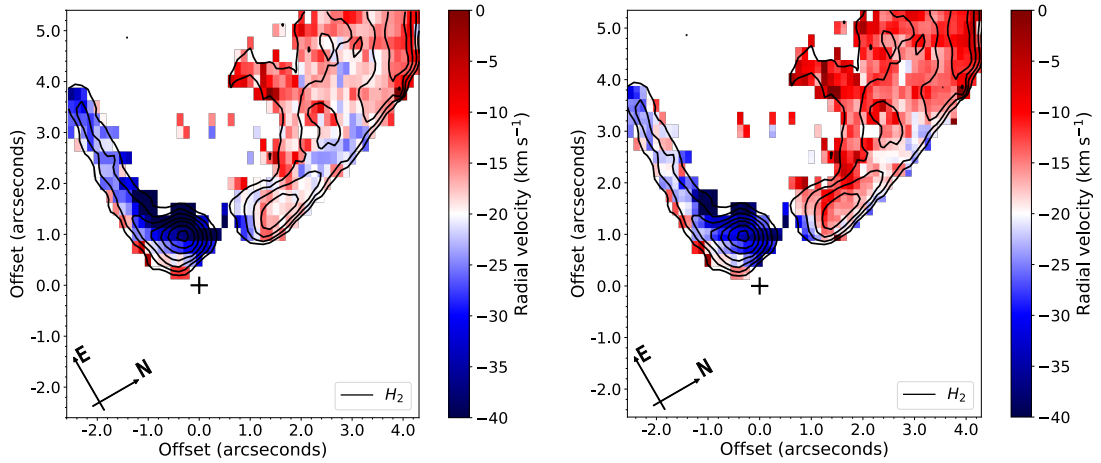


FIGURE 3.9: Velocity centroid maps of $H_2$ emission before (*left*), and after (*right*), the wavelength correction map required to amend illusory wavelength/velocity shifts due to uneven slit illumination (Figure 3.8), is applied. The radial velocity of the $H_2$ emission varies from $v = 0$ to $-40$ km s$^{-1}$. The continuum peak position is marked with a black plus symbol. Contour levels for both panels begin at $3\sigma$ of the background emission and increase by factors of 1.5.

possess well-known and precisely measured flux values over a range of wavelengths. Correlating the counts detected from standard star observations with their known flux values allows the determination of how the instruments detector detects light at various wavelengths. As these standards were observed on the same night as the science observations, they possess a similar airmass to the science observation. Airmass is a measure of the amount of atmosphere, or air, along the line of sight when observing a star or other celestial source from below Earth's atmosphere. It is formulated as the integral of the air density along the ray of light. Airmass is defined as the ratio of the atmospheric path length at some angle (the zenith angle) to the path length at the zenith, which is defined as having an airmass of 1. As light passes through the atmosphere it is attenuated by scattering and absorption, and the denser the atmosphere the greater the attenuation (Green, 1992).

The standard star observations, HD 67954 (HIP 39774) and HD 73105 (HIP 42038), were reduced using the SINFONI data reduction pipeline in the same fashion as the science cube. The standard star's known magnitudes in the J, H and K bands were obtained from the 2MASS (Two Micron All-Sky Survey) catalogue (Skrutskie et al., 2006). These magnitudes were converted to flux densities using the relation shown in Equation 3.7, derived from the difference

TABLE 3.1: Flux values for zero-magnitude stars in the J, H and K passbands, and the central wavelengths of the bands.

| Band | $\lambda_c$ (μm) | $F_0$(Band) ($10^{-13}$ W cm$^{-2}$ μm$^{-1}$) |
|---|---|---|
| J | $1.235 \pm 0.006$ | $3.129 \pm 0.055$ |
| H | $1.662 \pm 0.009$ | $1.662 \pm 0.022$ |
| $K_s$ | $2.159 \pm 0.011$ | $0.428 \pm 0.0081$ |

in apparent magnitudes expression shown in Equation 3.6.

$$m_1 - m_2 = -2.5 \times \log\left(\frac{F_1}{F_2}\right) \tag{3.6}$$

$$F_{\text{Standard}}(\text{Band}) = F_0(\text{Band}) \times 10^{-m(\text{Band})/2.5} \tag{3.7}$$

Here, $F_0(\text{Band})$ is the zero-magnitude flux of a star in a particular observation band, $m(\text{Band})$ is the known magnitude of the star, both taken from the 2MASS catalogue, and $F_{\text{Standard}}(\text{Band})$ is the flux of the standard star in the corresponding band. The J, H, and K observation bands are well defined passbands or filters in the NIR part of the electromagnetic spectrum that make up the JHK photometric system. J is centred on 1.220 μm and has a FWHM of 0.213 μm, H is centred on 1.630 μm and has a FWHM of 0.307 μm and K is centred on 2.190 μm and has a FWHM of 0.390 μm. The zero magnitude fluxes ($F_0(\text{Band})$) from Cohen, Wheaton, and Megeath (2003) are shown in Table 3.1. The magnitudes of the standard stars, HD 67954 (HIP 39774) & HD 73105 (HIP 42038), in the J, H, & K bands, taken from the 2MASS catalogue, and their calculated flux densities ($F_\lambda$) in these bands using Equation 3.7 are displayed in Table 3.2. Uncertainties associated with the calculated flux densities ($\sigma_{\text{F}}$), as shown in the table, were estimated using the propagation of uncertainty associated with the expression shown in Equation 3.7. The propagation of uncertainty expression is displayed in Equation 3.8.

$$\sigma_{\text{F}}^2 = (10^{-m/2.5})^2\, \sigma_{F_0}^2 + \left(\frac{2\, F_0 \ln(10)\, (10^{-2m/5})}{5}\right)^2 \sigma_m^2 \tag{3.8}$$

TABLE 3.2: Magnitudes and calculated flux densities of the standard stars HD 67954 & HD 73105 in the J, H, & K bands.

| Standard star | Magnitude[a] | $F_\lambda$ ($10^{-16}$ W cm$^{-2}$ μm$^{-1}$) |
|---|---|---|
| HD 67954 | J: 7.864 ± 0.027 | 2.238 ± 0.068 |
| (HIP 39774) | H: 7.870 ± 0.059 | 0.806 ± 0.047 |
| | K: 7.840 ± 0.029 | 0.313 ± 0.010 |
| HD 73105 | J: 7.013 ± 0.020 | 4.900 ± 0.124 |
| (HIP 42038) | H: 7.050 ± 0.040 | 1.715 ± 0.072 |
| | K: 7.089 ± 0.024 | 0.625 ± 0.018 |

[a] Band magnitudes are from the 2MASS catalogue.

Planck's radiation law (Equation 3.9) describes the spectral energy distribution of electromagnetic radiation emitted by a blackbody at a given temperature, $T$. Here, $h$ is Planck's constant, $\nu$ is the frequency of light, $c$ is the speed of light, and $k$ is Boltzmann's constant (Planck, 1901). The law is also expressed as a function of wavelength ($\lambda$) in Equation 3.9. The Rayleigh-Jeans' approximation (Equation 3.10) for Planck's radiation law holds if $hc/\lambda kT < 1$, in other words at long wavelengths/low frequencies. This approximation is also expressed as a function of wavelength ($\lambda$) in Equation 3.10. Both standard stars HD 67954 & HD 73105 are of spectral type B5, meaning they are bright, hot stars with effective temperatures of $\sim$ 15,200 K. The Rayleigh-Jeans' approximation is utilised here as $h\nu < kT$ in the J, H & K bands. At 1.95 μm, the lower bound of the K band, $h\nu \approx 0.49\ kT$ and at 2.45 μm, the upper bound of the K band, $h\nu \approx 0.39\ kT$. Flux varies with wavelength as $\lambda^{-4}$, and therefore this relation can be expressed as a simple linear function with the use of a log-log plot. Monomials appear as straight lines in log-log plots. A log(flux) vs. log(wavelength) plot was produced and a linear function was fit to the flux densities of each standard star in the J, H & K bands. These linear fits are shown in Figures 3.10 & 3.11. The equations of these lines of best fit allows the fluxes of the standard stars to be obtained at various wavelengths. The linear equations for the standard stars are shown in Equation 3.11, for HD 67954, and Equation 3.12, for HD 73105.

$$B(\nu, T) = \frac{2h\nu^3}{c^2} \frac{1}{e^{\frac{h\nu}{kT}} - 1} \quad , \quad B(\lambda, T) = \frac{2hc^2}{\lambda^5} \frac{1}{e^{\frac{hc}{\lambda kT}} - 1} \tag{3.9}$$

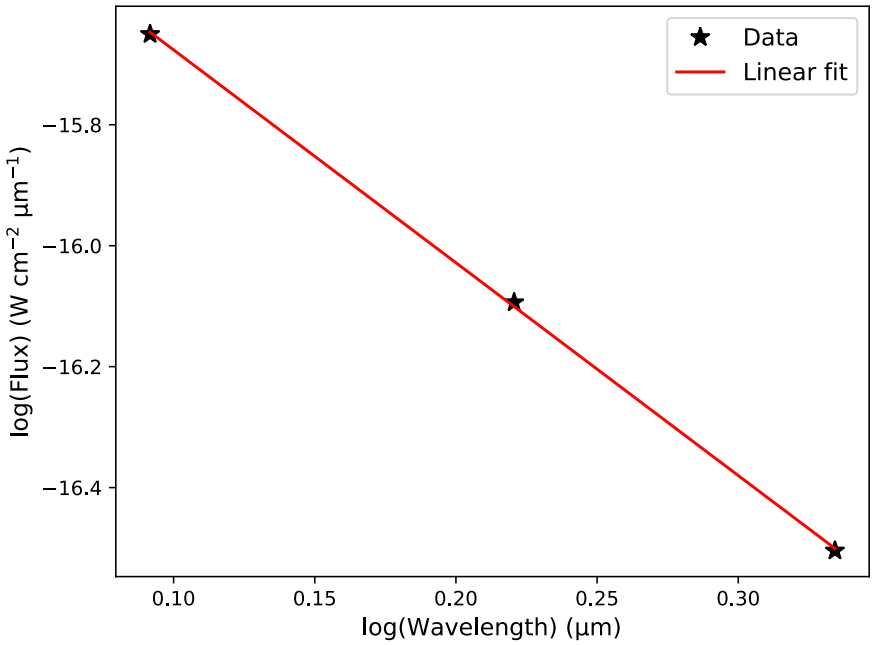


FIGURE 3.10: log(flux) vs. log(wavelength) plot with linear function fit to the flux densities of HD 67954 in the J, H, & K bands.

$$B(\nu, T) = \frac{2h\nu^3 kT}{c^2} \quad , \quad B(\lambda, T) = \frac{2hc^2}{\lambda^4 kT} \tag{3.10}$$

$$\log_{10}(F) = -3.159 \times \log_{10}(\lambda) - 15.324 \tag{3.11}$$

$$\log_{10}(F) = -3.682 \times \log_{10}(\lambda) - 14.966 \tag{3.12}$$

Following this, the standard stars were flux calibrated using these linear equations. Apertures, slightly larger in size than the seeing discs, were placed over the standard star's stellar positions and integrated to obtain the total intensity within the aperture. Annuli were used to estimate the contribution from the local background, which was subsequently subtracted from the aperture integration. Integrated stellar spectra from the standard stars were extracted using this method. Polynomial fits were then applied to these stellar spectra, an example of such is displayed in Figure. 3.12. A correction function was then calculated for each of the integrated stellar spectra. This correction function is a correction between the polynomial fits to the integrated

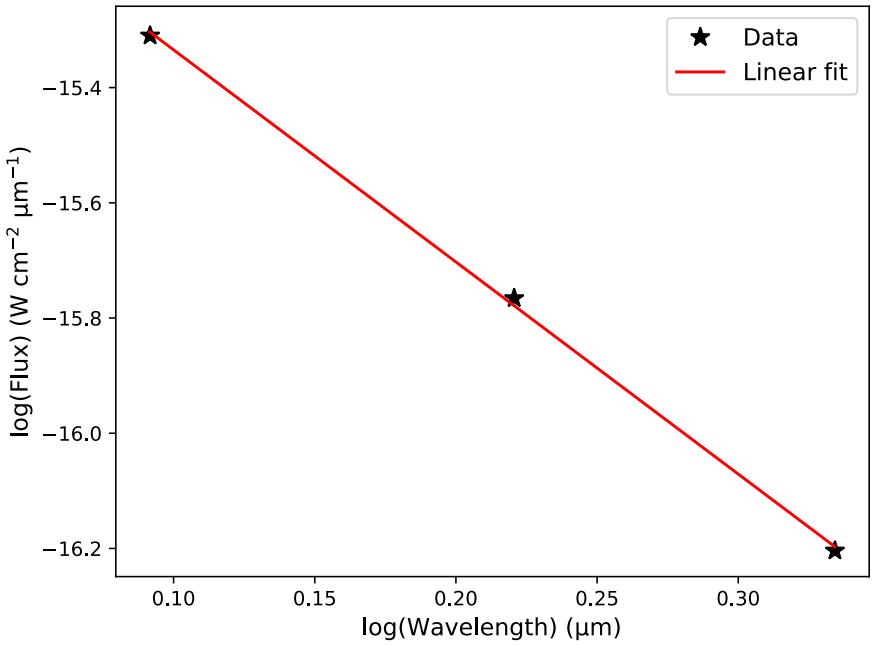


FIGURE 3.11: log(flux) vs. log(wavelength) plot with linear function fit to the flux densities of HD 73105 in the J, H, & K bands.

stellar spectra and their corresponding Rayleigh-Jeans' Flux vs. wavelength calibration curves, which appear linear in Figures 3.10 & 3.11. This correction function makes the polynomial fit to the integrated stellar spectra match the calibration curves. This results in a conversion between the arbitrary detector counts present in the polynomial fit to physical flux units. The integrated stellar spectra from the standard stars are then multiplied by their corresponding correction functions, subsequently flux calibrating the standard stars' stellar spectra. The integrated, flux calibrated stellar spectra from HD 67954 and HD 73105 are displayed in figures 3.13 and 3.14, respectively. These spectra possess large telluric absorption features.

The correction functions can then be applied to the science observation to flux calibrate it. The average calibration curve obtained independently from both of the standard star observations was used to flux calibrate the science data cube (Figure 3.15). The differing exposure times of the standard star observations and the science observation was also taken into account. The exposure time of the standard star observations was divided by the exposure time of the of the object and subsequently, the calibration curves were multiplied by these factors. Every spectrum at each spaxel in the science cube was then multiplied by this correction spectrum, flux calibrating the science data cube. This

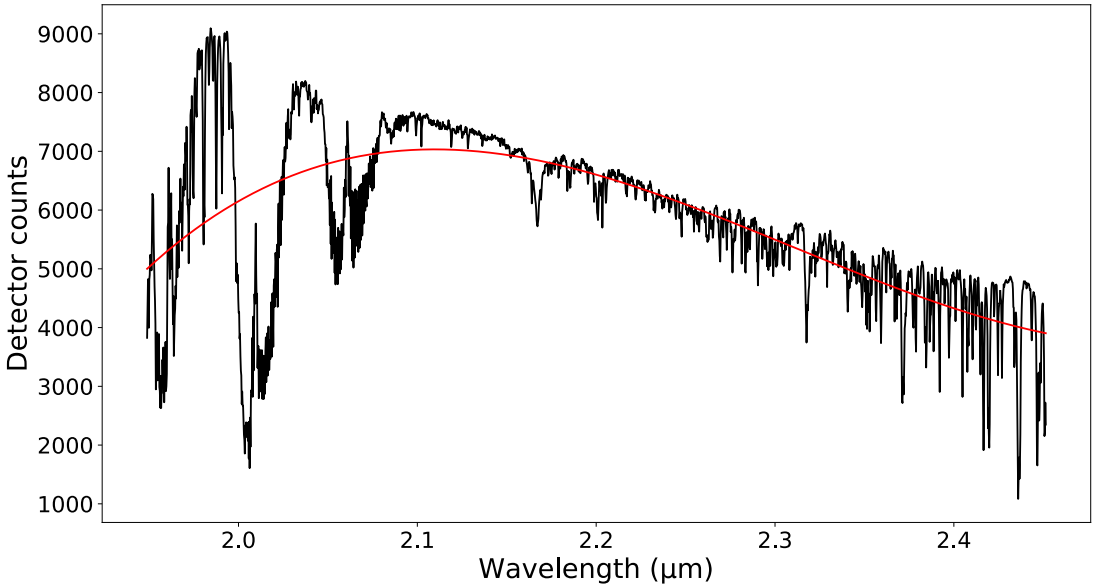


FIGURE 3.12: Integrated stellar spectrum from HD 67954 with polynomial fit applied.

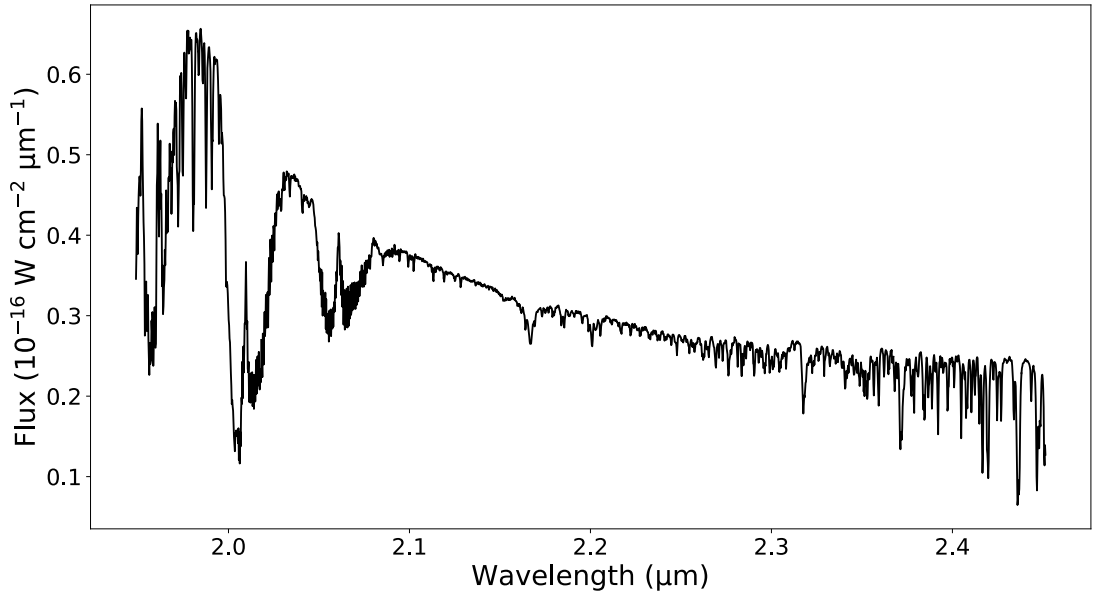


FIGURE 3.13: Flux calibrated integrated stellar spectrum from HD 67954.

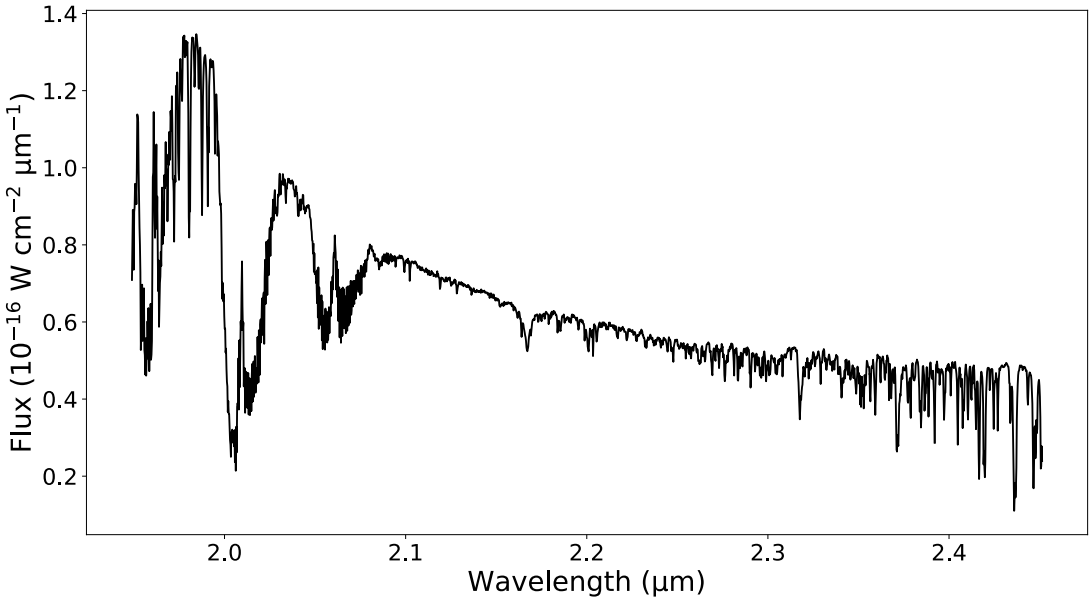


FIGURE 3.14: Flux calibrated integrated stellar spectrum from HD 73105.

spectral calibration formula is shown in Equation 3.13. Here, $\mathrm{Spec}_{\mathrm{cal}}$ is the flux calibrated spectrum, $\mathrm{Spec}_{\mathrm{obs}}$ is the uncalibrated observation spectrum, $C(\lambda)$ is the correction function displayed in Figure 3.15, and the ratio $t_{\mathrm{std}}/t_{\mathrm{obs}}$ is the ratio of the standard star exposure time to the science observation exposure time. The flux calibrated science cube has units; $10^{-23}$ W cm$^{-2}$ μm$^{-1}$, or equivalently, $10^{-16}$ erg s$^{-1}$ cm$^{-2}$ μm$^{-1}$.

$$\mathrm{Spec}_{\mathrm{cal}} = \mathrm{Spec}_{\mathrm{obs}} \times C(\lambda) \times \frac{t_{\mathrm{std}}}{t_{\mathrm{obs}}} \times 10^{23} \tag{3.13}$$

### 3.3.5 Telluric correction

Ground-based observations can be contaminated by emission or absorption of molecules in Earths atmosphere, this is known as telluric contamination. Molecules such as water and oxygen are two of the major contributors to this contamination, and the NIR is particularly affected, as water is a strong absorber at these wavelengths. In order to retrieve accurate flux measurements of line emission from observations it is necessary to remove the contribution from telluric sources. Telluric standard stars can be used to mitigate the effects of telluric contamination.

Here, the standard star used as a model template for telluric features was

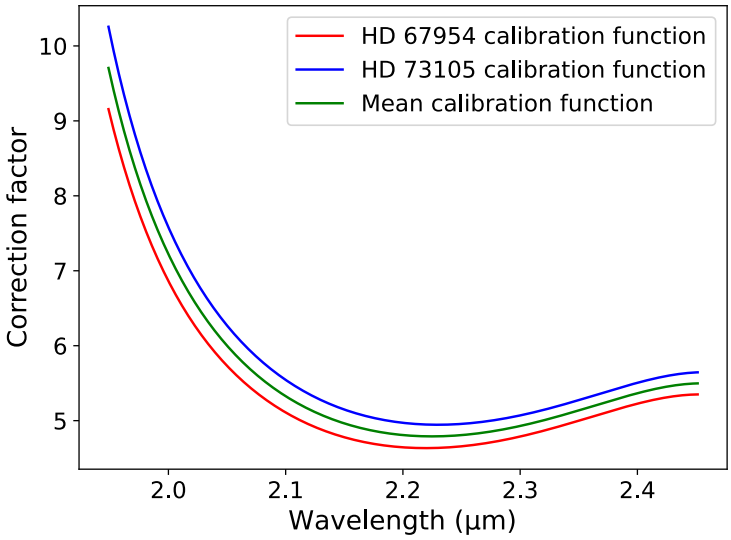


FIGURE 3.15: Mean flux correction function derived from those calculated from the standard star observations.

HD 73105. An integrated spectrum was extracted from the standard star and used as the telluric standard. The absorption feature centred around 2.16 μm (the Br-$\gamma$ absorption) was masked as this absorption line is not due to telluric contamination, but rather intrinsic to the stellar spectrum. Other photospheric lines, absorption lines originating in the photosphere of the star, were not detected in the science observation, indicating heavy veiling. A smooth spline was fit to the telluric standard spectrum, with care taken not to fit the deep absorption bands. This spline fit is displayed in Figure 3.16. The spectrum was then normalised so that the continuum level is unity, by dividing the telluric standard spectrum by the spline fit. The normalised telluric standard spectrum is shown in Figure 3.17.

An exponential correction factor was then applied to the normalised telluric standard spectrum. This factor[4] was applied to account for the difference in airmass between the observation of the standard star and the airmass of the science observation. Smooth splines were also fit to the spectra located at each pixel in the science data cube and subsequently, divided by this fit. This normalised each spectrum in the science cube to unity.

The telluric correction spectrum then needed to be shifted in wavelength

[4]The normalised telluric standard star spectrum is multiplied by the factor: $1^A$, where $A = Airmass_{\rm obs} / Airmass_{\rm std}$

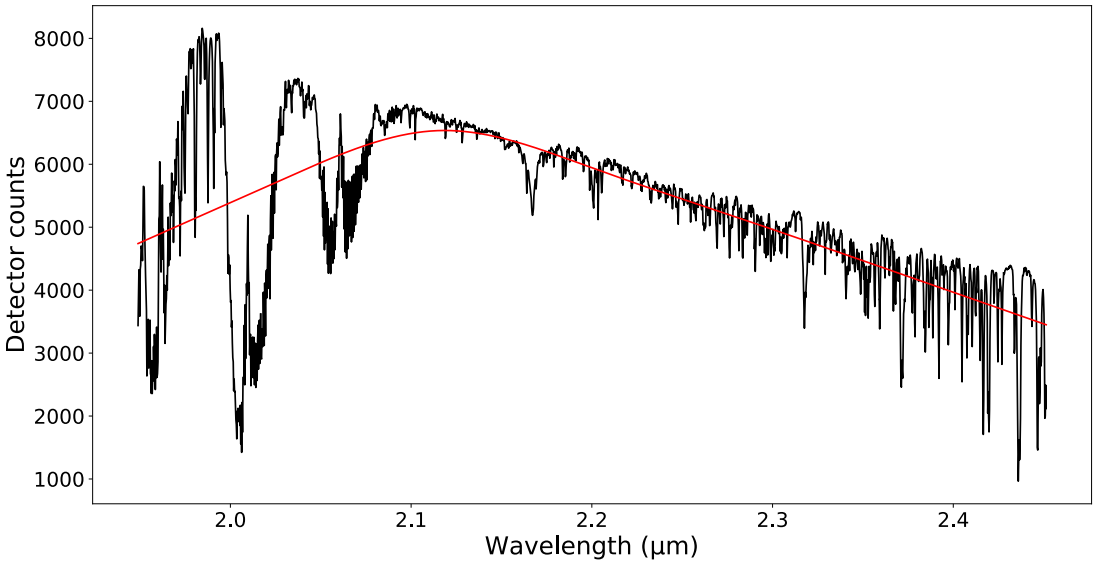


FIGURE 3.16: Telluric standard star HD 73105 spectrum with smooth spline fit applied.

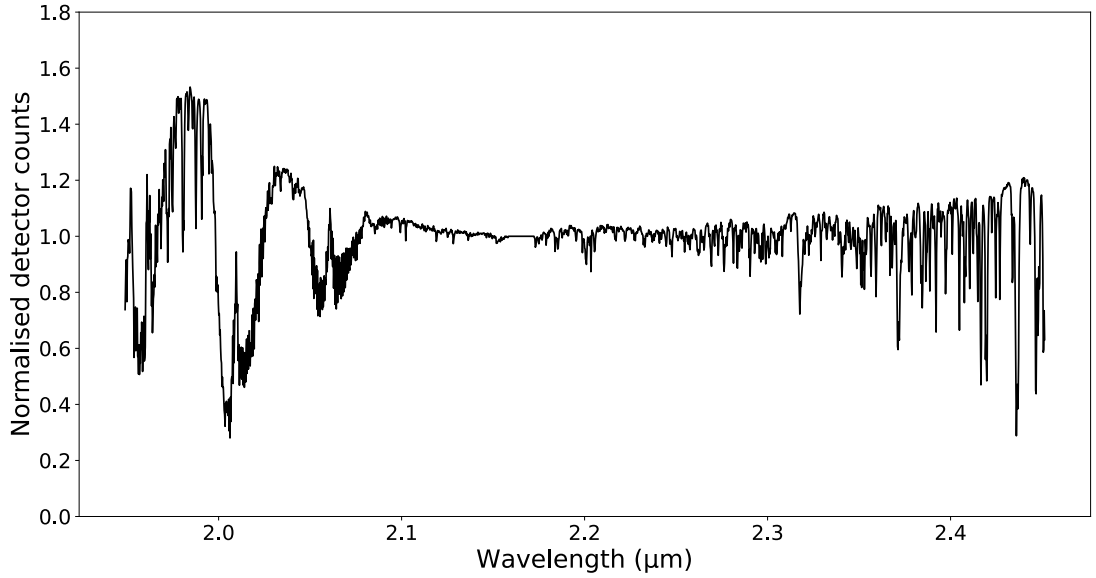


FIGURE 3.17: Normalised telluric standard star HD 73105 spectrum.

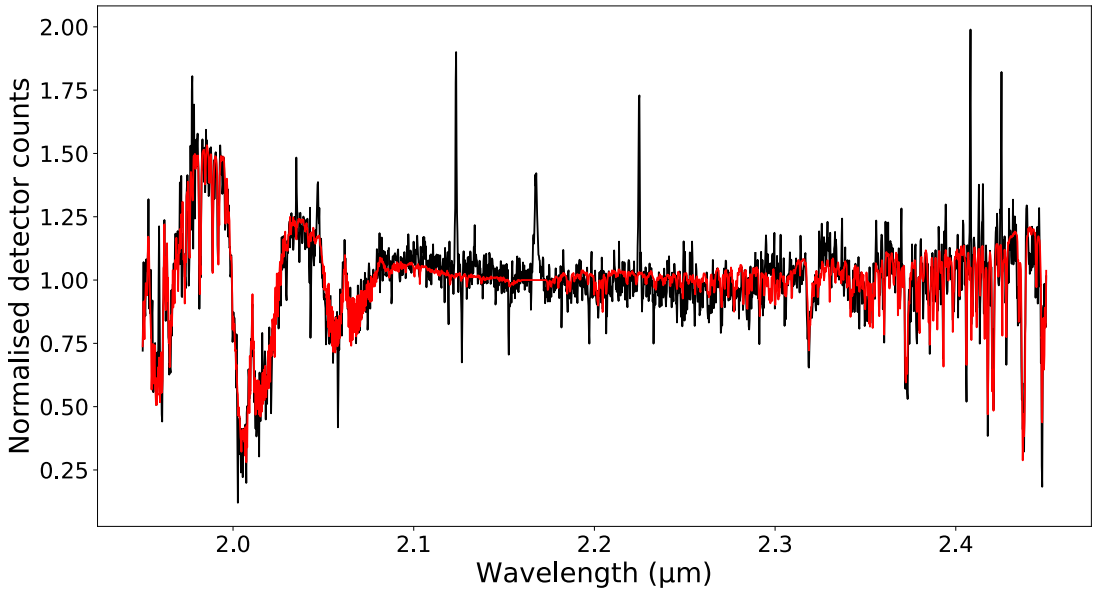


FIGURE 3.18: Normalised telluric standard spectrum, in red, overplotted on science spectrum, in black. The wide absorption bands match in location.

so that the telluric lines present in the standard spectrum matched the positions of the same telluric lines present in the science observation. This was achieved by isolating a spectral region of strong telluric absorption in both the science observation and telluric standard, then cross-correlating these spectral regions. An example of the wavelength-shifted and airmass corrected, normalised telluric standard spectrum overplotted on a selected normalised science spectrum is displayed in Figure 3.18. Following this, the spectra located at each pixel in the normalised science cube were divided by the wavelength-shifted and airmass-corrected, normalised telluric standard spectrum. This process mitigated the contribution from telluric contamination in the science cube observation. Each spectrum in the science cube was then multiplied by the original spline fit corresponding to that spectrum, in order to restore the original spectrum's shape and flux. An example of a spectrum extracted from the science observation before and after telluric correction is displayed in figure 3.19. Notable changes include the mitigation of the wide telluric absorption features, the intensity of the emission line at approximately 1.95 μm is increased, now that it is no longer suppressed by the deep telluric absorption band present in that spectral region, and also, the bandhead emission feature at approximately 2.32 μm is no longer obscured.

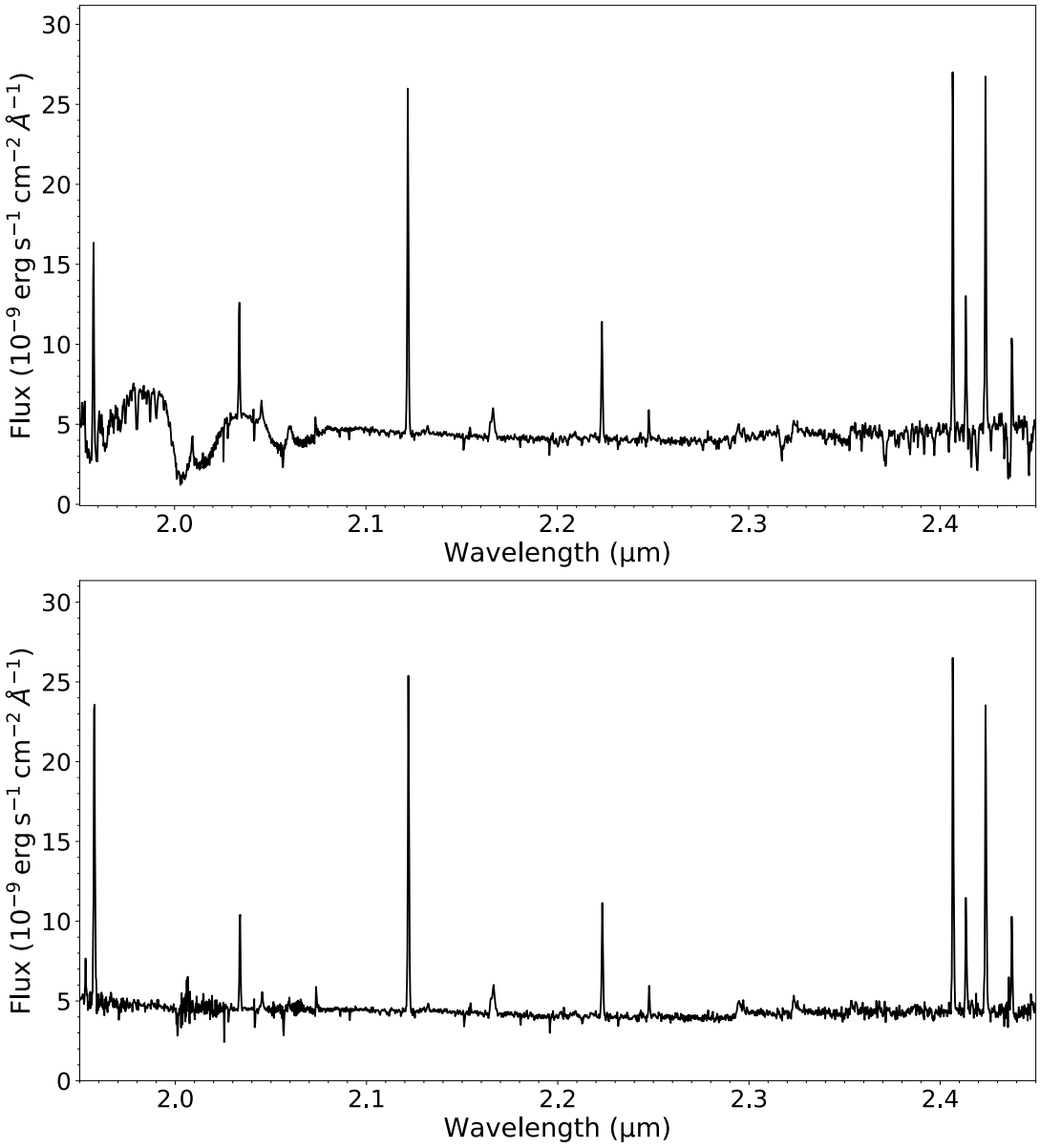


FIGURE 3.19: Spectrum extracted from science observation before (*Top*) and after (*Bottom*) telluric correction.

### 3.3.6 Spatial resampling

SINFONI's pixels are rectangular, as discussed in Section 2.3.1, in that the FOV is sliced into 32 slitlets which is imaged onto 64 vertical pixels of the detector. In the case of the SINFONI observations presented here, the spaxel size is $0''.125 \times 0''.250$, with each spaxel being imaged onto two vertical pixels in the square grid, resulting in two identical pixels. Some analyses therefore required a spatial resampling of the FOV in order to produce a square grid of pixels whereby each pixel represents a unique spatial location. Spatial resampling does not alter the spatial resolution of the image, but rather improves the appearance by providing a clearer visualisation of the features present in the image (Menezes, Steiner, and Ricci, 2014). The spatial resampling technique chosen involved the compression of adjacent vertical pixels into a single pixel. This was achieved by resampling the FOV onto a pixel grid, where every odd-indexed horizontal row of pixels is discarded, as these rows represent duplicate pixel values from the even-indexed rows. After this vertical compression, a uniform pixel grid is achieved where each pixel value represents a unique spatial point in the image. In order to maintain the correct aspect ratio of the FOV when plotting, the vertical direction requires a scaling factor of two, essentially stretching the square pixels to double their size in the vertical direction. This ensures an accurate representation of the original spatial dimensions of the FOV.

### 3.3.7 Continuum subtraction and scattered emission removal

As the goal of the study is to investigate the HH 46/47 outflow, the stellar continuum emission must be subtracted in order to isolate specific outflow features from stellar light. An image of the continuum emission, integrated over $\lambda$2.190 μm – $\lambda$2.191 μm, is displayed in Figure 3.20. The continuum emission is tracing a reflection nebula with an approximately parabolic shape. The position of the driving source of the outflow is marked with a red plus symbol. This reflection nebula is illuminated by stellar light from the driving source of the outflow scattered off the walls of a cavity carved by the outflow into the surrounding ambient material. This continuum image reveals the extent of the scattered light component present in these images. This contribution of scattered stellar light is present at all wavelengths in the observation. The

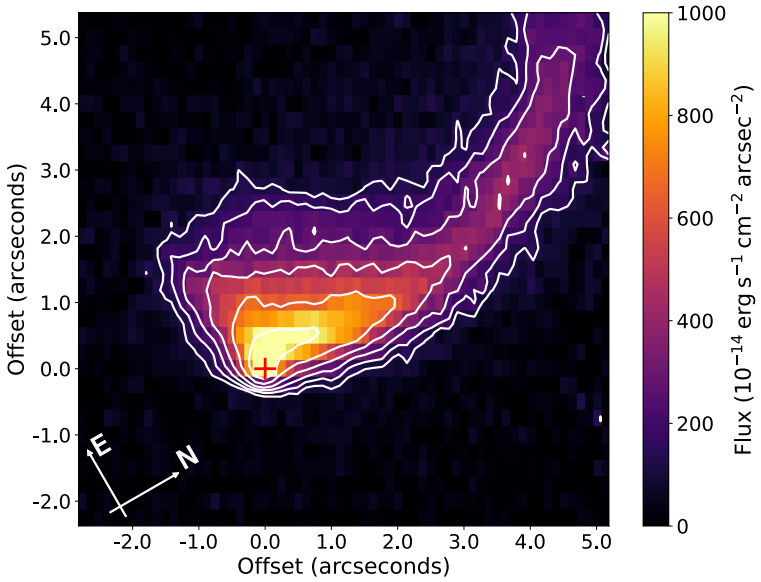


FIGURE 3.20: Integrated intensity map displaying the morphology of the continuum emission displaying a wide, approximately parabolic shape. The source position is marked with a red plus symbol. Contour levels begin at $3\sigma$ of the background emission and increase by factors of 1.5. The vertical axis of the image is aligned with central axis of HH 46/47 outflow in CO emission (PA = 60° from Zhang et al. (2019)).

morphology of the continuum emission, as well as the determination of the continuum peak position, is further discussed in Section 4.2.1.

The observations presented here probe the launching region of an outflow, tracing the outflow very close to the embedded driving source. Strong contributions of scattered light from the central engine is expected in these regions. As the investigation of the outflow in intrinsic outflow-tracing line emission was desired, the scattered emission first needed to be removed, or mitigated to the greatest extent. As the cavity seen in continuum emission was fully illuminated throughout the spectral axis, an assumption was made that the scattered light component was entirely light from the unresolved central binary reflecting off the cavity. A spectrum was therefore extracted from the continuum peak position, or the driving source position, to best represent the contribution from scattered emission. A polynomial fit was applied to this source spectrum (representing the scattered light) in order to rescale the source spectrum to the same level as the continuum level at each spaxel in the data cube. Subsequently, the rescaled source spectrum was subtracted from the spectra located at each spaxel in the data cube, hypothetically removing the scattered light

component from the data and leaving only intrinsic outflow emission. However, it was concluded that performing this scattered emission removal routine for the entire spectral axis of the data cube was not ideal.

Instead, the rescaled source spectrum was subtracted locally in wavelength around each emission line of interest from the spectra at each spaxel. This effectively removed the scattered light component and continuum emission from the emission line of interest, leaving only the intrinsic, outflow-tracing, line emission. This scattered emission removal routine was performed locally in the spectral region around each emission line of interest to ensure an accurate subtraction of scattered light. An example of applying this scattered light subtraction routine to the bright $H_2$ 1-0 S(1) emission line at 2.12 μm, in a single spectrum in the cube, is displayed in Figure 3.21. After this rescaled spectrum is subtracted, as seen represented by the solid black line in the bottom panel of Figure 3.21, the continuum level is centred around zero. An important aspect to consider is that subtracting the rescaled spectrum extracted from the continuum peak subtracts a portion of line emission, where this subtracted line emission may be entirely scattered emission or could harbour some intrinsic line emission. Therefore emission line flux measurements from this dataset, free from scattered emission, may not be representative of the real flux from the emission lines. If the continuum peak spectrum is assumed to be entirely scattered light, then the flux measurements are accurate.

Line to continuum ratio plots are an effective tool for investigating the contribution of scattered emission to intrinsic emission, and for checking the effectiveness of any process for removing it. These plots display the result of calculating the ratio between an integrated emission line image and an integrated continuum image, taken spectrally nearby to the line of interest. The contribution from scattered light to the integrated line images will be represented by a constant ratio in these plots, as the scattered light follows the same spatial distribution as the continuum emission, assuming the scattered light is entirely stellar light. In contrast, the real, intrinsic local emission will appear bright in these images, exceeding the constant ratio that represents the contribution from scattered light.

Line to continuum ratio plots were generated for the $H_2$ 1-0 S(1) emission line, the singly-ionised iron FEL, [Fe II] at 2.05 μm, and the Br-$\gamma$ emission line at 2.16 μm. The top panel of Figure 3.22 displays the result for $H_2$ emission.

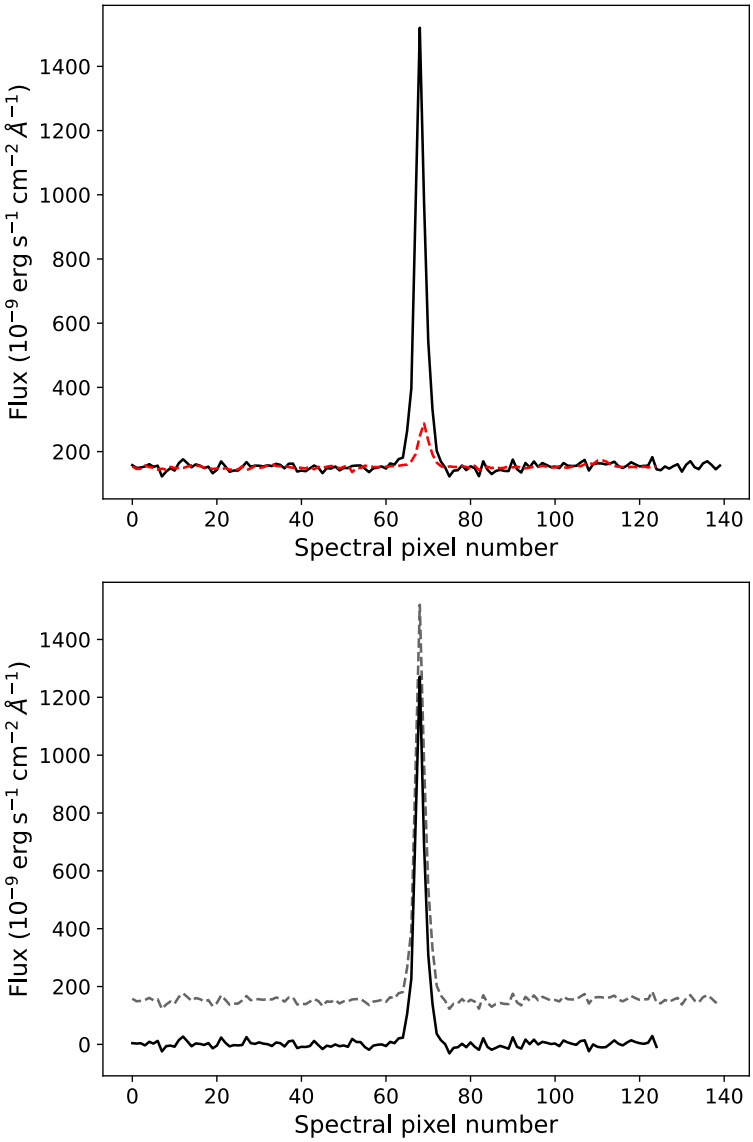


FIGURE 3.21: The scattered emission removal routine applied to the $H_2$ 1-0 S(1) emission line. *Top*: $H_2$ 1-0 S(1) emission line before the contribution from scattered light is subtracted, shown here in black. The rescaled source spectrum, representing the scattered light, is overplotted in a red, dashed line. This rescaled spectrum is subsequently subtracted. *Bottom*: The $H_2$ 1-0 S(1) emission line displayed before (in a grey dashed line) and after (in a solid black line) the rescaled source spectrum is subtracted.

The source position is marked with a red plus. A signal-to-noise threshold, set at 3 times the background noise, is implemented in these images to reject background emission, meaning the morphologies one sees in these panels is due to a combination of the continuum and the intrinsic line emission. The panel displays ratio values approximately between 1 and 2 in the inner region of the cavity traced in $H_2$ emission, close to the source, and along the outer side of the northern pointing cavity wall. Here, as the ratio is close to unity, the contribution from scattered light is strongest. It is seen that the intrinsic line emission here is coming from the cavity walls and the $H_2$ knots at the bases of the cavity walls. The morphology of $H_2$ emission is discussed further in Section 4.2.1. Intrinsic emission appears brighter as offset from the source increases, as the contribution from scattered light decreases with distance from the source. This is why the tips of the northern and eastern cavity walls have significantly larger ratio values. Figure 3.23 displays the integrated intensity map of the $H_2$ emission before, in the top panel, and after, in the bottom panel, the scattered emission removal routine was implemented. When comparing between these two images, it is clear that after the scattered light is subtracted, there is a steeper intensity gradient associated with the intrinsic $H_2$ emission, which is most readily observable in the closeness of contour lines surrounding bright $H_2$ emission, such as the features labelled *A1* & *A2*. Nebulous emission close the apex of the cavity has been diminished, which is in agreement with the $H_2$ line to continuum ratio map predicting a strong contribution from scattered photons in this region.

As the scattered emission subtraction process samples the representative scattered emission spectrum from the continuum peak, the base of the jet, traced in forbidden iron emission and Br-$\gamma$ emission, is removed as an unavoidable by-product of the process, as jet emission is more compact and located closer to the source position. This implies that some intrinsic atomic jet emission is present in the representative scattered emission spectrum or source spectrum due to the diameter of the aperture used to sample the spectrum, and also the angular resolution of the observation.

The bottom panel of Figure 3.22 presents the line to continuum plot for the [Fe II] emission at 2.05 μm. This emission is a well established jet tracing line. The morphology of this emission is discussed in Section 4.2.1. It is seen that at the continuum peak position, the line to continuum ratio is distinctly higher than that in the surrounding nebulous region, confirming that there is indeed

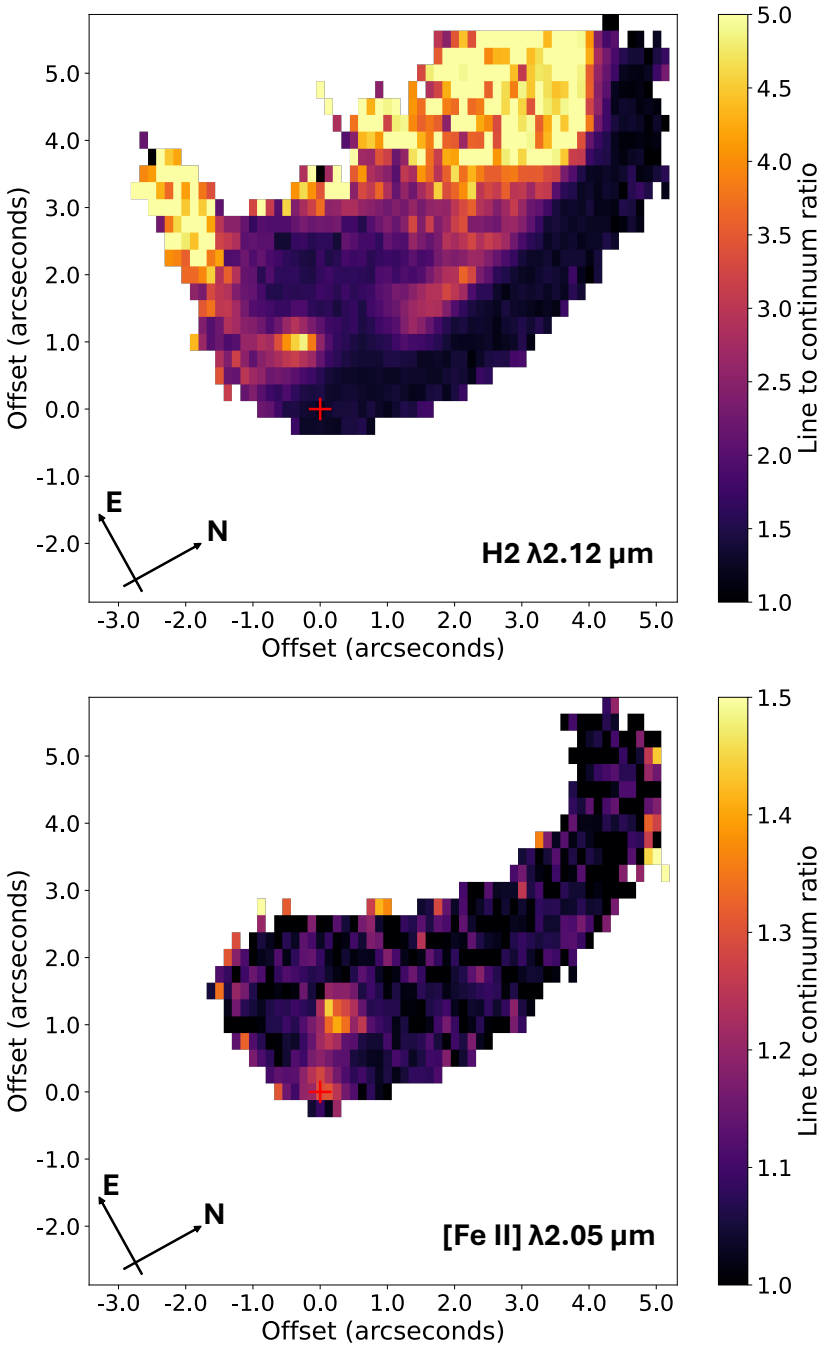


FIGURE 3.22: Line to continuum ratio plots of $H_2$ and [Fe II] emission. Intrinsic emission appears bright in these images, whereas scattered light is represented by a constant ratio close to unity. The source position is represented with a red plus symbol. *Top panel*: Integrated $H_2$ emission between $-$ 140 km s$^{-1}$ and $+$ 60 km s$^{-1}$, divided by nearby continuum. Intrinsic line emission here is coming from the cavity walls and a $H_2$ knot at the base of the left cavity wall. *Bottom panel*: Integrated [Fe II] emission between $-$ 310 km s$^{-1}$ and $-$ 100 km s$^{-1}$, divided by nearby continuum. Intrinsic line emission one sees here traces the high velocity atomic jet.

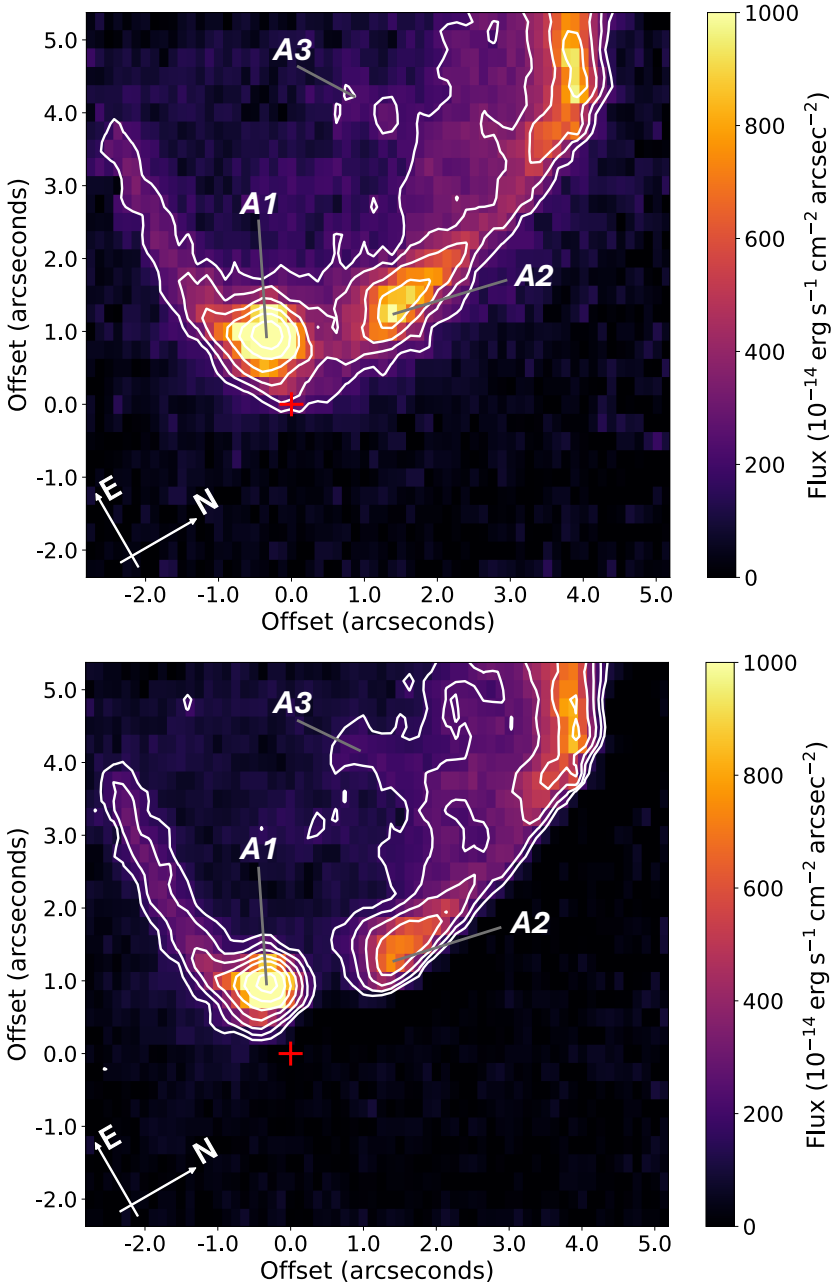


FIGURE 3.23: Figure displaying integrated $H_2$ line emission before (*top*) and after (*bottom*) the scattered emission removal routine is preformed. The source position is represented with a red plus symbol. Contour levels for both panels begin at $3\sigma$ of the background emission and increase by factors of 1.5.

intrinsic jet emission co-located with the continuum peak. Therefore the representative scattered emission spectrum extracted from the continuum peak position cannot be used to subtract the scattered light in [Fe II] emission, as this would result in an overcorrection and subsequently subtract intrinsic jet emission. This is further supported in Figure 6 from Nisini et al. (2024). The [Fe II] $\lambda$1.87 μm jet as observed using NIRCam (Near-InfraRed Camera) on JWST (James Webb Space Telescope) is displayed in the top right panel. The first jet knot that is seen is offset from the binary source, separated only by a thin dark lane. The angular resolution provided by the SINFONI observations presented here do not spatially resolve the [Fe II] jet knot from the central binary. This results in an artificially increased line to continuum ratio at the source position as jet emission coincides with the source position. In contrast, the bottom left panel of Figure 6 from Nisini et al. (2024) highlights that the innermost bright peak in $H_2$ emission, *A1*, is sufficiently separated from the binary source to be spatially resolved by SINFONI. This justifies that the spectrum extracted from the source position is representative of the true stellar spectrum illuminating the cavity, and therefore can be used for correcting the scattered light in $H_2$ emission. As applying the scattered light removal process to jet tracing emission lines, such as the [Fe II] emission line at 2.05 μm, resulted in sacrificing the ability to trace the jet back to the source position, it was decided not to perform this routine on the jet tracing lines. Furthermore, the lack of scattered emission removal is not critical in the analysis of the jet tracing lines because the narrow and collimated jet emission stands out clearly from the fainter surrounding nebulous emission allowing the accurate determination of the jet PA and morphology.

The line to continuum ratio plots generated for Br-$\gamma$ emission are displayed in Figure 3.24. The Br-$\gamma$ emission has been split into high velocity and low velocity channels. The top panel of Figure 3.24 presents the high-velocity ($-$ 230 km s$^{-1}$ to $-$ 130 km s$^{-1}$) Br-$\gamma$ emission line to continuum plot. This emission is seen to trace the jet also. Therefore, scattered emission subtraction was not performed on this emission line either. In the bottom panel of Figure 3.24, a line to continuum map of low velocity Br-$\gamma$ emission is presented, integrated from $-$ 100 km s$^{-1}$ to $+$ 100 km s$^{-1}$. In this line to continuum map, the ratio of integrated line emission to continuum is approximately constant across the morphology of the cavity, and equal to the ratio located at the continuum peak position. It can be inferred from this that any spatially extended Br-$\gamma$ emission

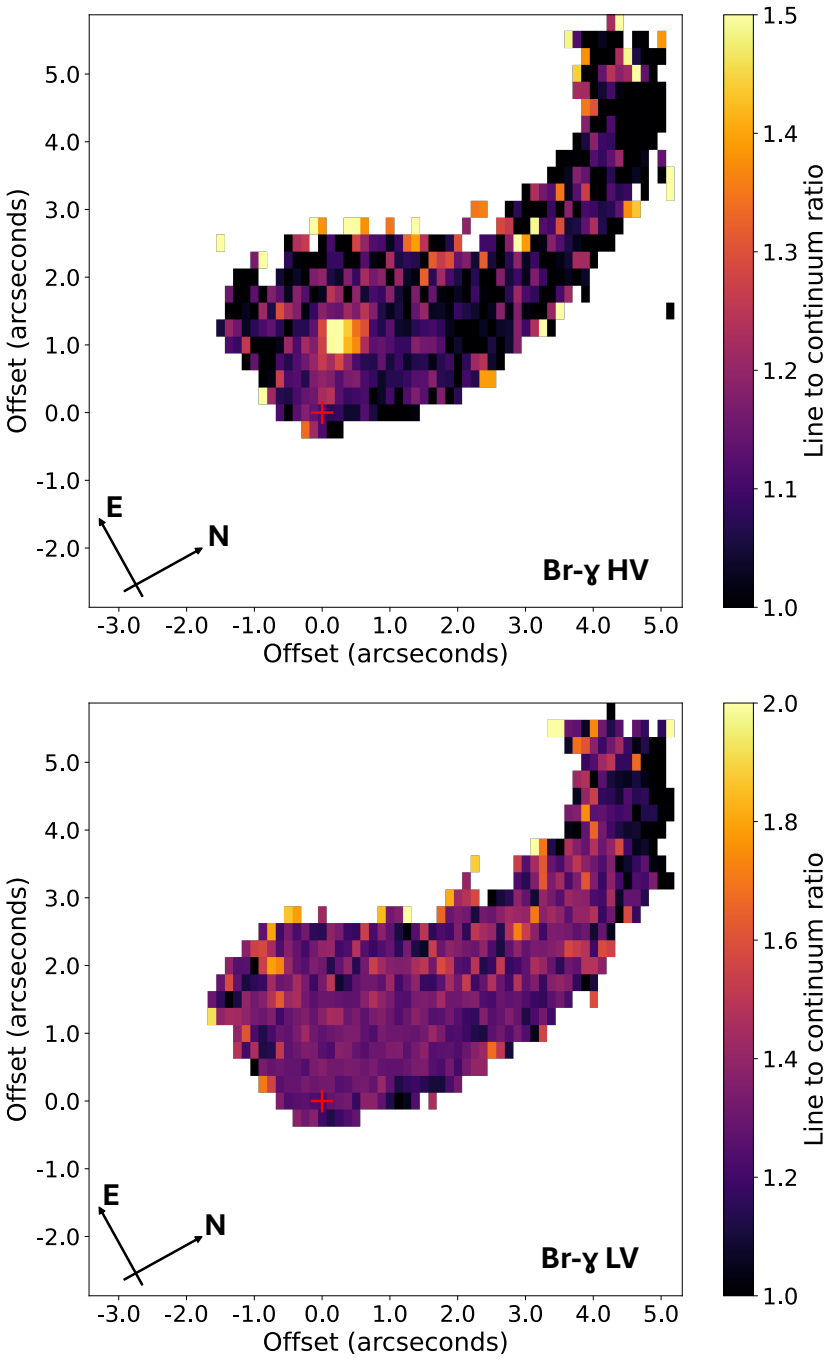


FIGURE 3.24: Line to continuum ratio plots of Br-$\gamma$ emission. The source position is represented with a red plus symbol. *Bottom left*: Integrated high-velocity Br-$\gamma$ emission between $-$ 230 km s$^{-1}$ and $-$ 130 km s$^{-1}$, divided by nearby continuum. Intrinsic line emission one sees here, again, traces the high velocity atomic jet. *Bottom right*: Integrated low-velocity Br-$\gamma$ emission between $-$ 100 km s$^{-1}$ and $+$ 100 km s$^{-1}$, divided by nearby continuum. There is no spatially extended intrinsic emission detected here.

one sees in the low velocity channel follows the same spatial distribution as the scattered light seen in continuum. This implies that any spatially extended, low velocity Br-$\gamma$ emission is not intrinsic emission, and is instead dominated by scattering of the central source spectrum off of the dusty, nebulous cavity material traced by the continuum.

As the scattered emission removal process could not be applied to the jet tracing lines, such as [Fe II] and Br-$\gamma$ emission, a baseline continuum subtraction routine was instead implemented. This method is performed locally around emission lines of choice. A sub-cube is extracted from the data cube, centred on an emission line of choice, with some continuum emission located either side of the line. At each spatial pixel in sub-cube, a polynomial is fit to the local continuum on either side of the emission line, with care taken to omit the emission line region from the fit. This is achieved by masking the spectral region where the emission line resides. Figure 3.25 illustrates the process of fitting a $n^{\text{th}}$ order polynomial to the continuum baseline level at a single spaxel spectrum for sub-cubes extracted around the [Fe II] $\lambda$2.05 μm, and Br-$\gamma$ emission lines. The order of polynomial of best fit to the continuum is manually selected. These polynomial fits are then subtracted from every spectrum in the sub-cube, effectively reducing the continuum level to zero.

## 3.4 MUSE observations

Observations of the CTTS RU Lupi were obtained with ESO's MUSE in July and August 2021 as part of two separate ESO observing programmes, 106.21-EN.001 and 0104.C-0919(B), respectively. Both sets of data were accessed through the ESO science archive[5]. The target, RU Lupi is discussed in Section 5.1.1.

### 3.4.1 0104.C-0919(B) observations

The 0104.C-0919(B) observations (PI: A. Müller) of RU Lupi were taken in August 2021. The observations were taken using MUSE's Narrow Field Mode (NFM), with a spectral resolving power varying from $R \approx 1700$ in the blue end of the wavelength range to $R \approx 3400$ in the red end, and a spectral sampling of 0.125 nm pixel$^{-1}$. The average spectral resolving power is $R$ = 2595. The FOV offered with MUSE's NFM is $7\farcs5 \times 7\farcs5$ with a spatial sampling of $0\farcs025$

[5]ESO Science archive

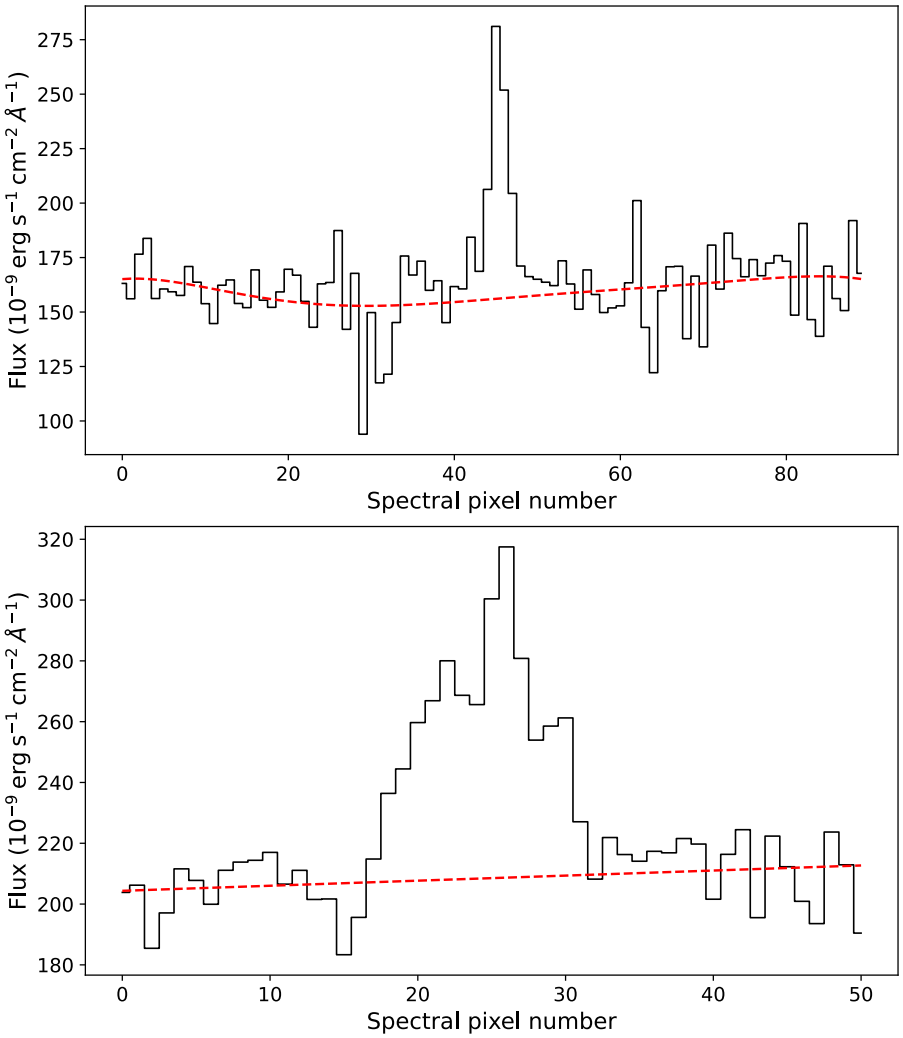


FIGURE 3.25: $n^{\text{th}}$ order polynomial fitting to the continuum baseline level at a single spaxel spectrum for sub-cubes extracted around the [Fe II] emission line at 2.05 µm (*Top*), and the Br-$\gamma$ emission line (*Bottom*).

pixel$^{-1}$ (Bacon et al., 2010). This FOV facilitated the investigation of the outflow from RU Lupi as it is known to be relatively compact. The observation run consisted of three observations of exposure times 390 s, 1500 s, and 1800 s. The average seeing of the observation $0\farcs061$ and the airmass varied from 1.102 to 1.151. The instruments AO correction was used.

### 3.4.2 106.21EN.001 observations

The 106.21EN.001 observations (PI: L. Pérez) of RU Lupi were taken in July 2021. The observations were also taken using MUSE's Narrow Field Mode (NFM). The average spectral resolving power is $R$ = 2595. The observation run consisted of four observations and was later included in ESO's MUSE DEEP data collection, where the individual observations were aligned and combined to form a higher signal to noise ratio (S/N) observation, resulting in a final exposure time of 3400 s. The laser tomography AO provided an angular resolution of $0\farcs074$. The 106.21EN.001 data was found to be of better quality due to the MUSE-DEEP data collection, and so the results presented in Section 5.2 are from this data set.

## 3.5 MUSE data reduction and analysis

As both sets of data were accessed through the ESO science archive, the data was pre-reduced using the MUSE data reduction pipeline. Therefore, in the cases of both observations, standard calibration files were used in the reductions. These include pixel tables, bias frames, dark frames, flat-field frames, sky frames, wavelength calibration tables, and astrometric corrections. More information on the calibration files and the pipeline can be found in the MUSE pipeline user manual[6]. The MUSE pipeline also performs flux calibration using a flux standard star observation. The reduced data cubes required some further processing for accurate analysis.

Wavelength recalibration was not deemed necessary for the analysis. This was verified by measuring the spectral positions of several OH telluric emission lines using Gaussian fitting of line profiles. The measured centroids of these Gaussian fits resulted in values averaging $\sim 0$ km s$^{-1}$, as one expects for emission lines originating in Earth's upper atmosphere. Telluric correction

[6]MUSE Pipeline user manual

was also not performed on these data sets as the effect of telluric contamination is not as pronounced at optical wavelengths as in NIR wavelengths, and where telluric features are present, they do not affect emission line regions that are relevant to the analysis.

### 3.5.1 Data cube coadding

As the 0104.C-0919(B) observations consisted of three data cubes, the alignment and combining of these into a single data cube was desired, as this would increase the S/N of the observation. The data cube with the longest exposure time (1800 s) was selected as the reference observation. 2D image slices were extracted from the data cube at spectral positions containing only continuum emission throughout the spectral axis. The point source was fit with a 2D Gaussian profile in order to retrieve the centroid of the PSF. This PSF centroid measurement was also performed on the other two data cubes and subsequently, these two cubes were spatially shifted in $x$ and $y$ coordinates so that their centroid positions matched that of the data cube with the longest exposure time. Once the three cubes were spatially aligned, they were integrated or coadded, where each 2D image slice in the cube was added to the corresponding 2D image slices in the other two cubes. This produced a single data cube that combined the three observations into one, effectively increasing the S/N.

### 3.5.2 Continuum subtraction

The emission line signal tracing outflow features in these observations was relatively weak, meaning it was difficult to isolate the line emission from the background and continuum emission. As a result of this weak signal, two methods of continuum subtraction were attempted.

As the goal of the study was to investigate the outflow emanating from the CTTS RU Lupi, the stellar contribution as well as background emission needed to be subtracted in order to probe the outflow tracing emission lines. Similar to the analysis performed with the SINFONI data, a continuum subtraction method that would also remove the contribution of light scattered from the central source, in effect, leaving only intrinsic line emission, was attempted. This was achieved in the same way as discussed in Section 3.3.7, where a reference spectrum is extracted such that it best represents pure stellar light.

This spectrum was extracted form the source position by placing an aperture slightly larger in size than the seeing of the observation over the stellar position and integrating to obtain the total flux within the aperture. Annuli, larger than the aperture, were implemented to estimate the background contribution which was subsequently subtracted. The reference spectrum, which best represents the continuum emission and the scattered light, was extracted in this way. This reference spectrum was then scaled so that it matched the continuum level at each spaxel in the data cube, locally around each emission line of interest, then subtracted from the cube. This results in a data cube free from continuum emission and scattered light.

However, a complication arose using this method, in that there was a problem of oversubtraction. This was due to a combination of the outflow tracing lines being relatively weak and the spatial resolution of the observation not being sufficient to extract a pure stellar spectrum. This resulted in the artificial diminishing of the outflow tracing lines, and the loss of information in the vicinity of the base of the outflow where the adverse effects of oversubtraction were the strongest. An example image of high-velocity [S II] $\lambda$6731 Å emission, an outflow tracing emission line, after this method of continuum subtraction is employed is displayed in Figure 3.26. In this figure, the loss of information in the vicinity of the source position can be clearly seen.

As this method of continuum subtraction could not be applied to the outflow tracing lines due to loss of information, a baseline continuum subtraction routine was instead implemented. The same baseline continuum subtraction process as described in Section 3.3.7 in reference to the jet tracing lines is used here. Figure 3.27 illustrates the process of fitting a $n^{\text{th}}$ order polynomial to the continuum baseline level at a single spaxel spectrum for sub-cubes extracted around the [O I] $\lambda$6300 Å and [S II] $\lambda\lambda$6716,6731 Å emission lines. These polynomial fits are subsequently subtracted from every spectrum in the sub-cube, effectively reducing the continuum level to zero. Using this method of continuum subtraction does not remove scattered light, originating from the central source, meaning emission line flux measurements may contain contribution from scattered emission depending on how embedded the driving source is. Line to continuum ratio maps are produced for RU Lupi to investigate the contribution of scattered emission to intrinsic line emission, and these are presented in Section 5.2.1.

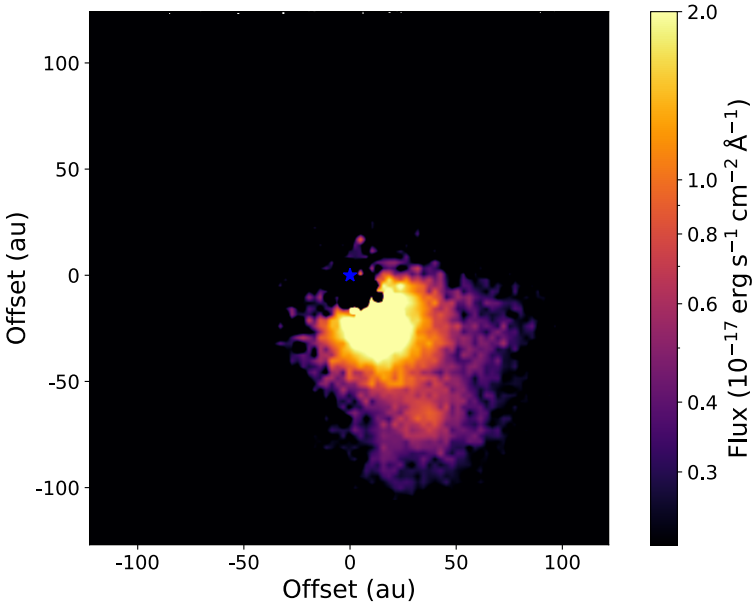


FIGURE 3.26: Integrated high-velocity [S II] $\lambda$6731 Å emission. The source is marked with a blue star. Notice the effect of oversubtraction of the outflow emission in the vicinity of the source position.

## 3.6 ERIS observations

Observations of the HH 46/47 outflow were obtained with ESO's ERIS on the 3$^{rd}$ of December 2022, as part of ERIS's science verification phase, under ESO observing programme ID 110.257N.001 (PI: M. Birney). The target, HH 46/47 is discussed in Section 4.1.1. The NIR observations were obtained using the 'K_short' band grating (1.95 – 2.20 µm) with a resolving power of R = 11,200. The FOV chosen was $8\farcs0 \times 8\farcs0$ providing a spatial sampling of $0\farcs125 \times 0\farcs250$. This FOV was chosen as it was well suited to encompass the base of the blueshifted outflow, and for ease of comparison with the SINFONI observations discussed in Section 3.2. Furthermore, the detector was also rotated by 60° so that the vertical axis of the detector was parallel to the approximate CO outflow position angle (PA) (Zhang et al., 2019).

The observations consisted of twelve exposures of 150 s each providing an on target exposure time of 1800 s. The average seeing of the science observation was $1\farcs42$ and the airmass varied from 1.54 to 1.57. As the observation was part of the ERIS science verification programme, a short trial run of observations aimed at demonstrating the scientific capability of the new instrument, the observation was taken outside of observational quality constraints. This resulted in the observation having a poor angular resolution or seeing. It was

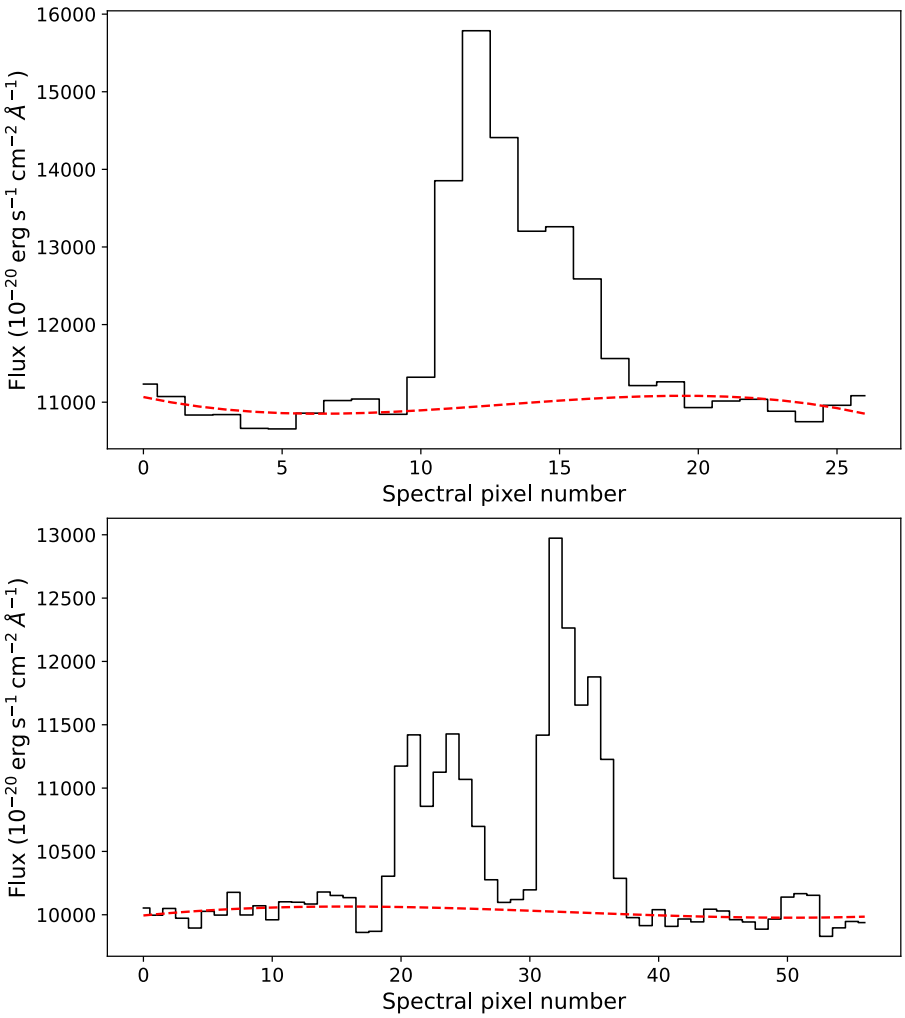


FIGURE 3.27: $n^{\text{th}}$ order polynomial fitting to the continuum baseline level at a single spaxel spectrum for sub-cubes extracted around the [O I] $\lambda$6300 Å (*Top*), and [S II] $\lambda$6716,6731 Å emission lines (*Bottom*).

also not possible to use the instruments AO correction due to a lack of a suitable bright point source nearby. Six exposures of 150 s were also taken for sky exposures. One standard star, HD 73105 (HIP 042038), was also observed for flux calibration and telluric correction. The goal of the observations was to further investigate the transverse velocity gradient observed with SINFONI in the blueshifted outflow cavity in $H_2$, discussed in Section 4.2.3, with greater spectral resolution.

## 3.7 ERIS data reduction and analysis

The data was reduced using ESO's ERIS-SPIFFIER data reduction pipeline (Version 1.6.1) and run with ESOReflex (Freudling et al., 2013). Standard calibration files were used in the reduction. Input files include reference files (reference bad pixel map & arc line reference table), the raw frames (dark frames, flat fields, fibre frames, arc lamp frames, sky frames, flux standard star frames, PSF standard star frames & science frames), and calibration products (bad pixel maps, distortion table, master flat field, master darks, slitlet positions, & wavelength maps). More information on these input files can be found in the ERIS-SPIFFIER pipeline user manual[7].

The data reduction pipeline was run using ESOReflex. The data cube was corrected for bad pixels, flat-fielding, geometric distortions, bias and dark signal, sky emission and a first order wavelength calibration was done using arc lamp wavelength solutions. The pipeline performs flux calibration. The reduced data cubes required some further processing for accurate analysis.

### 3.7.1 Continuum subtraction

Like the SINFONI observations of HH 46/47, the ERIS observations presented here probe the launching region of the outflow, tracing the outflow very close to the embedded driving source. Therefore strong contributions of scattered light from the central engine was expected. As discussed in Section 3.3.7, the scattered emission was subtracted from the outflow cavity-tracing emission lines ($H_2$). Again, an assumption was made that the scattered light component was entirely light from the unresolved central binary reflecting off the cavity. A spectrum was therefore extracted from the continuum peak position, or

[7]ERIS-SPIFFIER pipeline user manual.

the driving source position, to best represent the contribution from scattered emission. This spectrum was then rescaled and subtracted locally in wavelength around each emission line of interest from the spectra at each spaxel, effectively removing the scattered light component and continuum emission from the emission line of interest. As in the case with the SINFONI observations, and discussed in Section 3.3.7, this process of scattered light removal resulted in the loss of intrinsic jet emission ([Fe II] and Br-$\gamma$) close to the driving source. Again, as the scattered emission removal process could not be applied to the jet tracing lines, a baseline continuum subtraction routine was instead implemented. This method is described in Sections 3.3.7 and 3.5.2.

### 3.7.2 Principal component analysis

When inspecting the reduced data cube, visual artefacts, or aberrations, were present across the FOV. These aberrations appear as clusters of hot pixels in each 2D image slice in the data cube, and their positions vary from slice-to-slice. Figure 3.28 displays three subsequent image slices extracted from the reduced data cube. The visual aberrations, which vary in position and intensity across multiple slices, are clear in this succession of 2D images. As the analysis of the ERIS observations presented here is preliminary, the cause of these visual aberrations is not yet identified. In an effort to minimise the contribution from these aberrations, the statistical method of principal component analysis (PCA) was implemented. PCA was implemented locally around emission lines of interest, and the PCA implementation available in the Python package `scikit-learn` was used (Pedregosa et al., 2011).

PCA is a widely-used linear dimensionality reduction technique, where data is linearly transformed to a new coordinate system such that the orthogonal directions, called principal components, in this coordinate system, preserve the information in the original data (Joliffe, 2002). The first principal component describes the greatest variance in the data, therefore capturing an approximation of the global signal present in the data, or the most important structure in the data. The second principal component, aligned orthogonal to the first, describes greatest variance in the data, once the effect of the first component is removed, therefore capturing an approximation of the second most important global structure present in the data. This process is then iterated until all of the variance present in the dataset is explained. As this technique

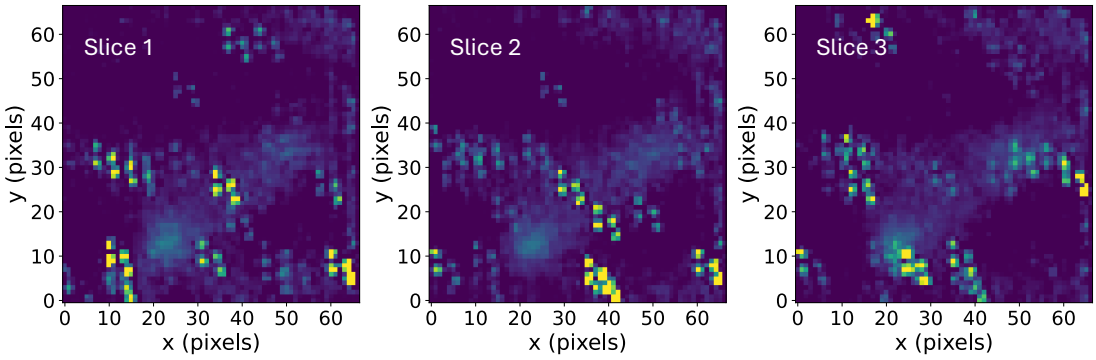


FIGURE 3.28: Three successive 2D image slices from the reduced data cube displaying visual artefacts or aberrations present. These aberrations appear as clusters of hot pixels.

identifies patterns in the data, it can be used to perform noise filtering, as noise is generally unsystematic, and will vary randomly. For a recent review of PCA see Greenacre et al. (2022).

In the case of the visual artefacts present in the IFS observations, since these artefacts appear in different positions across the data cube slices, PCA can help identify patterns that are inconsistent with real astrophysical signal. PCA was implemented locally around emission lines of interest by extracting small sub-cubes, with narrow-wavelength intervals, from the larger data cube. In these sub-cubes the intrinsic line emission representing the outflow, follows a smooth variation across wavelength slices, with a consistent spatial structure, and therefore is correlated over multiple slices. In contrast, the artefacts across the image slices are uncorrelated and display a random appearance, with their positions and intensities varying slice-to-slice. As each principal component represents a different mode of variation in the data, the first few will capture the global structure present in the sub-cube, in other words the intrinsic outflow emission. The higher-order principal components will capture random variations in the image slices, including noise, cosmic rays, and artefacts. Therefore, reconstructing the data using only the low-order principal components, and discarding the higher-order ones, results in a sub-cube with the artefacts removed. A limitation of PCA, that does not apply strongly here, is that it does not work well if artefacts are highly structured across many slices, such that the artefacts are correlated over multiple slices, for example, persistent detector effects.

In order to perform PCA, the 3D sub-cube was flattened into a 2D matrix,

where one axis represented the spectral information and one represented the spatial information. This was achieved by taking the dimensions of the 3D sub-cube ($N_\lambda$, $N_y$, $N_x$) and reshaping the spatial axes so that they were represented by a single dimension, resulting in a 2D matrix with dimensions ($N_\lambda$, $N_y \times N_x$). In this new 2D matrix, each column represents a spaxel's spectrum, and each row corresponds to a different wavelength slice. PCA is then applied to this 2D matrix. The number of principal components kept in the reconstructed 3D sub-cube was done by visual inspection, where $n$, the number of principal components retained, was tuned until the large-scale, intrinsic structure was present and the artefacts and random noise were mitigated.

# Chapter 4

# A kinematical study of the launching region of the blueshifted HH 46/47 outflow with SINFONI and ERIS K-band observations

## 4.1 Introduction

In this chapter, I will present the kinematical study of the launching region of the blueshifted HH 46/47 outflow with SINFONI and ERIS K-band observations. As discussed in Section 1.3.4, measurements of outflow rotation, that subsequently lead to estimates of specific angular momentum removed by the outflow, are critical for constraining magneto-centrifugally launched MHD outflow models, and for determining the role of outflows in angular momentum extraction from the star-disc system (Frank et al., 2014; Pudritz and Ray, 2019; Pascucci et al., 2023). Disc wind models predict a greater fraction of angular momentum removal from the star-disc system, in comparison to X-wind models, as the outflow launching region extends further radially along the disc from the driving source, and specific angular momentum contained in the outflow increases with disc radii (Anderson et al., 2003; Ferreira, Dougados, and Cabrit, 2006; Pudritz and Ray, 2019; Lee et al., 2021). The measurement of rotation in wide-angled outflow components can offer much information about angular momentum transport. As the lateral component of these wide-angled winds can more readily be spatially resolved, obtaining outflow rotation measurements is more promptly achievable (Tabone et al., 2017; Zhang et

al., 2018). Measuring outflow rotation signatures using only the high-velocity jet components is more challenging, and requires high-angular resolution observations to spatially resolved the narrow jet structure (Bacciotti et al., 2002; Coffey et al., 2004; Coffey et al., 2007; Lee et al., 2017). Furthermore, observing protostars, or class 0/I sources, is essential to gaining insights on the most active period of accretion and ejection (Ray and Ferreira, 2021). At these early stages, the outflows are at their most powerful and therefore brightest, making them ideal targets in the search for rotation signatures, especially in their wide-angled components. However, protostars are challenging to observe due to their heavily embedded nature. Their dusty and gaseous envelopes cause strong extinction, making it difficult to probe the inner regions of the discs where accretion occurs and where the earliest instances of planet formation are beginning. In order to search for rotation in the outflow, one must first understand the morphological and kinematical structure of the outflow. The large-scale morphology and kinematics of the HH 46/47 outflow is probed further in a proper motions study presented in Chapter 6.

As discussed in Section 1.3.2, outflow emission arises primarily from the cooling regions of the shocks generated when higher-velocity material catches up with and impacts material ahead of it (Tsukamoto et al., 2023). While outflows are observed in all wavelength regimes, class 0/I outflows are best observed with IR and sub-millimetre observations, as these wavelengths allow one to peer through the dusty envelope (Yang et al., 2022; Harsono et al., 2023; Beuther et al., 2023; Ray et al., 2023; Nisini et al., 2024; Delabrosse et al., 2024). In particular, these outflows can be studied using IR iron FELs and $H_2$ rovibrational emission lines, as these lines emit brightly near their bases, and interestingly these two species trace different outflow components (Davis et al., 2011). [Fe II] emission traces hot, dense, and partially ionised high-velocity gas ($T \sim$ 10,000 K; $n_e \sim 10^5$ cm$^{-3}$; $v \sim$ 100 km s$^{-1}$ – 400 km s$^{-1}$; Nisini et al. 2002; Davis et al. 2003), whilst $H_2$ traces an emission line region associated with lower excitation, shocked molecular gas, or UV fluoresced gas at much lower velocities ($T \sim$ 2,000 K; $n_e \sim 10^3$ cm$^{-3}$; $v \sim$ 10 km s$^{-1}$ – 50 km s$^{-1}$; Davis 2002; Caratti o Garatti et al. 2006; Frank et al. 2014). These typical gas properties are summarised in Table 4.1. Therefore, [Fe II] emission is a well-established jet tracer (Davis et al., 2003), and shocked $H_2$ emission is an important means of tracing molecular winds and cavities (Nisini et al., 2024). The CO rotational emission lines at sub-millimetre wavelengths are also found in

TABLE 4.1: Summary of typical gas properties for emission tracers present in SINFONI data.

| Emission tracer | $T$ (K) | $n_e$ (cm$^{-3}$) | $v$ (km s$^{-1}$) |
|---|---|---|---|
| [Fe II][(1)] | 10,000 | $10^5$ | 100 – 400 |
| $H_2$[(2)] | 2,000 | $10^3$ | 10 – 50 |
| CO[(3)] | 100 | $10^3$ | 5 – 30 |

(1) Nisini et al. (2002) and Davis et al. (2003)
(2) Davis (2002), Caratti o Garatti et al. (2006), and Frank et al. (2014)
(3) Scoville et al. (1987), Frank et al. (2014), and Baug et al. (2021)

outflows from class 0/I YSOs. The component of the outflow that CO likely maps is the resulting ambient gas after it has been swept up and entrained by some wide-angled wind and later left to cool (Arce et al., 2013). However, in some cases it is thought to trace the disc wind itself (Louvet et al., 2018; de Valon et al., 2022). The CO emission traces molecular gas at low velocities also and is cooler than the $H_2$ emission ($T \sim 100$ K; $n_e \sim 10^3$ cm$^{-3}$; $v \sim 5$ km s$^{-1}$ – 30 km s$^{-1}$ Scoville et al. 1987; Frank et al. 2014; Baug et al. 2021). Therefore, CO emission complements snapshots of current shock interactions, obtained with $H_2$ and [Fe II] observations, by providing insight into the outflow history of the protostar (Richer et al., 2000).

In this chapter, SINFONI IFS observations of the HH 46/47 outflow system in the K-band (1.95 – 2.45 μm) with a resolving power of R = 4000 are presented. The field of view (FOV) chosen was $8\farcs0 \times 8\farcs0$, resulting in an observation of the base of the blueshifted outflow. These observations allowed the investigation of both the base of the fast axial jet and the wide-angled outflow component in NIR [Fe II] and $H_2$ emission and to subsequently make a comparison with previous CO sub-millimetre observations. In particular, the use of a wavelength recalibration technique based on OH lines to search for a rotation signature in the HH 46/47 outflow was desired. The target is discussed in Section 4.1.1. In Section 4.2, the results of the study are presented, namely the morphologies and kinematics of the continuum emission, the wide-angled $H_2$ outflow cavity, and the base of the atomic jet. Also presented is a velocity gradient transverse to the outflow axis observed in the $H_2$ outflow cavity.

In Section 4.3, the results are discussed. Included in the discussion is the observed layering of different emission tracers and the origin of the velocity gradient associated with the $H_2$ outflow cavity. The conclusions are summarised in Section 4.4.

### 4.1.1 HH 46/47

Discovered by Schwartz (1977), HH 46/47 is a well-studied complex of Herbig-Haro (HH) objects, a series of internal working surfaces or shock fronts in a larger outflow (See Figure 4.1). The driving source of the outflow system (HH 46 IRS, HH 47 IRS, IRAS 08242-5050, 2MASS J08254384-5100326) is a deeply embedded ($A_V > 35$), low-mass, class I YSO binary system of $\sim 0\farcs26$ separation or 117 au (Reipurth et al., 2000; Nisini et al., 2024), taking a distance to the system of 450 pc (Graham and Heyer, 1989). The system has a combined mass of approximately 1.2 $M_\odot$ and bolometric luminosity of < 15 $L_\odot$ (Antoniucci et al., 2008), and is located at the northeastern edge of the Bok globule, ESO 210-6A, in the Gum nebula. Bok globules are dark, optically opaque clouds which have long been associated with low-mass star formation (Bok and Reilly, 1947). Molecular cloud cores, discussed in Section 1.1.1, are thought to be essentially equivalent to dense Bok globules. The bipolar outflow system consists of wide-angled low-velocity molecular outflows accompanied by highly collimated high-velocity, mainly atomic, jets. The blueshifted side of the jet emanates northeasterly from the Bok Globule, making it easily visible at optical wavelengths (Heathcote et al., 1996; Hartigan et al., 2011). The redshifted side of the jet penetrates southwesterly, deep into the cloud, making it, and the driving source itself, visible at only infrared wavelengths (Eisloeffel and Mundt, 1994; Reipurth et al., 2000; Noriega-Crespo et al., 2004; Erkal et al., 2021b).

The blueshifted jet displays a screw-like structure that spirals counter clockwise towards the observer with an angle of inclination of 37° with respect to the plane of the sky (Hartigan et al., 2005). Proper motions at the base of the jet are approximately 270 km $s^{-1}$ and increase to 300 km $s^{-1}$ (Hartigan et al., 2005; Erkal et al., 2021b). Wide-field images reveal that HH 46/47 extends at least 2.6 pc from the driving source, setting a lower limit to the dynamical age of the outflow of $10^4$ – $10^5$ years old (Stanke, McCaughrean, and Zinnecker,

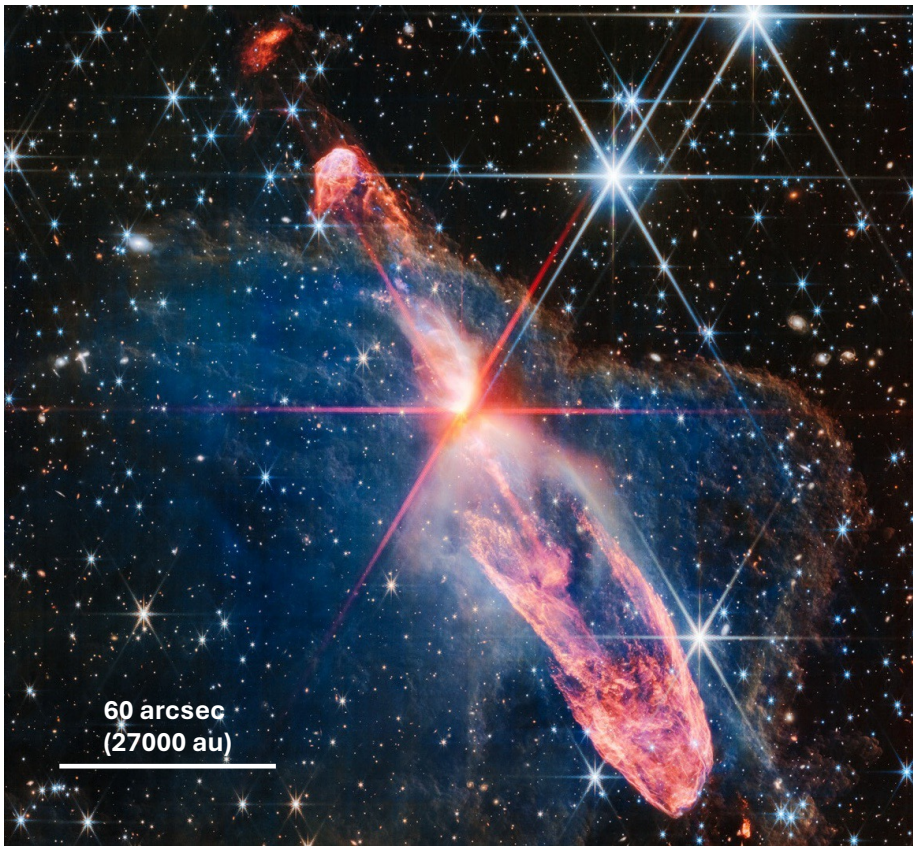


FIGURE 4.1: The HH 46/47 bipolar outflow as imaged by JWST NIRCam. Credit: NASA, ESA, CSA, J. DePasquale, A.M. Koekemoer.

1999). The jets display a prominent 'wiggling'. It was postulated that the orbital motion of an unresolved tertiary component caused the meandering of the jet (Reipurth et al., 2000), as the separation of the binary system was too large to explain the short wiggling period of $\sim$ 200 yr seen at large scales. The jet also displays a highly structured morphology, with knots seen along the outflow implying episodic ejection of material from the driving source.

The wide-angled molecular outflows have been well studied using ALMA CO (1-0) observations (Arce et al., 2013; Zhang et al., 2016) and CO (2-1) observations (Zhang et al., 2019). The low-velocity wide-angled CO outflow is highly asymmetric, with the redshifted lobe extending four times further than blueshifted lobe, a lack of dense material in the path of the blueshifted flow is responsible for this. This wide-angled component displays multiple shell-like structures and these shells trace the ejection variability just like the collimated component of the outflow (Zhang et al., 2019). The variability timescales of the multiple outbursts seen in the wide-angle wind is consistent with episodic knots along the jet of HH 46/47. This suggests that the multiple shell structure seen in wide-angle component may arise from the same high accretion rate episodes that is reflected in the knots in the jets.

$H_2$ emission was first detected in the HH 46/47 system by Schwartz (1983) with the identification of six fluorescent UV emission lines produced by Ly-$\alpha$ pumping of $H_2$. These molecules had to be first warmed to the second vibrational state of the electronic ground state. Later, NIR $H_2$ quadrupole emission in HH 46/47 was detected by Wilking et al. (1990). Eisloeffel and Mundt (1994) first presented the $H_2$ morphology of the HH 46/47 system using the IRAC2 instrument on the ESO/MPI 2.2 m telescope. Noriega-Crespo et al. (2004) imaged the system in the near to mid-infrared using the Spitzer Space Telescope revealing the optically invisible redshifted jet propagating southwesterly exhibiting a loop-like morphology, with both outflow lobes being narrower than those observed in CO emission. Garcia Lopez et al. (2010) used long-slit NIR spectroscopic observations of the system using ISAAC and investigated the kinematics of the atomic and molecular emission, namely $H_2$ and [Fe II] emission, along the jet.

Erkal et al. (2021b) mapped the HH 46/47 system with HST with, at the time, unprecedented detail and recently, the HH 46/47 driving source and outflow were mapped at higher angular resolution of $\sim 0\farcs2$ with JWST using the

NIRSpec (Near-Infrared Spectrograph) IFU and MIRI MRS (Mid-Infrared Instrument Medium Resolution Spectroscopy) as part of the PROJECT-J program (ID 1706, P: B. Nisini; Nisini et al. 2024). These observations provide unprecedented detail of the structure of the jet, the associated molecular outflow, and the cavity. Emission in $H_2$ reveals a complex molecular outflow, where the bright outflow cavity, expanding molecular shells and jet-driven bow-shocks interact with, and are influenced by ambient conditions. The superior spectral resolution provided by the SINFONI observations with respect to JWST ($R \approx 4000$ vs. 2700), allows the outflow kinematics to be studied with unprecedented detail.

## 4.2 Results

The SINFONI observations of HH 46/47 reveals emission lines tracing outflow and accretion activity, in agreement with previous spectroscopic studies (Antoniucci et al., 2008; Garcia Lopez et al., 2010). A table of identified emission lines present in the SINFONI observations is presented in Table 4.2. In this chapter, the morphology and kinematics of the jet and wide-angled outflow, with a particular focus on the kinematics of the outflow, are discussed. The source is heavily veiled (Antoniucci et al., 2008; Nisini et al., 2024) and therefore partially embedded at these wavelengths, but a point source at the apex of the cavity as traced in continuum emission is detected. The continuum peak position was fit with a 2D Gaussian profile and the centroid of this fit was used as the source position throughout. The spatial resolution of the SINFONI observations is not sufficient to resolve the binary system. It is important to note that this continuum peak is not necessarily coincident with the position of the HH 46 IRS (infrared source) millimetre position derived by Arce et al. (2013) using the peak intensity of thermal dust emission at 100 GHz with ALMA observations, as in the IR it is possible that the significant contribution of scattered light could shift the barycentre of the source continuum peak. The thermal dust emission at 100 GHz originates from the inner region of the accretion disc making the centroid of this emission an accurate indicator of the source position.

Spectra were extracted at various positions across the FOV of the observation. These spectral extraction positions are highlighted in Figure 4.2, which displays a three-colour image produced from the SINFONI observation of the

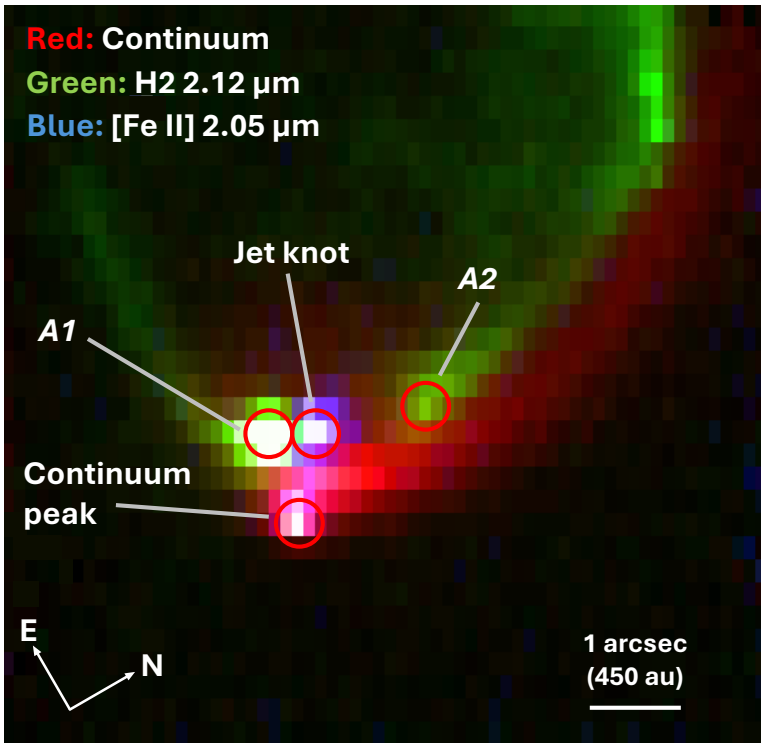


FIGURE 4.2: Spectral extraction locations presented in Figures 4.3, 4.4, and 4.5. Spectra were extracted from these positions using circular apertures of radius 0″.41, approximately half of the average seeing of the observation, 0″.81. The red emission here traces integrated continuum emission. The green emission traces the continuum-subtracted integrated $H_2$ emission at 2.12 μm. Blue emission traces [Fe II] emission at 2.05 μm, displaying collimated atomic jet emission.

outflow. Integrated continuum emission, or scattered light from the outflow driving source, is traced here in red. The continuum subtracted and scattered light-subtracted, integrated $H_2$ emission at 2.122 μm is traced here in green. The [Fe II] continuum subtracted emission at 2.047 μm, tracing the collimated atomic jet is displayed here in blue. The spectra were extracted using circular apertures of radius 0″.41, approximately half of the average seeing of the observation, 0″.81, from the continuum peak, the atomic jet knot, and the bright $H_2$ features labelled *A1* & *A2*. The extracted spectra are presented in Figures 4.3, 4.4, and 4.5, and are subsequently discussed briefly.

Figure 4.3 displays a spectrum extracted from the source position adopted from the continuum peak at the apex of the cavity in continuum emission. The spectrum was extracted using a circular aperture of radius 0″.41. Atomic jet emission is identified in the FELs of [Fe II], and in Br-$\gamma$ emission. Several $H_2$ ro-vibrational emission lines ($v = 1 \rightarrow 0$ & $2 \rightarrow 1$) are detected, likely due to a

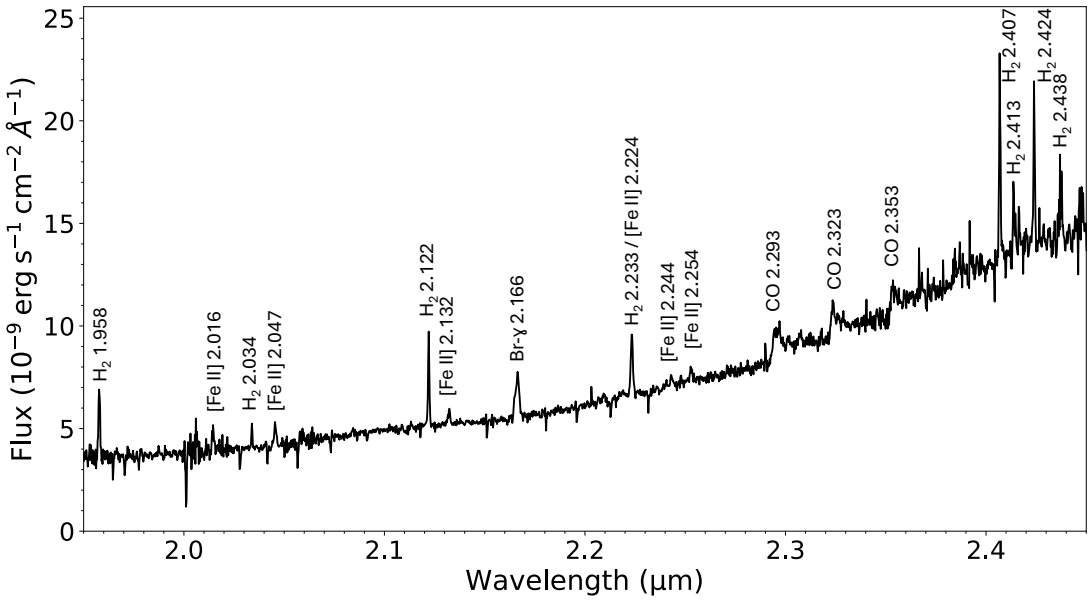


FIGURE 4.3: Spectrum extracted using a circular aperture of radius 0.″41, or approximately half the seeing, from the continuum peak. The jet emission is identified in the FELs of [Fe II], and in Br-$\gamma$ emission. The outflow is detected in the $H_2$ emission lines. In addition, CO overtone bandhead emission at 2.29 – 2.36 μm, which traces the inner gaseous disc, is also seen. A characteristic reddening slope is evident in this spectrum as expected, as the source is heavily extincted and only visible at infrared wavelengths. Stellar absorption lines were not identified in this spectrum, it was concluded that the central source is too heavily extincted to study these lines.

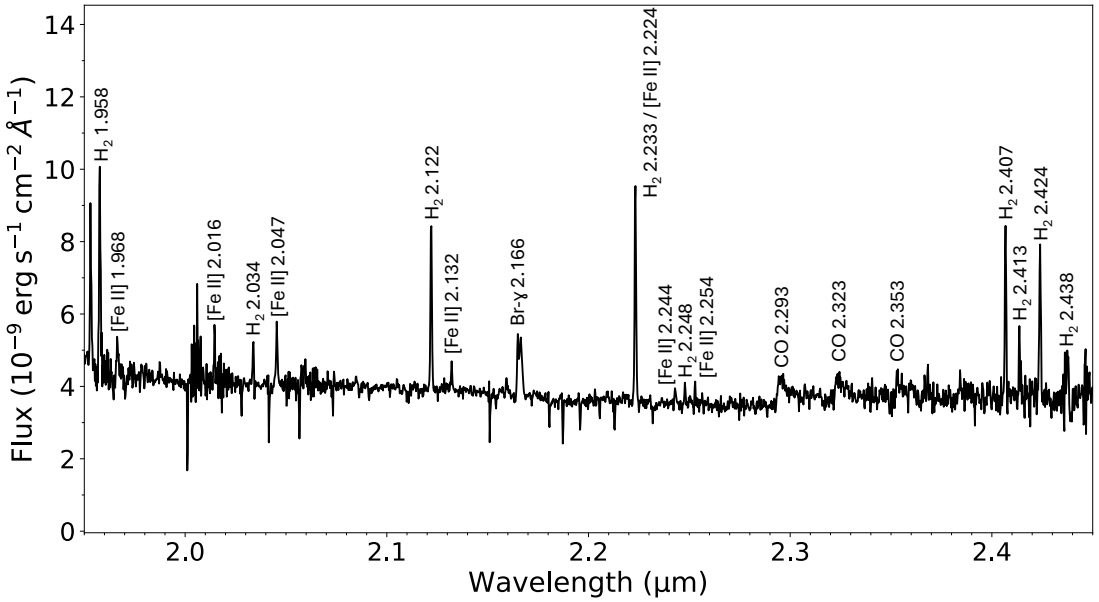


FIGURE 4.4: Spectrum extracted using a circular aperture of radius 0.″41 from the atomic jet knot. The jet knot is located approximately 450 au, or 1.″0, from the source position, along the jet direction. Jet tracing emission lines such as ([Fe II]) lines are bright here.

wide-angled outflow cavity (see Sect. 4.2.1). In addition, CO overtone band-head emission ($^{12}C^{16}O$) at 2.29 – 2.36 μm, which traces the inner gaseous disc, is also seen. As stated in Section 3.3.5, stellar absorption lines, absorption lines originating in the photosphere of the star, are not identified in this spectrum indicating the strong veiling present. Photospheric lines were therefore not present to study in this work. The spectrum is highly reddened in that a characteristic reddening slope of the continuum is visible where bluer wavelengths are more heavily extincted.

Figure 4.4 displays a spectrum extracted using a circular aperture of radius 0.″41 from an atomic jet knot located approximately 450 au, or 1.″0, from the source position, along the jet direction (see Section 4.2.1). This knot allowed the study of the jet very close to the base of the outflow. Atomic FELs, such as bright [Fe II] lines, are identified in this spectrum, tracing the collimated jet emanating from the source. Br-$\gamma$ is also identified here with the emission line profile displaying a double peak. This is indicative that Br-$\gamma$ emission here is tracing not only accretion processes onto the star but also ejection, namely the base of the atomic jet. Molecular hydrogen ($H_2$) emission lines also tracing the outflow are identified.

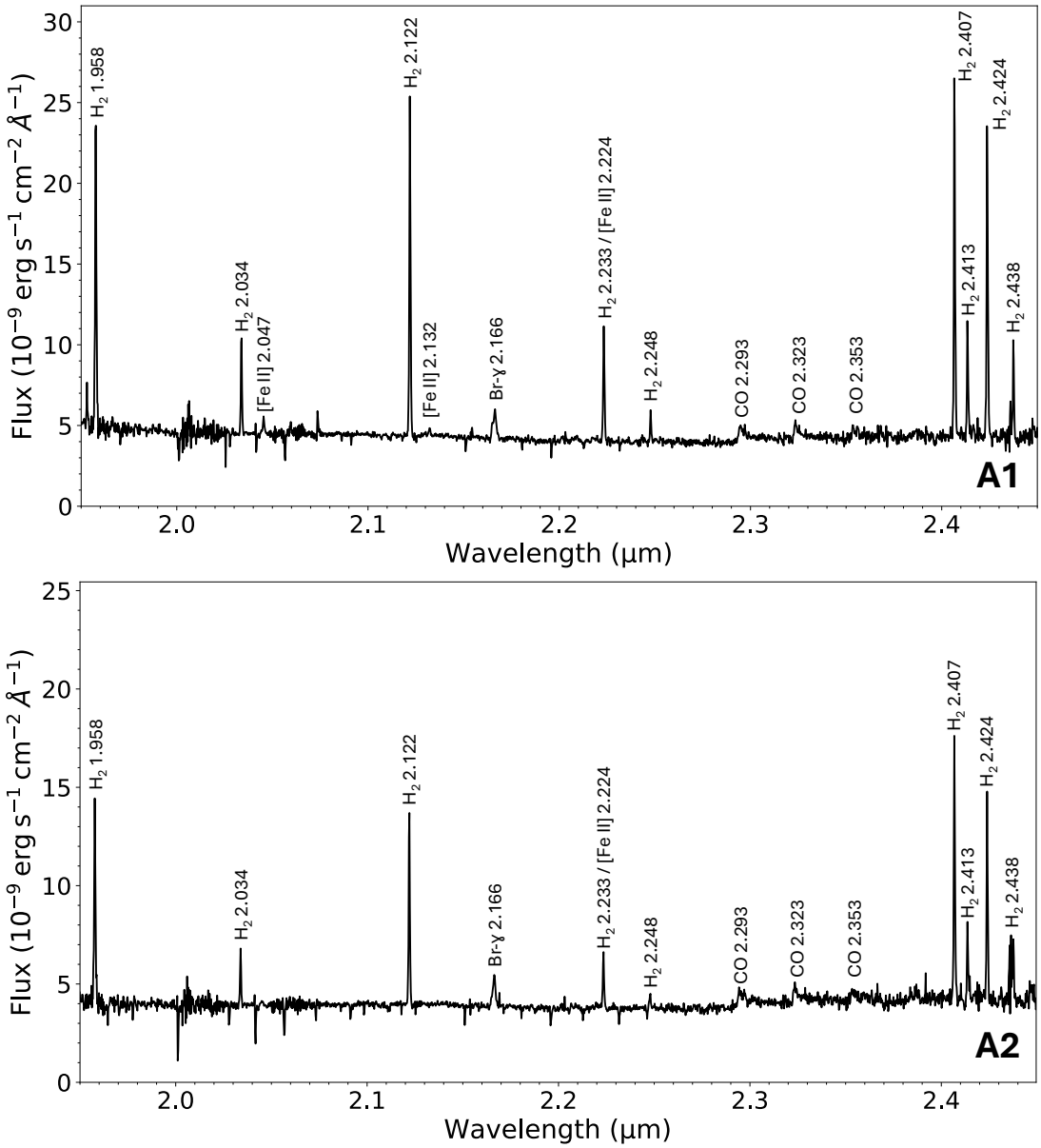


FIGURE 4.5: Spectra extracted from the bright $H_2$ features labelled *A1* & *A2*. Top: Integrated spectrum extracted using a circular aperture of radius 0.″41 from base of left cavity wall traced in $H_2$, position *A1*. Bottom: Integrated spectrum extracted using a circular aperture of radius 0.″41 from base of right cavity wall, position *A2*.

TABLE 4.2: Identified emission lines present in the SINFONI observations of HH 46/47. The wavelengths of these lines, $\lambda_{vac}$, are expressed as their rest wavelengths in a vacuum.

| Line | $\lambda_{vac}$ (μm) |
|---|---|
| $H_2$ 1-0 S(3) | 1.958 |
| [Fe II] | 1.968 |
| [Fe II] | 2.016 |
| $H_2$ 1-0 S(2) | 2.034 |
| [Fe II] | 2.047 |
| $H_2$ 1-0 S(1) | 2.122 |
| [Fe II] | 2.133 |
| Br-$\gamma$ | 2.166 |
| $H_2$ 1-0 S(0)/[Fe II] | 2.223/2.224 |
| [Fe II] | 2.244 |
| $H_2$ 2-1 S(1) | 2.248 |
| [Fe II] | 2.254 |
| CO 2-0 | 2.294 |
| CO 3-1 | 2.323 |
| CO 4-2 | 2.353 |
| $H_2$ 1-0 Q(1) | 2.407 |
| $H_2$ 1-0 Q(2) | 2.413 |
| $H_2$ 1-0 Q(3) | 2.424 |
| $H_2$ 1-0 Q(4) | 2.438 |

Figure 4.5 displays two spectra extracted using circular apertures of radii $0''.41$ from bright features in $H_2$ emission. The top panel displays the spectrum extracted from the bright $H_2$ knot located at the base of the left side of the limb-brightened V-shaped cavity. This feature is later labelled *A1* (See Section 4.2.1). The $H_2$ emission lines here are very bright. Comparatively, the spectrum in the bottom panel of Figure 4.5 was extracted from the base of the right side of the V-shaped cavity. This feature is later labelled *A2*. The $H_2$ emission lines here are not as strong as they appear on the left side of the V-shaped cavity, feature *A1*. This is expected, as the left knot of the cavity has a significantly greater intensity when compared with the knot on the right side.

### 4.2.1 Morphology

The morphology of the outflow was investigated in various tracers. Integrated intensity maps were produced to showcase the morphology of the base of the

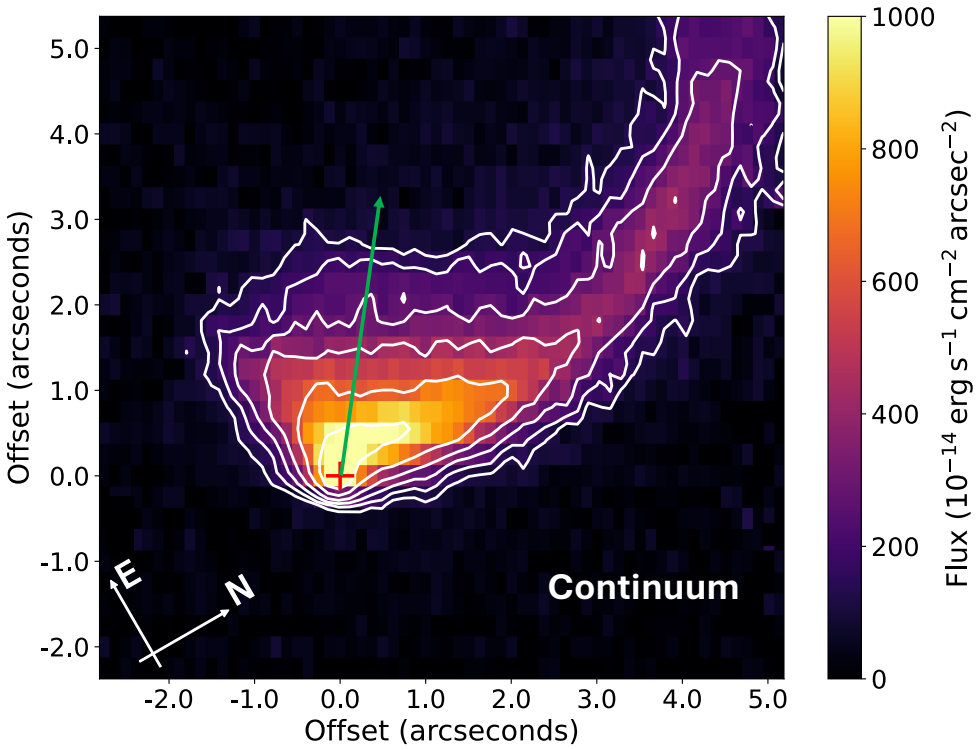


FIGURE 4.6: Integrated intensity map displaying the morphology of the outflow in continuum emission. The morphology shows a wide, approximately parabolic shape. The average jet PA of 52.3° is indicated by a green arrow. The source position is marked with a red plus. Contour levels begin at $3\sigma$ of the background emission and increase by factors of 1.5. The vertical axis is aligned with the central axis of the outflow as traced in CO emission (PA = 60°).

HH 46/47 blueshifted outflow. Figure 4.6 displays the morphology of the outflow in continuum emission, integrated over $\lambda$2.190 µm – $\lambda$2.191 µm. The continuum emission is tracing a reflection nebula with an approximately parabolic shape that is asymmetric in intensity about the average jet PA of 52.3° from Erkal et al. (2021b) indicated by a green arrow. The position of the driving source of the outflow is marked with a red plus symbol. The morphology of the continuum emission delineates the boundary region between the outflow and the ambient material, where the outflow has swept out a wide-angled hollow cavity in the quiescent material. The boundary region one sees is essentially the limb-brightened cavity walls. The northern-pointing arm of the cavity extends further from the source than the eastern-pointing arm, suggesting a dissymmetry in the distribution of ambient material surrounding the outflow. As discussed in Section 3.3.7, this reflection nebula is light from the driving source of the outflow scattered off the walls of the cavity.

Figure 4.7 displays the continuum subtracted and scattered emission subtracted $H_2$ 1-0 S(1) emission at 2.12 μm, integrated over radial velocities of $v_{\rm rad}$ = − 95 km s$^{-1}$ to + 110 km s$^{-1}$. The source position is marked with a red plus symbol. The $H_2$ emission line at 2.12 μm is the brightest molecular hydrogen emission line in the dataset that does not suffer any negative effects due to closeness to the spectral edge of the detector. The integrated $H_2$ emission has a striking V-shaped morphology tracing the limb-brightened cavity walls of the outflow. The shocked northern-pointing cavity wall traced by $H_2$ emission lies within the cavity structure seen in continuum emission (Figure 4.6), meaning the $H_2$ emission is confined within the outflow cavity seen in scattered light. This narrowing of the cavity walls suggests that the $H_2$ emission is probing deeper into the outflow cavity, allowing one to see within the cavity walls traced in scattered light. The $H_2$ cavity is again asymmetric about the jet PA with the northern wall appearing significantly brighter and extending further than the eastern wall. There is also some faint emission present within the cavity, especially apparent close to the interior side of northern cavity wall. This emission within the cavity walls signifies that the cavity structure one sees has a 3D inverted-conical shape extending from the source and surrounding the atomic jet. The collimated jet is not detected in $H_2$ emission, however, a bright knot of $H_2$ emission is seen at the base of the eastern cavity wall at a distance of approximately 1$''\!.$0 (450 au) from the source position. This bright $H_2$ peak has been labelled *A1* following precedent set by Nisini et al. (2024). The dimmer $H_2$ peak at the base of the northern cavity wall, at approximately 1$''\!.$4 from the source position, has been labelled *A2*, and the arc-like structure extending from the interior of the northern cavity wall curling towards the jet axis has been labelled *A3*, again, following Nisini et al. (2024).

Figure 4.8 displays the continuum subtracted and scattered emission subtracted intensity maps for the other $H_2$ emission lines present in the dataset (see Table 4.2). The radial velocity integration ranges are displayed in the individuals panels of the figure. These integrated $H_2$ intensity maps also display the V-shaped morphology tracing the limb-brightened cavity walls of the outflow, but not as comprehensibly as the $H_2$ 1-0 S(1) emission line. The bright $H_2$ knot labelled *A1* in Figure 4.7 is present in all emission lines. The intensity map of the $H_2$ 1-0 S(0) line at 2.223 μm is not spectrally resolved from the [Fe II] line at 2.224 μm and therefore is contaminated by atomic jet emission. This is clearly evidenced by investigating the brightness peak located above

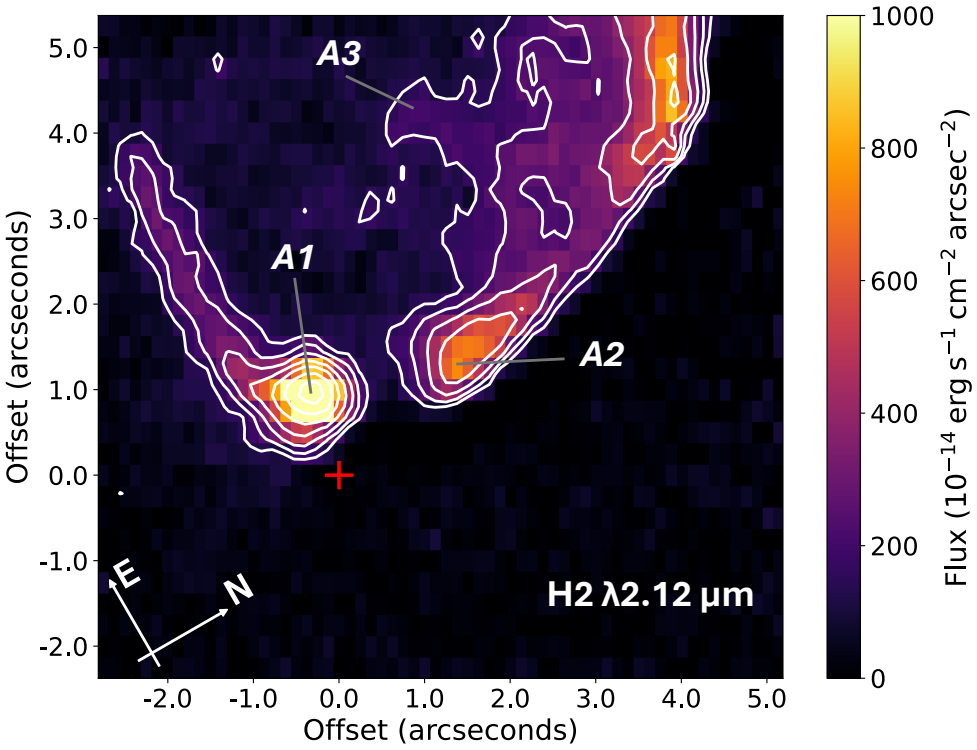


FIGURE 4.7: Integrated intensity map displaying the morphology of the outflow in continuum-subtracted and scattered light subtracted $H_2$ 1-0 S(1) emission. The morphology shows a wide, V-shaped outflow cavity. The source position is marked with a red plus. Contour levels begin at $3\sigma$ of the background emission and increase by factors of 1.5. The vertical axis is aligned with the central axis of the outflow as traced in CO emission (PA = 60°).

the source which does not spatially coincide with the bright $H_2$ knot labelled *A1*. The morphology of the [Fe II] emission is presented next.

Figure 4.9 displays the continuum subtracted, but not scattered emission subtracted, [Fe II] emission line at 2.047 μm, integrated over radial velocities of $v = -280$ km s$^{-1}$ to $-65$ km s$^{-1}$ in the top panel. In the bottom panel the continuum subtracted, but not scattered emission subtracted, high-velocity Br-$\gamma$ emission at 2.166 μm, integrated over radial velocities of $v = -230$ km s$^{-1}$ to $-130$ km s$^{-1}$, is displayed. The reason that the contribution from scattered light was not subtracted for these lines is discussed in Section 3.3.7. These intensity plots are tracing the fast-moving and collimated atomic jet. [Fe II] emission lines are well-established atomic jet tracers, and the emission line at 2.047 μm is the brightest iron emission line in the dataset. The [Fe II] and Br-$\gamma$ emission traces the base of the high-velocity collimated jet, culminating in a bright knot or bow shock approximately 1$''$.0 (450 au) from the source position. The jet bends slightly, tending towards the northern cavity wall. This is expected as the established jet PA of 52.3° differs from the central axis or PA of the wide-angled molecular outflow traced in CO emission, which is 60°. An interesting observation is that the jet knot that one sees, traced by [Fe II] and Br-$\gamma$ emission, does not coincide with the bright knot, *A1*, seen in $H_2$ emission. There is a horizontal offset of approximately 0$''$.53 (240 au) between the centres of these outflow emission knots. This offset between the jet knot seen in [Fe II] and Br-$\gamma$ and the outflow knot, *A1*, seen in $H_2$ suggests that the atomic jet emanates within the $H_2$ cavity, extending between the bases of the cavity walls seen in $H_2$. Again, this indicates that the conical outflow cavity traced by molecular hydrogen surrounds the more collimated and faster moving atomic jet.

Figure 4.10 displays the continuum subtracted, but not scattered emission subtracted, intensity maps for the remainder of the [Fe II] emission lines present in the dataset (see Table 4.2). The radial velocity integration ranges are also displayed in the individuals panels of the figure. These integrated [Fe II] intensity maps also trace the base of the high-velocity collimated jet, culminating in a bright knot or bow shock approximately 1$''$.0 (450 au) from the source position, but with less clarity than seen in the as the [Fe II] emission line at 2.047 μm.

Figure 4.11 displays the integrated intensity maps of the CO overtone bandhead emission ($^{12}C^{16}O$) at 2.29 – 2.36 μm (CO 2-0, CO 3-1, & CO 4-2), which

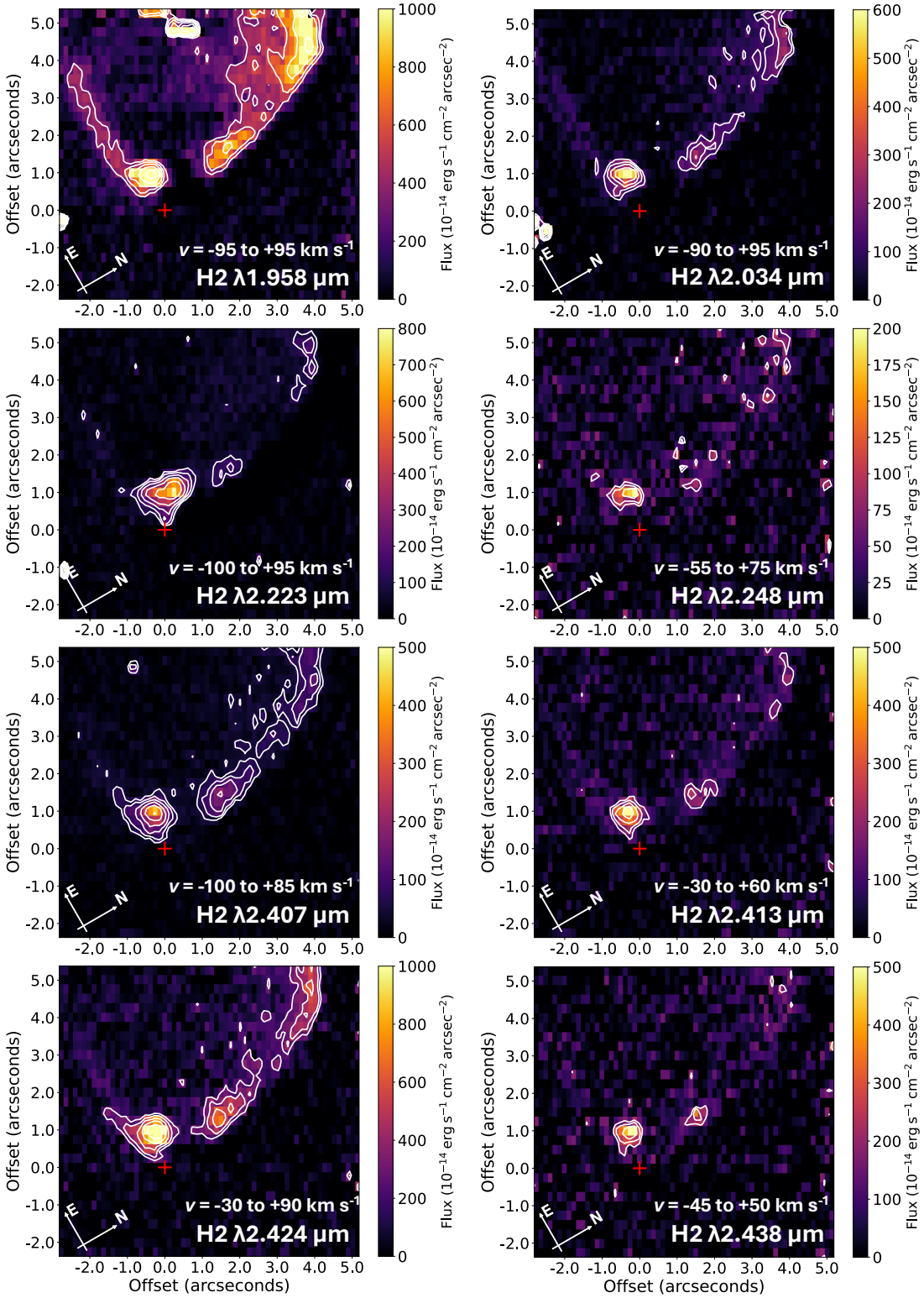


FIGURE 4.8: Integrated intensity maps displaying the morphology of the outflow in continuum-subtracted and scattered light subtracted $H_2$ emission. The source positions are marked with a red plus. Contour levels for all begin at $3\sigma$ of the background emission and increase by factors of 1.5.

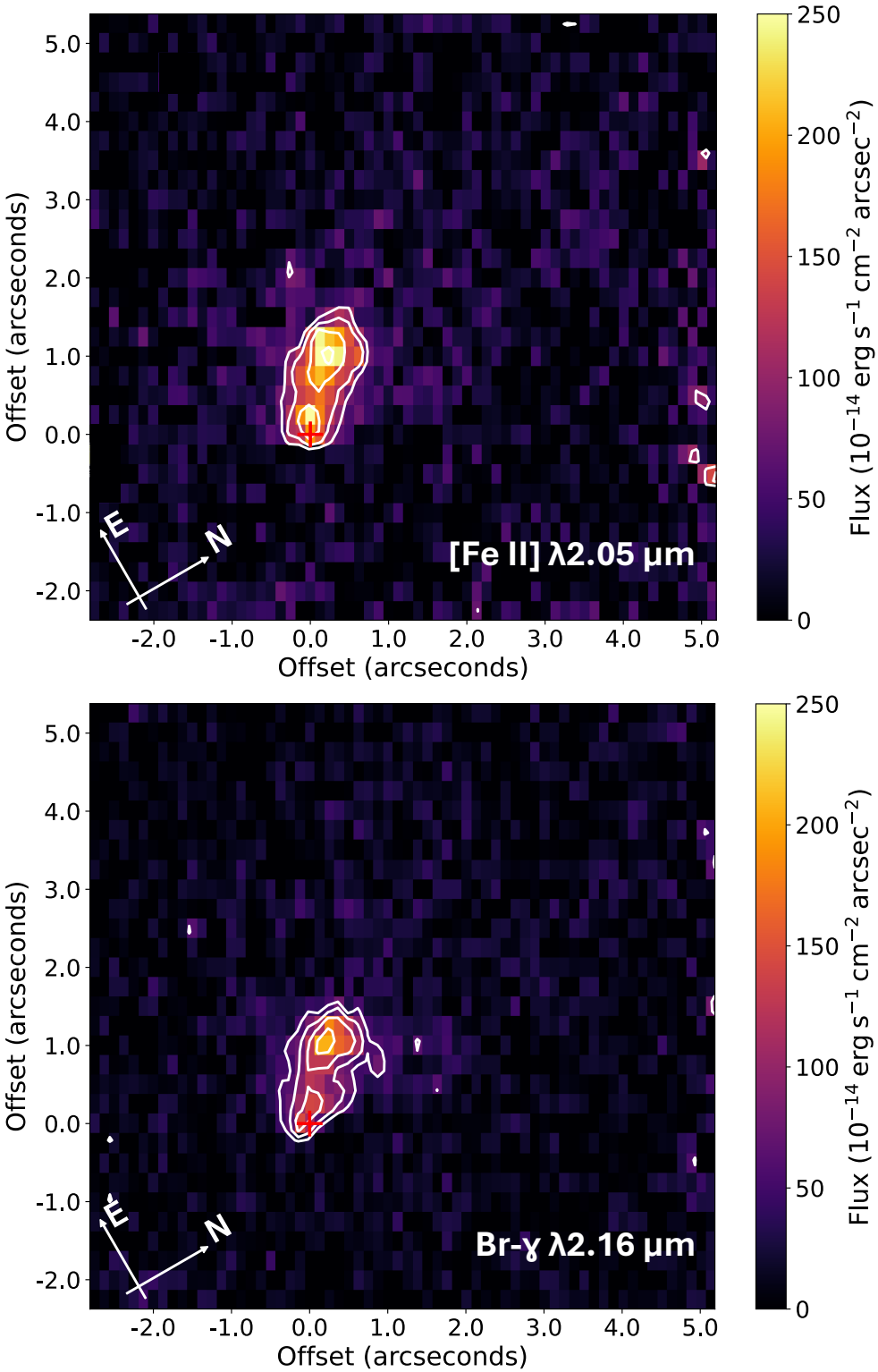


FIGURE 4.9: Integrated intensity maps displaying the morphology of the outflow in continuum-subtracted [Fe II] emission at 2.047 μm, and high-velocity Br-$\gamma$ emission. These lines trace the base of the collimated jet. The source positions are marked with a red plus. Contour levels for all begin at 3$\sigma$ of the background emission and increase by factors of 1.5.

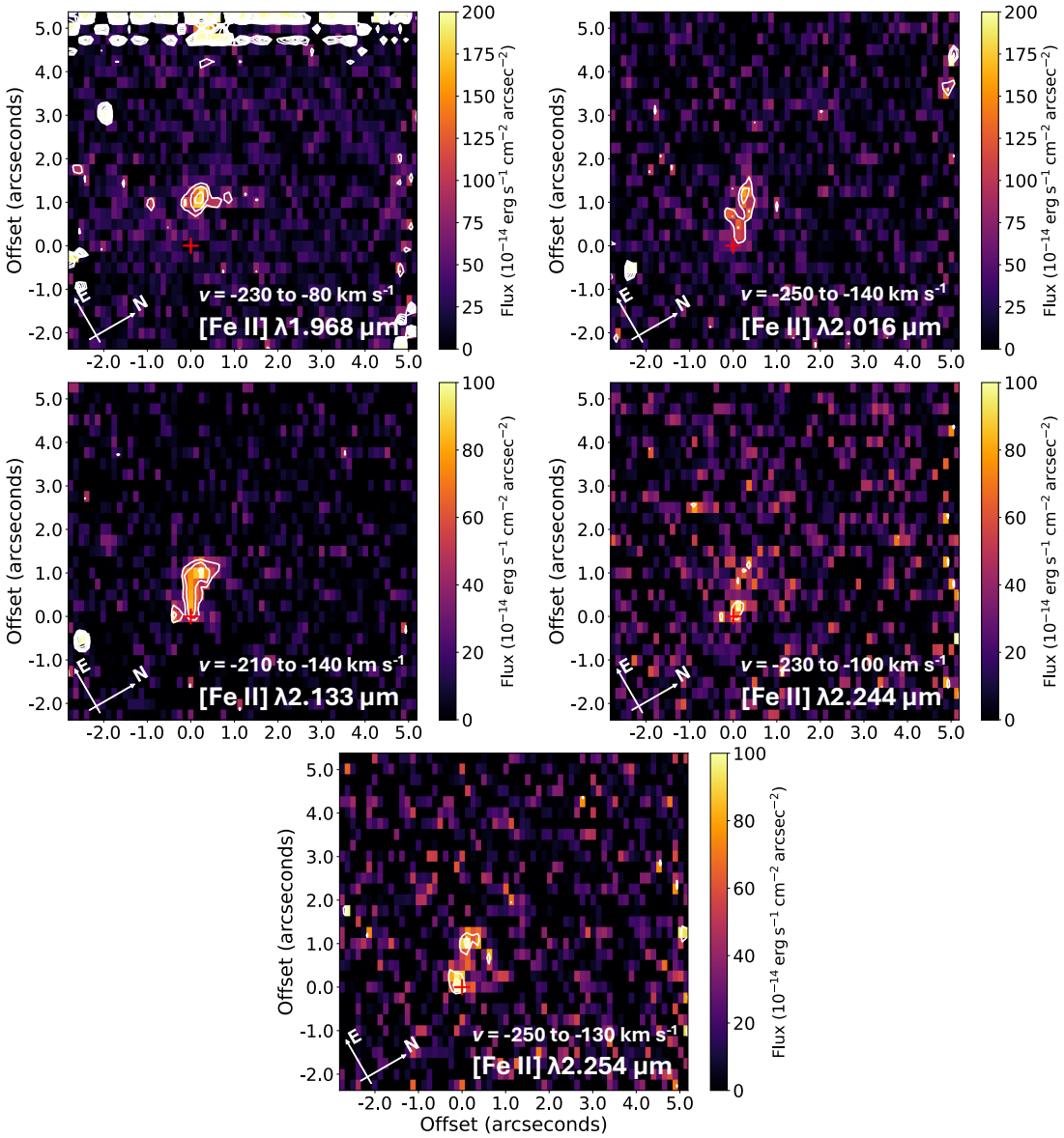


FIGURE 4.10: Integrated intensity maps displaying the morphology of the outflow in continuum-subtracted, but not scattered light subtracted, [Fe II] emission. The source positions are marked with a red plus. Contour levels for all begin at $3\sigma$ of the background emission and increase by factors of 1.5.

traces the inner gaseous disc. The CO $v = 2 \rightarrow 0$ map is integrated between $\lambda$: 2.294 μm and 2.296 μm, the CO $v = 3 \rightarrow 1$ map is integrated between $\lambda$: 2.323 μm and 2.325 μm, and the CO $v = 4 \rightarrow 2$ map is integrated between $\lambda$: 2.353 μm and 2.355 μm. The morphology in these intensity maps reveal the cavity as seen in continuum emission. This is due to the intrinsic CO bandhead emission being very compact, and therefore not spatially resolved in these observations. As the intrinsic CO emission is entirely co-located with the continuum source, the scattered emission removal routine, as described in Section 3.3.7, cannot be performed on this emission, as the intrinsic CO emission is consequently subtracted. Instead, the baseline continuum subtraction procedure is implemented. However, as the intrinsic CO emission is compact, the morphology of these integrated CO intensity maps trace the cavity seen in continuum light because the intrinsic CO emission is scattered off the nebulous cavity material.

### 4.2.2 Kinematics

In order to study the kinematics of the various outflow components in the outflow tracing emission lines, channel maps and position velocity diagrams were produced. As IFU instruments produce data cubes, with two spatial axes and one spectral axis, channel maps can be extracted from them, where a channel map is an image that represents the spatial distribution of emission at a specific velocity interval. The spectral interval in the cube can be converted to a radial velocity interval using Doppler shift (Equation 3.4) and the rest wavelength of the emission line in question. The SINFONI instrument utilises vacuum rest wavelengths. Position velocity (PV) diagrams can also be extracted from IFS data. A pseudo-slit of chosen length and width is placed along the desired emission region. The spatial information within the slit is collapsed and represented by one axis of the diagram, and the wavelength information is again converted into radial velocities using Doppler shift, and represented on the other axis. All emission line velocities discussed throughout the chapter are corrected for the Barycentric Earth Radial Velocity (BERV) and the Local Standard of Rest (LSR) velocity of the cloud that the outflow emanates from, which is + 5.3 km $s^{-1}$ (van Kempen et al., 2009), as discussed in Section 3.3.2. The kinematical measurements presented here are therefore expressed with respect to the frame of the central source.

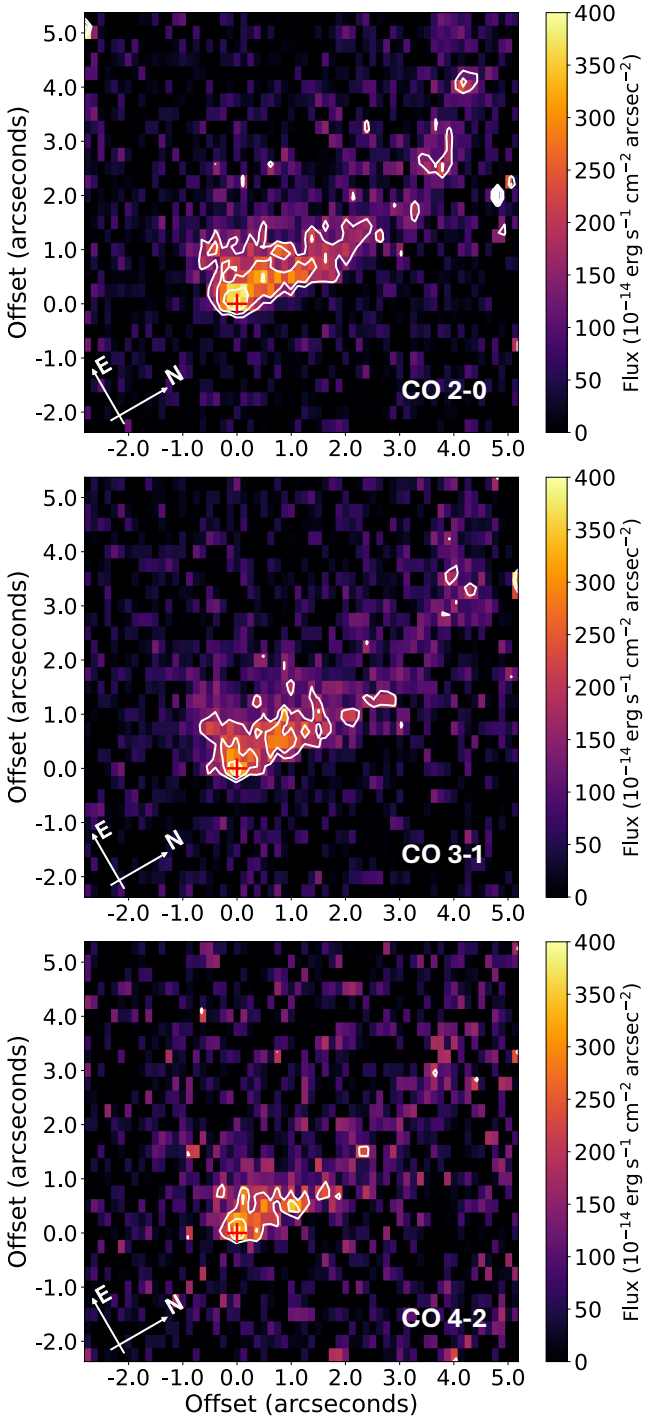


FIGURE 4.11: Integrated intensity maps displaying the morphology of the continuum-subtracted CO overtone bandhead emission at 2.29 – 2.36 μm. The morphology in these intensity maps reveal the cavity as seen in continuum emission as intrinsic CO emission is compact and therefore one sees the cavity illuminated by scattered CO emission. The source positions are marked with a red plus. Contour levels begin at $3\sigma$ of the background emission and increase by factors of 1.5.

Figure 4.12 displays the continuum subtracted and scattered emission subtracted channel map for the brightest molecular hydrogen line in the dataset, $H_2$ 1-0 S(1) emission at 2.12 μm. The source position is marked with a red plus symbol. The channel map displays the spatial distribution of the $H_2$ emission through a velocity interval of $v_{\rm rad} \approx -190$ km s$^{-1}$ to $+120$ km s$^{-1}$. The V-shaped morphology tracing the limb-brightened cavity walls of the outflow is again apparent throughout velocity space, and appears to peak in intensity in the $v_{\rm rad} = -55$ km s$^{-1}$ to $-20$ km s$^{-1}$ interval. The knot of bright $H_2$ emission labelled *A1* in Figure 4.7 exhibits a wide velocity range, appearing first in velocity space, as one moves from higher to lower blueshifted velocities, and persisting into high redshifted velocities.

Figure 4.13 displays the continuum subtracted, but not scattered emission subtracted channel map for the brightest forbidden iron emission line in the data set, [Fe II] emission at 2.047 μm. This figure shows the spatial distribution of the [Fe II] emission through a velocity interval of $v_{\rm rad} \approx -340$ km s$^{-1}$ to $-15$ km s$^{-1}$. The atomic jet is apparent here and possesses much higher radial velocities than the $H_2$ emission shown in Figure 4.12. The jet is collimated and appears to peak in intensity in the $v_{\rm rad} = -231$ km s$^{-1}$ to $-195$ km s$^{-1}$ interval. The morphology of the cavity, as seen in continuum emission and shown in Figure 4.6, is not reproduced here, meaning the jet is bright in comparison to the scattered emission, standing out clearly from the fainter surrounding nebulous emission. This further confirms that the lack of scattered emission removal for this emission line is not critical to the analysis of the jet emission, as discussed in Section 3.3.7. One sees the base of the jet in the highest velocity channels here, with the jet knot, located at approximately $1\farcs0$ (450 au) from the source position, only conclusively appearing in the $v_{\rm rad} = -266$ km s$^{-1}$ to $-231$ km s$^{-1}$ interval. This implies that the base of the jet is moving at a higher velocity before impacting the knot, or shock feature, and subsequently decreasing in velocity.

Figure 4.14 displays the continuum subtracted, but not scattered emission subtracted channel map for Br-$\gamma$ emission at 2.166 μm. This figure shows the spatial distribution of the Br-$\gamma$ emission through a velocity interval of $v_{\rm rad} \approx -285$ km s$^{-1}$ to $+20$ km s$^{-1}$. The atomic jet and jet knot at approximately $1\farcs0$ (450 au) from the source position is again apparent here, but only in the velocity range $v_{\rm rad} = -283$ km s$^{-1}$ to $-113$ km s$^{-1}$. In the lower velocity

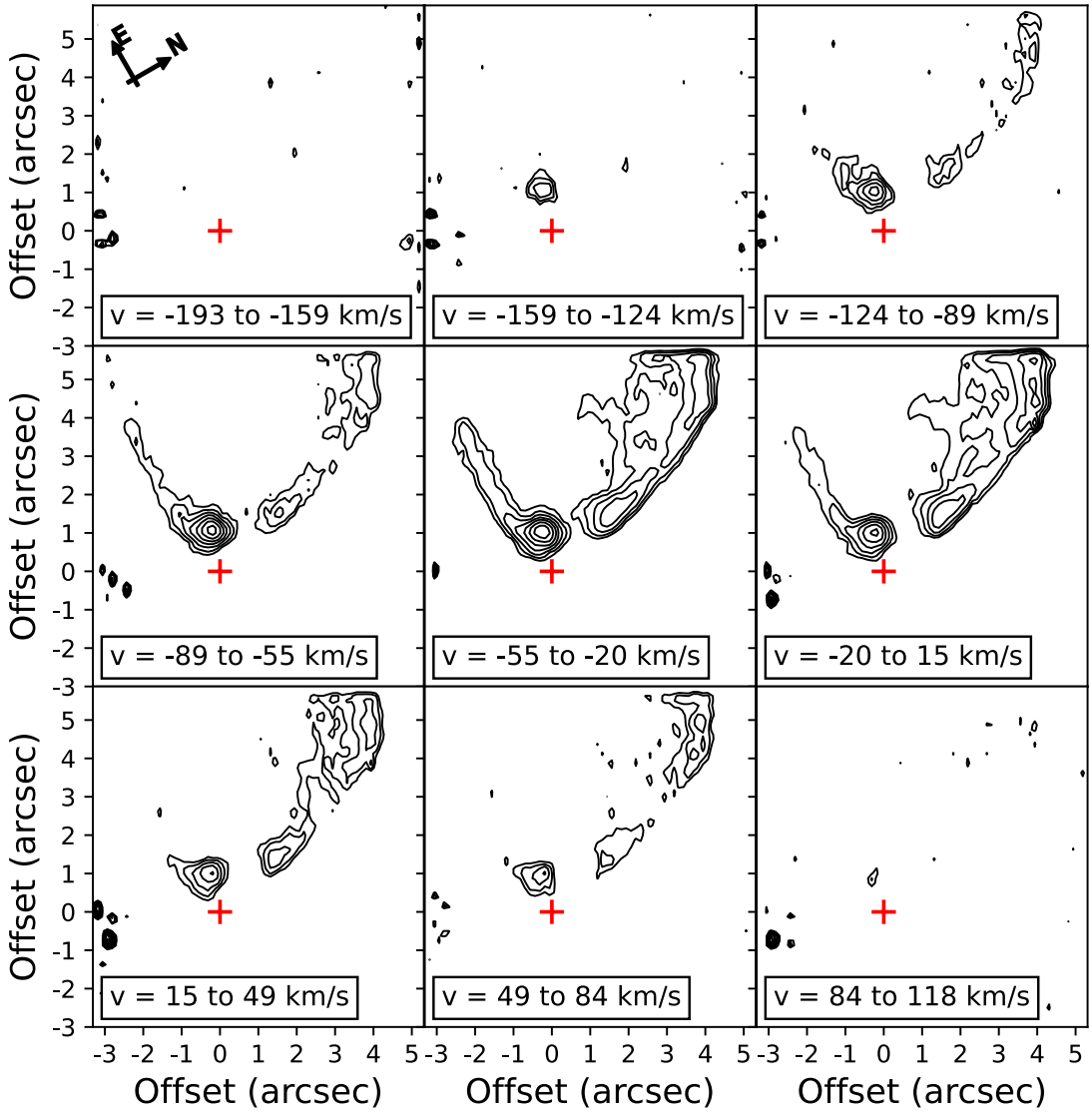


FIGURE 4.12: Continuum-subtracted and scattered light subtracted $H_2$ 1-0 S(1) emission channel map displaying the spatial distribution of the $H_2$ emission through a velocity interval of $v_{\rm rad} \approx -190$ km s$^{-1}$ to $+120$ km s$^{-1}$. The source position is marked with a red plus symbol. Contour levels begin at $3\sigma$ of the background emission and increase by factors of 1.5.

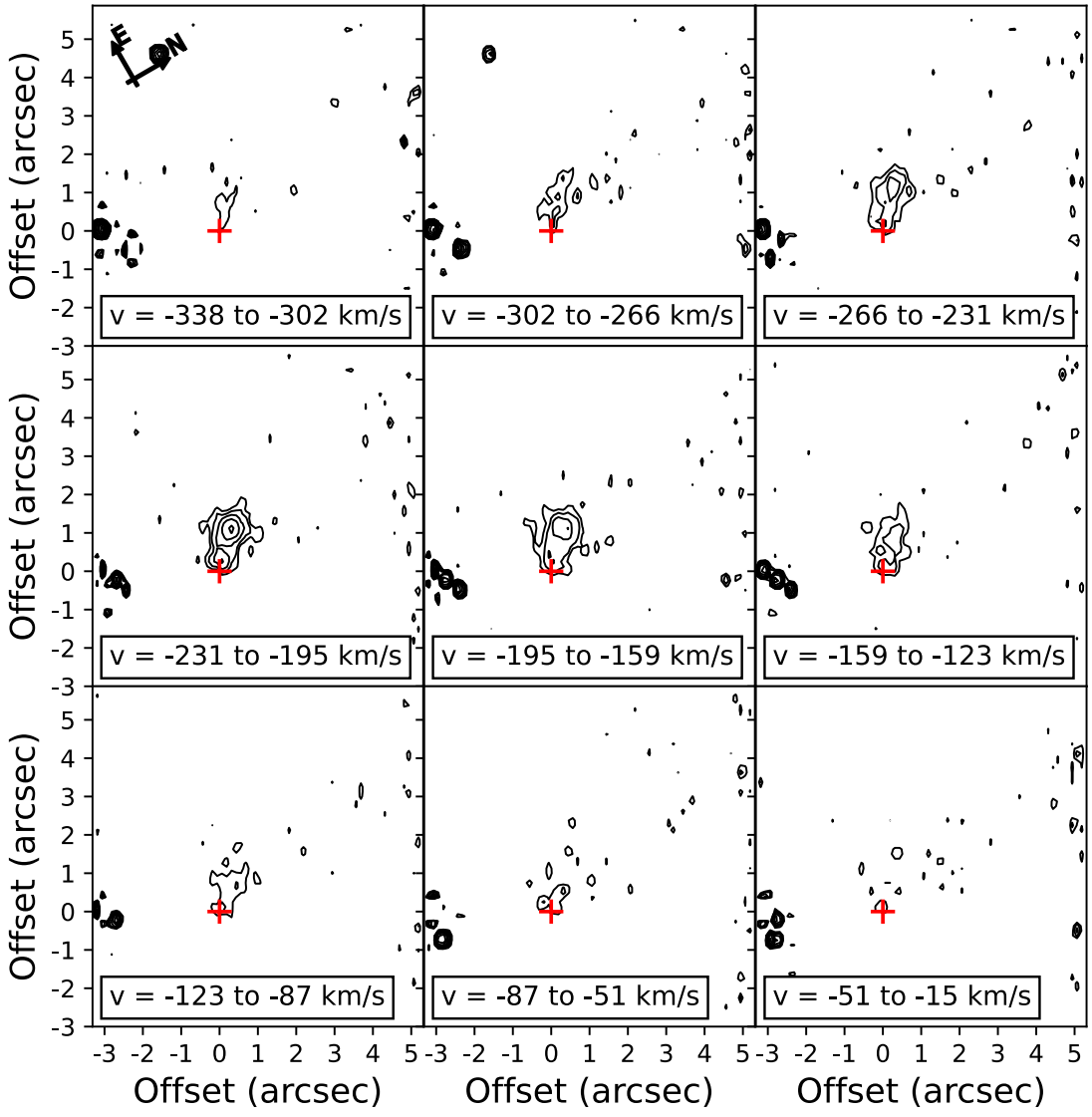


FIGURE 4.13: Continuum-subtracted, but not scattered light subtracted [Fe II] emission at 2.047 μm channel map displaying the spatial distribution of the [Fe II] emission through a velocity interval of $v_{\rm rad} \approx -340$ km s$^{-1}$ to $-15$ km s$^{-1}$. The source position is marked with a red plus symbol. Contour levels begin at $3\sigma$ of the background emission and increase by factors of 1.5.

channels ($< -113$ km s$^{-1}$) the emission begins to reproduce the same morphology of the cavity, as seen in continuum emission. This points to scattered continuum emission dominating at these lower velocities, as evidenced by the lack of intrinsic Br-$\gamma$ emission in the line to continuum ratio plot for low radial velocities presented in Figure 3.24 in Section 3.3.7.

Position velocity diagrams were also prepared to study the kinematics of the outflow in different emission tracers in more detail. Figures 4.15 and 4.16 display PV diagrams extracted along the outflow axis, with a PA of 60°, from Zhang et al. (2019), and a pseudo-slit width of 1.″0. Figure 4.15 displays a PV diagram extracted along the PA of the CO outflow axis in [Fe II] emission at at 2.047 μm. Here, one sees emission traced from the source position located at the zero position and culminating in a jet knot at $\sim$ 1.″0 or 450 au offset. The radial velocity of the emission peaks at approximately $-$ 200 km s$^{-1}$, as is expected for a collimated atomic jet. A Gaussian profile was fit to the emission peak located at an offset of 1.″0, along the velocity axis, and a Gaussian centroid velocity of $v_{\rm rad} = -208.7 \pm 3.6$ km s$^{-1}$ was retrieved. These radial velocities are consistent with previous observations of the HH 46/47 atomic jet (e.g. Garcia Lopez et al., 2010; Nisini et al., 2024). Figure 4.16 displays a PV diagram, again taken along the PA of the CO outflow axis, traced by Br-$\gamma$. The high-velocity emission ($\sim -200$ km s$^{-1}$) in this PV diagram is almost identical to that traced by [Fe II], implying that they are both tracing the jet. The high-velocity emission again culminates in a knot at $\sim$ 1.″0 or 450 au. Again, a Gaussian profile was fit to the emission peak at offset 1.″0, along the velocity axis, and a Gaussian centroid velocity of $v_{\rm rad} = -211.9 \pm 3.5$ km s$^{-1}$ was retrieved. A strong, low-velocity component, centred at $\sim$ 0 km s$^{-1}$ with a full width extending to approximately $\pm$ 150 km s$^{-1}$, is also evident in this PV diagram. As discussed in Section 3.3.7, the line to continuum ratio map of this low-velocity Br-$\gamma$ emission, displayed in Figure 3.24, implies that all of the spatially extended low-velocity Br-$\gamma$ emission is not intrinsic emission and is instead dominated by scattering. The intrinsic emission traced at approximately 0 km s$^{-1}$ and having a full width extending to approximately $\pm$ 150 km s$^{-1}$, is most likely very compact and spatially unresolved emission, entirely co-located with the source position. This intrinsic emission is then scattered off the nebulous cavity traced in continuum emission. The compact intrinsic emission here is possibly tracing accretion processes, such as accretion shocks on the stars surface or accretion flows, and compact disc winds.

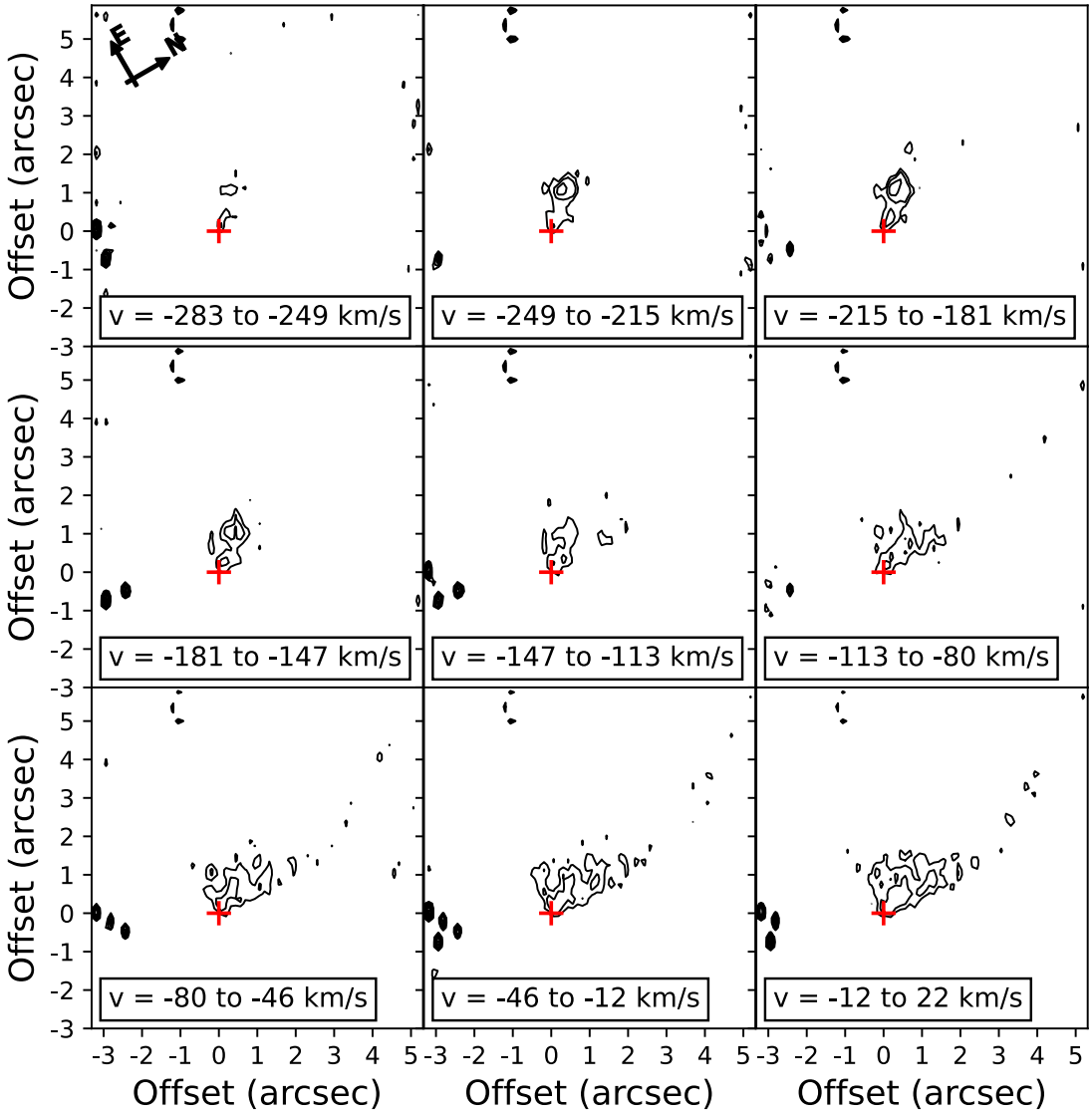


FIGURE 4.14: Continuum-subtracted, but not scattered light subtracted Br-$\gamma$ channel map displaying the spatial distribution of Br-$\gamma$ emission through a velocity interval of $v_{\rm rad} \approx -285$ km s$^{-1}$ to $+20$ km s$^{-1}$. The source position is marked with a red plus symbol. Contour levels begin at $3\sigma$ of the background emission and increase by factors of 1.5.

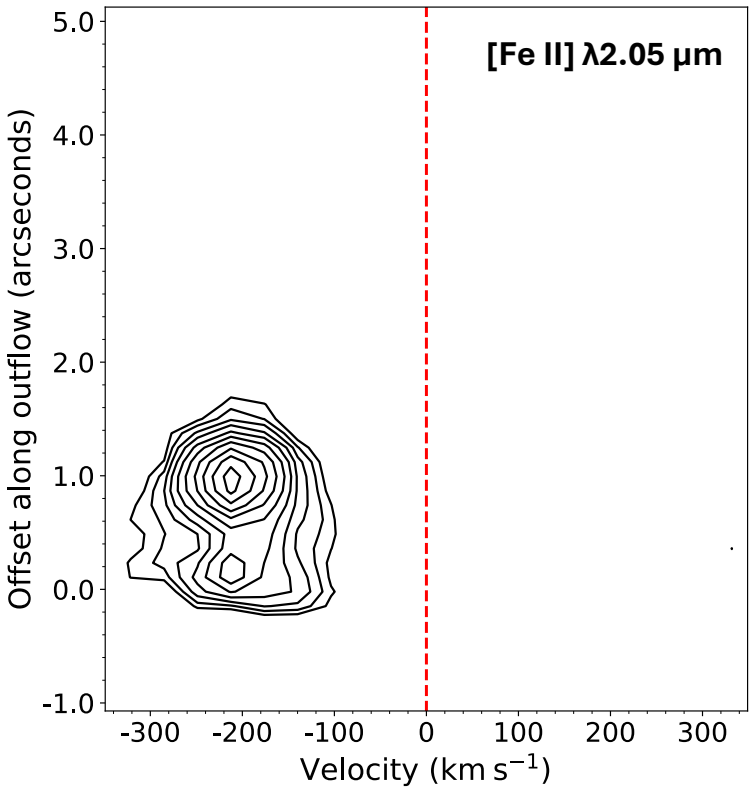


FIGURE 4.15: Position velocity diagram of the [Fe II] emission line region. The PV diagram is extracted along the outflow axis (PA = 60°) with a pseudo slit width of 1.″0. The emission is traced from the source at the zero offset position and culminates in a jet knot at $\sim$ 1.″0 (450 au). The radial velocity of the jet emission traced in this line peaks at approximately $-$ 200 km s$^{-1}$, in agreement with previous observations. Contour levels begin at 3$\sigma$ of the background emission and increase by factors of 1.2. Velocities are expressed with respect to the LSR.

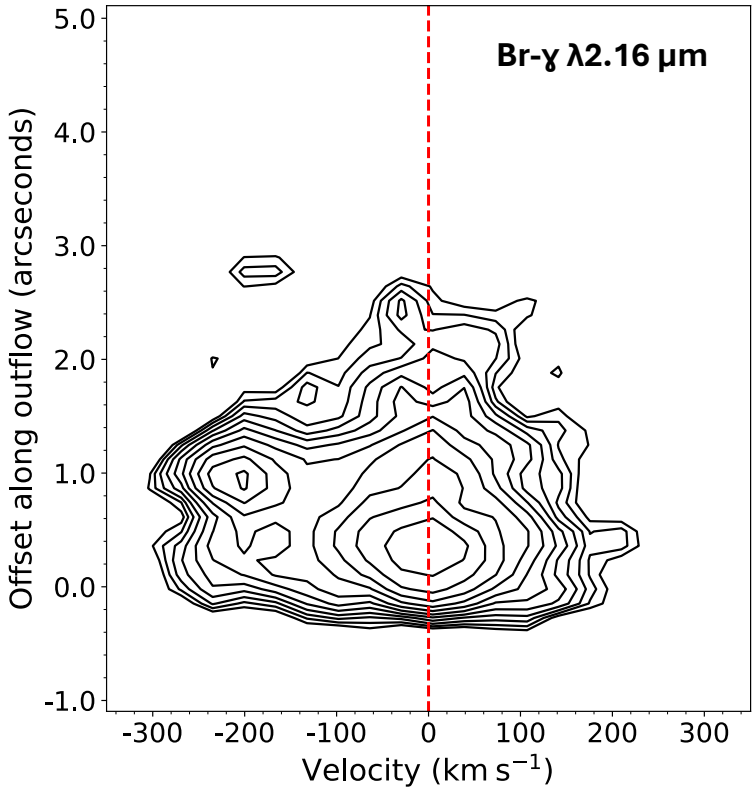


FIGURE 4.16: Position velocity diagram of the Brackett-$\gamma$ emission line region. The PV diagram is extracted along the outflow axis (PA = 60°) with a pseudo slit width of 1.″0. The emission is again traced from the source and culminates in a bow shock at $\sim$ 1.″0 (450 au). The radial velocity of the jet emission traced in this line peaks at approximately $-$ 200 km s$^{-1}$. The spatially extended low-velocity Br-$\gamma$ emission here, that is, the emission centred around 0 km s$^{-1}$ and having a full width extending to approximately $\pm$ 150 km s$^{-1}$, is not intrinsic emission, it is instead light scattered off of the nebulous cavity material. Contour levels begin at 3$\sigma$ of the background emission and increase by factors of 1.2. Velocities are expressed with respect to the LSR.

Position velocity diagrams were also produced for $H_2$ emission. However, unlike the [Fe II] and Br-$\gamma$ emission, the spatial distribution of $H_2$ emission is not aligned with the jet axis. Taking this into consideration, position velocity diagrams transverse to the outflow direction were instead extracted. In the bottom panel of Figure 4.17 a PV diagram taken transverse to the outflow direction, at a PA of 150° and at a distance of $1''.2$ above the source position, is shown, traced by $H_2$ emission after scattered emission removal. The pseudo-slits position and width on the $H_2$ cavity is shown in the top panel, represented by a red rectangle. The offset along the outflow of $1''.2$ was chosen so that the bright $H_2$ features labelled *A1* and *A2* would be within the pseudo-slit. This PA of 150° is perpendicular to the PA of the CO outflow axis (60°). The width of the pseudo-slit used to extract this PV diagram is $0''.5$. The radial velocity of material traced by $H_2$ is much lower than that traced by [Fe II] emission and Br-$\gamma$. Two emission peaks are seen either side of the source position, also labelled *A1* and *A2*. These emission peaks are the bases of each outflow cavity wall seen in $H_2$ emission. One sees that the emission peak from the eastern cavity wall (*A1*) peaks at a slightly higher radial velocity than the emission from the northern cavity wall (*A2*). A Gaussian fit was applied to both emission peaks in the velocity axis to retrieve the Gaussian centre of the emission. The Gaussian centroid velocity of the emission peak *A1* is $v_{\rm rad} = -33.9 \pm 1.4$ km s$^{-1}$. The Gaussian centroid velocity of the emission peak *A2* is $v_{\rm rad} = -16.9 \pm 1.5$ km s$^{-1}$. These Gaussian peak velocities are highlighted on the figure. This difference in centroid velocity between the two sides of the cavity walls hints at the presence of a velocity gradient in the molecular cavity, transverse to the outflow direction.

### 4.2.3 $H_2$ velocity centroid maps

The transverse position velocity diagram in $H_2$ emission (Figure 4.17) hinting that both sides of the V-shaped outflow cavity had different radial velocities, prompted the production of a 2D radial velocity map of the $H_2$ emission after scattered emission removal. This map would allow the spatial kinematics of the outflow cavity, as traced in $H_2$ emission, to be studied in detail. The $H_2$ emission line at 2.122 μm is again chosen here as it possesses the highest S/N of all of the $H_2$ emission lines in our observation and does not suffer any erroneous effects that are common near the spectral edges of IFU observations. The

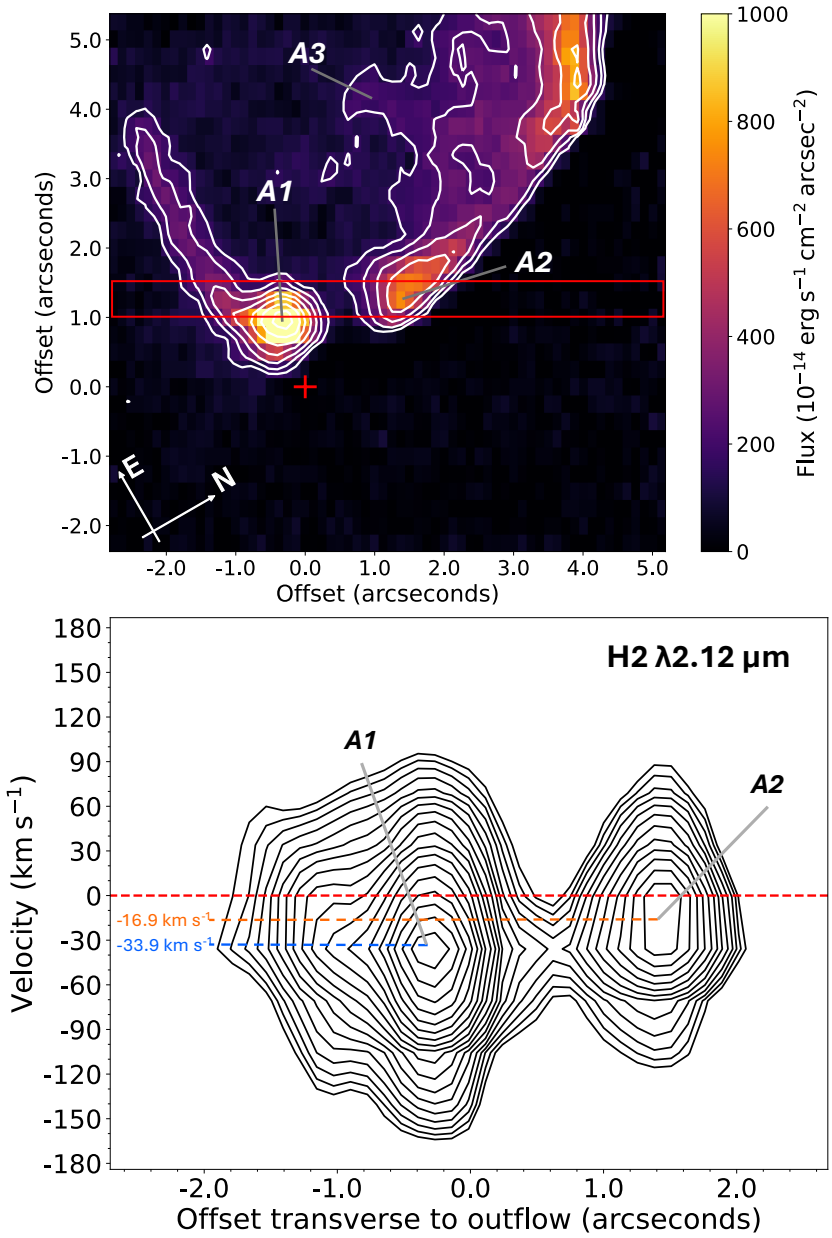


FIGURE 4.17: Transverse PV diagram of the $H_2$ emission line region extracted at a projected $z$ of $1\farcs2$ and with a pseudo slit width of $0\farcs5$. The radial velocity of the molecular emission is much lower than that of the atomic emission. Two emission peaks can be seen on either side of the source position, labelled *A1* and *A2*. The emission peak on the left side of the cavity (*A1*) has a slightly higher radial velocity of $-33.9$ km s$^{-1}$ than the emission peak on the right side of the cavity (*A2*) at $-16.9$ km s$^{-1}$. This hints at the presence of a velocity gradient transverse to the outflow direction in the cavity. The top panel displays a red rectangle, the position and width of the pseudo-slit used to extract the PV diagram. Contour levels begin at $3\sigma$ of the background emission and increase by factors of 1.2.

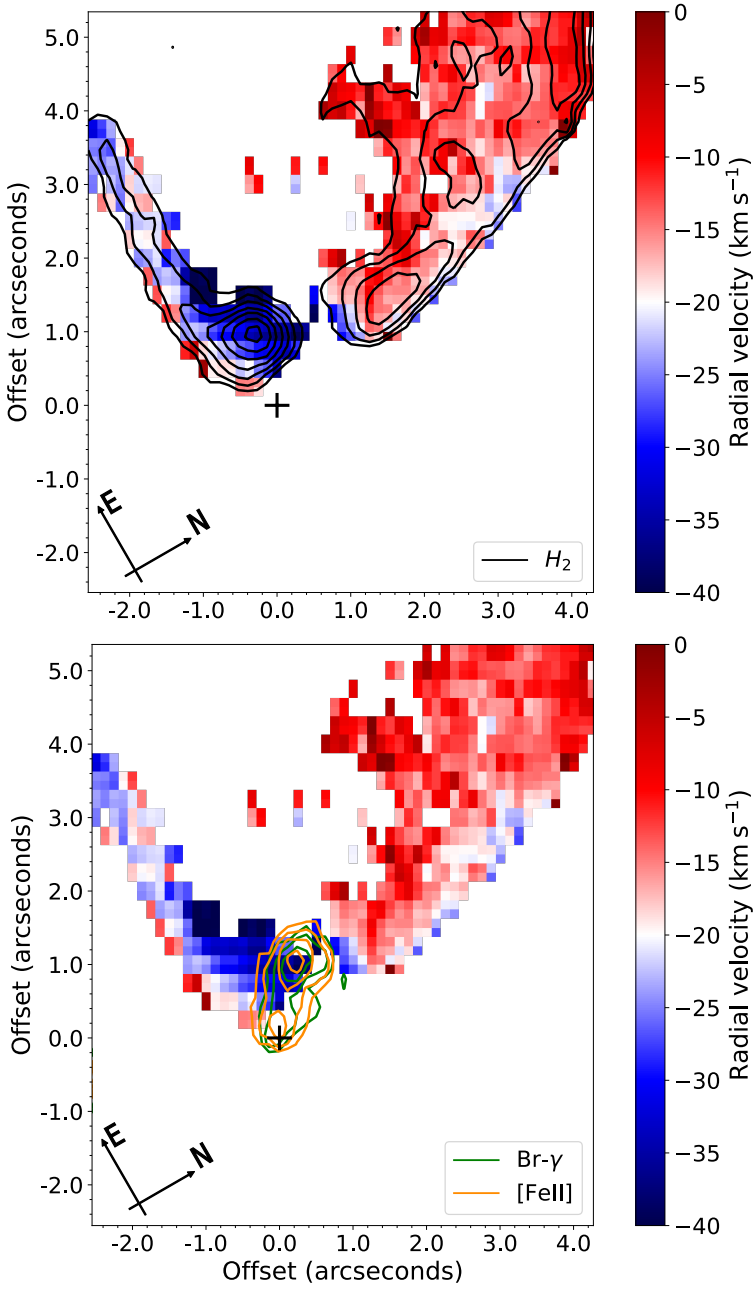


FIGURE 4.18: Scattered light-corrected $H_2$ emission radial velocity centroid maps. The radial velocity centroid maps display a clear velocity gradient between both sides of the V-shaped cavity. The left side of the cavity has, on average, a greater radial velocity when compared with the right side. The difference in velocity between both sides is $\sim$ 10 km s$^{-1}$. The source position is marked with a black plus symbol. Contour levels for both begin at 3$\sigma$ of the background emission and increase by factors of 1.5. Top panel: $H_2$ velocity centroid map with integrated $H_2$ emission overplotted in black contour lines. Bottom panel: Same $H_2$ velocity centroid map but with integrated [Fe II] emission (in orange contours) and integrated Br-$\gamma$ emission (in green contours) overplotted.

TABLE 4.3: Velocity difference between the eastern and northern pointing $H_2$ cavity walls at various heights along the outflow.

| $z$ ($''$) | $v_{\rm rad,\ left}$ (km s$^{-1}$) | $v_{\rm rad,\ right}$ (km s$^{-1}$) | $\Delta v_{\rm rad}$ (km s$^{-1}$) |
|---|---|---|---|
| 1.0 | $31.3 \pm 1.5$ | $17.3 \pm 2.5$ | $14.0 \pm 2.9$ |
| 1.5 | $25.1 \pm 2.0$ | $13.4 \pm 1.4$ | $11.7 \pm 2.4$ |
| 2.0 | $24.0 \pm 2.1$ | $15.2 \pm 1.4$ | $8.8 \pm 2.5$ |
| 2.5 | $22.0 \pm 2.3$ | $16.6 \pm 2.9$ | $5.4 \pm 3.7$ |
| 3.0 | $22.8 \pm 2.5$ | $14.5 \pm 2.0$ | $8.3 \pm 3.2$ |

production of a 2D radial velocity map of the $H_2$ emission was achieved by fitting Gaussian profiles to the $H_2$ emission line at every spatial pixel in the data cube and rejecting fits with a S/N below a certain threshold. The centres of each of the Gaussian profiles were taken as the centroid radial velocities of the emission line. This resulted in a 2D velocity centroid map of the $H_2$ 2.122 μm emission region shown in Figure 4.18. The velocities in this map are expressed with respect to the LSR velocity of the cloud that the outflow emanates from. The error associated with the velocity centroid map is a combination of the uncertainty associated with the Gaussian fitting, namely the accuracy of the Gaussian centroid measurement (Equation 3.3), and the uncertainty involved with the OH emission line wavelength recalibration, as discussed in Section 3.3.2. Thus, summing the relative and absolute errors in quadrature, I derive a $1\sigma$ uncertainty associated with the velocity centroid map of $\pm$ 1.0 km s$^{-1}$ to $\pm$ 3.0 km s$^{-1}$ depending on the brightness or S/N of the $H_2$ line at the corresponding spatial pixel.

One sees the V-shaped cavity morphology reproduced in velocity centroid maps. The top panel in Figure 4.18 displays the integrated $H_2$ emission intensity map overplotted in black contour lines. The source position is marked with a black plus symbol. Here, $-$ 20 km s$^{-1}$ was chosen as the central point for the radial velocity gradient map. One sees that the left outflow cavity wall has, on average, higher radial velocity peaks when compared to the right wall of the cavity. The velocity difference between both sides of the cavity is $\sim$ 10 km s$^{-1}$. In order to recover a more quantitative value for the radial velocity difference between both sides of the $H_2$ cavity, transverse PV cuts, similar to that presented in Figure 4.17, were taken at different heights ($z$) along the outflow direction. PV cuts of width $0\farcs25$ were taken at $z$ = $1\farcs0$, $1\farcs5$, $2\farcs0$,

2.″5, and 3.″0. The emission peaks corresponding to each side of the $H_2$ cavity in each PV plot were fit with Gaussian profiles along the velocity axis to retrieve the centroid velocity in the same way the Gaussian centroid velocities were retrieved in Figure 4.17. The difference in radial velocity centroid measurements ($\Delta v_{\rm rad}$) between the left side of the $H_2$ cavity ($v_{\rm rad,\ left}$) and the right side ($v_{\rm rad,\ right}$), at each height ($z$) along the outflow, is presented in Table 4.3. The uncertainties associated with the centroid velocities are quadrature summations of the Gaussian centroid error and the uncertainty obtained with wavelength recalibration. The uncertainty associated with the velocity difference is the quadrature sum of the uncertainties on the left and right centroid velocities.

The bottom panel of Figure 4.18 presents the same $H_2$ velocity centroid map, but integrated jet emission traced by [Fe II] in orange contours, and integrated Br-$\gamma$ emission in green contours are overplotted instead. These emission lines are tracing the base of the jet. One sees that the jet emission flows in-between either side of the $H_2$ cavity walls. This further illustrates that the $H_2$ low-velocity gas is surrounding the high-velocity jet in a conical morphology. This velocity gradient pattern observed between the eastern and northern pointing walls of the outflow cavity is also seen in the other molecular hydrogen emission lines present in the observation but with reduced clarity.

Figure 4.19 displays the continuum subtracted, but not scattered emission subtracted velocity centroid map for the brightest forbidden iron emission line in the data set, [Fe II] emission at 2.047 μm. Integrated [Fe II] emission is overplotted in orange contours. The radial velocity map varies in velocity from $-$ 170 km s$^{-1}$ to $-$ 230 km s$^{-1}$, as the jet emission is much faster-moving when compared to the $H_2$ emission. One sees a similar result to that in the [Fe II] channel maps, in that the central axis of the base of the jet possesses the highest velocity emission, implying that the base of the jet is moving at a higher velocity before impacting the knot, or shock feature, located at approximately 1.″0 (450 au) from the source position, and subsequently decelerating. There is no conclusive velocity gradient transverse to the jet direction here, although there exists a tentative gradient signal located at the base of the jet, either side of the central jet axis, between $\sim$ 0.″1 and 0.″4 (45 to 180 au) offset from the source position. Spatial pixels on the right side of the central jet axis possibly display a lower radial velocity peak when compared to the spatial pixels located on the left of the central axis.

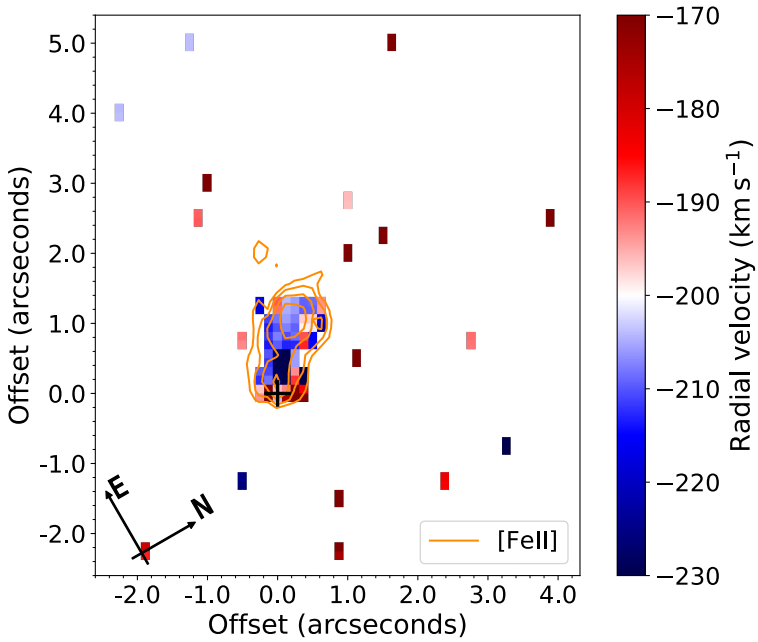


FIGURE 4.19: Continuum subtracted [Fe II] $\lambda$2.047 µm emission radial velocity centroid map. Integrated [Fe II] emission is overplotted in orange contours. The radial velocity centroid map shows that the base of the jet possesses the highest velocity emission. The source position is marked with a black plus symbol. Contour levels begin at 3$\sigma$ of the background emission and increase by factors of 1.5.

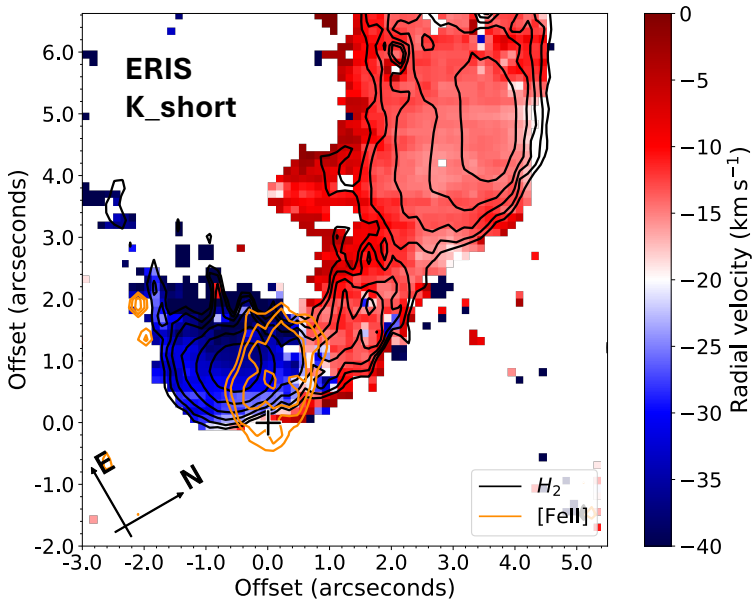


FIGURE 4.20: ERIS observation scattered light-corrected $H_2$ $\lambda$2.12 µm emission radial velocity centroid map. The left side of the cavity has a greater radial velocity when compared with the right side. The difference in velocity between both sides is $\sim$ 15 km s$^{-1}$. The source position is marked with a black plus symbol. Integrated $H_2$ emission is overplotted in black contour lines and integrated [Fe II] $\lambda$2.047 µm emission is overplotted in orange contour lines. Contour levels begin at 3$\sigma$ of the background emission and increase by factors of 1.5.

### Preliminary ERIS results

A velocity centroid map in $H_2$ $\lambda$2.122 µm emission was also produced using the ERIS observations of HH 46/47. This velocity centroid map is presented in Figure 4.20. The velocities in this map are expressed with respect to the LSR velocity of the cloud that the outflow emanates from. The error associated with the velocity centroid map has not been computed. Unlike the SINFONI observations, a careful wavelength recalibration using OH skylines, as discussed in Section 3.3.2, and a computation of the contribution from the uneven slit effect, as discussed in Section 3.3.3, was not performed on the ERIS observations. These processes will be applied to the observations in the future to acquire a low uncertainty associated with the velocity centroid measurements. Having said this, the transverse velocity gradient present in the SINFONI observations of the $H_2$ outflow cavity are reproduced here. In Figure 4.20, the morphology of the V-shaped cavity is seen, although the morphology looks different to that in the SINFONI observations. This change is likely due to the lower angular resolution of the ERIS observations. The overplotted black contour lines

display the integrated $H_2$ emission intensity map, and the overplotted orange contour lines display the integrated [Fe II] $\lambda$2.047 μm emission intensity map. The source position is marked with a black plus symbol and $-$ 20 km s$^{-1}$ was chosen as the central point for the radial velocity gradient map. Like the SINFONI observation, one sees that the left outflow cavity wall has, on average, higher radial velocity peaks when compared to the right wall of the cavity. The velocity difference between both sides of the cavity is $\sim$ 15 km s$^{-1}$.

## 4.3 Discussion

The main contribution that this study provides to the knowledge of the HH 46/47 outflow is the combination of spatial and kinematical information in one observation, made possible with integral field spectroscopy with SINFONI. Nisini et al. (2024) also present spectacular observations of the HH 46/47 molecular outflow, cavity, and atomic jet using JWST NIRSpec and MIRI. Their NIRSpec $6\farcs0 \times 6\farcs0$ FOV encompasses a similar region to the SINFONI observations presented in this chapter. They suggest that the $H_2$ feature, labelled *A1*, is an expanding bubble ejected by the secondary component of the binary system, implying that the second source is also driving an outflow. They hypothesise this as the *A1* knot has a shell-like morphology revealed by the higher spatial resolution NIRSpec observations, when compared with SINFONI's spatial resolution, and additional Near-Infrared Camera (NIRCam) images. They also associate both *A2* and *A3* with material entrained by the primary jet. The morphology of the $H_2$ emission obtained with SINFONI and seen in Figure 4.7 further supports these conclusions. However, one cannot rule out with the SINFONI data alone that the $H_2$ features labelled *A1* and *A2* instead trace the base of the cavity walls surrounding the jet. The spectral resolution of the Nisini et al. (2024) observations is R $\sim$ 2700, which translates to $\sim$ 110 km s$^{-1}$ of velocity resolution. The spectral resolution provided with SINFONI in the K-band (R $\sim$ 4000) is superior. Furthermore the possibility of being able to perform a wavelength recalibration using OH telluric emission lines, as described in Section 3.3.2, means that one can extract important kinematical information about the molecular emission and the atomic jet, which is not possible using the space-based JWST observations. This is the significant advantage of these SINFONI observations over previous studies of the HH 46/47 outflow.

### 4.3.1 Layering of emission and axial asymmetries

The hollow cavity carved out by the outflowing material as seen in continuum emission (Figure 4.6) surrounds the cavity traced by $H_2$ emission (Figure 4.7), which in turn encompasses the collimated jet (Figure 4.9) thus revealing a layered outflow structure. To investigate this layering of emission further, the SINFONI observations were compared with HST and ALMA observations. The left panel of Figure 4.21 displays a continuum subtracted [Fe II] $\lambda$1.64 μm emission image of HH 46/47, obtained using HST Wide Field Camera 3 (WFC3) with the narrowband filter, F164N (Program ID: 15178, PI: B. Nisini; Erkal et al. 2021b). This filter is centred on 1.6435 μm with a FWHM of 0.01646 μm to capture the [Fe II] emission line at 1.64 μm. In this observation, one can see the blueshifted jet extending northeasterly and the redshifted jet extending southwesterly. The inset in the right panel of this figure shows a three-colour image made from the SINFONI observation of the outflow cavity and jet. Integrated continuum emission, or scattered light from the outflow driving source, is traced here in red. The continuum subtracted and scattered light-subtracted, integrated $H_2$ emission at 2.122 μm is traced here in green, displaying the V-shaped outflow cavity. The SINFONI [Fe II] continuum subtracted emission at 2.047 μm, tracing the collimated atomic jet is displayed here in blue. Finally, the inner part of the HST [Fe II] $\lambda$1.64 μm emission tracing the jet is overplotted in orange contours. For the inset, the HST contours have been rotated to match the 60° rotation that the SINFONI observations underwent. The HST image was aligned with the SINFONI image by coinciding the continuum peak positions located at the apex of the cavity in each observation. These continuum centroid positions were retrieved using 2D Gaussian fitting. Figure 4.22 displays an adapted figure from Zhang et al. (2019) of the blueshifted and redshifted molecular outflows from the HH 46/47 system in $^{12}$CO (2-1) emission as observed with ALMA. Here, the blue area traces integrated CO emission from $-$ 35 km s$^{-1}$ to $-$ 10 km s$^{-1}$, the green area traces the 1.3 mm dust continuum emission, and the red area traces integrated CO emission from + 10 km s$^{-1}$ to + 50 km s$^{-1}$. The blueshifted cavity as traced by $H_2$ emission is overplotted. The $H_2$ cavity has been rotated anticlockwise by 90° with respect to the SINFONI results presented earlier in the chapter so that the outflow cavity axis points along the horizontal axis. The continuum peak position in the SINFONI image, marked with a red plus symbol, was aligned

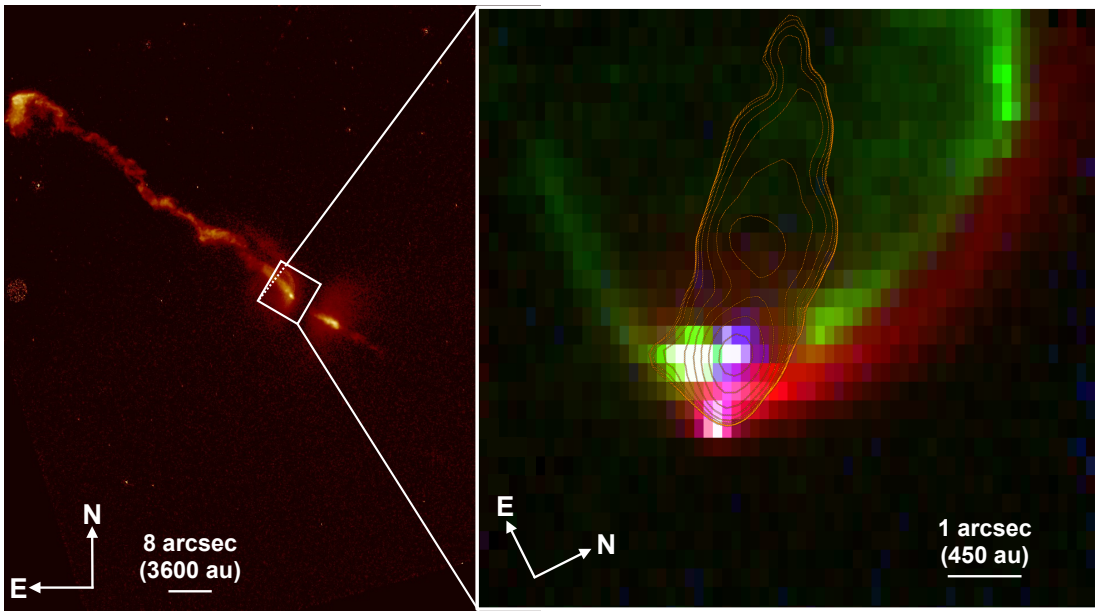


FIGURE 4.21: SINFONI three-colour image displaying the outflow cavity and jet compared to HST observations of the jet in [Fe II] $\lambda$1.64 µm emission. Background: Continuum-subtracted [Fe II] $\lambda$1.64 µm emission image of HH 46/47. The observation was obtained using HST WFC3 with the narrowband filter F164N (Program ID: 15178, PI: B. Nisini; Erkal et al. 2021b). Inset: SINFONI three-colour image displaying the outflow cavity and jet. The red emission traces the integrated continuum emission or scattered light from the outflow driving source. The green emission traces the continuum-subtracted integrated $H_2$ emission. The shocked $H_2$ cavity walls lie within the cavity structure seen in continuum emission. Blue emission traces [Fe II] emission, displaying collimated atomic jet emission. The jet culminates in a bright knot or bow shock approximately 1$''$.0 (450 au) from the source position. This knot does not spatially coincide with the outflow knot seen in $H_2$ emission. The inner part of the HST [Fe II] $\lambda$1.64 µm is rotated clockwise by 60° and overplotted in orange contours.

with the centroid of the 1.3 mm dust continuum emission in the ALMA image. An inset in the top right of the figure displays a zoomed image of the $H_2$ emission overplotted on the blueshifted CO outflow to better illustrate that the $H_2$ emission is nested within the blueshifted CO outflow. This inset has been rotated clockwise by 90° to match the convention of figures presented in this chapter, where the CO outflow axis of 60° is aligned with the vertical axis.

The comparison between SINFONI and HST shows that both sets of observations are consistent with one another. The bending of the atomic jet towards the northern $H_2$ cavity wall does not only occur for the $\sim$ 675 au long SINFONI jet but continues out to $>$ 1000 au in the HST jet. Also, the bright knot seen in

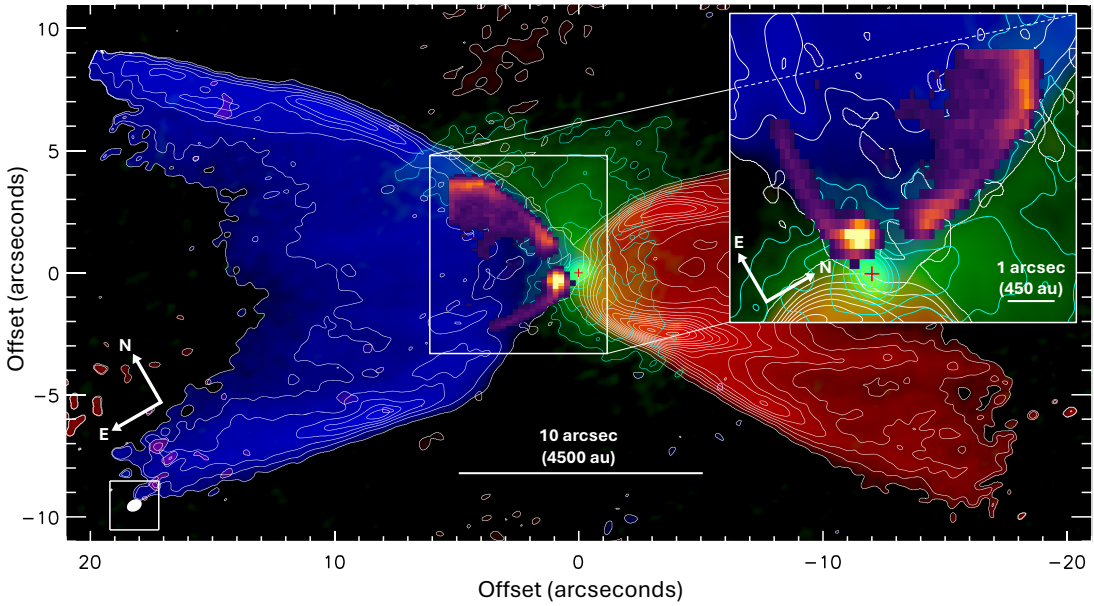


FIGURE 4.22: SINFONI $H_2$ emission overplotted on the blueshifted molecular outflow traced by $^{12}$CO (2-1) as observed by ALMA (Zhang et al., 2019). The blue area traces integrated CO emission from $-$ 35 km s$^{-1}$ to $-$ 10 km s$^{-1}$. The green area highlights the 1.3 mm dust continuum. The red area traces integrated CO emission from + 10 km s$^{-1}$ to + 50 km s$^{-1}$. The shocked cavity walls traced by $H_2$ lie within the cavity structure seen in the CO emission. The red plus indicates the continuum peak position in the SINFONI data. An inset displays a zoomed image of the $H_2$ emission overplotted on the blueshifted CO outflow to better illustrate that the $H_2$ emission is nested within the CO outflow. This inset has been rotated clockwise by 90° to match the convention of figures presented in this paper, where the outflow axis is aligned with the vertical axis. Figure adapted from Zhang et al. (2019).

[Fe II] $\lambda$2.047 μm emission in the SINFONI dataset coincides with a knot traced by the [Fe II] $\lambda$1.64 μm emission from the HST dataset. This is apparent in Figure 4.21 where the innermost jet knot in [Fe II] $\lambda$1.64 μm emission shown in orange contour lines is co-located with the peak in blue emission, tracing the [Fe II] $\lambda$2.047 μm emission. This is expected as the SINFONI observations took place in November 2018 and HST observations took place in March 2019, just four months later. As the radial velocity of the jet knot traced by [Fe II] $\lambda$2.047 μm emission is $\sim -200$ km s$^{-1}$, the jet velocity in the plane of the sky is $\sim -265$ km s$^{-1}$, or 56 au yr$^{-1}$, using a jet inclination value of 37° with respect to the plane of the sky from Hartigan et al. (2005). Assuming that the velocity of the jet knot remains invariable over this short period of time, one would expect the jet knot to have moved by just 14 au between the two observations. The pixel scale of the SINFONI observations is $\sim$ 56 au, meaning the expected offset would not be measurable. The [Fe II] $\lambda$1.64 μm emission displayed in orange contours appears to possess an additional knot coinciding with the bright $H_2$ feature *A1* seen here in green, suggesting that the knot may also be traced in [Fe II] emission. However, due the low S/N, its absence in the SINFONI line to continuum map, and the observation that this knot is not traced by any of the other [Fe II] emission lines, this emission is instead attributed to residual unsubtracted continuum emission, scattered light or real emission not detected in these SINFONI observations due to poorer angular resolution.

The layered structure one sees clearly in Figures 4.21 and 4.22 is a radial stratification, not only morphological in nature but also in temperature, between hot gas ($T_{[\mathrm{Fe\,II}]} \sim 10^4$ K and $T_{\mathrm{H_2}} \sim 10^3$ K) and the bulk of the surrounding colder material ($T_{\mathrm{CO}} \sim 10^1$ K). Not only does one see that the $H_2$ emission lies within the infrared continuum emission, but one also sees that the $H_2$ outflow cavity is nested within the blueshifted $^{12}$CO (2-1) cavity. The $H_2$ outflow cavity existing within the CO molecular outflow has been observed in HH 46/47 in Noriega-Crespo et al. (2004), with different emission lines than those presented here, and more recently in Nisini et al. (2024), showing that the mid-infrared $H_2$ emission is nested within the CO cavity in both the blueshifted and redshifted outflow lobes. In Figure 4.22 at $\sim 4\farcs0$ along the outflow axis, the northern-pointing $H_2$ cavity wall begins to curl inwards towards the jet axis. This curling of the $H_2$ cavity is also seen in Nisini et al. (2024), which they interpret as material entrained by the expanding primary jet. Similarly, the eastern cavity wall in $H_2$ emission lies within the CO molecular outflow and appears

to possess a narrower opening angle. However, one notes that the CO opening angle, close to the base of the molecular outflow, is narrower than the CO cone farther away from the source, indicating that there is some sudden increase of the CO opening angle. This opening of the blueshifted molecular outflow cone is especially evident in the eastern pointing side at $\sim 2\farcs0$ to $4\farcs0$ offset from the source position. The inner, narrower CO cone has a morphology more consistent with the $H_2$ emission morphology. This comparison of the different emission tracers reveals a stratification between continuum emission, CO emission, $H_2$ emission, and the jet implying that outflowing material from the star-disc system is spatially layered as radial distance from the jet axis increases. The highest velocity, highest temperature, and most strongly collimated emission is located at the centre of the outflow axis and surrounding it is the slower-moving, cooler, wide-angled molecular component of the outflow. This onion-like layered flow structure with stratification of emission in velocity, temperature, and chemistry has been observed in some cases (e.g. Delabrosse et al., 2024), and is predicted by MHD disc wind models (Ferreira, 1997; Panoglou et al., 2012; Bai et al., 2016; Zhu and Stone, 2018; Wang, Bai, and Goodman, 2019). In these models, material is accelerated along flow streamlines, poloidal magnetic field lines anchored in the rotating disc. Hot, high-velocity emission travels along streamlines originating in the very inner disc region, whilst cooler, lower velocity emission travels along streamlines originating further out in the disc. This stratified structure can be identified observationally when tracing the disc wind directly or tracing the winds interaction with surrounding ambient material. In this case, the CO emission is thought to be entrained material, tracing material located outside the cavity wall, whilst the $H_2$ emission is likely tracing the interaction region that put the entrained material into motion. The origin of such an interaction can be explained by an MHD disc wind, but can also be produced by the primary jet alone. Consequently, one cannot conclusively attribute the onion-like stratification structure exclusively to being produced by an MHD disc wind.

The $H_2$ cavity is likely an interaction region between some layers in a wide-angled component of the outflow. This wide-angled outflow component traced in $H_2$ could be an uncollimated or poorly collimated disc wind, an expanding shell of material produced by a wide-angled wind and the surrounding ambient material, or a feature produced by the stacking of successive jet bow shocks

from a collimated, variable inner jet propagating into a density-stratified surrounding medium (Rabenanahary et al., 2022). It is possible that in these observations one sees nested cavities traced in $H_2$, similar to those seen in cooler CO emission caused by multiple expanding shells. These expanding shells of material have been observed in both the blueshifted and redshifted outflows of HH 46/47, traced by $^{12}$CO emission (Zhang et al., 2019). These shells, which are highly coherent in space and velocity, have a parabolic morphology. The origin of these outflowing shells can be explained by entrainment of surrounding ambient material by an episodic wide-angle wind (Li and Shu, 1996; Lee et al., 2000), which produces radially expanding parabolic shells, or by successive jet bow shocks. The general morphology of the $H_2$ cavity that lies within the cavity traced by continuum emission could be produced by expanding shells of material, interior to the shells identified in CO by Zhang et al. (2019). Furthermore, the emission peaks labelled *A1* and *A2* could potentially be tracing shocked interaction regions between a more evolved shell, traced by the outer cavity walls, and a smaller scale, asymmetric $H_2$ shell nested within, produced by a subsequent outburst of the wide-angled wind or a successive jet bow shock. The arc-shaped morphological component labelled *A3* could also be associated with a cavity or shocked region created by an expanding shell. In terms of the shock conditions in the $H_2$ cavity one can look at the spectra presented in Figure 4.5, those extracted from the bright $H_2$ features *A1* and *A2*. When one compares the intensities of $H_2$ 1-0 emission lines, those originating from the $v$ = 1-0 vibrational transition such as the $H_2$ 1-0 S(1) line at 2.122 μm, to the $H_2$ 2-1 lines, those originating from the $v$ = 2-1 vibrational transition such as the $H_2$ 2-1 S(1) line at 2.248 μm, one sees that the $v$ = 1-0 lines are much brighter than the $v$ = 2-1 lines. This indicates that the shocks in the $H_2$ cavity are low velocity and non-dissociative. The shock velocities are not high enough to dissociate the molecular hydrogen, or heat the gas to a sufficient temperature to significantly populate higher vibrational levels such as $v$ = 2 or higher.

It is clear that both the outflow cavity traced by $H_2$ emission and the atomic jet traced by [Fe II] and Br-$\gamma$ emission are asymmetric about the CO outflow PA. The emission region of the left side of the cavity, that is, the eastern-pointing cavity wall, traced by $H_2$ is spatially more compact when compared to the right side, the northern-pointing cavity wall. The right side of the cavity also extends further from the driving source, both vertically and laterally. If the

surrounding medium on the right side of the cavity is denser than that of the left side, then this would naturally lead to brighter shocked wall regions on the right side of the cavity, as there is simply more material to impact and create shocked emission. The suggestion that the surrounding ambient material is denser on the right side of the cavity is further supported by the morphology of the scattered light emission seen in Figure 4.6. Here, the cavity as seen in scattered light is highly asymmetric about the CO outflow axis with the northern arm extending much further from the driving source than the eastern arm. This further suggests a dissymmetry in the distribution of the surrounding ambient material. This inhomogeneous ambient material is further testified by the morphology of the reflection nebula seen at optical wavelengths that extends mostly in the northern direction (Heathcote et al., 1996). Furthermore, in Figure 4.22, the 1.3 mm dust continuum is clearly brighter on the northern side, supporting this argument. As mentioned earlier in this section, there is some sudden increase of the CO opening angle, especially evident in the east side between $2\farcs0$ and $4\farcs0$, additionally reinforcing this argument. The northern side of the outflow is facing the cloud edge that the blueshifted outflow is emanating from, which may be shaped or compressed by radiation from outside the cloud. This may provide a rationale for why the ambient material on the northern side appears to be denser. There also exists an offset between the average PA of the atomic jet, 52.3° from Erkal et al. (2021b), and the central axis of the wide-angled CO outflow, $\sim 60°$ from Zhang et al. (2019). This difference between the jet PA and molecular outflow PA can be interpreted as being due to an inhomogeneous surrounding medium, with the eastern molecular cavity wall expanding quicker than the northern molecular cavity wall and therefore shifting the central axis of the CO outflow to a larger PA than the jet PA.

One can also see that the atomic jet is deflected away from the left side of the cavity, tending towards the northern wall. Also, the jet knot traced by [Fe II] and Br-$\gamma$ emission does not coincide with either peak traced at the bases of the cavity walls seen in $H_2$ labelled *A1* and *A2*. The bending of the atomic jet towards the northern cavity wall is consistent with the [Fe II] $\lambda$1.64 μm emission from the HST observations. This bending of the atomic jet is indicative of jet wiggling, which is clearly seen in large scale observations of the jet (e.g. Reipurth et al., 2000; Erkal et al., 2021b). Jet wiggling can be induced by an orbiting companion to the outflow driving source (Murphy et al., 2021). These axial asymmetries seen in the blueshifted outflow, both in the atomic jet and

the wide-angled outflow and cavity may also arise due to the influence of two outflows being driven by each of the components of the binary system (Nisini et al., 2024). The difference between the jet PA and molecular outflow PA can also be interpreted as being due to the secondary jet pushing on the material making up the eastern-pointing cavity wall, again shifting the central axis of the CO outflow to a different PA when compared to the jet PA.

### 4.3.2 Origin of the $H_2$ transverse velocity gradient

The V-shaped, parabolic outflow cavity observed in the integrated $H_2$ emission in Figure 4.18 displays a clear transverse velocity gradient of approximately 10 km $s^{-1}$ between the eastern and northern pointing cavity walls (see Table 4.3 for more quantitative velocity differences). This transverse velocity gradient is also observed in the preliminary ERIS results shown in Figure 4.20. A transverse velocity difference, though lower in magnitude, is also present in $^{12}$CO emission in the same sense as the velocity gradient presented here (2024, priv. comm Y. Zhang). Whilst the spectral resolution of the SINFONI dataset is R = 4000 or 2.45 Å, which translates to a spectral sampling of 38 km $s^{-1}$ at 1.95 μm and 30 km $s^{-1}$ at 2.45 μm, one can be confident in a velocity difference of $\sim$ 10 km $s^{-1}$ between either side of the cavity due to the wavelength recalibration performed using the OH lines from the upper atmosphere and discussed in Section 3.3.2. The estimated $1\sigma$ uncertainty associated with this velocity centroid map is $\pm$ 1.0 km $s^{-1}$ to $\pm$ 3.0 km $s^{-1}$, which encompasses absolute and relative errors associated with Gaussian centroid accuracy and the OH wavelength calibration.

Initially, one may interpret that this velocity gradient is due to the anticlockwise rotation of the $H_2$ cavity, with the eastern-pointing cavity wall approaching the observer at a higher radial velocity with respect to the northern-pointing cavity wall. This apparent rotation could be tracing a rotating disc wind directly (Zhang et al., 2016), or tracing the rotation of entrained material, where the angular momentum present in the envelope is provided for by the outflow (Gaudel et al., 2020). This rotation would support the MHD driven wind model, as one expects a rotation of the outflow if the wind is removing angular momentum from the star-disc system. Rotating cavities have been observed in early to late stages of low-mass star formation (e.g. Bjerkeli et al., 2016; Tabone et al., 2017; Zhang et al., 2018; Louvet et al., 2018; Tabone et al.,

2020; de Valon et al., 2022; Launhardt et al., 2023). In order to investigate the plausibility of this velocity gradient being caused by a rotation of the cavity, it was assumed that the velocity gradient was purely due to rotational motion and the specific angular momentum of this apparent rotation at different heights along the outflow was calculated. The velocity differentials are derived from the $H_2$ velocity centroid map provided in Figure 4.18, by extracting a transverse PV cut at a specific height along the outflow. Gaussian profiles are then fit along the velocity axis to both of the emission peaks corresponding to each side of the $H_2$ cavity, allowing the determination of the centroid velocity of each side of the $H_2$ cavity. This is the same process as described in Section 4.2.3 when calculating the velocity difference between the eastern and northern pointing $H_2$ cavity walls and presented in Table 4.3. The rotational radius, $r$, is estimated, assuming the rotation is axisymmetric, as half of the distance between the two emission peaks corresponding to each side of the $H_2$ cavity. The uncertainties associated with the centroid velocities are quadrature summations of the Gaussian centroid error and the uncertainty obtained with wavelength recalibration, as discussed in Section 3.3.2. The specific angular momentum ($J = r \times v_{\rm rot}$) of a rotation or orbit is defined as the angular momentum associated with the rotation divided by the systems mass, in other words, the angular momentum per unit mass. Assuming that the flow is axisymmetric, one can calculate the specific angular momentum as follows:

$$J(r) \;=\; r \times v_{\rm rot}(r) \;=\; r \times \frac{v_{\rm left} \;-\; v_{\rm right}}{2\sin(i)}, \tag{4.1}$$

where $v_{\rm rot}(r)$ is the rotational velocity and $i$ is the angle of inclination of the flow with respect to the line of sight. Here, $i$ = 53° is taken as the inclination of the outflow, as 37° is the angle of inclination with respect to the plane of the sky (Hartigan et al., 2005). Using Equation 4.1, the specific angular momentum of the apparent cavity rotation at various heights ($z$) along the outflow in the plane of the sky is calculated. These heights are; $z$ = 450 au, 675 au, and 900 au ($z$ = 1.″0, 1.″5, 2.″0). The specific angular momentum results are presented in Table 4.4. The specific angular momenta values calculated are $J(r)$ = 3217 $\pm$ 658 km s$^{-1}$au, at 1.″0 offset from the central source, to $J(r)$ = 3867 $\pm$ 1125 km s$^{-1}$au, at 2.″0 offset.

TABLE 4.4: Specific angular momenta calculations of the $H_2$ cavity rotation at various heights ($z$) along the outflow.

| $z$ (au) | $v_{\rm left}$ (km s$^{-1}$) | $v_{\rm right}$ (km s$^{-1}$) | $v_{\rm rot}$ (km s$^{-1}$) | $r$ (au) | $r$ ($10^{-3}$ pc) | $J(r)$ (km s$^{-1}$au) | $J(r)$ ($10^{-2}$ km s$^{-1}$pc) |
|---|---|---|---|---|---|---|---|
| 450 | $31.3 \pm 1.5$ | $17.3 \pm 2.5$ | $8.8 \pm 1.8$ | 365.6 | 1.8 | $3217 \pm 658$ | $1.6 \pm 0.3$ |
| 675 | $25.1 \pm 2.0$ | $13.4 \pm 1.4$ | $7.3 \pm 1.5$ | 506.3 | 2.5 | $3696 \pm 759$ | $1.8 \pm 0.4$ |
| 900 | $24.0 \pm 2.1$ | $15.2 \pm 1.4$ | $5.5 \pm 1.6$ | 703.1 | 3.4 | $3867 \pm 1125$ | $1.9 \pm 0.6$ |

In the case that the $H_2$ velocity gradient is directly tracing an outflow rotation one can compare to previous outflow rotation observations. Pascucci et al. (2023) present a review where they summarise published results for rotating molecular winds from low-mass class 0/I/II sources in various molecular tracers of winds. They show that the measured disc wind angular momenta for class 0 sources range from 20 – 100 km $s^{-1}$au in SO and $SO_2$ emission, for class I sources range from 40 – 250 km $s^{-1}$au in $H_2$ and CO emission, and for class II sources range from 20 – 300 km $s^{-1}$au in $H_2$ and CO emission. Bjerkeli et al. (2016) measure the specific angular momentum, in $^{12}$CO emission, of the rotating outflow associated with the TMC1A protostellar system to be less than 200 km $s^{-1}$au, using $r$ values an order of magnitude lower than those used here. Zhang et al. (2018) measure the mean specific angular momentum, in $C^{18}O$ emission, in the rotating NGC 1333 IRAS 4C outflow to be 100 km $s^{-1}$au. Louvet et al. (2018) measure the specific angular momentum, in $^{12}$CO emission, of the rotating HH 30 outflow to be $\sim$ 40 km $s^{-1}$au. In de Valon et al. (2022), they measure the specific angular momentum, in $^{12}$CO emission, of the rotating outflow from DG Tauri B to be $\sim$ 65 km $s^{-1}$au. Launhardt et al. (2023) measure the specific angular momentum, in $^{12}$CO emission, of the rotating outflow from a young T Tauri star in the CB 26 Bok globule to be less than 200 km $s^{-1}$au. Zhang et al. (2016) estimated the specific angular momentum in the equatorial plane of the envelope surrounding the object in question here, HH 46/47, in $^{13}$CO and $C^{18}O$ emission. They found specific angular momentum values for the rotation of $J$ = 450 – 540 km $s^{-1}$au ($J = 2.2 \times 10^{-3}$ to $2.6 \times 10^{-3}$ km $s^{-1}$pc), an order of magnitude lower than the specific angular momenta estimated here. As this rotation is measured in the equatorial plane, it is indicative of an upper limit for the specific angular momentum in this system. In the case that the $H_2$ velocity gradient is instead tracing the rotation of entrained material, where the angular momentum present in the envelope is provided for by the jet one can compare with Gaudel et al. (2020). They measure the specific angular momentum of the midplanes of circumstellar environments of a sample of class 0/I protostellar envelopes. In their sample, the maximum specific angular momenta values, at similar $r$ values presented here, are $\sim$ 400 km $s^{-1}$au ($2 \times 10^{-3}$ km $s^{-1}$pc), an order of magnitude below what is measured here.

The specific angular momenta calculated here at various heights along the

outflow cavity are significantly larger than what has been seen before for rotating outflow cavities based on either rotational motion traced directly by the outflow or by rotating entrained material. Furthermore, the apparent anti-clockwise rotation one sees here is opposite to the clockwise rotation of the flattened structure around the central source perpendicular to the outflow axis traced by $^{13}$CO and C$^{18}$O from Zhang et al. (2016). Whilst this flattened structure has a size of approximately $10\farcs0$ (4500 au) across, which is much larger than what is expected for a rotationally supported Keplerian disc, it is indicative of the disc rotation direction as the sense of rotation remains consistent as the beam size, in $^{13}$CO and C$^{18}$O, is scaled down to its smallest size, approximately $1\farcs5$ (675 au). They conclude that the structure is a rotating envelope that feeds the accretion disc. Although some outflows present transverse velocity gradients in the opposite sense to the disc rotation (Cabrit et al., 2006; Louvet et al., 2016), it is unclear if these gradients (of a few kilometres per second and variable in time) truly trace counter-rotation of the jet, or if they are contaminated by other effects such as jet precession (wiggling of the jet) or shock asymmetries. The large specific angular momenta calculated here, coupled with the fact that the apparent rotation is opposite to the sense of the disc rotation, lead the ruling out of the interpretation that the velocity gradient observed in the $H_2$ cavity is entirely tracing a rotation signature, and other effects must be considered.

Another possible explanation for the velocity gradient could be ascertained from the observation that the cavity seen in $H_2$ is clearly asymmetric about the outflow direction. If the surrounding medium in the region of the northern-pointing cavity wall is denser than that in the region around the eastern-pointing cavity wall, as discussed in Section 4.3.1, then the outflowing material, or expanding shells of material, would encounter and impact denser quiescent material in the region of the northern cavity wall, causing the outflow to decelerate more quickly. This could explain why the northern wall of the cavity displays lower radial velocities when compared to that seen in the eastern wall. The denser quiescent material at the right side of the cavity could naturally explain the velocity gradient one sees in the $H_2$ emission. The production of transverse velocity gradients due to dissymmetry in density of surrounding ambient material has been discussed by De Colle, Cerqueira, and Riera (2016).

Lastly, the velocity gradient seen in the cavity traced by $H_2$ emission could be that the dominating outflow driver for the northern and eastern cavity walls

originate from different sources. The driving source of the HH 46/47 outflow system is known to be a binary source (Reipurth et al., 2000). Nisini et al. (2024) suggest that the bright $H_2$ knot seen at the base of the eastern cavity wall, *A1*, is a expanding bubble ejected by the secondary component of the binary system. This could imply that the emission one sees in the eastern wall of the $H_2$ cavity could have been strongly influenced by this secondary outflow driver. The outflow from this secondary source in the binary system could be strongly contributing to the shocked $H_2$ emission in the eastern wall of the cavity, potentially increasing it's radial velocity in comparison to the northern wall. This is further testified by the $H_2$ knot *A1* possessing the highest blueshifted radial velocity in the velocity centroid maps provided in Fig. 4.18.

One point I would like to emphasise in this discussion is that velocity gradient signatures observed transverse to the outflow direction can easily be misinterpreted as being due to rotational motion, and this interpretation is further motivated by current MHD disc wind models. However, other effects, such as ambient material density variations and the presence of multiple outflows, as discussed above, can produce transverse velocity gradient signals. In addition, further effects such as kink instabilities (Staff et al., 2015) and twin-jet structures (Soker, Bublitz, and Kastner, 2022), to name a few, can reproduce transverse velocity gradients. In this analysis, other interpretations of the observed velocity gradient are investigated, due to the specific angular momentum values being significantly larger than that seen before for rotating outflow cavities, and due to the apparent counter-rotation of the outflow with respect to the conjectured disc rotation direction. However, other effects that can produce similar velocity gradient signatures must be considered in cases where specific angular momentum estimates are as expected and apparent rotation direction is in the same sense as the disc.

## 4.4 Summary and conclusions

The morphology and kinematics of the launching region of the blueshifted HH 46/47 outflow emanating from the class I binary system HH 46 IRS have been investigated with SINFONI K-band observations. The achieved angular resolution was $0\farcs81$, and a precision in velocity centroids, in $H_2$ 1-0 S(1) emission, of $\pm$ 1 to 3 km s$^{-1}$. These observations allowed the study of both the base of

the atomic jet traced by [Fe II] and Br-$\gamma$ emission and the wide-angled molecular hydrogen outflow cavity. The main results of this chapter are summarised as follows:

- I have presented the morphology of the NIR continuum, $H_2$ 1-0 S(1), [Fe II] $\lambda$2.047 $\mu$m and Br-$\gamma$ emission. The continuum emission displays an approximately parabolic and asymmetric reflection nebula that is interpreted as a boundary region between the outflow and the ambient material, where the outflow has carved a wide-angled cavity in the quiescent material. A point source at the apex of this cavity is recovered and established as the source position. The $H_2$ emission displays a striking V-shaped morphology tracing the limb-brightened cavity walls of the outflow. It is inferred that the cavity structure one observes has a 3D inverted-conical shape surrounding the atomic jet. The forging of this outflow cavity, which is determined to be an interaction region between the outflow and the surrounding quiescent material, may be due to some wide-angled wind, or expanding shells of material produced by an episodic wide-angled wind, or by the stacking of successive jet bow shocks from a collimated variable inner jet propagating into a density-stratified surrounding medium. The morphological components labelled *A1*, *A2*, and *A3* may arise due to multiple expanding shells, with a smaller scale shell associated with the shocked emission peaks *A1* and *A2* expanding within a slightly larger scale shell associated with the outer cavity walls produced by an earlier outburst of the wide-angled wind or by a successive jet bow shock. The high-velocity [Fe II] and Br-$\gamma$ emission traces the base of the atomic jet that culminates in a jet knot at approximately 1$\farcs$0 or 450 au from the source position.

- Radial stratification of the outflow in different emission tracers, which produces an onion-like flow structure, as discussed in Section 4.3.1 is found, favouring the disc wind launching model. The slow-moving, wide-angled molecular outflow cavity traced in $H_2$ emission surrounds the base of the hotter, high-velocity atomic jet traced in [Fe II] and Br-$\gamma$ emission. The $H_2$ outflow cavity lies within the reflection nebula seen in continuum emission, extending less laterally, and has a narrower opening angle. The $H_2$ outflow cavity is also nested within the molecular

outflow traced in $^{12}$CO (2-1) emission, and it appears to curl inward towards the outflow axis at a distance along the outflow of approximately $4\farcs0$.

- The reflection nebula seen in continuum emission, the $H_2$ outflow cavity, and the atomic jet traced in [Fe II] and Br-$\gamma$ are all asymmetric about the CO outflow direction. This is discussed in Section 4.3.1. Explanations for the origin of the $H_2$ outflow cavity asymmetries are provided, including density variations in the surrounding ambient material and the influence of multiple outflows. It is plausible that both components of the binary source drive outflows. A bending of the atomic jet, which emanates from the source position and tends towards the northern-pointing cavity wall, is observed, which is indicative of the jet wiggling that has been observed in this jet at larger scales.

- Position velocity diagrams, as seen in Section 4.2.2, are employed to investigate the kinematics of the atomic jet and the $H_2$ outflow cavity. The radial velocity of the atomic jet emission traced by [Fe II] and Br-$\gamma$ peaks at $\sim -210$ km s$^{-1}$, which is consistent with previous measurements. The Gaussian centroid velocity of the atomic jet knot at an offset of $1\farcs0$ from the source position is $v_{\rm rad} = -208.7 \pm 3.6$ km s$^{-1}$ in [Fe II] emission and $v_{\rm rad} = -211.9 \pm 3.5$ km s$^{-1}$ in Br-$\gamma$ emission. A position velocity diagram taken transverse to the outflow axis was produced to investigate the kinematics of the $H_2$ emission. The radial velocity of the $H_2$ emission is significantly lower than that of the atomic jet emission, peaking around $\sim -15$ km s$^{-1}$ to $-30$ km s$^{-1}$. Two emission peaks located at the base of each cavity wall on either side of the source position, labelled *A1* and *A2* are observed. The emission peak from the base of the eastern cavity wall (*A1*) peaks at a slightly higher radial velocity ($-33.9 \pm 1.4$ km s$^{-1}$) than the emission peak (*A2*) from the base of the northern cavity wall ($-16.9 \pm 1.5$ km s$^{-1}$).

- The presence of a velocity gradient in the outflow cavity, transverse to the outflow axis, traced in $H_2$ emission, is confirmed. A velocity centroid map was generated to probe this observed velocity gradient. The

magnitude of this velocity difference is $\sim 10$ km s$^{-1}$, and exists between the northern and eastern pointing cavity walls (see Table 4.3). Some possible explanations for the origin of this velocity gradient are discussed (Section 4.3.2). Outflow rotation as the sole origin is ruled out due to large specific angular momenta values, $J(r) = 3217 \pm 658$ to $3867 \pm 1125$ km s$^{-1}$au, calculated from $1\farcs0$ to $2\farcs0$ offset from the central source, and the fact that the sense of apparent rotation detected is opposite to that of the CO envelope emission. Instead, a dissymmetry in the ambient material surrounding the outflow as the origin is favoured, or the presence of multiple outflows.

This chapter displays the wealth of information that can be extracted from IFU observations of protostellar outflows on intermediate scales in the NIR, and highlights the morphological and kinematical complexity that needs to be considered when interpreting various aspects of outflows at these scales. In particular, I want to emphasise that radial velocity gradients observed transverse to the outflow axis can be misinterpreted as rotation signatures when other effects, such as those discussed, can produce equivalent transverse velocity gradients.

# Chapter 5

# Forbidden emission line spectro-imaging of the RU Lupi jet and low-velocity component

## 5.1 Introduction

In this chapter, I will present the FEL spectro-imaging study of the outflow emanating from the CTTS RU Lupi, using MUSE NFM observations. CTTSs are young, low-mass stars in the earliest stages of forming planets and thus are analogues of the early evolution of our own Solar System (Ray, 2007). As discussed in Section 1.3.3, CTTSs are further into their evolution than their class 0/I counterparts, therefore, their accretion rates are lower and consequently their outflows are less powerful. However, they are still actively accreting, meaning that angular momentum must be extracted from the system. Characterising how angular momentum is extracted from CTTSs therefore provides constraints on how CTTSs accrete mass, and how their discs evolve and form planets (Pascucci et al., 2023). CTTSs are observed to have slow rotation rates, with typical periods of 8 – 10 days, or approximately 10% of their break-up speed (Bouvier et al., 1986; Bertout, 1989). Furthermore, it has been observed that for CTTSs, as long as a disc is present, the central star maintains a constant period, even as the central star is contracting. This is referred to as disc-locking (Gallet and Bouvier, 2013). Outflows are therefore thought to be essential to this period of star formation as a means to remove angular momentum from the star-disc system, regulating accretion and preventing the spinning-up of the central star (Pudritz and Ray, 2019; Lesur, 2021; Pascucci et al., 2023).

Early observations of the spectra from CTTSs revealed that outflow-tracing FEL line profiles displayed two distinct components, a HVC and LVC (Kwan and Tademaru, 1988). As discussed in Section 1.3.2, the HVC is thought to trace the high-velocity, collimated jet component of the MHD outflow, with the emission region extending to several hundred au (Hirth, Mundt, and Solf, 1997; Hartigan and Morse, 2007). The exact physical origin of the LVC is less certain, as discussed in Section 1.3.2, however, it has long been a strong candidate for an MHD disc wind tracer (Kwan and Tademaru, 1988; Kwan and Tademaru, 1995). In contrast to the HVC, the LVC is spatially compact, limiting what it can reveal about MHD winds (Fang et al., 2023b). A further complication is that the LVC likely also traces a thermally driven photoevaporative wind (Rab et al., 2023), which does not contribute to angular momentum removal.

To uncover the origin of the LVC, studies have focused on kinematics (Banzatti et al., 2019; Nisini et al., 2024) and spectro-astrometry (Whelan et al., 2021; Whelan, Murphy, and Pascucci, 2023). The observed high velocities of the LVC coupled with emitting regions existing within the gravitational potential well of the central star revealed by these studies cannot easily be explained by photoevaporative winds (Pascucci et al., 2023). AO-assisted IFS, such as can be done with the MUSE instrument, has the capability to spatially resolve the LVC, allowing its width and height to be measured (e.g. Fang et al., 2023b; Flores-Rivera et al., 2023). The width of this outflow component provides an upper limit of the launch radius of the outflow, providing a key differentiator between MHD outflow launching models. The height of the emitting region is required to estimate the mass outflow rate. In combination with the mass accretion rate, the mass outflow rate provides quantitative estimates of how much angular momentum is being extracted from the system (Frank et al., 2014; Pudritz and Ray, 2019; Whelan et al., 2021). Therefore, MUSE observations could potentially distinguish between the different physical origins for the LVC, differentiating between outflow launching mechanisms, as discussed in Section 1.3.4, and verify whether MHD winds regulate accretion. Current work is focused on identifying direct tracers of MHD winds to test for their presence and their ability to remove angular momentum. As the [O I] $\lambda$6300 Å line is the brightest FEL[1] almost always displaying an LVC and frequently, a

[1]Due to the large abundance of oxygen and the favourable excitation conditions in the gas.

HVC, it is considered a touchstone for the LVC (McGinnis et al., 2018; Nisini et al., 2018).

In this chapter, MUSE narrow-field mode (NFM) observations of the jet and wide-angled wind of the CTTS RU Lupi are presented. The outflow from RU Lupi is well suited in regards to untangling the origin of the LVC, as it has a distinctly separated HVC and LVC, and has previously been investigated with high-resolution spectroscopy and spectro-astrometry (Takami et al., 2001; Whelan et al., 2021). The motivation for this study of the object was to see what additional information the use of IFS can provide to solve what outflow component the LVC is tracing, and to resolve the compact nature of the LVC. The observational technique of spectro-astrometry measures the spatial displacement of spectral features from an unresolved source, typically at milliarcsecond scales. In regards to using this technique to study outflows, spectro-astrometry examines how the centroid of an emission line shifts relative to the continuum position as a function of velocity. If the outflowing gas is moving in an organized way, for example in a bipolar outflow, then its emission can be displaced from the star's position at different velocities, allowing the inference of spatial and kinematic information. This technique can provide the minimum extent of an outflow, but yields no information on the width or collimation of the outflow. In Banzatti et al. (2019), the [O I] $\lambda$6300 Å and [S II] $\lambda$6731 Å FELs were shown to have three distinct velocity components in their line profiles. Whelan et al. (2021) classified these components as a HVC with a peak velocity $v_{\rm p} \sim 200$ km s$^{-1}$ (HVC2), a second, intermediate HVC that they suggested was the base of the jet (HVC1; $v_{\rm p}$ = 60 – 100 km s$^{-1}$) and an LVC narrow component (NC) ($v_{\rm p}$ = 13 – 24 km s$^{-1}$). The spectro-astrometric analysis of Whelan et al. (2021) using data from the Ultraviolet and Visual Echelle Spectrograph (UVES) installed on the 2$^{\rm nd}$ unit telescope (UT2) of the VLT, revealed three new pieces of information about the LVC NC from RU Lupi that were interpreted as it tracing an MHD wind. These were; that the position angle (PA) of the LVC NC matched the PA of the jet, the emitting region was traced within 2 au of the star, which is unlikely for a photoevaporative wind, and a negative velocity gradient with increasing offset from the central star, opposite to that seen for the jet. The MUSE observations now described offer the first images of the RU Lupi jet and NC along with measurements of their width and height.

### 5.1.1 RU Lupi

RU Lupi (RU Lup, HD 142560, Sz 83) is a CTTS with an apparent magnitude of 10.5 located in the Lupus star forming region at a distance of approximately 140 pc (Hughes et al., 1994; Zeeuw et al., 1999; Bertout, Robichon, and Arenou, 1999; Takami et al., 2001; Herczeg et al., 2005; Whelan et al., 2021). The object is approximately 2 – 3 million years old and has a luminosity of $L_\star = 2.1\ L_\odot$, a mass of $M_\star = 0.55\ M_\odot$, and a radius of $R_\star = 2.48\ R_\odot$ (Hughes et al., 1994; Herczeg et al., 2005; Lommen et al., 2009; Fang et al., 2018). The estimated optical extinction for RU Lupi is approximately zero ($A_V = 0$ – $0.07$) (Herczeg et al., 2005; Robrade and Schmitt, 2007; Fang et al., 2018). RU Lupi is notable for its high accretion activity for a CTTS, and therefore exhibits significant variability in its luminosity (Stock et al., 2022). The stellar spectrum is known to display evidence of an outflow comprising both a jet and a wider-wind (Takami et al., 2001; Podio et al., 2008), in both permitted line emission and forbidden line emission. Banzatti et al. (2019), and later, Whelan et al. (2021), have shown that the line profiles of the [O I] $\lambda$6300 Å and [S II] $\lambda$6731 Å FELs display three distinct velocity components, most likely tracing jet and wind activity. Herczeg et al. (2005) have shown that there also exists a molecular wind in $H_2$ emission, and Pontoppidan, Blake, and Smette (2011) have shown with spectro-astrometry that there exists a wide-angled molecular wind in CO emission. The estimated PA of the disc surrounding RU Lupi is $121^\circ \pm 5^\circ$ (Huang et al., 2018), which is approximately perpendicular to the outflow direction estimated by Takami et al. (2001) and Whelan et al. (2021). The disc also has an almost face-on inclination of $\theta_i = 19^\circ \pm 2^\circ$ with respect to the plane of the sky (Huang et al., 2018).

## 5.2 Results

In this chapter the results from the 106.21EN.001 observations (PI: L. Pérez) are presented due to them being of higher quality than the 0104.C-0919(B) observations (PI: A. Müller), as discussed in Section 3.4.2. All emission line velocities discussed throughout the chapter are corrected for the Barycentric Earth Radial Velocity (BERV). The MUSE NFM observations of RU Lupi reveal emission lines tracing accretion and outflow activity. A table of identified emission lines in the observation is presented in Table 5.1. In this chapter, the morphology, kinematics, and efficiency of the outflow emanating from the CTTS RU Lupi,

are discussed. As the star is a class II object and therefore more evolved in its formation process when compared with the HH 46/47 system, the source is not heavily veiled. The source can therefore be observed at optical wavelengths, as the envelope of material surrounding the star has mostly dispersed. The determination of the source position is subsequently not a challenge in these observations. The peak of the continuum emission was fit with a 2D Gaussian profile and the recovered centroid of the fitted profile was used as the source position throughout. Figure 5.1 displays a spectrum from the RU Lupi source position extracted using a circular aperture of radius 0.″1, or 14 au, taking a distance of 140 pc to RU Lupi. The outflow is identified in the forbidden emission lines [O I] $\lambda\lambda$ 6300,6363 Å, [N II] $\lambda$ 6583 Å, [S II] $\lambda\lambda$ 6716,6731 Å, and [Fe II] $\lambda$ 7155 Å. Typical gas properties of these emission tracers are summarised in Table 5.2. Emission lines tracing accretion activity are also identified and discussed further in Section 5.2.3. There is a gap in the spectral range from 5780 – 6050 Å due to the sodium laser adaptive optics system that MUSE employs. There also is a telluric absorption feature at $\sim$ 7600 Å due to molecular oxygen ($O_2$).

### 5.2.1 Morphology of the outflow components

The outflow was identified in the forbidden emission lines [O I] $\lambda\lambda$ 6300,6363 Å, [N II] $\lambda$ 6583 Å, [S II] $\lambda\lambda$ 6716,6731 Å, and [Fe II] $\lambda$ 7155 Å. This prompted the production of integrated intensity maps to showcase the morphology of the jet emission. These are the first images of the outflow emanating from RU Lupi. Deconvolved intensity maps are also presented later in this section purely to better visualise the morphological differences present between various emission tracers. Figure 5.2 displays the integrated continuum-subtracted intensity maps of the jet in [O I] 6300 Å emission in the left panel and [O I] 6363 Å emission in the right panel. The [O I] 6300 Å emission is integrated over the velocity range $v_{\rm rad}$ = − 265 km s$^{-1}$ to − 325 km s$^{-1}$ and the [O I] 6363 Å emission is integrated over the velocity range $v_{\rm rad}$ = − 250 km s$^{-1}$ to − 310 km s$^{-1}$. The measured source position is marked with a blue star symbol. The intensity follows a logarithmic scale. The jet propagates in the southwesterly direction, with the jet appearing more evidently in the [O I] 6300 Å emission line. The [O I] 6363 Å intensity map possesses a slight offset in the southwesterly direction of the jet but there is no conclusive collimated jet emission seen here. A faint shock feature or jet knot is apparent in the left panel of this figure, located

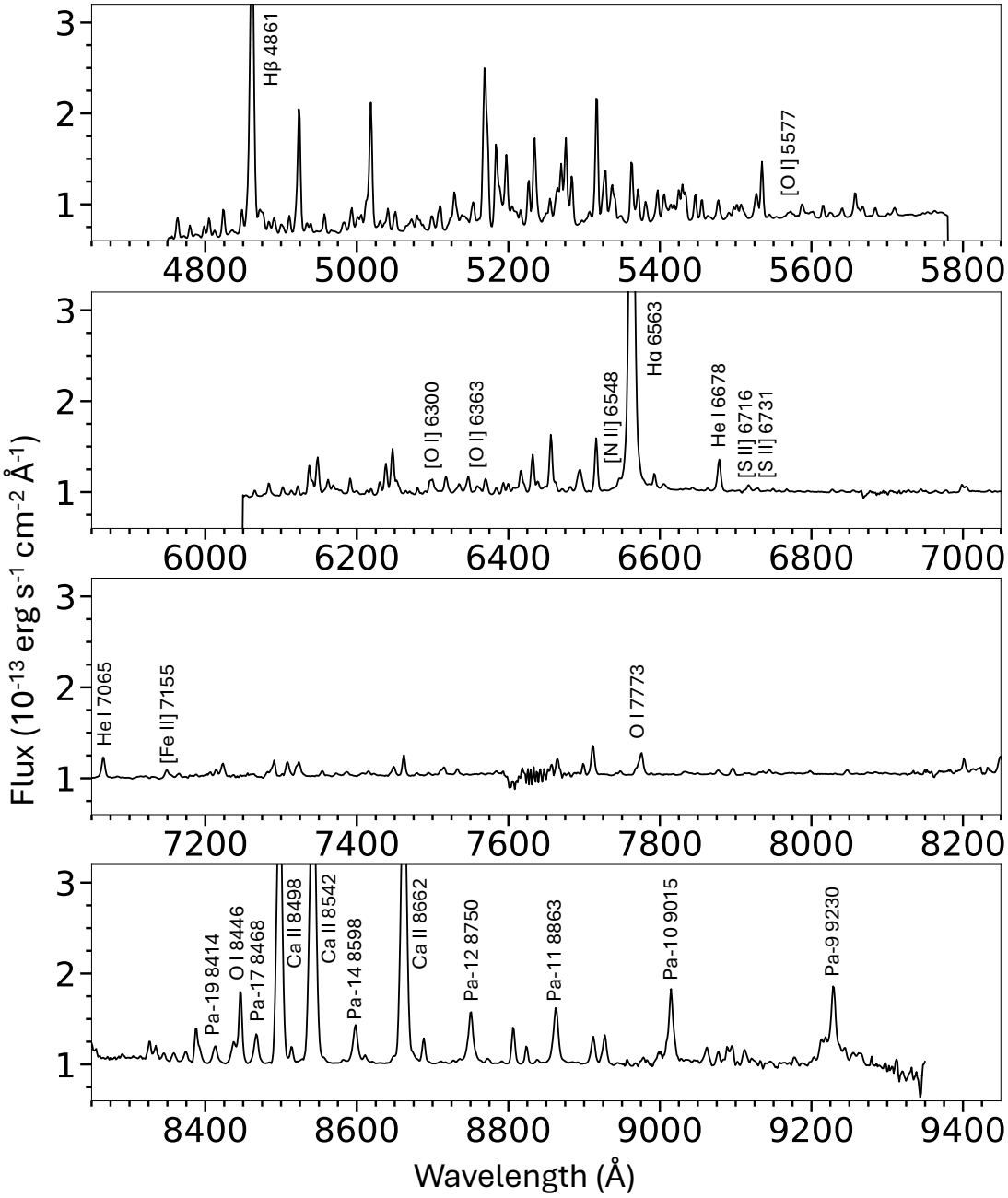


FIGURE 5.1: Spectrum extracted using a circular aperture of radius 0.″1 (14 au) from the RU Lupi source position. The outflow is identified in forbidden emission lines. Accretion tracing emission lines are also identified.

TABLE 5.1: Identified emission lines present in the MUSE observations of RU Lupi. The wavelengths of these lines, $\lambda_{air}$, are expressed as their rest wavelengths in air.

| Line | $\lambda_{air}$ (Å) |
|---|---|
| H$\beta$ | 4861 |
| [O I] | 5577 |
| [O I] | 6300 |
| [O I] | 6363 |
| H$\alpha$ | 6563 |
| [N II] | 6583 |
| He I | 6678 |
| [S II] | 6716 |
| [S II] | 6731 |
| He I | 7065 |
| [Fe II] | 7155 |
| O I | 7773 |
| Pa-19 | 8414 |
| O I | 8446 |
| Pa-17 | 8468 |
| Ca II | 8498 |
| Ca II | 8542 |
| Pa-14 | 8598 |
| Ca II | 8662 |
| Pa-12 | 8750 |
| Pa-11 | 8863 |
| Pa-10 | 9015 |
| Pa-9 | 9230 |

TABLE 5.2: Summary of typical gas properties for outflow emission tracers present in MUSE data.

| Emission tracer | $T$ (K) | $n_e$ (cm$^{-3}$) | Velocity components |
|---|---|---|---|
| [O I](1) | 8,000 – 15,000 | $10^3$ – $10^4$ | HVC + LVC |
| [N II](2) | 10,000 – 20,000 | $10^3$ – $10^5$ | HVC only |
| [S II](3) | 8,000 – 15,000 | $10^2$ – $10^4$ | HVC + LVC |
| [Fe II](4) | 8,000 – 15,000 | $10^4$ – $10^6$ | HVC dominates |

(1) Hartigan, Morse, and Raymond (1994) and Bacciotti and Eislöffel (1999)
(2) Hartigan, Morse, and Raymond (1994), Hirth, Mundt, and Solf (1997), and Bacciotti and Eislöffel (1999)
(3) Hartigan, Morse, and Raymond (1994) and Bacciotti and Eislöffel (1999)
(4) Bacciotti and Eislöffel (1999) and Nisini et al. (2005)

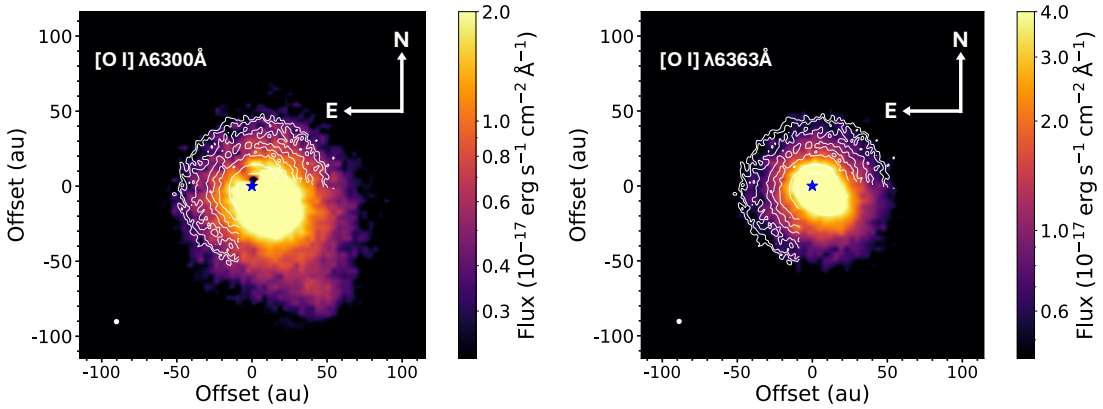


FIGURE 5.2: Integrated continuum-subtracted intensity maps of the jet in [O I] 6300 Å emission in the left panel and [O I] 6363 Å emission in the right panel. A sector of the ALMA 1.25 mm dust continuum disc is shown in white contours (Andrews et al., 2018). The ALMA beam size (3.5 × 3.4 au) is shown in the lower left corner of each panel. The jet is propagating southwesterly. In the [O I] 6300 Å emission line, a faint shock feature or jet knot is apparent, located at approximately 85 au from the source position along the jet axis.

at approximately 85 au from the source position, along the jet axis. The jet possesses a wide morphology at the base of the outflow, close to the driving source, in both emission lines. The outflow is also clearly brightest at the base of the outflow. As the accretion disc surrounding RU Lupi has an almost face-on inclination of $\theta_i = 19° \pm 2°$ (Huang et al., 2018) with respect to the plane of the sky, the blueshifted jet one sees is emanating towards the observer. One is essentially looking down the barrel of the outflow as it propagates towards us. As a visual aid to help with the geometry of the system, a sector of the RU Lupi accretion disc is overplotted in these intensity maps in white contour lines. Only a sector of the disc is plotted, with an artificial wedge removed from the disc, so that the disc contours do not inhibit the visibility of the outflow emission. The disc image is from the Disc Substructures at High Angular Resolution Project (DSHARP) (Andrews et al., 2018), carried out with ALMA using an observing frequency in the vicinity of 240 GHz (ALMA Band 6) so as to capture 1.25 mm continuum emission from the disc surface. This continuum emission traces the dust disc. The ALMA beam size, which refers to the observatory's angular resolution is displayed in the bottom left of each panel. The beam size is $0\farcs025 \times 0\farcs024$ (Andrews et al., 2018), or 3.5 au × 3.4 au, taking the distance to the object to be 140 pc.

Figure 5.3 displays the integrated continuum-subtracted intensity maps of

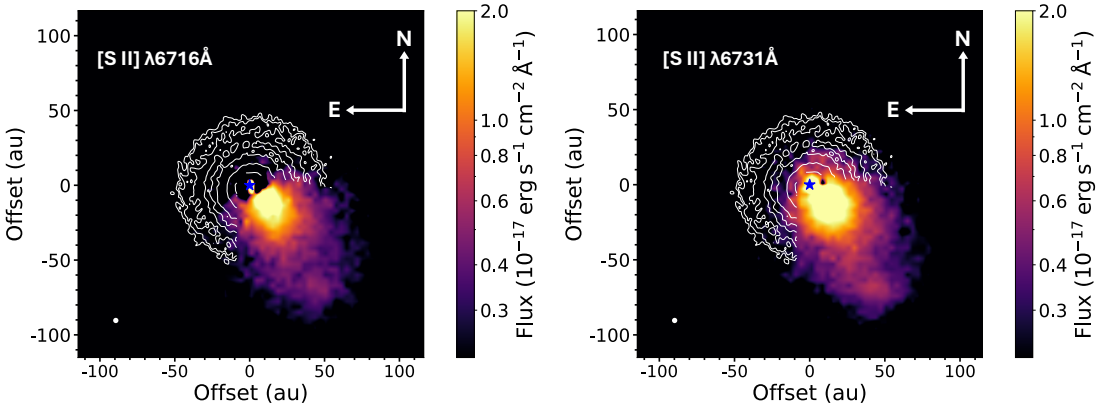


FIGURE 5.3: Integrated continuum-subtracted intensity maps of the jet in [S II] 6716 Å emission in the left panel and [S II] 6731 Å emission in the right panel. A sector of the ALMA 1.25 mm dust continuum disc is shown in white contours (Andrews et al., 2018). The ALMA beam size (3.5 × 3.4 au) is shown in the lower left corner of each panel. The jet is propagating southwesterly. The jet knot is apparent in both intensity maps, located at approximately 85 au from the source position along the jet axis.

the jet in [S II] 6716 Å emission in the left panel and [S II] 6731 Å emission in the right panel. The [S II] 6716 Å emission is integrated over the velocity range $v_{\rm rad}$ = − 245 km s$^{-1}$ to − 300 km s$^{-1}$ and the [S II] 6731 Å emission is integrated over the velocity range $v_{\rm rad}$ = − 270 km s$^{-1}$ to − 325 km s$^{-1}$. The measured source position is marked with a blue star symbol. The intensity follows a logarithmic scale. The jet propagates in the southwesterly direction, with the jet appearing more clearly than in the [O I] emission lines. The jet culminates in the shock feature or jet knot, located at approximately 85 au from the source position along the jet axis. Again, the outflow is also evidently brightest at the base of the outflow. A sector of the ALMA 1.25 mm continuum dust disc is again overplotted in white contour lines as a visual aid.

Figure 5.4 displays the integrated continuum-subtracted intensity maps of the jet in [N II] 6583 Å emission in the left panel and [Fe II] 7155 Å emission in the right panel. The [N II] 6583 Å emission is integrated over the velocity range $v_{\rm rad}$ = − 230 km s$^{-1}$ to − 280 km s$^{-1}$ and the [Fe II] 7155 Å emission is integrated over the velocity range $v_{\rm rad}$ = − 280 km s$^{-1}$ to − 330 km s$^{-1}$. The measured source position is again marked with a blue star symbol and the intensity follows a logarithmic scale. The [Fe II] 7155 Å intensity map shown in the right panel bears resemblance to the [O I] 6363 Å intensity map, in that there exists a slight offset in the southwesterly direction of the jet, but there is no conclusive collimated jet emission seen here. The [N II] 6583 Å intensity map,

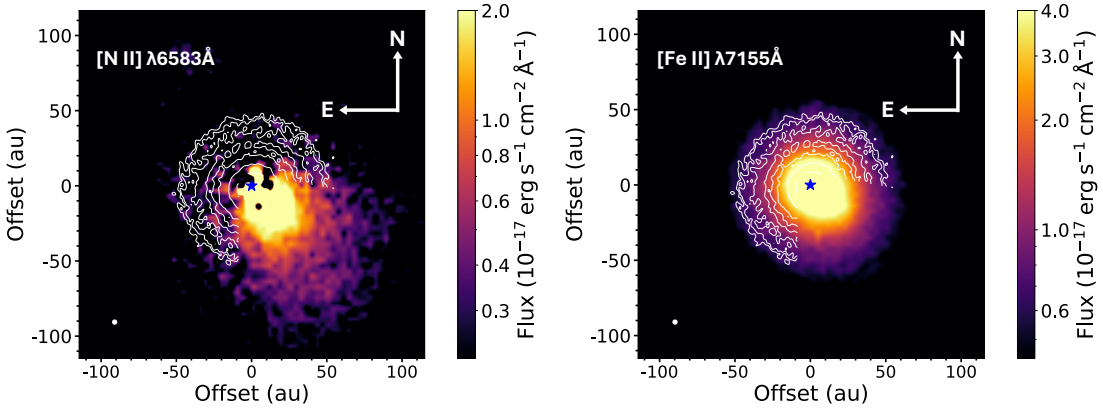


FIGURE 5.4: Integrated continuum-subtracted intensity maps of the jet in [N II] 6583 Å emission in the left panel and [Fe II] 7155 Å emission in the right panel. A sector of the ALMA 1.25 mm dust continuum disc is shown in white contours (Andrews et al., 2018). The ALMA beam size (3.5 × 3.4 au) is shown in the lower left corner of each panel. The jet is propagating southwesterly. The morphology in N II emission is quite wide at the base of the jet.

shown in the left panel, possesses extended emission along the southwesterly direction. The morphology of the outflow in [N II] emission is relatively wide at the base of the jet. The outflow is again clearly brightest at the base, close to the driving source. The sector of the ALMA 1.25 mm continuum dust disc is again overplotted in white contour lines.

The position angle of the disc has been estimated to be 121° ± 5° by Huang et al. (2018). As the integrated intensity maps presented here are the first images of the RU Lupi jet, the measurement of the position angle of the jet was desired. In order to retrieve the PA of the jet, the integrated intensity maps of emission lines displaying conclusive collimated jet emission were selected to perform the measurements on. The selected lines were [O I] $\lambda$ 6300 Å, [S II] $\lambda$ 6716Å, and [S II] $\lambda$ 6731 Å emission. Firstly, these three intensity maps were rotated by eye, so that the jet axis lay along the positive horizontal direction. Following this, spatial profiles perpendicular to the jet axis were extracted at numerous positions along the jet axis. These spatial profiles were fit with Gaussian profiles to measure the centroids of the emission, which are indicative of the jet axis position. Linear fits were then applied to the centroid data points measured along the jet axis in order to retrieve the jet position angle. In this way, using these three emission lines, the jet PA was measured to be 213° ± 2°, which is perpendicular, within the uncertainties of the observations, to the estimated disc PA of 121° ± 5° (Huang et al., 2018), as one would expect. To

illustrate this, Figure 5.5 displays the continuum-subtracted integrated intensity map for [S II] $\lambda$ 6731 Å emission with the disc PA and newly measured jet PA overplotted. The red arrow delineates the disc PA and radius from Huang et al. (2018) ($121^\circ \pm 5^\circ$, $63 \pm 1$ au). The dashed green line shows the jet PA measured here ($213^\circ \pm 2^\circ$). The jet and outer shock feature or knot are perpendicular to the disc. In the bright inner region of the jet emission, at $< 50$ au from the source, the emission appears to be asymmetric about the green line, with the northwestern side appearing brighter than the southeastern side, of this inner jet region. Close to the source, the outflow is wide and bright. The shock feature, or knot, that the jet culminates in at $\sim 85$ au is located at 250 au along the jet axis if one deprojects the jet into the plane of the sky, assuming that the jet is indeed launched perpendicularly to the disc. Assuming that the jet is launched perpendicularly to the almost face-on accretion disc of inclination $\theta_i = 19^\circ \pm 2^\circ$ (Huang et al., 2018) results in a jet inclination of $\theta_i = 109^\circ$, with respect to the plane of the sky, if one measures from the same side as the inclined disc, or equivalently, $\theta_i = 71^\circ$, if one measures the smaller angle with respect to the sky.

As some optical FEL profiles are known to possess both high and low-velocity components, as discussed in Section 1.3.2, this was investigated in the MUSE observation of RU Lupi. Figure 5.6 displays the line profiles of the [O I] emission line at 6300 Å and the [S II] emission line at 6731 Å, as the jet emission was clearest in these lines. The line profiles are extracted from the source position, shown here in red, and from the jet shock feature, or knot, located at approximately 85 au from the source position, shown here in black. The spectral extraction apertures for both had the same radius, $0\farcs1$ or 14 au. The wavelength axis in this figure has been converted to radial velocities with the 0 km s$^{-1}$ value corresponding the rest wavelength of the corresponding emission line as measured in air. As the flux is much greater at the source position in comparison to the jet shock feature in both emission lines, as evidenced by the integrated intensity images in figures 5.2 and 5.3, the two spectra were independently normalised. This was done in order to investigate how the shape of the line profile changed from on-source emission to on-jet emission. In both line profiles, it is clear that there are two distinct velocity components that comprise the profiles, in that the summation of two Gaussian profiles are required to reproduce the observed profile shape. In the source spectra, shown in red, it is clear that the low-velocity component dominates. In contrast, the

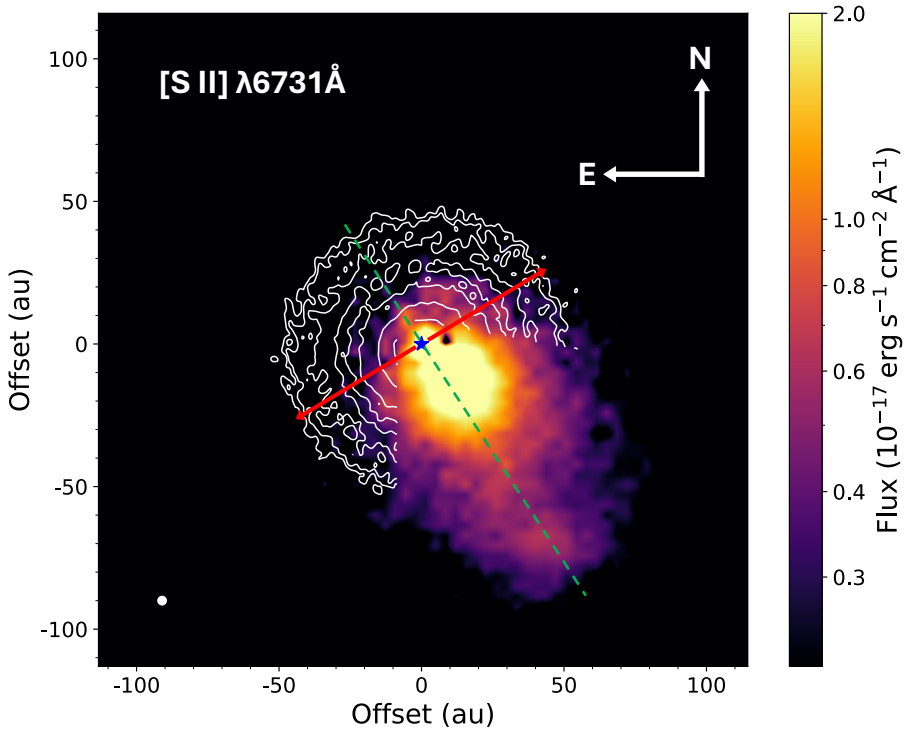


FIGURE 5.5: Integrated continuum-subtracted intensity map of the jet in [S II] 6731 Å emission. A sector of the ALMA 1.25 mm dust continuum disc is shown in white contours (Andrews et al., 2018). The ALMA beam size (3.5 × 3.4 au) is shown in the lower left corner. The red arrow delineates the disc PA and radius from Huang et al. (2018) (121° ± 5°, 63 ± 1 au), and the dashed green line shows the jet PA measured here (213° ± 2°). The jet and outer knot are perpendicular to the disc, but the inner bright region of the jet at < 50 au from the source is asymmetric about the green line.

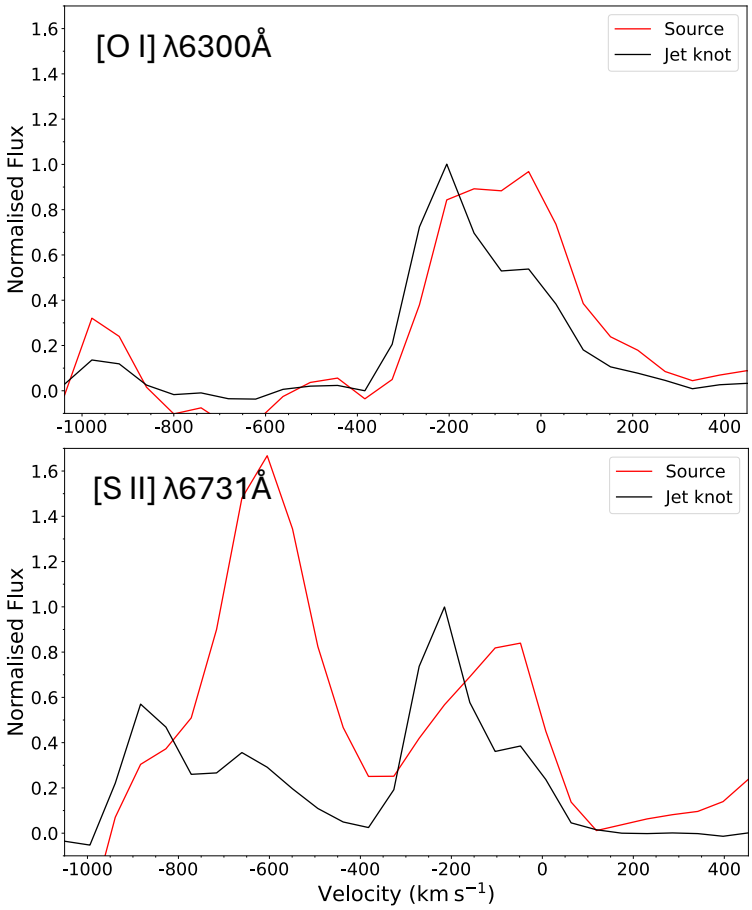


FIGURE 5.6: The line profiles of [O I] 6300 Å and [S II] 6731 Å emission. The red profiles display the spectra extracted from the source position using a circular aperture of radius 0.″1. The black profiles display the spectra extracted using a circular aperture of radius 0.″1 from the jet knot position located at approximately 85 au along the jet.

jet spectra, shown in black, display that the high-velocity component dominates. This implies that the jet emission is strongest in the spectrum extracted from the jet and that the low-velocity component fades in intensity as offset from the driving source increases. Banzatti et al. (2019) have shown that the [O I] emission line at 6300 Å and the [S II] emission line at 6731 Å have three distinct velocity components in their line profiles. In Figure 5.6 three velocity components are not resolved due to the insufficient spectral resolution of the MUSE instrument.

In order to investigate the morphology of the distinct velocity components present in these emission lines, channel maps of the outflow were produced. As discussed in Section 4.2.2, a channel map is an image that represents the

spatial distribution of emission at a specific velocity interval, where the spectral interval in the data cube is converted to a radial velocity interval using Doppler shift (Equation 3.4) and the rest wavelength of the emission line in question. Furthermore, the continuum-subtracted data cube was rotated so that the measured PA of $\sim 213^{\circ}$ lay along the horizontal axis to facilitate the analysis of the extended outflow emission. Channel maps of the outflow in [O I] 6300 Å and [S II] 6731 Å emission are displayed in Figure 5.7. The dashed-red line highlights the measured jet PA. The channel maps are integrated over spectral or velocity regions that correspond to the three distinct velocity components present in the line profiles as shown by Banzatti et al. (2019). As stated in Section 5.1, Whelan et al. (2021) classified these three velocity components as *HVC2*, a HVC with a peak velocity $v_{\rm p} \sim 200$ km s$^{-1}$, *HVC1*, a second, intermediate HVC with a peak velocity $v_{\rm p} \sim 60$ – 100 km s$^{-1}$, and *LVC NC*, an LVC narrow component (NC) with a peak velocity of $v_{\rm p} \sim 13$ – 24 km s$^{-1}$. Hereafter, I will refer to the velocity component *HVC2* as the jet, *HVC1* as HVC1, and *LVC NC* as LVC. In Figure 5.7 the jet emission is integrated in the velocity region $v_{\rm rad} = -205$ km s$^{-1}$ to $-325$ km s$^{-1}$ in [O I] 6300 Å emission and $v_{\rm rad} = -215$ km s$^{-1}$ to $-325$ km s$^{-1}$ in [S II] 6731 Å emission. The velocity component HVC1 is integrated in the velocity region $v_{\rm rad} = -85$ km s$^{-1}$ to $-150$ km s$^{-1}$ in [O I] 6300 Å emission and $v_{\rm rad} = -105$ km s$^{-1}$ to $-160$ km s$^{-1}$ in [S II] 6731 Å emission. The velocity component LVC is integrated in the velocity region $v_{\rm rad} = +30$ km s$^{-1}$ to $-30$ km s$^{-1}$ in [O I] 6300 Å emission and $v_{\rm rad} = +5$ km s$^{-1}$ to $-50$ km s$^{-1}$ in [S II] 6731 Å emission. Due to the insufficient spectral resolution of MUSE, the three outflow velocity components are not fully resolved, as evident in Figure 5.6, and any conclusions that one makes from these channel maps should consider this. Morphological differences are however present between the velocity components of the outflow.

Channel maps were also prepared in [N II] 6583 Å emission and in high-velocity redshifted [S II] 6731 Å. These are presented in Figure 5.8. The [N II] 6583 Å emission line is known to lack a low-velocity component in its line profile. [N II] does not posses an LVC because of the lack of strong ionising conditions in the denser, slower-moving region associated with low-velocity components of outflows (Hirth, Mundt, and Solf, 1997). The region of the outflow associated with low-velocity components simply does not have the ionisation necessary to produce [N II] emission, and therefore [N II] emission does not trace low-velocity gas. As a result of this, only a channel map for the

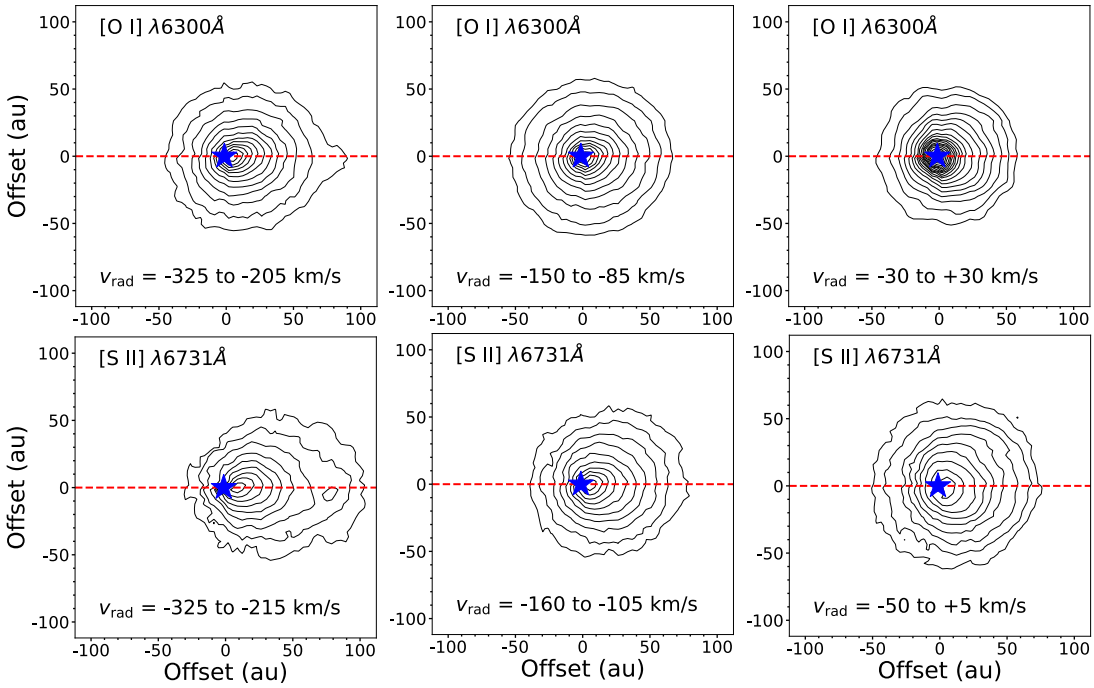


FIGURE 5.7: Channel maps of the jet, HVC1, and LVC in continuum subtracted [O I] 6300 Å and [S II] 6731 Å emission. The source position is marked with a blue star symbol. The velocity intervals of the channel maps are highlighted in the panels. The contour levels begin at $3\sigma$ of the background emission and increase by factors of 1.5.

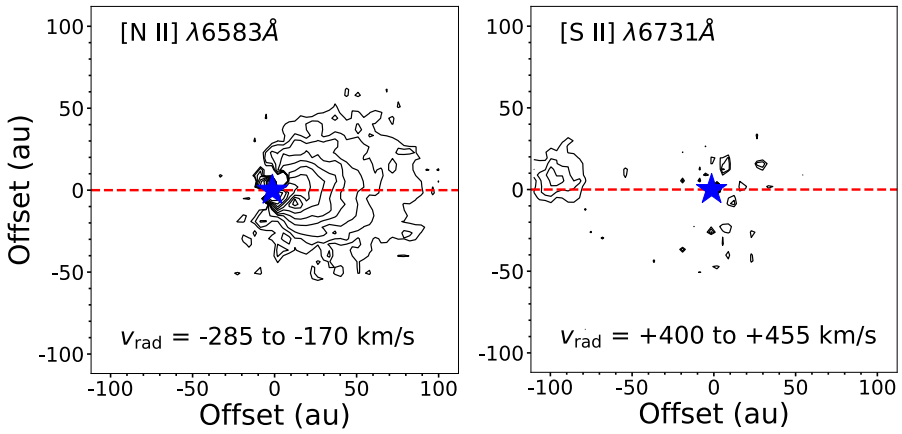


FIGURE 5.8: Channel maps of the jet in continuum subtracted [N II] 6583 Å emission and high-velocity redshifted emission in [S II] 6731 Å. The source position is marked with a blue star symbol. The velocity intervals of the channel maps are highlighted in the panels. The contour levels begin at $3\sigma$ of the background emission and increase by factors of 1.5.

jet emission in [N II] emission is presented in Figure 5.8, in the left panel, displaying a clear image of the jet without contamination from the other velocity components. The jet emission is integrated in the velocity region $v_{\rm rad} = -170$ km s$^{-1}$ to $-285$ km s$^{-1}$. A faint knot of high-velocity redshifted emission in the [S II] 6731 Å line is also seen, shown in the right panel of Figure 5.8. The redshifted emission is integrated in the velocity region $v_{\rm rad} = +400$ km s$^{-1}$ to $+455$ km s$^{-1}$. This redshifted knot has a higher velocity than the blueshifted jet emission has in the same emission line. This faint knot of emission is located at an offset from the central driving source where the 1.25 mm continuum dust disc would no longer block the redshifted counter-flow and therefore could be tracing emission from the redshifted outflow. The velocity of this emission points to a kinematical asymmetry between the blue and redshifted jet lobes.

In each outflow-tracing emission line, there existed faint line emission across the entire field of view. In continuum emission, faint emission was seen to fill the entire field also, with the intensity of this emission dropping as offset from the source increased. One expects to find faint continuum emission relatively close to the source as this emission represents the tail of the point spread function. However, in the case of the MUSE observation, continuum emission was present at extended offsets from the source position. This pointed to the presence of scattered light filling the field of view, potentially due to light from the central source scattering off the almost face-on accretion disc surrounding RU Lupi, or scattering off ambient material in the vicinity of the

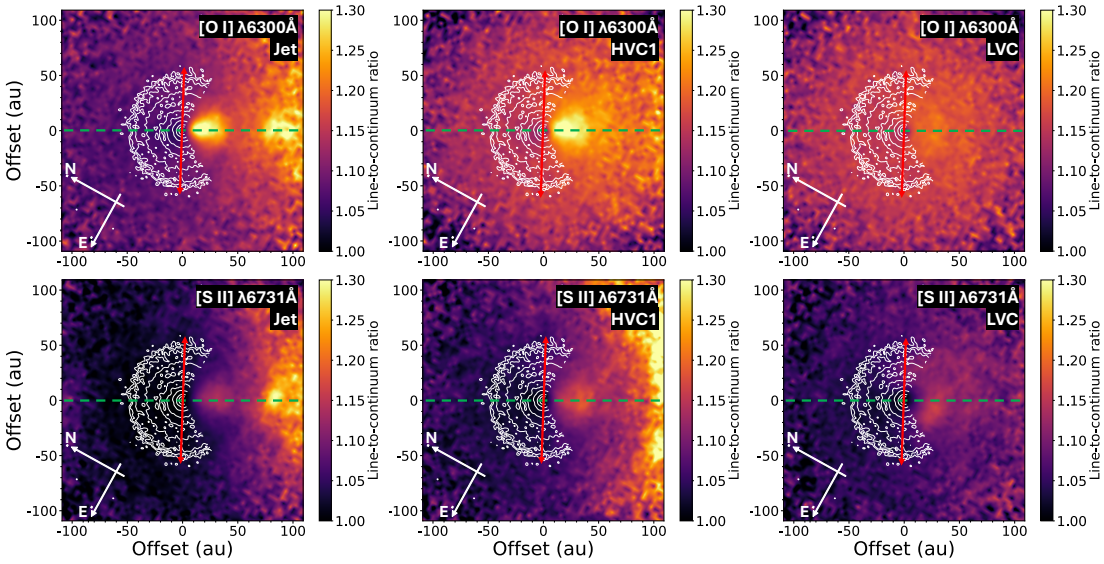


FIGURE 5.9: Line to continuum ratio maps of the jet, HVC1, and LVC in [O I] 6300 Å and [S II] 6731 Å emission. Intrinsic emission appears bright in these images, whereas scattered light is represented by a constant ratio close to unity. A sector of the ALMA 1.25 mm dust continuum disc is shown in white contours (Andrews et al., 2018). The red arrow delineates the disc PA and radius from Huang et al. (2018) ($121^\circ \pm 5^\circ$, $63 \pm 1$ au), and the dashed green line shows the jet PA measured here ($213^\circ \pm 2^\circ$).

outflow. To investigate the nature of the scattered emission, line to continuum ratio maps were produced. Line to continuum ratio plots are an effective tool for investigating the contribution of scattered emission to intrinsic line emission (Delabrosse et al., 2024; Birney et al., 2024a), and have been discussed in detail in Section 3.3.7 in relation to SINFONI observations. These figures display the result of calculating the ratio between an integrated line image, before continuum subtraction, and an integrated continuum image that is taken spectrally nearby to the line of interest. An assumption is made that the scattered emission is entirely light from the driving source of the outflow scattered off the disc and surrounding nebulous material. Therefore, the contribution from scattered light to the integrated line images will be represented by a constant ratio in these plots, as the scattered light follows the same spatial distribution as the continuum emission. In contrast, the real, intrinsic local emission will appear bright in these images, exceeding the constant ratio that represents the contribution from scattered light. Figure 5.9 displays the line to continuum ratio maps for the [O I] 6300 Å and [S II] 6731 Å emission channel maps shown in Figure 5.7. A sector of the ALMA 1.3 mm dust continuum disc image is shown in white contours (Andrews et al., 2018).

The intrinsic outflow emission, delineated by bright regions in the line to continuum ratio maps, showcases the morphologies of the outflow velocity components more clearly than in the channel maps. In the high-velocity channels in both emission lines, the jet emission, one sees the intrinsic collimated jet emission extending from the source position and culminating in a jet knot at an offset from the source of approximately 85 au. In the intermediate velocity channel (HVC1) one also sees the base of the outflow in intrinsic line emission, but comparatively less collimated than the jet emission. Also present in the jet and HVC1 line to continuum ratio maps is a wide, arc-like feature, located just beyond the jet knot at 85 au seen in the jet channels. This arc-like feature is not detected in the channel maps shown in Figure 5.7. Intrinsic emission in line to continuum ratio maps appears brighter as offset from the source increases, as the contribution from scattered light decreases with distance from the source. As this wide arc-like feature is not detected in the channel maps, it is likely that it is intrinsic, very low-intensity line emission that appears bright in these line to continuum maps, as the contribution from scattered light is very low in the region, resulting in an overly inflated line to continuum ratio. As the feature displays an arc-like morphology, it may indicate the location of the edge of the gas disc surrounding RU Lupi, where the inner edge of the arc-like feature is the outer edge of the gas disc. Small dust particles responsible for scattering at optical wavelengths follow the spatial distribution of the gas disc, that can extend two to three times further than dust disc as seen in millimetre continuum emission. As the contribution from scattered light is likely very low in the region where the arc-like feature is located, this indicates a rapid decrease in the density of scattering particles which would coincide with the gas disc edge. In the low-velocity channels (LVC) one sees intrinsic wide-angled outflow emission, that is comparatively dimmer than the jet emission and the HVC1 emission. The intrinsic LVC emission is also wider than both the jet and HVC1 emission. Also present in the HVC1 and LVC channels, in [O I] emission, is significant line emission across the entire FOV. This is attributed to residual scattered line emission from the outflow itself. Light originating from the outflow that is scattered off the disc and nebulous surrounding material does not follow the same spatial distribution as scattered light from the source. This results in the outflow emission illuminating surrounding ambient material. This scattered outflow light appears bright in these line to continuum ratio maps, just like the intrinsic jet emission because it does not follow the spatial distribution of the continuum emission. Figure 5.10 displays the

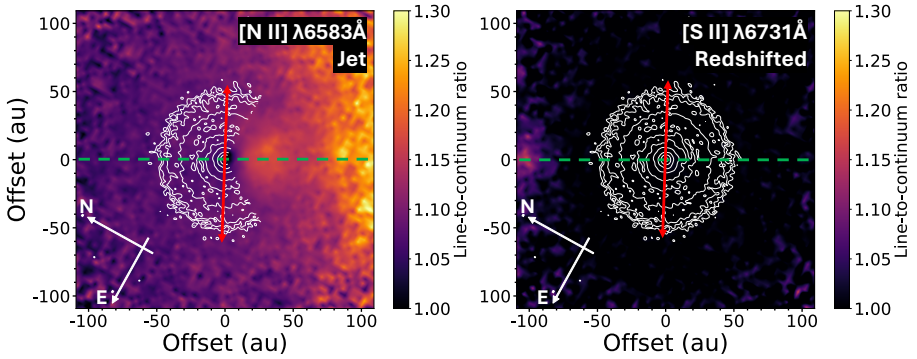


FIGURE 5.10: Line to continuum ratio maps of the jet in [N II] 6583 Å emission and high-velocity redshifted emission in [S II] 6731 Å. Intrinsic emission appears bright in these images, whereas scattered light is represented by a constant ratio close to unity. A sector of the ALMA 1.25 mm dust continuum disc is shown in white contours (Andrews et al., 2018). The red arrow delineates the disc PA and radius from Huang et al. (2018) (121° ± 5°, 63 ± 1 au), and the dashed green line shows the jet PA measured here (213° ± 2°).

line to continuum ratio maps of the jet in [N II] 6583 Å emission and the faint knot of high-velocity redshifted emission in [S II] 6731 Å. The morphology of the intrinsic jet emission traced by [N II] here is relatively wide and quite faint. In the high-velocity redshifted [S II] emission, labelled 'Redshifted' in Figure 5.10, one sees the intrinsic knot of line emission at an offset of approximately 100 au from the source position, in the opposite direction of the blueshifted outflow.

In order to gain a better picture of the morphological differences between the various outflow velocity components than that provided by the continuum subtracted channel maps, a Lucy-Richardson deconvolution was applied to the channel maps presented in Figures 5.7 and 5.8. A Lucy-Richardson deconvolution enhances the observation quality, achieving a sharper image by deconvolving the PSF from the true original observation. The observed image is a convolution of the true observation and the PSF. The deconvolution process attempts to recover the true observation by iteratively estimating the true observation based on the difference between the actual observation and the predicted true image based on the current estimate. The PSF of MUSE in narrow-field mode is best reproduced using a combination of two Moffat profiles making up the core of the PSF and the extended wings, or halo, of the PSF[2]. The PSF can also be well approximated by a combination of Gaussian

[2]See the MUSE user manual for more information about the PSF: MUSE user manual

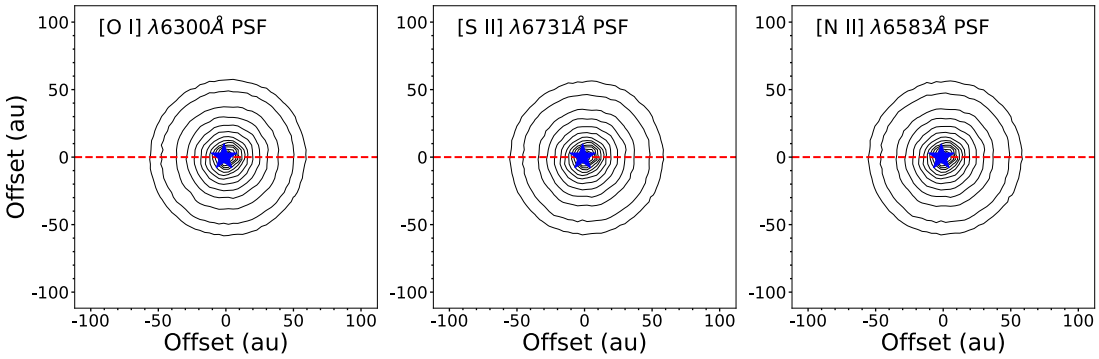


FIGURE 5.11: The PSFs used when deconvolving the [O I], [S II], and [N II] emission. The source position is marked with a blue star. The contour levels begin at $3\sigma$ of the background emission and increase by factors of 1.5.

components. The PSF is wavelength dependent, in that it gets broader with increasing wavelength. As the PSF is wavelength dependent, instead of modelling the PSF, the local continuum emission was chosen as the PSF. The PSFs used when deconvolving the [O I], [S II], and [N II] emission are displayed in Figure 5.11. These PSFs were extracted from continuum emission located spectrally nearby to the corresponding emission lines. The `lucy` package in IRAF was used to perform the deconvolution and the routine was allowed to run for twenty iterations to enhance the morphology of the outflow components without introducing any artefacting.

Figure 5.12 displays the channel maps of the jet, HVC1, and LVC in [O I] 6300 Å emission, before and after deconvolution. The post-deconvolution channel maps are shown in the bottom panels. The morphologies of the outflow velocity components are more apparent. In the jet emission channel map, a small-scale jet culminating in a shock feature at $\sim$ 85 au is seen. Both the HVC1 and LVC channel maps display emission that is both less extended and wider than the jet. This suggests a layering in the outflow, with faster moving material being more collimated than slower-moving material. Similarly, Figure 5.13 displays the channel maps of the jet, HVC1, and LVC in [S II] 6731 Å emission, before (top panels) and after (bottom panels) deconvolution. The small-scale jet culminating in a shock feature at $\sim$ 85 au is again seen in the highest velocity channel. Both the HVC1 and LVC channel maps also display emission that is both less extended and wider than the jet. The asymmetry across the inner region of the outflow with respect to the jet PA is also visible in these deconvolved channel maps, especially in the HVC1 channel map.

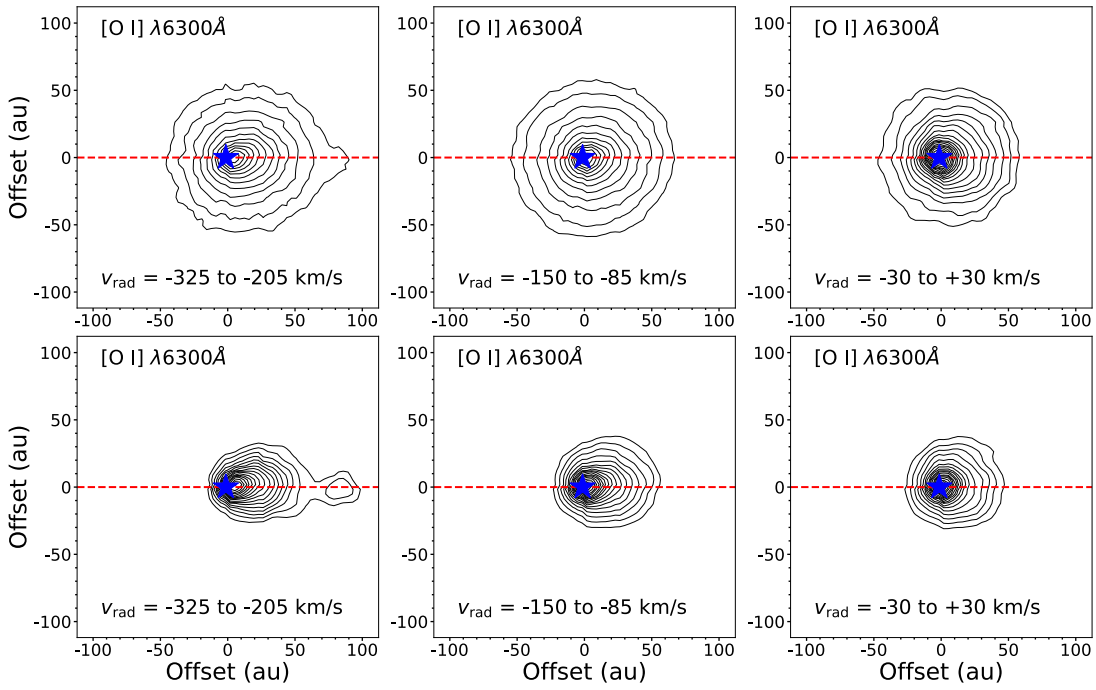


FIGURE 5.12: Channel maps of the jet, HVC1, and LVC in [O I] 6300 Å emission before (top panels) and after (bottom panels) the deconvolution routine is performed. The jet emission displays a shock feature at an offset of $\sim$ 85 au. The source position is marked with a blue star symbol. The velocity intervals of the channel maps are highlighted in the panels. The contour levels begin at $3\sigma$ of the background emission and increase by factors of 1.5.

Figure 5.14 displays the channel maps of the jet in [N II] 6583 Å emission and the high-velocity redshifted material in [S II] 6731 Å emission, again, before and after the deconvolution routine. The morphology of the jet in [N II] emission, shown in the left panel, is wide at the base, possessing a wide opening angle. The shock feature seen in [O I] and [S II] emission is also visible in the [N II] emission after the deconvolution routine. The faint redshifted emission along the jet PA, shown in the right panel, is still seen in [S II] emission post-deconvolution, at a higher velocity than in the blueshifted jet.

As a comparison to the 106.21EN.001 observations (PI: L. Pérez), which were selected to perform the analysis of the RU Lupi outflow, channel maps were prepared using the 0104.C-0919(B) observations (PI: A. Müller) also. This data was analysed in the same way as those just described in this chapter. Figures 5.15 and 5.16 display the channel maps of the jet, the HVC1 and the LVC generated using this data set in [O I] 6300 Å and [S II] 6731 Å emission respectively before and after the deconvolution routine. The deconvolved channel

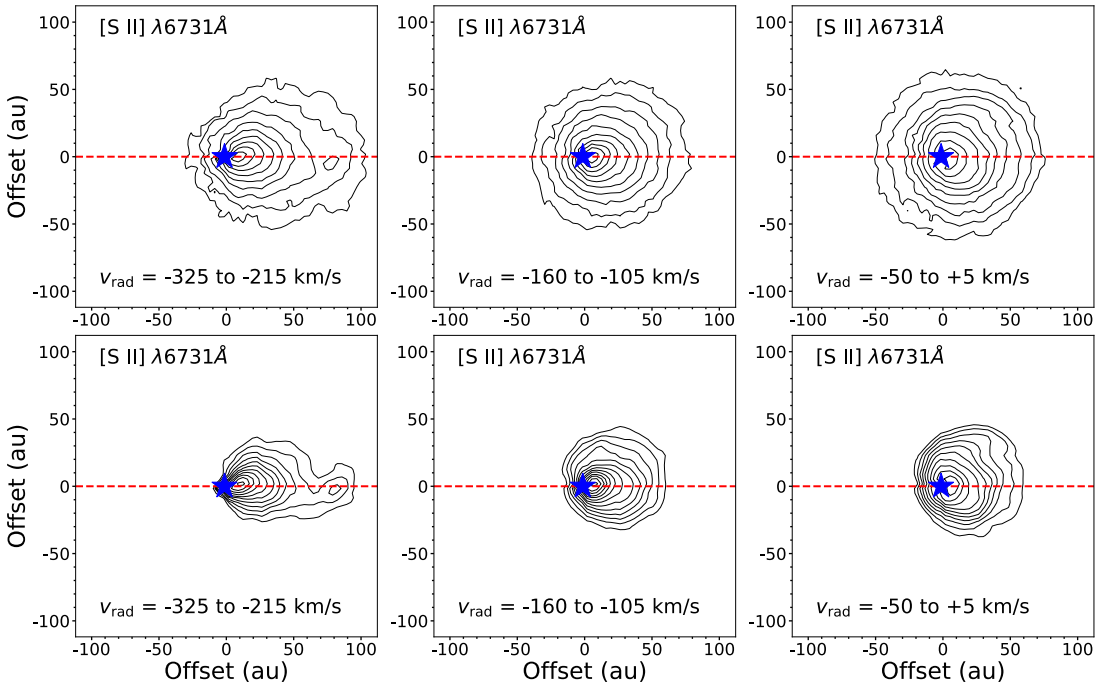


FIGURE 5.13: Channel maps of the jet, HVC1, and LVC in [S II] 6731 Å emission before (top panels) and after (bottom panels) the deconvolution routine is performed. The jet emission again displays a shock feature at an offset of $\sim$ 85 au. The source position is marked with a blue star symbol. The velocity intervals of the channel maps are highlighted in the panels. The contour levels begin at $3\sigma$ of the background emission and increase by factors of 1.5.

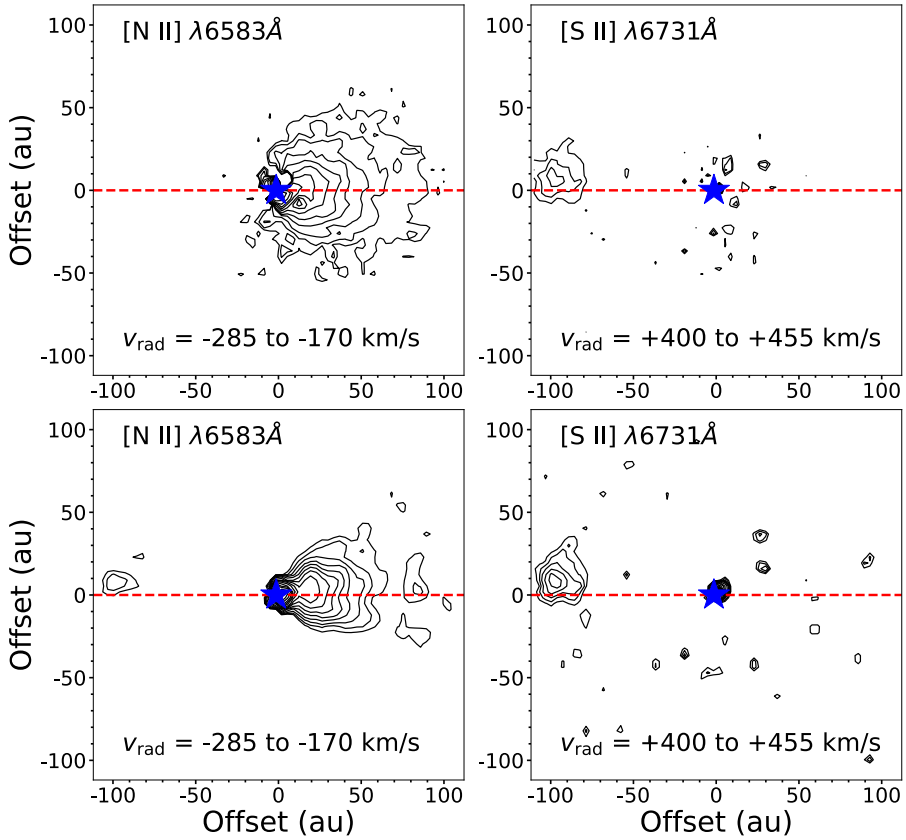


FIGURE 5.14: Channel maps of the jet in [N II] 6583 Å emission and high-velocity redshifted emission in [S II] 6731 Å before (top panels) and after (bottom panels) the deconvolution routine is performed. The jet in [N II] emission is wide at the base, and the shock feature at an offset of $\sim$ 85 au is visible post-deconvolution. The faint redshifted emission along the jet PA is seen in [S II] emission post-deconvolution at a higher velocity than in the blueshifted jet. The source position is marked with a blue star symbol. The velocity intervals of the channel maps are highlighted in the panels. The contour levels begin at $3\sigma$ of the background emission and increase by factors of 1.5.

maps are shown in the bottom panels. In the jet emission channels the shock feature is also apparent in both emission lines post-deconvolution, with the knot appearing tentatively in the [S II] emission before deconvolution. The morphologies of the HVC1 and LVC emission is less extended than the jet emission and not as collimated. In comparison to the 106.21EN.001 observations already presented in this chapter, these possess a reduced S/N. Additionally, this dataset is affected by a MUSE artefact known as a spike (See the MUSE user manual: Section 3.9.1 for more information on known MUSE artefacts)[3]. This artefact affected the morphology of the emission and is most evident in the LVC channels in both [O I] and [S II] emission. The morphology of the LVC in these channel maps displays a strong asymmetry of emission about the jet PA indicated by the dashed-red line. Although this artefact is most apparent in the LVC channel maps, it is present at all wavelengths and significantly affected the measurement of the outflow PA among other problems. Figure 5.17 displays the channel maps of the jet in [N II] 6583 Å emission and the high-velocity redshifted material in [S II] 6731 Å emission, before and after deconvolution. The morphology of the jet in [N II] emission before deconvolution, shown in the upper left panel, is again wide at the base, in agreement with the 106.21EN.001 observations. After the deconvolution routine is performed the jet displays a narrow jet that no longer showcases the wide opening angle. This is attributed to the low S/N in the emission line, where the deconvolution routine has suppressed faint but intrinsic jet emission. Both the channel map of the jet in [N II] emission shown in Figure 5.14 and the line to continuum ratio map of the jet in [N II] emission shown in Figure 5.10 present the jet morphology to be wide at the launching region of the jet, close to the driving source. The collimated jet emission seen in the deconvolved channel map in the lower left panel of Figure 5.17 is therefore misleading, as the true jet emission is not collimated to this degree. The faint high-velocity redshifted emission along the jet PA, shown in the right panels, in [S II] emission is also seen in in this data set. For the reasons discussed in this paragraph, the 106.21EN.001 observations, included in ESO's MUSE DEEP data collection, where the individual observations were aligned and combined to form a higher signal to noise ratio (S/N) observation, were selected for the analysis of RU Lupi.

[3]MUSE user manual

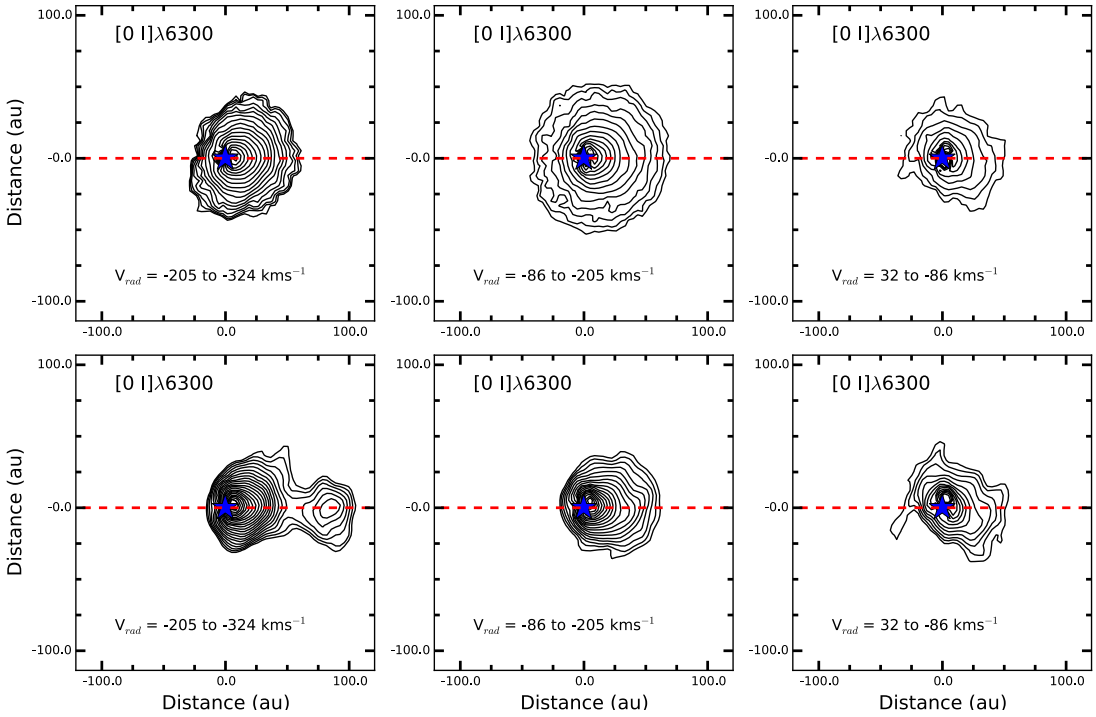


FIGURE 5.15: Channel maps prepared using the 0104.C-0919(B) observations of the jet, HVC1, and LVC in [O I] 6300 Å emission before (top panels) and after (bottom panels) the deconvolution routine is performed. The jet emission displays a shock feature at an offset of $\sim$ 85 au, only in the deconvolved image. The LVC is particularly affected by the MUSE artefact, displaying a strong asymmetry about the jet PA. The source position is marked with a blue star symbol. The velocity intervals of the channel maps are highlighted in the panels. The contour levels begin at $3\sigma$ of the background emission and increase by factors of 1.5.

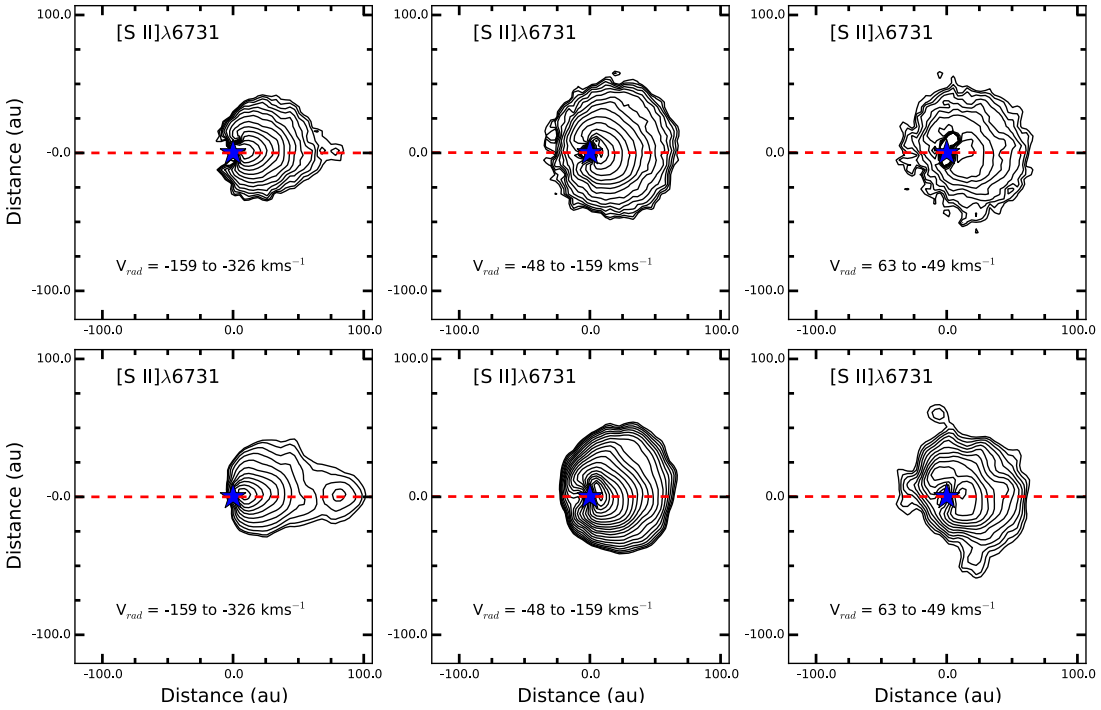


FIGURE 5.16: Channel maps prepared using the 0104.C-0919(B) observations of the jet, HVC1, and LVC in [S II] 6731 Å emission before (top panels) and after (bottom panels) the deconvolution routine is performed. The jet emission again displays a shock feature at and offset of $\sim$ 85 au, and is marginally resolved in the channel pre-deconvolution. The LVC is again strongly affected by the MUSE artefact. The source position is marked with a blue star symbol. The velocity intervals of the channel maps are highlighted in the panels. The contour levels begin at $3\sigma$ of the background emission and increase by factors of 1.5.

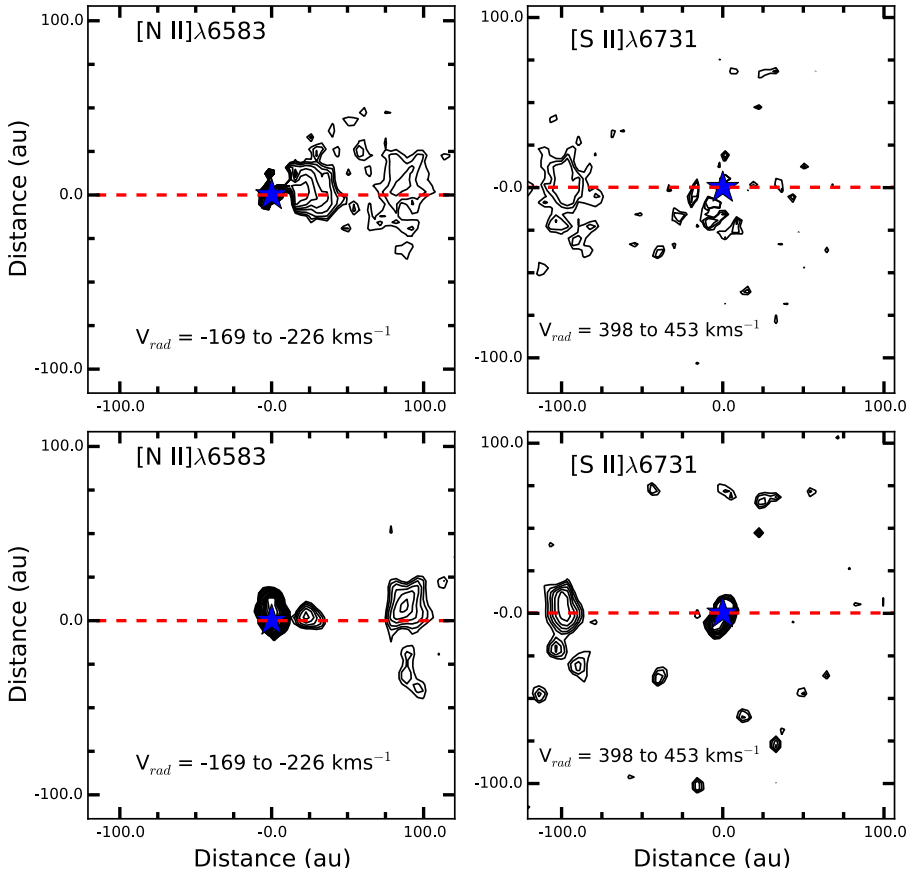


FIGURE 5.17: Channel maps prepared using the 0104.C-0919(B) observations of the jet in [N II] 6583 Å emission and high-velocity redshifted emission in [S II] 6731 Å before (top panels) and after (bottom panels) the deconvolution routine is performed. The jet in [N II] emission is wide at the base, only in the pre-deconvolved channel, and the shock feature at an offset of $\sim$ 85 au is visible in both. The wide morphology of the jet emission is not reproduced in the deconvolved channel due to the low S/N of the emission line. The faint redshifted emission along the jet PA is seen in [S II] emission is also present in this data set. The source position is marked with a blue star symbol. The velocity intervals of the channel maps are highlighted in the panels. The contour levels begin at $3\sigma$ of the background emission and increase by factors of 1.5.

### 5.2.2 Structure of the outflow components

In order to study the kinematical structure of the distinct outflow velocity components in greater detail, position velocity diagrams of the outflow were also prepared. As discussed in Section 4.2.2, PV diagrams can be extracted from IFU observations where a pseudo-slit is placed along the desired emission region. The spatial information within the slit is collapsed and represented by one axis of the diagram and the wavelength information is converted into a radial velocity using Doppler shift and represented on the other axis. Figure 5.18 displays position velocity diagrams extracted along the jet axis, with a PA of 213° and a narrow pseudo-slit width of $0\farcs075$. In the top panel, the position velocity diagram in [O I] 6300 Å emission is shown, and in the bottom panel the position velocity diagram in [S II] 6731 Å emission is shown. The dashed red line in these diagrams denotes the zero offset position, or the measured source position. Also present in these diagrams are the velocities of the outflow components (jet, HVC1 and LVC) as measured by Whelan et al. (2021), denoted by the dashed-lines. Black, green, and blue correspond to the measured velocities of the jet, HVC1, and LVC respectively, in [O I] 6300 Å and [S II] 6731 Å emission, from the higher spectral resolution observations in Whelan et al. (2021). These outflow component velocities ($v_{\rm component}$) are highlighted in the bottom right of both panels Figure 5.18. In both position velocity diagrams one sees the high-velocity jet emission extending furthest from the source position, to approximately 150 au in [O I] emission and 160 au in [S II] emission. The radial velocity of the jet emission in both emission lines peaks at $\sim -200$ km s$^{-1}$, as expected for a collimated atomic jet, and in accordance with previous spectroscopic measurements (e.g. Whelan et al., 2021). The jet emission is also seen to decrease in radial velocity as offset from the source increases, this is clear looking at the peaks of the contour lines. The peak radial velocity in the jet emission shifts to lower blueshifted velocities at offsets of approximately $>$ 100 au, implying that the fastest jet emission originates in the base of the jet, within the inner 100 au of the outflow. The LVC in both diagrams does not extend to the same offset form the driving source as the jet emission, being more compact. This clearly highlights that the jet is a separate outflow component from the LVC. Interestingly in these diagrams, there exists significant high and low-velocity emission at negative offsets from the source position. In other words, blueshifted emission originating from the side of the driving source opposite to where the outflow is emanating from. Also present in the position

velocity diagrams, and to a greater extent in the [O I] emission, is redshifted emission at both positive and negative offsets from the central star.

Figure 5.19 displays position velocity diagrams, again extracted along the jet axis, with a PA of 213° and a narrow pseudo-slit width of 0.″075. In the top panel, the position velocity diagram in [N II] 6583 Å emission is shown, and in the bottom panel the position velocity diagram in [Fe II] 7155 Å emission is shown. Channel maps were not produced using the [Fe II] 7155 Å emission line as the jet emission was not well resolved, as evidenced in the right panel of Figure 5.4, and the HVC1 and LVC emission was not significantly extended beyond continuum emission. However, the position velocity diagram in [Fe II] emission shows useful information. The dashed red line in these diagrams denotes the zero offset position and the velocities of the outflow components (jet, HVC1 and LVC) as measured by Whelan et al. (2021) are denoted by the dashed-lines. Only the measured velocity of the jet in [S II] emission by Whelan et al. (2021) is shown in the top panel, as the [N II] emission only possesses a HVC. The bottom panel has the measured velocities of the jet, HVC1 and LVC in [S II] emission by Whelan et al. (2021) overplotted. In [N II] emission, the high-velocity jet is clear, extending to $\sim$ 140 au, and again decreasing in velocity as offset from the driving source increases, at approximately $>$ 100 au. The radial velocity of the jet is centred at $\sim -200$ km s$^{-1}$. There also exists faint high-velocity blueshifted emission at negative offset from the source position centred around $-$ 100 au. In the [Fe II] emission, one sees the high-velocity jet, again extending far from the source and peaking at $\sim$ 200 km s$^{-1}$. The jet emission in this line possesses a large wing, with emission extending to almost $-$ 400 km s$^{-1}$, not conclusively seen in [O I], [S II], or [N II] emission. The LVC does not extend as far from the source as the jet. Also present in the [Fe II] emission is significant high and low-velocity emission at negative offsets from the source position.

Position velocity diagrams were also extracted transverse to the outflow direction. This was achieved by rotating the pseudo-slit, previously positioned along the jet PA, by 90° resulting in a slit PA of 303°. 0.″05 was selected as the pseudo-slit width. These transverse position velocity diagrams were extracted at various heights along the outflow, namely at 0 au, 10 au, 50 au, and 80 au from the source position, or 0 au, 29 au, 145 au, and 232 au if one deprojects the outflow into the plane of the sky. Figure 5.20 displays the position velocity diagrams, in [O I] 6300 Å emission, in the top panels, and in [S II] 6731 Å

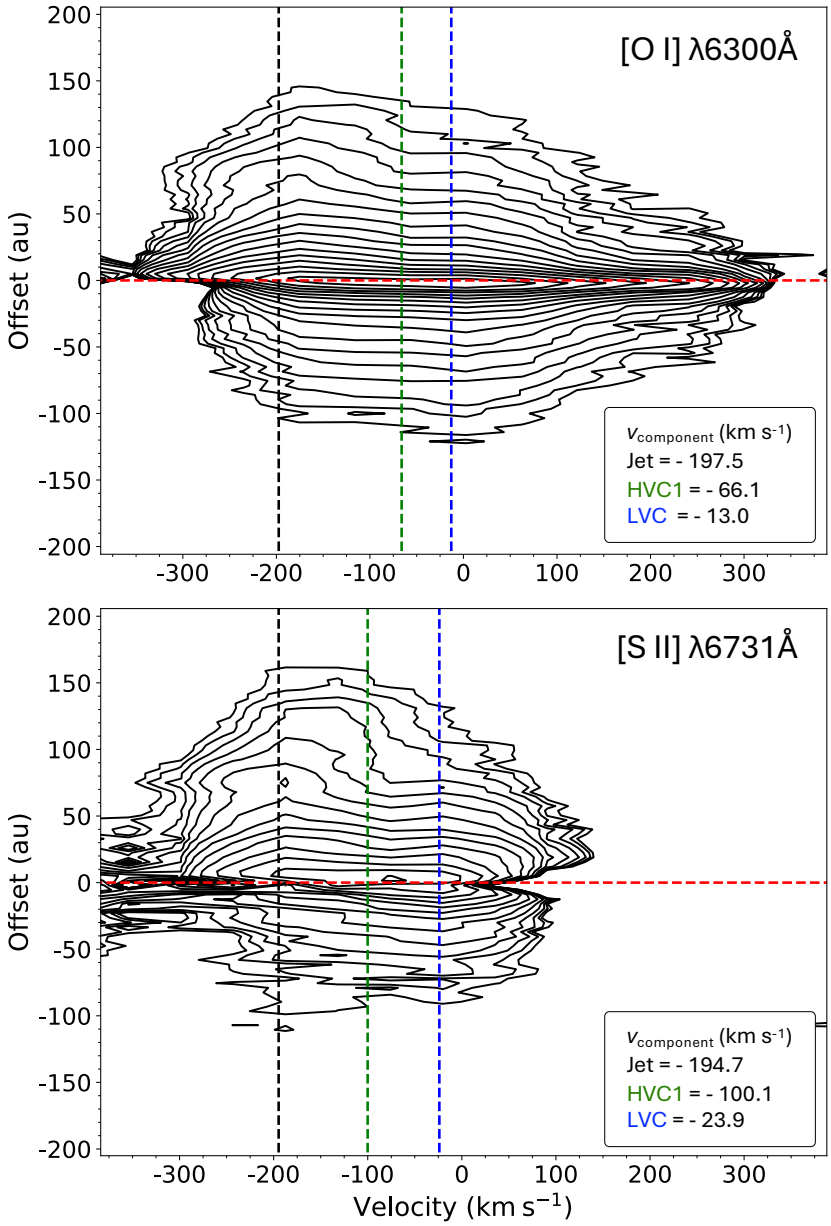


FIGURE 5.18: Position velocity diagrams of [O I] 6300 Å and [S II] 6731 Å emission. The PV diagram is extracted along the measured jet axis (PA = 213°) using a narrow pseudo-slit width of 0.″075. The velocities of the jet, HVC1 and LVC as measured by Whelan et al. (2021) are marked by the dashed lines. The LVC appears as a clear second component distinct from the jet, extending to a lesser offset. The radial velocity of the jet emission traced in these emission lines peaks at approximately $-200$ km s$^{-1}$, in agreement with previous observations. The contour levels begin at $3\sigma$ of the background emission and increase by factors of 1.5.

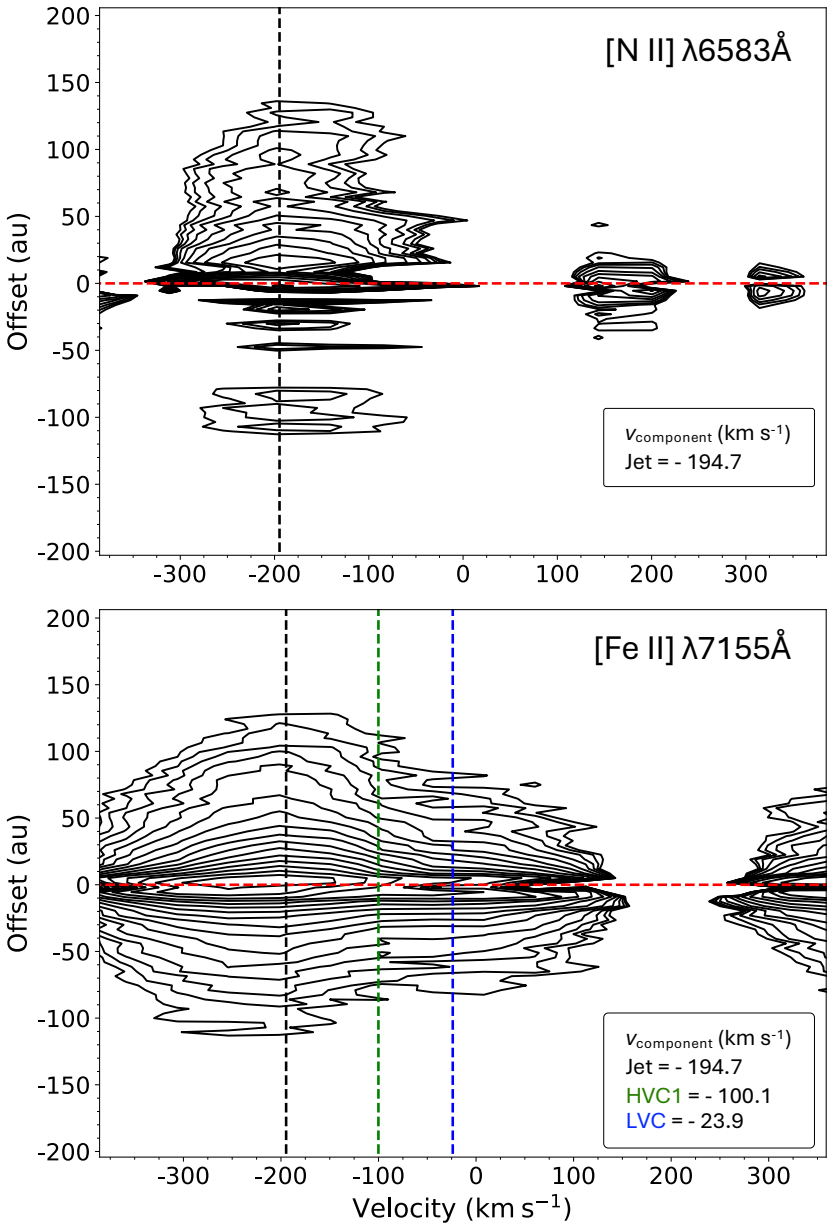


FIGURE 5.19: Position velocity diagrams of [N II] 6583 Å and [Fe II] 7155 Å emission. The PV diagram is extracted along the measured jet axis (PA = 213°) using a narrow pseudo-slit width of 0.″075. The velocities of the jet, HVC1 and LVC as measured by Whelan et al. (2021) are marked by the dashed lines, with only the jet velocity overplotted in the top panel. The radial velocity of the jet emission traced in these emission lines peaks at approximately $-$ 200 km s$^{-1}$. The contour levels begin at 3$\sigma$ of the background emission and increase by factors of 1.5.

emission in the bottom panels, extracted transverse to the outflow at various distances along the outflow axis. Again, the measured velocities of the outflow components from Whelan et al. (2021) are denoted by the dashed lines. These outflow component velocities ($v_{\text{component}}$) are highlighted in the rightmost panels in Figure 5.20. One sees emission at both positive and negative offsets from the source position in every panel, as expected for an axisymmetric outflow. In the position velocity diagrams extracted transverse to the outflow at the source position, and at those extracted at 10 au along the outflow, one sees the presence of two velocity components in both emission lines. The high-velocity jet and an LVC is seen. However, it is seen that as the distance along the outflow axis increases, the LVC begins to fade, appearing to possess significantly lower flux than the jet emission at the same distance. This is clear in the position velocity diagrams extracted transverse to the outflow at distances along the outflow of 50 au and 80 au. The jet emission remains strong, whilst the LVC fades. This evidences that the LVC is a separate outflow component to the jet, as the jet extends much further from the source position than the LVC does. Also present in the position velocity diagrams, and to a greater degree in the [O I] emission, is a significant proportion of redshifted emission. To further illustrate that the LVC was a distinct outflow component from the jet emission, line profiles were extracted along the 0 au offset position, indicated by the horizontal dashed-red lines in Figure 5.20. These line profiles are extracted from the [O I] and [S II] emission line regions at distances of 0 au, 10 au, 50 au, and 80 au from the source position, and are presented in Figure 5.21. In these line profiles, there are two distinct velocity components; the high-velocity jet and the lower intensity LVC. The LVC is seen to decrease in intensity relative to the jet intensity as distance from the source increases, in accordance with that seen in Figure 5.20. The jet emission and LVC emission are not resolved from one another at the source position (0 au) in the [S II] line. This is likely an effect of the emission lines critical density. The [O I] emission line at 6300 Å possesses a higher critical density than the [S II] emission line at 6731 Å. This means that [O I] emission can trace denser and more compact material (See Section 1.3.2). As the [S II] line is not a good tracer of dense material, one only begins to see the LVC as the density decreases further from the driving source. Furthermore, Whelan et al. (2021) report no [S II] emission in the LVC within 2 au of the source.

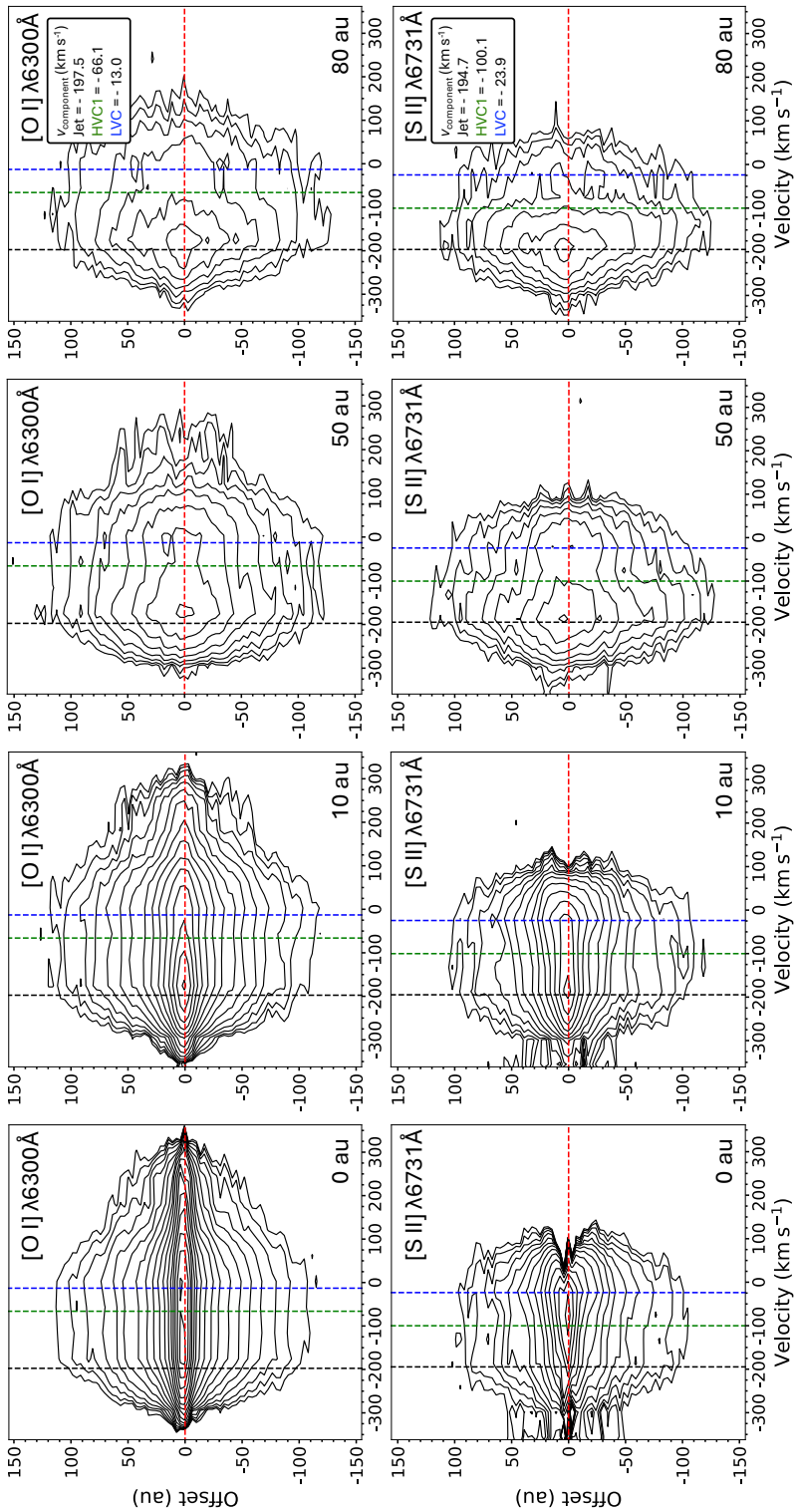


FIGURE 5.20: Position Velocity diagrams made transverse to the outflow axis for the [O I] 6300 Å and [S II] 6731 Å emission line regions. Pseudo-slits, of width 0.″05, were placed at the source position and at distances of 10 au, 50 au and 80 au from the star. Distances are not deprojected and these positions correspond to 29 au, 145 au and 232 au when corrected for the inclination of the system. The velocities of the jet, HVC1 and LVC as measured by Whelan et al. (2021) are marked by the dashed lines. The LVC appears as a clear second component distinct from the jet. The intensity of the LVC decreases with distance from the source, whereas the jet emission remains strong. The contour levels begin at $3\sigma$ of the background emission and increase by factors of 1.5.

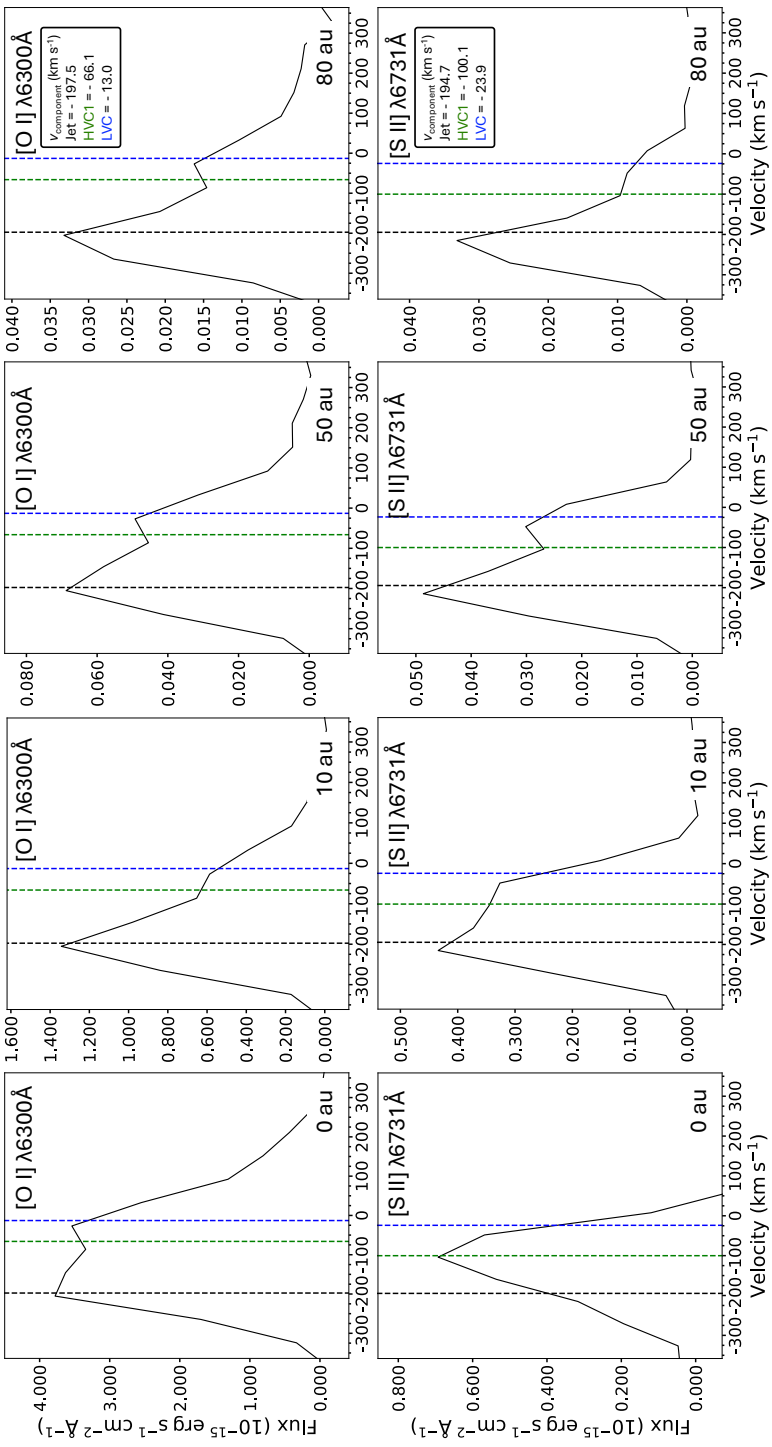


FIGURE 5.21: Line profiles extracted along the 0 au offset position (dashed-red lines) from the position velocity diagrams made transverse to the outflow axis, shown in Figure 5.20, for the [O I] 6300 Å and [S II] 6731 Å emission line regions. These PV slices were extracted at the source position, and at distances of 10 au, 50 au and 80 au from the star. Distances are not deprojected and these positions correspond to 29 au, 145 au and 232 au when corrected for the inclination of the system. The velocities of the jet, HVC1 and LVC as measured by Whelan et al. (2021) are marked by the dashed lines. The line flux decreases as the offset from the central source increases. The LVC appears as a clear secondary component distinct from the jet and is seen to decrease in intensity relative to the jet intensity as distance from the source increases.

Figure 5.22 displays the position velocity diagrams, in [N II] 6583 Å emission, in the top panels, and in [Fe II] 7155 Å emission in the bottom panels, extracted transverse to the outflow at various distances along the outflow axis. The pseudo-slit width and PA were 0.″05 and 303° respectively. Again, the measured velocities of the outflow components from Whelan et al. (2021) are denoted by the dashed lines. These outflow component velocities ($v_{\text{component}}$) are highlighted in the rightmost panels in Figure 5.19. One again sees emission at both positive and negative offsets from the source position in every panel, as expected for an axisymmetric outflow. In [Fe II] emission, in the position velocity diagram extracted transverse to the outflow at the source position, and at that extracted at 10 au along the outflow, one sees the presence of two velocity components; the high-velocity jet and LVC. Again, it is seen that as the distance along the outflow axis increases, the LVC begins to fade, whereas the jet emission remains strong. This is clear in the position velocity diagrams extracted transverse to the outflow at distances along the outflow of 50 au and 80 au, evidencing that the LVC is a separate outflow component to the jet. In [N II] emission, one only sees jet emission as discussed in Section 5.2.1, and the jet emission region tentatively appears to grow wider as distance from the source increases. To further investigate the differences between the outflow components, line profiles were again extracted along the 0 au offset position, indicated by the horizontal dashed-red lines in Figure 5.19. These line profiles are extracted from the [N II] and [Fe II] emission line regions at distances of 0 au, 10 au, 50 au, and 80 au from the source position, and are presented in Figure 5.23. The line profiles suggest that the jet emission, in these emission lines, peaks at a slightly higher radial velocity than the peak radial velocity of [S II] emission as measured by Whelan et al. (2010). In [Fe II] emission in the bottom panels, one sees the jet emission and the LVC. The LVC in this emission line appears weak with respect to the jet emission, when compared with the strength of the LVC with respect to the jet emission in both [O I] and [S II] emission.

To better understand the structure of the outflow components the spatial widths of the outflow components in [O I] 6300 Å, [S II] 6731 Å, and [N II] 6583 Å emission were mapped with distance from the source (e.g. Murphy et al., 2021; Kirwan et al., 2022). This was achieved by extracting spatial profiles from the pre-deconvolution channel maps of the jet, HVC1, and LVC components presented in Figures 5.7 and 5.8. These spatial components were extracted transverse to the outflow axis at various distances along the outflow.

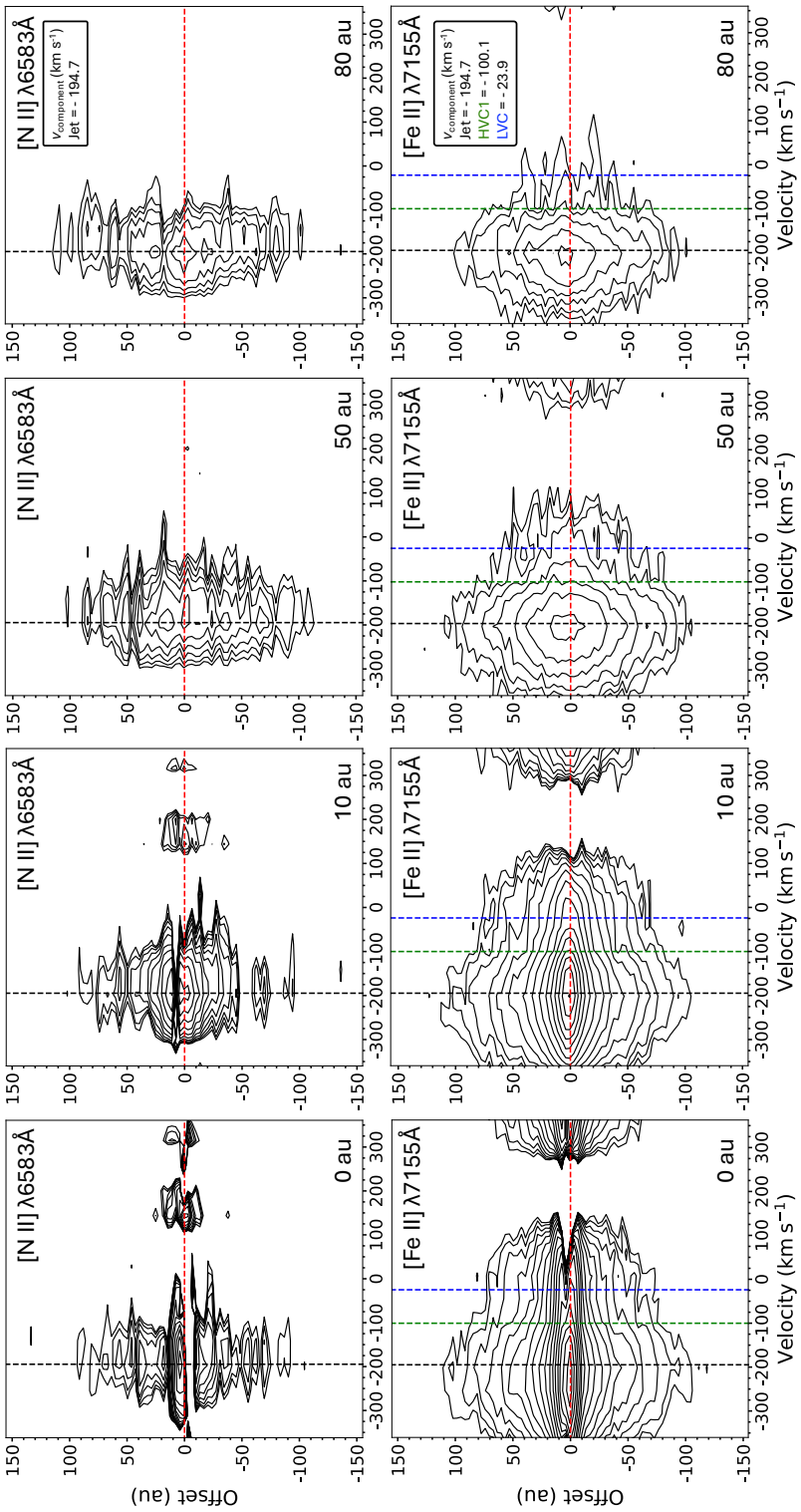


FIGURE 5.22: Position velocity diagrams made transverse to the outflow axis for the [N II] 6583 Å and [Fe II] 7155 Å emission line regions. Pseudo-slits, of width 0″.05, were placed at the source position and at distances of 10 au, 50 au and 80 au from the star. Distances are not deprojected and these positions correspond to 29 au, 145 au and 232 au when corrected for the inclination of the system. The velocities of the jet, HVC1 and LVC as measured by Whelan et al. (2021) are marked by the dashed lines. The LVC in [Fe II] emission decreases in intensity as distance from the source increases. In [N II] emission, the jet emission region tentatively appears to grow wider as distance from the source increases. The contour levels begin at $3\sigma$ of the background emission and increase by factors of 1.5.

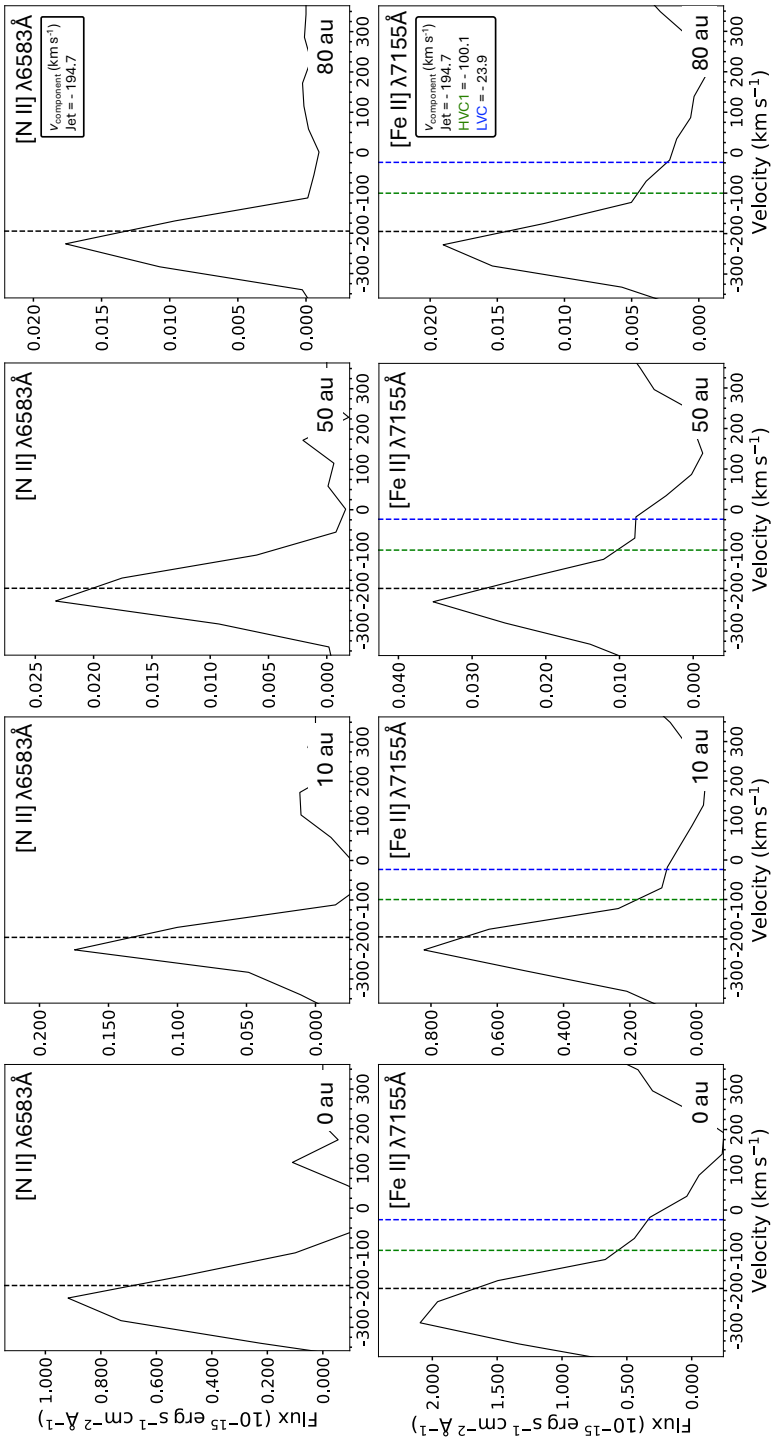


FIGURE 5.23: Line profiles extracted along the 0 au offset position (dashed-red lines) from the position velocity diagrams made transverse to the outflow axis, shown in Figure 5.23, for the [N II] 6583 Å and [Fe II] 7155 Å emission line regions. These PV slices were extracted at the source position, and at distances of 10 au, 50 au and 80 au from the star. Distances are not deprojected and these positions correspond to 29 au, 145 au and 232 au when corrected for the inclination of the system. The velocities of the jet, HVC1 and LVC as measured by Whelan et al. (2021) are marked by the dashed lines. The line flux decreases as the offset from the central source increases. The line profiles suggest that the jet emission, in both emission lines, peaks at a slightly higher radial velocity than the peak radial velocity of [S II] emission as measured by Whelan et al. (2010).

These spatial components were fit with Gaussian profiles, and the centroids, FWHMs, and fluxes associated with the fitted profiles were recorded. Beyond approximately 50 au from the source position, the spatial profiles were not well fit by Gaussian profiles. In order to retrieve the intrinsic width of the outflow components, the angular resolution of the observation was subtracted in quadrature from the measured FWHMs, and measurements below the FWHM of the source PSF were excluded. Figure 5.24 displays the outflow component widths, or FWHMs, for the jet, HVC1, and LVC, in [O I] 6300 Å emission in the top panel, and in [S II] 6300 Å and [N II] 6583 Å emission in the bottom panel. The jet width measurements are represented by the black data points, the HVC1 by the green data points, and the LVC by the blue data points. This is to remain consistent with colour scheme used in the position velocity diagrams shown previously. The jet width as measured from the [N II] emission is represented by the orange data points, and is overplotted with the outflow width measurements in [S II] emission. The error bars on the FWHM data points are the uncertainty of the FWHM in the Gaussian fitting routine, which appear small here due to the high S/N of the transverse spatial profiles. The distances from the source position, or distance along the outflow axis, were deprojected into the plane of the sky, assuming that the outflow is launched perpendicularly to the disc. The data points were subsequently fit with linear profiles which allowed the estimation of the full opening angles associated with the outflow components and also an estimation of the launching radius from the disc.

In Figure 5.24, it is clear that in [O I], [S II], and [N II] emission, the jet is most collimated, possessing the narrowest width of all the outflow components. The HVC1 component is wider than the jet, and the LVC is the widest outflow component in both emission lines. The linear fits to the FWHM measurements were used to estimate the opening angle associated with the outflow components. The full opening angle of the outflow is a measure of the degree of collimation of the flow, with the jet expected to be most collimated. For the jet, the angle between the linear fit to the FWHM measurements and the y-intercept of the fit is used as a lower limit of the full opening angle. The upper limit is estimated as being the angle between the linear fit through the origin. The opening angle of the HVC1 outflow component is estimated in the same way. As the width of the LVC is larger than both the jet and HVC1, especially in the case of [S II] emission, the angle between the linear fit to the LVC

TABLE 5.3: Launch radii ($r_{max}$) and full opening angles ($\theta$) of the jet, HVC1, and LVC in [O I] 6300 Å, [S II] 6731 Å, and [N II] 6583 Å emission, derived from the measured outflow component widths presented in Figure 5.24.

| | Line | $r_{max}$ (au) | $\theta$ (°) |
|---|---|---|---|
| Jet | [O I] 6300 Å | $< 1.0$ | 24.8 – 26.1 |
| | [S II] 6731 Å | $< 3.7$ | 21.0 – 26.8 |
| | [N II] 6583 Å | $< 1.2$ | 26.7 – 28.4 |
| HVC1 | [O I] 6300 Å | $< 1.5$ | 31.8 – 33.9 |
| | [S II] 6731 Å | $< 4.4$ | 25.2 – 31.6 |
| LVC | [O I] 6300 Å | $< 2.0$ | 36.9 – 38.4 |
| | [S II] 6731 Å | $< 9.0$ | 19.9 – 33.2 |

FWHM measurements and the y-intercept likely underestimates the opening angle, therefore this angle is used as a lower limit. The angle between the linear fit to the FWHM measurements through the y-intercept of the jet emission is used as a reasonable upper limit of the LVC opening angle. These full opening angle ($\theta$) estimations are shown in Table 5.3. The radial distance along the disc from which the outflow components are launched from, or the footpoint of flows, was also estimated. To retrieve these launching radii, the y-intercepts of the linear fits to the FWHM measurements were used. As the outflow component width plots shown in Figure 5.24 display the full width of the outflow components, it was necessary to half the lower bounds of the FWHM measurements, or the y-intercepts, to estimate the disc radius from which the flows were launched from. This provided upper limits of the launching radii ($r_{max}$), and these measurements are presented in Table 5.3. It is clear that the jet is launched from the inner disc region, the slower-moving HVC1 outflow component is launched at larger disc radii, and the LVC is launched at the largest disc radii. The opening angles of the flows also get progressively larger as the outflow component velocity decreases, the highest velocity material is the most collimated.

To further probe the structure of the outflow components, the flux measurements associated with the Gaussian fits to the spatial profiles extracted transverse to the outflow axis were plotted with distance from the source position. The flux values were normalised to compare how the flux along the outflow varied between the components. Figure 5.25 displays these normalised flux measurements along the outflow axis in [O I] 6300 Å, [S II] 6731 Å, and [N II]

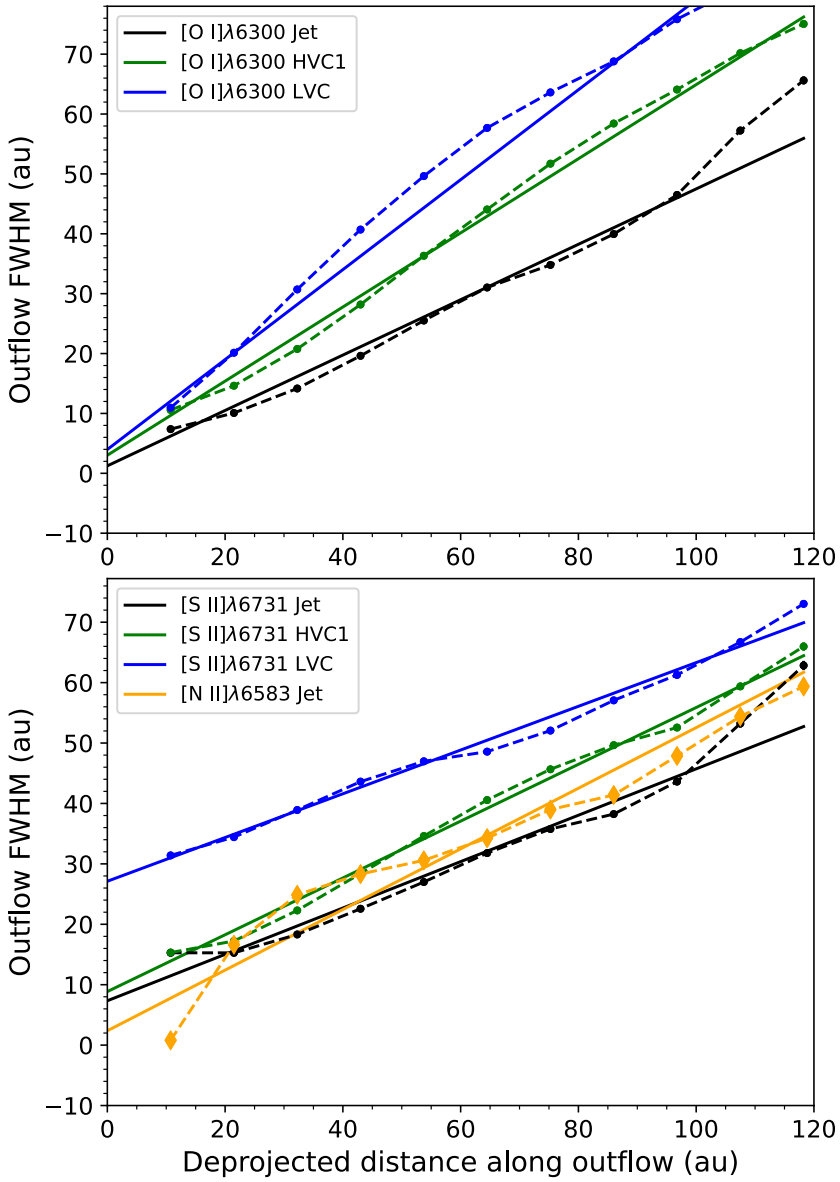


FIGURE 5.24: Full width at half maximum (FWHM) measurements along the outflow axis of the jet, HVC1, and LVC, in [O I] 6300 Å emission in the top panel, and in [S II] 6300 Å and [N II] 6583 Å emission in the bottom panel. The error bars on the FWHM data points are the uncertainty of the FWHM in the Gaussian fitting routine which appear small here due to the high S/N of the transverse spatial profiles. The distance along the outflow axis is deprojected into the plane of the sky. The jet emission is most collimated. The HVC1 component is wider than the jet, and the LVC is the widest outflow component in both emission lines.

6583 Å emission. All outflow components here tend to decrease in flux as distance from the driving source increases. In both the [O I] and [S II] emission lines, the jet emission appears to follow a different spatial distribution when compared to the HVC1 and LVC. The HVC1 and LVC tend to decrease in flux near the immediate vicinity of the source position, and continue to decrease in flux along the outflow axis. In contrast the jet emission displays a peak in brightness at $\sim$ 25 au in [O I] emission and at $\sim$ 45 au in [S II] and [N II] emission. In other words there is a spatial offset between the peak brightness in the HVC1 and LVC, and the jet.

The centroids of the Gaussian fits to the spatial profiles extracted transverse to the outflow axis were also plotted with distance from the source position. These outflow centroid measurements along the outflow axis of the jet, HVC1, and LVC in [O I] 6300 Å and [S II] 6731 Å emission, and the jet in [N II] 6583 Å emission are presented in Figure 5.26. The centroids of the Gaussian fits to the transverse spatial profiles are indicative of the outflow axis position. The error bars on these data points are the difference in centroid position as measured in the pre-deconvolved channel maps and the deconvolved channel maps. Centroid measurements of the LVC narrow component (NC), in [O I] 6300 Å and [S II] 6731 Å emission, as measured from the spectro-astrometric study presented in Whelan et al. (2021) are also over-plotted in magenta. The centroid measurements do not reveal any significant deviations from the position of the outflow axis, neither do they display any prominent periodic outflow wiggling, which is indicative of an orbital companion (Murphy et al., 2021).

### 5.2.3 Outflow efficiency

The outflow efficiency ($\eta_{\rm out}$) is defined as the ratio of the mass outflow rate ($\dot{M}_{\rm out}$) to the mass accretion rate ($\dot{M}_{\rm acc}$), as shown in Equation 5.1, and is an important parameter for constraining outflow launching models. An outflow efficiency close to unity, or 100%, implies that the mass outflow rate approximately equals the mass accretion rate. This condition is required in order to agree with current disc wind models (Gressel and Pessah, 2015; Béthune, Lesur, and Ferreira, 2017; Bai, 2017).

$$\eta_{\rm out} = \frac{\dot{M}_{\rm out}}{\dot{M}_{\rm acc}} \tag{5.1}$$

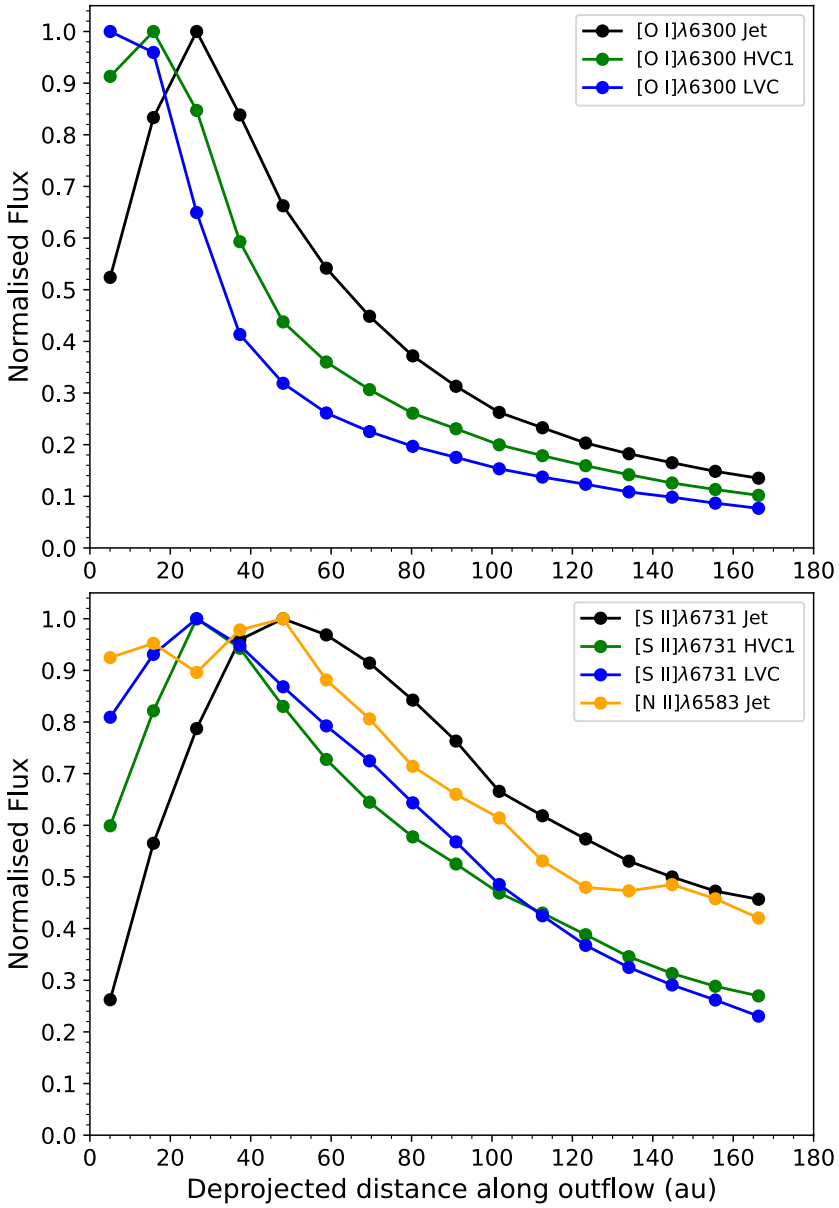


FIGURE 5.25: Normalised flux measurements along the outflow axis of the spatial profiles extracted transverse to the outflow in [O I] 6300 Å, [S II] 6731 Å, and [N II] 6583 Å emission. The distance along the outflow axis is deprojected into the plane of the sky. All outflow components decrease in flux as distance from the driving source increases. The jet emission follows a different spatial distribution when compared to the HVC1 and LVC.

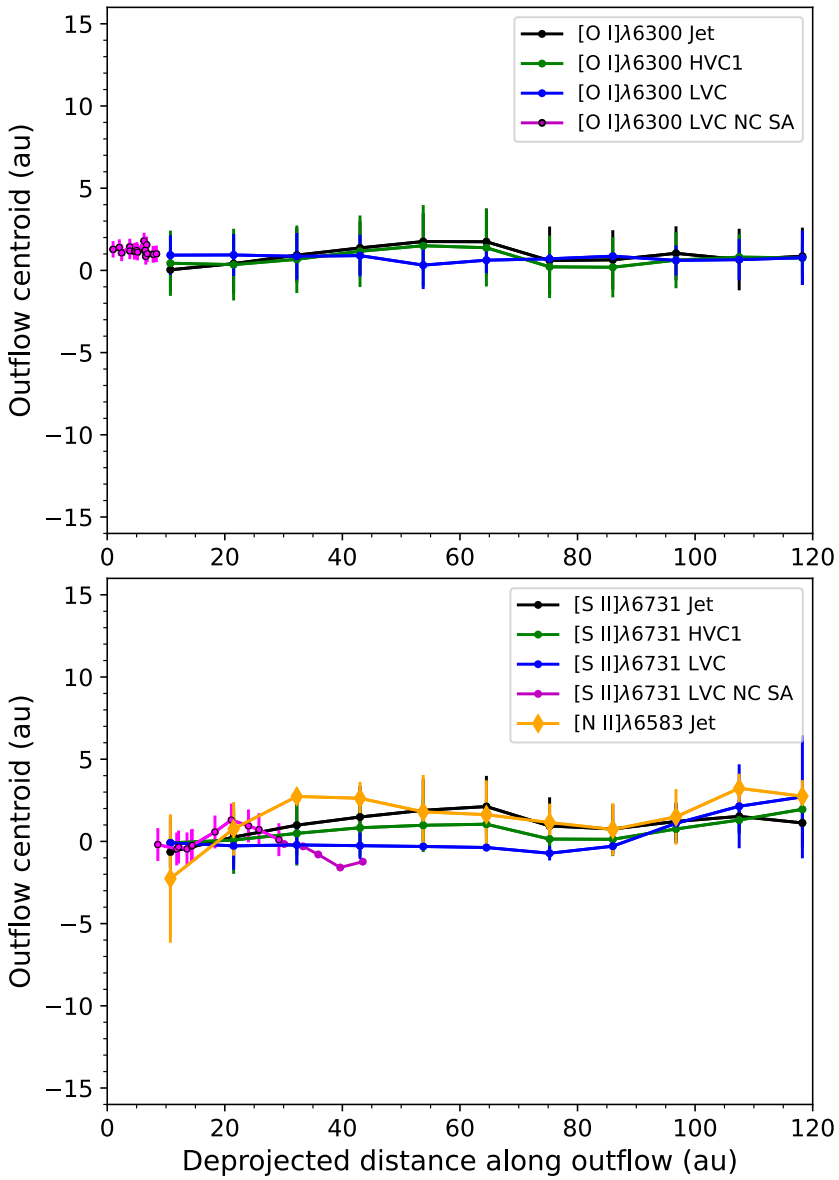


FIGURE 5.26: Outflow centroid measurements along the outflow axis of the jet, HVC1, and LVC in [O I] 6300 Å, [S II] 6731 Å, and [N II] 6583 Å emission. The error bars are the difference in centroid position as measured in the pre-deconvolved channel maps and the deconvolved channel maps. Centroid measurements of the LVC narrow component (NC), in [O I] 6300 Å, [S II] 6731 Å emission, as measured from the spectro-astrometric (SA) study presented in Whelan et al. (2021) are over-plotted in magenta. The centroid measurements do not reveal any significant deviations from the position of the outflow axis.

To estimate the mass accretion rates, the method outlined in Alcalá et al. (2017) was followed. Magnetospheric accretion refers to material at the inner edge of the accretion disc being funnelled along magnetic field lines and impacting the stellar surface producing strong shocks, thus generating emission lines and excess that span from ultraviolet to optical wavelengths. The method outlined in Alcalá et al. (2017) estimates mass accretion rates by converting the luminosity of these select emission lines into accretion luminosities, the release of accretion energy, using empirical relationships established between the emission line luminosities and the accretion luminosity. Emission lines within the MUSE spectral range whose luminosities were known to correlate well with accretion luminosities were selected. Hydrogen recombination line luminosities such as those in the Balmer and Paschen series are known to correlate well with the accretion luminosity (e.g. Muzerolle, Calvet, and Hartmann, 1998; Muzerolle et al., 2003; Natta et al., 2004; Muzerolle et al., 2005; Herczeg and Hillenbrand, 2008; Fang et al., 2009). The Ca II triplet ($\lambda$8498 Å, $\lambda$8542 Å, and $\lambda$8662 Å) emission lines are commonly attributed to accretion shocks close to the stellar surface (e.g. Batalha et al., 1996; Muzerolle, Calvet, and Hartmann, 1998; Rigliaco et al., 2012). Helium and oxygen emission lines are also associated with accretion activity (e.g. Fang et al., 2009; Rigliaco et al., 2012; Alcalá et al., 2014; Alcalá et al., 2017).

$$F_{\text{line}} = A\sigma\sqrt{2} \tag{5.2}$$

$$L_{\text{line}} = F_{\text{line}} \times 4\pi D^2 \tag{5.3}$$

To retrieve the luminosities of these emission lines the relation shown in Equation 5.3 was used. Here, $F_{\text{line}}$ is the integrated flux of the emission line and $D$ is the distance to RU Lupi, which is taken to be 140 pc. The flux of the emission lines was estimated using Equation 5.2, by calculating the integrated flux of the Gaussian profile fit to the emission line profiles, where $A$ is the amplitude and $\sigma$ is the standard deviation of the fit. In order to calculate the flux of the accretion-tracing emission lines, a spectrum from the source position needed to be extracted. Generally, the spectral extraction aperture size for this stellar spectrum should be slightly larger than the seeing disc of the observations to ensure that only stellar light, and therefore radiation originating

from accretion, is contained within the aperture. However, in the case of these observations, a spectral extraction aperture slightly larger than the seeing disc resulted in lower than expected emission line fluxes. Figure 5.27 displays how the measured emission line flux and mass accretion rate ($\dot{M}_{\rm acc}$), the calculation of which will be discussed subsequently, increase as the radius of the spectral extraction aperture placed at the source position increased. This analysis was performed using the H$\beta$ $\lambda$4861 Å and O I $\lambda$ 7773 Å emission lines to provide confirmation that this effect was present throughout the spectral axis. The aperture size is given in units of arcseconds and astronomical units, assuming a distance to the source of 140 pc. The angular resolution of the observation after adaptive optics is $\sim 0\farcs07$, and the measured seeing is $0\farcs45$. However, utilising the observations seeing as the aperture size, an aperture radius of $\sim 0\farcs23$, for spectral extraction clearly results in a significant portion of the line flux not being accounted for, existing outside of the aperture radius. Instead, an aperture size was chosen where both the line flux and consequently, the resulting mass accretion rate, began to asymptote to a constant value. The aperture size chosen to extract spectra from the source position was that of radius of $0\farcs7$ (98 au). This is approximately three times the seeing of the observation. The results shown in Figure 5.27 point to a large aperture correction factor for MUSE NFM data, as could be expected due to MUSE's extended PSF wings.

Line fluxes were then computed utilising the accretion spectrum extracted from the source position, using a circular aperture of radius $0\farcs7$. The source spectrum was not corrected for extinction as the estimated extinction for RU Lupi is approximately zero (Fang et al., 2018). The emission lines chosen, whose luminosities were known to correlate with the accretion luminosity, are listed in Table 5.4, as well as their measured fluxes and computed line luminosities. The H$\alpha$ and the Ca II triplet emission lines are saturated at the source position and thus accurate flux measurements could not be measured. The uncertainties associated with the line fluxes and luminosities are the uncertainties in the line flux calculation. The calculated luminosities of these emission lines were converted into accretion luminosities using the empirical linear relation between $\log(L_{\rm acc})$ and $\log(L_{\rm line})$, shown in Equation 5.4 from Alcalá et al. (2017). This relation was empirically derived by plotting $\log(L_{\rm acc})$ vs. $\log(L_{\rm line})$ for a large sample of young stellar objects. The linear coefficients $a$ and $b$ from Alcalá et al. (2017) for the selected emission lines are presented in Table 5.5.

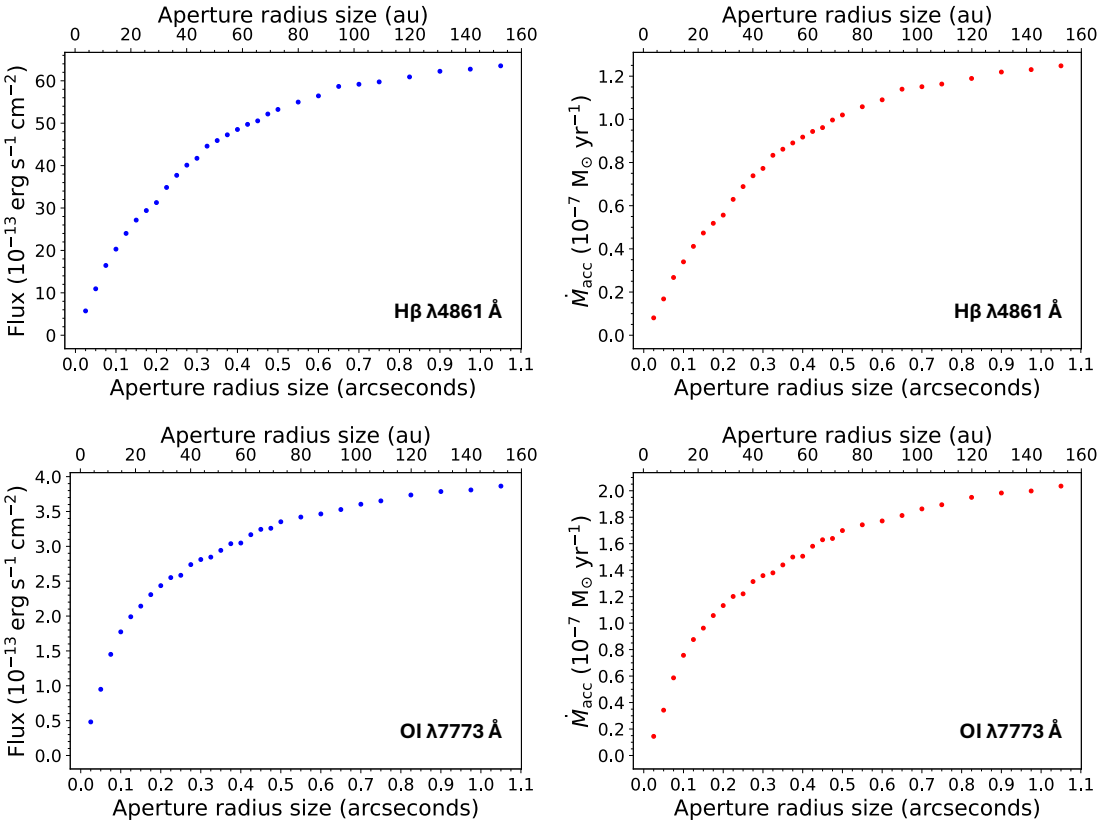


FIGURE 5.27: Measured line flux, shown in the left panels, and mass accretion rate ($\dot{M}_{acc}$), shown in the right panels, for the H$\beta$ $\lambda$4861 Å and O I $\lambda$ 7773 Å emission lines as a function of spectral extraction aperture size. The aperture size in units of au is also displayed assuming a distance to RU Lupi of 140 pc.

TABLE 5.4: Measured line fluxes ($F_{line}$) and computed line luminosities ($L_{line}$) for the selected accretion-tracing emission lines.

| Line | $F_{line}$ ($10^{-13}$ erg s$^{-1}$ cm$^{-2}$) | $L_{line}$ ($10^{-4}$ $L_\odot$) |
|---|---|---|
| H$\beta$ $\lambda$4861 Å | $65.51 \pm 0.55$ | $39.78 \pm 0.33$ |
| [O I] $\lambda$6300 Å | $2.82 \pm 0.52$ | $1.72 \pm 0.31$ |
| H$\alpha$ $\lambda$6563 Å | - | - |
| He I $\lambda$6678 Å | $4.05 \pm 0.04$ | $2.47 \pm 0.02$ |
| He I $\lambda$7065 Å | $2.64 \pm 0.03$ | $1.61 \pm 0.02$ |
| O I $\lambda$7773 Å | $3.72 \pm 0.04$ | $2.27 \pm 0.02$ |
| O I $\lambda$8446 Å | $9.01 \pm 0.37$ | $5.51 \pm 0.23$ |
| Ca II $\lambda$8498 Å | - | - |
| Ca II $\lambda$8542 Å | - | - |
| Ca II $\lambda$8662 Å | - | - |
| Pa-10 $\lambda$9015 Å | $10.92 \pm 0.31$ | $6.68 \pm 0.19$ |
| Pa-9 $\lambda$9230 Å | $1.42 \pm 0.25$ | $0.87 \pm 0.15$ |

TABLE 5.5: Results of the $L_{acc}$ – $L_{line}$ linear fits from Alcalá et al. (2017). The relations are of the form shown in Equation 5.4.

| Line | $a \pm$ error | $b \pm$ error |
|---|---|---|
| H$\beta$ $\lambda$4861 Å | $1.14 \pm 0.04$ | $2.59 \pm 0.16$ |
| [O I] $\lambda$6300 Å | $0.91 \pm 0.01$ | $2.49 \pm 0.41$ |
| H$\alpha$ $\lambda$6563 Å | $1.13 \pm 0.05$ | $1.74 \pm 0.19$ |
| He I $\lambda$6678 Å | $1.25 \pm 0.06$ | $4.70 \pm 0.33$ |
| He I $\lambda$7065 Å | $1.18 \pm 0.05$ | $4.47 \pm 0.29$ |
| O I $\lambda$7773 Å | $1.27 \pm 0.09$ | $4.66 \pm 0.49$ |
| O I $\lambda$8446 Å | $1.08 \pm 0.12$ | $3.46 \pm 0.62$ |
| Ca II $\lambda$8498 Å | $0.99 \pm 0.05$ | $2.60 \pm 0.29$ |
| Ca II $\lambda$8542 Å | $0.97 \pm 0.06$ | $2.43 \pm 0.29$ |
| Ca II $\lambda$8662 Å | $0.93 \pm 0.06$ | $2.30 \pm 0.30$ |
| Pa-10 $\lambda$9015 Å | $1.15 \pm 0.10$ | $3.60 \pm 0.52$ |
| Pa-9 $\lambda$9230 Å | $1.18 \pm 0.08$ | $3.71 \pm 0.43$ |

$$\log(L_{acc}/L_{\odot}) = a \cdot \log(L_{line}/L_{\odot}) + b \tag{5.4}$$

The derived accretion luminosities could then be used to estimate the mass accretion rate using Equation 5.5 (Gullbring et al., 1998; Hartmann et al., 1998). This equation requires the mass ($M_{\star}$) and the radius ($R_{\star}$) of the star in question. The values of $M_{\star} = 0.55\ M_{\odot}$ and $R_{\star} = 2.48\ R_{\odot}$ from Fang et al. (2018) are adopted for RU Lupi. This equation also requires the inner disc radius ($R_{in}$), or the magnetic truncation radius, where the stellar magnetic field has truncated the inner disc, typically near, but within, the co-rotation radius. It has been shown that $R_{in}$ varies from $3R_{\star}$ to $10R_{\star}$ in CTTSs (Johns-Krull, 2007), however, the prevailing assumption that $R_{in} \approx 5R_{\star}$ is adopted here for consistency with previous studies (e.g. Gullbring et al., 1998; Hartmann et al., 1998; Johns-Krull, 2007; Herczeg and Hillenbrand, 2008; Rigliaco et al., 2012; Manara et al., 2016; Alcalá et al., 2017). Rigliaco et al. (2012) has shown that this assumption produces uncertainties of $< 20\%$ on calculated mass accretion rates. The derived accretion luminosities and corresponding mass accretion rates for the accretion-tracing emission lines are presented in Table 5.6. The uncertainties associated with the accretion luminosities and the corresponding mass accretion rates are the quadrature sums of the errors associated with the line luminosities and the errors associated with the linear coefficients $a$ and $b$, presented in Table 5.5. The H$\alpha$ and the Ca II triplet emission lines are saturated

TABLE 5.6: Measured accretion luminosities ($L_{acc}$) and mass accretion rates ($\dot{M}_{acc}$) in the selected accretion-tracing emission lines. H$\alpha$ and the Ca II triplet are saturated at the source position and thus could not be used as reliable accretion tracers. Furthermore, the mass accretion rate derived from the [O I] $\lambda$6300 Å line was not used in the mean calculation, as this line is used to measure the mass outflow rates in the jet and LVC.

| Line | Log $L_{acc}$ ($L_\odot$) | Log $\dot{M}_{acc}$ ($M_\odot$ yr$^{-1}$) | $\dot{M}_{acc}$ ($10^{-7}$ $M_\odot$ yr$^{-1}$) |
|---|---|---|---|
| H$\beta$ $\lambda$4861 Å | $-$ 0.15 $\pm$ 0.16 | $-$ 6.89 $\pm$ 0.16 | 1.28 $\pm$ 0.47 |
| [O I] $\lambda$6300 Å | $-$ 0.91 $\pm$ 0.41 | $-$ 7.66 $\pm$ 0.41 | 0.22 $\pm$ 0.21 |
| H$\alpha$ $\lambda$6563 Å | - | - | - |
| He I $\lambda$6678 Å | + 0.19 $\pm$ 0.33 | $-$ 6.55 $\pm$ 0.33 | 2.79 $\pm$ 2.12 |
| He I $\lambda$7065 Å | $-$ 0.01 $\pm$ 0.29 | $-$ 6.75 $\pm$ 0.29 | 1.78 $\pm$ 1.19 |
| O I $\lambda$7773 Å | + 0.03 $\pm$ 0.49 | $-$ 6.71 $\pm$ 0.49 | 1.94 $\pm$ 2.19 |
| O I $\lambda$8446 Å | $-$ 0.06 $\pm$ 0.62 | $-$ 6.81 $\pm$ 0.62 | 1.57 $\pm$ 2.24 |
| Ca II $\lambda$8498 Å | - | - | - |
| Ca II $\lambda$8542 Å | - | - | - |
| Ca II $\lambda$8662 Å | - | - | - |
| Pa-10 $\lambda$9015 Å | $-$ 0.04 $\pm$ 0.43 | $-$ 6.78 $\pm$ 0.43 | 1.65 $\pm$ 1.64 |
| Pa-9 $\lambda$9230 Å | $-$ 1.08 $\pm$ 0.43 | $-$ 7.83 $\pm$ 0.43 | 0.15 $\pm$ 0.15 |

at the source position and thus could not be used as reliable accretion tracers. The [O I] 6300 Å is not included in the mean calculation of the mass accretion rate as this line evidently also traces ejected material, and thus will be used to calculate the mass outflow rate instead. The mean value of the measured accretion rate is $\dot{M}_{acc} = 1.6 \times 10^{-7}\ M_\odot\ \mathrm{yr}^{-1}$.

$$\dot{M}_{acc} = \left(1 - \frac{R_\star}{R_{in}}\right)^{-1} \frac{L_{acc} R_\star}{G M_\star} \approx 1.25 \frac{L_{acc} R_\star}{G M_\star} \tag{5.5}$$

The mass outflow rate ($\dot{M}_{out}$) was estimated using the method described in Fang et al. (2018). This method was selected as it allowed the estimation of the mass outflow rate in the high-velocity jet ($\dot{M}_{jet}$) and the low-velocity wind ($\dot{M}_{wind}$) independently. This method uses the luminosity of the [O I] 6300 Å emission line, as this line traces both high and low-velocity outflowing material. The high-velocity component of the [O I] 6300 Å line profile, referred to as the jet in this chapter, can be used to estimate $\dot{M}_{jet}$, and the low-velocity, narrow-component of the [O I] 6300 Å line profile, referred to as the LVC in this chapter, can be used to estimate $\dot{M}_{wind}$. Equation 5.6 displays the equation provided in Fang et al. (2018) for the mass outflow rate in the low-velocity

wind. Here, $C(T)$ is a gas temperature dependent function that varies from 2.4 $\times$ $10^{-4}$ to 2.6 $\times$ $10^{-5}$, taking a temperature of 5000 K to 10,000 K respectively. $V_{\rm wind}$ is the peak velocity of the wind, taken as the centroid of the Gaussian profile fit to the LVC in the [O I] line profile. $l_{\rm wind}$ is the vertical extent of the wind emitting region, and $L_{\rm OI6300}$ is the luminosity of the LVC component of the [O I] line profile calculated using Equation 5.3. The low spectral resolution provided by MUSE posed in a challenge here for the measurement of the peak velocity and the luminosity of the LVC. Therefore, values obtained from higher spectral resolution studies, namely, from Whelan et al. (2021) and Fang et al. (2018), were used in the calculation in place of the MUSE measurements. A wind, or LVC, velocity of $V_{\rm wind} = -4$ km s$^{-1}$ was taken from Whelan et al. (2021), and the luminosity of the LVC, $L_{\rm OI6300} = 9.54 \times 10^{-6}$ $L_{\odot}$ was taken from Fang et al. (2018). Although the jet component of the RU Lupi outflow is known to experience temporal variability (Whelan et al., 2021), the LVC is seen to remain stable with time, allowing the use of these previously measured parameters. The vertical extent of the wind emitting region is a key parameter in the estimation of the mass outflow rate in the wind. The spatially resolved observations of the LVC presented for the first time in this chapter allow the height of the wind to be estimated. The height is estimated using Figure 5.25, by taking the width of the [O I] 6300 Å LVC emission at half the peak flux. This results in a wind height of $\sim$ 35 au. Using these parameters, the mass outflow rate of the LVC or wind emission is calculated to be $\dot{M}_{\rm wind} = 2.6 \times 10^{-11}$ $M_{\odot}$ yr$^{-1}$, assuming a gas temperature of 5000 K. Instead, assuming a gas temperature of 10,000 K reduces the mass outflow rate by an order of magnitude ($\dot{M}_{\rm wind} = 2.8 \times 10^{-12}$ $M_{\odot}$ yr$^{-1}$), but a gas temperature of this magnitude is unlikely for the slow-moving LVC, otherwise emission lines from ionised oxygen would have also been easily detected (Simon et al., 2016; Fang et al., 2018). Calculating the outflow efficiency ($\eta_{\rm out}$), shown in Equation 5.1, and assuming a gas temperature of 5000 K, results in an outflow efficiency of $\eta_{\rm out} \approx 0.02\%$.

$$\dot{M}_{\rm wind} = C(T) \left( \frac{V_{\rm wind}}{10 \text{ km s}^{-1}} \right) \left( \frac{l_{\rm wind}}{1 \text{ au}} \right)^{-1} \left( \frac{L_{\rm OI6300}}{L_{\odot}} \right) \text{M}_{\odot} \text{ yr}^{-1} \qquad (5.6)$$

Equation 5.7 displays the equation provided in Fang et al. (2018) for the mass outflow rate in the high-velocity jet. Here, $C(T, n_{\rm e})$ is a gas temperature and electron density dependent function. $C(T, n_{\rm e})$ values at $T$ = 10,000 K are 9.0 $\times$ $10^{-5}$, 6.1 $\times$ $10^{-5}$, and 4.6 $\times$ $10^{-5}$ for $n_{\rm e} = 5.0 \times 10^4$, 7.5 $\times$ $10^4$, and 1.0 $\times$

$10^5$ cm$^{-3}$, respectively. $V_\perp$ is the peak velocity of the jet emission, taken as the centroid of the Gaussian profile fit to the jet component of the [O I] line profile, deprojected into the plane of the sky. $l_\perp$ is the projected length of the jet contained within the spectral extraction aperture. $L_{\rm OI6300}$ is the luminosity of the jet component of the [O I] line profile calculated using Equation 5.3. Since the jet component is moderately resolved in the MUSE observations, the luminosity and the peak velocity of the component can be better estimated than the LVC. For the calculation, a tangential jet velocity of $V_\perp = -$ 52 km s$^{-1}$ from Fang et al. (2018) is adopted, and this value agrees well with that measured in the MUSE observations, $V_\perp = -$ 50 km s$^{-1}$. The luminosity of the jet emission in [O I] 6300 Å emission is estimated to be $L_{\rm OI6300} = 7.43 \times 10^{-5}$ $L_\odot$ from the MUSE observations, and $L_{\rm OI6300}$ = 9.77 $\times$ $10^{-5}$ $L_\odot$ is taken from Fang et al. (2018). The difference in the line luminosities between the two studies can be attributed to the known variability in the jet emission (Whelan et al., 2021). The projected size of the jet within the spectral extraction aperture is estimated in the MUSE observations to be $l_\perp = 98$ au. Using these parameters, and setting $C(T, n_{\rm e})$ at 9.0 $\times$ $10^{-5}$ ($T$ = 10,000 K; $n_{\rm e} = 5.0 \times 10^4$ cm$^{-3}$), the mass outflow rate of the jet emission is calculated to be $\dot{M}_{\rm jet} = 3.6 \times 10^{-9}$ $M_\odot$ yr$^{-1}$. The mass outflow rate increases to $\dot{M}_{\rm jet}$ = 4.7 $\times$ $10^{-9}$ $M_\odot$ yr$^{-1}$ using $L_{\rm OI6300}$ from Fang et al. (2018). The assumed gas temperature of 10,000 K in this calculation is appropriate for the base of the T-Tauri jets (e.g. Agra-Amboage et al., 2011). For gas temperatures of $T$ = 7000 – 15,000 K, the electron density varies in the range $n_{\rm e} = (2 - 6) \times 10^4$ cm$^{-3}$ at the base of T-Tauri jets (e.g. Hartigan and Morse, 2007; Agra-Amboage et al., 2011; Giannini et al., 2013; Maurri et al., 2014), justifying the electron density of $n_{\rm e} = 5.0 \times 10^4$ used in the calculation. Calculating the outflow efficiency ($\eta_{\rm out}$), shown in Equation 5.1, results in an outflow efficiency of $\eta_{\rm out} \approx 2.22\%$ using the measured $L_{\rm OI6300}$ from the MUSE observations, and increases to $\eta_{\rm out} \approx 2.92\%$ using $L_{\rm OI6300}$ from Fang et al. (2018). These outflow efficiencies are as expected for high-velocity jets (Ray, 2007).

$$\dot{M}_{\rm jet} = C(T, n_{\rm e}) \left( \frac{V_\perp}{100 \text{ km s}^{-1}} \right) \left( \frac{l_\perp}{100 \text{ au}} \right)^{-1} \left( \frac{L_{\rm OI6300}}{L_\odot} \right) \text{M}_\odot \text{ yr}^{-1} \qquad (5.7)$$

## 5.3 Discussion

The main contribution that this study provides to the knowledge of the CTTS RU Lupi is the combination of spatial and kinematical information, made possible with IFS with MUSE in NFM. Although it was known that there existed a bipolar outflow from RU Lupi (e.g. Takami et al., 2001), the blueshifted outflow has been imaged for the first time. This provided important constraining information such as the true PA of the jet, and the height of the LVC, necessary for informed mass outflow rate estimations. The spectral resolution provided with MUSE allowed the decomposition of the outflow into its constituent parts, allowing the analysis of the jet and LVC emission independently.

### 5.3.1 Interpretation of the outflow structure

It is clear from both the channel maps in Section 5.2.1 and the position velocity diagrams presented in Section 5.2.2 that the high-velocity jet emission extends furthest from the source position, culminating in a shock feature at approximately 85 au along the jet axis. Both slower-moving outflow components, the HVC1 and LVC, display emission that is less extended and wider than the jet. In the outflow component width measurements along the jet axis shown in Figure 5.24, it is clear that the jet emission is the most collimated component of the outflow. These results, that there is a radial stratification between the outflow components, point to a layering in the outflow structure, both spatially and kinematically. The highest-velocity material is collimated to the highest degree, and the lower-velocity material is spatially wider, surrounding the jet emission. Furthermore, the derived upper limits of the footpoints, or launching radii, of the different outflow components, presented in Table 5.3, show that the jet is launched in the inner disc region, closest to the outflow axis, whilst the LVC is launched at larger disc radii. This onion-like, layered flow structure with stratification of emission in velocity is predicted by MHD disc wind models (Ferreira, 1997; Panoglou et al., 2012; Bai et al., 2016; Zhu and Stone, 2018; Wang, Bai, and Goodman, 2019). As stated in Section 4.3.1, in these models, material is accelerated along flow streamlines, poloidal magnetic field lines anchored in the rotating disc. High-velocity emission travels along streamlines originating in the very inner disc region, whilst lower velocity emission travel along streamlines originating further out in the disc. The outflow launch radii extend to up to 9 au from the disc surface, implying that

outflows may significantly affect not only disc evolution, but also the planet forming regions of the disc.

The full opening angle of the jet, measured in [O I] 6300 Å, [S II] 6731 Å, and [N II] 6583 Å emission and presented in Table 5.3, is large, at approximately 21° to 28°, in comparison to other studies, where the jet full opening angle is typically measured at $< 5°$ (e.g. Murphy et al., 2021). In some cases, wide opening angles of jets have been seen (e.g. Pascucci et al., 2024), however. One rational explanation for this wide jet opening angle may be that the low spectral resolution of MUSE, compared to high-resolution spectroscopic studies, has resulted in spectral blending between the jet emission and the wider outflow components, such as the HVC1 and LVC. However, this is ruled out as the cause as the opening angle is also large when measured in [N II] 6583 Å emission, which only traces the high-velocity jet (Hirth, Mundt, and Solf, 1997). Another possible cause is that the jet width measurements could be impacted by the presence of an unresolved shock feature or jet knot along the outflow axis. In the plots of the flux measurements of the outflow components along the jet axis, shown in Figure 5.25, it is clear that the jet emission follows a different spatial distribution when compared to the HVC1 and LVC. In [O I] 6300 Å emission, there is a peak in jet brightness at $\sim$ 25 au, and in [S II] 6731 Å and [N II] 6583 Å emission there is a peak in jet brightness at $\sim$ 45 au. This peak in flux, offset from the source position, could be an unresolved shock feature at this distance, with the difference in the peak position in [O I] emission and [S II] and [N II] emission reflecting the different critical densities of the lines. The critical density of the [O I] 6300 Å emission line is much higher than the critical densities of the [S II] 6731 Å and [N II] 6583 Å emission lines, meaning it can trace denser material, and therefore trace material closer to the driving source. The wide-angled morphology at the base of the jet may also arise from emission scattered off some V-shaped cavity carved into the surrounding ambient medium by the outflow. As the line to continuum ratio maps of the high-velocity emission, especially apparent in the [N II] emission line displayed in Figure 5.10, also display this wide-angled morphology, one can rule out contribution from continuum light scattered off a cavity. However, one cannot dismiss the possibility that the spatial distribution of scattered jet emission differs from that of scattered continuum light, resulting in the cavity being illuminated entirely by jet emission. Conversely, the morphology of this wide-angled emission in the jet images does not match what is expected for a cavity of an almost face-on inclination

(Whitney et al., 2003; Habel et al., 2021).

Interestingly, the measured opening angles of the LVC are smaller ($\theta \approx 20^{\circ}$ to $38^{\circ}$) than what has been predicted for disc winds by other studies. Banzatti et al. (2019) showed that the kinematics of the BC and NC of the LVC correlate, and that the blueshifted velocities are maximised at a viewing angle of $\approx 35^{\circ}$. This was taken as evidence of the LVC possessing a conical wind geometry with a half-opening angle of $35^{\circ}$, or a full opening angle of $70^{\circ}$. Opening angles of this magnitude match the predictions for conical-shell MHD winds made by Kurosawa and Romanova (2012). However, the MHD wind models in Kurosawa and Romanova (2012), which give half-opening angles of $\sim 35^{\circ}$, are for sources with a moderate mass accretion rate, which they take to be $\dot{M}_{\rm acc} = 4 \times 10^{-8}\ M_{\odot}\ {\rm yr}^{-1}$. Kurosawa and Romanova (2012) also showed that smaller full opening angles, of the order of $40^{\circ}$, are achieved in cases of high accretion, which they take to be $\dot{M}_{\rm acc} = 3.4 \times 10^{-7}\ M_{\odot}\ {\rm yr}^{-1}$. This accretion rate is more comparable to what is measured here for RU Lupi, $\dot{M}_{\rm acc} = 1.6 \times 10^{-7}\ M_{\odot}\ {\rm yr}^{-1}$. A source of uncertainty in the outflow width measurements is the deprojection of the outflow into the plane of the sky. As the disc inclination measurements with respect to the plane of the sky are not constrained to a high degree ($\theta_{\rm i} = 16^{\circ} \pm^{+6}_{-8}$, Perraut et al., 2021), then uncertainty is introduced and amplified when deprojecting the outflow to derive width measurements. Having said this, the relative difference between the widths of the jet and LVC emission, being that the jet is more collimated than the LVC, remains unchanged when taking this uncertainty into account. Furthermore, the fact this uncertainty would affect the width measurements in one direction, meaning that the widths of both outflow components could be wider, or they could both be narrower, does not change the fact that the opening angle of the jet is larger than expected and the opening angle of the LVC is smaller than expected.

An unexpected finding is seen in the position velocity diagrams extracted along the outflow axis presented in Figures 5.18 and 5.19, in [O I] 6300 Å, [S II] 6731 Å, [N II] 6583 Å, and [Fe II] 7155 Å emission. That is, the existence of significant high and low-velocity emission at negative offsets from the source position, or blueshifted emission originating from the side of the driving source opposite to where the outflow is emanating from. One does not expect to see this emission as the outflow is not traced at these negative offsets. One possibility for this blueshifted material at negative offsets is that the emission could

originate from shock-entrained material, located at negative offset from the stars position in projection. If the outflow is emanating into, and interacting with, a dense surrounding medium, then it may shock and entrain the surrounding ambient material, resulting in the entrained material being excited and possessing blueshifted velocities. This scenario would suggest that the blueshifted emission at negative offsets one sees in the position velocity diagrams extracted along the outflow PA is intrinsic emission from wide, shock-entrained material that has been swept up and excited by the outflow. However, this scenario for RU Lupi is unlikely, as it requires that a powerful outflow interact strongly with a dense circumstellar envelope. RU Lupi is a class II object, and so does not possess a dense envelope obscuring the star. The star is visible at optical wavelengths and has an estimated visual extinction of $A_{\rm V} = 0$ (Fang et al., 2018). It is therefore unlikely that this blueshifted emission at negative offsets is tracing shock entrained material in a dense envelope.

Another explanation for this emission could be due to the scattering of intrinsic outflow emission. If a hollow cavity, carved out in the ambient material by the outflow is indeed present, then intrinsic outflow light, originating from both high and low-velocity material, could scatter off the cavity walls producing this signature of emission at negative offsets, that one sees in projection. The intrinsic outflow emission could scatter off the cavity wall closer to the observer, the near side of the cavity, creating the illusion of blueshifted emission at negative offsets. In contrast, the intrinsic outflow emission, and outflow emission scattered off the far side of the cavity, would appear as blueshifted emission at positive offsets with respect to the star, as one expects. As this 3D hollow cavity structure appears in observations as a 2D projection in the plane of the sky, the illusion of blueshifted emission either side of the source position, the red dashed lines in Figures 5.18 and 5.19, is created. Similarly, the outflowing emission may be scattered off the almost face-on disc surface surrounding the star, or scattered off surrounding ambient material near the source position. RU Lupi is known to possess a reflection nebulosity (Gupta et al., 2023; Winter et al., 2024), that could scatter outflow emission resulting in blueshifted emission appearing at negative offsets with respect to the source position.

The scattering scenario is the most likely cause for this emission. It can be seen in the channel maps, pre-deconvolution, presented in Figure 5.7, that

there exists emission at negative offsets with respect to the source position, opposite to the direction of the outflow PA, in the jet, HVC1, and LVC channels. This emission matches the signature seen in the PV diagrams, and extends to an offset of almost $-$ 50 au in these channel maps displaying blueshifted emission. It is unlikely that this emission at negative offsets in the channel maps is intrinsic outflow light, as confirmed by the line to continuum ratio maps presented in Figure 5.9. If this emission was indeed intrinsic light, it would appear bright in the line to continuum ratio maps, exceeding the ratio of unity. However, in these maps, there is no intrinsic outflow emission detected on the side of the star opposite to the outflow direction. Additionally, this blueshifted emission at negative offsets seen in the channel maps is greatly reduced in spatial extent after the deconvolution routine. This is evident in the channel maps of [O I] 6300 Å and [S II] 6731 Å emission, before and after deconvolution, as seen in Figures 5.12 and 5.13. Therefore, the scattering of intrinsic outflow emission is the most likely cause of this blueshifted emission seen at negative offsets with respect to the star position in the PV diagrams extracted along the outflow, whether it be scattered off a wide-angled cavity, nebulosity in the surrounding region of the star, or the disc surface. The fact that the MUSE PSF possesses significant wings further contributes to this extension of blueshifted emission into negative offsets.

Another potentially puzzling signature seen in the PV diagrams extracted both along and transverse to the outflow, most evident in [O I] emission, is significant compact redshifted emission. This signature is clearest in Figures 5.18 and 5.20. One may initially attribute this high-velocity redshifted emission to the counter-jet emanating away from the observer. However, this redshifted counter-flow is being obscured by the disc surrounding RU Lupi (Stock et al., 2022). Furthermore, the redshifted emission seen in the [O I] emission is spatially compact, centred around the source position and not extending far from the star. This is further supported in the transverse PV diagrams extracted along the outflow axis presented in Figure 5.20. As the distance from the source increases, this redshifted signature fades implying that it is entirely located in the vicinity of the star. As this emission is compact, and symmetric about the source position, it is possible that it is tracing infalling material or accretion shocks originating from the star-disc region. [O I] emission is not usually attributed to tracing infalling material, and is most closely associated with jets and winds, however it is possible that a minor component of the [O I]

emission is tracing accretion activity, resulting in this emission at redshifted velocities. Alternatively, this redshifted signature could be the extended tail of the [O I] 6300 Å line profile which has been observed to extend into redshifted velocities in the case of RU Lupi (Banzatti et al., 2019).

A tentative detection of velocity stratification transverse to the jet axis is also observed. This is most evident in the PV diagrams extracted across the outflow axis in [N II] 6583 emission, shown in Figure 5.22. There is a crescent shape in the PV diagram extracted at 80 au from the source position, where the velocity of material is highest centred on the outflow axis, the dashed-red line, and as one moves radially outward from the outflow axis the velocity of the jet emission decreases. This points to an onion-like velocity structure in the jet, as predicted by MHD outflow launching models, with the highest velocity material being closest to the jet axis.

### 5.3.2 Implications of the outflow efficiency

The outflow efficiency ($\eta_{\rm out}$) was calculated for the jet and the LVC independently using the derived mass accretion rate ($\dot{M}_{\rm acc}$) and the derived mass outflow rates ($\dot{M}_{\rm jet}$ and $\dot{M}_{\rm wind}$). Estimating the efficiency of an outflow, in terms of the mass flux, is important as it is thought that the mass flux correlates with angular momentum transport. A larger mass outflow rate for a magneto-centrifugally launched outflow results in a greater portion of angular momentum extraction from the star-disc system (Ray and Ferreira, 2021). The mass accretion rate was estimated using a combination of accretion tracing emission lines presented in Table 5.6, and an empirical relation between the luminosity of the emission lines and the accretion luminosity, shown in Equation 5.4. Whilst the connections between $L_{\rm line}$ and $L_{\rm acc}$ are strong, their use in estimating mass accretion rates for individual objects introduces significant uncertainties (e.g. Fiorellino et al., 2021; Bouvier et al., 2023; Herczeg et al., 2023; Nelissen et al., 2023; Wendeborn et al., 2024) and estimates of accretion rates can vary up to an order of magnitude (Gullbring et al., 1998). A caveat associated with using empirical relationships between $L_{\rm line}$ and $L_{\rm acc}$ is the fact that the emission lines trace not only accretion, but other processes also, such as chromospheric activity, stellar flaring, and winds (Manara et al., 2013; Alcalá et al., 2014). Furthermore, there is an uncertainty introduced in the aperture size selected to extract the accretion spectrum, as discussed in Section 5.2.3. The aperture size

chosen in this study was of radius 0.″7 (98 au), or three times the seeing of the observation. This pointed to a large aperture correction factor for the MUSE NFM data, as could be expected due to MUSE's extended PSF wings, which can extend beyond 1.″0. The complication associated with using an aperture of this size is that background emission will contribute to the spectrum. There is significant scattering of continuum emission present throughout the spectral axis of the observation, as evidenced by comparing the morphology of the emission in the pre-deconvolved channel maps, in Figures 5.7 and 5.8, to the line to continuum ratio maps, in Figures 5.9 and 5.10. There is also likely the scattering of emission from the base of the outflow, and the scattering of emission originating from accretion activity. All of this emission is scattering off the surface of the disc, nebulous ambient material, or some wide-angled cavity, potentially contributing significantly to the integrated line fluxes within the aperture, and therefore artificially inflating the measured line luminosities. However, Rigliaco et al. (2012) and others (e.g. Alcalá et al., 2017) have shown that the measurement of the accretion luminosity using a significant number of emission lines ($\sim$ 5 – 6) leads to accurate measurements of the accretion luminosity with relatively small uncertainties of the order of $\sim$ 0.2 – 0.3 dex.

Having stated these large uncertainties associated with estimating $\dot{M}_{\rm acc}$ values using line luminosities (see Table. 5.6), and acknowledging that varying the spectral extraction aperture size when measuring the mass accretion rate, seen in Figure 5.27, can result in a difference of an order of magnitude, one can be confident in the mass accretion rate of $\dot{M}_{\rm acc} = 1.6 \times 10^{-7}\ M_{\odot}\ {\rm yr}^{-1}$ that is estimated here. The result for the mass accretion rate agrees well with previous studies. Fang et al. (2018) reported a value of $\dot{M}_{\rm acc} = 1.7 \times 10^{-7}\ M_{\odot}\ {\rm yr}^{-1}$ for RU Lupi, using a different set of emission lines. Wendeborn et al. (2024) reported a value of $\sim 1 \times 10^{-7}\ M_{\odot}\ {\rm yr}^{-1}$ using three methods of estimating the mass accretion rate. They used accretion shock modelling, flow modelling, and the method that is used here, from Alcalá et al. (2017), all with the luminosity of the H$\alpha$ emission line ($L_{\rm H\alpha}$), a well-established accretion tracer, and also mitigating the effect of wind absorption, which allowed H$\alpha$ to be a more reliable accretion tracer.

The mass outflow rate for both the jet and the wind are estimated using the luminosity of the [O I] 6300 Å emission line, and various other parameters, as discussed in Section 5.2.3. The mass outflow rate derived for the jet, $\dot{M}_{\rm jet} = (3.6 – 4.7) \times 10^{-9}\ M_{\odot}\ {\rm yr}^{-1}$, when compared to the mass accretion rate, gives

an outflow efficiency of $\eta_{\rm out} = 2.22\%$ – $2.92\%$. An outflow efficiency of this magnitude is expected for high-velocity jets, which tend to lie in the region of $\eta_{\rm out} = 1\%$ to $10\%$ (Ray, 2007). However, in the case of the mass outflow rate derived for the LVC, or wind, the mass loss rate calculated is significantly low.

As the LVC from RU Lupi was spatially resolved for the first time, the vertical height of the wind could be accurately measured, a key parameter in the estimation of the mass outflow rate. This highlights the power of IFS for similar observations, where the height of the outflow can be estimated much better than it can using a technique such as spectro-astrometry, which only provides a minimum offset of the wind from the source position. The mass outflow rate calculated for the LVC, $\dot{M}_{\rm wind} = 2.6 \times 10^{-11}\ M_{\odot}\ {\rm yr}^{-1}$, when compared to the mass accretion rate, gives an outflow efficiency of $\eta_{\rm out} \approx 0.02\%$. An outflow efficiency of this magnitudes implies that the LVC traced in [O I] 6300 Å emission is not removing a significant portion of mass from the system, and subsequently not contributing strongly to angular momentum extraction.

This small mass flux contained in the LVC may indicate that the wind traced by [O I] emission is tracing some transition layer between atomic and molecular emission in an underlying MHD disc wind. Pascucci et al. (2023) argued that in the case of strongly accreting CTTSs, such as RU Lupi, the slow-moving wind is predominantly molecular. This implies that atomic wind tracers, such as the [O I] 6300 Å emission line, do not trace the bulk of the mass flux contained in the wind, and instead provide a lower limit on $\dot{M}_{\rm wind}$ (Nisini et al., 2024). For RU Lupi, Pontoppidan, Blake, and Smette (2011) reported that the CO fundamental line at $\sim 4.7\mu$m traces a wind, and they estimated the mass outflow rate of the CO wind at $\dot{M}_{\rm wind} = 4 \times 10^{-9}\ M_{\odot}\ {\rm yr}^{-1}$. This value is two orders of magnitude higher than the mass outflow rate measured for the wind traced by [O I] emission here. This higher mass flux contained in the molecular wind from Pontoppidan, Blake, and Smette (2011) supports the explanation for the low mass loss rate in the LVC in [O I] emission offered by Pascucci et al. (2023), however, the outflow efficiency of the CO wind ($\eta_{\rm out} \approx 2.5\%$) is comparable to that of the atomic jet, insinuating that the CO wind does not dominate angular momentum removal either.

The low mass outflow rate may also be explained by the size of the emitting region of the LVC in [O I] emission. The mass outflow rate in the wind ($\dot{M}_{\rm wind}$) depends critically on the radial area of the emitting region. If the LVC in [O I]

emission is tracing a narrow radial region from the disc, then the mass outflow rate from this narrow region would naturally be low (See Equation 17 in de Valon et al., 2022). Nisini et al. (2024) show that the [O I] 6300 Å emission line may only trace the very inner portion of the wind region, where this region is most likely not the main contributor to the mass loss. Another hypothesis for the low mass outflow rate in [O I] emission is that the emission line could be primarily tracing a thermally-launched photoevaporative wind, where high-energy radiation (UV and X-rays) originating from the central source generate a thermal pressure in the disc surface. It is now accepted that photoevaporative winds can exist in the inner few astronomical units of the accretion disc in low mass stars (Rab et al., 2022; Rab et al., 2023; Fang et al., 2023a). However, the derived mass outflow rate for the LVC is low even for a photoevaporative wind, which typically have mass loss rates of $\dot{M}_{\rm wind} = 10^{-10} - 10^{-8}\ M_{\odot}\ {\rm yr}^{-1}$ (Font et al., 2004; Wang and Goodman, 2017; Picogna et al., 2019; Pascucci et al., 2023).

Nisini et al. (2024) state that the [O I] 6300 Å emission line is not a good tracer to probe the mass outflow rate contained in low-velocity winds. They argue that there is significant emission from the disc surface that contributes to the forbidden emission lines' flux. Also, they argue that without more accurate knowledge of the wind geometry and the spatial extent of the wind, the mass outflow rates estimated from the blueshifted LVC cannot be constrained better than a factor of 100. However, even if the estimated mass outflow rate derived here increased by a factor of this magnitude, the mass outflow rate would still be too low to be significantly contributing to angular momentum removal. The mass loss rate value that is estimated here, even taking all of these uncertainties into account, places the outflow efficiency of the outflow component that is traced by the LVC at $< 1\%$, while models suggest that $\dot{M}_{\rm out} \approx \dot{M}_{\rm acc}$ for the wind if it dominates angular momentum removal (Gressel and Pessah, 2015; Béthune, Lesur, and Ferreira, 2017; Bai, 2017). I therefore cannot conclude whether the narrow component of the LVC in the case of RU Lupi is tracing an MHD disc wind, or some interaction region, or if it is tracing a photoevaporative flow, based solely on the outflow efficiency.

## 5.4 Summary and conclusions

I have investigated the outflow emanating from the CTTS RU Lupi, probing the high-velocity jet emission and the low-velocity emission separately, using MUSE NFM observations achieving a spectacular spatial resolution of $0\farcs074$. This work provides new insights into the outflow, building on what was previously learned from spectroscopic and spectro-astrometric studies. The results presented in this chapter most closely align with the existing conclusion that the narrow component of the LVC in [O I] 6300 Å and [S II] 6731 Å emission trace an MHD wind. I summarise the main conclusions of the chapter as follows:

- The jet was imaged for the first time in the forbidden emission lines [O I] $\lambda\lambda$ 6300,6363 Å, [N II] $\lambda$ 6583 Å, [S II] $\lambda\lambda$ 6716,6731 Å, and [Fe II] $\lambda$ 7155 Å. The morphology of the jet is presented in integrated line intensity images, line to continuum ratio maps, and in the high-velocity channels of the channel maps. The jet emission displays a wide full-opening angle ($\theta \approx 21^\circ$ to $28^\circ$) and culminates in a shock feature or jet knot at $\approx 85$ au (or 250 au deprojected into the plane of the sky) along the outflow axis. The opening angle of the jet is large compared to other studies (typically $< 5^\circ$), but the jet width measurements could be impacted by the presence of an unresolved knot in the inner outflow region, or by jet emission scattered off a V-shaped cavity. It is possible that the jet possesses a kinematical asymmetry when the high-velocity redshifted emission detected in [S II] $\lambda$ 6731 Å emission is considered.

- The jet extends to double the minimum distance suggested by spectro-astrometric analysis, and the jet PA, measured here accurately to be $213^\circ \pm 2^\circ$, is perpendicular to the PA of the RU Lupi disc ($121^\circ \pm 5^\circ$) within the uncertainties.

- The outflow efficiency ($\eta_{\rm out}$) of the jet is at a few percent, which is in line with the values derived for other CTTSs (Ray, 2007). The outflow efficiency in the LVC in [O I] 6300 Å emission is very low, even when all the uncertainties in the calculations are considered, such as poorly understood wind geometries, spatial extents, and contribution to emission

from the disc surface (Nisini et al., 2024). The mass-loss rate value places the efficiency of the outflow component that is traced by the LVC at $<$ 0.1%, while models suggest that $\dot{M}_{\rm out} \sim \dot{M}_{\rm acc}$ for the wind if it dominates angular momentum removal (Bai, 2017). The measured mass outflow rate in the LVC is also relatively low for photoevaporative winds (Pascucci et al., 2023). The mass outflow rate for the LVC in [O I] 6300 Å emission is therefore likely a lower limit on $\dot{M}_{\rm wind}$, with the wind from CTTSs being predominately molecular.

- The LVC was also imaged for the first time, allowing its height in [O I] 6300 Å emission to be estimated. The measured value of $\sim$ 35 au is higher than the 8 au from the spectro-astrometric measurement, which only provides a minimum offset. The full opening angles for the LVC ($\theta \approx 20^{\circ}$ to $38^{\circ}$) are smaller than what has been predicted for low-velocity winds by other studies ($\approx 70^{\circ}$). However, narrower opening angles are predicted in cases of high accretors, such as RU Lupi.

- Radial stratification of the outflow in the different outflow components, producing an onion-like flow structure, is observed, favouring the disc wind launching model. The slow-moving, wide-angled LVC surrounds the high-velocity jet emission. The measured launch radii upper limits suggest that the jet is launched in the inner disc region, closest to the outflow axis, whilst the LVC is launched at larger disc radii. This nested velocity structure supports the wind origin for the LVC.

- Position velocity diagrams are used to investigate the kinematics of the outflow. The radial velocity of the jet emission peaks at $v_{\rm rad} \approx -$ 200 km s$^{-1}$, which is consistent with previous measurements and is expected for atomic jets. It is seen that the LVC is a separate outflow component to the jet, and does not extend as far from the source position. The LVC fades as offset from the star increases, as expected for a low-velocity wind.

This work strongly highlighted the power of IFS for advancing our understanding of the best MHD wind tracer and whether they should be considered important to angular momentum removal in forming stars. VLT/ERIS observations of RU Lupi would be a logical next step, as spatially extended and

blueshifted $H_2$ emission, indicative of an outflow, has been observed spectrally (Herczeg et al., 2006). The molecular wind in $H_2$ emission could be analysed in the same way as was done here, and with an improved spectral resolution.

# Chapter 6

# The proper motions of the HH 46/47 outflow in [S II] and $H_2$ emission

## 6.1 Introduction

In this chapter, I will present the proper motions study of the HH 46/47 outflow, with wide-field imaging observations spanning from 1991 to 2018 in [S II] emission, and from 2001 to 2019 in $H_2$ emission. Proper motions studies involve the measurement of the apparent motion of objects over time by comparing observations from different epochs. In the context of outflows from forming stars, one can study the outflowing material by identifying internal shocks within the outflow, or terminal shocks, where the outflow impacts ambient material, and trace their movements. The identification of this shocked emission can be performed in different shock tracers, such as those molecular, for example $H_2$ and CO, and atomic, such as H$\alpha$, [S II], [Fe II], and [O II]. Proper motions studies of outflows provide insight into their physical properties. One can derive the true 3D velocity of the outflow by combining the tangential velocities, obtained with the proper motions, with radial velocities, derived from spectroscopy. The acceleration and deceleration of shock features can be investigated, providing information about the interaction of the flow with the ambient material, entrainment of material by the flow, and recent high ejection events. The variability in the flows motion can also be studied, identifying episodic ejection events that can be subsequently linked to accretion bursts. Proper motions can also help constrain outflow launching mechanisms, as different mechanisms predict different kinematic structures and outflow collimation. One can also estimate the dynamical age of the outflow from proper

motions, and learn about shock properties in the outflow. Ultimately, the investigation of the dynamical changes in the outflow's large scale structure and kinematics over time better informs the findings of the SINFONI observations of HH 46/47, presented in Chapter 4.

Prominent features of the well-studied HH 46/47 outflow have established nomenclatures. The blueshifted jet emanates northeasterly from the Bok Globule, ESO 210-6A, and the redshifted side of the jet penetrates southwesterly, deep into the cloud. The blueshifted jet terminates in a bright bow shock known as HH 47A, the bow shock that the redshifted counter-flow terminates in is known as HH 47C. There is also a bubble-like bow shock located beyond the HH 47A bow shock, thought to have arisen from an earlier outflow episode, known as HH 47D (Dopita, Schwartz, and Evans, 1982; Reipurth and Heathcote, 1991). The base of the blueshifted outflow is embedded in a bright reflection nebula. These features are labelled in Figure 6.1, which displays a FORS2 H$\alpha$ image of the outflow.

A comprehensive profile of the HH 46/47 outflow is provided in Section 4.1.1, but here, it is expanded to provide an overview of the previous proper motion studies performed on this outflow. The results of these studies are summarised in Table 6.1. Schwartz, Jones, and Sirk (1984) measured the proper motions of the HH 46/47 jet, from 1976 – 1983, in H$\alpha$ and [S II] emission to be $v_\perp = 195$ km s$^{-1}$ near the base of the jet, the bright HH 47A bow shock to be $v_\perp = 165$ km s$^{-1}$, and the HH 47C bow shock that the redshifted outflow terminates in to be $v_\perp = 234$ km s$^{-1}$, using the University of Michigan Curtis Schmidt telescope and the Víctor M. Blanco Telescope at the Cerro Tololo Inter-American Telescope (CTIO). Eisloeffel and Mundt (1994) measured the proper motions of jet knots in the blueshifted HH 46/47 jet and redshifted counter-jet from 1987 – 1991 in [S II] emission using the ESO-MPI telescope. They found that the outflowing motion was aligned with the outflow axis, that the knot velocities further from the outflow axis decreased, and that the blueshifted jet had average tangential velocities of $v_\perp = 200$ km s$^{-1}$ and increased in velocity up until the HH 47A bow shock. The apex of the HH 47A bow shock had a proper motion of $v_\perp = 182$ km s$^{-1}$. The proper motions of HH 47D were found to range from $v_\perp = 100$ – 250 km s$^{-1}$, from the wings of the bow shock to the apex. The proper motions of the HH 47C bow shock were found to be on average $v_\perp = 150$ km s$^{-1}$. Hartigan et al. (2005) measured the proper motions of the jet between 1994 and 1995 in [S II] and H$\alpha$ emission, using WFPC2 (Wide

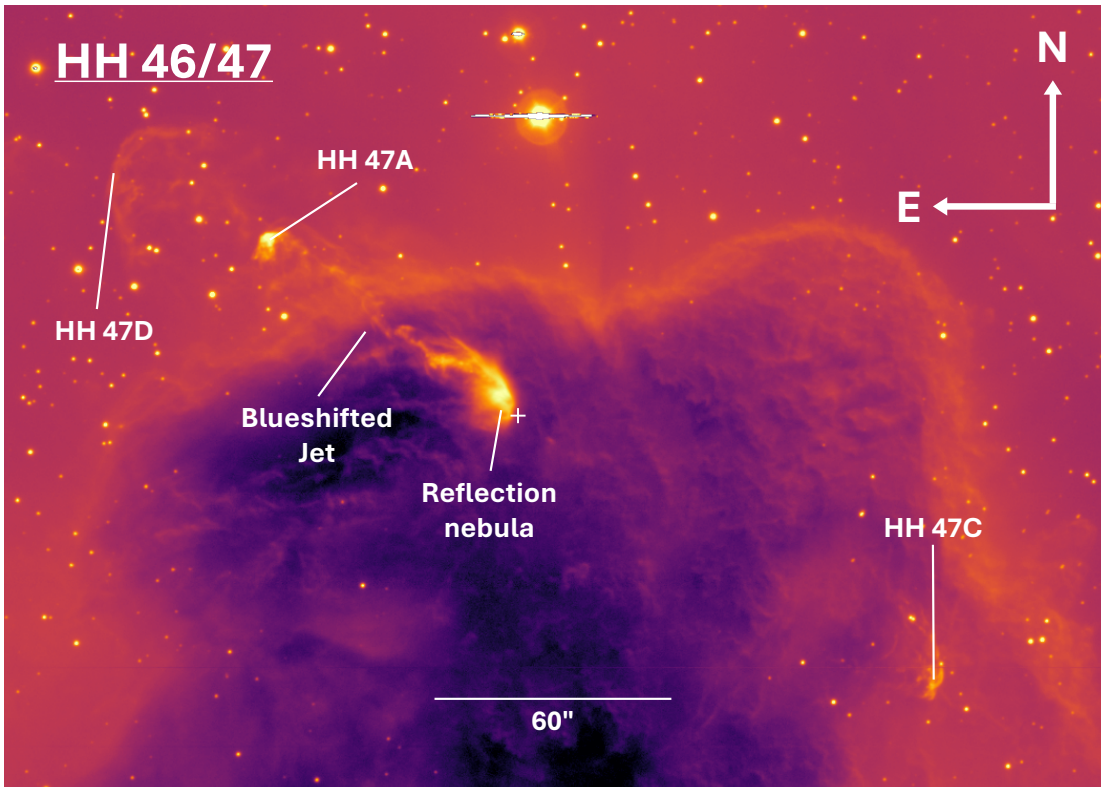


FIGURE 6.1: FORS2 H$\alpha$ image of the HH 46/47 outflow with prominent features labelled. The embedded driving source is located at the apex of the reflection nebula and its approximate location is marked with a white plus symbol. The blueshifted jet emanates northeasterly from the Bok Globule, ESO 210-6A, and the redshifted side of the jet penetrates southwesterly, deep into the cloud. The blueshifted jet terminates in the HH 47A bow shock, with a fainter, bow shock HH 47D which is more extended. The redshifted jet terminates in the HH 47C bow shock.

Field and Planetary Camera 2) on HST. The proper motions of the jet were $v_\perp$ = 235 ± 24 km s$^{-1}$, the HH 47A bow shock, $v_\perp$ = 201 km s$^{-1}$, and the HH 47D bow shock, $v_\perp$ = 179 ± 40 km s$^{-1}$. Raga, Velázquez, and Noriega-Crespo (2018), using HST observations, measured the proper motions of the jet to be 264 ± 30 km s$^{-1}$ in [S II] emission and 240 ± 42 km s$^{-1}$ in H$\alpha$ emission, in the epoch 1994 – 1999, and subsequently measured 229 ± 17 km s$^{-1}$ in [S II] emission and 216 ± 24 km s$^{-1}$ in H$\alpha$ emission, in the epoch of 1999 – 2008. They also measured the proper motions of the HH 47A bow shock to be 215 ± 13 km s$^{-1}$ in [S II] emission and 217 ± 16 km s$^{-1}$ in H$\alpha$ emission in the epoch 1994 – 1999, and 199 ± 8 km s$^{-1}$ in [S II] emission and 204 ± 9 km s$^{-1}$ in H$\alpha$ emission in the subsequent epoch 1999 – 2008. Erkal et al. (2021b) reported a tangential velocity of $v_\perp$ = 245 ± 15 km s$^{-1}$ for the jet, again using HST observations, in [S II] and [Fe II] emission between 2005 and 2019.

The proper motions of the molecular outflow, in $H_2$ 2.12 μm emission, were probed in a multi-epoch study spanning 1993 – 1997 by Micono et al. (1998), using the ESO-MPI telescope. This emission generally has a wider morphology when compared to the narrow jet, instead tracing shock-heated outflow cavities and wide-angled components of the outflow. They found that the fastest-moving $H_2$ knots were in, or close to, the central axis of the outflow and knots constituting the wings of the large scale bow were found to move much more slowly. They measured proper motions of shocks in the central axis of the redshifted flow to be in excess of 200 km s$^{-1}$, and much lower velocities in features along the wide wings of the outflow lobe (40 – 81 km s$^{-1}$). In the HH 47A bow shock, they found proper motions of $v_\perp$ = 184 km s$^{-1}$, in close agreement with proper motions traced by optical emission lines.

In this chapter, the dataset used for the proper motions study is presented in Section 6.2. Section 6.3 presents the astrometric alignment technique employed to measure shock feature movement between subsequent observing epochs. The shock feature identification in each epoch, and the corresponding proper motions measured, are presented in Section 6.4. The results are discussed in Section 6.5 and a summary of the findings and conclusions are presented in Section 6.6.

TABLE 6.1: Summary of previous proper motion measurements of large scale outflow features in the HH 46/47 outflow.

| Feature – tracer[a] | $v_\perp$ (km s$^{-1}$) | | | | | | |
|---|---|---|---|---|---|---|---|
| | 76 – 83$^{(1)}$ | 87 – 91$^{(2)}$ | 93 – 97$^{(3)}$ | 94 – 95$^{(4)}$ | 94 – 99$^{(5)}$ | 99 – 08$^{(5)}$ | 05 – 19$^{(6)}$ [b] |
| Jet – H$\alpha$ | 195 | - | - | $235 \pm 24$ | $240 \pm 42$ | $216 \pm 24$ | - |
| Jet – [S II] | 195 | 200 | - | $235 \pm 24$ | $264 \pm 30$ | $229 \pm 17$ | $245 \pm 15$ |
| Jet – [Fe II] | - | - | - | - | - | - | $245 \pm 15$ |
| HH 47A – H$\alpha$ | 165 | - | - | 201 | $217 \pm 16$ | $204 \pm 9$ | - |
| HH 47A – [S II] | 165 | 182 | - | 201 | $215 \pm 13$ | $199 \pm 8$ | - |
| HH 47A – $H_2$ | - | - | 184 | - | - | - | - |
| HH 47C – H$\alpha$ | 234 | - | - | - | - | - | - |
| HH 47C – [S II] | 234 | 150 | - | - | - | - | - |
| HH 47D – H$\alpha$ | - | - | - | $179 \pm 40$ | - | - | - |
| HH 47D – [S II] | - | 100 – 250 | - | $179 \pm 40$ | - | - | - |

[a] The large scale outflow features are given an identifier. Jet refers to the axis of the blueshifted jet. HH 47A refers to the bright bow shock that the blueshifted jet terminates in. HH 47D refers to the fainter, and further extended from the source position, bow shock in the blueshifted outflow. HH 47C refers to the bow shock observed in the redshifted outflow. The emission tracers are also noted.

[b] Observation epochs.

References: (1)Schwartz, Jones, and Sirk (1984), (2)Eisloeffel and Mundt (1994), (3)Micono et al. (1998), (4)Hartigan et al. (2005), (5)Raga, Velázquez, and Noriega-Crespo (2018), (6)Erkal et al. (2021b)

TABLE 6.2: Proper motions study imaging data

| Epoch | Instrument | Program ID[a] | Filter | Exp. (s) |
|---|---|---|---|---|
| 1991 Dec | EMMI | 043.03.003 | S II | 2700 |
| 1995 Feb | EMMI | 054-d-0828 | S II | 1800 |
| 2001 May | ISAAC | 67.C-0600(A) | NB 2.13 | 480 |
| 2002 Feb | EFOSC2 | 060.A-9018(A) | [SII] | 3000 |
| 2006 May | EMMI | 77.C-0047(B) | S II | 3600 |
| 2018 Nov | FORS2 | 102.C-0473(B) | SII+62 | 600 |
| 2019 Feb | HAWK-I | 102.C-0473(D) | H2 | 1680 |

[a] ESO program IDs.

## 6.2 Observations and data reduction

The dataset for the proper motions study consists of optical and NIR narrow-band imaging of the outflow. The proper motions of the outflow are investigated in the [S II] narrow-band filter in the optical domain, centred around the bright [S II] emission line at 6731 Å. The proper motions of the outflow are also investigated in the $H_2$ narrow-band filter in the NIR, centred around the bright molecular hydrogen emission line at 2.12 μm. The images were reduced following the standard procedure outlined by the respective instruments manuals. These procedures are largely similar and consist of bias and dark frame subtraction, flat-fielding, sky subtraction, alignment of multiple exposures, and median combining.

Table 6.2 summarises the dataset used for the project. What is listed in this table is the epoch of the observation, the instrument used, the program ID, the narrow-band filter used, and the total exposure time. These observations are presented in more detail below. Figure 6.2 displays a schematic of the observations timeline, including the time interval between subsequent observations.

### 6.2.1 EMMI 1991 observations

Imaging observations of the HH 46/47 outflow were obtained with ESO's EMMI, installed on the NTT at La Silla Observatory, on the 19$^{\text{th}}$ of December 1991 under ESO Program ID 043.03.003. The observations were obtained using the 'S II' narrow-band filter, centred at 6732 Å and having a FWHM of 72 Å, using EMMI's 'red arm' imager. The FOV of the observation was $7\farcm5 \times 7\farcm5$, which provided a spatial sampling of $0\farcs44$ pixel$^{-1}$ using EMMI's THX31156

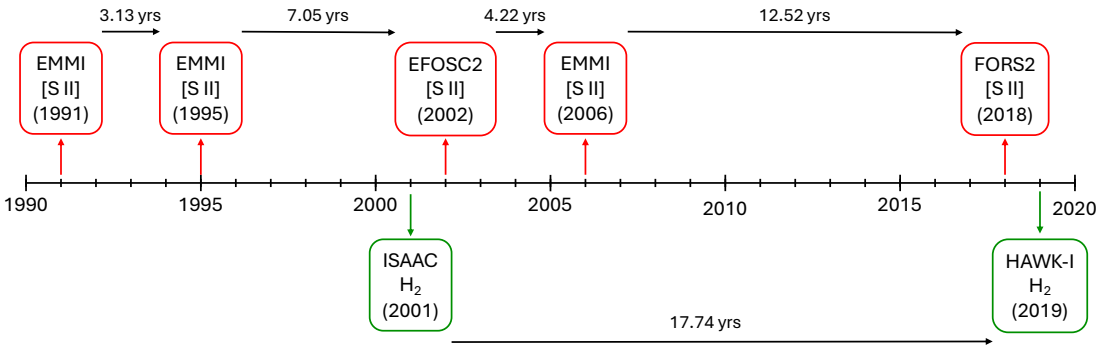


FIGURE 6.2: Schematic of the observation timeline for data used in the proper motion study.

1024 detector (ESO CCD#18) (D'Odorico, 1990). The observations consisted of three exposures of 900 s each, providing an on target exposure time of 2700 s. The average seeing of the science observation was $0\farcs84$ and the average airmass was 1.150.

### 6.2.2 EMMI 1995 observations

Imaging observations of the HH 46/47 outflow were obtained with ESO's EMMI, installed on the NTT at La Silla Observatory, on the 7$^{\text{th}}$ of February 1995 under ESO Program ID 054-d-0828 (PI: B. Reipurth). The observations were obtained using the 'S II' narrow-band filter, centred at 6732 Å and having a FWHM of 72 Å, using EMMI's 'red arm' imager. The FOV of the observation was $8\farcm9 \times 8\farcm9$, which provided a spatial sampling of $0\farcs26$ pixel$^{-1}$ using EMMI's TEK 2048EB detector (ESO CCD#36)[1]. The observations consisted of a single exposure of 1800 s. The average seeing of the science observation was $1\farcs12$ and the average airmass was 1.105.

### 6.2.3 EFOSC2 2002 observations

Imaging observations of the HH 46/47 outflow were obtained with ESO's EFOSC2, installed on the ESO-3.6 metre telescope at La Silla Observatory, on the 25th of February 2002 under ESO Program ID 060.A-9018(A). The observations were obtained using the '[SII]' narrow-band filter, centred at 6730 Å and having a FWHM of 62 Å. The FOV of the observation was $4\farcm1 \times 4\farcm1$, which

[1]EMMI and SUSI operating manual

provided a spatial sampling of $0\farcs12$ pixel$^{-1}$ using EFOSCS2's MPP 2048 detector (ESO CCD#40)[2]. A $2 \times 2$ binning was applied, resulting in the observation having a spatial resolution of $0\farcs24$ pixel$^{-1}$. The observations consisted of five exposure of 600 s each, resulting in a total integration time of 3000 s. The average seeing of the science observation was $0\farcs95$ and the average airmass was 1.407.

### 6.2.4 EMMI 2006 observations

Imaging observations of the HH 46/47 outflow were obtained with ESO's EMMI, installed on the NTT at La Silla Observatory, on the 14$^{\text{th}}$ of May 2006 under ESO Program ID 077.C-0047(B) (PI: A. Caratti o Garatti). The observations were obtained using the 'S II' narrow-band filter, centred at 6732 Å and having a FWHM of 72 Å, using EMMI's 'red arm' imager. The FOV of the observation was $4\farcm5 \times 9\farcm0$, which provided a spatial sampling of $0\farcs1665$ pixel$^{-1}$ using EMMI's 2048 $\times$ 4096 MIT LL mosaic detector (ESO CCD#20-14-5-3)[3]. The observations consisted of a two exposures of 1800 s each, providing a total integration time of 3600 s. The average seeing of the science observation was $0\farcs85$ and the average airmass was 1.298.

### 6.2.5 FORS2 2018 observations

Imaging observations of the HH 46/47 outflow were obtained with ESO's FORS2, installed on UT1 of ESO's VLT at Paranal Observatory, on the 15th of November 2018 under ESO Program ID 0102.C-0473(B) (PI: B. Reipurth). The observations were obtained using the 'SII+62' narrow-band filter, centred at 6728 Å and having a FWHM of 66 Å. The FOV of the observation was $7\farcm1 \times 7\farcm1$, which provided a spatial sampling of $0\farcs25$ pixel$^{-1}$, using FORS2's standard resolution collimator and the 2k $\times$ 4k MIT CCD[4]. The observations consisted of a sixteen exposures of 37.5 s each, providing a total integration time of 600 s. The average seeing of the science observation was $0\farcs66$ and the average airmass was 1.214.

[2]EFOSC2 user manual
[3]EMMI ESO information webpage
[4]FORS2 user manual

### 6.2.6 ISAAC 2001 observations

Imaging observations of the HH 46/47 outflow were obtained with ESO's ISAAC, installed on UT3 of ESO's VLT at Paranal Observatory, on the 2$^{nd}$ of May 2001 under ESO Program ID 67.C-0600(A) (PI: H. Zinnecker). The observations were obtained using the 'NB 2.13' narrow-band filter, centred at 2.13 μm and having a FWHM of 0.03 μm. The FOV of the observation was 2′.5 × 2′.5, which provided a spatial sampling of 0″.148 pixel$^{-1}$, using ISAAC's short-wavelength (SW) imaging mode and the Hawaii 1024 × 1024 Rockwell CCD[5]. The observations consisted of a eight exposures of 60 s each, providing a total integration time of 480 s. The average seeing of the science observation was 0″.56 and the average airmass was 1.124.

In the $H_2$ observation obtained with ISAAC, the sky-subtraction step of data reduction could not be performed, as the sky frames were not offset from the outflow by a sufficient amount, and therefore contained outflow emission. These sky frames could not be subtracted from the science observations as this resulted in spurious dark regions in the science image that corresponded to outflow emission in the sky frames. As the sky-subtraction could not be performed a known instrumental aberration is present in the science image, that is normally eliminated, or greatly reduced, with sky subtraction. This aberration appears as circular arcs caused by instrumental scattered light due to the long-wavelength (LW) imaging mode open filter position which is immediately adjacent to the SW filter.

### 6.2.7 HAWK-I 2019 observations

Imaging observations of the HH 46/47 outflow were obtained with ESO's HAWK-I, installed on UT4 of ESO's VLT at Paranal Observatory, on the 23$^{rd}$ of January 2019 under ESO Program ID 0102.C-0473(D) (PI: B. Reipurth). The observations were obtained using the 'H2' narrow-band filter, centred at 2.124 μm and having a FWHM of 0.030 μm. The FOV of the observation was 7′.5 × 7′.5, which provided a spatial sampling of 0″.106 pixel$^{-1}$, using HAWK-I's mosaic of four Hawaii 2RG 2048 × 2048 detectors[6]. The observations consisted of a twenty exposures of 84 s each, providing a total integration time of 1680 s.

[5]ISAAC user manual
[6]HAWK-I user manual

The average seeing of the science observation was $0\farcs63$ and the average airmass was 1.12.

## 6.3 Astrometric alignment

In order to study the temporal evolution of the outflow between observing epochs, an astrometric solution, or a geometric shifting, rotating, and scaling solution, needed to be derived between two epochs. This solution was derived by identifying point sources present in the FOVs of both observations. The background stars, which are assumed to have negligible proper motions in comparison to that of the outflow, were used as a reference point for this astrometric solution, and identified stars with high proper motions were not used. The python package ASTROALIGN (Beroiz, Cabral, and Sanchez, 2020) was used to calculate the astrometric solution. This package registers or aligns two images by finding similar 3-point asterisms, or constellations, in both images and estimates the affine transformation between the two asterisms. This method improves upon generic registration routines which attempt to match single point sources using corner detection routines to make the point-to-point correspondence. As the dataset used in this study contained observations taken with different instruments and telescopes, and the fact that point sources are relatively indistinguishable from one another, asterism matching was selected to reproject the images, therefore aligning them. This method is robust as it is not affected by differences between PSFs and seeing conditions. The routine does not suffer from lack of background stars, as there are many background stars in the fields, and so uncertainties in the registration are low. Point sources not bright enough to pass a $5\sigma$ threshold were not considered in the source detection process.

In order to avoid the routine interpreting adverse effects such as hot pixels in the images as source detections, the images were first cleaned using CCDProc's (Craig et al., 2017) `cosmicray_lacosmic` routine. This routine detects and removes unfavourable pixel detections, such as cosmic rays, from astronomical images. The algorithm is based on the cosmic ray identification algorithm (Dokkum, 2001), which identifies bright, sharp, and isolated pixels in astronomical images, using Laplacian edge detection, and replaces these pixels with interpolated values from neighbouring pixels. The outflow region was masked before the registration process so that outflow features would not

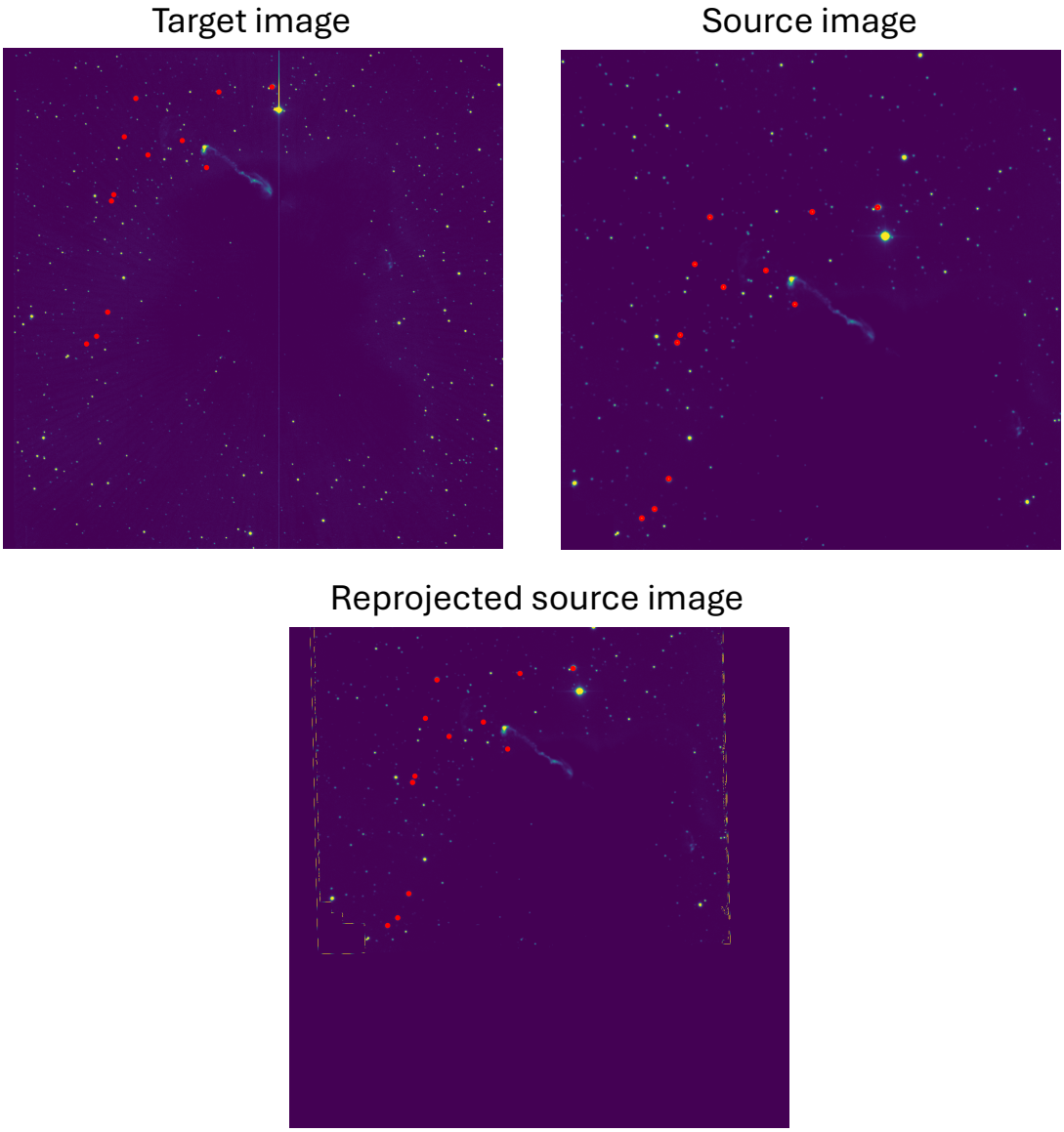


FIGURE 6.3: Example affine transformation solution between two epochs of observations using the ASTROALIGN package.

be considered. In order to achieve a more accurate transformation, the ASTROALIGN package was given an estimated affine transformation retrieved from manual star centroid measurements. A selection of corresponding suitable background stars were identified in both images and the centroids of the stars were measured using 2D Gaussian fitting. These star-to-star correspondences were input to the ASTROALIGN package as an initial guess of the transformation required to align the two observations. An example of this routine is illustrated in Figure 6.3 where the red-dots represent manually measured star centroids as the initial estimate of the affine transformation.

## 6.4 Results

The following describes the shock feature identification and centroid measurement performed on each pair of observations. Bright shock features in the outflow were identified manually in each observation. Identified shock features common to both epochs were selected to perform proper motions measurements. The centroids of the shock features were measured using 2D Gaussian fitting, as this method was the most robust, allowed sub-pixel accuracy, and handled noise well, as the Gaussian fit averages over the pixels. Other methods were ruled out for different reasons. Intensity based centroiding, obtaining the weighted mean of the brightness distribution, was found to be heavily affected by noise in the image, therefore shifting the measured centroid, and did not work as expected for fainter shock features. PSF photometry was also not selected as this method requires a well-chosen PSF for accurate fitting of the shock features, and requires the assumption that the shock features are relatively point-like. A potentially more accurate method for finding the centroids of the shock features is a 2D cross-correlation method. This method works well with faint shock features and the template used in the cross-correlation can be the shock feature itself, meaning that assuming the shock is approximately Gaussian-shaped is not required. However, this method was deemed too slow and computationally expensive for the number of identified shock features.

As the 2D Gaussian fitting method was selected to measure the positions of shock features, an assumption was made that the shock features could be approximated well by Gaussian profiles. In reality the shock features were not symmetric around their peak like Gaussian profiles. Instead, the brightness

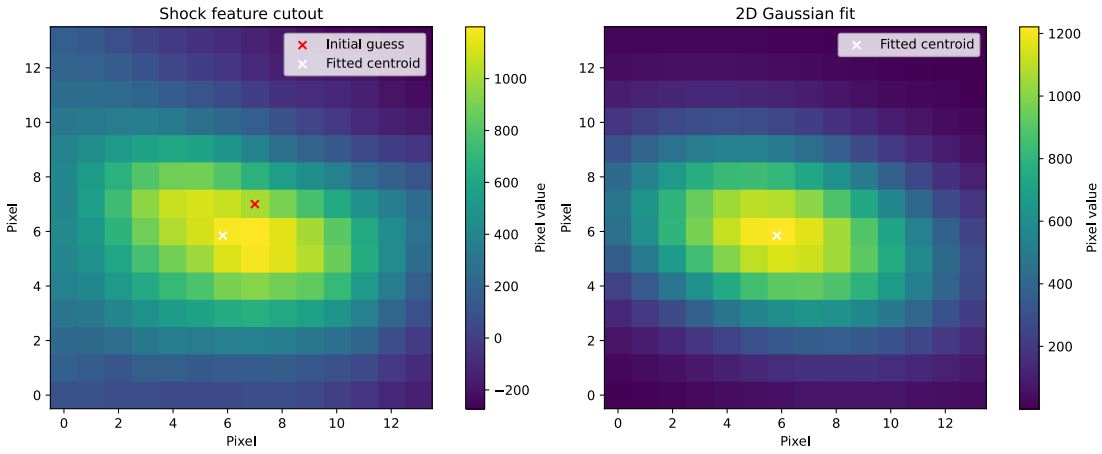


FIGURE 6.4: Example of shock feature centroid retrieval using 2D Gaussian fitting routine. The initial guess of the centroid position is represented by a red cross symbol, and the centroid of the fit is represented by the white cross symbol.

peaks of the shock features tended to be shifted in direction of the flow. However, this potential mismeasurement in the centroid positions is mitigated by the fact that this Gaussian profile assumption was applied in the measurement of the shock feature centroid in both observations, resulting in the relative motion of the centroid position being accurate. Furthermore, the morphology of the shock features did not change drastically between observations and therefore similar Gaussian profiles were fit to corresponding shock features between the observations. The approximate positions of the identified shock features were input into the 2D Gaussian fitting routine and a small rectangular region was extracted around this position. A 2D Gaussian profile was then fit to the shock feature in the region and the centroid of the fit was returned. Each Gaussian fit was inspected visually, and the residual between the shock feature and fit was calculated, to ensure accurate fits. An example of the 2D Gaussian fitting routine is illustrated in Figure 6.4.

### 6.4.1 The proper motions in [S II] emission

Firstly, the proper motions of the HH 46/47 outflow in the [S II] emission line at 6731 Å were investigated. It was decided that the better spatial resolution and seeing observations would be reprojected to match the corresponding lesser spatially resolved images. This approach was chosen to avoid introducing interpolation errors associated with reprojecting lower spatial resolution observations onto the higher. A caveat of this decision is that the superior spatial

resolution data is degraded in order to align with the coarser pixel grid of the lower spatial resolution data, potentially obscuring fine shock features. However, this loss is not critical to the analysis, as the finer shocks are inherently not resolved in the lower spatial resolution data, meaning that they are not relevant in the measurement of proper motions. The shock features were labelled numerically with approximately increasing distance from the driving source of the outflow. The prefix 'B' was assigned to denote shock features identified in the blueshifted outflow, and the prefix 'R' was assigned to denote shock features identified in the redshifted outflow. Further to this, the shock features are preceded by another prefix to denote which pair of observations the proper motions are calculated from. The identified corresponding shock features present in the EMMI 1991 data and EMMI 1995 data are preceded by the prefix '9195', with '91' representing the epoch of the older observations and '95' representing the epoch of the newer observations. This prefix convention is used for each subsequent proper motion observation pair. This section presents difference images that highlight the movement of the outflow between observing epochs. In the case of these difference images, the two individual images are independently normalised prior to subtraction. Furthermore, as the driving source of the outflow is not visible at optical wavelengths, the source position is not measured in these observations. However, the approximate source position, obtained from an infrared IRAC (Infrared Array Camera) Spitzer image (Hartigan et al., 2005), is marked with a plus symbol to provide a reference point.

**1991 – 1995 epoch**

The EMMI 1995 data was first reprojected onto the EMMI 1991 data. Figure 6.5 displays the difference between the two observation epochs in [S II] 6731 Å emission, where white represents the EMMI 1995 observation, and black represents the preceding EMMI 1991 observation. It is clear from this figure that the outflow moves radially away from the source position, with the shock features exhibiting a leading white edge and a trailing black edge. The tip of the reflection nebula along the outflow cavity, on the northern side of the outflow, varied between the two observation epochs, appearing bright in this image, meaning that this region of the reflection nebula increased in brightness between the observations. This may arise due the quasi-stationary deflection shock, where the jet collides obliquely with the edge of the evacuated cavity

(Hartigan et al., 2011). The faint bow shock, extended further from the source position than the bright bow shock that the northeastern outflow terminates in, is very faint in this image due to the low intensity of the shock in both observations. This faint bow shock is shown in panel 1 of Figure 6.6.

Figure 6.6 displays the EMMI 1991 narrow-band image of the HH 46/47 outflow in [S II] 6731 Å emission. Fifteen resolved shock features, labelled 'B1 – B15', were identified in the blueshifted outflow, pointing north-east, in both observations. Four resolved shock features, labelled 'R1 – R4', were identified in the redshifted outflow, pointing south-west, in both observations. These identified shock features, which are resolved in both observations, are labelled in Figure 6.6. The proper motions of these shock features were derived by calculating the differences in their centroid positions as measured by the 2D Gaussian fitting. Table 6.3 presents the proper motions of the shock features. The first column of the table displays the shock feature identifications, preceded by the prefix '9195', corresponding to those in Figure 6.6. The table presents the difference ($\Delta x$ and $\Delta y$) in the $x$ and $y$ positions of the centroids in units of milliarcseconds, where the positive $x$ axis is west-pointing, and the positive $y$ axis is north-pointing. The proper motions of the shocks are presented in milliarcseconds per year (mas yr$^{-}$1), where the time elapsed between the EMMI 1991 and EMMI 1995 observations is approximately 3.13 years. The PA of the shock features is also presented, estimated by deriving the trajectory of the shock features movement between observations. The tangential velocities ($v_{\perp}$) of the shocks are given, and the true, 3D space velocity ($v_{\rm space}$) of the shocks was estimated assuming that the outflow has an inclination angle of 37° with respect to the plane of the sky (Hartigan et al., 2005).

The average tangential velocity of the internal shocks within the blueshifted jet, calculated by obtaining the mean tangential velocities of the 9195B1 – 9195-B11 shock features from Table 6.3, is $v_{\perp} = 287$ km s$^{-1}$. The bright bow shock that the twisting blueshifted jet terminates in, known as HH 47A (Dopita, Schwartz, and Evans, 1982) and visible in the upper left of panel 2 in Figure 6.6, has a tangential velocity of $v_{\perp} = 295$ km s$^{-1}$, estimated here from the 9195B12 shock feature. The bright HH 47A feature is however more complex than a single bow shock and instead contains numerous clumps that move relative to one another creating a complex morphology within the bow shock (Hartigan et al., 2005). Here, the bulk proper motions of the bow shock are presented. The fainter bow shock, extended further than the HH 47A bow shock, known

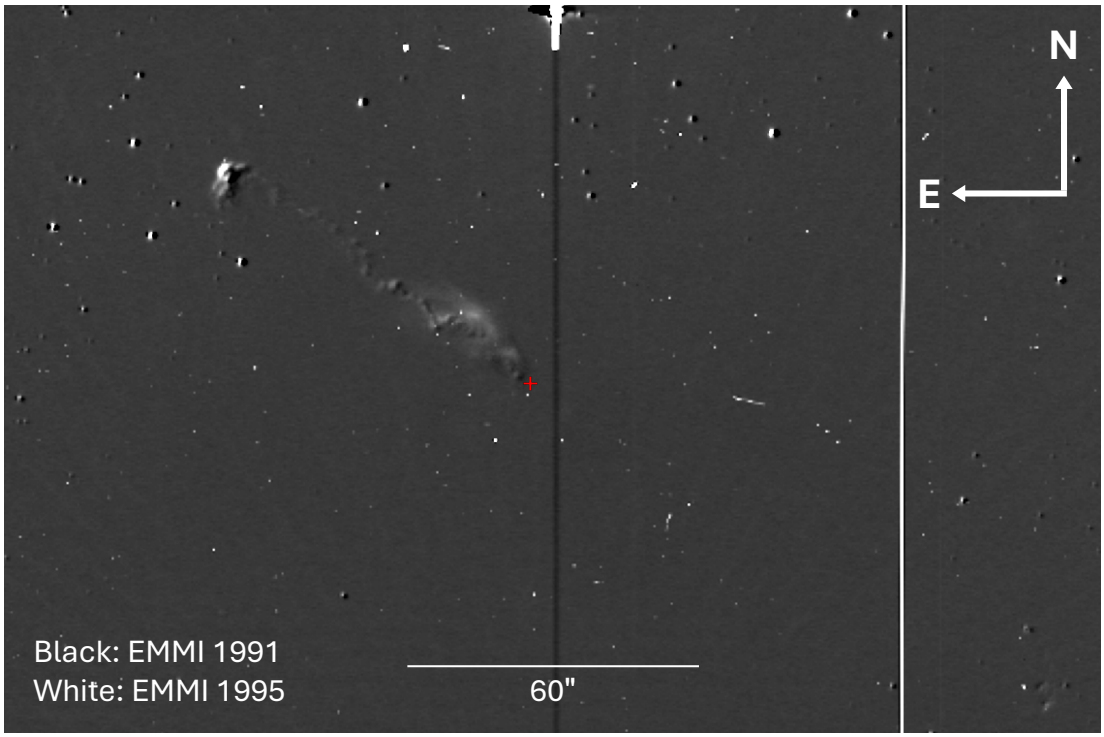


FIGURE 6.5: Difference between the EMMI 1995 observation and the EMMI 1991 observation in [S II] 6731 Å emission. White represents the EMMI 1995 observation, and black represents the preceding EMMI 1991 observation. The approximate source position is marked with a red-plus symbol. The shock features in the outflow move radially away from the source position, exhibiting leading white edges and a trailing black edges. The tip of the reflection nebula along the outflow cavity, on the northern side of the outflow, appears bright in this image.

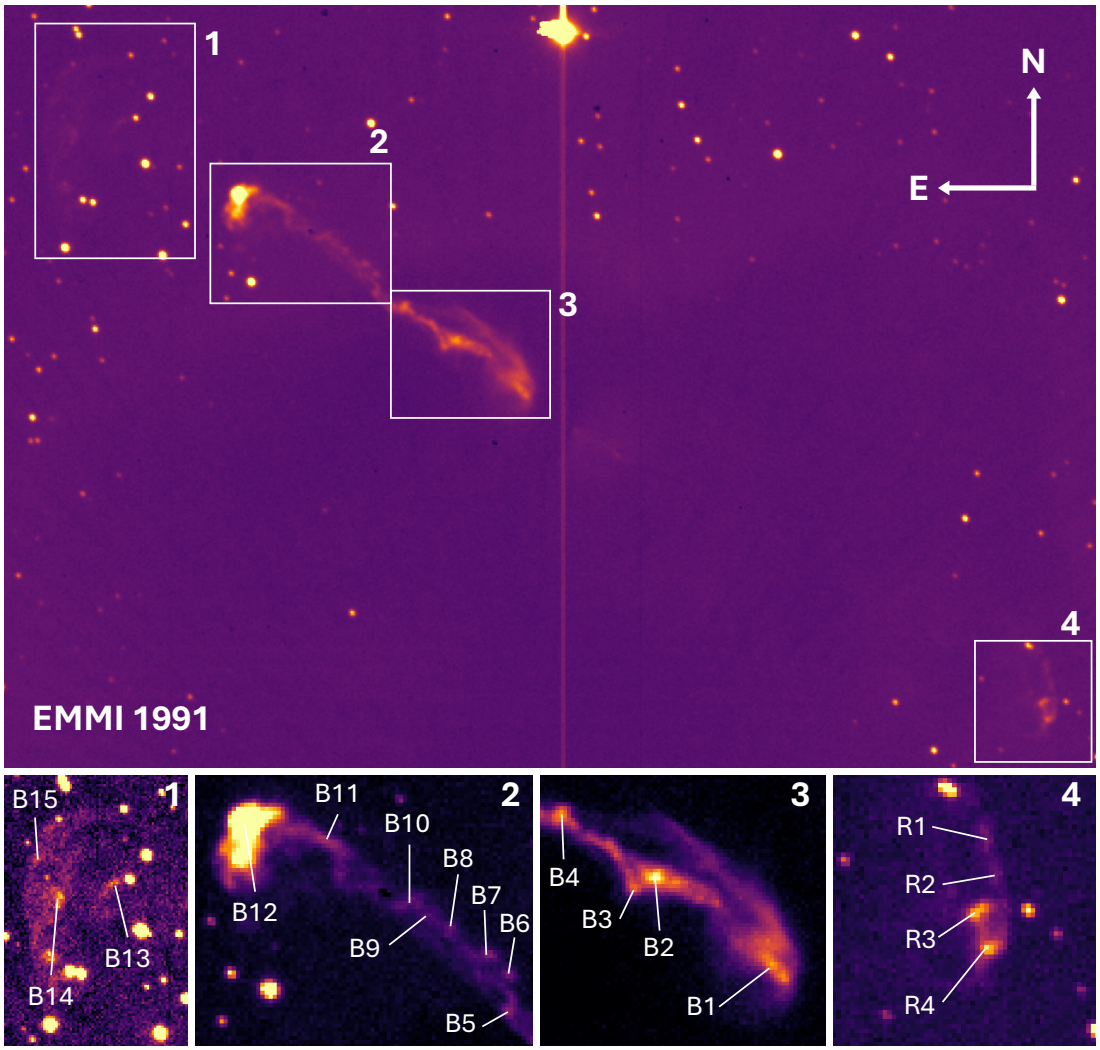


FIGURE 6.6: EMMI 1991 narrow-band image of the HH 46/47 outflow in [S II] 6731 Å emission. Identified shock features, resolved in both the EMMI 1991 data and EMMI 1995 data, are labelled in the panels 1, 2, 3, and 4. The prefix 'B' denotes shock features identified in the blueshifted outflow, and the prefix 'R' denotes those identified in the redshifted outflow.

TABLE 6.3: Proper motions of identified shock features in HH 46/47 outflow in [S II] 6731 Å emission from December 1991 – February 1995.

| ID[a] | $\Delta x$ [b] | $\Delta y$ [b] | $\mu$ (mas yr$^{-1}$) | PA (°) | $v_\perp$ [c] | $v_{\rm space}$ [c] |
|---|---|---|---|---|---|---|
| B1 | − 282 | + 172 | 106 | 59 | 226 | 283 |
| B2 | − 393 | + 216 | 144 | 61 | 306 | 384 |
| B3 | − 401 | + 125 | 134 | 73 | 287 | 359 |
| B4 | − 433 | + 231 | 157 | 62 | 335 | 419 |
| B5 | − 455 | + 85 | 148 | 79 | 316 | 395 |
| B6 | − 448 | + 347 | 181 | 52 | 386 | 484 |
| B7 | − 455 | + 204 | 159 | 66 | 340 | 426 |
| B8 | − 317 | + 77 | 104 | 76 | 222 | 278 |
| B9 | − 526 | + 307 | 195 | 59 | 416 | 520 |
| B10 | − 21 | + 285 | 91 | 4 | 195 | 244 |
| B11 | − 181 | + 30 | 59 | 80 | 125 | 157 |
| B12 | − 416 | + 119 | 138 | 74 | 295 | 370 |
| B13 | − 530 | + 30 | 170 | 87 | 362 | 454 |
| B14 | − 66 | − 190 | 64 | 161 | 137 | 171 |
| B15 | − 86 | − 107 | 44 | 141 | 94 | 118 |
| R1 | + 68 | − 400 | 130 | 190 | 278 | 348 |
| R2 | + 79 | − 87 | 37 | 222 | 80 | 100 |
| R3 | + 108 | − 73 | 42 | 236 | 89 | 112 |
| R4 | + 49 | − 208 | 68 | 193 | 146 | 182 |

[a] Identified shock features are preceded by the prefix 9195.
[b] $\Delta x$ and $\Delta y$ are measured in mas.
[c] $v_\perp$ and $v_{\rm s}$ are measured in km s$^{-1}$.

as HH 47D (Dopita, Schwartz, and Evans, 1982) and highlighted in panel 1 of Figure 6.6, has a mean tangential velocity of $v_{\perp} = 197$ km s$^{-1}$, obtained from the mean velocities of the 9195B13 – 9195B15 shock features. The faint shock features near the base of the redshifted outflow were not well-fit by 2D Gaussian profiles in both observations and therefore their proper motions are not reported here. The bow shock that the redshifted outflow terminates in, known as HH 47C (Dopita, Schwartz, and Evans, 1982) and highlighted in panel 4 of Figure 6.6, has a mean tangential velocity of $v_{\perp} = 157$ km s$^{-1}$, obtained from the mean velocities of the 9195R1 – 9195R4 shock features.

The PAs of the shock features in the blueshifted outflow approximate to the same direction as the average PA of the atomic jet, 52.3° from Erkal et al. (2021b), and the central axis of the wide-angled CO outflow, $\sim 60°$ from Zhang et al. (2019). The PA of the atomic jet, calculated from the mean PAs of the 9195B1 – 9195B11 shock features, is 67°, implying that the shock features movement between the epochs is more easterly than the average jet PA of 52.3° obtained from HST 2019 observations of the jet. The shock 9195B10 is an outlier within the jet axis, with an estimated PA of 4°, implying the shock has moved almost vertically in the northern direction between the observations. The PAs of the shock features (9195B13 – 9195B15) in the faint HH 47D bow shock are higher than that of the atomic jet, with PAs of 87° to 161°. This implies that these regions of the bow shock are moving laterally away from the jet axis to a greater extent than in the direction of the flow, displaying that the bow shock is most likely expanding in all directions and growing wider. This is further supported by the negative difference ($-\Delta y$) in the $y$ positions of the 9195B14 and 9195B15 centroids in Table 6.3. The average PA of the redshifted outflow bow shock, HH 47C, is 210° calculated from the average of the 9195R1 – 9195R4 PAs.

**1995 – 2002 epoch**

Next, the EMMI 1995 data was reprojected onto the EFOSC2 2002 data. Although the EFOSC2 observation was more recent, the spatial resolution of the EMMI data was higher and therefore it was reprojected onto the lower spatial resolution EFOSC2 data. Figure 6.7 displays the difference between the two observation epochs in [S II] 6731 Å emission, where white represents the EFOSC2 2002 observation, and black represents the preceding EMMI 1995 observation.

It is again clear that the outflow moves radially away from the source position, with the shock features exhibiting a leading white edge and a trailing black edge. Interestingly, the reflection nebula along the outflow cavity, on the northern side of the outflow, again varied between the two observation epochs, appearing dark in this image. This implies that this region of the reflection nebula dimmed between the observations.

Figure 6.8 displays the EMMI 1995 narrow-band image of the HH 46/47 outflow in [S II] 6731 Å emission. Thirteen resolved shock features, labelled 'B1 – B13', were identified in the blueshifted outflow, pointing north-east, in both observations. Five resolved shock features, labelled 'R1 – R5', were identified in the redshifted outflow, pointing south-west, in both observations. These identified shock features are labelled in Figure 6.8. These features do not have a shock-to-shock correspondence with those identified in the EMMI 1991 to EMMI 1995 observations labelled in Figure 6.6, hence the prefix '9502'. Table 6.4 presents the proper motions of these shock features. The first column again displays the shock feature identifications, preceded by the prefix '9502', corresponding to those in Figure 6.8. The difference ($\Delta x$ and $\Delta y$) in the $x$ and $y$ positions of the centroids in units of milliarcseconds are presented, and the proper motions of the shocks are presented in milliarcseconds per year (mas yr$^{-}$1), where the time elapsed between the EMMI 1995 and EFOSC2 2002 observations is approximately 7.05 years. The PA of the shock features is also presented, estimated by deriving the trajectory of the shock features movement between observations. The tangential velocities ($v_{\perp}$) of the shocks are given, and the true, 3D space velocity ($v_{\rm space}$) of the shocks was estimated assuming that the outflow has an inclination angle of 37° with respect to the plane of the sky (Hartigan et al., 2005).

The average tangential velocity of the internal shocks within the blueshifted jet, calculated by obtaining the mean tangential velocities of the 9502B1 – 9502-B9 shock features from Table 6.4, is $v_{\perp} = 190$ km s$^{-1}$, lower than in the 1991 – 1995 epoch (287 km s$^{-1}$). The bright HH 47A bow shock, visible in the upper left of panel 2 in Figure 6.8, has a tangential velocity of $v_{\perp} = 128$ km s$^{-1}$, estimated here from the 9502B10 shock feature, which is lower than what is measured in the 1991 – 1995 epoch (295 km s$^{-1}$). The fainter HH 47D bow shock, highlighted in panel 1 of Figure 6.8, has a mean tangential velocity of $v_{\perp} = 68$ km s$^{-1}$, obtained from the mean velocities of the 9502B11 – 9502B13 shock features, again much lower than in the 1991 – 1995 epoch (197 km s$^{-1}$).

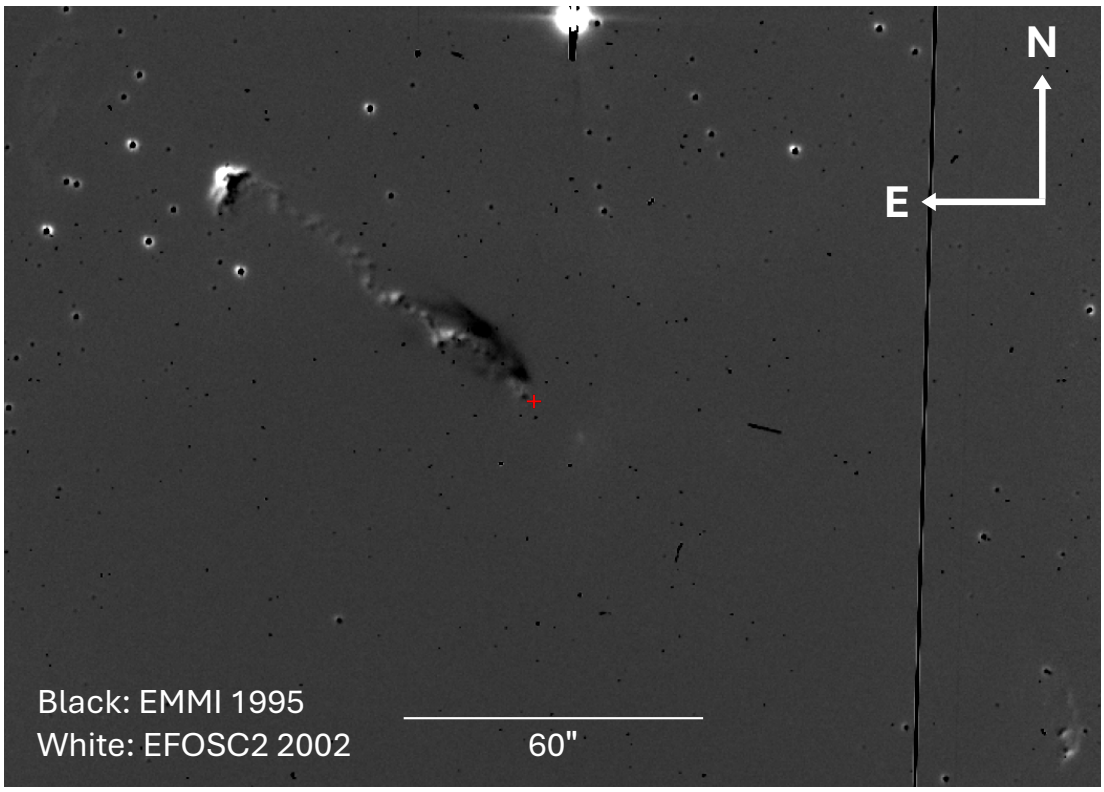


FIGURE 6.7: Difference between the EFOSC2 2002 observation and the EMMI 1995 observation in [S II] 6731 Å emission. White represents the EFOSC2 2002 observation, and black represents the preceding EMMI 1995 observation. The approximate source position is marked with a red-plus symbol. The shock features in the outflow move radially away from the source position, again exhibiting leading white edges and a trailing black edges. The reflection nebula along the outflow cavity, on the northern side of the outflow, appears dark in this image.

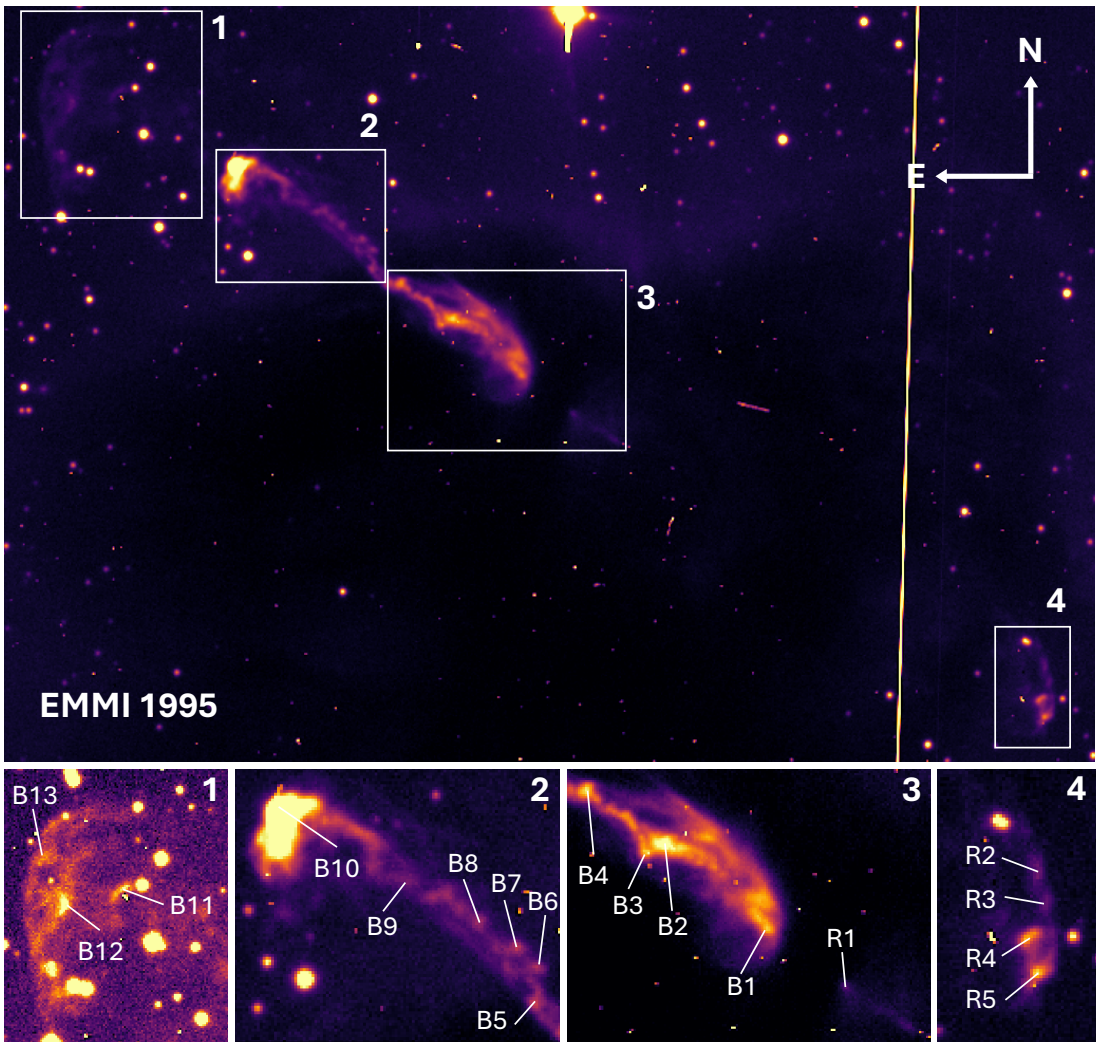


FIGURE 6.8: EMMI 1995 narrow-band image of the HH 46/47 outflow in [S II] 6731 Å emission. Identified shock features, resolved in both the EMMI 1995 data and EFOSC2 2002 data, are labelled in the panels 1, 2, 3, and 4. The prefix 'B' denotes shock features identified in the blueshifted outflow, and the prefix 'R' denotes those identified in the redshifted outflow.

TABLE 6.4: Proper motions of identified shock features in HH 46/47 outflow in [S II] 6731 Å emission from February 1995 – February 2002.

| ID[a] | $\Delta x$ [b] | $\Delta y$ [b] | $\mu$ (mas yr$^{-1}$) | PA (°) | $v_\perp$ [c] | $v_{\rm space}$ [c] |
|---|---|---|---|---|---|---|
| B1 | − 677 | + 873 | 157 | 38 | 334 | 418 |
| B2 | − 639 | + 291 | 99 | 65 | 212 | 265 |
| B3 | − 520 | + 395 | 93 | 53 | 197 | 247 |
| B4 | − 454 | + 324 | 79 | 55 | 169 | 211 |
| B5 | − 600 | + 406 | 103 | 56 | 219 | 274 |
| B6 | − 10 | − 29 | 4 | 161 | 9 | 12 |
| B7 | − 662 | + 240 | 100 | 70 | 213 | 267 |
| B8 | − 535 | + 338 | 90 | 58 | 191 | 240 |
| B9 | − 466 | + 284 | 77 | 59 | 165 | 207 |
| B10 | − 350 | + 237 | 60 | 56 | 128 | 160 |
| B11 | − 26 | + 45 | 7 | 30 | 16 | 20 |
| B12 | − 229 | + 210 | 44 | 47 | 94 | 118 |
| B13 | − 202 | + 242 | 45 | 40 | 95 | 119 |
| R1 | + 167 | − 65 | 25 | 249 | 54 | 68 |
| R2 | + 288 | − 255 | 55 | 228 | 116 | 146 |
| R3 | + 177 | + 48 | 26 | 285 | 55 | 69 |
| R4 | + 225 | − 179 | 41 | 231 | 87 | 109 |
| R5 | + 222 | − 303 | 53 | 216 | 114 | 142 |

[a] Identified shock features are preceded by the prefix 9502.
[b] $\Delta x$ and $\Delta y$ are measured in mas.
[c] $v_\perp$ and $v_{\rm s}$ are measured in km s$^{-1}$.

One faint shock feature, labelled 9502R1, near the base of the redshifted outflow was well-fit by a 2D Gaussian profile in both observations and therefore its proper motions could be reported, in contrast to the 1991 – 1995 epoch. The HH 47C bow shock that the redshifted outflow terminates in, seen in panel 4 of Figure 6.8, has a mean tangential velocity of $v_{\perp} = 93$ km s$^{-1}$, obtained from the mean velocities of the 9502R2 – 9502R5 shock features.

The PA of the atomic jet, calculated from the mean PAs of the 9502B1 – 9502B9 shock features, is 68°, implying that the shock features movement between the epochs is again more easterly than the average jet PA of 52.3° (Erkal et al., 2021b). The shock 9502B6 is an outlier within the jet axis, with an estimated PA of 161°, implying the shock has moved almost horizontally in the eastern direction between the observations. The PAs of the shock features (9502B11 – 9502B13) in the faint HH 47D bow shock are lower than that of the atomic jet, with PAs of 30° to 47°. This is in contrast with the 1991 – 1995 epoch, with the shocks exhibiting movement in a more northerly direction to the jet axis. The average PA of the redshifted outflow bow shock, HH 47C, is 240° calculated from the average of the 9502R2 – 9502R5 PAs.

**2002 – 2006 epoch**

Next, the EMMI 2006 data was reprojected onto the EFOSC2 2002 data. Figure 6.9 displays the difference between the two observation epochs in [S II] 6731 Å emission, where white represents the EMMI 2006 observation, and black represents the preceding EFOSC2 2002 observation. It is again clear that the outflow moves radially away from the source position, with the shock features exhibiting a leading white edge and a trailing black edge. Similar to the 1991 – 1995 difference image, presented in Figure 6.5, the reflection nebula along the outflow cavity, on the northern side of the outflow appears slightly bright in this image. This implies that this region of the reflection nebula has increased in brightness between the observations.

Figure 6.10 displays the EFOSC2 2002 narrow-band image of the HH 46/47 outflow in [S II] 6731 Å emission. Twelve resolved shock features, labelled 'B1 – B12', were identified in the blueshifted outflow, pointing north-east, in both observations. Five resolved shock features, labelled 'R1 – R5', were identified in the redshifted outflow, pointing south-west, in both observations. These identified shock features are labelled in Figure 6.10. Table 6.5 presents the

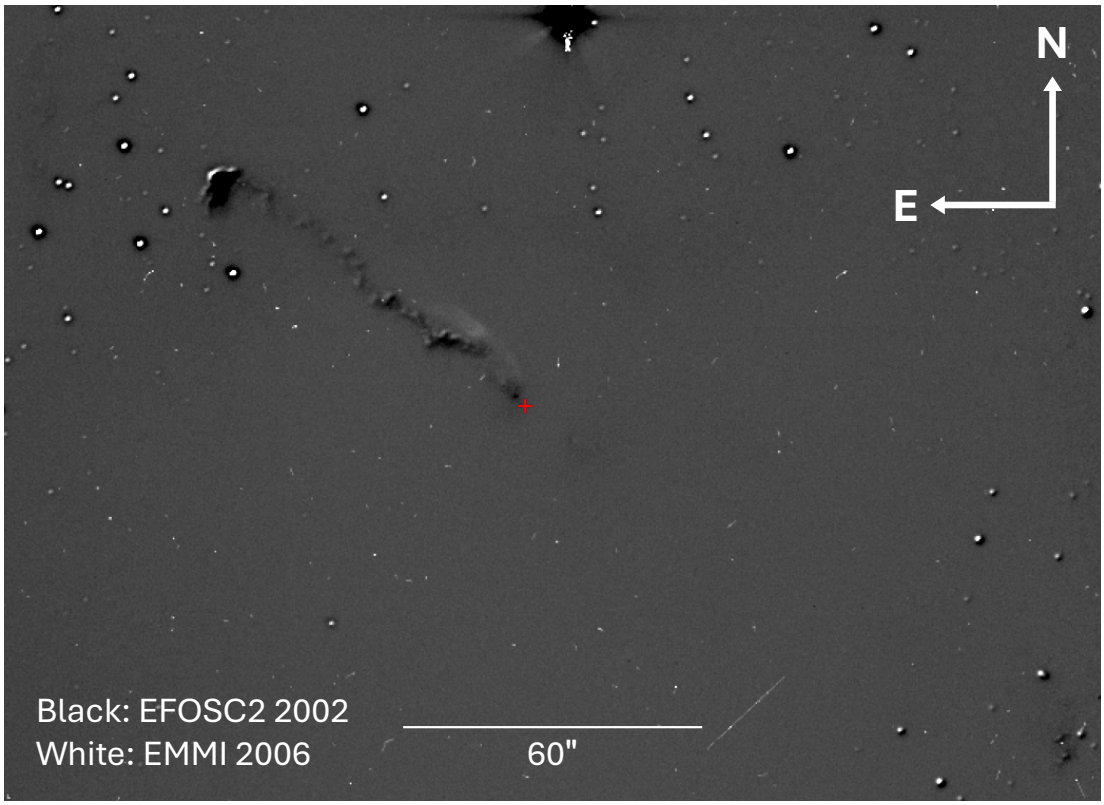


FIGURE 6.9: Difference between the EMMI 2006 observation and the EFOSC2 2002 observation in [S II] 6731 Å emission. White represents the EMMI 2006 observation, and black represents the preceding EFOSC2 2002 observation. The approximate source position is marked with a red-plus symbol. The shock features in the outflow move radially away from the source position, again exhibiting leading white edges and a trailing black edges. The reflection nebula along the outflow cavity, on the northern side of the outflow, appears bright in this image.

proper motions of these shock features. The first column again displays the shock feature identifications, preceded by the prefix '0206', corresponding to those in Figure 6.10. The difference ($\Delta x$ and $\Delta y$) in the $x$ and $y$ positions of the centroids in units of milliarcseconds are presented, and the proper motions of the shocks are presented in milliarcseconds per year (mas yr$^{-}$1), where the time elapsed between the EFOSC2 2002 and EMMI 2006 observations is approximately 4.22 years. The PA of the shock features is also presented, estimated by deriving the trajectory of the shock features movement between observations. The tangential velocities ($v_{\perp}$) of the shocks are given, and the true, 3D space velocity ($v_{\rm space}$) of the shocks was estimated assuming that the outflow has an inclination angle of 37° with respect to the plane of the sky (Hartigan et al., 2005).

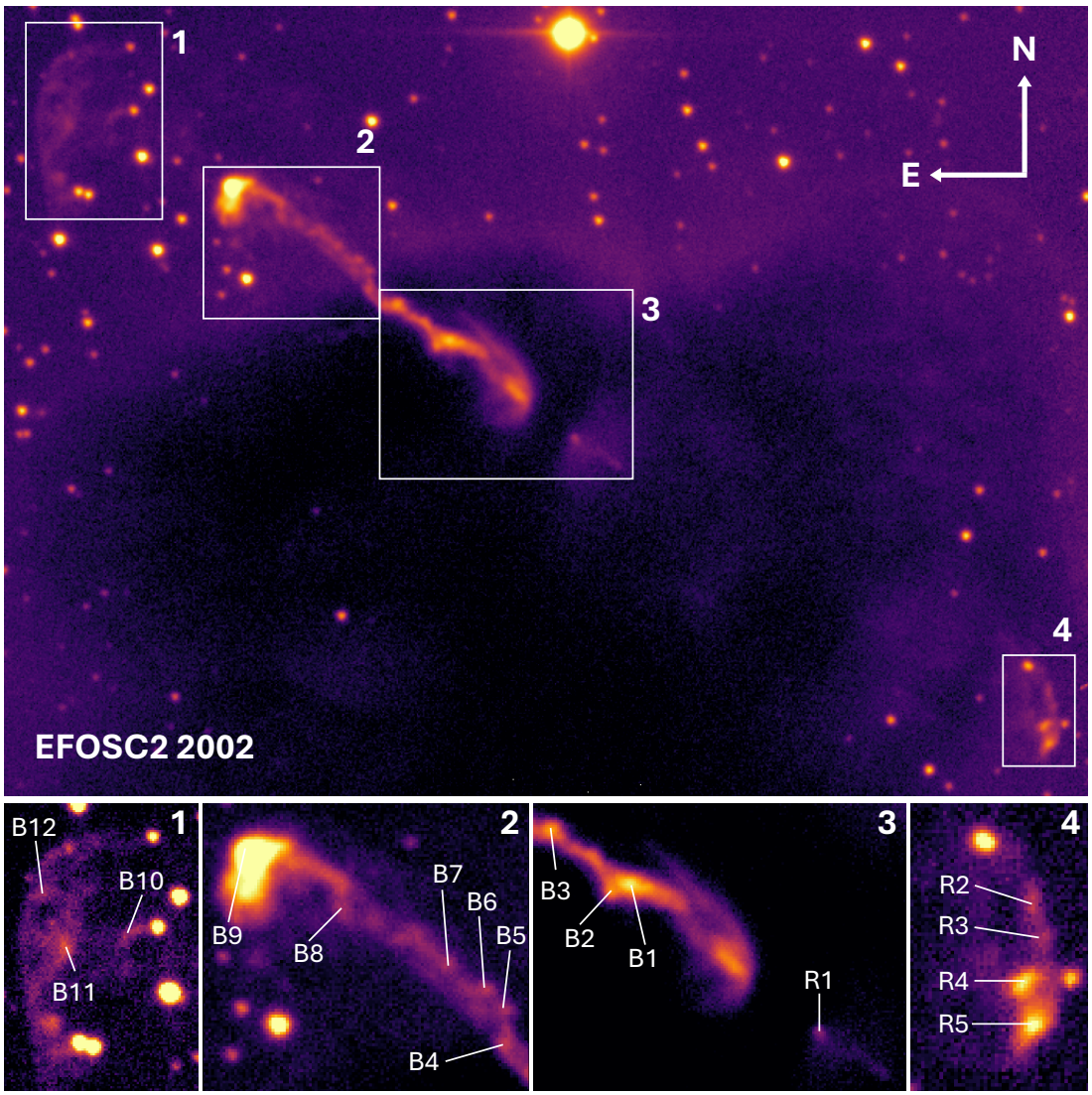


FIGURE 6.10: EFOSC2 2002 narrow-band image of the HH 46/47 outflow in [S II] 6731 Å emission. Identified shock features, resolved in both the EFOSC2 2002 data and the EMMI 2006 data, are labelled in the panels 1, 2, 3, and 4. The prefix 'B' denotes shock features identified in the blueshifted outflow, and the prefix 'R' denotes those identified in the redshifted outflow.

TABLE 6.5: Proper motions of identified shock features in HH 46/47 outflow in [S II] 6731 Å emission from February 2002 – May 2006.

| ID[a] | $\Delta x$ [b] | $\Delta y$ [b] | $\mu$ (mas yr$^{-1}$) | PA (°) | $v_\perp$ [c] | $v_{\rm space}$ [c] |
|---|---|---|---|---|---|---|
| B1 | − 165 | + 354 | 93 | 25 | 197 | 247 |
| B2 | − 182 | + 58 | 45 | 72 | 97 | 121 |
| B3 | − 219 | + 324 | 93 | 34 | 198 | 248 |
| B4 | − 231 | + 223 | 76 | 46 | 162 | 203 |
| B5 | − 51 | + 460 | 110 | 6 | 234 | 293 |
| B6 | − 211 | + 398 | 107 | 28 | 228 | 286 |
| B7 | − 207 | + 328 | 92 | 32 | 196 | 246 |
| B8 | − 366 | + 143 | 93 | 68 | 199 | 249 |
| B9 | − 181 | + 459 | 117 | 22 | 250 | 313 |
| B10 | − 35 | + 304 | 73 | 7 | 155 | 194 |
| B11 | − 58 | + 43 | 17 | 54 | 37 | 46 |
| B12 | − 166 | + 144 | 52 | 49 | 111 | 140 |
| R1 | + 195 | − 3 | 46 | 269 | 96 | 123 |
| R2 | + 41 | − 69 | 19 | 211 | 40 | 51 |
| R3 | + 128 | + 649 | 157 | 348 | 335 | 419 |
| R4 | + 4 | + 49 | 12 | 355 | 25 | 31 |
| R5 | + 1 | + 267 | 63 | 0 | 135 | 169 |

[a] Identified shock features are preceded by the prefix 0206.
[b] $\Delta x$ and $\Delta y$ are measured in mas.
[c] $v_\perp$ and $v_{\rm s}$ are measured in km s$^{-1}$.

The average tangential velocity of the internal shocks within the blueshifted jet, calculated by obtaining the mean tangential velocities of the 0206B1 – 0206-B8 shock features from Table 6.5, is $v_{\perp} = 189$ km s$^{-1}$, lower than in the 1991 – 1995 epoch (287 km s$^{-1}$), but in agreement with the 1995 – 2002 epoch (190 km s$^{-1}$). The bright HH 47A bow shock, visible in the upper left of panel 2 in Figure 6.10, has a tangential velocity of $v_{\perp} = 250$ km s$^{-1}$, estimated here from the 0206B9 shock feature. This velocity is higher than in the 1995 – 2002 epoch (128 km s$^{-1}$), and more in line with that measured in the 1991 – 1995 epoch (295 km s$^{-1}$). The faint HH 47D bow shock, seen in panel 1 of Figure 6.10, has a mean tangential velocity of $v_{\perp} = 101$ km s$^{-1}$, obtained from the mean velocities of the 0206B10 – 0206B12 shock features, lower than in the 1991 – 1995 epoch (197 km s$^{-1}$), but higher than the 1995 – 2002 epoch (68 km s$^{-1}$). The faint shock feature, labelled 0206R1, near the base of the redshifted outflow has a tangential velocity of $v_{\perp} = 96$ km s$^{-1}$, slightly higher than the same shock feature's velocity in the 1995 – 2002 epoch (54 km s$^{-1}$). The HH 47C bow shock that the redshifted outflow terminates in, seen in panel 4 of Figure 6.10, has a mean tangential velocity of $v_{\perp} = 134$ km s$^{-1}$, obtained from the mean velocities of the 0206R2 – 0206R5 shock features.

The PA of the atomic jet, calculated from the mean PAs of the 0206B1 – 0206B8 shock features, is 39°, implying that the shock features movement between the epochs is more northerly than the average jet PA of 52.3° (Erkal et al., 2021b), in contrast with the previous measurements presented in this chapter. The average PA of the shock features 0206B10 – 0206B12 in the faint HH 47D bow shock are in line with that of the atomic jet, with a mean PA of 37°. This is in agreement with the estimated PA in the 1995 – 2002 epoch (39°), but in contrast with the 1991 – 1995 epoch, where the shocks exhibit movement in a more easterly direction with respect to the jet axis. The average PA of the redshifted outflow bow shock, HH 47C, is 240° calculated from the average of the 0206R2 – 0206R5 PAs. This is in agreement with that estimated for the 1995 – 2002 epoch (240°), and similar to that estimated for the 1991 – 1995 epoch (210°).

**2006 – 2018 epoch**

Next, the FORS2 2018 data was reprojected onto the EMMI 2006 data. Figure 6.11 displays the difference between the two observation epochs in [S II] 6731 Å emission, where white represents the FORS2 2018 observation, and

black represents the preceding EMMI 2006 observation. Again, the shock features exhibit a leading white edge and a trailing black edge, displaying the radial movement of the flow away from the source position. Here, the entire reflection nebula along the outflow cavity appears bright, implying that the V-shaped reflection nebula increased in brightness between the two observations. This may imply a clearing of obscuring dust in the vicinity of the outflow cavity (Hartigan et al., 2005).

Figure 6.12 displays the EMMI 2006 narrow-band image of the HH 46/47 outflow in [S II] 6731 Å emission. Seventeen resolved shock features, labelled 'B1 – B17', were identified in the blueshifted outflow, pointing north-east, in both observations, and five resolved shock features, labelled 'R1 – R5', were identified in the redshifted outflow, pointing south-west. These identified shock features are labelled in Figure 6.12. Table 6.6 presents the proper motions of the shock features. The first column again displays the shock feature identifications, preceded by the prefix '0618', corresponding to those in Figure 6.12. The difference ($\Delta x$ and $\Delta y$) in the $x$ and $y$ positions of the centroids in units of milliarcseconds are presented, and the proper motions of the shocks are presented in milliarcseconds per year (mas yr$^{-}$1), where the time elapsed between the EMMI 2006 and FORS2 2018 observations is approximately 12.52 years. The PA of the shock features is also presented, estimated by deriving the trajectory of the shock features movement between observations. The tangential velocities ($v_{\perp}$) of the shocks are given, and the true, 3D space velocity ($v_{\rm space}$) of the shocks was estimated assuming that the outflow has an inclination angle of 37° with respect to the plane of the sky (Hartigan et al., 2005).

The average tangential velocity of the internal shocks within the blueshifted jet, calculated by obtaining the mean tangential velocities of the 0618B1 – 0618-B12 shock features from Table 6.6, is $v_{\perp} = 246$ km s$^{-1}$, slightly lower than in the 1991 – 1995 epoch (287 km s$^{-1}$), but higher than the 1995 – 2002 epoch (190 km s$^{-1}$) and the 2002 – 2006 epoch (189 km s$^{-1}$). The bright HH 47A bow shock, visible in the upper left of panel 2 in Figure 6.12, has a tangential velocity of $v_{\perp} = 197$ km s$^{-1}$, estimated here from the 0618B13 shock feature. This velocity is higher than in the 1995 – 2002 epoch (128 km s$^{-1}$), and lower than both the 1991 – 1995 epoch (295 km s$^{-1}$) and 2002 – 2006 epoch (250 km s$^{-1}$). The faint HH 47D bow shock, seen in panel 1 of Figure 6.12, has a mean tangential velocity of $v_{\perp} = 184$ km s$^{-1}$, obtained from the mean velocities of the 0618B14 – 0618B17 shock features. This estimation is in line with that from the

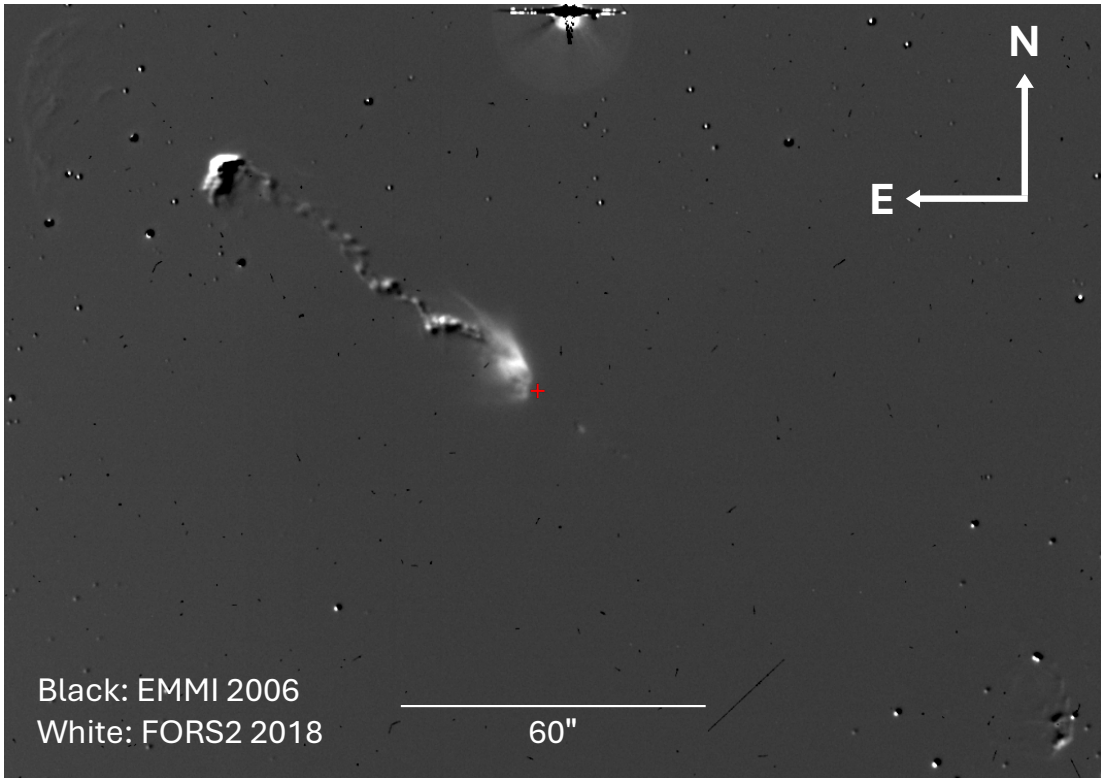


FIGURE 6.11: Difference between the FORS2 2018 observation and the EMMI 2006 observation in [S II] 6731 Å emission. White represents the FORS2 2018 observation, and black represents the preceding EMMI 2006 observation. The approximate source position is marked with a red-plus symbol. The shock features in the outflow move radially away from the source position, again exhibiting leading white edges and a trailing black edges. The entire reflection nebula along the outflow cavity appears bright in this image.

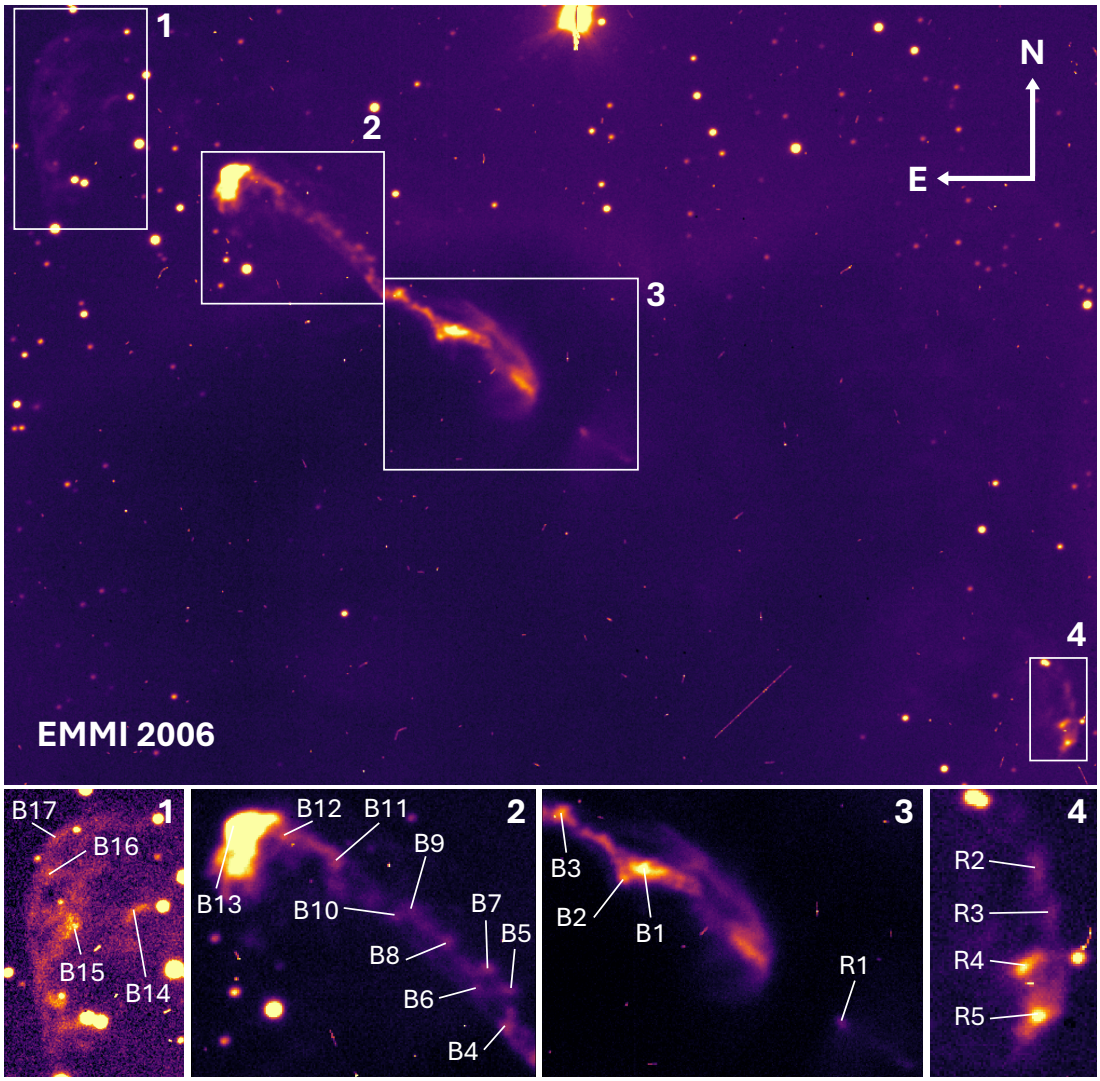


FIGURE 6.12: EMMI 2006 narrow-band image of the HH 46/47 outflow in [S II] 6731 Å emission. Identified shock features, resolved in both the EMMI 2006 data and the FORS2 2018 data, are labelled in the panels 1, 2, 3, and 4. The prefix 'B' denotes shock features identified in the blueshifted outflow, and the prefix 'R' denotes those identified in the redshifted outflow.

TABLE 6.6: Proper motions of identified shock features in HH 46/47 outflow in [S II] 6731 Å emission from May 2006 – November 2018.

| ID[a] | $\Delta x$ [b] | $\Delta y$ [b] | $\mu$ (mas yr$^{-1}$) | PA (°) | $v_\perp$ [c] | $v_{\rm space}$ [c] |
|---|---|---|---|---|---|---|
| B1 | − 912 | + 537 | 85 | 60 | 180 | 226 |
| B2 | − 1009 | + 516 | 91 | 63 | 193 | 242 |
| B3 | − 1142 | + 558 | 102 | 64 | 217 | 271 |
| B4 | − 1127 | + 706 | 106 | 58 | 227 | 284 |
| B5 | − 1164 | + 737 | 110 | 58 | 235 | 294 |
| B6 | − 1186 | + 920 | 120 | 52 | 256 | 320 |
| B7 | − 1152 | + 836 | 114 | 54 | 243 | 304 |
| B8 | − 1228 | + 849 | 119 | 55 | 254 | 319 |
| B9 | − 1804 | + 1070 | 168 | 59 | 358 | 448 |
| B10 | − 1341 | + 866 | 128 | 57 | 272 | 341 |
| B11 | − 1185 | + 671 | 109 | 60 | 232 | 291 |
| B12 | − 1393 | + 969 | 136 | 55 | 289 | 362 |
| B13 | − 889 | + 738 | 92 | 50 | 197 | 247 |
| B14 | − 824 | − 170 | 67 | 102 | 143 | 179 |
| B15 | − 1470 | + 206 | 119 | 82 | 253 | 317 |
| B16 | − 765 | + 400 | 69 | 62 | 147 | 184 |
| B17 | − 952 | + 593 | 90 | 58 | 191 | 239 |
| R1 | + 608 | − 541 | 65 | 228 | 139 | 174 |
| R2 | + 230 | − 384 | 36 | 211 | 76 | 95 |
| R3 | + 409 | − 865 | 76 | 205 | 163 | 204 |
| R4 | + 468 | − 1230 | 105 | 201 | 224 | 281 |
| R5 | + 240 | − 1474 | 119 | 189 | 254 | 319 |

[a] Identified shock features are preceded by the prefix 0618.
[b] $\Delta x$ and $\Delta y$ are measured in mas.
[c] $v_\perp$ and $v_{\rm s}$ are measured in km s$^{-1}$.

1991 – 1995 epoch (197 km $s^{-1}$), but higher than the 1995 – 2002 epoch (68 km $s^{-1}$) and the 2002 – 2006 epoch (101 km $s^{-1}$). The faint shock feature, labelled 0618R1, near the base of the redshifted outflow has a tangential velocity of $v_{\perp}$ = 139 km $s^{-1}$, which is higher than the same shock feature's velocity in the 1995 – 2002 epoch (54 km $s^{-1}$) and in the 2002 – 2006 epoch (96 km $s^{-1}$). The HH 47C bow shock that the redshifted outflow terminates in, seen in panel 4 of Figure 6.12, has a mean tangential velocity of $v_{\perp}$ = 179 km $s^{-1}$, obtained from the mean velocities of the 0618R2 – 0618R5 shock features.

The PA of the atomic jet, calculated from the mean PAs of the 0618B1 – 0618B12 shock features, is 53°, agreeing well with the average jet PA of 52.3° measured from HST 2019 observations of the jet (Erkal et al., 2021b). The PAs of the shock features (0618B14 – 0618B17) in the faint HH 47D bow shock are higher than that of the atomic jet, with PAs of 58° to 102°, implying the features in the bow shock is moving in a more easterly direction in comparison to the jet. This direction of movement is in agreement with the 1991 – 1995 epoch, but in contrast to both the 1995 – 2002 and 2002 – 2006 epochs. The average PA of the redshifted outflow bow shock, HH 47C, is 202° calculated from the average of the 0618R2 – 018R5 PAs.

### 6.4.2 The proper motions in $H_2$ emission

Following the proper motions study of the HH 46/47 outflow in the [S II] emission line at 6731 Å, the proper motions in the bright $H_2$ line at 2.12 μm were investigated. In the case of this emission line, only two datasets were used, ISAAC observations in 2001 and HAWK-I observations in 2019. Investigating the proper motions in this emission line provides intrinsically different information to the [S II] 6731 Å proper motions, as $H_2$ traces different physical processes. The [S II] emission traces the fast-moving, hot, partially ionised gas, such as that found in the collimated jet. In contrast, $H_2$ emission traces slower-moving, cooler gas, where the shocks are not energetic enough to dissociate molecular hydrogen. This emission generally has a wider morphology when compared to the narrow jet, instead tracing shock-heated outflow cavities and wide-angled components of the outflow. Studying the outflow in this emission line therefore allows the investigation of temporal evolution of bow shock wings, wide-angled winds, and interactions of the outflow with the surrounding ambient medium. This information complements that provided with

proper motions in [S II] emission, providing knowledge of parts of the outflow not seen in [S II] emission.

The higher spatial resolution HAWK-I 2019 data was reprojected onto the lower resolution ISAAC 2001 data. Figure 6.13 displays the difference between the two observation epochs in $H_2$ 2.12 μm emission, where white represents the HAWK-I 2019 observation, and black represents the preceding ISAAC 2001 observation. The circular arcs aberration discussed in Section 6.2.6 is apparent here. Although this aberration is significant, it did not affect the measurement of the positions of shock features in the observation, as these measurements were performed locally around the individual shocks where the oscillatory variation in the image intensity caused by the aberration is spatially larger than the shock features. However, careful measurement of the background intensity, around the shock feature, was required for each identified shock to ensure good Gaussian profile fits. The driving source of the outflow is still embedded at these NIR wavelengths, however a brightness peak is identified at the apex of the blueshifted outflow cavity. This peak in brightness was established as the source position in these images and its position was measured by retrieving the centroid of a 2D Gaussian profile fit. This source position is marked by a red-plus symbol in Figure 6.13. Similar to what was observed in [S II] emission, the shock features exhibit a leading white edge and a trailing black edge, displaying the radial movement of the outflow away from the source position. The blueshifted outflow cavity displays variation between the two observations. Firstly, the northern-pointing wing of the outflow cavity appears dark in this image, signifying that it has dimmed between observations. Secondly, the tip of the northern-pointing wing of the cavity has expanded outward from the jet axis. In the ISAAC 2001 observation (black) the northern-pointing tip of the cavity curls inward towards the jet axis, in contrast, in the HAWK-I 2019 observation (white), the tip of the cavity points more northerly, more so in the direction of the jet axis. This change in the morphology of the outflow cavity in $H_2$ emission points to an expanding shell or bubble of material, potentially driven by a wide-angled component of the outflow or by the narrow jet if the surrounding medium is stratified in density, blowing out the tip of the cavity away from the jet axis.

Figure 6.14 displays the HAWK-I 2019 narrow-band image of the HH 46/47 outflow in $H_2$ 2.12 μm emission. Nine resolved shock features, labelled 'B1 –

B9', were identified in the blueshifted outflow, pointing north-east, in both observations, and twenty six resolved shock features, labelled 'R1 – R26', were identified in the redshifted outflow, pointing south-west. These identified shock features are labelled in Figure 6.14. The identified shock features are presented in the HAWK-I 2019 observation instead of the ISAAC 2001 observation due to the aberration present in the ISAAC data. Table 6.7 presents the proper motions of the shock features. The first column again displays the shock feature identifications, preceded by the prefix '0119', corresponding to those in Figure 6.14. The difference ($\Delta x$ and $\Delta y$) in the $x$ and $y$ positions of the centroids in units of milliarcseconds are presented, and the proper motions of the shocks are presented in milliarcseconds per year (mas yr$^{-}$1), where the time elapsed between the ISAAC 2001 and HAWK-I 2019 observations is approximately 17.74 years. The PA of the shock features is also presented, estimated by deriving the trajectory of the shock features movement between observations. The tangential velocities ($v_{\perp}$) of the shocks are given, and the true, 3D space velocity ($v_{\rm space}$) of the shocks was estimated assuming that the outflow has an inclination angle of 37° with respect to the plane of the sky (Hartigan et al., 2005).

In $H_2$ emission the fast-moving, collimated jet is not traced. Instead, one sees the bright bow shock HH 47A, displayed in the left of panel 1 in Figure 6.14, appearing connected, along the northern side of the outflow, to the cavity at the base of the blueshifted outflow. This lobe-like outflow morphology is associated with molecular material, where some wide angled component of the outflow, or the narrow jet propagating into a density-stratified medium (Rabenanahary et al., 2022), has caused the outflow to carve out a loop-like lobe in the surrounding ambient material. Here, a number of clumps in HH 47A bow shock were resolved, and so could be investigated independently in contrast to the bow shock in [S II] emission, where only the bulk movement of the feature was presented. The average tangential velocity of shock features in the bow shock is $v_{\perp} = 155$ km s$^{-1}$, with individual velocities of the 0119B3 – 0119B9 shock features ranging from 90 km s$^{-1}$ to 217 km s$^{-1}$. This average velocity is lower than the bulk velocity of the bow shock measured in all observation epoch in [S II] emission. This implies that the HH 47A bow shock has decreased in velocity from the previous proper motion measurements of Micono et al. (1998) spanning 1993 – 1997, where they estimate $v_{\perp} = 184$ km s$^{-1}$. As the HH 47A bow shock is visible in $H_2$ emission, molecular hydrogen

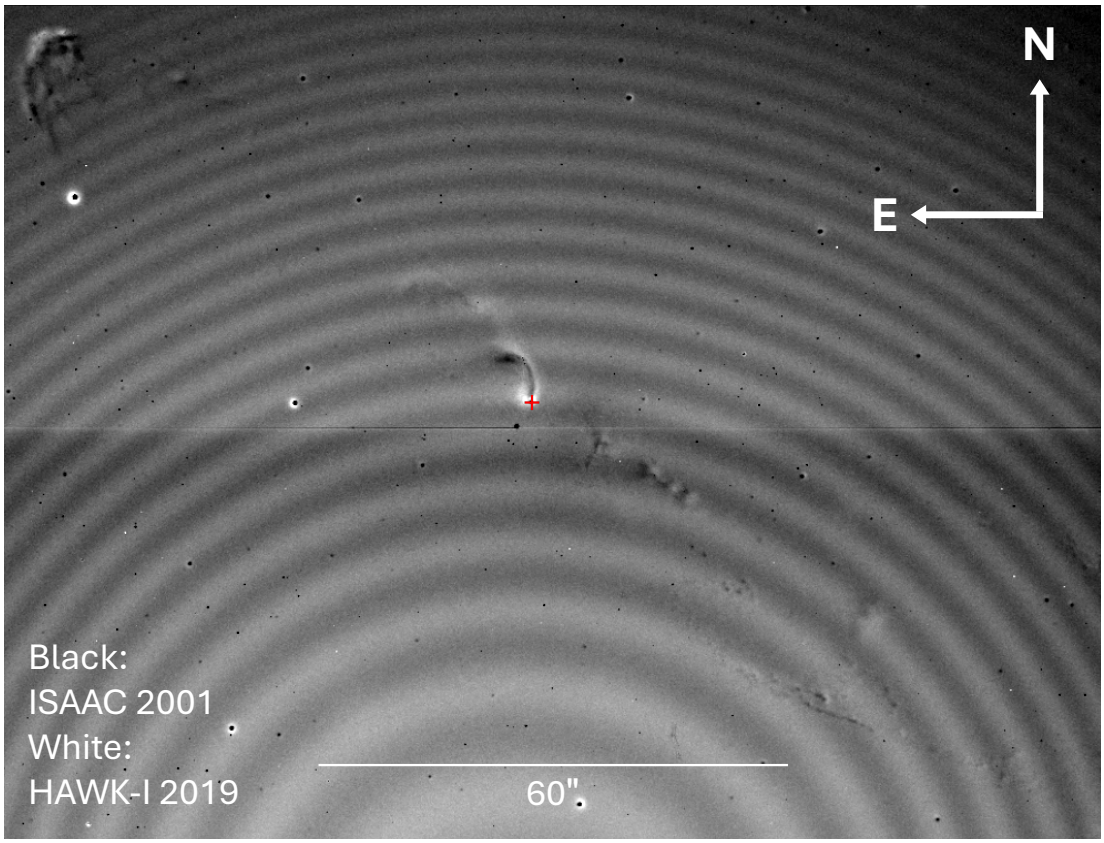


FIGURE 6.13: Difference between the HAWK-I 2019 observation and the ISAAC 2001 observation in $H_2$ 2.12 μm emission. White represents the HAWK-I 2019 observation, and black represents the preceding ISAAC 2001 observation. The source position is marked with a red-plus symbol. The shock features in the outflow move radially away from the source position, exhibiting leading white edges and a trailing black edges. The northern-pointing tip of the blueshifted outflow cavity has been blown out, away from the jet axis.

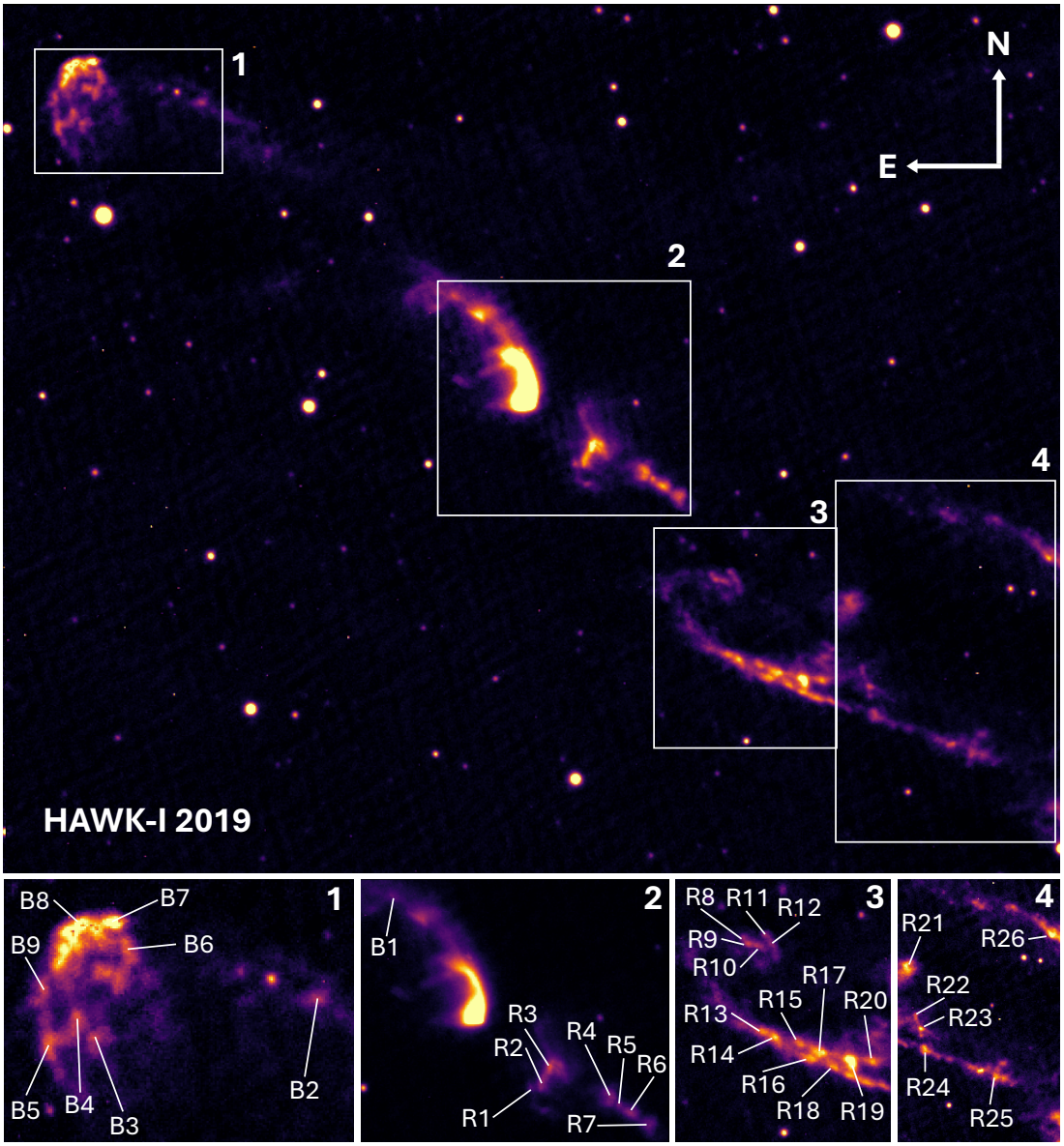


FIGURE 6.14: HAWK-I 2019 narrow-band image of the HH 46/47 outflow in $H_2$ 2.12 μm emission. Identified shock features, resolved in both the ISAAC 2001 data and the HAWK-I 2019 data, are labelled in the panels 1, 2, 3, and 4. The prefix 'B' denotes shock features identified in the blueshifted outflow, and the prefix 'R' denotes those identified in the redshifted outflow.

TABLE 6.7: Proper motions of identified shock features in HH 46/47 outflow in $H_2$ 2.12 μm emission from May 2001 – February 2019.

| ID[a] | $\Delta x$ [b] | $\Delta y$ [b] | $\mu$ (mas yr$^{-1}$) | PA (°) | $v_\perp$ [c] | $v_{\rm space}$ [c] |
|---|---|---|---|---|---|---|
| B1 | − 826 | + 1024 | 74 | 39 | 158 | 198 |
| B2 | − 568 | + 730 | 52 | 38 | 111 | 139 |
| B3 | − 1060 | + 1461 | 102 | 36 | 217 | 272 |
| B4 | − 1111 | + 264 | 64 | 77 | 137 | 172 |
| B5 | − 1207 | + 700 | 79 | 60 | 168 | 210 |
| B6 | − 758 | + 487 | 51 | 57 | 108 | 136 |
| B7 | − 8 | + 747 | 42 | 1 | 90 | 112 |
| B8 | − 1663 | + 736 | 100 | 66 | 214 | 268 |
| B9 | − 1280 | − 33 | 72 | 91 | 154 | 193 |
| R1 | + 159 | + 52 | 9 | 288 | 20 | 25 |
| R2 | + 105 | − 118 | 9 | 222 | 19 | 24 |
| R3 | + 170 | − 81 | 11 | 244 | 23 | 28 |
| R4 | + 1156 | − 181 | 66 | 261 | 141 | 176 |
| R5 | + 1240 | − 632 | 78 | 243 | 167 | 210 |
| R6 | + 1185 | − 550 | 74 | 245 | 157 | 197 |
| R7 | + 1111 | − 842 | 79 | 233 | 167 | 210 |
| R8 | + 281 | − 158 | 18 | 241 | 39 | 49 |
| R9 | + 395 | − 9 | 22 | 269 | 48 | 60 |
| R10 | + 347 | − 112 | 21 | 252 | 44 | 55 |
| R11 | + 291 | − 83 | 17 | 254 | 36 | 46 |
| R12 | + 425 | − 388 | 32 | 228 | 69 | 87 |
| R13 | + 321 | − 24 | 18 | 266 | 39 | 49 |
| R14 | + 64 | + 55 | 5 | 311 | 10 | 13 |
| R15 | + 333 | − 324 | 26 | 226 | 56 | 70 |
| R16 | + 131 | + 46 | 8 | 289 | 17 | 21 |
| R17 | + 101 | + 16 | 6 | 279 | 12 | 15 |
| R18 | + 170 | + 114 | 12 | 304 | 25 | 31 |
| R19 | + 309 | − 28 | 17 | 265 | 37 | 47 |
| R20 | + 21 | − 20 | 2 | 227 | 4 | 4 |
| R21 | + 117 | − 1020 | 58 | 187 | 123 | 155 |
| R22 | + 161 | − 20 | 9 | 263 | 20 | 24 |
| R23 | + 71 | − 75 | 6 | 223 | 12 | 16 |
| R24 | + 261 | − 196 | 18 | 233 | 39 | 49 |
| R25 | + 317 | − 181 | 21 | 240 | 44 | 55 |
| R26 | + 197 | + 18 | 11 | 275 | 24 | 30 |

[a] Identified shock features are preceded by the prefix 0119.
[b] $\Delta x$ and $\Delta y$ are measured in mas.
[c] $v_\perp$ and $v_{\rm s}$ are measured in km s$^{-1}$.

must recombine from post-shock atomic gas in the bow shock, or the shock is not energetic enough to dissociate $H_2$ (Böhm, Scott, and Solf, 1991). The faint HH 47D bow shock is not observed in $H_2$ emission.

In the redshifted outflow, shock features can be approximately categorised into those along the central axis of the outflow and those in the wide-angled outflow lobe, again displaying a loop-like morphology (Noriega-Crespo et al., 2004; Raga et al., 2004; Arce et al., 2013). The redshifted counter-lobe of the outflow joins to the HH 47C bow shock, however, this bow shock is beyond the FOV of these observations. The features 0119R4 – 0119R7, and 0119R21 appear as knots along the central outflow axis. As one would expect, these shock features possess the highest velocities, with the average velocity of the chain of knots labelled 0119R4 – 0119R7 being $v_\perp = 158$ km s$^{-1}$. Again, this implies a deceleration compared to the measurements made by Micono et al. (1998), where they report velocities in excess of 200 km s$^{-1}$ for these central axis shock features. The other shock feature along the outflow axis, 0119R21 has a tangential velocity of $v_\perp = 123$ km s$^{-1}$, implying a deceleration of molecular material along the central outflow axis. The features labelled 0119R1 – 0119R3 appear to be part of a bow shock-like feature, possibly driven by the redshifted jet (Nisini et al., 2024), and have lower velocities with those in the central axis, having an average tangential velocity of $v_\perp = 21$ km s$^{-1}$. The remainder of the shock features in the redshifted outflow are those in the walls of the lobe. These shock features have lower proper motions in comparison to those along the central outflow axis, as one would expect as outflows have an onion-like velocity structure, with the highest velocity material at the central outflow axis and with progressively lower velocity material as one moves radially away from the outflow axis (e.g. Ferreira, 1997; Panoglou et al., 2012; Bai et al., 2016; Zhu and Stone, 2018; Wang, Bai, and Goodman, 2019). The average velocity of these shock features, obtained by calculating the mean velocity of the 0119R8 – 0119R26 shock features and excluding 0119R21, is $v_\perp = 32$ km s$^{-1}$. Micono et al. (1998) also measure lower velocities in the wings of the outflow lobe, with measurements of 40 – 81 km s$^{-1}$, but again, these are greater in velocity to the measurements presented here.

The PAs of the shock features in the northern wall of the blueshifted outflow lobe are lower than the PA of the central axis of the molecular outflow in CO emission, $\approx 60°$ (Zhang et al., 2019), with 0119B1 and 0119B2 having PAs of 39° and 38° respectively, showing that they are moving more northerly

than the outflow direction, moving away from the outflow axis. The PAs of the shock features (0119B3 – 0119B9) in the HH 47A bow shock have a large spread of values, ranging from 1° to 91°, most likely a result of the complex motion of the knots within the bow shock moving relative to one another and interacting with one another. However, the average PA of these shock features is 55° in good agreement with the direction of the blueshifted flow.

The movement of features in the redshifted outflow is again complex. The average PA of all features (0119R1 – 0119R26) is 253°, which is almost antiparallel to the blueshifted molecular outflow in CO emission, $\approx 60°$ (Zhang et al., 2019). The majority of the shock features in the redshifted outflows have a negative difference ($-\ \Delta y$) in the $y$ positions of their centroids in Table 6.7, as they are moving either in the bulk direction of the redshifted outflow, or, those with the lowest PAs, radially away from the central outflow axis in a more southern direction. Some features, however, have positive differences ($+\ \Delta y$) in the $y$ positions of their centroids. A cluster of these features is 0119R14 – 0119R18, excluding 0119R15. These shock features lie in a chain along the wall of some shell of molecular material, which lies within the southern side of the larger redshifted outflow lobe. Only one shock feature in the northern wall of the redshifted outflow lobe is identified in both observations, 0119R26. This shock also has a positive difference ($+\ \Delta y$) in the $y$ positions of its measured centroid between the observations as expected, as this wall of the outflow lobe is expanding away from the central axis in a more northerly direction.

## 6.5 Discussion

Figure 6.15 displays position velocity diagrams of the proper motions results from all epochs. The radial distance from the approximate source position, in arcseconds, is plotted against the measured tangential velocities of the identified shock features. Here, positive offsets were designated to the blueshifted outflow and negative offsets to the redshifted outflow. For ease of interpretation, the tangential velocities of the shock features in the blueshifted outflow were converted to negative values, in order to resemble the intuitive convention of radial velocity measurements, where blueshifted outflows possess negative velocities. These negative velocities, representing the tangential velocities of the shock features in the blueshifted outflow, are of course positive values, as reported throughout in the chapter. The approximate source position

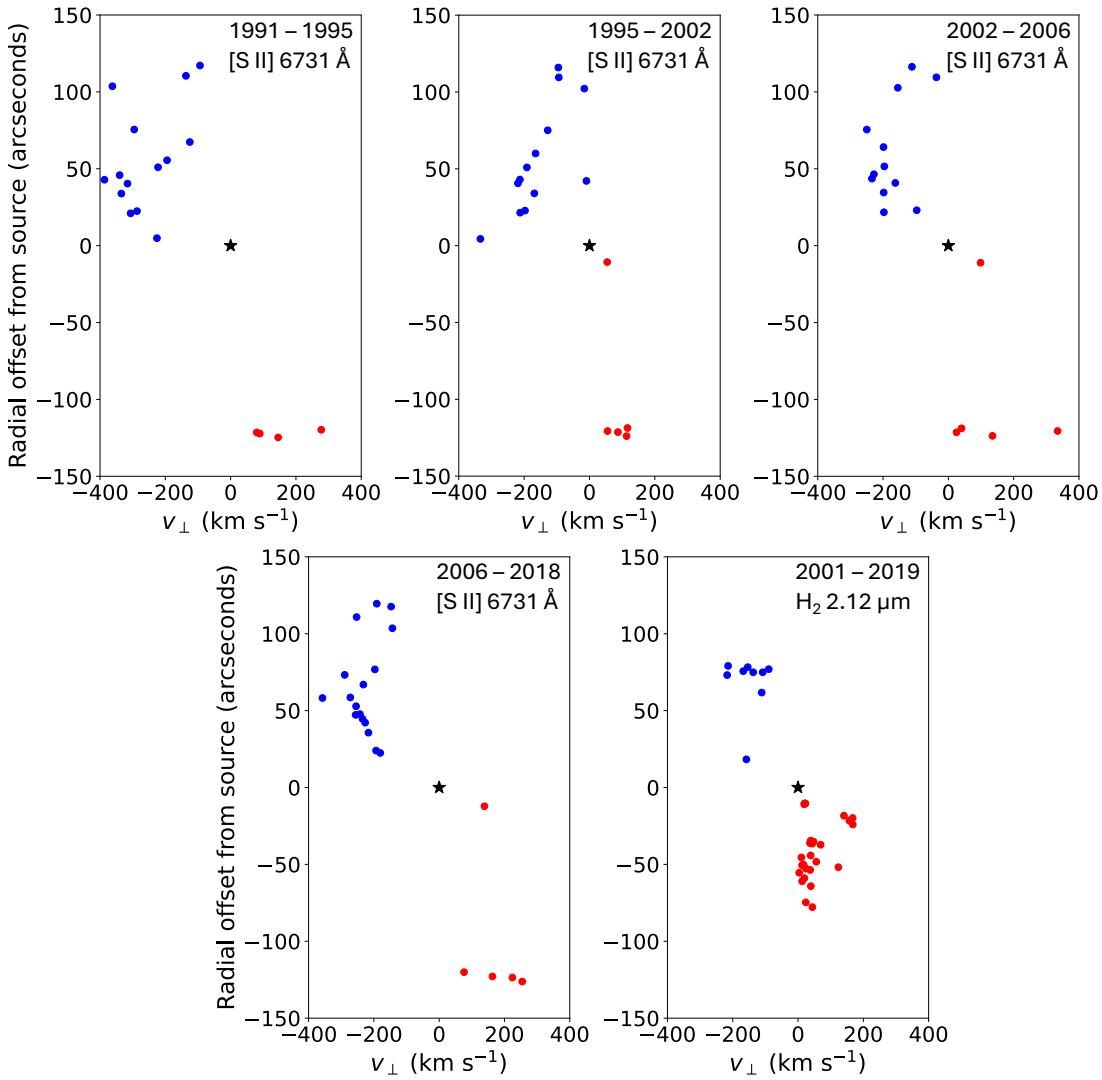


FIGURE 6.15: Position velocity diagrams of the proper motions measurements for the HH 46/47 outflow. The radial distance from the approximate source position, in arcseconds, is plotted against the measured tangential velocities of the identified shock features. Positive offsets represent shock features in the blueshifted outflow and negative offsets represent those in the redshifted outflow. Negative tangential velocities represent those measured in the blueshifted outflow and positive tangential velocities represent those measured in the redshifted outflow. The approximate source position is marked with a black-star symbol. Blue data points represent shock features in the blueshifted outflow and red data points represent those in the redshifted outflow.

is marked with a black-star symbol. In the blueshifted atomic jet, there is an initial acceleration of material up to approximately 50 arcseconds in [S II] 6731 Å emission, excluding the 1995 – 2002 epoch, where the signal is less clear. This initial acceleration of material in the collimated jet axis is in agreement with that seen in Eisloeffel and Mundt (1994), and is somewhat expected, as jet emission arises primarily from the cooling regions of the shocks generated when higher-velocity material catches up with and impacts material ahead of it (Tsukamoto et al., 2023). The shock features in the faint HH 47D bow shock in the blueshifted outflow, data points beyond $\approx$ 100 arcseconds here, have lower tangential velocities when compared to the average jet velocity. In the HH 47C bow shock, in the redshifted outflow, there is large spread of tangential velocities in [S II] 6731 Å emission, with only the data points in the 1995 – 2002 epoch appearing to be clustered. In the redshifted outflow in $H_2$ 2.12 μm emission, the majority of data points are clustered around low velocities, as one would expect for molecular material. However, a selection of data points, those corresponding to the shock features 0119R4 – 0119R7, and 0119R21, have higher tangential velocities ($> 100$ km s$^{-1}$) as these features are along the central axis of the redshifted outflow, as discussed above. The data point with the highest offset in this selection of data points has a lower tangential velocity than the other, less-offset points in the central axis, implying a deceleration of the redshifted jet.

A collection of shock features, identified in the various observing epochs, are common to all epochs in [S II] 6731 Å emission. This allows a multi-epoch study of the shock features, where the motion of these shock features are traced over all epochs, allowing the derivation of feature acceleration or deceleration. The tangential velocities derived from the proper motions of shock features identified in [S II] 6731 Å emission, common to all observing epochs, are presented in Table 6.8. Overall, there seems to be few clear trends in the proper motions of these shock features, however, some can be identified. Blueshifted jet knots closest to the driving source ($\alpha$B2, $\alpha$B3, $\alpha$B4, and subsequent epoch labels) display a general deceleration over time, with some variability in individual epochs. One expects a deceleration of jet knots with increasing distance from the driving source due to interactions with material in the flow itself, or from interactions with the ambient medium (e.g. Cabrit and Raga, 2000). The faint HH 47D bow shock harbours one shock feature that shows a clear acceleration with time ($\alpha$B15), whereas the other two shock features in the bow

shock ($\alpha$B13 and $\alpha$B14) display less clear trends, with periods of deceleration and acceleration. The shock feature located closest to the driving source in the redshifted jet ($\beta$R1) shows a clear acceleration over time. The rest of the shock features ($\alpha$R1, $\alpha$R2, $\alpha$R3, $\alpha$R4) in the redshifted outflow are those contained in the HH 47C bow shock. These features display no clear trend with some features decelerating (e.g. $\alpha$R1) and some accelerating (e.g. $\alpha$R3). The overarching trend in this data is that there exists tangential velocity variability, where there is no clear acceleration or deceleration of jet material. This variation in velocity is somewhat expected when measuring interacting shock features, as the shock features are accelerating material in front of them and decelerating material behind them (Caratti o Garatti et al., 2009). This is especially true when studying features further from the driving source, where the loss of initial launching condition information is greater, due to the knots interaction with the flow itself, or the ambient material. Furthermore, the shock features are likely not smooth entities, instead being complex working surfaces with turbulent gas interacting with itself, creating substructures (Hartigan et al., 2011). This may explain the large variations in the velocities of common shock features, whereby in one epoch the brightest emission is coming from a deceleration zone, where jet material is impacting material ahead of it, and in another epoch, the brightest emission is coming from an acceleration zone of the working surface. Another explanation for the apparent acceleration and deceleration of shock features with time is the precession of the outflow. As the outflow is precessing, the shock features may follow curved or helical trajectories resulting in transverse velocity variations over multiple epochs due to projection effects.

The results of the proper motion study over all epochs are summarised in Table 6.9. The average proper motions ($\mu$), PAs, and tangential velocities ($v_\perp$) of large scale outflow structures are presented. The jet refers to the twisting, collimated atomic jet in the blueshifted side of the outflow. HH 47A refers to the bright bow shock that the blueshifted jet terminates in. HH 47D refers to the fainter, and further extended from the source position, bow shock in the blueshifted outflow. HH 47C refers to the bow shock observed in the redshifted outflow. Only the proper motions of the HH 47A bow shock are presented here in the $H_2$ emission proper motions study as the atomic jet and the fainter HH 47D bow shock are not seen in this emission, and the HH 47C bow

TABLE 6.8: Multi-epoch proper motions, expressed as tangential velocities, of shock features in the HH 46/47 outflow in [S II] 6731 Å emission common to all the observing epochs; 1991 – 1995, 1995 – 2002, 2002 – 2006, 2006 – 2018.

| Shock IDs[a] | $v_\perp$ (km s$^{-1}$) | | | |
|---|---|---|---|---|
| | 91 – 95 | 95 – 02 | 02 – 06 | 06 – 18[b] |
| $\alpha$B2, $\beta$B2, $\gamma$B1, $\delta$B1 | 306 | 212 | 197 | 180 |
| $\alpha$B3, $\beta$B3, $\gamma$B2, $\delta$B2 | 287 | 197 | 97 | 193 |
| $\alpha$B4, $\beta$B4, $\gamma$B3, $\delta$B3 | 335 | 169 | 198 | 217 |
| $\alpha$B5, $\beta$B5, $\gamma$B4, $\delta$B4 | 316 | 219 | 162 | 227 |
| $\alpha$B6, $\beta$B6, $\gamma$B5, $\delta$B5 | 386 | 9 | 234 | 235 |
| $\alpha$B7, $\beta$B7, $\gamma$B6, $\delta$B7 | 340 | 213 | 228 | 243 |
| $\alpha$B8, $\beta$B8, $\gamma$B7, $\delta$B8 | 222 | 191 | 196 | 254 |
| $\alpha$B13, $\beta$B11, $\gamma$B10, $\delta$B14 | 362 | 16 | 155 | 143 |
| $\alpha$B14, $\beta$B12, $\gamma$B11, $\delta$B15 | 137 | 94 | 37 | 253 |
| $\alpha$B15, $\beta$B13, $\gamma$B12, $\delta$B16 | 94 | 95 | 111 | 147 |
| —- , $\beta$R1, $\gamma$R1, $\delta$R1 | - | 54 | 96 | 139 |
| $\alpha$R1, $\beta$R2, $\gamma$R2, $\delta$R2 | 278 | 116 | 40 | 76 |
| $\alpha$R2, $\beta$R3, $\gamma$R3, $\delta$R3 | 80 | 55 | 335 | 163 |
| $\alpha$R3, $\beta$R4, $\gamma$R4, $\delta$R4 | 89 | 87 | 25 | 224 |
| $\alpha$R4, $\beta$R5, $\gamma$R5, $\delta$R5 | 146 | 114 | 135 | 254 |

[a] Common shock features across all epochs. The identified shocks are highlighted in Figures 6.6, 6.8, 6.10, and 6.12. The symbols $\alpha$, $\beta$, $\gamma$, and $\delta$ are used to represent the prefixes '9195', '9502', '0206', and '0618', respectively.

[b] Proper motions measured across epochs 1991 – 1995, 1995 – 2002, 2002 – 2006, 2006 – 2018.

shock is not contained within the FOV of the $H_2$ observations. There is significant variation in the proper motions of the blueshifted jet over the epochs, ranging from $\mu = 89$ – 134 mas yr$^{-1}$, corresponding to tangential velocities of $v_\perp = 189$ – 287 km s$^{-1}$. This variation in the proper motions of the jet may be attributed to physical changes in the average velocity of the outflow between different epochs, however, it is more likely influenced by the broad range of instruments used for the observations, the spatial resolution and seeing conditions differences, and the selection of shock features in the jet in each observation epoch pair. The identified shock features differ between each epoch pair. The average proper motions of the jet over all epochs is $\mu = 107 \pm 19$ mas yr$^{-1}$, and the average tangential velocity is $v_\perp = 228 \pm 41$ km s$^{-1}$, where the uncertainty associated with these estimations is the standard deviation of the set of measurements. This is in good agreement with proper motion measurements of the jet in [S II] and H$\alpha$ emission, using WFPC2 (Wide Field and Planetary Camera 2) on HST between 1994 and 1999, where they reported the tangential velocity of the jet to be $v_\perp = 235 \pm 24$ km s$^{-1}$ (Hartigan et al., 2005). Raga, Velázquez, and Noriega-Crespo (2018) used HST observations of the HH 46/47 outflow and measured the proper motions of the jet to be 264 $\pm$ 30 km s$^{-1}$ in [S II] emission and 240 $\pm$ 42 km s$^{-1}$ in H$\alpha$ emission, in the epoch 1994 – 1999, and measured 229 $\pm$ 17 km s$^{-1}$ in [S II] emission and 216 $\pm$ 24 km s$^{-1}$ in H$\alpha$ emission, in a subsequent epoch of 1999 – 2008. Erkal et al. (2021b) reported a tangential velocity of $v_\perp = 245 \pm 15$ km s$^{-1}$ for the jet, again using HST observations in [S II] and [Fe II] emission between 2005 and 2019. This value agrees very well with the estimated tangential jet velocity in the 2006 – 2018 epoch presented here, $v_\perp = 246$ km s$^{-1}$, where the intervals are of similar duration and epochs. Schwartz, Jones, and Sirk (1984) measured the proper motions over a seven year period, in H$\alpha$ and [S II] emission, to be $v_\perp = 195$ km s$^{-1}$ near the base of the jet, and Eisloeffel and Mundt (1994) measured the proper motions of $v_\perp = 200$ km s$^{-1}$ and increased in velocity up until the HH 47A bow shock. The PA of the jet also displays variation, with estimated PAs ranging from 39° to 68°. The twisting jet axis is known to have a variable ejection angle from the driving source (Hartigan et al., 1993; Hartigan et al., 2005). This, coupled with the differing selection of shock features in the jet, explains the large spread of estimated PAs presented here. The average PA over all epochs is 57 $\pm$ 12°.

In the HH 47A bow shock, there is again significant variation in the proper

TABLE 6.9: Summary of proper motions of large scale outflow features in the HH 46/47 outflow in [S II] 6731 Å and $H_2$ 2.12 μm emission from 1991 – 2019.

| Epochs[a] | Feature[b] | $\mu$ (mas yr$^{-1}$) | PA (°) | $v_\perp$ (km s$^{-1}$) |
|---|---|---|---|---|
| 1991 – 1995 | Jet | 134 | 67 | 287 |
| 1995 – 2002 | Jet | 89 | 68 | 190 |
| 2002 – 2006 | Jet | 89 | 39 | 189 |
| 2006 – 2018 | Jet | 116 | 53 | 246 |
| 2001 – 2019 | Jet | - | - | - |
| 1991 – 1995 | HH 47A | 138 | 74 | 295 |
| 1995 – 2002 | HH 47A | 60 | 56 | 128 |
| 2002 – 2006 | HH 47A | 117 | 22 | 250 |
| 2006 – 2018 | HH 47A | 92 | 50 | 197 |
| 2001 – 2019 | HH 47A | 73 | 55 | 155 |
| 1991 – 1995 | HH 47D | 93 | 130 | 197 |
| 1995 – 2002 | HH 47D | 32 | 39 | 68 |
| 2002 – 2006 | HH 47D | 47 | 37 | 101 |
| 2006 – 2018 | HH 47D | 86 | 76 | 184 |
| 2001 – 2019 | HH 47D | - | - | - |
| 1991 – 1995 | HH 47C | 69 | 210 | 157 |
| 1995 – 2002 | HH 47C | 44 | 240 | 93 |
| 2002 – 2006 | HH 47C | 63 | 240 | 134 |
| 2006 – 2018 | HH 47C | 84 | 202 | 179 |
| 2001 – 2019 | HH 47C | - | - | - |

[a] This displays the epochs of the observation pairs that the corresponding proper motions measurements come from.

[b] The large scale outflow features are given an identifier. Jet refers to the axis of the blueshifted jet. HH 47A refers to the bright bow shock that the blueshifted jet terminates in. HH 47D refers to the fainter, and further extended from the source position, bow shock in the blueshifted outflow. HH 47C refers to the bow shock observed in the redshifted outflow.

motions with $\mu$ ranging from 60 – 138 mas yr$^{-1}$, corresponding to tangential velocities of $v_\perp = 128$ – 295 km s$^{-1}$. This variation can possibly be attributed to the fact that the bow shock has a complex morphology, comprising multiple clumps that move relative to one another with a spread of $\pm$ 40 km s$^{-1}$ (Hartigan et al., 2005). It is likely that the measured centroid of the bow shock as a whole (excluding the ISAAC 2001 – HAWK-I 2019 observations, where multiple shock features are identified), taken as the brightness centroid, varies with time as shocked clumps or knots within the bow shock dim or increase in intensity with time. This results in the brightest clump within the bow shock at a certain epoch, being a different clump at a different epoch. As the velocity of different shock features are being measured in each observation pair, then this naturally leads to a difference in the measured proper motions for HH 47A. The average proper motions of HH 47A over all epochs is $\mu = 96 \pm 28$ mas yr$^{-1}$, and the average tangential velocity is $v_\perp = 205 \pm 61$ km s$^{-1}$. This is in good agreement with the average proper motions of HH 47A measured by Hartigan et al. (2005), $v_\perp = 201$ km s$^{-1}$. Raga, Velázquez, and Noriega-Crespo (2018) measured the average proper motions of the bow shock to be 215 $\pm$ 13 km s$^{-1}$ in [S II] emission and 217 $\pm$ 16 km s$^{-1}$ in H$\alpha$ emission in the epoch 1994 – 1999, and subsequently measured the proper motions at 199 $\pm$ 8 km s$^{-1}$ in [S II] emission and 204 $\pm$ 9 km s$^{-1}$ in H$\alpha$ emission in the epoch 1999 – 2008. These measurements agree well with those presented here. Schwartz, Jones, and Sirk (1984) measured the proper motions to be $v_\perp = 165$ km s$^{-1}$, and Eisloeffel and Mundt (1994) reported the apex of the bow shock to have a proper motion of $v_\perp = 182$ km s$^{-1}$. The PA of HH 47A also displays strong variation, with estimated PAs ranging from 22° to 74°. Again, the sparse number of data points representing the complex bow shock, and the movement of individual clumps within the bow shock, is most likely responsible for this range of values. If indeed different clumps are being measured in different observation epoch pairs then this uncertainty is to be expected. The average PA of HH 47A over all epochs is 51 $\pm$ 17°.

In the fainter HH 47D bow shock in the blueshifted outflow, there is again significant variation in the proper motions with $\mu$ ranging from 32 – 93 mas yr$^{-1}$, corresponding to tangential velocities of $v_\perp = 68$ – 197 km s$^{-1}$. Eisloeffel and Mundt (1994) found the proper motions to range from $v_\perp = 100$ – 250 km s$^{-1}$, from the wings of the bow shock to the apex. Although there is a strong variation in the proper motions of the bow shock, most likely caused

by the selection of shock features in the larger scale structure, a conclusion can be drawn. That is, that the shock features in HH 47D exhibit lower proper motions than both the collimated jet and the brighter HH 47A bow shock in all epochs. The average proper motions of HH 47D over all epochs is $\mu = 65 \pm 26$ mas yr$^{-1}$, and the average tangential velocity is $v_\perp = 138 \pm 54$ km s$^{-1}$. This result is somewhat lower, but in agreement within the uncertainties, than that presented in Hartigan et al. (2005), where they estimated a tangential velocity of $v_\perp = 179 \pm 40$ km s$^{-1}$. The average PAs of the HH 47D bow shock also display variation between epochs, with some displaying low PAs, 1995 – 2002 and 2002 – 2006, and some displaying high PAs, 1991 – 1995 and 2006 – 2018. The average PA over all epochs is $71 \pm 38°$, with the large range attributed to the outlying 1991 – 1995 south-easterly-pointing PA estimation of 130°.

In the redshifted bow shock HH 47C, the proper motions vary with $\mu$ ranging from 44 – 84 mas yr$^{-1}$, corresponding to tangential velocities of $v_\perp = 93$ – 189 km s$^{-1}$. The average proper motions of HH 47C over all epochs is $\mu$ = 65 ± 14 mas yr$^{-1}$, and the average tangential velocity is $v_\perp = 141 \pm 32$ km s$^{-1}$. These results are similar to those in the HH 47D bow shock in the blueshifted outflow ($\mu = 65 \pm 26$ mas yr$^{-1}$, $v_\perp = 138 \pm 54$ km s$^{-1}$). This can be expected as HH 47D and HH 47C are located symmetrically about the driving source of the outflow (Heathcote et al., 1996) and possess similar transverse velocities (Reipurth and Heathcote, 1991). This naturally leads to the conclusion that these two opposing bow shocks originated in the same outburst event. Schwartz, Jones, and Sirk (1984) measured the proper motions to be significantly higher at $v_\perp = 234$ km s$^{-1}$ and Eisloeffel and Mundt (1994) found proper motions in better agreement with those presented here at $v_\perp$ = 150 km s$^{-1}$. The average PA of the HH 47C bow shock over all epochs is 223 ± 17°.

The large scale structure of the outflow does not vary significantly over the range of observation epochs. However, in $H_2$ emission a morphological change is observed in the blueshifted outflow cavity, where the tip of the northern-pointing wing of the cavity has expanded outward from the jet axis between the observations. In [S II] emission, the reflection nebula along the outflow cavity at the base of the blueshifted outflow experienced significant variability in intensity, with the reflection nebula appearing to dim and brighten between successive observations. In the 1991 – 1995 epoch, the northern-pointing tip of the reflection nebula increased in brightness. Conversely, in the

1995 – 2002 epoch, the entire northern side of the reflection nebula dimmed significantly between observations. In the 2002 – 2006 epoch, the northern side of the reflection nebula brightened slightly, and in the 2006 – 2018 epoch the entirety of the reflection nebula increased in brightness. This variation in intensity has been attributed to processes happening in the inner jet region, such as heightened ejection episodes producing new jet knots, the presence of a quasi-stationary deflection shock obliquely impacting the northern cavity wall, and the clearing of obscuring dust in the region.

In the case of new knot ejections, one can refer to the higher spatial resolution observations of the base of the outflow presented in Chapter 4. In these observations, taken in November 2018, the jet traced in [Fe II] $\lambda$2.047 μm culminates in a knot at an offset from the source position of $1\farcs0$, or 450 au. The average proper motion of the blueshifted jet derived here is $v_\perp = 228 \pm 41$ km s$^{-1}$, or equivalently $v_\perp = 48 \pm 9$ au yr$^{-1}$. If one assumes that the ejection velocity remains constant, the dynamical age of this knot is 9.4 $\pm$ 1.8 years, placing its time of approximate ejection in July 2009. The same jet knot is observed in [Fe II] $\lambda$1.87 μm emission in recent JWST observations of HH 46/47 with NIRSpec (Figure 6(a) in Nisini et al., 2024). The approximate offset of the knot in these observations, taken in February 2023, is 650 au. Again, assuming the tangential velocity derived here remains constant, one would expect the knot observed in the SINFONI observations to have moved by 200 au, from 450 au to 650 au, in the 4 years, 2 months, and $\sim$ 20 days elapsed between the observations, agreeing very well with that observed. If one instead takes the knot position in the NIRSpec observations and assumes that the ejection velocity remains constant, the dynamical age of the knot is 13.5 $\pm$ 2.5 years, placing its time of approximate ejection in August 2009, in good agreement with the SINFONI observations. Furthermore, in the NIRSpec observations there is a new jet knot at an offset from the source position of approximately 300 au, placing it's dynamical age, assuming a constant ejection velocity, at 6.3 $\pm$ 1.2 years, placing its time of approximate ejection in November 2016. The dynamical ages of these two recently ejected, bright jet knots observed in [Fe II] emission, place their ejections within the observation epoch between 2006 and 2018. This suggests that these heightened ejection events could be contributing to the significant brightening of the reflection nebula seen in this period.

In the SINFONI observations, the cause of the transverse velocity gradient observed in the $H_2$ outflow cavity, discussed in Section 4.3.2, was proposed to

be due to the asymmetric nature of the density of the ambient medium surrounding the base of the outflow. It was suggested that the quiescent material in the region near the northern side of the reflection nebula was denser than the region near the eastern or southern side, supported by the brighter emission on the northern side. This dissymmetry in the distribution of the surrounding ambient material is further supported here, in the [S II] emission images (Figures 6.1, 6.6, 6.8, 6.10, 6.12) with the northern side of the reflection nebula appearing much brighter than the southern side, and extending further from the source position. In $H_2$ emission (Figure 6.14), again, the northern side of the outflow cavity is brighter further supporting this argument.

## 6.6 Summary and conclusions

The precise proper motions of the HH 46/47 outflow have been measured over five epochs totalling approximately 27 years in [S II] 6731 Å emission, and over two epochs, 18 years apart, in $H_2$ emission. In all sets of observations it is seen that the shock features primarily move radially away from the source position. The average proper motions of large scale structures present in the outflow were presented, consisting of the collimated, blueshifted, atomic jet, the HH 47A and HH 47D bow shocks in the blueshifted outflow, and the HH 47C bow shock in the redshifted outflow. Table 6.8 presents a multi-epoch tracking of shock features common to all observing epochs in [S II] emission, and Table 6.9 summarises the average proper motion results over all epochs.

The overarching trend in the multi-epoch tracing of shock features is that there exists tangential velocity variability, where there is no clear acceleration or deceleration of jet material. This variation is somewhat expected when measuring interacting shock features, as the shock features are accelerating material in front of them and decelerating material behind them. The precession of the outflow could also be producing apparent velocity variations due to projection effects. Furthermore, the shock features are likely not smooth entities, instead being complex working surfaces with turbulent gas interacting with itself, creating substructures.

The average proper motions of the jet are $\mu = 107 \pm 19$ mas yr$^{-1}$, corresponding to an average tangential velocity of $v_\perp = 228 \pm 41$ km s$^{-1}$. This is in good agreement with previous proper motion measurements of the jet in

[S II], H$\alpha$, and [Fe II] emission. The average proper motions of the HH 47A bow shock are $\mu = 96 \pm 28$ mas yr$^{-1}$, or $v_{\perp} = 205 \pm 61$ km s$^{-1}$, again in agreement with previous measurements, and lower than the atomic jet, as expected as it is more distant from the driving source. The average proper motions of the fainter HH 47D bow shock are $\mu = 65 \pm 26$ mas yr$^{-1}$, or $v_{\perp} = 138 \pm 54$ km s$^{-1}$, which is lower than previous estimates, implying a deceleration, but in agreement within uncertainties. The proper motions of HH 47D are also lower than both the atomic jet and the HH 47A bow shock. The average proper motions of the redshifted HH 47C bow shock are $\mu = 65 \pm 14$ mas yr$^{-1}$, or $v_{\perp} = 141 \pm 32$ km s$^{-1}$, which is similar to the proper motions in the HH 47D bow shock, where the opposing bow shocks are located symmetrically about the driving source of the outflow and likely originated in the same ejection event. The jet is observed to initially accelerate with increasing offset from the source position, within the first $\sim 50$ arcseconds, in all observation epoch pairs, excluding the 1995 – 2002 epoch where the signal is less clear. This acceleration of material within the jet axis is expected for the bright atomic jet, as internal shocks are produced when higher-velocity material catches up with and impacts material ahead of it. True, 3D space velocities of the shock features were also derived, assuming that outflow has an inclination angle of 37° with respect to the plane of the sky.

In $H_2$ emission, the fast-moving and collimated atomic jet is not traced. Instead, an opposing and wide, loop-like outflow lobe morphology is observed, which is associated with molecular outflows. The HH 47A bow shock is however observed, implying that either molecular hydrogen has recombined from post-shock atomic gas in the bow shock, or that the shock is not energetic enough to dissociate $H_2$. In the redshifted outflow, the shock features have been approximately categorised into those along the central axis of the outflow, and those in the wide-angled outflow lobe. The shock features along the central axis of the outflow possess the highest tangential velocities in the redshifted outflow, and there is evidence of a deceleration of this molecular material with increasing distance from the driving source. The remainder of the shock features in the redshifted outflow, those in the walls of the lobe, have lower tangential velocities.

The morphology of the large scale outflow does not vary significantly over the range of observation epochs. However, the reflection nebula along the

outflow cavity seen at the base of the blueshifted outflow experienced significant variability in intensity, with the reflection nebula appearing to dim and brighten between successive observations in [S II] 6731 Å emission. This variation in intensity may indicate processes happening in the inner jet region, close to the driving source, where periods of increased ejection produce new shock features or jet knots which in turn illuminate the reflection nebula surrounding the base of the outflow. This proposition is supported by recent jet knot ejections observed in the SINFONI observations presented in this thesis, and more recent JWST observations. Further to this, Hartigan et al. (2011) argued that the brightening of the cavity is due to the presence of a quasi-stationary deflection shock, where the jet collides obliquely with the edge of the evacuated cavity. Or the increases in cavity intensity could correspond to the clearing of obscuring dust in the vicinity of the outflow cavity (Hartigan et al., 2005). In $H_2$ emission a morphological change is observed in the blueshifted outflow cavity, where the tip of the northern-pointing wing of the cavity has expanded outward from the jet axis between the observations. Furthermore, the cause for the transverse velocity gradient observed in the $H_2$ outflow cavity in the SINFONI observations, attributed to a dissymmetry in the density of ambient material surrounding the base of the outflow, is supported here. In the [S II] emission images and the $H_2$ emission images, the northern side of the reflection nebula or outflow cavity appears much brighter than the southern side, and extends further from the source position, reinforcing this argument.

The average PAs of large scale outflow features is also presented here, estimated by deriving the trajectory of the shock features movement between observations. The average PA of the jet over all epochs is $57 \pm 12°$. The average PA of the HH 47A bow shock is $51 \pm 17°$, and the fainter HH 47D bow shock, $71 \pm 38°$, which is most likely too large, being influenced by a significant outlier. The average PA of the redshifted HH 47C bow shock is $223 \pm 17°$. The average atomic jet PA is reported to be 52.3° by Erkal et al. (2021b), and the central axis of the blueshifted molecular outflow in CO emission is reported to be $\approx 60°$ from Zhang et al. (2019). The average PA of all shock features in the redshifted outflow in $H_2$ emission is 253°, which is almost antiparallel to the blueshifted molecular outflow in CO emission, as one expects from a bipolar outflow. There is evidence of shock features, in both the blue and redshifted lobes in $H_2$ emission, expanding away from the central jet axis.

# Chapter 7

# Conclusions and future work

This thesis has explored bipolar outflows from young forming stars, an aspect of the star formation process that may be fundamental. These outflows are ubiquitous to accreting stars, and are thought to be the primary mechanism for the removal of angular momentum from the star-disc system, thus permitting accretion onto the central star. The study of outflows therefore provides a window into the star formation process, disc evolution, planet formation, and feedback into the natal cloud. This work has specifically probed outflows in the optical and NIR wavelength regimes, primarily using the observational technique of IFS. A plethora of permitted and forbidden emission lines tracing ionised, atomic, and molecular shocked gas is available for investigation in this region of the electromagnetic spectrum. This allowed for the study of many aspects of the outflow, and the disentangling of the high-velocity, collimated jet component, and the slower-moving, wider-angled outflow component. In particular, the powerful HH 46/47 outflow emanating from the class I source was investigated using SINFONI K-band IFS observations, and subsequently, the proper motions of this outflow were derived over a 27 year period in [S II] emission, and over an 18 year period in $H_2$ emission, using wide-field imaging. The weaker outflow emanating from the more evolved CTTS, RU Lupi, was probed using MUSE NFM observations. The main findings of these studies are summarised in Section 7.1.

The technique of IFS, discussed in Section 2.2, and the advances in IFU instrumentation in recent years has proven an effective tool in the study of outflows. Their ability to provide both spatial and spectral information is advantageous, in that the morphology of the outflow can be studied in various emission lines and velocity bins. In doing so, the outflow can be decomposed

into high and low-velocity components. Localised spectra can be extracted from various positions across the FOV, allowing the determination of fundamental physical outflow properties such as radial velocities, gas temperatures, densities and ionisation fractions. The advances in AO techniques, especially in the domain of optical wavelengths, has allowed sharper observations with high angular resolutions, and the advances in both spectral range and resolution has allowed better determinations of physical properties and the decomposition of emission lines into their constituent components.

An open question in star formation is the exact mechanism for magneto-centrifugal outflow launching. The work presented in this thesis aims to provide constraints to this question, and in particular, focuses on the angular momentum extraction from the star-disc system. In regards to this, this work has provided evidence of layering in the radial structure of outflows. Confirmation of kinematical layering, exhibiting an onion-like velocity structure, has been shown, where the velocity of the flow decreases with increasing radial distance from the outflow axis. Layering in different emission tracers has been shown, indicating a radially-stratified structure in both temperature and chemistry. Evidence of outflow launching regions originating from extended disc radii has been shown, by geometrically tracing emission back to the disc plane, providing upper limits to launch radii. The feasibility of performing outflow rotation measurements close to the launching region with IFS has been demonstrated. The estimation of accurate mass outflow rates, critical for constraining launching mechanisms, has been shown to be achievable with IFU observations.

These constraints, provided by the main findings of this work, favour the disc wind model as the dominant mechanism for magneto-centrifugal outflow launching. However, as discussed in Section 1.3.1, it is likely somewhat of a combination of the models discussed that are contributing to the overall driving of outflows, producing a layered, multi-component MHD outflow structure. High-velocity, collimated jets originate in the inner disc region, and possibly from the protostar itself, where magnetisation is expected to be the strongest. At this region near the co-rotation radius, the interface where the stellar magnetosphere interacts directly with the inner disc edge, there likely exists a high density of magnetic field lines threading the disc, launching a hot, highly-collimated, fast flow. Furthermore, due to the proximity to the

central star, the inner disc is fully ionised, resulting in a strong coupling between the magnetic field and the disc gas. Moving to more radially extended disk radii, where rotational velocities are increasingly lower, open magnetic field lines likely launch cooler, wide-angled, slower winds, mirroring the disc wind model. This outflow structure, stratified in kinematics, temperature, and chemistry, is what an increasing number of observational evidence is indicating. Evidence of outflows originating from extended disc radii places these energetic phenomena at the forefront for the extraction of angular momentum from the star-disc system.

Important data analysis techniques have been implemented here which facilitate the study of outflows using IFS, and should be considered by other similar studies. One implemented here is the wavelength recalibration technique using OH lines present in the spectra as a reference point, rather than the wavelength solution provided with arc lamps, as discussed in Section 3.3.2. This precise method of wavelength calibration provides a significantly more accurate spectral calibration than that offered with standard data reduction pipelines, with achieved uncertainties of $< 1/10^{\text{th}}$ of the spectral pixel size. This method can be implemented in any ground-based IFU observations, resulting in greater confidence in radial velocity measurements. In fact, the new ESO ERIS data reduction pipeline incorporates the generation of wavelength solutions using OH emission lines to recalibrate the wavelength axis after the first order wavelength solution is derived from the arc lamp. This has yet to be applied to the ERIS observations presented in this work, having been reduced using an earlier version of the pipeline. Another important data analysis technique beneficial to the study of outflows using IFS, is the generation of line to continuum ratio maps. These maps allow the deduction of the contribution that scattered continuum light makes to intrinsic line emission, as discussed in Section 3.3.7. The disentangling of true line emission from scattered nebulosity is critical when investigating the morphology of an emitting region, especially true close to the driving source where the contribution from scattered light is greater. The production of these maps is particularly powerful in the study of the youngest, most powerful outflows which are heavily embedded.

## 7.1 Summary of findings

### 7.1.1 The kinematical study of the HH 46/47 outflow with SINFONI

In Chapter 4, NIR SINFONI K-band IFU observations of the blueshifted HH 46/47 outflow base was presented. The morphology and kinematics of the launching region were investigated, focusing on $H_2$ 1–0 S(1), [Fe II], and Br-$\gamma$ emission. The angular resolution achieved was $0\farcs81$, and, employing a wavelength recalibration technique based on OH telluric lines, an accuracy of $\sim$ 1 km s$^{-1}$ – 3 km s$^{-1}$ was obtained in the radial velocity of $H_2$ emission.

The continuum emission displayed an approximately parabolic and asymmetric reflection nebula, delineating a boundary region between the outflow and the ambient material, where the outflow has carved a wide-angled cavity in the quiescent material. The $H_2$ emission, lying within the reflection nebula traced in continuum emission, displayed a V-shaped morphology surrounding the atomic jet. The forging of this outflow cavity may be due to some wide-angled wind, or expanding shells of material produced by an episodic wide-angled wind, carving into the ambient material, or by successive jet bow shocks from a collimated variable inner jet propagating into a density-stratified medium. The high-velocity [Fe II] and Br-$\gamma$ emission displayed the base of the atomic jet, that culminated in a knot at approximately $1\farcs0$ or 450 au from the source position. Radial stratification of the outflow in different emission tracers was confirmed, exhibiting an onion-like kinematical structure, supporting the disc wind outflow launching model. In addition to the wide-angled outflow cavity traced in $H_2$ emission lying within the reflection nebula traced in continuum emission, and surrounding the hotter, high-velocity atomic jet, it was also nested within the molecular outflow traced in $^{12}$CO (2-1) emission. The reflection nebula, outflow cavity, and atomic jet were all shown to be asymmetric about the CO outflow axis. This asymmetry was attributed to density variations in the surrounding ambient material, and the possible influence of multiple outflows from each of the sources in the binary system. The bending of the atomic jet towards the northern-pointing cavity wall is in agreement with the jet wiggling that has been observed at larger scales.

The radial velocity of the atomic jet peaked at $\approx -210$ km s$^{-1}$, consistent with previous measurements. The slower-moving $H_2$ emission ($\approx -15$ km s$^{-1}$

to $-$ 30 km s$^{-1}$) displayed a velocity gradient in the PV diagrams, where the eastern cavity wall peaked at a higher radial velocity than the northern cavity wall. This velocity gradient in the outflow cavity, transverse to the outflow axis, was confirmed, using velocity centroid maps. The magnitude of this velocity difference is $\sim$ 10 km s$^{-1}$. The origin of this transverse velocity gradient was attributed to the outflow expanding into an inhomogeneous, in density, ambient medium, or the presence of a secondary outflow. Although outflow rotation may be contributing to this signal, it was ruled out as the sole origin, due to large specific angular momenta values, $J(r)$ = 3217 $\pm$ 658 to 3867 $\pm$ 1125 km s$^{-1}$au, calculated from 1$''$.0 to 2$''$.0 offset from the central source, and the fact that the sense of apparent rotation detected is opposite to that of the CO envelope emission. In particular, it was emphasised that radial velocity gradients observed transverse to the outflow axis can be misinterpreted as rotation signatures when other effects, such as those discussed in Section 4.3.2, can produce equivalent transverse velocity gradients.

This chapter displayed the wealth of information that can be extracted from a single IFU observation and highlighted the morphological and kinematical complexity that needs to be considered when interpreting various aspects of outflows at these scales and wavelengths.

### 7.1.2 The spectro-imaging study of the RU Lupi outflow

In Chapter 5, MUSE NFM IFU observations of the CTTS RU Lupi were presented. The morphology and kinematics of the high-velocity jet and the low-velocity outflow component were investigated in optical FEL emission, with a high angular resolution of 0$''$.074. This work built on what was previously uncovered with spectroscopic and spectro-astrometric studies, aligning with the existing conclusion that the narrow component of the LVC in [O I] 6300 Å and [S II] 6731 Å emission traces an MHD disc wind.

Images of the jet and low-velocity component emanating from RU Lupi were presented for the first time. The jet displayed a wide full-opening angle ($\theta \approx 21^\circ$ to $28^\circ$) and culminated in a shock feature or knot at $\approx$ 85 au (or 250 au deprojected into the plane of the sky) along the outflow axis. The opening angle of the jet was comparatively large compared to other studies, typically $< 5^\circ$, but the jet width measurements were hypothesised to be impacted by the presence of an unresolved knot in the inner outflow region, or by jet emission

scattered off a V-shaped cavity. A possible kinematical asymmetry in the jet and counter-jet was also presented. The jet PA, which was measured here accurately for the first time, was $213^\circ \pm 2^\circ$, perpendicular to the PA of the disc, $121^\circ \pm 5^\circ$, as expected. The opening angles for the LVC ($\theta \approx 20^\circ$ to $38^\circ$) are smaller than what has been predicted for low-velocity winds by other studies, $\approx 70^\circ$, however, narrower opening angles are predicted in cases of high accretors, such as RU Lupi. The height of the LVC emitting region could be accurately measured here for the first time, where the measured height of $\sim$ 35 au is higher than the 8 au from the spectro-astrometric measurement, which only provides a minimum offset. This measurement is critical for constraining the mass outflow rate.

Again, radial stratification of the outflow, producing an onion-like flow structure, was confirmed. The slow-moving wide-angled LVC surrounded the high-velocity jet emission. Furthermore, the geometrically measured launch radii upper limits suggested that the jet is launched in the inner disc region, closest to the outflow axis, whilst the LVC is launched at larger disc radii. This nested velocity structure supports the disc wind origin for the LVC. The radial velocity of the jet emission peaks at $v_{\rm rad} \approx -200$ km s$^{-1}$, consistent with previous measurements. The LVC is shown to be a distinct outflow component from the jet, spatially extending less from the source position, therefore fading as offset from the star increases, as expected for a low-velocity wind.

The outflow efficiency ($\eta_{\rm out}$) of the jet was measured to be a few percent, in line with values derived for other CTTSs. The outflow efficiency in the LVC in [O I] 6300 Å emission was shown to be very low, even when uncertainties in the calculations were considered, such as poorly understood wind geometries, spatial extents, and contribution to emission from the disc surface. The mass-loss rate placed the efficiency of the outflow component traced by the LVC at $< 0.1\%$, while models suggest that $\dot{M}_{\rm out} \sim \dot{M}_{\rm acc}$ for a disc wind if it dominates angular momentum removal. The mass outflow rate in the LVC was also shown to be relatively low for a photoevaporative wind. The mass outflow rate for the LVC in [O I] 6300 Å emission was therefore concluded to be a lower limit on $\dot{M}_{\rm wind}$, with the wind from CTTSs instead hypothesised to be predominately molecular. This chapter strongly highlighted the power of IFS for advancing the understanding of the best MHD disc wind tracer, and whether they should be considered important to angular momentum removal in forming stars.

### 7.1.3 The proper motions study of the HH 46/47 outflow

In Chapter 6, the precise proper motions of the HH 46/47 outflow were measured over five epochs totalling approximately 21 years in [S II] 6731 Å emission, and over two epochs, 18 years apart, in $H_2$ emission. This was achieved using wide-field imaging from the EMMI, EFOSC2, FORS2, ISAAC and HAWK-I instruments. This study was undertaken to better understand the large scale structure and motions of the outflow to better inform the findings resulting from the SINFONI observations. The identified shock features were shown to primarily move radially away from the source position. A multi-epoch tracking of shock features common to all observing epochs in [S II] emission, and the average proper motion results over all epochs were presented.

The overarching trend in the multi-epoch tracing of shock features is that there exists tangential velocity variability over time, which is expected when measuring interacting shock features. The average proper motions of the jet were measured to be $v_\perp = 228 \pm 41$ km s$^{-1}$, in good agreement with previous proper motion measurements of the jet in [S II], H$\alpha$, and [Fe II] emission. The average proper motions of the HH 47A bow shock were $v_\perp = 205 \pm 61$ km s$^{-1}$, again in agreement with previous measurements, and lower than the atomic jet, as expected as it is more distant from the driving source. The average proper motions of the fainter, and extended further from the source, HH 47D bow shock were $v_\perp = 138 \pm 54$ km s$^{-1}$, lower than previous estimates, implying a deceleration, but in agreement within uncertainties. The average proper motions of the redshifted HH 47C bow shock were $v_\perp = 141 \pm 32$ km s$^{-1}$, similar to the proper motions in the HH 47D bow shock, where the opposing bow shocks are located symmetrically about the driving source of the outflow and likely originated in the same ejection event. True, 3D space velocities of the shock features were also derived, using a previously derived inclination angle of the outflow.

In $H_2$ emission, the proper motions of the opposing, loop-like molecular outflow lobes was investigated. The HH 47A bow shock was observed in this emission, implying that either molecular hydrogen has recombined from post-shock atomic gas in the bow shock, or that the shock is not energetic enough to dissociate $H_2$. In the redshifted outflow, the identified shock features were

approximately categorised into those along the central axis of the outflow, possessing the highest tangential velocities in the redshifted outflow, and exhibiting evidence of deceleration with distance from the source, and those in the wide-angled outflow lobe which displayed lower tangential velocities.

The large scale morphology of the outflow did not exhibit significant variations over the range of observation epochs. However, the reflection nebula along the outflow cavity seen at the base of the blueshifted outflow experienced variability in intensity, dimming and brightening between successive observations in [S II] emission. This variation was attributed to periodic ejections illuminating the reflection nebula, supported by recent jet knot ejections observed in the SINFONI observations presented in this thesis, and more recent JWST observations, and the presence of a quasi-stationary deflection shock, where the jet collides obliquely with the edge of the evacuated cavity. In $H_2$ emission, a morphological change was observed in the blueshifted outflow cavity, where the tip of the northern-pointing wing of the cavity expanded outward from the jet axis between the observations. The origin of the transverse velocity gradient observed in the $H_2$ outflow cavity in the SINFONI observations, attributed to a dissymmetry in the density of ambient material surrounding the base of the outflow, is supported here, with the northern side of the reflection nebula or outflow cavity appearing much brighter than the southern side in the [S II] and $H_2$ emission images.

The average PAs of large scale outflow features, derived from the trajectories of shock features, were also presented. Those estimated largely agreed with previous estimates. In the wide-angled molecular lobes in $H_2$ emission, shock trajectories exhibited movement, not only radially away from the source, but also away from the outflow axis, implying that the molecular lobes are expanding in all directions.

## 7.2 Future work

As highlighted throughout this thesis, the identification of the dominant outflow launching mechanism, and how significant a role this plays in the extraction of mass and angular momentum from the system is an outstanding question in the field of star formation. The implications that outflows may have on star and planet formation, and disc evolution is substantial. I aim to further

work towards the understanding of the connection between the outflow and the star-disc system, and the intrinsic relationship between outflow launching and accretion.

While case studies, like those presented in this work, are important to understand details of individual outflow systems, the study of large samples allows the investigation of systematic trends in outflow properties. Such a study could consist of a sample of CTTSs in nearby star-forming regions, with evidence of spatially extended emission, provided with high-resolution spectroscopy or spectro-astrometry, or confirmed outflows, like in the case of RU Lupi. Utilising MUSE NFM IFS data cubes, either with new observations or leveraging those already available in the ESO archive, the investigation and findings of the RU Lupi outflow (Chapter 5) could be extended to a sample of objects using the data reduction and analysis techniques developed in this work. This would allow for the study of the morphology and kinematics of their high-velocity jet components and low-velocity, wide-angled outflow components, across a wide spectral window, containing many permitted and forbidden emission lines. Measuring the outflow widths would contribute to the knowledge of jet collimation, and the opening angles of winds near the launching region. The centroids of the outflow emission could be mapped with distance from the source, allowing the exploration of periodic outflow wiggling, an indicator of orbital companions. Employing IFS, the velocity components can be resolved, allowing for the investigation of kinematically layered outflow structures, providing knowledge on launching mechanisms. Further to this, the geometric tracing of emission back to the disc plane allows for the derivation of upper limits of launch radii. Measuring the spatial extents of the LVCs of these resolved outflows from CTTSs, coupled with their radial velocities and emitting luminosities, allows the accurate characterisation of mass outflow rates. Coupling the mass outflow rates with readily measurable mass accretion rates from the many accretion tracing emission lines available in CTTSs, would allow for the derivation of the outflow efficiency in both the jets and winds. One avenue to pursue is the low outflow efficiency measured in the RU Lupi wind in [O I] emission. Is this low efficiency typical for all CTTS winds in this emission line? If so, this tracer is likely not well suited to study the bulk emission from MHD winds originating from extended disc radii, and likely the wind traced by this emission line does not contribute significantly

to mass extraction, and subsequently, angular momentum extraction. A logical complementary dataset to this sample of objects, would be observations of CTTSs that show evidence of spatially extended molecular emission with ERIS in the NIR. Utilising this instrument, the same spatial region of the outflows could be mapped with similar angular resolutions, but in a different wavelength window. This would allow the comparison of the LVC in optical emission to the molecular winds traced by species such as $H_2$. Furthermore, this would allow the estimation of the mass outflow rate contained in the molecular wind, where CTTS winds are hypothesised to be predominantly molecular, allowing the estimation of the outflow efficiencies of the molecular wind components. Wind mass loss rates that are comparable to, or exceed, the mass accretion rate onto the star are consistent with MHD disc wind models, and imply that outflows are the primary driver of accretion in the planet-forming regions of discs.

In regards to the proper motions study presented in Chapter 6, I wish to further investigate the temporal evolution of the HH 46/47 outflow using this dataset. The logical next step in this study is to flux calibrate the wide-field observations. This will allow the determination of true shock intensities, and the exploration of shock dimming and brightening, permitting the examination of shock properties such as gas densities, heating processes, and cooling rates, which can be compared to current models.

Additionally, I have access to MUSE WFM observations of HH 46/47 outflow, providing a $60\farcs0 \times 60\farcs0$ view of the outflow at optical wavelengths. The outflow in the MUSE observations has been identified in many emission lines, such as H$\alpha$, H$\beta$, [Fe II], [N I], [N II], [O I], [S II], [Ni II], and [Cr II]. The investigation of the MUSE observations of HH 46/47 will compliment the SINFONI observations well, allowing a greater spatial extent of the outflow to be studied in different emission tracers. Physical outflow properties will be obtained, such as gas densities, temperatures, and ionisation fractions, using well-established line ratio diagnostics. Furthermore, combining radial velocity measurements of shock features from the MUSE data with derived tangential velocities of corresponding features from the proper motions study will generate accurate estimations of inclination angles for sections of this well-studied outflow.

As the NIR is suitable to study the embedded launching region of outflows from class I sources, as evidenced with the SINFONI observations of HH

46/47 presented in Chapter 4, SINFONI's successor, ERIS, could be utilised to study a sample of these outflow regions in a similar manner to the kinematical and morphological study of HH 46/47. Further to this, JWST NIRSpec in IFU mode, and MIRI can be employed to investigate the nested kinematical, chemical, and thermal morphologies of outflows at even longer wavelengths, permitting even the study of launch regions of class 0 objects. With the use of IFS, making measurements of outflow rotation has been shown to be feasible, especially in the case the of the easily resolvable, laterally extended morphologies of wide-angled outflow components. Rotation signatures are easier to detect in these wide-angled components as opposed to the narrow axial jet components. In class 0/I sources, the outflow launching mechanism can be well-constrained with rotation measurements, providing both disc launching radii, and specific angular momentum contained in the flow. The search for more examples of outflow rotation is progressively becoming more achievable with the advent of new telescopes, instrumentation, and analysis techniques, however, rotation studies are pushing the limits of current telescope capabilities.

Further to the use of current generation IFUs to investigate the launching region of outflows with spatial and kinematical information, the closer evaluation of the dominant launching mechanism through observations of rotation and launch radii will be hugely altered with the delivery of ESO's Extremely Large Telescope (ELT) in the late 2020's to early 2030's. New instrumentation such as HARMONI (the High Angular Resolution Monolithic Optical and Near-infrared Integral field spectrograph), and the IFU modes of METIS (Mid-infrared ELT Imager and Spectrograph) and MOSAIC (Multi-Object Spectrograph) will allow for measurements with very high angular and spectral resolution in the optical and IR wavelength regimes, probing the outflow at au scales in nearby star-forming regions such as Taurus. These close-in observations will enable the study of the innermost region of discs around forming stars, where Earth-like planets may form, and shed light on the earliest phases of star and planet formation. This will bring us even closer to understanding the fundamental question about the origins of our planet, Sun, and Solar System.

# Bibliography


Agra-Amboage, V et al. (2011). "Sub-arcsecond [Fe ii] spectro-imaging of the DG Tauri jet-Periodic bubbles and a dusty disk wind?" In: *Astronomy and Astrophysics* 532, A59.

Agra-Amboage, V. et al. (2014). "Origin of the wide-angle hot $H_2$ in DG Tauri. New insight from SINFONI spectro-imaging". In: *Astronomy and Astrophysics* 564, A11, A11. DOI: 10.1051/0004-6361/201220488. arXiv: 1402.1160 [astro-ph.SR].

Alcalá, J. M. et al. (2014). "X-shooter spectroscopy of young stellar objects-IV. Accretion in low-mass stars and substellar objects in Lupus". In: *Astronomy and Astrophysics* 561, A2.

Alcalá, J. M. et al. (2017). "X-shooter spectroscopy of young stellar objects in Lupus. Accretion properties of class II and transitional objects". In: *Astronomy and Astrophysics* 600, A20, A20. DOI: 10.1051/0004-6361/201629929. arXiv: 1612.07054.

Alexander, R. et al. (2014). "The Dispersal of Protoplanetary Disks". In: *Protostars and Planets VI*. Ed. by Henrik Beuther et al., pp. 475–496. DOI: 10.2458/azu_uapress_9780816531240-ch021. arXiv: 1311.1819 [astro-ph.EP].

Anderson, J. M. et al. (2003). "Locating the Launching Region of T Tauri Winds: The Case of DG Tauri". In: *The Astrophysical Journal Letters* 590.2, pp. L107–L110. DOI: 10.1086/376824. arXiv: astro-ph/0304127 [astro-ph].

André, P. (2002). "The Initial Conditions for Protostellar Collapse: Observational Constraints". In: *EAS Publications Series*. Ed. by Jerome Bouvier and Jean-Paul Zahn. Vol. 3. EAS Publications Series, pp. 1–38. DOI: 10.1051/eas:2002043.

André, P. (2017). "Interstellar filaments and star formation". In: *Comptes Rendus Geoscience* 349.5, pp. 187–197.

André, P., D. Ward-Thompson, and M. Barsony (1993). "Submillimeter Continuum Observations of rho Ophiuchi A: The Candidate Protostar VLA

1623 and Prestellar Clumps". In: *The Astrophysical Journal* 406, p. 122. DOI: 10.1086/172425.

André, P. et al. (2004). "Submillimeter studies of prestellar cores and protostars: Probing the initial conditions for protostellar collapse". In: *Astrophysics and Space Scince* 292.1-4, pp. 325–337.

André, P. et al. (2010). "From filamentary clouds to prestellar cores to the stellar IMF: Initial highlights from the Herschel Gould Belt Survey". In: *Astronomy and Astrophysics* 518, p. L102.

André, P. et al. (2014). "From filamentary networks to dense cores in molecular clouds: toward a new paradigm for star formation". In: *Protostars and Planets VI* 27.

Andrews, S. M. (2020). "Observations of protoplanetary disk structures". In: *Annual Review of Astronomy and Astrophysics* 58.1, pp. 483–528.

Andrews, S. M. et al. (2018). "The Disk Substructures at High Angular Resolution Project (DSHARP). I. Motivation, Sample, Calibration, and Overview". In: *The Astrophysical Journal Letters* 869.2, L41, p. L41. DOI: 10.3847/2041-8213/aaf741. arXiv: 1812.04040 [astro-ph.SR].

Ansdell, M. et al. (2018). "ALMA survey of lupus protoplanetary disks. II. Gas disk radii". In: *The Astrophysical Journal* 859.1, p. 21.

Antoniucci, S. et al. (2008). "Accretion and ejection properties of embedded protostars: the case of HH26, HH34, and HH46 IRS". In: *Astronomy and Astrophysics* 479.2, pp. 503–514. DOI: 10.1051/0004-6361:20077468. arXiv: 0710.5609 [astro-ph].

Arce, H. G. et al. (2007). "Molecular Outflows in Low- and High-Mass Star-forming Regions". In: *Protostars and Planets V*. Ed. by Bo Reipurth, David Jewitt, and Klaus Keil, p. 245. DOI: 10.48550/arXiv.astro-ph/0603071. arXiv: astro-ph/0603071 [astro-ph].

Arce, H. G. et al. (2013). "ALMA Observations of the HH 46/47 Molecular Outflow". In: *The Astrophysical Journal* 774.1, 39, p. 39. DOI: 10.1088/0004-637X/774/1/39. arXiv: 1304.0674 [astro-ph.SR].

Armitage, P. J. (2011). "Dynamics of protoplanetary disks". In: *Annual Review of Astronomy and Astrophysics* 49.1, pp. 195–236.

Armitage, P. J. (2015). "Physical processes in protoplanetary disks". In: *arXiv e-prints*, arXiv:1509.06382, arXiv:1509.06382. DOI: 10.48550/arXiv.1509.06382. arXiv: 1509.06382 [astro-ph.SR].

Armitage, P. J., C. J. Clarke, and F. Palla (2003). "Dispersion in the lifetime and accretion rate of T Tauri discs". In: *Monthly Notices of the Royal Astronomical Society* 342.4, pp. 1139–1146.

Arzoumanian, D. et al. (2021). "Dust polarized emission observations of NGC 6334. BISTRO reveals the details of the complex but organized magnetic field structure of the high-mass star-forming hub-filament network". In: 647, A78, A78. DOI: 10.1051/0004-6361/202038624. arXiv: 2012.13060 [astro-ph.GA].

Astropy Collaboration et al. (2013). "Astropy: A community Python package for astronomy". In: *Astronomy and Astrophysics* 558, A33, A33. DOI: 10.1051/0004-6361/201322068. arXiv: 1307.6212 [astro-ph.IM].

Astropy Collaboration et al. (2018). "The Astropy Project: Building an Open-science Project and Status of the v2.0 Core Package". In: *The Astronomical Journal* 156.3, 123, p. 123. DOI: 10.3847/1538-3881/aabc4f. arXiv: 1801.02634 [astro-ph.IM].

Astropy Collaboration et al. (2022). "The Astropy Project: Sustaining and Growing a Community-oriented Open-source Project and the Latest Major Release (v5.0) of the Core Package". In: *The Astrophysical Journal* 935.2, 167, p. 167. DOI: 10.3847/1538-4357/ac7c74. arXiv: 2206.14220 [astro-ph.IM].

Bacciotti, F. and J. Eislöffel (1999). "Ionization and density along the beams of Herbig-Haro jets". In: *Astronomy and Astrophysics* 342, pp. 717–735.

Bacciotti, F. et al. (2000). "Hubble space telescope stis spectroscopy of the optical outflow from dg tauri: Structure and kinematics on subarcsecond scales". In: *The Astrophysical Journal* 537.1, p. L49.

Bacciotti, F. et al. (2002). "Hubble Space Telescope/STIS Spectroscopy of the Optical Outflow from DG Tauri: Indications for Rotation in the Initial Jet Channel". In: *The Astrophysical Journal* 576.1, pp. 222–231. DOI: 10.1086/341725. arXiv: astro-ph/0206175 [astro-ph].

Bacon, R. et al. (2010). "The MUSE second-generation VLT instrument". In: *Ground-based and Airborne Instrumentation for Astronomy III*. Vol. 7735. SPIE, pp. 131–139.

Bae, J. et al. (2023). "Structured Distributions of Gas and Solids in Protoplanetary Disks". In: *Protostars and Planets VII*. Ed. by S. Inutsuka et al. Vol. 534. Astronomical Society of the Pacific Conference Series, p. 423. DOI: 10.48550/arXiv.2210.13314. arXiv: 2210.13314 [astro-ph.EP].

Bai, X. N. (2017). "Global Simulations of the Inner Regions of Protoplanetary Disks with Comprehensive Disk Microphysics". In: *The Astrophysical Journal* 845.1, 75, p. 75. DOI: 10.3847/1538-4357/aa7dda. arXiv: 1707.00729 [astro-ph.EP].

Bai, X. N. and J. M. Stone (2013). "Local study of accretion disks with a strong vertical magnetic field: Magnetorotational instability and disk outflow". In: *The Astrophysical Journal* 767.1, p. 30.

Bai, X. N. et al. (2016). "Magneto-thermal Disk Winds from Protoplanetary Disks". In: *The Astrophysical Journal* 818.2, 152, p. 152. DOI: 10.3847/0004-637X/818/2/152. arXiv: 1511.06769 [astro-ph.EP].

Balbus, S. A. and J. F. Hawley (1991). "A powerful local shear instability in weakly magnetized disks. I-Linear analysis. II-Nonlinear evolution". In: *Astrophysical Journal, Part 1 (ISSN 0004-637X), vol. 376, July 20, 1991, p. 214-233.* 376, pp. 214–233.

Bally, J. (2016). "Protostellar Outflows". In: *Annual Review of Astronomy and Astrophysics* 54, pp. 491–528. DOI: 10.1146/annurev-astro-081915-023341.

Bally, J. et al. (1987). "Filamentary structure in the Orion molecular cloud". In: *Astrophysical Journal, Part 2-Letters to the Editor (ISSN 0004-637X), vol. 312, Jan. 15, 1987, p. L45-L49.* 312, pp. L45–L49.

Banzatti, A. et al. (2019). "Kinematic Links and the Coevolution of MHD Winds, Jets, and Inner Disks from a High-resolution Optical [O I] Survey". In: *The Astrophysical Journal* 870.2, 76, p. 76. DOI: 10.3847/1538-4357/aaf1aa. arXiv: 1811.06544 [astro-ph.HE].

Batalha, C. C. et al. (1996). "The narrow emission lines of T Tauri stars". In: *Astrophysical Journal Supplement v. 103, p. 211* 103, p. 211.

Baug, T et al. (2021). "An ALMA study of outflow parameters of protoclusters: outflow feedback to maintain the turbulence". In: *Monthly Notices of the Royal Astronomical Society* 507.3, pp. 4316–4334.

Beck, T. L. et al. (2008). "Spatially resolved molecular hydrogen emission in the inner 200 AU environments of classical T Tauri stars". In: *The Astrophysical Journal* 676.1, p. 472.

Belloche, A. (2013). "Observation of rotation in star forming regions: clouds, cores, disks, and jets". In: *EAS Publications Series*. Ed. by P. Hennebelle and C. Charbonnel. Vol. 62. EAS Publications Series, pp. 25–66. DOI: 10.1051/eas/1362002. arXiv: 1305.0627 [astro-ph.GA].

Beroiz, M., J.B. Cabral, and B. Sanchez (2020). "Astroalign: A Python module for astronomical image registration". In: *Astronomy and Computing* 32,

p. 100384. ISSN: 2213-1337. DOI: https://doi.org/10.1016/j.ascom.2020.100384. URL: http://www.sciencedirect.com/science/article/pii/S221313372030038X.

Bertout, C. (1989). "T Tauri stars: wild as dust." In: *Annual Review of Astronomy and Astrophysics* 27, pp. 351–395. DOI: 10.1146/annurev.aa.27.090189.002031.

Bertout, C., N. Robichon, and F. Arenou (1999). "Revisiting Hipparcos data for pre-main sequence stars". In: *Astronomy and Astrophysics* 352, pp. 574–586.

Béthune, W., G. Lesur, and J. Ferreira (2017). "Global simulations of protoplanetary disks with net magnetic flux-i. non-ideal mhd case". In: *Astronomy and Astrophysics* 600, A75.

Beuther, H. et al. (2023). "JWST Observations of Young protoStars (JOYS) - Outflows and accretion in the high-mass star-forming region IRAS 23385+6053". In: *Astronomy and Astrophysics* 673, A121.

Biazzo, K. et al. (2012). "The Chamaeleon II low-mass star-forming region: radial velocities, elemental abundances, and accretion properties". In: *Astronomy and Astrophysics* 547, A104.

Birney, M. et al. (2024a). "A kinematical study of the launching region of the blueshifted HH 46/47 outflow with SINFONI K-band observations". In: *Astronomy and Astrophysics* Vol. 692, A143. DOI: 10.1051/0004-6361/202451433. arXiv: 2407.07233 [astro-ph.SR].

Birney, M. et al. (2024b). "Forbidden emission line spectro-imaging of the RU Lupi jet and low-velocity component". In: *Astronomy and Astrophysics* Vol. 692, L5. DOI: 10.1051/0004-6361/202452402. arXiv: 2409.19112 [astro-ph.SR].

Bjerkeli, P. et al. (2016). "Resolved images of a protostellar outflow driven by an extended disk wind". In: *Nature* 540.7633, pp. 406–409. DOI: 10.1038/nature20600. arXiv: 1612.05148 [astro-ph.SR].

Bjerkeli, P. et al. (2019). "Kinematics around the B335 protostar down to au scales". In: *Astronomy and Astrophysics* 631, A64.

Blandford, R. D. and D. G. Payne (1982). "Hydromagnetic flows from accretion discs and the production of radio jets". In: *Monthly Notices of the Royal Astronomical Society* 199.4, pp. 883–903.

Bohlin R. C. Savage, B. D. and J. F. Drake (1978). "A survey of interstellar HI from L-alpha absorption measurements. II". In: *Astrophysical Journal* 224, pp. 132–142.

Böhm, K. H., D. M. Scott, and J. Solf (1991). "The ultraviolet continuum and the fluorescent H2 lines in low-excitation Herbig-Haro objects". In: *Astrophysical Journal, Part 1 (ISSN 0004-637X), vol. 371, April 10, 1991, p. 248-253.* 371, pp. 248–253.

Bohr, N. (1913). "I. On the constitution of atoms and molecules". In: *The London, Edinburgh, and Dublin Philosophical Magazine and Journal of Science* 26.151, pp. 1–25.

Bok, B. J. and E. F. Reilly (1947). "Small dark nebulae." In: *Astrophysical Journal, vol. 105, p. 255* 105, p. 255.

Bonnefoy, M. et al. (2014). "A library of near-infrared integral field spectra of young M–L dwarfs". In: *Astronomy and Astrophysics* 562, A127.

Bonnell, I. A. et al. (1998). "Magnetospheric accretion and pre-main-sequence stellar masses". In: *Monthly Notices of the Royal Astronomical Society* 299.4, pp. 1013–1018.

Bouvier, J. et al. (1986). "Rotation in T Tauri stars. I-Observations and immediate analysis". In: *Astronomy and Astrophysics (ISSN 0004-6361), vol. 165, no. 1-2, Sept. 1986, p. 110-119.* 165, pp. 110–119.

Bouvier, J. et al. (1997). "COYOTES IV: the rotational periods of low-mass Post-T Tauri stars in Taurus." In: *Astronomy and Astrophysics, v. 318, p. 495-505* 318, pp. 495–505.

Bouvier, J. et al. (2007). "Magnetospheric accretion-ejection processes in the classical T Tauri star AA Tauri". In: *Astronomy and Astrophysics* 463.3, pp. 1017–1028.

Bouvier, J. et al. (2023). "Stable accretion and episodic outflows in the young transition disk system GM Aurigae-A semester-long optical and near-infrared spectrophotometric monitoring campaign". In: *Astronomy and Astrophysics* 672, A5.

Bracco, A. et al. (2017). "Probing changes of dust properties along a chain of solar-type prestellar and protostellar cores in Taurus with NIKA". In: *Astronomy and Astrophysics* 604, A52.

Cabrit, S. (2007). "Jets from young stars: The need for MHD collimation and acceleration processes". In: *Jets from Young Stars: Models and Constraints*. Springer, pp. 21–53.

Cabrit, S. and A. Raga (2000). "Theoretical interpretation of the apparent deceleration in the HH 34 superjet". In: *Astronomy and Astrophysics, v. 354, p. 667-673 (2000)* 354, pp. 667–673.

Cabrit, S. et al. (2006). "Tidal stripping and disk kinematics in the RW Aurigae system". In: *Astronomy and Astrophysics* 452.3, pp. 897–906. DOI: 10.1051/0004-6361:20054047.

Calvet, N. and L. Hartmann (1992). "Balmer line profiles for infalling T Tauri envelopes". In: *Astrophysical Journal, Part 1 (ISSN 0004-637X), vol. 386, Feb. 10, 1992, p. 239-247.* 386, pp. 239–247.

Camenzind, M (1990). "Magnetized disk-winds and the origin of bipolar outflows". In: *Accretion and Winds*. Springer, pp. 234–265.

Caratti o Garatti, A. et al. (2006). "$H_2$ active jets in the near IR as a probe of protostellar evolution". In: *Astronomy and Astrophysics* 449.3, pp. 1077–1088. DOI: 10.1051/0004-6361:20054313.

Caratti o Garatti, A. et al. (2009). "First detection of acceleration and deceleration in protostellar jets?-Time variability in the Chamaeleontis II outflows". In: *Astronomy & Astrophysics* 502.2, pp. 579–597.

Carrera, D. et al. (2017). "Planetesimal formation by the streaming instability in a photoevaporating disk". In: *The Astrophysical Journal* 839.1, p. 16.

Čemeljić, Miljenko, Hsien Shang, and T-Y Chiang (2013). "Magnetospheric Accretion and Ejection of Matter in Resistive Magnetohydrodynamic Simulations". In: *The Astrophysical Journal* 768.1, p. 5.

Cerqueira, A. H. et al. (2006). "Emission lines from rotating proto-stellar jets with variable velocity profiles-I. Three-dimensional numerical simulation of the non-magnetic case". In: *Astronomy and Astrophysics* 448.1, pp. 231–241.

Chen, X. et al. (2016). "Rotating bullets from a variable protostar". In: *The Astrophysical Journal* 824.2, p. 72.

Chevance, M. et al. (2023). "The Life and Times of Giant Molecular Clouds". In: *Protostars and Planets VII*. Ed. by S. Inutsuka et al. Vol. 534. Astronomical Society of the Pacific Conference Series, p. 1. DOI: 10.48550/arXiv.2203.09570. arXiv: 2203.09570 [astro-ph.GA].

Choi, M., M. Kang, and K. Tatematsu (2011). "Rotation of the NGC 1333 IRAS 4A2 protostellar jet". In: *The Astrophysical Journal Letters* 728.2, p. L34.

Cieza, L. et al. (2007). "The Spitzer c2d survey of weak-line T Tauri stars. II. New constraints on the timescale for planet building". In: *The Astrophysical Journal* 667.1, p. 308.

Coffey, D. (2017). "Star formation: Desperately seeking spin". In: *Nature Astronomy* 1, 0180, p. 0180. DOI: 10.1038/s41550-017-0180.

Coffey, D. et al. (2004). "Rotation of Jets from Young Stars: New Clues from the Hubble Space Telescope Imaging Spectrograph". In: *The Astrophysical Journal* 604.2, pp. 758–765. DOI: 10.1086/382019. arXiv: astro-ph/0312300 [astro-ph].

Coffey, D. et al. (2007). "Further Indications of Jet Rotation in New Ultraviolet and Optical Hubble Space Telescope STIS Spectra". In: *The Astrophysical Journal* 663.1, pp. 350–364. DOI: 10.1086/518100. arXiv: astro-ph/0703271 [astro-ph].

Coffey, D. et al. (2015). "A search for consistent jet and disk rotation signatures in RY Tau". In: *The Astrophysical Journal* 804.1, p. 2.

Cohen, M., Wm. A. Wheaton, and S. T. Megeath (2003). "Spectral Irradiance Calibration in the Infrared. XIV. The Absolute Calibration of 2MASS". In: *The Astronomical Journal* 126.2, pp. 1090–1096. DOI: 10.1086/376474. arXiv: astro-ph/0304350 [astro-ph].

Costigan, G. et al. (2014). "Temperaments of young stars: rapid mass accretion rate changes in T Tauri and Herbig Ae stars". In: *Monthly Notices of the Royal Astronomical Society* 440.4, pp. 3444–3461.

Craig, M. et al. (2017). *astropy/ccdproc: v1.3.0.post1*. DOI: 10.5281/zenodo.1069648. URL: https://doi.org/10.5281/zenodo.1069648.

Cranmer, S. R. (2008). "Turbulence-driven polar winds from T Tauri stars energized by magnetospheric accretion". In: *The Astrophysical Journal* 689.1, p. 316.

Dame, T. M., D. Hartmann, and P. Thaddeus (2001). "The Milky Way in molecular clouds: a new complete CO survey". In: *The Astrophysical Journal* 547.2, p. 792.

Davis, C. J. (2002). "H[2] Observations of Outflows from Young Stars". In: *Revista Mexicana de Astronomia y Astrofisica Conference Series*. Ed. by William J. Henney et al. Vol. 13. Revista Mexicana de Astronomia y Astrofisica Conference Series, pp. 36–42.

Davis, C. J. et al. (2003). "Near-IR echelle spectroscopy of Class I protostars: Mapping Forbidden Emission-Line (FEL) regions in [FeII]". In: *Astronomy and Astrophysics* 397, pp. 693–710. DOI: 10.1051/0004-6361:20021545.

Davis, C. J. et al. (2011). "VLT integral field spectroscopy of embedded protostars: using near-infrared emission lines as tracers of accretion and outflow". In: *Astronomy and Astrophysics* 528, A3, A3. DOI: 10.1051/0004-6361/201015897.

De Colle, F., A. H. Cerqueira, and A. Riera (2016). "Transverse Velocity Shifts in Protostellar Jets: Rotation or Velocity Asymmetries?" In: *The Astrophysical Journal* 832.2, 152, p. 152. DOI: 10.3847/0004-637X/832/2/152. arXiv: 1609.04858 [astro-ph.SR].

de Valon, A. et al. (2020). "ALMA reveals a large structured disk and nested rotating outflows in DG Tauri B". In: *Astronomy and Astrophysics* 634, p. L12.

de Valon, A. et al. (2022). "Modeling the CO outflow in DG Tauri B: Swept-up shells versus perturbed MHD disk wind". In: *Astronomy and Astrophysics* 668, A78, A78. DOI: 10.1051/0004-6361/202141316. arXiv: 2212.00514 [astro-ph.SR].

Delabrosse, V. et al. (2024). "JWST study of the DG Tau B disk-wind candidate-I. Overview and nested H2-CO outflows". In: *Astronomy and Astrophysics* 688, A173.

Demars, D. et al. (2023). "Emission line variability of young 10-30 $M_{Jup}$ companions. I. The case of GQ Lup b and GSC 06214-00210 b". In: *Astronomy and Astrophysics* 676, A123, A123. DOI: 10.1051/0004-6361/202346221. arXiv: 2305.09460 [astro-ph.EP].

Dobbs, C. L., A. Burkert, and J. E. Pringle (2011). "Why are most molecular clouds not gravitationally bound?" In: *Monthly Notices of the Royal Astronomical Society* 413.4, pp. 2935–2942.

Dobbs, C. L. et al. (2014). "Formation of Molecular Clouds and Global Conditions for Star Formation". In: *Protostars and Planets VI*. Ed. by Henrik Beuther et al., pp. 3–26. DOI: 10.2458/azu_uapress_9780816531240-ch001. arXiv: 1312.3223 [astro-ph.GA].

D'Odorico, S. (1990). "EMMI, the ESO multi-mode instrument, successfully installed at the NTT." In: *The Messenger, vol. 61, p. 51-56* 61, pp. 51–56.

Dokkum, P. G. van (2001). "Cosmic-ray rejection by laplacian edge detection". In: *Publications of the Astronomical Society of the Pacific* 113.789, p. 1420.

Donati, J-F. et al. (2005). "Direct detection of a magnetic field in the innermost regions of an accretion disk". In: *Nature* 438.7067, pp. 466–469.

Donati, J-F. et al. (2010). "Magnetospheric accretion and spin-down of the prototypical classical T Tauri star AA Tau". In: *Monthly Notices of the Royal Astronomical Society* 409.4, pp. 1347–1361.

Donati, J-F. et al. (2020). "The magnetic field and accretion regime of CI Tau". In: *Monthly Notices of the Royal Astronomical Society* 491.4, pp. 5660–5670.

Dopita, M. A. (1976). "Optical emission from shock waves. I-Abundances in N49". In: *Astrophysical Journal, vol. 209, Oct. 15, 1976, pt. 1, p. 395-401.* 209, pp. 395–401.

Dopita, M. A., R. D. Schwartz, and I. Evans (1982). "Herbig-Haro Objects 46 and 47-Evidence for bipolar ejection from a young star". In: *Astrophysical Journal, Part 2-Letters to the Editor, vol. 263, Dec. 15, 1982, p. L73-L77.* 263, pp. L73–L77.

Dougados, C. (2008). "Observing YSO Jets with Adaptive Optics: Techniques and Main Results". In: *Jets from Young Stars II: Clues from High Angular Resolution Observations*. Springer, pp. 105–121.

Dougados, C. et al. (2000). "T Tauri stars microjets resolved by adaptive optics". In: *Astronomy and Astrophysics* 357, pp. L61–L64.

Draine, B. T. and C. F. McKee (1993). "Theory of interstellar shocks." In: *Annual Review of Astronomy and Astrophysics* 31, pp. 373–432. DOI: 10.1146/annurev.aa.31.090193.002105.

Drazkowska, J. et al. (2023). "Planet Formation Theory in the Era of ALMA and Kepler: from Pebbles to Exoplanets". In: *Astronomical Society of the Pacific Conference Series*. Vol. 534, p. 717.

Dunham, M. M. et al. (2014). "The evolution of protostars: Insights from ten years of infrared surveys with Spitzer and Herschel". In: *Protostars and Planets VI* 195.

Edwards, S. (2009). "Winds and Accretion in Young Stars". In: *15th Cambridge Workshop on Cool Stars, Stellar Systems, and the Sun*. Ed. by Eric Stempels. Vol. 1094. American Institute of Physics Conference Series. AIP, pp. 29–38. DOI: 10.1063/1.3099106. arXiv: 0809.3603 [astro-ph].

Edwards, S. et al. (1994). "Spectroscopic Evidence for Magnetospheric Accretion in Classical T Tauri Stars". In: *The Astronomical Journal* 108, p. 1056. DOI: 10.1086/117134.

Einstein, Albert (1965). "Concerning an heuristic point of view toward the emission and transformation of light". In: *American Journal of Physics* 33.5, p. 367.

Eisenhauer, F. et al. (2003). "SINFONI: integral field spectroscopy at 50-milliarcsecond resolution with the ESO VLT". In: *Instrument Design and Performance for Optical/Infrared Ground-based Telescopes*. Vol. 4841. SPIE, pp. 1548–1561.

Eisenhauer, F. et al. (2011). "GRAVITY: observing the universe in motion". In: *The Messenger*.

Eisloeffel, J. and R. Mundt (1994). "Proper motion measurements and high resolution imaging of the HH 46/47 outflow." In: *Astronomy and Astrophysics* 284, pp. 530–544.

Ercolano, B. and J. E. Owen (2010). "Theoretical spectra of photoevaporating protoplanetary discs: an atlas of atomic and low-ionization emission lines". In: *Monthly Notices of the Royal Astronomical Society* 406.3, pp. 1553–1569.

Ercolano, B. and I. Pascucci (2017). "The dispersal of planet-forming discs: theory confronts observations". In: *Royal Society Open Science* 4.4, 170114, p. 170114. DOI: 10.1098/rsos.170114. arXiv: 1704.00214 [astro-ph.EP].

Erkal, J. et al. (2021a). "Launching the asymmetric bipolar jet of DO Tau". In: *Astronomy and Astrophysics* 650, A46, A46. DOI: 10.1051/0004-6361/202038977. arXiv: 2104.07484 [astro-ph.SR].

Erkal, J. et al. (2021b). "Probing Jets from Young Embedded Sources: Clues from HST Near-IR [Fe II] Images". In: *The Astrophysical Journal* 919.1, 23, p. 23. DOI: 10.3847/1538-4357/ac06c5. arXiv: 2106.04414 [astro-ph.SR].

Espaillat, C. et al. (2014). "An observational perspective of transitional disks". In: *arXiv preprint arXiv:1402.7103*.

Fang, M. et al. (2009). "Star and protoplanetary disk properties in Orion's suburbs". In: *Astronomy and Astrophysics* 504.2, pp. 461–489.

Fang, M. et al. (2018). "A New Look at T Tauri Star Forbidden Lines: MHD-driven Winds from the Inner Disk". In: *The Astrophysical Journal* 868.1, 28, p. 28. DOI: 10.3847/1538-4357/aae780. arXiv: 1810.03366 [astro-ph.SR].

Fang, M. et al. (2023a). "A High-resolution Optical Survey of Upper Sco: Evidence for Coevolution of Accretion and Disk Winds". In: *The Astrophysical Journal* 945.2, 112, p. 112. DOI: 10.3847/1538-4357/acb2c9. arXiv: 2301.09240 [astro-ph.SR].

Fang, M. et al. (2023b). "High-resolution [O I] line spectral mapping of TW Hya supportive of a magnetothermal wind". In: *Nature Astronomy*. DOI: 10.1038/s41550-023-02004-x. arXiv: 2305.07929 [astro-ph.SR].

Fendt, Christian (2009). "FORMATION OF PROTOSTELLAR JETS AS TWO-COMPONENT OUTFLOWS FROM STAR–DISK MAGNETOSPHERES". In: *The Astrophysical Journal* 692.1, p. 346.

Ferreira, J. (1997). "Magnetically-driven jets from Keplerian accretion discs." In: *Astronomy and Astrophysics* 319, pp. 340–359. DOI: 10.48550/arXiv.astro-ph/9607057. arXiv: astro-ph/9607057 [astro-ph].

— (2009). "Self-Collimated Jets from Accretion Discs and Star-disc Interaction Zones". In: *Protostellar Jets in Context*. Ed. by Kanaris Tsinganos, Tom Ray,

and Matthias Stute. Vol. 13. Astrophysics and Space Science Proceedings, pp. 99–110. DOI: 10.1007/978-3-642-00576-3_12.

Ferreira, J. (2013). "Braking down an accreting protostar: disc-locking, disc winds, stellar winds, X-winds and Magnetospheric Ejecta". In: *European Astronomical Society Publications Series* 62, pp. 169–225.

Ferreira, J., C. Dougados, and S. Cabrit (2006). "Which jet launching mechanism(s) in T Tauri stars?" In: *Astronomy and Astrophysics* 453.3, pp. 785–796. DOI: 10.1051/0004-6361:20054231. arXiv: astro-ph/0604053 [astro-ph].

Fiorellino, E. et al. (2021). "KMOS study of the mass accretion rate from Class I to Class II in NGC 1333". In: *Astronomy and Astrophysics* 650, A43.

Fischer, W. J. et al. (2023). "Accretion Variability as a Guide to Stellar Mass Assembly". In: *Protostars and Planets VII*. Ed. by S. Inutsuka et al. Vol. 534. Astronomical Society of the Pacific Conference Series, p. 355. DOI: 10.48550/arXiv.2203.11257. arXiv: 2203.11257 [astro-ph.SR].

Flores-Rivera, L. et al. (2023). "Forbidden emission lines in protostellar outflows and jets with MUSE". In: *Astronomy and Astrophysics* 670, A126, A126. DOI: 10.1051/0004-6361/202141664. arXiv: 2301.02559 [astro-ph.SR].

Font, A. S. et al. (2004). "Photoevaporation of circumstellar disks around young stars". In: *The Astrophysical Journal* 607.2, p. 890.

Frank, A. et al. (2014). "Jets and Outflows from Star to Cloud: Observations Confront Theory". In: *Protostars and Planets VI*. Ed. by Henrik Beuther et al., pp. 451–474. DOI: 10.2458/azu_uapress_9780816531240-ch020. arXiv: 1402.3553 [astro-ph.SR].

Freudling, W. et al. (2013). "Automated data reduction workflows for astronomy. The ESO Reflex environment". In: *Astronomy and Astrophysics* 559, A96, A96. DOI: 10.1051/0004-6361/201322494. arXiv: 1311.5411 [astro-ph.IM].

Fromang, S. et al. (2013). "Local outflows from turbulent accretion disks". In: *Astronomy and Astrophysics* 552, A71.

Fukui, Y. and A. Kawamura (2010). "Molecular clouds in nearby galaxies". In: *Annual Review of Astronomy and Astrophysics* 48.1, pp. 547–580.

Fukui, Y. et al. (2001). "On the mass spectrum of giant molecular clouds in the large magellanic cloud". In: *Publications of the Astronomical Society of Japan* 53.6, pp. L41–L44.

Gallet, F. and J. Bouvier (2013). "Improved angular momentum evolution model for solar-like stars". In: *Astronomy and Astrophysics* 556, A36.

Galli, D. and F. H. Shu (1993). "Collapse of magnetized molecular cloud cores. I. Semianalytical solution". In: *Astrophysical Journal v. 417, p. 220* 417, p. 220.

Garcia Lopez, R. et al. (2010). "IR diagnostics of embedded jets: kinematics and physical characteristics of the HH46-47 jet". In: *Astronomy and Astrophysics* 511, A5, A5. DOI: 10.1051/0004-6361/200913304. arXiv: 0912.2043 [astro-ph.SR].

Garcia Lopez, R. et al. (2013). "Spatially resolved H2 emission from a very low-mass star". In: *Astronomy and Astrophysics* 552, p. L2.

Garufi, A. et al. (2020). "ALMA chemical survey of disk-outflow sources in Taurus (ALMA-DOT)-I. CO, CS, CN, and H2CO around DG Tau B". In: *Astronomy and Astrophysics* 636, A65.

Gaudel, M. et al. (2020). "Angular momentum profiles of Class 0 protostellar envelopes". In: *Astronomy and Astrophysics* 637, A92, A92. DOI: 10.1051/0004-6361/201936364. arXiv: 2001.10004 [astro-ph.SR].

Giannini, T. et al. (2013). "The diagnostic potential of Fe lines applied to protostellar jets". In: *The Astrophysical Journal* 778.1, p. 71.

Ginski, C. et al. (2016). "Direct detection of scattered light gaps in the transitional disk around HD 97048 with VLT/SPHERE". In: *Astronomy and Astrophysics* 595, A112, A112. DOI: 10.1051/0004-6361/201629265. arXiv: 1609.04027 [astro-ph.EP].

Ginski, C. et al. (2021). "Disk Evolution Study Through Imaging of Nearby Young Stars (DESTINYS): Late Infall Causing Disk Misalignment and Dynamic Structures in SU Aur". In: *The Astrophysical Journal Letters* 908.2, L25, p. L25. DOI: 10.3847/2041-8213/abdf57. arXiv: 2102.08781 [astro-ph.EP].

Gorti, U., D. Hollenbach, and C. P. Dullemond (2015). "The impact of dust evolution and photoevaporation on disk dispersal". In: *The Astrophysical Journal* 804.1, p. 29.

Gorti, U. et al. (2011). "Emission lines from the gas disk around TW Hydra and the origin of the inner hole". In: *The Astrophysical Journal* 735.2, p. 90.

Graham, J. A. and M. H. Heyer (1989). "Young Stars of Low Mass in the GUM Nebula". In: *Publications of the Astronomical Society of the Pacific* 101, p. 573. DOI: 10.1086/132471.

Green, D. W. (1992). "Magnitude corrections for atmospheric extinction". In: *International Comet Quarterly* 14, p. 55.

Greenacre, M. et al. (2022). "Principal component analysis". In: *Nature Reviews Methods Primers* 2.1, p. 100.

Greene, T. P. et al. (1994). "Further mid-infrared study of the rho Ophiuchi cloud young stellar population: Luminosities and masses of pre-main - sequence stars". In: *Astrophysical Journal, Part 1 (ISSN 0004-637X), vol. 434, no. 2, p. 614-626* 434, pp. 614–626.

Gressel, O. and M. E. Pessah (2015). "Characterizing the mean-field dynamo in turbulent accretion disks". In: *The Astrophysical Journal* 810.1, p. 59.

Güdel, M. et al. (2018). "ALMA detects a radial disk wind in DG Tauri". In: *Astronomy and Astrophysics* 620, p. L1.

Gullbring, E. et al. (1998). "Disk accretion rates for T Tauri stars". In: *The Astrophysical Journal* 492.1, p. 323.

Gupta, A. et al. (2023). "Reflections on nebulae around young stars. A systematic search for late-stage infall of material onto Class II disks". In: *Astronomy and Astrophysics* 670, L8, p. L8. DOI: 10.1051/0004-6361/202245254. arXiv: 2301.02994 [astro-ph.SR].

Habel, N. M. et al. (2021). "An HST Survey of Protostellar Outflow Cavities: Does Feedback Clear Envelopes?" In: *The Astrophysical Journal* 911.2, p. 153.

Hacar, A. et al. (2023). "Initial Conditions for Star Formation: A Physical Description of the Filamentary ISM". In: *Protostars and Planets VII*. Ed. by S. Inutsuka et al. Vol. 534. Astronomical Society of the Pacific Conference Series. Astron. Soc. Pac San Francisco, p. 153.

Haro, G. (1952). "Herbig's nebulous objects near NGC 1999." In: *Astrophysical Journal, vol. 115, p. 572* 115, p. 572.

Harsono, D. et al. (2023). "JWST Peers into the Class I Protostar TMC1A: Atomic Jet and Spatially Resolved Dissociative Shock Region". In: *The Astrophysical Journal Letters* 951.2, p. L32.

Hartigan, P. (2003). "Shock waves in outflows from young stars". In: *Jets in Young Stellar Objects: Theory and Observations*, pp. 111–122.

— (2008). "Measurement of Physical Conditions in Stellar Jets". In: *Jets from Young Stars II: Clues from High Angular Resolution Observations*. Ed. by Francesca Bacciotti, Leonardo Testi, and Emma Whelan. Berlin, Heidelberg: Springer Berlin Heidelberg, pp. 15–42. ISBN: 978-3-540-68032-1. DOI: 10.1007/978-3-540-68032-1_2. URL: https://doi.org/10.1007/978-3-540-68032-1_2.

Hartigan, P., S. Edwards, and L. Ghandour (1995). "Disk Accretion and Mass Loss from Young Stars". In: *The Astrophysical Journal* 452, p. 736. DOI: 10.1086/176344.

Hartigan, P. and J. A. Morse (2007). "Collimation, proper motions, and physical conditions in the HH 30 jet from Hubble Space Telescope slitless spectroscopy". In: *The Astrophysical Journal* 660.1, p. 426.

Hartigan, P., J. A. Morse, and J. Raymond (1994). "Mass-Loss Rates, Ionization Fractions, Shock Velocities, and Magnetic Fields of Stellar Jets". In: *The Astrophysical Journal* 436, p. 125. DOI: 10.1086/174887.

Hartigan, P. et al. (1993). "Observations of entrainment and time variability in the HH 47 jet". In: *Astrophysical Journal, Part 2-Letters (ISSN 0004-637X), vol. 414, no. 2, p. L121-L124.* 414, pp. L121–L124.

Hartigan, P. et al. (2005). "Proper Motions of the HH 47 Jet Observed with the Hubble Space Telescope". In: *The Astronomical Journal* 130.5, pp. 2197–2205. DOI: 10.1086/491673. arXiv: astro-ph/0507526 [astro-ph].

Hartigan, P. et al. (2011). "Fluid Dynamics of Stellar Jets in Real Time: Third Epoch Hubble Space Telescope Images of HH 1, HH 34, and HH 47". In: *The Astrophysical Journal* 736.1, 29, p. 29. DOI: 10.1088/0004-637X/736/1/29. arXiv: 1104.4341 [astro-ph.SR].

Hartmann, L. (2009). *Accretion Processes in Star Formation: Second Edition*. Cambridge University Press.

Hartmann, L., E. Avrett, and S. Edwards (1982). "Wave-driven winds from cool stars. II-Models for T Tauri stars". In: *Astrophysical Journal, Part 1, vol. 261, Oct. 1, 1982, p. 279-292. Research supported by the Smithsonian Institution;* 261, pp. 279–292.

Hartmann, L., G. Herczeg, and N. Calvet (2016). "Accretion onto pre-main-sequence stars". In: *Annual Review of Astronomy and Astrophysics* 54.1, pp. 135–180.

Hartmann, L., R. Hewett, and N. Calvet (1994). "Magnetospheric accretion models for T Tauri stars. 1: Balmer line profiles without rotation". In: *Astrophysical Journal, Part 1 (ISSN 0004-637X), vol. 426, no. 2, p. 669-687* 426, pp. 669–687.

Hartmann, L. et al. (1998). "Accretion and the evolution of T Tauri disks". In: *The Astrophysical Journal* 495.1, p. 385.

Heathcote, S. et al. (1996). "Hubble Space Telescope Observations of the HH 47 Jet: Narrowband Images". In: *The Astronomical Journal* 112, p. 1141. DOI: 10.1086/118085.

Henshaw, J. D. et al. (2014). "The dynamical properties of dense filaments in the infrared dark cloud G035. 39- 00.33". In: *Monthly Notices of the Royal Astronomical Society* 440.3, pp. 2860–2881.

Herbig, G. H. (1951). "The spectra of two nebulous objects near NGC 1999." In: *Astrophysical Journal, vol. 113, p. 697-699* 113, pp. 697–699.

Herbig, G. H. (1962). "The Properties and Problems of T Tauri Stars and Related Objects". In: *Advances in Astronomy and Astrophysics* 1, pp. 47–103. DOI: 10.1016/B978-1-4831-9919-1.50006-6.

Herbig, George H. (1960). "The Spectra of Be- and Ae-Type Stars Associated with Nebulosity". In: *The Astrophysical Journal Supplement* 4, p. 337. DOI: 10.1086/190050.

Herczeg, G. J. and L. A. Hillenbrand (2008). "UV excess measures of accretion onto young very low mass stars and brown dwarfs". In: *The Astrophysical Journal* 681.1, p. 594.

Herczeg, G. J. et al. (2005). "The loopy ultraviolet line profiles of RU Lupi: accretion, outflows, and fluorescence". In: *The Astronomical Journal* 129.6, p. 2777.

Herczeg, G. J. et al. (2006). "The origins of fluorescent H2 emission from T Tauri stars". In: *The Astrophysical Journal Supplement Series* 165.1, p. 256.

Herczeg, G. J. et al. (2023). "Twenty-five Years of Accretion onto the Classical T Tauri Star TW Hya". In: *The Astrophysical Journal* 956.2, p. 102.

Hillenbrand, L. A. et al. (1992). "Herbig Ae/Be Stars: Intermediate-Mass Stars Surrounded by Massive Circumstellar Accretion Disks". In: *The Astrophysical Journal* 397, p. 613. DOI: 10.1086/171819.

Hirota, T. et al. (2017). "Disk-driven rotating bipolar outflow in Orion Source I". In: *Nature Astronomy* 1, 0146, p. 0146. DOI: 10.1038/s41550-017-0146. arXiv: 1712.04606 [astro-ph.SR].

Hirth, G. A., R. Mundt, and J. Solf (1997). "Spatial and kinematic properties of the forbidden emission line region of T Tauri stars". In: *Astronomy & Astrophysics Supplement* 126, pp. 437–469. DOI: 10.1051/aas:1997275.

Hoare, M. G. et al. (2007). "Ultracompact Hii Regions and the Early Lives of Massive Stars". In: *Protostars and Planets V*. Ed. by Bo Reipurth, David Jewitt, and Klaus Keil, p. 181. DOI: 10.48550/arXiv.astro-ph/0603560. arXiv: astro-ph/0603560 [astro-ph].

Huang, J. et al. (2018). "The Disk Substructures at High Angular Resolution Project (DSHARP). II. Characteristics of Annular Substructures". In: *The Astrophysical Journal Letters* 869.2, L42, p. L42. DOI: 10.3847/2041-8213/aaf740. arXiv: 1812.04041 [astro-ph.EP].

Hughes, J. et al. (1994). "The stellar population of the Lupus clouds". In: *The Astronomical Journal, vol. 108, no. 3, p. 1071-1090* 108, pp. 1071–1090.

Hugoniot, H (1887). "Mémoire sur la propagation du mouvement dans un fluide indéfini (première partie)". In: *Journal de Mathématiques Pures et Appliquées* 3, pp. 477–492.

Hunter, J. D. (2007). "Matplotlib: A 2D graphics environment". In: *Computing in Science & Engineering* 9.3, pp. 90–95. DOI: 10.1109/MCSE.2007.55.

Inutsuka, S. (2012). "Present-day star formation: From molecular cloud cores to protostars and protoplanetary disks". In: *Progress of Theoretical and Experimental Physics* 2012.1, 01A307.

Jeans, J. H. (1902). "The Stability of a Spherical Nebula". In: *Philosophical Transactions of the Royal Society of London Series A* 199, pp. 1–53. DOI: 10.1098/rsta.1902.0012.

Jhan, K. S. and C. F. Lee (2021). "25 au Angular Resolution Observations of HH 211 with ALMA: Jet Properties and Shock Structures in SiO, CO, and SO". In: *The Astrophysical Journal* 909.1, p. 11.

Johns-Krull, C. M., J. A. Valenti, and C. Koresko (1999). "Measuring the magnetic field on the classical T Tauri star BP Tauri". In: *The Astrophysical Journal* 516.2, p. 900.

Johns-Krull, Christopher M (2007). "The magnetic fields of classical T Tauri stars". In: *The Astrophysical Journal* 664.2, p. 975.

Joliffe, I.T. (2002). "Principal Component Analysis for Special Types of Data". In: *Principal Component Analysis*. New York, NY: Springer New York, pp. 338–372. ISBN: 978-0-387-22440-4. DOI: 10.1007/0-387-22440-8_13. URL: https://doi.org/10.1007/0-387-22440-8_13.

Jones, A. et al. (2013). "An advanced scattered moonlight model for Cerro Paranal". In: *Astronomy and Astrophysics* 560, A91, A91. DOI: 10.1051/0004-6361/201322433. arXiv: 1310.7030 [astro-ph.IM].

Joy, A. H. (1945). "59. T Tauri Variable Stars". In: *Astrophysical Journal* 102, pp. 168–195.

Kirwan, A. et al. (2022). "The morphology of the HD 163296 jet as a window on its planetary system". In: *Astronomy and Astrophysics* 663, A30, A30. DOI: 10.1051/0004-6361/202142862. arXiv: 2205.06569 [astro-ph.SR].

Koenigl, A. (1991). "Disk Accretion onto Magnetic T Tauri Stars". In: *The Astrophysical Journal Letters* 370, p. L39. DOI: 10.1086/185972.

Kogure, T. and K. C. Leung (2010). *The astrophysics of emission-line stars*. Vol. 342. Springer Science & Business Media.

Konigl, A. and R. E. Pudritz (2000). "Disk Winds and the Accretion-Outflow Connection". In: *Protostars and Planets IV*. Ed. by V. Mannings, A. P. Boss,

and S. S. Russell, p. 759. DOI: 10.48550/arXiv.astro-ph/9903168. arXiv: astro-ph/9903168 [astro-ph].

Krumholz, M. R. (2017). *Star Formation*. World Scientific. DOI: 10.1142/10091.

Kuffmeier, M. (2024). "Magnetohydrodynamical modeling of star-disk formation: from isolated spherical collapse towards incorporation of external dynamics". In: *Frontiers in Astronomy and Space Sciences* 11, p. 1403075.

Kurosawa, R. and M. M. Romanova (2012). "Line formation in the inner winds of classical T Tauri stars: testing the conical-shell wind solution". In: *Monthly Notices of the Royal Astronomical Society* 426.4, pp. 2901–2916. DOI: 10.1111/j.1365-2966.2012.21853.x. arXiv: 1203.5154 [astro-ph.SR].

Kwan, J. and E. Tademaru (1988). "Jets from T Tauri Stars: Spectroscopic Evidence and Collimation Mechanism". In: *The Astrophysical Journal Letters* 332, p. L41. DOI: 10.1086/185262.

— (1995). "Disk Winds from T Tauri Stars". In: *The Astrophysical Journal* 454, p. 382. DOI: 10.1086/176489.

Labdon, A. et al. (2019). "Dusty disk winds at the sublimation rim of the highly inclined, low mass young stellar object SU Aurigae". In: *Astronomy and Astrophysics* 627, A36.

Lada, C. J. (1976). "Detailed observations of the M17 molecular cloud complex." In: *Astrophysical Journal, Suppl. Ser., Vol. 32, p. 603-629* 32, pp. 603–629.

— (1987). "Star formation: from OB associations to protostars". In: *Symposium-International astronomical union*. Vol. 115. Cambridge University Press, pp. 1–18.

Larson, R. B. (1969). "Numerical calculations of the dynamics of a collapsing proto-star". In: *Monthly Notices of the Royal Astronomical Society* 145.3, pp. 271–295.

— (1981). "Turbulence and star formation in molecular clouds". In: *Monthly Notices of the Royal Astronomical Society* 194.4, pp. 809–826.

Launhardt, R. et al. (2009). "Rotating molecular outflows: the young T Tauri star in CB 26". In: *Astronomy and Astrophysics* 494.1, pp. 147–156. DOI: 10.1051/0004-6361:200810835. arXiv: 0811.3910 [astro-ph].

Launhardt, R. et al. (2023). "A resolved rotating disk wind from a young T Tauri star in the Bok globule CB 26". In: *Astronomy and Astrophysics* 678, A135, A135. DOI: 10.1051/0004-6361/202347483. arXiv: 2309.01629 [astro-ph.SR].

Lavalley-Fouquet, C., S. Cabrit, and C. Dougados (2000). "DG Tau: A shocking jet". In: *Astronomy and Astrophysics, v. 356, p. L41-L44 (2000)* 356, pp. L41–L44.

Lee, C. F. (2020). "Molecular jets from low-mass young protostellar objects". In: *The Astronomy and Astrophysics Review* 28.1, p. 1.

Lee, C. F. et al. (2000). "CO Outflows from Young Stars: Confronting the Jet and Wind Models". In: *The Astrophysical Journal* 542.2, pp. 925–945. DOI: 10.1086/317056.

Lee, C. F. et al. (2017). "A rotating protostellar jet launched from the innermost disk of HH 212". In: *Nature Astronomy* 1.7, p. 0152.

Lee, C. F. et al. (2018). "ALMA observations of the very young Class 0 protostellar system HH211-mms: A 30 au dusty disk with a disk wind traced by SO?" In: *The Astrophysical Journal* 863.1, p. 94.

Lee, C. F. et al. (2021). "First Detection of Interaction between a Magnetic Disk Wind and an Episodic Jet in a Protostellar System". In: *The Astrophysical Journal Letters* 907.2, L41, p. L41. DOI: 10.3847/2041-8213/abda38. arXiv: 2101.03293 [astro-ph.GA].

Lesur, G. (2021). "Magnetohydrodynamics of protoplanetary discs". In: *Journal of Plasma Physics* 87.1, 205870101, p. 205870101. DOI: 10.1017/S0022377820-001002. arXiv: 2007.15967 [astro-ph.SR].

Lesur, G. et al. (2023). "Hydro-, Magnetohydro-, and Dust-Gas Dynamics of Protoplanetary Disks". In: *Protostars and Planets VII*. Ed. by S. Inutsuka et al. Vol. 534. Astronomical Society of the Pacific Conference Series, p. 465. DOI: 10.48550/arXiv.2203.09821. arXiv: 2203.09821 [astro-ph.EP].

Li, Z. Y. and F. H. Shu (1996). "Interaction of Wide-Angle MHD Winds with Flared Disks". In: *The Astrophysical Journal* 468, p. 261. DOI: 10.1086/177688.

Littlefair, S. P. et al. (2004). "Evidence for high accretion rates in weak-line T Tauri stars?" In: *Monthly Notices of the Royal Astronomical Society* 347.3, pp. 937–941.

Lommen, D. et al. (2009). "Large grains in discs around young stars: ATCA observations of WW Chamaeleontis, RU Lupi, and CS Chamaeleontis". In: *Astronomy and Astrophysics* 495.3, pp. 869–879.

López-Vázquez, J. A. et al. (2024). "Multiple Shells Driven by Disk Winds: ALMA Observations in the HH 30 Outflow". In: *The Astrophysical Journal* 962.1, 28, p. 28. DOI: 10.3847/1538-4357/ad132a. arXiv: 2312.03272 [astro-ph.SR].

Louvet, F. et al. (2016). "ALMA observations of the <ASTROBJ>Th 28</ASTROBJ> protostellar disk. A new example of counter-rotation between disk and optical jet". In: *Astronomy and Astrophysics* 596, A88, A88. DOI: 10.1051/0004-6361/201628474. arXiv: 1607.08645 [astro-ph.SR].

Louvet, F. et al. (2018). "The HH30 edge-on T Tauri star. A rotating and precessing monopolar outflow scrutinized by ALMA". In: *Astronomy and Astrophysics* 618, A120, A120. DOI: 10.1051/0004-6361/201731733. arXiv: 1808.03285 [astro-ph.GA].

Manara, C. F. et al. (2013). "X-shooter spectroscopy of young stellar objects. II. Impact of chromospheric emission on accretion rate estimates". In: *Astronomy and Astrophysics* 551, A107, A107. DOI: 10.1051/0004-6361/201220921. arXiv: 1301.3058 [astro-ph.GA].

Manara, C. F. et al. (2016). "X-Shooter study of accretion in Chamaeleon I". In: *Astronomy and Astrophysics* 585, A136.

Manara, C. F. et al. (2017). "An extensive VLT/X-shooter library of photospheric templates of pre-main sequence stars". In: *Astronomy and Astrophysics* 605, A86, A86. DOI: 10.1051/0004-6361/201730807. arXiv: 1705.10075 [astro-ph.SR].

Manara, C. F. et al. (2023). "Demographics of Young Stars and their Protoplanetary Disks: Lessons Learned on Disk Evolution and its Connection to Planet Formation". In: *Protostars and Planets VII*. Ed. by S. Inutsuka et al. Vol. 534. Astronomical Society of the Pacific Conference Series, p. 539. DOI: 10.48550/arXiv.2203.09930. arXiv: 2203.09930 [astro-ph.SR].

Marconi, A. et al. (2003). "Is There Really a Black Hole at the Center of NGC 4041? Constraints from Gas Kinematics". In: *The Astrophysical Journal* 586.2, pp. 868–890. DOI: 10.1086/367764. arXiv: astro-ph/0211650 [astro-ph].

Marsh, K. A. et al. (2016). "A census of dense cores in the Taurus L1495 cloud from the Herschel Gould Belt Survey". In: *Monthly Notices of the Royal Astronomical Society* 459.1, pp. 342–356.

Martel, É. and G. Lesur (2022). "Magnetised winds in transition discs-I. 2.5 D global simulations". In: *Astronomy and Astrophysics* 667, A17.

Matsushita, Y. et al. (2021). "Super-fast Rotation in the OMC 2/FIR 6b Jet". In: *The Astrophysical Journal* 916.1, p. 23.

Matt, S. P. and R. E. Pudritz (2005). "Accretion-powered stellar winds as a solution to the stellar angular momentum problem". In: *The Astrophysical Journal* 632.2, p. L135.

Matt, S. P. et al. (2012). "Spin evolution of accreting young stars. II. Effect of accretion-powered stellar winds". In: *The Astrophysical Journal* 745.1, p. 101.

Maucó, K. et al. (2018). "Herschel PACS Observations of 4–10 Myr Old Classical T Tauri Stars in Orion OB1". In: *The Astrophysical Journal* 859.1, p. 1.

Maurri, L. et al. (2014). "Physical properties of the jet from DG Tauri on subarcsecond scales with HST/STIS". In: *Astronomy and Astrophysics* 565, A110, A110. DOI: 10.1051/0004-6361/201117510. arXiv: 1401.0483 [astro-ph.SR].

McGinnis, P. et al. (2018). "Ejection processes in the young open cluster NGC 2264-A study of the [OI] $\lambda$6300Å emission line". In: *Astronomy and Astrophysics* 620, A87.

Menezes, R. B., J. E. Steiner, and T. V. Ricci (2014). "A treatment procedure for Gemini North/NIFS data cubes: application to NGC 4151". In: *Monthly Notices of the Royal Astronomical Society* 438.3, pp. 2597–2620.

Mestel, L. (1966). "The magnetic field of a contracting gas cloud. I,Strict flux-freezing". In: *Monthly Notices of the Royal Astronomical Society* 133, p. 265. DOI: 10.1093/mnras/133.2.265.

Micono, M. et al. (1998). "Proper motions and variability of the H2 emission in the HH 46/47 system". In: *The Astrophysical Journal* 494.2, p. L227.

Miotello, A. et al. (2023). "Setting the Stage for Planet Formation: Measurements and Implications of the Fundamental Disk Properties". In: *Astronomical Society of the Pacific Conference Series*. Vol. 534, p. 501.

Morbidelli, A. and S. N. Raymond (2016). "Challenges in planet formation". In: *Journal of Geophysical Research: Planets* 121.10, pp. 1962–1980.

Murphy, A. et al. (2021). "A MUSE spectro-imaging study of the Th 28 jet: Precession in the inner jet". In: *Astronomy and Astrophysics* 652, A119, A119. DOI: 10.1051/0004-6361/202141315. arXiv: 2107.08065 [astro-ph.SR].

Muzerolle, J., N. Calvet, and L. Hartmann (1998). "Magnetospheric accretion models for the hydrogen emission lines of T Tauri stars". In: *The Astrophysical Journal* 492.2, p. 743.

Muzerolle, J. et al. (2003). "Accretion in young stellar/substellar objects". In: *The Astrophysical Journal* 592.1, p. 266.

Muzerolle, J. et al. (2005). "Measuring accretion in young substellar objects: approaching the planetary mass regime". In: *The Astrophysical Journal* 625.2, p. 906.

Najita, J. R. and E. A. Bergin (2018). "Protoplanetary disk sizes and angular momentum transport". In: *The Astrophysical Journal* 864.2, p. 168.

Natta, A. et al. (2004). "Accretion in brown dwarfs: An infrared view". In: *Astronomy and Astrophysics* 424.2, pp. 603–612.

Natta, A. et al. (2014). "X-shooter spectroscopy of young stellar objects-V. Slow winds in T Tauri stars". In: *Astronomy and Astrophysics* 569, A5.

Nelissen, M. et al. (2023). "Correlation between the optical veiling and accretion properties-A case study of the classical T Tauri star DK Tau". In: *Astronomy and Astrophysics* 677, A64.

Nelson, R. P., O. Gressel, and O. M. Umurhan (2013). "Linear and non-linear evolution of the vertical shear instability in accretion discs". In: *Monthly Notices of the Royal Astronomical Society* 435.3, pp. 2610–2632.

Nisini, B. et al. (2002). "1-2.5 mu m spectra of jets from young stars: Strong Fe II emission in HH111, HH240-241 and HH120". In: *Astronomy and Astrophysics* 393, pp. 1035–1051. DOI: 10.1051/0004-6361:20021062.

Nisini, B. et al. (2015). "[OI] 63 $\mu$m jets in class 0 sources detected by Herschel". In: *The Astrophysical Journal* 801.2, p. 121.

Nisini, B. et al. (2018). "Connection between jets, winds and accretion in T Tauri stars. The X-shooter view". In: *Astronomy and Astrophysics* 609, A87, A87. DOI: 10.1051/0004-6361/201730834. arXiv: 1710.05587 [astro-ph.SR].

Nisini, B. et al. (2024). "GIARPS High-resolution Observations of T Tauri stars (GHOsT). V. New insights into disk winds from 3 km $s^{-1}$ resolution spectroscopy". In: *Astronomy and Astrophysics* 683, A116, A116. DOI: 10.1051/0004-6361/202346742. arXiv: 2312.10777 [astro-ph.SR].

Nisini, B. et al. (2024). "PROJECT-J: JWST Observations of HH46 IRS and Its Outflow. Overview and First Results". In: *The Astrophysical Journal* 967.2, p. 168.

Nisini, Brunella et al. (2005). "A combined optical/infrared spectral diagnostic analysis of the HH1 jet". In: *Astronomy & Astrophysics* 441.1, pp. 159–170.

Noll, S. et al. (2012). "An atmospheric radiation model for Cerro Paranal. I. The optical spectral range". In: *Astronomy and Astrophysics* 543, A92, A92. DOI: 10.1051/0004-6361/201219040. arXiv: 1205.2003 [astro-ph.IM].

Noriega-Crespo, A. et al. (2004). "A New Look at Stellar Outflows: Spitzer Observations of the HH 46/47 System". In: *The Astrophysical Journal Supplement* 154.1, pp. 352–358. DOI: 10.1086/422819.

Offner, S. S. R. et al. (2011). "Radiation-hydrodynamic Simulations of Protostellar Outflows: synthetic observations and data comparisons". In: *The Astrophysical Journal* 743.1, p. 91.

Ogihara, M., A. Morbidelli, and T. Guillot (2015). "Suppression of type I migration by disk winds". In: *Astronomy and Astrophysics* 584, L1, p. L1. DOI: 10.1051/0004-6361/201527117. arXiv: 1510.06010 [astro-ph.EP].

Osterbrock, D.E. and G.J. Ferland (2006). *Astrophysics Of Gas Nebulae and Active Galactic Nuclei*. University Science Books. ISBN: 9781891389344.

Ostriker, E. C. and F. H. Shu (1995). "Magnetocentrifugally driven flows from young stars and disks. IV. The accretion funnel and dead zone". In: *Astrophysical Journal v. 447, p. 813* 447, p. 813.

Palma-Bifani, P. et al. (2023). "Peering into the young planetary system AB Pic. Atmosphere, orbit, obliquity, and second planetary candidate". In: *Astronomy and Astrophysics* 670, A90, A90. DOI: 10.1051/0004-6361/202244294. arXiv: 2211.01474 [astro-ph.EP].

Palmeirim, P. et al. (2013). "Herschel view of the Taurus B211/3 filament and striations: evidence of filamentary growth?" In: *Astronomy and Astrophysics* 550, A38.

Panoglou, D. et al. (2012). "Molecule survival in magnetized protostellar disk winds. I. Chemical model and first results". In: *Astronomy and Astrophysics* 538, A2, A2. DOI: 10.1051/0004-6361/200912861. arXiv: 1112.3248 [astro-ph.SR].

Pascucci, I. et al. (2020). "The Evolution of Disk Winds from a Combined Study of Optical and Infrared Forbidden Lines". In: *The Astrophysical Journal* 903.2, 78, p. 78. DOI: 10.3847/1538-4357/abba3c. arXiv: 2009.09114 [astro-ph.SR].

Pascucci, I. et al. (2023). "The Role of Disk Winds in the Evolution and Dispersal of Protoplanetary Disks". In: *Protostars and Planets VII*. Ed. by S. Inutsuka et al. Vol. 534. Astronomical Society of the Pacific Conference Series, p. 567. DOI: 10.48550/arXiv.2203.10068. arXiv: 2203.10068 [astro-ph.EP].

Pascucci, I. et al. (2024). "The nested morphology of disk winds from young stars revealed by JWST/NIRSpec observations". In: *Nature Astronomy*, pp. 1–9.

Pattle, K. et al. (2023). "Magnetic Fields in Star Formation: from Clouds to Cores". In: *Protostars and Planets VII*. Ed. by S. Inutsuka et al. Vol. 534. Astronomical Society of the Pacific Conference Series, p. 193. DOI: 10.48550/arXiv.2203.11179. arXiv: 2203.11179 [astro-ph.GA].

Pedregosa, F. et al. (2011). "Scikit-learn: Machine learning in Python". In: *the Journal of machine Learning research* 12, pp. 2825–2830.

Pelletier, G. and R. E. Pudritz (1992). "Hydromagnetic disk winds in young stellar objects and active galactic nuclei". In: *Astrophysical Journal, Part 1 (ISSN 0004-637X), vol. 394, no. 1, July 20, 1992, p. 117-138. Research supported by NATO and NSERC.* 394, pp. 117–138.

Perraut, K. et al. (2021). "The GRAVITY young stellar object survey-VII. The inner dusty disks of T Tauri stars". In: *Astronomy and Astrophysics* 655, A73.

Persson, M. V. (2014a). "Current view of protostellar evolution". In: DOI: 10.6084/m9.figshare.654555.v7. URL: https://figshare.com/articles/figure/Current_view_of_protostellar_evolution/654555.

— (2014b). "SEDs of the different protostellar evolutionary stages". In: DOI: 10.6084/m9.figshare.1121574.v2. URL: https://figshare.com/articles/figure/SEDs_of_the_different_protostellar_evolutionary_stages/1121574.

Petrus, S. et al. (2021). "Medium-resolution spectrum of the exoplanet HIP 65426 b". In: *Astronomy and Astrophysics* 648, A59, A59. DOI: 10.1051/0004-6361/202038914. arXiv: 2012.02798 [astro-ph.EP].

Picogna, G. et al. (2019). "The dispersal of protoplanetary discs–I. A new generation of X-ray photoevaporation models". In: *Monthly Notices of the Royal Astronomical Society* 487.1, pp. 691–701.

Pineda, J. E. et al. (2023). "From Bubbles and Filaments to Cores and Disks: Gas Gathering and Growth of Structure Leading to the Formation of Stellar Systems". In: *Protostars and Planets VII*. Ed. by S. Inutsuka et al. Vol. 534. Astronomical Society of the Pacific Conference Series, p. 233. DOI: 10.48550/arXiv.2205.03935. arXiv: 2205.03935 [astro-ph.GA].

Planck, Max (1901). "On the law of distribution of energy in the normal spectrum". In: *Annalen der physik* 4.553, p. 1.

Podio, L. et al. (2008). "Tracing the origins of permitted emission lines in RU Lupi down to AU scales". In: *Astronomy and Astrophysics* 480.2, pp. 421–430.

Podio, L. et al. (2016). "First image of the L1157 molecular jet by the CALYPSO IRAM-PdBI survey". In: *Astronomy and Astrophysics* 593, p. L4.

Pontoppidan, K. M., G. A. Blake, and A. Smette (2011). "The Structure and Dynamics of Molecular Gas in Planet-forming Zones: A CRIRES Spectro-astrometric Survey". In: *The Astrophysical Journal* 733.2, 84, p. 84. DOI: 10.1088/0004-637X/733/2/84. arXiv: 1103.3000 [astro-ph.EP].

Priest, E. and T. Forbes (2000). *Magnetic Reconnection: MHD Theory and Applications*. Cambridge Universiy Press. DOI: 10.1017/CBO9780511525087.

Pudritz, R. E. and C. A. Norman (1983). "Centrifugally driven winds from contracting molecular disks". In: *The Astrophysical Journal* 274, pp. 677–697. DOI: 10.1086/161481.

Pudritz, R. E. and T. P. Ray (2019). "The Role of Magnetic Fields in Protostellar Outflows and Star Formation". In: *Frontiers in Astronomy and Space Sciences* 6, 54, p. 54. DOI: 10.3389/fspas.2019.00054. arXiv: 1912.05605 [astro-ph.SR].

Pudritz, R. E. et al. (2007). "Disk Winds, Jets, and Outflows: Theoretical and Computational Foundations". In: *Protostars and Planets V*. Ed. by Bo Reipurth, David Jewitt, and Klaus Keil, p. 277. DOI: 10.48550/arXiv.astro-ph/0603592. arXiv: astro-ph/0603592 [astro-ph].

Rab, C. et al. (2022). "Interpreting molecular hydrogen and atomic oxygen line emission of T Tauri disks with photoevaporative disk-wind models". In: *Astronomy and Astrophysics* 668, A154.

Rab, C. et al. (2023). "High-resolution [O I] Line Spectral Mapping of TW Hya Consistent with X-Ray-driven Photoevaporation". In: *The Astrophysical Journal Letters* 955.1, L11, p. L11. DOI: 10.3847/2041-8213/acf574. arXiv: 2309.01832 [astro-ph.EP].

Rabenanahary, M. et al. (2022). "Wide-angle protostellar outflows driven by narrow jets in stratified cores". In: *Astronomy and Astrophysics* 664, A118, A118. DOI: 10.1051/0004-6361/202243139. arXiv: 2204.05850 [astro-ph.SR].

Raga, A. C., P. F. Velázquez, and A. Noriega-Crespo (2018). "Is HH 47 Slowing down?" In: *Revista mexicana de astronomía y astrofísica* 54.1, pp. 0–0.

Raga, A. C. et al. (2004). "Models for the Infrared Cavity of HH 46/47". In: *The Astrophysical Journal Supplement Series* 154.1, p. 346.

Rankine, William John Macquorn (1870). "XV. On the thermodynamic theory of waves of finite longitudinal disturbance". In: *Philosophical Transactions of the Royal Society of London* 160, pp. 277–288.

Ray, T. P. (2007). "The First Three Million Years". In: *Jets from Young Stars: Models and Constraints*. Ed. by Jonathan Ferreira, Catherine Dougados, and Emma Whelan. Berlin, Heidelberg: Springer Berlin Heidelberg, pp. 3–19. ISBN: 978-3-540-68035-2. DOI: 10.1007/978-3-540-68035-2_1. URL: https://doi.org/10.1007/978-3-540-68035-2_1.

Ray, T. P. and J. Ferreira (2021). "Jets from young stars". In: *New Astronomy Review* 93, 101615, p. 101615. DOI: 10.1016/j.newar.2021.101615. arXiv: 2009.00547 [astro-ph.SR].

Ray, T. P. et al. (2007). "Toward Resolving the Outflow Engine: An Observational Perspective". In: *Protostars and Planets V*. Ed. by Bo Reipurth, David Jewitt, and Klaus Keil, p. 231. DOI: 10.48550/arXiv.astro-ph/0605597. arXiv: astro-ph/0605597 [astro-ph].

Ray, T. P. et al. (2023). "Outflows from the youngest stars are mostly molecular". In: *Nature* 622.7981, pp. 48–52.

Redaelli, E. et al. (2019). "Magnetic properties of the protostellar core IRAS 15398-3359". In: *Astronomy and Astrophysics* 631, A154, A154. DOI: 10.1051/0004-6361/201936271. arXiv: 1910.05573 [astro-ph.SR].

Reipurth, B. and J. Bally (2001). "Herbig-Haro Flows: Probes of Early Stellar Evolution". In: *Annual Review of Astronomy and Astrophysics* 39, pp. 403–455. DOI: 10.1146/annurev.astro.39.1.403.

Reipurth, B. and S. Heathcote (1991). "The jet and energy source of HH 46/47." In: *Astronomy and Astrophysics* 246, p. 511.

Reipurth, B. et al. (2000). "Hubble Space Telescope NICMOS Images of Herbig-Haro Energy Sources: [Fe II] Jets, Binarity, and Envelope Cavities". In: *The Astronomical Journal* 120.3, pp. 1449–1466. DOI: 10.1086/301510.

Rice, W. K. M., G. Lodato, and P. J. Armitage (2005). "Investigating fragmentation conditions in self-gravitating accretion discs". In: *Monthly Notices of the Royal Astronomical Society: Letters* 364.1, pp. L56–L60.

Richer, J. S. et al. (2000). "Molecular Outflows from Young Stellar Objects". In: *Protostars and Planets IV*. Ed. by V. Mannings, A. P. Boss, and S. S. Russell, p. 867. DOI: 10.48550/arXiv.astro-ph/9904097. arXiv: astro-ph/9904097 [astro-ph].

Rigliaco, E. et al. (2012). "X-shooter spectroscopy of young stellar objects-I. Mass accretion rates of low-mass T Tauri stars in $\sigma$ Orionis". In: *Astronomy and Astrophysics* 548, A56.

Rigliaco, E. et al. (2013). "Understanding the Origin of the [O I] Low-velocity Component from T Tauri Stars". In: *The Astrophysical Journal* 772.1, p. 60.

Robinson, C. E. and Catherine C. Espaillat (2019). "Multiepoch Ultraviolet HST Observations of Accreting Low-mass Stars". In: *The Astrophysical Journal* 874.2, 129, p. 129. DOI: 10.3847/1538-4357/ab0d8d. arXiv: 1903.01987 [astro-ph.SR].

Robrade, J. and JHMM Schmitt (2007). "X-rays from RU Lupi: accretion and winds in classical T Tauri stars". In: *Astronomy & Astrophysics* 473.1, pp. 229–238.

Rousselot, P. et al. (2000). "Night-sky spectral atlas of OH emission lines in the near-infrared". In: *Astronomy and Astrophysics, v. 354, p. 1134-1150 (2000)* 354, pp. 1134–1150.

Saigo, K., K. Tomisaka, and T. Matsumoto (2008). "Evolution of first cores and formation of stellar cores in rotating molecular cloud cores". In: *The Astrophysical Journal* 674.2, p. 997.

Sanchis, E. et al. (2021). "Measuring the ratio of the gas and dust emission radii of protoplanetary disks in the Lupus star-forming region". In: *Astronomy and Astrophysics* 649, A19, A19. DOI: 10.1051/0004-6361/202039733. arXiv: 2101.11307 [astro-ph.EP].

Sauty, C., E. Trussoni, and K. Tsinganos (2002). "Nonradial and nonpolytropic astrophysical outflows-V. Acceleration and collimation of self-similar winds". In: *Astronomy and Astrophysics* 389.3, pp. 1068–1085.

Sauty, C. and K. Tsinganos (1994). "Nonradial and nonpolytropic astrophysical outflows III. A criterion for the transition from jets to winds". In: *Astronomy and Astrophysics, Vol. 287, p. 893-926 (1994)* 287, pp. 893–926.

Scholz, A., J. Eislöffel, and R. Mundt (2009). "Long-term monitoring in IC4665: fast rotation and weak variability in very low mass objects". In: *Monthly Notices of the Royal Astronomical Society* 400.3, pp. 1548–1562.

Schwartz, R. D. (1977). "Evidence of star formation triggered by expansion of the Gum Nebula." In: *Astrophysical Journal, Lett., Vol. 212, p. L25-L26* 212, pp. L25–L26.

Schwartz, R. D. (1983). "Ultraviolet continuum and H2 fluorescent emission in Herbig-Haro objects 43 and 47." In: *The Astrophysical Journal Letters* 268, pp. L37–L40. DOI: 10.1086/184025.

Schwartz, R. D., B. F. Jones, and M. Sirk (1984). "Proper motions of Herbig-Haro objects. V-Southern HH objects". In: *Astronomical Journal (ISSN 0004-6256), vol. 89, Nov. 1984, p. 1735-1739.* 89, pp. 1735–1739.

Scoville, NZ et al. (1987). "Molecular clouds and cloud cores in the inner Galaxy". In: *Astrophysical Journal Supplement Series (ISSN 0067-0049), vol. 63, April 1987, p. 821-915. NASA-supported research.* 63, pp. 821–915.

Shang, H. et al. (2020). "A Unified Model for Bipolar Outflows from Young Stars: The Interplay of Magnetized Wide-angle Winds and Isothermal Toroids". In: *The Astrophysical Journal* 905.2, 116, p. 116. DOI: 10.3847/1538-4357/abbdb0.

Shu, F. H., F. C. Adams, and S. Lizano (1987). "Star formation in molecular clouds: observation and theory." In: *Annual Review of Astronomy and Astrophysics* 25, pp. 23–81. DOI: 10.1146/annurev.aa.25.090187.000323.

Shu, F. H. et al. (1994). "Magnetocentrifugally driven flows from young stars and disks. 1: A generalized model". In: *The Astrophysical Journal, vol. 429, no. 2, pt. 1, p. 781-796* 429, pp. 781–796.

Shu, F. H. et al. (2000). "X-Winds Theory and Observations". In: *Protostars and Planets IV*. Ed. by V. Mannings, A. P. Boss, and S. S. Russell, pp. 789–814.

Shull, J. M. and C. F. McKee (1979). "Theoretical models of interstellar shocks. I-Radiative transfer and UV precursors". In: *Astrophysical Journal, Part 1, vol. 227, Jan. 1, 1979, p. 131-149.* 227, pp. 131–149.

Simon, M. N. et al. (2016). "Tracing Slow Winds from T Tauri Stars via Low-velocity Forbidden Line Emission". In: *The Astrophysical Journal* 831.2, 169, p. 169. DOI: 10.3847/0004-637X/831/2/169. arXiv: 1608.06992 [astro-ph.SR].

Skrutskie, M. F. et al. (2006). "The Two Micron All Sky Survey (2MASS)". In: *The Astronomical Journal* 131.2, pp. 1163–1183. DOI: 10.1086/498708.

Soker, N., J. Bublitz, and J. H. Kastner (2022). "A Twin-jet Structure Rather than Jet Rotation in the Young Stellar Object OMC 2/FIR 6b". In: *The Astrophysical Journal* 928.2, 159, p. 159. DOI: 10.3847/1538-4357/ac5827. arXiv: 2108.01303 [astro-ph.SR].

Staff, J. E. et al. (2015). "Hubble Space Telescope scale 3D simulations of MHD disc winds: a rotating two-component jet structure". In: *Monthly Notices of the Royal Astronomical Society* 446.4, pp. 3975–3991.

Stanke, T., M. J. McCaughrean, and H. Zinnecker (1999). "HH 46/47: Also a parsec scale flow". In: *Astronomy and Astrophysics* 350, pp. L43–L46. DOI: 10.48550/arXiv.astro-ph/9909357. arXiv: astro-ph/9909357 [astro-ph].

Sternberg, Amiel et al. (2014). "H i-to-H2 transitions and H i column densities in galaxy star-forming regions". In: *The Astrophysical Journal* 790.1, p. 10.

Stock, C. et al. (2022). "Accretion variability in RU Lup". In: *Astronomy and Astrophysics* 668, A94.

Strom, Karen M. et al. (1989). "Circumstellar Material Associated with Solar-Type Pre-Main-Sequence Stars: A Possible Constraint on the Timescale for Planet Building". In: *The Astronomical Journal* 97, p. 1451. DOI: 10.1086/115085.

Strom, S. E. (1972). "Optical and infrared observations of young stellar objects–an informal review". In: *Publications of the Astronomical Society of the Pacific* 84.502, pp. 745–756.

Suzuki, T. K. and S. Inutsuka (2009). "Disk winds driven by magnetorotational instability and dispersal of protoplanetary disks". In: *The Astrophysical Journal* 691.1, p. L49.

Symington, N. H. et al. (2005). "T Tauri stellar magnetic fields: He I measurements". In: *Monthly Notices of the Royal Astronomical Society* 358.3, pp. 977–984.

Tabone, B. et al. (2017). "ALMA discovery of a rotating $SO/SO_2$ flow in HH212. A possible MHD disk wind?" In: *Astronomy and Astrophysics* 607, L6, p. L6. DOI: 10.1051/0004-6361/201731691. arXiv: 1710.01401 [astro-ph.SR].

Tabone, B. et al. (2020). "Constraining MHD disk winds with ALMA-Apparent rotation signatures and application to HH212". In: *Astronomy and Astrophysics* 640, A82.

Tacconi, L. J., R. Genzel, and A. Sternberg (2020). "The evolution of the star-forming interstellar medium across cosmic time". In: *Annual Review of Astronomy and Astrophysics* 58.1, pp. 157–203.

Takami, M. et al. (2001). "Circumstellar structure of RU Lupi down to au scales". In: *Monthly Notices of the Royal Astronomical Society* 323.1, pp. 177–187. DOI: 10.1046/j.1365-8711.2001.04172.x. arXiv: astro-ph/0103311 [astro-ph].

Tscharnuter, W. M. (1987). "A collapse model of the turbulent presolar nebula". In: *Astronomy and Astrophysics (ISSN 0004-6361), vol. 188, no. 1, Dec. 1987, p. 55-73.* 188, pp. 55–73.

Tsukamoto, Y. et al. (2023). "The Role of Magnetic Fields in the Formation of Protostars, Disks, and Outflows". In: *Protostars and Planets VII*. Ed. by S. Inutsuka et al. Vol. 534. Astronomical Society of the Pacific Conference Series, p. 317.

Turner, N. J. et al. (2014). "Transport and accretion in planet-forming disks". In: *Protostars and Planets VI* 411, p. 411.

Uchida, Y. and K. Shibata (1985). "Magnetodynamical acceleration of CO and optical bipolar flows from the region of star formation". In: *Astronomical Society of Japan, Publications (ISSN 0004-6264), vol. 37, no. 3, 1985, p. 515-535. Sponsorship: Ministry of Education, Science, and Culture of Japan.* 37, pp. 515–535.

van der Marel, N. (2023). "Transition disks: the observational revolution from SEDs to imaging". In: *The European Physical Journal Plus* 138.3, p. 225.

van Kempen, T. A. et al. (2009). "APEX-CHAMP$^+$ high-J CO observations of low-mass young stellar objects. I. The HH 46 envelope and outflow". In:

*Astronomy and Astrophysics* 501.2, pp. 633–646. DOI: 10.1051/0004-6361/200912013. arXiv: 0905.2878 [astro-ph.SR].

van't Hoff, M. L. R. et al. (2023). "Early Planet Formation in Embedded Disks (eDisk). III. A First High-resolution View of Submillimeter Continuum and Molecular Line Emission toward the Class 0 Protostar L1527 IRS". In: *The Astrophysical Journal* 951.1, p. 10.

Vázquez-Semadeni, E. et al. (2019). "Global hierarchical collapse in molecular clouds. Towards a comprehensive scenario". In: *Monthly Notices of the Royal Astronomical Society* 490.3, pp. 3061–3097.

Venuti, L. et al. (2014). "Mapping accretion and its variability in the young open cluster NGC 2264: a study based on u-band photometry". In: *Astronomy and Astrophysics* 570, A82.

Virtanen, P. et al. (2020). "SciPy 1.0: Fundamental Algorithms for Scientific Computing in Python". In: *Nature Methods* 17, pp. 261–272. DOI: 10.1038/s41592-019-0686-2.

Wang, L., X. N. Bai, and J. J. Goodman (2019). "Global simulations of protoplanetary disk outflows with coupled non-ideal magnetohydrodynamics and consistent thermochemistry". In: *The Astrophysical Journal* 874.1, p. 90.

Wang, L. and J. J. Goodman (2017). "Wind-driven accretion in transitional protostellar disks". In: *The Astrophysical Journal* 835.1, p. 59.

Waters, L. B. F. M. and C. Waelkens (1998). "Herbig ae/be stars". In: *Annual Review of Astronomy and Astrophysics* 36.1, pp. 233–266.

Weilbacher, P. M. et al. (2020). "The data processing pipeline for the MUSE instrument". In: *Astronomy and Astrophysics* 641, A28.

Wendeborn, J. et al. (2024). "A Multiwavelength, Multiepoch Monitoring Campaign of Accretion Variability in T Tauri Stars from the ODYSSEUS Survey. III. Optical Spectra". In: *The Astrophysical Journal* 972.1, p. 100.

Whelan, E. T. and P. Garcia (2008). "Spectro-astrometry: the method, its limitations, and applications". In: *Jets from Young Stars II: Clues from High Angular Resolution Observations*, pp. 123–149.

Whelan, E. T., A. Murphy, and I. Pascucci (2023). "Optical Forbidden Emission Line Spectro-astrometry of T CrA: Evidence for a Multiple System and Multiple Jets". In: *The Astrophysical Journal* 951.1, 1, p. 1. DOI: 10.3847/1538-4357/acd542. arXiv: 2305.15537 [astro-ph.SR].

Whelan, E. T. et al. (2010). "The 2008 Outburst in the Young Stellar System Z CMa: The First Detection of Twin Jets". In: *The Astrophysical Journal Letters*

720.1, pp. L119–L124. DOI: 10.1088/2041-8205/720/1/L119. arXiv: 1008.0111 [astro-ph.SR].

Whelan, E. T. et al. (2021). "Evidence for an MHD Disk Wind via Optical Forbidden Line Spectroastrometry". In: *The Astrophysical Journal* 913.1, 43, p. 43. DOI: 10.3847/1538-4357/abf55e. arXiv: 2104.05561 [astro-ph.SR].

Whitney, B. A. et al. (2003). "Two-dimensional Radiative Transfer in Protostellar Envelopes. II. An Evolutionary Sequence". In: *The Astrophysical Journal* 598.2, pp. 1079–1099. DOI: 10.1086/379068. arXiv: astro-ph/0309007 [astro-ph].

Wichittanakom, C. et al. (2020). "The accretion rates and mechanisms of Herbig Ae/Be stars". In: *Monthly Notices of the Royal Astronomical Society* 493.1, pp. 234–249. DOI: 10.1093/mnras/staa169. arXiv: 2001.05971 [astro-ph.SR].

Wilking, B. A. et al. (1990). "Shocked Molecular Hydrogen Emission from Herbig-Haro Objects and Their Exciting Stars". In: *The Astronomical Journal* 99, p. 344. DOI: 10.1086/115333.

Wilson, C. D. and N. Scoville (1990). "The properties of individual giant molecular clouds in M33". In: *Astrophysical Journal, Part 1 (ISSN 0004-637X), vol. 363, Nov. 10, 1990, p. 435-450.* 363, pp. 435–450.

Winter, A. J. et al. (2024). "Spatially correlated stellar accretion in the Lupus star-forming region-Evidence for ongoing infall from the interstellar medium". In: *Astronomy and Astrophysics* 691, A169.

Woitas, J. et al. (2005). "Jet rotation: Launching region, angular momentum balance and magnetic properties in the bipolar outflow from RW Aur". In: *Astronomy and Astrophysics* 432.1, pp. 149–160.

Wood, D. O. S. and E. Churchwell (1989). "The Morphologies and Physical Properties of Ultracompact H II Regions". In: *The Astrophysical Journal Supplement* 69, p. 831. DOI: 10.1086/191329.

Xu, W. and P. J. Armitage (2023). "Revisiting collisional dust growth in class 0/I protostellar disks: sweep-up can convert a few 10 M of dust into kilogram pebbles in 0.1 Myr". In: *The Astrophysical Journal* 946.2, p. 94.

Yang, Y. L. et al. (2022). "CORINOS. I. JWST/MIRI spectroscopy and imaging of a class 0 protostar IRAS 15398–3359". In: *The Astrophysical Journal Letters* 941.1, p. L13.

Zapata, L. A. et al. (2015). "Kinematics of the Outflow from the Young Star DG Tau B: Rotation in the Vicinities of an Optical Jet". In: *The Astrophysical Journal* 798.2, 131, p. 131. DOI: 10.1088/0004-637X/798/2/131. arXiv: 1411.0173 [astro-ph.SR].

Zeeuw, P. T. de et al. (1999). "A HIPPARCOS census of the nearby OB associations". In: *The Astronomical Journal* 117.1, p. 354.

Zhang, Qizhou et al. (2014). "Magnetic Fields and Massive Star Formation". In: 792.2, 116, p. 116. DOI: 10.1088/0004-637X/792/2/116. arXiv: 1407.3984 [astro-ph.GA].

Zhang, S. et al. (2018). "The disk substructures at high angular resolution project (DSHARP). VII. The planet–disk interactions interpretation". In: *The Astrophysical journal letters* 869.2, p. L47.

Zhang, Y. et al. (2016). "ALMA Cycle 1 Observations of the HH46/47 Molecular Outflow: Structure, Entrainment, and Core Impact". In: *The Astrophysical Journal* 832.2, 158, p. 158. DOI: 10.3847/0004-637X/832/2/158. arXiv: 1602.02388 [astro-ph.SR].

Zhang, Y. et al. (2018). "Rotation in the NGC 1333 IRAS 4C Outflow". In: *The Astrophysical Journal* 864.1, 76, p. 76. DOI: 10.3847/1538-4357/aad7ba. arXiv: 1808.00346 [astro-ph.GA].

Zhang, Y. et al. (2019). "An Episodic Wide-angle Outflow in HH 46/47". In: *The Astrophysical Journal* 883.1, 1, p. 1. DOI: 10.3847/1538-4357/ab3850. arXiv: 1908.00689 [astro-ph.GA].

Zhu, Z. and J. M. Stone (2018). "Global Evolution of an Accretion Disk with a Net Vertical Field: Coronal Accretion, Flux Transport, and Disk Winds". In: *The Astrophysical Journal* 857.1, 34, p. 34. DOI: 10.3847/1538-4357/aaafc9. arXiv: 1701.04627 [astro-ph.EP].